

ANCHAM

ANALYTICAL CHEMISTRY

NOVEMBER 1, 1995



The Nucleic Acid Ligand 663 A

In a changing world...

Burdick & Jackson
always delivers the best
in high purity solvents



*Quality and Consistency
You Can Count On.*

Burdick & Jackson, Inc. • 1953 South Harvey Street • Muskegon, MI 49442-6184 • 616.726.3171 • 800.368.0050 EST • FAX: 616.726.8226

A Subsidiary of Dade International Inc.
CIRCLE 13 ON READER SERVICE CARD

Quality you can count on!

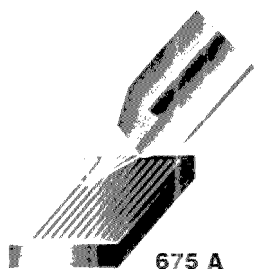
We're the Laboratory Products Association. When you buy from an LPA member company you can count on choosing from the best products & value, the broadest line of laboratory products, guaranteed delivery & service from well established & dependable companies. By purchasing from an LPA member company you tap an invaluable source of leading manufacturers & distributors serving the scientific community. Our membership is constantly growing & expanding its network of information & services; all with the goal of providing you with what you need.



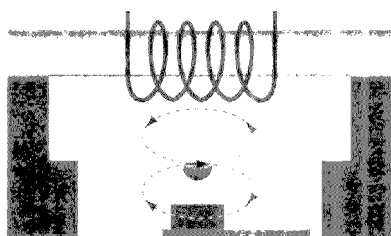
and still counting...

225 Reinekers Lane, Suite 625 • Alexandria • Virginia • 22314 • 703-836-1360 • Fax 703-836-6644

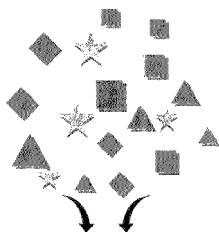
CIRCLE 6 ON READER SERVICE CARD



675 A



671 A



663 A

SFC MS

650 A

REPORT

650 A Guidelines for successful SFC/MS

Making the proper chromatographic and mass spectrometric choices can make the difference between success and failure in SFC/MS. J. David Pinkston and Thomas L. Chester of the Procter & Gamble Company consider the factors involved in planning a successful SFC/MS experiment and describe how SFC/MS can be used to determine components in industrial and consumer products.

REPORT

663 A ON THE COVER. Using nucleic acid ligands for molecular recognition

Oligonucleotide ligands can provide specific and high-affinity binding with selected target molecules. Linda B. McGown and colleagues at Duke University and the Becton Dickinson Research Center describe the chemistry of nucleic acid ligands and explore their use as reagents for chemical analysis.

ANALYTICAL CHEMISTRY

NOVEMBER 1, 1995

ANCHAM
67(21) 629 A-686 A/3829-4032 (1995)
ISSN 0003-2700

Registered in U.S. Patent and Trademark Office
©Copyright 1995 by the American Chemical Society

DEPARTMENTS

633 A In AC Research

641 A Editorial

Off-shore authors welcome. Cutting-edge analytical chemistry has no nationality, and in 1994 37% of the papers published in *Analytical Chemistry* were by non-resident authors.

643 A Analytical Currents

648 A News

Laboratory profile: Making cutting-edge technology work for day-to-day use. • FDA rekindles symposium on applied MS. • Division of Analytical Chemistry officers for 1995-96. • Nominations solicited for DAC's Findeis Award.

658 A Software

Tracking calibration records. *Calibration Manager*, a relational database package for managing calibration of analytical instrumentation, is reviewed by F. C. McElroy of Exxon Research and Engineering Company. • Software released.

660 A Books

Predicting retention in LC. *Retention and Selectivity in LC* is reviewed by C. H. Lochmüller of Duke University. • Determining drugs of abuse. *Analysis of Addictive and Misused Drugs* is reviewed by John T. Cody of Lackland Air Force Base. • Books received.

669 A Meetings

671 A Focus

MRFM. Combining magnetic resonance with atomic force microscopy results in a new technique with the potential for providing single-spin sensitivity for 3-D characterization of individual molecules in situ.

675 A Product Review

X-ray photoelectron spectroscopy. Small-area analysis, imaging, and depth-profiling capabilities have broadened the scope of research instruments for XPS. We review recent innovation and differences in instrument design for advanced techniques.

680 A New Products

An X-ray imaging module for SEM, a multi-dimensional XRF spectrometer, and a triple-quadrupole mass spectrometer are featured. • Instrumentation. • Literature. • Catalogs.

684 A Information Express

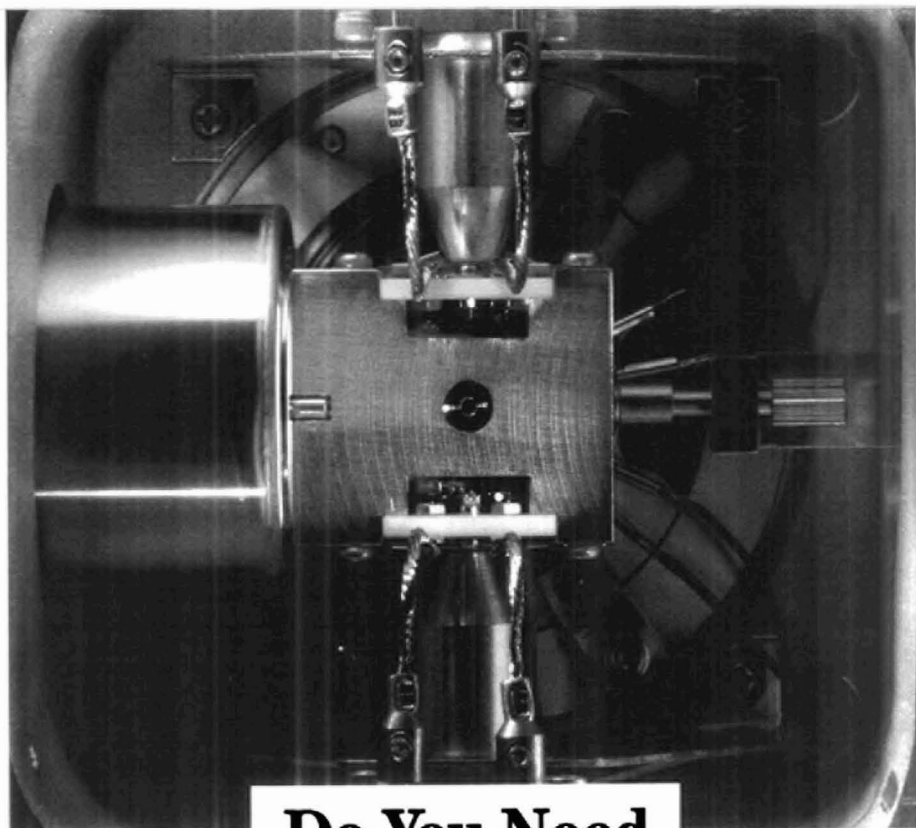
1C AC Research Contents

3829-4031 AC Research

4032 Author Index

Analytical Chemistry (ISSN 0003-2700) is published semimonthly by the American Chemical Society, 1155 Sixteenth St., N.W., Washington, DC 20036. Second-class postage paid at Washington, DC, and additional mailing offices. Postmaster: Send address changes to *Analytical Chemistry*, Member & Subscriber Services, P.O. Box 3337, Columbus, OH 43210.

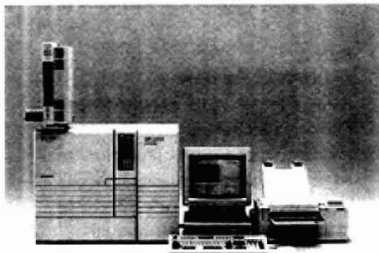
Canadian GST Reg. No. 127571347.



Do You Need A Comprehensive GC/MS Solution?

The Shimadzu GC/MS QP-5000. The new generation. Compact and complete.

Regardless of whether you work in water, air, or soil analysis, or whether you are looking for environmental analysis, additives in food, or forensics drug abuse, our new GC/MS QP-5000 is sure to exceed your expectations. Its mass spectrometer, covering the range 10 amu to 700 amu, is coupled to the proven performance of the GC-17A gas chromatograph, including AFC for setting carrier related flows and pressures. Our new GC/MS QP-5000 has been designed for the most stringent analytical methodology as well as routine analytical laboratory work. Its compactness and range



of features are truly impressive. The overall width of the GC and MS is just 72.5 cm (28.5"). All system operations are controlled by Microsoft® Windows™-based software. The GC/MS QP-5000 is a highly sensitive bench-top GC/MS with computer-simulation-optimized ion optics and fully automated vacuum control. Available options include a jet-separator interface, a high capacity turbomolecular pump, chemical-ionization, and a direct inlet system for low volatiles. Call your nearest Shimadzu Representative today for more details on the GC/MS QP-5000. You can count on a prompt response from us.

Microsoft® Windows™ is a registered trademark of Microsoft Corporation, Redmond, WA, USA.

SHIMADZU CORPORATION,
International Marketing Division
3, Kanda-Nishikicho 1-chome, Chiyoda-ku, Tokyo 101, Japan
Phone: 81(3)3219-5641 Fax: 81(3)3219-5710

SHIMADZU SCIENTIFIC INSTRUMENTS, INC.
7102 Riverwood Drive, Columbia, Maryland 21046, U.S.A.
Phone: 1(410)381-1227 Fax: 1(410)381-1222

SHIMADZU EUROPA GmbH
Phone: 49(203)7687-0 Fax: 49(203)766625 Germany.

SHIMADZU (ASIA PACIFIC) PTE LTD.
Phone: 65-778 6280 Fax: 65-779 2935 Singapore.

SHIMADZU OCEANIA PTY. LTD.
Phone: 61(2)684-4200 Fax: 61(2)684-4055 Australia.

CIRCLE 3 ON READER SERVICE CARD

**For more information, please contact us.*

 **SHIMADZU**
Solutions for Science
since 1875

Brief introductions to the research articles appearing in the November 1 issue and tentatively scheduled to appear in the November 15 issue

Accelerated Article

Measuring the more toxic PCBs by immunoassay

Most analyses of polychlorinated biphenyls (PCBs) detect the congeners most abundant in commercial formulations such as the Aroclors. However, PCBs differ in their toxicology, and determining the environmental impact by measuring the more toxic of these pollutants is generally difficult and expensive. Alexander E. Karu and colleagues at the University of California-Berkeley and ECOCHEM Research report deriving a monoclonal antibody that is the basis of highly selective enzyme immunoassays for nonortho-substituted, coplanar PCBs including the very toxic PCBs 77 and 126. ("A Monoclonal Immunoassay for the Coplanar Polychlorinated Biphenyls"; AC950675Y; p. 3829)

BIOANALYTICAL

Drug dispersion in a medicinal patch

Time-release drug delivery systems, such as skin patches, are becoming more important as peptide hormone drugs are developed to regulate growth, immune response, blood pressure, and other physiological processes. However,

the rate and efficiency of drug delivery depends on how the drug is distributed in the polymer matrix of the carrier. R. W. Odom and colleagues at the University of California-San Francisco, Charles Evans & Associates, and Abbott Laboratories analyze the distribution of a peptide hormone in a skin patch using TOF-SIMS and X-ray photoelectron spectroscopy. ("XPS and TOF-SIMS Microanalysis of a Peptide/Polymer Drug Delivery Device"; AC950439N; p. 3871)

Clinical impedance sensor

Electrochemical sensors for clinically important analytes have been based on amperometric or potentiometric measurements using enzyme electrodes that have disadvantages for certain analytes. Calum J. McNeil and colleagues at the University of Newcastle upon Tyne (U.K.) and Cambridge Life Sciences plc (U.K.) construct sensors based on enteric polymer coatings that dissolve in the presence of the analyte, causing a change in impedance in the underlying electrode. The utility of this technique is demonstrated by applying it to the measurement of urea and enzyme immunoassay. ("Electrochemical Sensors Based on Impedance Measurement of Enzyme-Catalyzed Polymer Dissolution: Theory and Applications"; AC950386+; p. 3928)

Aldehyde biosensor

To lessen the large overpotentials encountered when NADH is directly oxidized at electrodes, there is much interest in developing materials capable of electrocatalytically oxidizing the compound. H. D. Abruña and colleagues at Cornell University and the Universidad Autónoma de Madrid (Spain) develop an aldehyde biosensor by combining the electrocatalytic activity of glassy carbon electrodes (modified with electropolymerized 3,4-dihydroxybenzaldehyde film) with the enzymatic activity of immobilized aldehyde dehydrogenase. The detection limit is 5.0 μ M and the response time is \sim 1 min. ("Aldehyde Biosensor Based on the Determination of NADH Enzymatically Generated by Aldehyde Dehydrogenase"; AC950207O; p. 3936)

Detecting DNA hybridization

The most direct way to determine DNA sequences is to probe the unknown DNA specimen with probe DNA of a known sequence and monitor the occurrence of hybridization using separation techniques. Linda B. McGown and colleagues at Duke University and the Becton Dickinson Research Center use steady-state fluorescence anisotropy to monitor hybridization of fluorescein-labeled DNA oligomers in situ without a prior separation step. The oligomers included a binding site for the EcoRI restriction enzyme, which binds to double-stranded DNA and is used to enhance the difference between the anisotropies of the single-stranded and double-stranded oligomers. ("Hybridization of Fluorescein-Labeled DNA Oligomers Detected by Fluorescence Anisotropy with Protein Binding Enhancement"; AC950478Z; p. 3945)

Sequencing proteins from the C-terminal

The C-terminus is a region of proteins and peptides often not analyzed because of the lack of methods that could provide reliable information. Stephen A. Martin and colleagues at PerSeptive Biosystems discuss C-terminal sequencing using a time-dependent carboxypeptidase Y digestion, coupled with MALDI TOFMS analysis of the resulting peptide ladders. Of 22 peptides tested with the method, sequence information was derived from 19. ("C-Terminal Ladder Sequencing via Matrix-Assisted Laser Desorption Mass Spectrometry Coupled with Carboxypeptidase Y Time-Dependent and Concentration-Dependent Digestions"; AC950501G; p. 3971)

New method for characterizing phospholipids

Phospholipids are principal components of biological cell membranes and various subcellular organelles. Alan G. Marshall and colleagues at Florida State University and The Ohio State University demonstrate structural analysis of several key phospholipids using MALDI FT-ICRMS. Both positive and negative molecular or quasimolecular ions are generated in high abundance. ("Structural Characterization of Phospholipids by

Matrix-Assisted Laser Desorption/Ionization Fourier Transform Ion Cyclotron Resonance Mass Spectrometry"; AC950440M; p. 3979)

Determining enrichment of [¹⁵N]leucine by GC/MS

GC/MS is often used to determine the abundance of [¹⁵N]leucine and other amino acids in isotopic tracer experiments. François Guyon and colleagues at the Université René Descartes (France) study the effect of hydrogen rearrangement on the determination of the enrichment of the measured ratio of ¹⁵N/¹⁴N-labeled leucine using 11 esters of ¹⁵N-labeled and nonlabeled *N*-(heptafluorobutyl)leucine. They find that the labeling ratio increases with the length of the alkyl chain of the ester and the number of hydrogen atoms on the chain. ("Effect of Hydrogen Rearrangement on the Determination of the Enrichment of [¹⁵N]Leucine by GC/MS"; AC950434Q; p. 4000)

Testing drugs for electrolytic degradation

Nonoral and nonintravenous delivery systems are needed for some of the new peptide drugs, which would otherwise be digested or oxidized by the liver before reaching their targets. Delivery of ionic drugs through the skin can be achieved by applying a low-level electric current and could be used in a number of controlled-release drug delivery schemes. However, some drugs may degrade under an applied voltage. Hung-Yuan Cheng and co-workers at SmithKline Beecham Pharmaceuticals evaluate electrolytic degradation of growth-hormone-releasing peptide in a prototype transdermal iontophoresis system, using cyclic voltammetry, bulk electrophoresis, HPLC, LC/MS/MS, and spin-trapping EPR for structural analysis. ("Structural Study of Electrolysis-Induced Degradation of the Growth Hormone Releasing Peptide His-D-Trp-Ala-Trp-D-Phe-Lys-NH₂"; AC950607B)

Interactions of bile salts with heavy metal ions

It has been postulated that bile salts can act as metal ion buffers and prevent precipitation of heavy metal salts with other anions, but experimental evidence is limited. Using polarography, P. Zuman and colleagues at Clarkson University and the Università di Bologna (Italy) study the interaction of dihydroxy bile acid anions with divalent metal ions. They measure equilibrium constants for metal ion complexes with small bile acid aggregates, finding that the solubility depends primarily on the nature of the metal ion. ("Interaction between Dihydroxy Bile Salts and Divalent Heavy Metal Ions Studied by Polarography"; AC940519B)

Trace electrochemical measurement of RNA

Few studies have been devoted to electroanalysis of RNA. Joseph Wang and colleagues at New Mexico State University and the Academy of Sciences of the Czech Republic investigate the adsorptive accumulation of low levels of RNA on a carbon paste electrode combined with constant current potentiometric stripping analysis. They find that picogram quantities of RNA can be detected without a mercury surface or an oxygen removal step. ("Trace Measurements of RNA by Potentiometric Stripping Analysis at Carbon Paste Electrodes"; AC950520Q)



A modular detector for fluoride

Integration of several steps into a complex module is often used as a way of simplifying and miniaturizing analytical methods. M. D. Luque de Castro and I. Papaefstathiou of the University of Cordoba (Spain) develop a method for determining fluoride that integrates pervaporation with potentiometric detection in a laboratory-built module. The method is successfully applied to determination of fluoride in orange tree leaves. ("Integrated Pervaporation/Detection: Continuous and Discontinuous Approaches for Treatment/Determination of Fluoride in Liquid and Solid Samples"; AC950357Z; p. 3916)

Biosensor for phenol vapor

Nonbiological gas-phase sensors such as electrochemical, colorimetric, or semiconducting sensors are widely available but are often somewhat nonspecific and generally require analyte vapors to be reactive. Enzymes and antibodies have high selectivity for their substrates or target antigens and can be incorporated into electrode systems, but they require water for activity and gas-phase sensing is usually too dry for them. Anthony P. F. Turner and colleagues at Cranfield University (U.K.) fabricate a microbiosensor for phenol vapor by incorporating polyphenol oxidase in a water-retaining gel on a microelectrode. The sensor is stable for at least five days at room temperature and achieves 30 ppb detection limits. ("Gas-Phase Microbiosensor for Monitoring Phenol Vapor at ppb Levels"; AC950443Z; p. 3922)

Making troublesome polymers work as SAW sensors

Jay W. Grate of the Naval Research Laboratory and R. Andrew McGill of Geo-Centers report that well-behaved surface acoustic wave vapor sensors can be prepared using previously troublesome polymers. They observe that thin polymer films sometimes dewet the sensor surface, leading to isolated droplets of material and a degradation in sensor performance. In general, plasma precleaning methods alleviate these problems. ("Dewetting Effects on Polymer-Coated Surface Acoustic Wave Vapor Sensors"; AC950262X; p. 4015)

Decreasing stray capacitance in ultramicroelectrodes

Stray capacitance effects are a problem in fast-scan cyclic voltammetry using ultramicroelectrodes. J. Heinze and P. Tschuncky of the Universität Freiburg (Germany) discuss new methods for connecting the electrode microwire and development of shieldings that result in a fivefold drop in capacitive currents in a standard electrode solution. Electrodes with radii down to 1 μm are constructed. ("An Improved Method for the Construction of Ultramicroelectrodes"; AC950183L; p. 4020)

Fabricating ultrasmall carbon disk electrodes

Although disk-shaped microelectrodes with radii as small as 10 Å to 20 μm have been constructed, they are still too large for microenvironments such as the extracellular region of the brain or the cytoplasm of single cells. Danny K. Y. Wong and Lisa Y. F. Xu of Macquarie University (Australia) fabricate carbon disk electrodes with tip diameters approaching 100 nm.

The microelectrodes show a well-defined sigmoidal response for the oxidation of dopamine with minimal background charging current. ("Voltammetric Studies of Carbon Disk Electrodes with Submicrometer-Sized Structural Diameters"; AC9505211)

Microdisk voltammetry with a twist

Microelectrodes offer several advantages including quantitative electrochemical measurements in solutions with low ionic strengths. Henry S. White and Xiaoping Gao of the University of Utah investigate using a rotating microdisk electrode for steady state voltammetric studies in low-ionic-strength solutions. They find that fluid convection causes an increase in potential drop, resulting, for some reactions, in a dramatic decrease in the voltammetric current as the rotation rate increases. ("Rotating Microdisk Voltammetry"; AC9504124)



Tandem TOFMS

MS/MS structural confirmation is becoming more important for chromatographic methods, particularly in regulatory applications. However, GC peaks are so narrow that very rapid mass spectral collection is necessary. Single-reflectron TOF mass spectrometers collect full spectra very rapidly and have been adapted for MS/MS using photodissociation of precursor ions in the flight tube, but so far have not achieved unit mass resolution for both precursor and product ion spectra to m/z 1000. Christie G. Enke and colleagues at Michigan State University perform TOFMS/TOFMS with unit mass resolution for both stages using a dual-reflectron mass spectrometer and a timed pulsed laser for photodissociation of selected precursor ion packets. ("Tandem Reflectron Time-of-Flight Mass Spectrometer Utilizing Photodissociation"; AC9502880; p. 3952)

Detecting neutral analytes by electrospray MS

To further the utility of electrospray MS, a number of recent studies have investigated the various processes that generate gas-phase ions. Gary J. Van Berkel and Feimeng Zhou of Oak Ridge National Laboratory show that an electrospray ion source is analogous to a controlled-current electrolytic flow cell. Based on this model, they find that by meeting three key operating requirements even difficult-to-oxidize neutral analytes can be efficiently ionized and detected in the gas phase by electrospray MS. Neutral metallocenes, metalloporphyrins, and polycyclic aromatic hydrocarbons are presented as model compounds. ("Electrospray as a Controlled-Current Electrolytic Cell: Electrochemical Ionization of Neutral Analytes for Detection by Electrospray Mass Spectrometry"; AC950426+; p. 3958)

Flame-retarding additives by FT-ICRMS

Pyrolysis FT-ICRMS has many features that make it a powerful technique for identifying polymer additives. Ron M. A. Heeren and colleagues at the FOM-Institute for Atomic and Molecular Physics (The Netherlands) evaluate direct temperature resolved in-source pyrolysis with FT-ICRMS using polymers containing fire-retardants spiked with antimony-containing synergists. They obtain resolution sufficient to separate the nominally isobaric ions from the antimony (III) oxide synergist and the *n*-butyl ether derivative of tetrabromobisphenol-A. ("Direct Tem-

perature Resolved HRMS of Fire-Retarded Polymers by In-Source PyMS on an External Ion Source Fourier Transform Ion Cyclotron Resonance Mass Spectrometer"; AC950294K; p. 3965)

Determining purity of ginseng products

Because of the widespread interest in ginseng as an unconventional herbal medicine, analytical methods are needed to determine the integrity of these products. Richard B. van Breen and colleagues at the University of Illinois—Chicago describe an electrospray LC/MS method for the analysis of ginseng saponins (ginsenosides) from ginseng root extracts. They find that Korean and American ginseng extracts display substantial differences between the relative amounts of each ginsenoside. ("Electrospray Liquid Chromatography/Mass Spectrometry of Ginsenosides"; AC950420K; p. 3985)

MALDI-TOF fragmentation of peptides

MALDI is best known as a "soft" ionization method that leaves proteins and other large molecules intact. However, reflectron TOFMS reveals that these molecules can undergo significant postsource decay in the flight tube. Delayed pulsed ion extraction can be used to observe fast metastable fragmentation in a linear TOF spectrometer. Robert S. Brown and John J. Lennox of Utah State University use delayed pulsed ion extraction in a linear system to take advantage of fast metastable decay as a protein-sequencing method. They obtain overlapping fragment sequence information from both the C- and N-terminal ends of several proteins. ("Sequence-Specific Fragmentation of Matrix-Assisted Laser-Desorbed Protein/Peptide Ions"; AC9504225; p. 3990)

Measuring self-exchange rates by ICPMS

Knowing the accuracy of electron transfer self-exchange rate constants is important for comparing theoretical and experimental values for cross-reactions. However, because no net chemical change takes place during self-exchange, direct determination of k_{11} values is difficult. Michael E. Ketterer and Michael A. Fiorentino of John Carroll University perform timewise separation of Tl redox species in aqueous HClO_4 using enriched stable isotope labeling and ICPMS for determination of electron transfer self-exchange rates between Tl(III) and Tl(I). ("Measurement of Tl(III/I) Electron Self-Exchange Rates Using Enriched Stable Isotope Labels and Inductively Coupled Plasma Mass Spectrometry"; AC950285B; p. 4004)

Oligosaccharides by ESIMS

Researchers have attempted to overcome poor ionization efficiency in ESIMS studies of carbohydrate structure by using chromophores or fluorophores. Toshifumi Takao and colleagues at Osaka University (Japan) report on a method that uses 4-aminobenzoic acid 2-(diethylamino)ethyl ester, resulting in a derivative with high proton affinity, which enhances ionization efficiency. The detection limit for derivatized maltohexaose is 10 fmol, which represents a 5000-fold improvement in sensitivity over underivatized maltohexaose. ("Use of the Derivatizing Agent 4-Aminobenzoic Acid 2-(Diethylamino)ethyl Ester for High-Sensitivity Detection of Oligosaccharides by Electrospray Ionization Mass Spectrometry"; AC950250B; p. 4028)

Making MALDI MS better

The ion trap/reTOF device combines the storage capabilities of the ion trap with the speed and high mass capabilities of TOF

to produce an instrument that has several potential advantages for MALDI MS. David M. Lubman and colleagues at The University of Michigan use a continuous-flow probe to introduce peptide solutions into an ion trap/reTOF mass spectrometer for MALDI analysis. They demonstrate the ability of the trap to operate efficiently at the elevated pressures required for direct liquid introduction, obtain picomole-level sensitivity, and discuss the conditions required to optimize the instrument. ("Continuous-Flow MALDI Mass Spectrometry Using an Ion Trap/Reflectron Time-of-Flight Detector"; AC950605R)

Comparing LC/MS interfaces ♦

The main problem with LC/MS of polycyclic aromatic compounds is finding the right interface to do the job. Robert K. Boyd and colleagues at Dalhousie University (Canada), Health Canada, and the National Research Council of Canada compare the moving belt, particle beam, and heated pneumatic nebulizer interfaces for reversed-phase LC/MS of a carbon black sample. The advantages and disadvantages of each interface are discussed, although the heated pneumatic nebulizer interface provided the best overall performance. ("Comparison of Liquid Chromatography/Mass Spectrometry Interfaces for the Analysis of Polycyclic Aromatic Compounds"; AC950616K)

Mass analysis of biomolecules at attomole levels ♦

Alan G. Marshall and colleagues at Florida State University describe FT-ICR mass analysis of MALDI-generated ions from amol amounts of several different biomolecule samples. To achieve the higher sensitivity, they use microscope-monitored sample deposition onto the probe tip and multiple remeasurement of ions from a single laser shot. The authors report detection limits as low as 8 amol of sample. ("Attomole Biomolecule Mass Analysis by Matrix-Assisted Laser Desorption/Ionization Fourier Transform Ion Cyclotron Resonance"; AC950615S)

Detecting reaction intermediates with ESMS ♦

Because on-line ESMS is particularly useful for identification of unstable reaction products or short-lived intermediates, it has potential for use in reaction monitoring. Ryuichi Arakawa and colleagues at Osaka University (Japan) and Kagawa Nutrition University (Japan) use ESMS to detect photoproducts of (polypyridine)ruthenium (II) complexes. Intermediates with a monodentate ligand are detected for the first time in the electrospray mass spectra. ("Detection of Reaction Intermediates: Photosubstitution of (Polypyridine)ruthenium (II) Complexes Using On-Line Electrospray Mass Spectrometry"; AC9504272)

Remeasuring stored ions in a quadrupole ion trap ♦

In the commonly used mass-selective instability mode of ion trap operation, further manipulation of the original ion packet is precluded by ion ejection and subsequent collision with the detector surface. Douglas E. Goeringer and colleagues at Oak Ridge National Laboratory demonstrate multiple remeasurement of the same population of stored ions in an rf quadrupole ion trap. For a collection of $C_3F_5^+$ ions produced via a single electron ionization event, the remeasurement efficiency during 24 scans, as judged by the scan-to-scan loss in signal, was > 99%. ("Ion Remeasurement in the Radio Frequency Quadrupole Ion Trap"; AC9506185)

SEPARATIONS

Relating orthogonality and peak capacity in 2-D separations

Two-dimensional separations need a basis on which they can be evaluated and the analytical performance of different systems compared. Zaiyou Liu and colleagues at the Centers for Disease Control

and Brigham Young University describe a three-step procedure that computes correlation and peak spreading angle matrices for a set of data, calculates peak capacities in each dimension and estimates theoretical peak capacity, and calculates practical peak capacity. Using data from a 2-D GC separation, they demonstrate the usefulness of the equations. ("Geometric Approach to Factor Analysis for the Estimation of Orthogonality and Practical Peak Capacity in Comprehensive Two-Dimensional Separations"; AC9412286; p. 3840)

Identifying the source of underground fuel spills

The possible contamination of groundwater by fuels stored in leaking underground tanks or pipelines has prompted the development of methods for identifying fuel materials recovered from subsurface environments. Barry K. Lavine of Clarkson University and colleagues at Tyndall Air Force Base use pattern recognition methods to classify high-speed gas chromatograms of weathered and unweathered jet fuels. A total of 228 neat jet fuel samples representing common aviation fuels sold in the United States are characterized by 85-peak gas chromatograms. ("Source Identification of Underground Fuel Spills by Pattern Recognition Analysis of High-Speed Gas Chromatograms"; AC950475M; p. 3846)

Atmospheric gas sampling for IC-like CE

Ion suppression, which is widely used in ion chromatography, has been adapted to CE of small ions as suppressed conductometric CE. However, application of this CE method to atmospheric gas analysis has been hindered by the lack of a sample collection device that is compatible with the small scale of the capillaries. Purnendu K. Dasgupta and Satyajit Kar of Texas Tech University use a small wire loop with a liquid film in communication with the capillary as the gas sampling interface to determine 1 ppb SO_2 by suppressed conductometric CE. ("Measurement of Gases by a Suppressed Conductometric Capillary Electrophoresis Separation System"; AC950622G; p. 3853)

Separating latex aggregates

Because of the importance of nonspherical particles in many fields, it is important to better understand their steric behavior. J. Calvin Giddings and Bhajendra N. Barman of the University of Utah use sedimentation FFF of aggregated poly(methyl methacrylate) latex beads to examine steric perturbations of clusters of different mass and clusters of various shapes within a fixed mass category. They discuss the change in peak spacing as n increases and the factors affecting the transition from normal mode to steric mode. ("Separation of Colloidal Latex Aggregates by Cluster Mass and Shape Using Sedimentation Field-Flow Fractionation with Steric Perturbations"; AC950219+; p. 3861)

Polymer CE for chiral separations

The presence of linear poly(vinylpyrrolidone) in a CE electrolyte solution enhances stereoselectivity for separation of diaste-

reomers in a racemic mixture. In addition to its hydrophobicity, the polymer's aromatic and π -electron-rich moieties may play a significant role in the separation. Andreas Rizzi and colleagues at the University of Vienna (Austria) and the Istituto di Cromatografia del CNR (Italy) observe the stereoselectivity enhancement effects of these properties and the effects of chain length in three types of polymer additives for CE of diastereomeric derivatives of α -amino and α -hydroxy acids. ("Separation of Diastereomers by Capillary Zone Electrophoresis with Polymer Additives: Effect of Polymer Type and Chain Length"; AC950310D; p. 3866)

Using spacers in a stationary phase

The separation of organic bases is a problem for chromatographers using reversed-phase LC because these bases adsorb to unreacted silanols, leading to peak tailing. Mary J. Wirth and colleagues at the University of Delaware use methyl spacers in a mixed horizontally polymerized stationary phase to reduce silanol activity. Baseline resolution of a mixture of three cytochrome *c* genetic variants is used to demonstrate the high efficiency of the C_{18}/C_1 stationary phase. ("Use of Methyl Spacers in a Mixed Horizontally Polymerized Stationary Phase"; AC9504934; p. 3879)

A quaternized PEI-zirconia stationary phase

The recently developed polyethyleneimine (PEI)-coated zirconia stationary phase is useful for the separation of proteins but is unstable at extreme pHs. Peter W. Carr and Clayton McNeff of the University of Minnesota describe the synthesis of an acid- and alkali-stable quaternized PEI-coated zirconia stationary phase for use in anion-exchange chromatography. Because the quaternized PEI-zirconia phase does not shrink or swell appreciably upon addition of organic modifiers, such modifiers can be used to attenuate hydrophobic interactions or to effect a change in column selectivity. ("Synthesis and Use of Quaternized Polyethyleneimine-Coated Zirconia for High-Performance Anion-Exchange Chromatography"; AC950278N; p. 3886)

Measuring traces of uranium in nuclear fuel reprocessing

Although a most "unburned" uranium is recovered during the nuclear fuel reprocessing procedure, trace amounts remain in the last organic phase. Constant M. G. van den Berg and colleagues at the University of Liverpool (U.K.) and BNFL (U.K.) describe an in-line stripping procedure for extracting U(VI) from a mixture of tributyl phosphate and kerosene into aqueous sodium sulfate with detection by on-line cathodic stripping voltammetry. Constant recoveries of $\sim 50\%$ are obtained. ("Automated In-Line Extraction of Uranium (VI) from Raffinate Streams with On-Line Detection by Cathodic Stripping Voltammetry"; AC950071U; p. 3903)

Detection of sulfur-containing peptides

Electrochemical detection of easily oxidized and sulfur-containing amino acids, peptides, and proteins separated by reversed-phase HPLC has been hindered by incompatibility between the analytes and the detector solvent: requirements and detector fouling. Pulsed electrochemical detection (PED) reduces fouling at noble metal electrodes and has been used to detect sulfur-containing amino acids at a gold electrode. Cornelis Olieman and Johannes A. M. van Riel of the Netherlands Institute of Dairy Research evaluate oxidative PED of sulfur-containing amino acids at a Pt elec-

trode at low pH and achieve linearity over two orders of magnitude with picomole sensitivity. ("Selective Detection in RP-HPLC of Tyr-, Trp-, and Sulfur-Containing Peptides by Pulsed Amperometry at Platinum"; AC950127K; p. 3911)

Amperometric detector for CE

Although satisfactory results can be obtained from off-column and end-column detectors in CE, they are not yet applicable to routine analysis. Hsuan-Jung Huang and Mei-Cheng Chen of the National Sun Yat-sen University (Republic of China) demonstrate an electrochemical cell assembly similar to the off-column detector but used as an end-column detector. Detection limits of 3.0 amol for dopamine and 5.2 amol for catechol are obtained. ("An Electrochemical Cell for End-Column Amperometric Detection in Capillary Electrophoresis"; AC950428U; p. 4010)

Crown ethers for optical detection of mercury

The use of crown ethers for selective complexation with small ions in aqueous solution has led to the synthesis of numerous analogues tailored to specific applications. The addition of chromophores or fluorophores as side arms on the main ring allows for optical detection of the crown ether-ion complex. Marc D. Porter and co-workers at the DOE Ames Laboratory at Iowa State University and Richard A. Bartsch and co-workers at Texas Tech University determine extraction constants for two such analogues designed for selective extraction of Hg(II) from aqueous solution. Both crown ethers exhibit \sim million-fold selectivity for Hg(II) over the next most extractable divalent cation. ("Chromogenic and Fluorogenic Crown Ether Compounds for the Selective Extraction and Determination of Hg(II)"; AC950619X)

Determining methylsulfonyl-containing metabolites

Methylsulfonyl-containing metabolites of PCBs and DDE have received little attention as environmental contaminants, in contrast to their parent compounds. Ross J. Norstrom and colleagues at Carleton University (Canada), the Canadian Wildlife Service, and Stockholm University (Sweden) report on a GC method for determining PCBs, methylsulfonyl-containing metabolites of PCBs and DDE, and tris(4-chlorophenyl)methanol spiked into biological tissues. Overall mean recovery relative to the internal standard is 103% independent of analyte, substrate, and lipid extract weights up to ~ 0.7 g. MS results are also presented. ("An Integrated Analytical Method for Determination of Polychlorinated Aryl Methyl Sulfone Metabolites and Polychlorinated Hydrocarbon Contaminants in Biological Matrices"; AC950465L)

Separations on a microchip

Miniaturization of liquid phase separation devices is particularly attractive because analytical separation performance often improves when components decrease in size. J. Michael Ramsey and colleagues at Oak Ridge National Laboratory report on micellar electrokinetic capillary chromatography of three neutral coumarin dyes performed on glass microchips. Using laser-induced fluorescence detection, they find that at low applied electric field strengths on-chip injections yield separations with highly reproducible peak areas and migration times. ("Microchip Separations of Neutral Species via Micellar Electrokinetic Capillary Chromatography"; AC950629Y)

**Order your NEW
Pesticide/
Metabolite
Catalog NOW!**



Produced biennially, the Chem Service Pesticide/Metabolite Catalog contains the world's largest selection of pesticide standards. Included in the new expanded listing are the first A2LA Certified pesticide reference materials available anywhere. All Chem Service pesticide/metabolite standards are purity certified and expiration dated. Each chemical is cross referenced by generic, trade and chemical name, with metabolites listed under their base compound.

For a free copy, contact us at 800-452-9994.

ChemService

PO Box 3108 • 660 Tower Lane
West Chester • PA 19381

CIRCLE 1 ON READER SERVICE CARD

**Convert Scanned Images
to (x,y) Data
with**

UN-SCAN-IT™

Full
Scanner
Resolution

Free
Demo Disk!
(PC or Mac)

UN-SCAN-IT™

Turns Any Scanner into an
Automated (x,y) Digitizing System
for Under \$350.

Automatically Digitize:

- STRIP CHART OUTPUT
- INSTRUMENTAL OUTPUT
- OLD GRAPHS AND DRAWINGS
- (X,Y) RECORDER OUTPUT
- PUBLISHED GRAPHS
- ANY HARD COPY GRAPH...

The UN-SCAN-IT software converts scanned images to (x,y) data at Full Scanner Resolution! The (x,y) data can be saved in ASCII or HPGL format and imported into almost any commercial graphics or spreadsheet program.

The UN-SCAN-IT software can also be used to re-scale graphs, integrate peak areas, smooth data, perform regression analysis, take derivatives, etc.

ACS Software

Distribution Center
P.O. 57136, West End Station • Washington, DC 20037
Telephone: 1-800-227-5558 FAX: (202) 872-6067

In AC Research



Not moving the peak in liquid scintillation spectra

In liquid scintillation analysis, interaction of the sample matrix and analyte could affect response. Colin G. Ong and colleagues at Stanford University investigate the effects of pH, NaCl, and cocktail selection on the liquid scintillation spectra of ²³²U. They find that pH has a small effect and that NaCl has a large, but not deleterious, effect on the position of the analyte peak. ("Effect of pH, NaCl, and Cocktail Selection on ²³²U Liquid Scintillation Spectra"; AC950504T; p. 3893)

Dyes for O₂ and CO₂

Detection methods for O₂ and CO₂ range from colorimetry to amperometry, and advances in fiber-optic technology have made simultaneous detection of the two gases possible. However, no single indicator dye system has been developed to determine both gases along with pH. Ming Fat Choi and Peter Hawkins of the University of the West of England (U.K.) optimize an aniline dye-solvent solution that senses both gases independently and reversibly, based on contact charge transfer. ("Novel Dye-Solvent Solutions for the Simultaneous Detection of Oxygen and Carbon Dioxide"; AC9409849; p. 3897)

Spectroelectrochemical cell for ATR-FT-IR

Because of the close-to-ideal flow pattern developed with a channel-type electrode, Daniel A. Scherson and colleagues at Case Western Reserve University modify the same cell to probe the solution past the electrode surface with attenuated total reflection FT-IR spectroscopy. The cell is assessed using the reduction of 2 M bisulfite in an unbuffered aqueous electrolyte at pH 5.25. The spectrum is dominated by negative- and positive-pointing contributions from bisulfite, dithionite, and sulfite. ("Channel Flow Cell for Attenuated Total Reflection Fourier Transform Infrared Spectroelectrochemistry"; AC950436A; p. 4024)

The RON, MON, pump, and RVP of gas+

Based on seasonal and geographic considerations, gasoline must meet stringent environmental requirements, yet still provide an acceptable level of driving performance. John B. Cooper and colleagues at Old Dominion University and Ashland Petroleum describe the use of FT-Raman spectroscopy and partial least-squares regression analysis to build models for determining the research octane number, motor octane number, pump octane number, and Reid vapor pressure of 208 commercial fuel blends. ("Determination of Octane Numbers and Reid Vapor Pressure of Commercial Petroleum Fuels Using FT-Raman Spectroscopy and Partial Least-Squares Regression Analysis"; AC9504631)

Analyzing solid state NMR spectra+

When magic angle spinning NMR samples contain a mixture of chemically similar components with nearly identical isotropic chemical shifts, analysis of the resultant spectrum's line shape is often complex. Jeff M. Koons of the University of South Carolina and Paul D. Ellis of Pacific Northwest Laboratory describe an abstract factor analysis target transformation technique that can determine the number of constituents present and the component MAS NMR spectra. Compared to the conventional least-squares approach, the new technique provides improved precision and accuracy. ("Applicability of Factor Analysis in Solid State NMR"; AC950499T)

Discover four solutions to your analysis problems



Low pressure prep LC

Let us show how you can put a complete LC system on only about 40 x 40 cm of bench or coldroom space. Fractionate your proteins by time, drop count, or peak shape. Automate entire processes with a super-smart Foxy® fraction collector, and solve difficult separation problems with optional gradient programming. With our wide range of LC systems, we already have the right one for you.

circle number 9



HPLC

Robust, reliable HPLC systems give you modular flexibility at a fair price - so you can still get great HPLC value even on a tight budget. Our ProTeam LC® inert option assures maximum biocompatibility and corrosion resistance. And new ChemResearch® 150 software makes it easier than ever to manage your data and automate your entire system.

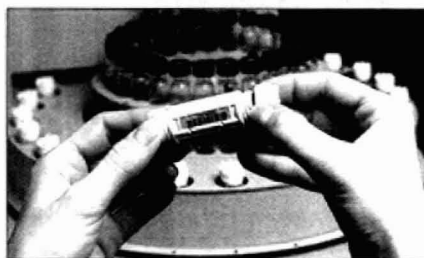
circle number 10



Precision fluid delivery

An Isco syringe pump beats reciprocating pumps cold for special jobs like precision reagent addition, low-flow and pulsation-sensitive LC, and supercritical fluid techniques. There are no check valves to cause flow noise, poor precision at low flow rates, or failure at high viscosities. You'll get pulsefree delivery throughout wide operating ranges: 0.1 µl/min to 200 ml/min; 0 to 10,000 psi.

circle number 11



Supercritical fluid extraction

Now SFE can mean super fast extraction! Exclusive tool-free sample cartridges help make Isco SFX® the fastest and most productive SFE systems available. Manual SFX systems give you top throughput with their dual chambers and no waiting for heat-up or cool-down between extractions. Our new fully automated system runs 24 samples overnight. And it's all done with non-hazardous, non-polluting CO₂!

circle number 12



**Phone today
(800)228-4250!**

Isco, Inc. • P.O. Box 5347 • Lincoln NE 68505
Phone: (402)464-0231 • Fax: (402)464-0318

ANALYTICAL CHEMISTRY

EDITOR ROYCE W. MURRAY
University of North Carolina

ASSOCIATE EDITORS: Catherine C. Fenselau, University of Maryland Baltimore County. William S. Hancock, Hewlett Packard. James W. Jorgenson, University of North Carolina. Robert A. Osteryoung, North Carolina State University. Edward S. Yeung, Iowa State University/Ames Laboratory

Editorial Headquarters, research section
Department of Chemistry
Venable and Keran Laboratories
University of North Carolina
Chapel Hill, NC 27599-3290
Phone: 919-962-2541
Fax: 919-962-2542
E-mail: analyt_chem@unc.edu

Editorial Headquarters, A-page section
1155 Sixteenth St., N.W.
Washington, DC 20036
Phone: 202-872-4570
Fax: 202-872-4574
E-mail: analytical@acs.org

Managing Editor: Mary Warner

Associate Editors: Alan R. Newman, Felicia Wach

Editorial Assistant: Deborah Noble

Contributing Editor: Marcia Vogel

Head, Graphics and Production: Leroy L. Corcoran

Division Art Director: Alan Kahan

Art Director: Michele Telschow

Manager, Copy Editing: Elizabeth Wood

Production Editor: John W. Laine

Electronic Composition: Wanda R. Gordon

Journals Dept., Columbus, Ohio

Editorial Office Manager: Mary E. Scanlan

Journals Editing Manager: Kathleen E. Duffy

Associate Editor: Lorraine Gibb

Assistant Editor: Stephanie L. Mallon

Advisory Board: Phyllis Brown, Karl Cammann, Brian Chait, Bruce Chase, Joseph Glajch, Joseph G. Gordon, David M. Haaland, Kiyokatsu Jimno, Peter Kissinger, Gary E. Maciel, Linda B. McGown, Scott McLuckey, Milos V. Novotny, Jeanne Pemberton, J. Michael Ramsey, James A. Yergey
Ex Officio: Henry Blount, III

A-page Advisory Panel: Frank V. Bright, Therese M. Cotton, Royce C. Engstrom, Curtis Marcott, Mary Ellen P. McNally, Jonathan V. Sweedler, Thomas Tiernan, Vicki Wysocki, Robert D. Voyksner

Publications Division

Director: Robert H. Marks

Director, Special Publishing Operations: Anthony Durniak

Director, Journal Publishing Operations: Charles R. Bertsch

Head, Publications Marketing: David Schulbaum

Copyright permission: Reprographic copying beyond that permitted by Section 107 or 108 of the U.S. Copyright Act is allowed, provided that the fee of \$9.00 per article copy is paid directly to the Copyright Clearance Center (CCC), 222 Rosewood Dr., Danvers, MA 01923, USA. A CCC code printed at the bottom of the first page of an article indicates that ACS owns copyright or has permission to collect the copying fee for that article. A record of that code should accompany payment. Direct reprint permission requests to ACS Copyright Office, Publications Division, 1155 Sixteenth St., N.W., Washington, DC 20036.

Registered names and trademarks, etc., used in this publication, even without specific indication thereof, are not to be considered unprotected by law.

1995 subscription rates include air delivery outside the U.S., Canada, and Mexico. Canadian subscriptions are subject to 7% GST.

	Members	Nonmembers (personal)	Nonmembers (institutional)
U.S.	\$ 40	\$ 85	\$ 570
Canada and Mexico	77	122	607
Europe	123	168	653
Other countries	148	193	678

Members may share/donate their personal subscriptions with/to libraries and the like but only after 5 years from publication.

Nonmember rates in Japan: Rates above do not apply to nonmember subscribers in Japan, who must enter subscription orders with Maruzen Company Ltd., 3-10, Nihonbashi 2-chome, Chuo-ku, Tokyo 103, Japan. Tel: (03) 272-7211.

For multi-year and other rates, call toll free 800-227-5558 in the U.S. and Canada; in the Washington, DC, metropolitan area and outside the U.S., call 202-872-4363; fax 202-872-4615.

Single issues, current year, \$24.00 except review issue, \$50.00, and LabGuide, \$50.00; back issues and volumes and microform editions available by single volume or back issue collection. For information or to order, call the number listed for subscription orders; or write the Microform & Back Issues Office at the Washington address.

Subscription orders by phone may be charged to VISA, MasterCard, or American Express. Call toll free 800-333-9511 in the continental U.S.; in the Washington, DC, metropolitan area and outside the continental U.S., call 202-872-8065. Mail orders for new and renewal subscriptions should be sent with payment to American Chemical Society, Department L-0011, Columbus, OH 43268-0011.

Changes of address must include both old and new addresses with ZIP code and a recent mailing label. Send all address changes to the ACS Columbus address. Please allow 6 weeks for change to become effective. Claims for missing issues will not be allowed if loss was due to failure of notice of change of address to be received in the time specified: if claim is dated (a) North America—more than 90 days beyond issue date, (b) all other foreign—more than 180 days beyond issue date. Hard copy claims are handled at the ACS Columbus address.

Instructions for authors of AC Research and guidelines for the Instrumentation, Report, Analytical Approach, and A/C Interface features are published in the Jan. 1 issue, p. 229, or can be obtained from our e-mail relector "acinfo@acs.org" using the keyword phrases "ac research" or "ac apguide," respectively. Please consult these instructions prior to submitting a manuscript for consideration for publication.

Manuscripts for publication in AC Research (4 copies of text and illustrative material) should be submitted to the Editor at the University of North Carolina address. Please include a signed copyright status form; a copy of this document appears on p. 235 of the Jan. 1 issue. Manuscripts for publication in the A-page section should be submitted to the Washington editorial staff.

Supporting information is noted in the table of contents with a ■. It is available as photocopy (\$12.00 for up to 3 pages and \$1.50 per page for additional pages, plus \$2.00 for foreign postage) or as 24x microfiche (\$12.00, plus \$1.00 for foreign postage). Canadian residents should add 7% GST. See supporting information notices at the end of journal article for number of pages. Orders must give complete title of article, names of authors, journal, issue date, and page numbers. Prepayment is required and prices are subject to change. In 1995, electronic supporting information is available to current journal subscribers via the Internet using either gopher or World Wide Web protocols. Most often, the material is available as PDF files, which may be viewed using Adobe's Acrobat Reader, a program that is freely available on the Internet. However, some articles may include computer programs, PostScript files, word-processing files, experimental data in a standard format (e.g., crystallographic parameters in CIF format), etc. In order to download the supplementary material files, users will need to enter their journal subscriber number, which can be found on the mailing label. Detailed instructions for using this service can be found on the Internet. With gopher, connect to pubs.acs.org, go to the "ACS Publications" selection, then to the "Supporting Information" selection. Read the README file in this directory for detailed instructions. When using a WWW client (e.g., Mosaic, Netscape), connect to the URL "http://pubs.acs.org/" and select the "Supporting Info. for Journals" link. For further information on electronic access, send electronic mail to gopher@acsinfo.acs.org, or phone (202) 872-4434. For information on microforms, contact Microforms & Back Issues at the ACS Washington address or phone (202) 872-4554. Supporting information, except structure factors, also appears in the microfiche edition.

The American Chemical Society and its editors assume no responsibility for the statements and opinions advanced by contributors. Views expressed in the editorials are those of the editors and do not necessarily represent the official position of the American Chemical Society.

Journals Department, American Chemical Society, 2540 Olentangy River Road, P.O. Box 3330, Columbus, OH 43210 (614-447-3600, Ext. 3171; TELEX 6842086; Fax 614-447-3745)

Member & Subscriber Services: American Chemical Society, P.O. Box 3337, Columbus, OH 43210 (614-447-3776; 800-333-9511)

Advertising Management: Centcom, Ltd., 1599 Post Rd. East, P.O. Box 231, Westport, CT 06881 (203-256-8211; fax 203-256-8175)

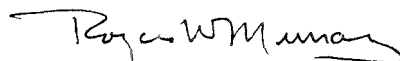
Off-Shore Authors Are Welcome

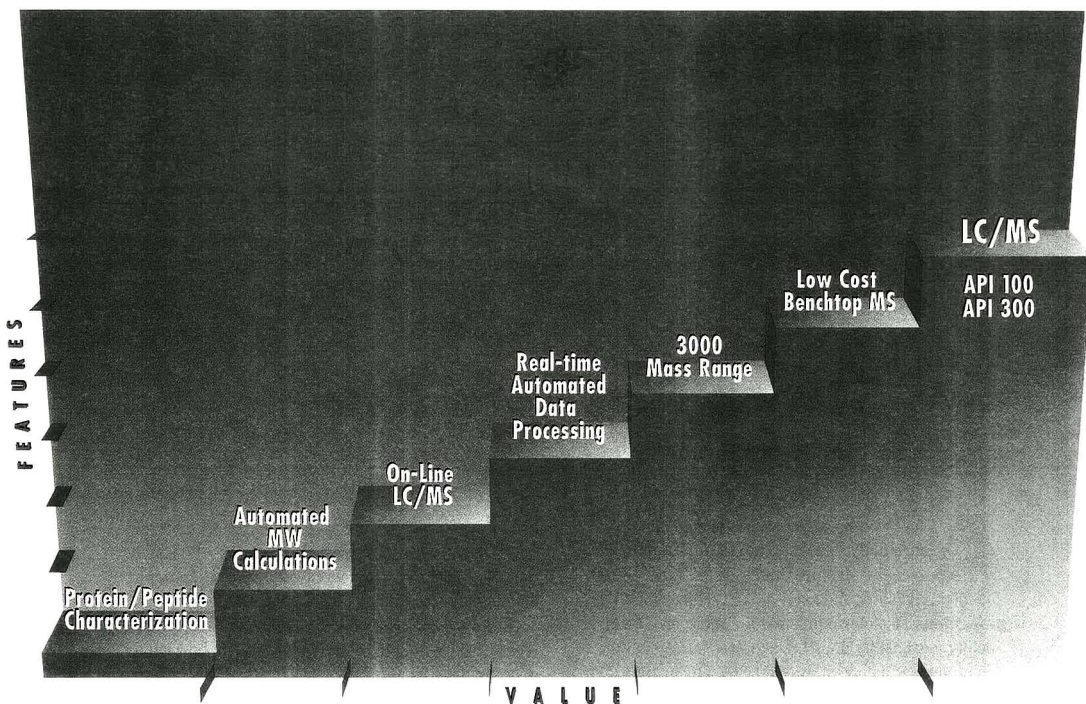
A few months ago an article in a popular science magazine made the claim that authors living outside the United States have special difficulty publishing their science in U.S. journals. The proportion of articles published in American Chemical Society journals by non-U.S. scholars suggests that this premise is incorrect. In 1989, 36% and, in 1994, 45% of the papers published in ACS journals were by non-resident authors. (Here, nonresident author refers to a corresponding (i.e., senior) author at an institution outside the United States; the above percentages would be much larger if the contributions of foreign students working at U.S. institutions were included.) For *Analytical Chemistry*, the comparable numbers were smaller but still considerable; 26% and 37% of the papers published in 1989 and 1994, respectively, were by nonresident authors. The proportion of foreign senior authorship is increasing; in 1994, *Analytical Chemistry* papers included research from 32 countries, signifying a broad geographical distribution of high-quality measurement science. This means to me that *Analytical Chemistry* is publishing an increasing worldwide portion of excellent analytical chemistry research. That's good.

Publication in *Analytical Chemistry*, and other ACS journals, is substantially guided by peer-review evaluations of submitted research manuscripts. My perception of reviewers is that there are no "favorite" countries. "Cutting-edge" analytical chemistry has no nationality. Reviewers are often non-U.S. residents. Our editorial responsibility is to identify and disseminate to our readership the most significant advances in chem-

ical measurement science. For those fine scholars and potential authors at non-U.S. institutions who suspect that *Analytical Chemistry* has a national bias, I would like to persuade you that is not the case.

It is important to realize that a potential author, anywhere, who is unfamiliar with a journal can best come to understand its requirements and standards with regard to quality of experiments, novelty of concepts and theory, and significance of the applications only by a careful reading of articles published in the journal, as well as its published instructions to authors. A potential author can be handicapped by lack of equipment or proper facilities, but in the above respect can be especially handicapped by a poor library resource. I examine each paper submitted to *Analytical Chemistry* before assigning it to an Associate Editor (or myself) for peer evaluation. Several times a month, I see papers submitted by non-U.S. authors that clearly reflect an incomplete and out-of-date awareness of the current literature and state of intellectual development of the subject at hand. To those authors I can only say try harder to find and read copies of *Analytical Chemistry* and other sources of good chemistry, and show this editorial to the local authorities who, if they wish to support analytical chemistry research, should provide the means for better access to the chemical literature.





PE SCIEX takes a step up with the new benchtop API 100 and API 300 LC/MS systems.



PE SCIEX is the world leader in API/LC/MS technology for both single and triple quadrupole mass spectrometers. In over

100 of the world's largest pharmaceutical and bioresearch labs, API/LC/MS technology from PE SCIEX is being used to analyze a wide variety of samples—from small pharmaceutical metabolites, through peptides, to large proteins and glycoproteins.

Outselling and outperforming all other dedicated LC/MS systems, the API I and API III have been accepted worldwide as the industry standard. Our innovative IonSpray™ and TurboIonSpray™ interfaces have made LC/MS a routine and reliable technique—even for complex biological samples.

Now we've taken API technology another step up: onto the lab bench. The new API 100 and API 300 are benchtop

quadrupole mass spectrometers offering a newly designed IonSpray interface with the option of μ IonSpray™. With the new μ IonSpray, protein sequencing, peptide mapping, and molecular weight determinations with biomolecular characterization at femtomole levels is now possible.

Both systems offer a mass range of up to 3000, highly reliable turbomolecular pumps, and improved sensitivity. New software, fully compatible with the latest computer technology, enables the user to take advantage of the increased performance of the Apple Power Macintosh®.

Our BioToolBox™ application software is ideal for complete characterization of proteins and peptides from LC/MS, CID/MS and MS/MS data.

For more information about the new benchtop API 100 and API 300, call 1-800-345-5224 in the U.S. or contact your local Perkin-Elmer representative.

PE SCIEX

Australia Tel: 3 212 8500 Fax: 3 212 8501 Latin America Tel: 11 578 9600 Fax: 11 276 1864 Italy Tel: (039) 23831 Fax: (039) 2383490
 France Tel: 1 3085 6363 Fax: 1 3085 6300 Germany Tel: 6150 101 0 Fax: 6150 101 101 UK Tel: 01494 67 6161 Fax: 01494 67 9331
 Japan Tel: 45 314 8010 Fax: 45 314 5142 Singapore Tel: 336 0322 Fax: 338 3991

All trademarks are the property of their respective owners.

CIRCLE 5 ON READER SERVICE CARD

Synopses of significant analytical articles from other publications

BIOWANALYTICAL

Detecting DNA strand breaks during apoptosis

Apoptosis, a physiological process for control and maintenance of tissue homeostasis, is increasingly being recognized as a factor in disease processes. During apoptosis, DNA fragments first into 300- and/or 500 kb fragments and ultimately into internucleosomal fragments of 180 bp by endogenous endonuclease activity. Gregory J. Gores and colleagues at the Mayo Clinic and Foundation have developed a quantitative assay for determining fragmentation in apoptosis by enzymatically labeling the 3'-OH ends of the DNA with a fluorescent dideoxynucleotide.

Because only one labeled dideoxynucleotide can be added per 3'-OH end of the DNA, the fluorescence intensity is directly proportional to the number of DNA strand breaks. The researchers first established the sensitivity of the method using isolated calf thymus DNA treated with the endonuclease DNase I and observed an excellent correlation between the results obtained by fluorophore end-labeling and those obtained using an isotopic approach. They then used the new assay to quantitate DNA strand breaks in nuclei isolated from hepatocytes undergoing apoptosis using fluorescent digitized microscopy, flow cytometry, and fluorometry. The researchers believe that the assay will be useful in studying the molecular mechanisms leading to DNA cleavage during apoptosis. (*Anal. Biochem.* 1995, 229, 229-35)

Magic angle spinning of photosynthetic reaction centers

The photosynthetic reaction center of *Rhodospirillum rubrum* R26 is a transmembrane protein complex that consists of three polypeptide chains and nine cofactors: two ubiquinones-10, four bacteriochlorophylls, two bacteriopheophytins, and one nonheme Fe. Upon illumination

of the protein complex, an electron is transported from a bacteriochlorophyll pair at the periplasmic side of the membrane to the primary quinone Q_A . Because quinones generally undergo two-step reduction to the corresponding quinols, rather than the one-step reaction to the semiquinone state observed here, it has been postulated that specific protein-cofactor interactions are responsible for the Q_A redox properties. H.J.M. de Groot and colleagues at Leiden University (The Netherlands) have used ^{13}C magic angle spinning NMR to characterize these protein- Q_A interactions.

Reaction centers dispersed in LDAO detergent were studied at temperatures between 180 and 240 K, whereas reaction centers precipitated by removal of the detergent were studied at ambient temperature and at temperatures as low as 180 K. The NMR data reveal an apolar Q_A site and show no evidence for electrostatic polarization of the quinoid ring by a particularly strong binding interaction of the protein. The researchers suggest that the detailed characterization of the redox process requires an in-depth study using both 1-D and 2-D NMR techniques at different temperatures. (*Biochemistry* 1995, 34, 10229-36)

MS tells which end is up for proteins

MS/MS methods for protein sequencing can determine peptide fragment order along with amino acid sequences for individual fragments so that large peptides and proteins don't have to be cleaved and mapped during sample preparation. However, being able to tell the N-terminus from the C-terminus of each peptide or fragment ion is essential and requires a distinction between the complementary b- and y-ions formed during cleavage of the amide bonds. Peptide and small protein studies have shown b-ions to be less stable than y-ions. Fred W. McLafferty and co-workers at Cornell University used ESI-FTMS to extend these studies to a 24-kDa protein.

They used both IR multiphoton (IR-MPD) and nozzle/skimmer dissociation

to fragment carbonic anhydrase and measured the relative abundances of complementary b- and y-ion pairs against irradiation time or potential difference, respectively, to determine ion stabilities. For both methods, b-ions were almost universally less stable than y-ions for all primary complementary pairs studied; with IR-MPD, the abundance for b-ions began to decrease ~ 50 ms before that of the y-ions. The researchers propose that amide bond cleavage involves charge migration from the C-terminus to the N-terminus and increases the charge density of b-ions at the expense of y-ions. (*Rapid Commun. Mass Spectrom.* 1995, 9, 871-76)

Opioid peptides by preparative and analytical CZE

Although research has shed some light on the mechanisms of opioid peptides in mammals, many of their clinical and pharmacological aspects are not yet well understood. Accurately determining trace amounts of these compounds in biological tissues is therefore critical to the understanding of their physiological effects and possible therapeutic value. Dominic M. Desiderio and colleagues at the University of Tennessee have used preparative and analytical CZE followed by liquid SIMS to resolve a complex mixture of opioid peptides (β -endorphin [BE], methionine enkephalin [ME], and leucine enkephalin [LE]) extracted from bovine pituitary.

After precipitation and solid-phase extraction, the peptide-enriched bovine pituitary homogenate was subjected to preparative CZE at pH 2.5 and 5.5, and fractions were collected within defined time windows for BE, ME, and LE. Preparative CZE was then performed at pH 2.5 for fractions collected at pH 5.5. LSIMS of the 2-D CZE fraction revealed the appropriate protonated molecular ion of LE at an m/z of 556.4. The authors note that this work shows the usefulness of preparative and analytical CZE, in combination with MS, for analyzing complex biological tissue mixtures. (*Anal. Biochem.* 1995, 229, 188-97)



Sol-gel-derived enzyme biosensors

Amperometric biosensors contain active enzymes immobilized within, or attached to, a supporting matrix. Although many methods of mass-producing low-cost, disposable biosensors have been developed, only two types of renewable biosensors, carbon paste and carbon-epoxy composite material sensors, have been successfully implemented. O. Lev and I. Pankratov of the Hebrew University of Jerusalem (Israel) have described a new class of renewable-surface amperometric biosensors based on the newly developed field of sol-gel bioceramics.

The sol-gel biosensors consist of enzymes immobilized in organically modified silica-carbon matrices. The silica backbone provides rigidity, the organically modified surface guarantees that water will not penetrate into the bulk of the electrode, the percolating carbon powder provides electric conductivity and shields the enzyme from the hostile environment during the sol-gel molding process, and the encapsulated enzyme provides biocatalysis and specificity. The researchers show that an amperometric sol-gel glucose biosensor has a linear range of 0–15 mM, which coincides with the required detection range for medical applications, and a dynamic range of up to 25 mM. (*J. Electroanal. Chem.* 1995, 393, 35–41)

Clay complexes in oxygen sensors

Many attempts have been made to design metalloporphyrin-modified electrode systems based on oxygen reduction of the two-electron transfer mechanism for use as oxygen sensors at ambient temperature and atmospheric pressure, including fixing metalloporphyrins using polymer supports, polymer ligands, and self-polymerization. Isao Sekine and colleagues at the Science University of Tokyo and Osaka Sanso Kogyo Co. Ltd. (Japan) complexed cobalt-porphyrins with monmorillonite, vermiculite, and acid-washed kaolin clays in an effort to modify pyrolytic graphite electrodes for use as oxygen sensors.

In the monmorillonite and vermiculite systems, the cobalt-porphyrins were incorporated into the interlayered regions, and in the acid-washed kaolin, they were adsorbed onto the surface. To improve the stability and increase conductance, the

researchers also added poly(vinyl alcohol) and poly(2-vinylpyridine) as polymer supports and silver colloid as a mediator. They found that the peak current density increased linearly with the concentration of oxygen, the response was reversible and rapid, and the electrodes using monmorillonite and vermiculite were stable for more than 6 h. The most effective electrodes were those modified with Co[5,10,15,20-tetrakis(*N*-methyl-4-pyr:dyl)-porphyrin] and Co[5,10,15,20-tetrakis(4-(trimethylammonio)phenyl)-porphyrin]-vermiculite-silver colloid-poly(vinyl alcohol)-poly(2-vinylpyridine). (*J. Electrochem. Soc.* 1995, 142, 2612–17)

Isomerization flips a single ion channel

Protein ion channels in cell membranes are difficult to characterize because they sit in a lipid environment and their action involves small conformational changes. Artificial ion channel-forming molecules such as gramicidin are easier to synthesize and study. G. Andrew Woolley and Dominic C. J. Jaikaran of the University of Toronto (Canada) used single-channel current measurement to study the *cis-trans* isomerization of a carbamate bond in gramicidin-ethylenediamine molecules incorporated into a lipid bilayer.

A lipid bilayer film was formed across the hole in a pipet tip containing electrodes and filled and surrounded with electrolyte in a cell. Gramicidin-ethylenediamine was added and, as dimers of the peptide incorporated into the bilayer and formed ion channels, channel events were detected as discrete steps for measurements taken over several hours at temperatures from 2 ° to 37 °C. Bond configurations for the carbamate were assigned based on molecular modeling of the channel and NMR studies with small molecules. As the temperature increased, the lifetimes of the individual *cis* and *trans* states for the carbamate bond decreased. The calculated activation parameters agreed with those found for simple carbamates using dynamic NMR spectroscopy. (*J. Phys. Chem.* 1995, 99, 13352–55)



Single-trap electrode for FT-ICRMS

In FT-ICRMS, the open-cell configuration is used to increase external ion injection efficiency, improve gas conductance, eliminate the formation and charging of dielectric sur-

faces, and eliminate ion trajectory perturbations. David A. Laufer and Victor H. Vartanian of the University of Texas–Austin reported on an open-geometry trapped ion cell with a single annular trap electrode located at the center of the excitation and detection region that creates a trapping well by applying a static potential of a polarity that is opposite the charge of the ion to be trapped.

The cell uses a combination of applied electric fields to eliminate the axial ejection of ions and generates a reduced radial electric field throughout a significant portion of the trapping volume. A mass resolving power of 1.45×10^6 was achieved for benzene, the highest among all the cells evaluated. Because there is no electrostatic barrier, ions can be externally generated and injected into the cell without discrimination on the basis of translational energy. However, continuous ion injection into the cell can occur simultaneously. This success of this open-geometry cell configuration demonstrated that, through the appropriate selection of electrodes and location, cell performance can be improved without increasing its complexity. (*J. Am. Soc. Mass Spectrom.* 1995, 6, 812–21)

Laser-desorption FT-MS reveals new fulvic acid molecular weights

Fulvic acid, a heterogeneous mixture of organic substances found in soils and peats, plays a key role in many geochemical processes. However, fulvic acid's molecular weight distribution has never been unambiguously determined. James A. Rice and colleagues at South Dakota State University and the 3M Corporation have reported the molecular weight of five fulvic acid samples using laser-desorption FT-MS.

The values were compared to molecular weights determined by gel filtration chromatography or vapor pressure osmometry. The authors found that LD-FT-MS consistently yielded number-averaged molecular weights ~ 50% lower than the other methods. To ensure that the MS results are correct, they used low laser power (0.05 J) to prevent formation of fragments and demonstrated that the technique could determine molecules in the higher mass range. The authors conclude that the LD-FT-MS values are correct and that other methods measure only a small proportion of the substances in fulvic acid. (*Environ. Sci. Technol.* 1995, 29, 2464–66)

Borane salts by electrospray MS

Although analysis of biochemical compounds by electrospray MS has received a great deal of attention, analysis of inorganic compounds has received little. Recently, Cornelis E.C.A. Hop and colleagues at the University of Wisconsin-Madison demonstrated that electrospray MS in the negative ion mode can be used to identify borane salts, which cannot be analyzed by other conventional MS techniques such as electron impact ionization, chemical ionization, and liquid secondary ion MS. In a continuation of their earlier work, these authors have reported the preliminary results of an examination of [(Me)₃N][B₃H₆]⁻ and Cs[B₃H₆]⁻ by electrospray MS in the positive ion mode and showed that the solvent is a critical parameter in these experiments.

They dissolved the borane salts in acetonitrile, methanol, water, and tetrahydrofuran and found that the acetonitrile solutions provided EI mass spectra that were characteristic of the borane and that virtually all signals corresponded to cationic cluster ions of the general formula [(cation^{m+})_x(anionⁿ⁻)_y]^{(m-x)(n-y)+}. In contrast, the methanol solutions produced only B(OCH₃)₃⁺ cluster ions. The researchers note that this was the first demonstration of an electrochemical reaction between an analyte and solvent in electrospray MS and concluded that, under certain conditions, electrospray is not a mild ionization method. (*J. Am. Soc. Mass Spectrom.* 1995, 6, 866-865)

Electron affinities of PAHs by the kinetic method

Electron affinity is an important thermochemical property, and several methods for determining values are available. The kinetic method is an approximate method based on the rates of competitive dissociation of mass-selected cluster ions. Guodong Chen and R. Graham Cooks of Purdue University have used the kinetic method to determine the electron affinities of several polycyclic aromatic hydrocarbons. Electron-bound dimers of PAHs are generated in the ion source and fragmented competitively to yield monomeric molecular radical anions, and the ratio of the resulting ion abundances reflects differences in electron affinities.

To collect the data, the researchers used electron attachment desorption chemical ionization MS and triple-quadrupole tandem MS. They found that alkyl-substituted PAHs have lower electron af-

finities than unsubstituted PAHs, in agreement with other studies. Values for halogenated PAHs are also reported. One key finding is that chemically similar species must be used for generating the electron-bound dimers. (*J. Mass Spectrom.* 1995, 30, 1167-73)

SEPARATIONS

Kinetic studies in a nanoliter volume

With the growing interest in determining kinetic parameters in small-volume biochemical reactions or single cells, there is a need for analytical methods that monitor multiple chemical species in real time in these nanoliter-volume, complex matrices. Spectroscopic methods and miniaturized electrochemical sensors meet some of these requirements, but they fail to measure a number of biochemically important compounds. Yi-Ming Liu and Jonathan V. Sweedler of the University of Illinois at Urbana-Champaign have developed an electrophoretic method for these types of measurements using a thin rectangular separation channel constructed from standard microscope slides.

Samples are introduced onto the separation channel by a capillary sampler. Movement of this sampling capillary is carefully controlled along the separation channel's width and provides a time axis for the reaction. Analytes were separated as they migrated along the channel's length and detected in this study by fluorescence. The authors demonstrated the new technique by following the first-order kinetics of a reaction taking place in a 200-nL solution, and found that this new system yielded > 10,000 theoretical plates and offered time resolution as fast as 100 ms. (*J. Am. Chem. Soc.* 1995, 117, 8871-72)

Studying the surface polarity of silica

Silica and silica-based materials are the most important stationary phases in LC and, although the surface properties of silica have been studied extensively, there are still many controversies and ambiguities about the origin of the surface acidity, the molecular interactions between solutes and the silica surface, and the surface polarity of silica. Sarah C. Rutan and Zengjiao Li of Virginia Commonwealth University have used the solvatochromic method to quantify the dipolarity-polariz-

ability, hydrogen-bonding acidity, and hydrogen-bonding basicity of the surface of silica under normal-phase chromatographic conditions.

The researchers obtained electronic absorption spectra using a flow cell with a 1-mm pathlength packed with the stationary phase of interest. These spectra were then used in conjunction with solution-phase dye spectra and measurements of the retention of dyes on the stationary phase to calculate the various solvatochromic parameters. Rutan and Li found that in *n*-hexane-chloroform mixtures, the surface dipolarity-polarizability and hydrogen-bonding acidity of silica are high and not affected by the composition of the mixture. The hydrogen-bonding basicity of silica is much lower and decreases as the concentration of chloroform increases in the mobile phase. (*Anal. Chim. Acta* 1995, 312, 127-39)

Postcapillary electrophoresis column derivatization

Because of its sensitivity, laser-induced fluorescence has become a popular detection method for biological analytes separated by capillary electrophoresis. However, many analytes of interest do not fluoresce and therefore require derivatization to be detected by LIF. S. Douglass Gilman and Andrew G. Ewing of Penn State University developed a postcolumn derivatization technique for CE using naphthalene-2,3-dicarboxaldehyde (NDA) and 2-mercaptoethanol to label analytes.

Although the NDA/2-mercaptoethanol reaction products are unstable, they form quickly and are very fluorescent. Compounds marked with NDA were excited with a He-Cd laser (442 nm line). The postcolumn approach avoided several problems of precolumn methods including dilution of low-volume samples, labeling multiple species in the unseparated mixture, and changes in the derivatization reaction due to the matrix. The authors demonstrated their technique by detecting amol amounts of glycine and transferrin. They also used the postcolumn method for LIF detection of homogenate samples of a snail brain and the separation of components in a single human erythrocyte. (*Anal. Methods Instrum.* 1995, 2, 133-41)

Ionic polymers as micellar media

Micellar electrokinetic chromatography (MEKC) has limited separation capabilities for strongly hydrophobic compounds,

which elute very near the migration time of the micelles. Adding organic solvents increases the elution window, but at high concentrations the solvents inhibit micelle formation. Morteza G. Khaledi and colleagues at North Carolina State University proposed that ionic polymers could be viewed as covalently bonded micelles that maintain their structural integrity in the presence of organic solvents.

They used poly(methylmethacrylate/ethyl acrylate/methacrylic acid) block copolymer as the micellar medium for MEKC separation of several types of hydrophobic compounds. The method provided near-baseline separation of alkylphenones with a wide range of polarities in 60% methanol; separation was improved for the more hydrophobic compounds by increasing methanol and for the more polar compounds by eliminating it. Polycyclic aromatic hydrocarbons were separated successfully both for different ring numbers and for geometric isomers such as pyrene, chrysene, and 2-benzo[*a*]anthracene. Finally, the researchers separated C_{60} and C_{70} fullerenes from fullerite in high-volume percentages of organic solvents with elution times ranging from 16 min for toluene to 175 min for C_{70} fullerene. (*J. High Resolut. Chromatogr.* 1995, 18, 443–45)



Visible-light FT-Raman spectrometer

Although they are used extensively in IR absorption and UV-vis spectroscopies, Fourier trans-

form techniques have only recently been applied to the spectral analysis of Raman-scattered light. Earlier work indicated that although FT-Raman spectroscopy with visible light was possible, design limitations inherent in the modified FT-IR spectrometer used in the work prevented the acquisition of Raman spectra with S/N comparable to those obtained using a single-channel dispersive Raman spectrometer. In an effort to demonstrate the intrinsic potential of FT-Raman spectroscopy with visible light excitation, Colin J. H. Brennan and Ian W. Hunter of the Massachusetts Institute of Technology have designed, constructed, and characterized a visible-light FT-Raman spectrometer to be used as a spectral analyzer subsystem in a confocal scanning laser Raman microscope.

The FT design features high étendue, large free-spectral range, intrinsic spectral

accuracy, spectral resolving power independent of input aperture diameter, spectral resolution under computer control, and increased Raman scattering efficiency with shorter wavelengths. Coupled with a low-noise, high-quantum-efficiency photodetector and high-optical-density Rayleigh line filters, the decreased étendue of the microscope optics was partially offset, and Raman signal shot noise operation was achieved. The measurements used to evaluate the spectrometer included Raman spectra from solids and liquids. (*Appl. Spectrosc.* 1995, 49, 1086–93)

ICPMS of chromium in tissues

Environmental chromium contamination poses a number of biological hazards. Trace chromium can be determined by isotope dilution inductively coupled plasma mass spectrometry (ID-ICPMS), but biological samples are high in carbon, which when combined with argon from the plasma (as ArC) interferes isobarically with ^{52}Cr , the most abundant isotope. Joseph W. H. Lam and colleagues at the National Research Council of Canada investigated a series of protocols for Cr determination in a biological standard reference material (SRM) in which they varied sample preparation, isotope dilution, standard addition, and plasma gas composition.

Nitric acid digestion of dogfish liver SRM and addition of enriched ^{53}Cr for ID-ICPMS gave a $^{52}\text{Cr}/^{53}\text{Cr}$ ratio much higher than the certified values, indicating that not all the carbon was removed. Similar digestion with measurement by standard additions at ^{53}Cr gave good agreement with the certificate value but was less sensitive than for the more abundant ^{52}Cr . Following on studies showing that $\text{O}_2\text{-Ar}$ plasmas remove carbon interferences but that maintaining the O_2 stoichiometry is difficult, the researchers optimized an air-Ar plasma method and were able to determine ^{52}Cr at 30 pg/mL detection limits, only a little higher than the 10 pg/mL limit obtained in a pure Ar plasma. (*J. Anal. At. Spectrom.* 1995, 10, 551–54)

Photodeposition on optical imaging fibers

Micrometer- and nanometer-scale structures such as nanotubes, nanowires, quantum dots, microspheres, and nanometer-size light-emitting diodes are generating considerable interest in the scientific community. Complex, well-defined micro-

structures have been produced by laser-assisted chemical vapor deposition and photoactivation. In a new photopolymerization technique, David R. Walt and colleagues at Tufts University have used the discrete light pathways in an optical imaging fiber to photopolymerize an array of individual polymer spots in a variety of sizes and patterns.

The distal end of the imaging fiber is first functionalized by treatment with 3-trimethoxysilylpropylmethacrylate to attach a photopolymerizable acrylate group to the glass surface, which facilitates the adhesion of the polymer. The fiber is then placed on the photodeposition system, and collimated light from a Hg/Xe arc lamp is passed through a neutral density filter slide and then through an excitation bandpass filter to isolate the appropriate initiation light, which passes through a mask and is imaged onto the proximal end of the fiber. Finally, the distal end of the fiber is coated with a thin film of prepolymer, and the fiber is illuminated for a fixed time by an electronic shutter. The excess polymerization solution is removed by rinsing with ethanol. Using this method, the researchers were able to produce monodisperse polymeric microarrays containing spots 2.5 μm in diameter spaced 4.5 μm apart. They note that the technique allows micrometer-scale photopatterning with masks larger than the desired dimensions. (*Science* 1995, 269, 1078–80)

Electric field effects on atomic species in a flame

Electric fields can substantially reduce the emission of excited atomic species in a flame. Although the effect is easily observed visually, little work has been done to study the phenomenon. James D. Winefordner and colleagues at the University of Florida at Gainesville and the National Institute of Standards and Technology used components from a conventional flame atomic absorption apparatus to quantitatively study the effect for sodium and strontium.

Relative decreases in emission and absorption were found to be related to applied voltage and analyte concentration at low voltages, but constant at high voltages of ~ 2000 V. The results are consistent with a disturbance of the equilibrium: $\text{Me} \leftrightarrow \text{Me}^+ + \text{e}^-$. Loss of positive ions from the equilibrium by, for example, deposition on the plates is also consistent with the results. The temporal behavior of the effect was also investigated. (*Appl. Spectrosc.* 1995, 49, 1137–41)

J.T.Baker laboratory reagents. Because at first you must succeed.

The wrong reagent can put you at risk. In terms of costly problem solving. Delays. Repeat analyses. And, embarrassing explanations.

The good news:
J.T.Baker laboratory chemicals have been rated number one for quality 18 years in a row.* High characterization. Low trace impurities. Made to tighter specifications than industry standards require. Full traceability. Signed Certificates of Analysis. SAF-T-DATA™ labels. And innovative leadership in safety packaging.

Specify
J.T.Baker
through
your local
distributor,

or call
1-800-JTBAKER,
Fax 908-859-9318.

Because even though reagents are only 3% of your laboratory budget, a minor misstep can cause major headaches. Just ask young William Tell.



*Right from
the Start.®*

*Based on studies by the Marketing Research Group, GENTCO, LTD.
Right from the Start® is a trademark of Mallinckrodt Baker, Inc.
©1995 Mallinckrodt Baker, Inc.

CIRCLE 8 ON READER SERVICE CARD



Making cutting-edge technology work for day-to-day use

When the basis of your business is at the cutting edge of science and technology, creating products and methods that harness this new technology to satisfy customers that are regulated, conservative, and quality-assurance-oriented is quite a challenge. Peter T. Kissinger of Bioanalytical Systems (BAS) has built his business by taking the fruits of biology-based analytical chemistry research and turning them into useful products and procedures for the pharmaceutical and clinical industries.

Kissinger began trying to determine small organic molecules in biological materials in the early 1970s. At that time, samples were typically homogenized in acid, a process that not only precipitated interfering proteins but also destroyed the spatial resolution of the sample. He tried to take measurements using electrodes implanted in living tissue, but this procedure was generally unacceptable at that time because of the need to monitor several substances simultaneously. Work is actively continuing on such in vivo electrode biosensors, however.

BAS was founded in the fall of 1974 when Kissinger was on the faculty at Michigan State University. "I pretty much worked all the time and needed a hobby. Building instruments became a way to focus my excess energy. I tried to interest existing companies in our

ideas for free—we didn't bother with patents—but they had ideas of their own and technology transfer was not the fad it is now. The primary motive was to have fun. It still is!"

In 1984, Kissinger began sampling *in vivo* and using dialysis membranes to exclude proteins from samples. "This change of direction," he says, "was inspired by Urban Ungerstedt of the Karolinska Institute in Sweden, a pioneer in this field with whom we began a collaboration. Lee Phebus of Eli Lilly and Jay Justice of Emory University were also a great influence in getting us started with this approach. Because all the early work was done with brain tissue, that's where the method is most highly developed." This simple idea had significant analytical consequences: The samples are free of proteins, there is no need to homogenize tissue or add acid to denature enzymes, and the samples are clean and very compatible with LC, capillary electrophoresis, and immunoassay.

To improve the reliability of microdialysis, Kissinger's company is working with Sue and Craig Lunte of the University of Kansas to explore hollow fiber dialysis and ultrafiltration sampling devices for both *in vitro* (enzymes, microsomes, cell cultures, and tissue slices) drug discovery work and *in vivo* pharmacokinetics and toxicokinetics. Kissinger says, "The challenge is to understand the details and to make the *in vivo* sampling process easy to use. When your focus is on developing instruments and methods, you tolerate a lot. You fiddle, adjust, and make it work long enough to submit a paper or a patent. Then you take it apart and redo it. When your interest is in obtaining quality data, you tend to be a lot more focused on validation, reliability, and convenience issues. QA makes you more conservative.

"We are interested in supporting drug discovery research and clinical trials with innovative analytical chemistry that can be trusted. I've gradually



acquired an appreciation for people who use and regulate analytical chemistry. I've likewise seen how hard it is to take the innovative cutting-edge methodology and make it really work for those who need it day in and day out. We are dealing with a highly regulated and conservative audience [the pharmaceutical industry] that is in a hurry and doesn't have a lot of time to explore new techniques unless the benefits are clearly drawn out. As a commercial entity, we need to clarify these benefits. It's what we have to sell."

Kissinger also enjoys his time in the classroom. "It was a real pleasure working at Purdue and developing BAS for fun. Now it's a pleasure working at BAS and keeping a hand in at Purdue for fun. Although I had a number of truly exceptional graduate students who could work independently, I eventually had to stop taking students a few years ago because I couldn't give them 'quality time,' and it just wasn't fair to them. My arrangement with Purdue worked because of their fabulous analytical faculty, very supportive department heads, and an enthusiastic university administration. I'm not sure that combination exists at too many other institutions.

"The most satisfying thing for me is to read the papers of scientists who use our equipment and cite our papers. Our work has had an enormous impact on neuroscience research for over 20 years. Our assays have been used to develop some of the most successful drugs in history. I think that's pretty neat!"

FDA rekindles symposium on applied MS

On September 12 and 13, the Food and Drug Administration (FDA) held its first technology symposium on MS in 15 years. The symposium, co-sponsored by the FDA National Center for Toxicology Research (NCTR) and the Center for Food Safety and Applied Nutrition (CFSAN), boasted a speaker list of many of the top names in the field. Organizers Jackson Lay, Jr., of NCTR and James Sphon of CFSAN say the symposium, which attracted 250 participants, reflects the agency's growing interest in applying modern MS methods to its regulatory work and research goals.

The FDA also used the symposium as an occasion to recognize Sphon, who received an award from the agency's Office of Science for sustained achievement in regulatory MS. Sphon, director of the Center's MS lab, developed the currently used three-ion-peak minimum criterion for valid regulatory MS identification.

Several trends were emphasized in the presentations. On-line LC/MS, especially with atmospheric pressure chemical ionization or electrospray ionization, is likely to be one of the most adaptable combinations for regulatory methods development. Ion trap MS, now available in most FDA labs, is also of growing interest to the regulatory labs because it can be used for

MS* and may enable those labs to pursue multianalyte determinations inexpensively. Graham Cooks of Purdue University described some of the recent advances that have made ion trap MS reliable enough for regulatory work, and Thomas Cairns, formerly of FDA, now of Psychomedics, described trace and multiresidue analyses in typically complex food matrices.

Lay, Michael Gross of Washington University, and Michelle Buchanan of Oak Ridge National Laboratory discussed applying MS/MS structural characterization methods to study carcinogen interactions with DNA. Bernard Schwetz, director of NCTR and the FDA's associate commissioner for science, discussed some regulatory implications of this research. "MS gives us a handle to look at the [mechanisms of carcinogenesis] directly and may let us get away from having to rely only on toxicological endpoint observations [in animal models]." Donald Hunt of the University of Virginia gave another perspective on the potential of MS in cancer research in his talk on characterizing signal peptides excreted by virus- or tumor-infected cells. Knowing the structures of these peptides could allow researchers to develop vaccines against tumors.

Schwetz announced plans to hold another FDA MS symposium within the next three years, in part to foster closer ties

between the MS research community and the FDA laboratories. He and Lay both believe increased cooperation may help the agency develop more cost-effective regulatory methods. "An example was Jon Wilkes's talk on pyrolysis MS for bacterial identification," says Lay. "That came out of Army research on biological defense. We were able to apply their R&D to our problems with bacterial contamination in foods."



Yeung



Wise



Thompson



Buchanan

NOMINATIONS

■ Findeis Award

The Division of Analytical Chemistry is soliciting nominations for a new award, the Arthur F. Findeis Award for Achievements by a Young Analytical Scientist. The award, sponsored by the Phillip Morris Companies, is in memory of Arthur F. Findeis, former head of the National Science Foundation Chemistry Division's Office of Special Projects, and is intended to recognize outstanding contributions to the fields of analytical chemistry by a young scientist. This first award will be presented at the Eastern Analytical Symposium in November 1996 and will consist of \$4000, a plaque, and a travel allowance to attend the ceremony.

Nominees must have earned their highest degree between Jan. 1, 1986, and Jan. 1, 1996. Contributions by a candidate that have been recognized by a prior Divisional or ACS national award will not be considered for this award. For additional information, contact Henry Blount at 3234 Valley La., Falls Church, VA 22044-1739 (703-306-1841; fax 703-306-0534). For this inaugural presentation only, deadline is Dec. 1.

New DAC officers

Edward S. Yeung of Iowa State University/Ames Laboratory began a one-year term as chair of the ACS Division of Analytical Chemistry on Oct. 1. He joins Stephen Wise of the National Institute of Standards and Technology, chair-elect; Robert Thompson of Oberlin College, secretary; Michelle Buchanan of Oak Ridge National Laboratory, treasurer; four councilors; and four alternate councilors as members of the executive committee of the Division. The chair also serves as an ex-officio member of the *Analytical Chemistry* Editorial Advisory Board. Elections are held each spring; winners are announced at the fall national meeting.

Putting Opposites

Guidelines for Successful SFC/MS

In the early days of on-line LC/MS, Arpino likened the union of these two instruments to the unlikely marriage of a bird and a fish: "Many believe this coupling is even more difficult to achieve than the love-match . . . between two creatures that are at ease in their own environments but are not at home in both" (1). At first consideration, this combination of high-pressure and vacuum techniques does seem preposterous. Removing a molecule from its high-pressure solvent, transporting it preferentially over vaporized solvent to a partial vacuum, and imparting a charge on the analyte does seem a challenging feat. However, great progress was made and LC/MS applications have become routine.

But what if the analyte were dissolved in a fluid that, at high pressure, solvated like a traditional liquid but transformed to an easily removed gas when the pressure dropped, leaving the analyte free to "fly like a bird"? This was the promise offered by supercritical fluid chromatography (SFC)/MS when research in the area began in the late 1960s (2-5). Admittedly, the analogy should not be carried too far. Nevertheless, the commonly used mobile phases in SFC/MS, such as CO₂, are much more easily pumped from a high to moderate vacuum system than are

The proper chromatographic and mass spectrometric choices can make the difference between success and failure

common LC mobile phases. Although modern instrumentation provides nearly routine LC/MS, SFC/MS still offers distinct advantages, some chromatographic, some mass spectrometric.

For example, the supercritical fluid mobile phase provides liquid-like interactions with solutes so that species with volatilities too low for GC can be eluted in SFC (6). In addition, because diffusion coefficients are generally higher in supercritical fluids than in liquids, separations of relatively nonpolar species can be performed more quickly in packed-column SFC than in LC (7). Similarly, because viscosities of supercritical fluids are lower than those of common solvents, the pressure drop required to produce mobile-phase flow is lower, and therefore longer packed columns can be used in SFC than in LC (with correspondingly higher total plate counts [8]). In the MS realm, the effluent from open-tubular SFC columns can be introduced directly into electron ioniza-

tion (EI) or chemical ionization (CI) ion sources with a very simple interface. EI and CI have been studied for years and offer great versatility in characterizing unknown mixtures.

Despite these advantages, there are relatively few practitioners of SFC/MS, although the range of potential applications warrants greater interest, particularly in industries such as consumer products, fossil fuels, food, and pharmaceuticals. The proper chromatographic and mass spectrometric choices made by the analyst can make the difference between success and failure.

SFC guidelines

Factors that must be considered for a successful SFC/MS marriage include the types of analytes, injection method, and hardware. Most of our experience has involved using open-tubular SFC combined with the direct fluid introduction (DFI) interface on a triple quadrupole mass spectrometer with an m/z range of 4000 Da per unit charge. Packed-column SFC/MS is possible with this interface and instrument but requires additional pumping or flow splitting to accommodate the larger mobile-phase mass flow rate, especially with a traditional 4.6-mm-i.d. packed column.

Analytes. Open-tubular SFC with CO₂ mobile phase works best for low-to-medium-polarity solutes. Analytes that are more polar can be eluted using CO₂ modified with a polar solvent, or they can often

J. David Pinkston
Thomas L. Chester
The Procter & Gamble Company

TOGETHER

SFC MS

be derivatized and then separated using pure CO₂. The disadvantage of this approach is not the derivatization but the mass of the derivatives—those derivatives that are double the mass of the original solute effectively halve the solute upper mass limit from the MS perspective. Nonetheless, this approach is very effective, and the added moieties may also aid in detection and/or structure elucidation.

Because SFC can be performed at low temperatures, solutes too labile for GC can be separated. Although the nominal temperatures at the tip of the interface and within the ion source are usually higher than in the chromatographic oven, the actual temperatures experienced by the analytes are much lower because of Joule-Thompson cooling. In addition, the analytes experience these temperatures for only a brief moment. Thus, any observed

degradation usually occurs in the chromatographic column rather than in the interface or mass spectrometer.

Injection. Injections of up to ~ 10 μ L are usually not difficult with packed-column SFC. Direct injection in a style essentially identical to that used in LC usually works well, even on microbore packed columns, as long as the analyst remembers that the injection solvent is usually stronger than the mobile phase. Injection conditions must be mild enough that solutes will be initially retained on the stationary phase in the presence of injection-solvent modifier. In some cases, the addition of well-swept volume between the injector and the column may improve the peak shapes by providing a means of diluting the injection solvent with mobile phase, weakening the binary mixture, and improving the solute focusing. However,

time must be allowed for transport of the solute through this extra volume.

Because the effects of sample inhomogeneity are greatly exaggerated by sub-microliter injection volumes, the solvent must completely dissolve the sample, and the transport behavior of the solvent in the mobile phase must be understood. This cannot be neglected or underestimated in open-tubular SFC. Solvents that are miscible in all proportions with liquid CO₂ are often chosen, and it is erroneously assumed that they stay mixed on transport to the oven. This is not necessarily the case, depending on the chosen temperature and pressure.

Figure 1 is a pressure-temperature phase diagram that shows how binary mixtures can exist in a single phase in the injector (at room temperature) and subsequently split into two phases upon trans-

port to the oven. It is not desirable to deliver large volumes of liquid or high vapor-phase concentrations of sample solvent to the analytical column, because these fluids are usually much stronger than the pure mobile phase and may deposit solutes over a large band before dissipating. Open-tubular SFC has historically used flow- or time-splitting injection to avoid these pitfalls, and solvent-venting injection and other solvent elimination techniques have been used with varying degrees of success. However, these techniques add more and often expensive hardware to the system and more steps to the analysis.

We prefer direct injection onto a retention gap. Solutes are distributed in broad bands on the retention gap, then focused by the solvent effect or by phase-ratio focusing before migration begins on the analytical column (9). We have injected sample volumes up to 1 μL onto 50- μm -i.d. columns with this approach. Its real beauty, aside from negligible cost, is that it is easy. We have already mapped the phase behavior of 13 CO_2 -solvent mixtures and can specify appropriate injection conditions (10). The actual injection technique requires no additional decisions and no special operator skills; the details of the rather complicated mass transfer process take place automatically. Relative standard deviations of absolute peak areas are $\sim 1\%$ for most solutes, which allows external standardization.

Hardware. SFC/MS of solutes with molecular masses up to 4000 Da is straightforward if the SFC instrument can elute the solutes. The pumps available on commercial open-tubular SFC systems are limited to 42.0 MPa (415 atm). A 68.9-MPa (680 atm, 10,000 psi) pump can greatly increase the analysis range. This pump can be added to a commercial SFC system with appropriate safety precautions, but needs a separate controller.

Because of relatively low flow rates and small volumes, making proper connections is also critical to success in open-tubular SFC. (Packed-column SFC is more forgiving.) An ideal union would be compatible with the full range of operating temperatures and pressures, easy to install, free of any dead volume, reusable, and inexpensive. A variety of low- and zero-dead-volume unions are available that

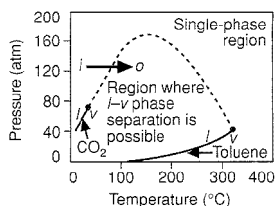


Figure 1. Pressure-temperature phase diagram for CO_2 -toluene mixtures.

All CO_2 -toluene mixtures, regardless of proportions, exist as a single liquid phase in the room-temperature injector *i*. However, when a plug of toluene is transported to the SFC oven *v*, the necessary liquid *l* to vapor *v* phase separation occurs as the fluid is heated. This phase separation is necessary for direct injection onto a retention gap.

have their advantages and drawbacks. We have recently begun to explore a unionless retention gap-column-restrictor system that greatly simplifies plumbing the chromatograph. These systems consist of an uncoated but deactivated retention gap and a coated column made from a single piece of fused-silica tubing with an integral flow restrictor fashioned on the end of the column. These work very well as long as the phase is stabilized.

In most SFC/MS separations using an unmodified supercritical fluid, the mobile-phase pressure is programmed to increase the strength of the mobile phase. Because fixed flow restrictors are most often used, the increased pressure means increased flow of mobile phase into the ion source. The rate of increase of mobile-phase flow depends significantly on the type of restrictor used: the frit restrictor (11), the short-tapered or integral restrictor (12), or the tapered capillary restrictor (13). Only the frit and integral restrictors are available commercially.

The rate of mobile-phase flow increase is less with restrictors that have more turbulent flow characteristics (e.g., integral, crimped metal capillary, and pinhole restrictors) than it is with restrictors that have more laminar flow characteristics (e.g., linear, thin-walled tapered, and multipath frit restrictors). The multipath frit restrictor is rugged but is not suitable for many solutes over ~ 2000 Da (14). Integral restrictors are rugged and

can be easily cleared by applying heat and pressure. To date, we have found no performance advantages of the tapered capillary over the integral restrictor, though some speculate that the tapered capillary may perform better with high molecular weight solutes. We recommend the integral restrictor for most SFC/MS applications.

The choice of restrictor flow rate involves a compromise. Fast-flowing restrictors (3–10 cm/s on a 50- μm open-tubular column) plug less frequently (and are easier to unplug when they do) than slow-flowing restrictors when used to analyze relatively nonvolatile analytes. On the other hand, the high mobile-phase velocity means less chromatographic efficiency and a higher gas load introduced into the mass spectrometer. For practical, day-to-day analyses, we opt for fast-flowing restrictors. A traditional, differentially pumped mass spectrometer can maintain a reasonable analyzer pressure when operated with a DFI interface, a 50- μm open-tubular column, and a fast-flowing, integral-style restrictor (15).

MS guidelines

Mass spectrometric choices that must be made for successful SFC/MS include the type of mass spectrometer, the configuration of the vacuum system, and the form of ionization. But perhaps the most obvious and visible choice involves the type of interface used to connect the chromatograph and the mass spectrometer.

Interfaces. Typically, mobile-phase flow rates in open-tubular SFC are such that the entire effluent may be directly introduced into the ion source of a modern mass spectrometer designed for GC/MS, resulting in a DFI interface (4, 16, 17). This simple interface consists of a stem that houses the chromatographic column or a transfer line that is held at the same temperature as the chromatographic oven. The tip of the interface houses the flow restrictor and is typically heated at 150–450 $^{\circ}\text{C}$ to counteract the Joule-Thompson cooling of the expansion and to provide some volatility to the eluting analytes. The tip is usually positioned so that the effluent is introduced directly into the ionization region. Given its simplicity and flexibility, the DFI interface is used most often.

Because the mobile-phase flow rates of conventional packed, microbore, and packed-capillary SFC columns are typically too high for direct introduction to the ion source, a variety of mobile-phase elimination and flow-splitting interfaces (based on similar LC/MS interfaces) have been devised for packed-column SFC/MS. The two primary mobile-phase elimination interfaces are the moving-belt (18) and particle-beam (19) interfaces. The advantage of these interfaces is that they can "divorce" the chromatograph from the mass spectrometer. Chromatographic separation, analyte ionization, and mass analysis can each be performed under optimized conditions.

Once transported into the ion source, the analytes are volatilized by heating the moving belt or the particle, so thermally labile analytes may suffer some degradation. Most attempts to use the particle-beam interface for SFC/MS have used interfaces designed for LC/MS with few modifications (19). These attempts have generally resulted in markedly poor limits of detection, which have been attributed to the differences between solvent evaporation and particle formation in LC and in SFC. A recent particle-beam interface designed specifically for SFC/MS performs much better (20).

The simplest splitting interface is the pre-expansion splitting interface, in which a portion of the chromatographic effluent from the packed column is directed to the mass spectrometer using a DFI interface (21). The balance of the effluent goes to other detectors or is discarded. Other packed-column interfaces may be characterized as postexpansion splitting interfaces, in which the entire expanded effluent is directed to an ionization region. Much of the effluent, as well as many of the ions formed, is pumped from the ionization region and never reaches the mass-analysis region of the mass spectrometer. Prominent members of this particular class of interfaces are the thermospray (22, 23), the heated nebulizer for atmospheric pressure CI (24, 25), the electrospray (26), and the "high-flow-rate" interfaces (27, 28).

These interfaces have an advantage over the pre-expansion interfaces in that focusing fields in the ion-sampling region may enhance the total number of ions di-

rected to the mass analysis region. Of the postexpansion interfaces, the thermospray and heated nebulizer, used for atmospheric pressure ionization (API), are used most often. They are both reasonably simple and have good performance characteristics. Because the heated nebulizer operates at atmospheric pressure, the chromatograph and mass spectrometer can operate more independently, and making alterations or adjustments to the interface is easier.

Instrumentation. The quadrupole mass spectrometer (4, 17) still holds the winner's hand of positive attributes for SFC/MS. High sensitivity, reasonable m/z range (up to 4000 for research-grade instruments), moderate cost, and straightforward interfacing are among the reasons most practitioners have chosen quadrupole instruments for their laboratories.

The most obvious and visible choice is the type of MS interface.

However, MS/MS is a sequential-in-space experiment with a quadrupole-based instrument and requires multiple quadrupoles, which raises the cost of quadrupole-based MS/MS instruments significantly. This stands in sharp contrast to the sequential-in-time MS/MS available at relatively little additional cost on the Fourier transform (FT) and Paul ion trap instruments. The low-energy (generally up to 200-eV) collision-induced dissociation (CID) available on quadrupole MS/MS instruments is sufficient for most analytes with m/z below a few thousand.

Modern sector mass spectrometers provide high sensitivity, high resolution, and higher m/z range (up to 8000–10,000 for research-grade instruments) than typical Paul ion trap or quadrupole mass spectrometers. They also provide high-energy CID for MS/MS, which can be critical for molecules with molecular

weight greater than a few thousand. Interfacing SFC to the ion source of sector mass spectrometers, which generally operate at voltages of 3–10 kV, has been accomplished with carefully designed probes (16, 29). The vacuum systems of most modern sector instruments can easily handle the gas load of open-tubular SFC. Traditionally, the primary disadvantage of sector instruments has been their high cost relative to that of quadrupole instruments. This differential is shrinking as lower cost sector instruments reach the market.

The FT-MS instrument offers ultrahigh resolution, simultaneous detection of all ions, and a wide mass range. Yet, the performance of most SFC/FT-MS combinations described in the literature suffers from the high SFC gas load and a longer-than-usual interface line (30, 31). A differentially pumped external ion source would remove these obstacles. The cost of an FT-MS instrument has traditionally been higher than that of many other mass spectrometers.

The Paul ion trap can provide high sensitivity and a reasonable mass range, despite its small size and relatively low cost. However, when used for SFC/MS, it has problems dealing with the high SFC gas load (32, 33). Ion traps usually operate with a relatively high pressure of helium as damping gas within the trap. Most SFC mobile phases are not good damping gases. As with the FT instrument, a differentially pumped external ion source coupled to a Paul ion trap should provide good performance.

Although time-of-flight (TOF) mass spectrometers designed for the detection of chromatographic effluents are not widely available today, advances in high-speed electronics and technology may soon give the nod to TOFMS for sensitivity, cost, and versatility (34, 35). However, even when the choice of mass spectrometer has been made, other choices remain that are at least as, if not more, critical to success. The two most important are the vacuum system and the m/z range of the instrument.

Vacuum system. Differential pumping became popular in the early GC/MS instruments. In this approach, the ion source and mass analyzer vacuum regions are isolated from each other, with

the exception of a small slit or hole to allow passage of the ions. The analyzer can operate at much lower pressure than the ion source and thus provide good performance despite a relatively high gas load entering the source.

Recent design improvements have made instruments more tolerant of high gas loads because economic pressures have pushed instrument companies to manufacture singly-pumped systems. Commercial quadrupole mass spectrometers are now available with a variety of vacuum systems, from low-end benchtop instrument systems with a single high-vacuum pump to high-end research-grade instruments that are differentially pumped. Most sector mass spectrometers are differentially pumped.

Although singly-pumped instruments perform satisfactorily under some conditions in SFC/MS, the analyzer pressure rises to unacceptable levels and the performance drops at higher SFC mobile-phase flow rates. For this reason, we strongly advise using a differentially pumped mass spectrometer for SFC/MS to provide satisfactory performance over a wide range of conditions. Under certain circumstances, supplemental pumping may be required for a differentially pumped system (15).

Range of m/z . Quadrupole mass spectrometers with upper m/z range limits between 650 and 4000 have been used for SFC/MS. What is the "best" m/z range for a mass spectrometer for SFC/MS? The answer depends on the application for which the instrument is intended. If the anticipated analytes are low molecular weight, thermally labile compounds, then an upper mass range limit below m/z 1000 may be satisfactory. However, if the analytes will be higher molecular weight compounds of relatively low volatility, such as non-ionic surfactants or oligomeric species, a higher upper m/z range limit may be appropriate. Ultimately, the choice in upper m/z limit often pits cost against anticipated applications. The higher-cost research-grade mass spectrometers will be applicable to a wider range of analytes.

Ionization mode. Open-tubular SFC using a DFI interface and a traditional EI or CI source gives the analyst a good deal of flexibility. EI is advantageous because

it is the most widely accepted ionization method for structure elucidation. EI fragmentation mechanisms have been studied for years, many are well understood, and large libraries of EI spectra have been compiled that may be used for automated searching and matching.

CI provides a great deal of flexibility in the amount of internal energy deposited in the analyte upon ionization. A spectrum can be produced with a little or a lot of fragmentation, depending on the proton affinities of the analyte and reagent ions produced in the CI plasma of the reagent gas. Thus, reagent ions with proton affinities near those of the analytes can be used to produce spectra with little fragmentation for mixture analysis or to provide precursor ions for tandem MS experiments. Lower proton-affinity reagent ions can be used to produce a spectrum with more fragmentation for single-stage MS structure elucidation.

There has been a good deal of discussion on the influence of the SFC mobile phase on ionization when the DFI interface is used (36, 37). With a fixed flow restrictor, the partial pressure of the mobile phase in the ion source increases over the course of a pressure-programmed separation. In addition, fast-flowing restrictors (higher linear velocities) mean higher pressures of mobile phase in the ion source.

Despite these variables, certain general conclusions can be drawn. In EI SFC/MS, mobile-phase-mediated charge-exchange ionization occurs at high mobile-phase flow rates (i.e., at high mobile-phase pressure or when using a fast-flowing restrictor). This is generally not a great disadvantage. The ions generated in the charge-exchange plasma of the CO_2 mobile phase have recombination energies that allow ionization and fragmentation of virtually all organic compounds. The spectra produced when charge-exchange conditions prevail in EI SFC/MS resemble EI spectra that can be searched in EI libraries. However, the charge-exchange spectra usually exhibit less fragmentation because of differences in the amount of internal energy deposited and because of collisional stabilization.

Recently we have shown that a more open EI source, combined with a relatively fast-flowing integral restrictor, pro-

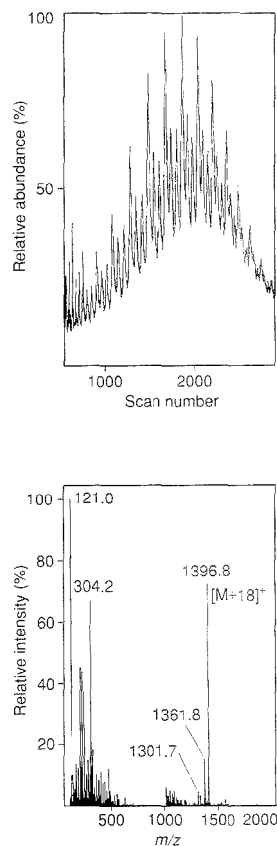


Figure 2. SFC/MS separation of a functionalized polydimethylsiloxane

(a) Reconstructed ion chromatogram of 0.06 μL of a solution of a modified polysiloxane injected directly onto a unionless retention gap-column-restrictor system. The mobile phase was CO_2 . The mass spectrometer was scanned from m/z 100 to 2000 every 1.9 s. (b) NH_3 CI spectrum of the oligomer containing 16 dimethylsiloxane units from the chromatogram in (a). The spectrum shows an ammonium adduct ion at m/z 1396.8, a small protonated molecule, and an ion corresponding to loss of water from the protonated molecule at m/z 1361.8.

vides true EI conditions up to the 56.7-MPa limit of our SFC pump. We obtained these results using probe analytes that bracket the recombination energies of the reagent ions that exist in the CO_2 charge-exchange plasma. CI spectra arc

inherently more variable because of the number of parameters that influence these spectra (reagent gas and its pressure, ion source configuration, and temperature). Therefore, there is less agreement in the literature on the influence of the SFC mobile phase on CI spectra. Collisional stabilization and charge-exchange ionization likely occur at high SFC flow rates.

Recently Sadoun described ESI for SFC/MS (26) using an interface that accommodated flow rates typical of open-tubular and packed-capillary SFC. The nebulizing effect of the expanding mobile phase allowed significantly higher flows of a polar organic modifier (methanol) than are possible in traditional ESI for LC/MS. However, memory effects were observed from analytes deposited on the electrospray needle and the authors suggested using a sheath flow of polar organic solvent to eliminate this problem. We have since designed and tested a sheath-flow interface for ESI SFC/MS (38). This interface allows the use of unmodified CO₂ for the mobile phase, is compatible with open-tubular and packed-column flow rates, and can be used for a variety of polar and nonpolar analytes.

Postexpansion splitting interfaces are most often used in packed-column SFC/MS. With these interfaces, the mode of ionization is often dictated by the interface and mobile phase. The high mobile-phase flow rate associated with these interfaces typically allows only high-pressure ionization mechanisms such as CI. When a polar organic modifier is added to the mobile phase, reagent ions from the modifier often dominate the CI plasma, but this is generally not a disadvantage. When an interface incorporating API is used, the CI mechanisms typical of API are usually observed. In many cases this consists of water CI, if traces of water are present in the ionization region.

Applications

Nonpolar polysiloxanes are important active components in many industrial and consumer products. They may be present at relatively low concentrations and found with many other components. The distribution of the polysiloxane, as well as the nature of the terminal groups or of a functionalized moiety, may reveal important information about the process used to syn-

thesize a larger, siloxane-containing polymer. Siloxanes with molecular weights of up to ~20,000 are readily amenable to characterization by SFC, provided the proper type of flow restrictor is used (14). Figure 2a shows the reconstructed ion chromatogram of a functionalized polydimethylsiloxane injected directly onto a unionless retention gap-column-restrictor system. Figure 2b shows the NH₃ CI spectrum of one of the peaks from Figure 2a, the oligomer containing 16 dimethylsiloxane groups. We believe that this oligomer is capped with a phenyl group on one end and an alkyl chain bearing a hydroxyl group on the other.

The analysis of more polar ethoxylated surfactants has been a traditional strength of SFC (39). For example, ethoxylated alcohols are complex mixtures of considerable industrial importance. Characterization of the chain lengths and branching patterns of these alcohols and the distribution of the ethoxylate chain are important to ensure not only proper performance but also environmental compatibility. Ethoxylate chains that are longer than ~10–15 units are not sufficiently volatile to be amenable to traditional GC separation, so a combination of GC and LC is used.

The alcohol distribution is characterized by GC after the ethoxylate chain is cleaved, and the ethoxylate distribution is obtained by LC after a chromophore is added by derivatization. In contrast, a sin-

gle SFC separation provides both alcohol and ethoxylate distribution data without derivatization because ethoxylated alcohols can be eluted with pure CO₂, which is compatible with flame-ionization detection. SFC/MS is used to confirm peak identities in new or unusual samples and is especially useful in studying byproducts or other species that are present at low levels.

Mebeverine, an antispasmodic agent marketed in Europe, is difficult to determine at trace and ultratrace levels because it irreversibly binds to GC columns and suffers thermal degradation. The LC method is satisfactory with a detection limit of ~10 ng/mL of plasma, but analysts seeking a lower detection limit came to us to see whether SFC/MS could do the job. Ammonia CI and selected ion monitoring of mebeverine and of D₄-mebeverine, the stable-isotope-labeled internal standard, provided the improved detection limit (40). As in GC and LC, proper deactivation of the SFC column was necessary to achieve these detection limits.

Organic ions are usually too polar to be eluted with pure CO₂. However, they can often be made soluble in CO₂ by chemical derivatization. We faced a problem involving low molecular weight (<~4500) poly(acrylic acid) (PAA). Project team members believed that certain terminal groups on the polymer chain might adversely affect the performance of the product into

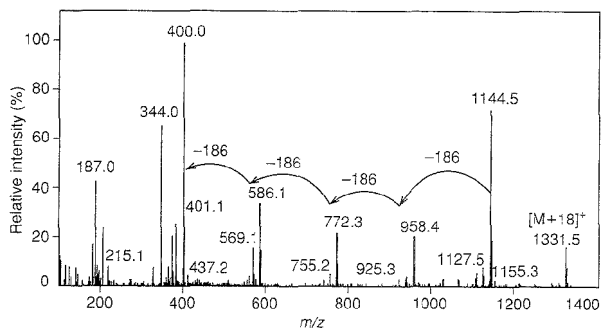
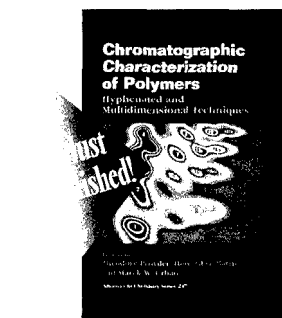


Figure 3. NH₃ CI mass spectrum of the *n* = 6 oligomer of derivatized poly(acrylic acid).

(Adapted with permission from Reference 41.)



Chromatographic Characterization of Polymers: Hyphenated and Multidimensional Techniques

This important new volume presents an overview of some of the significant developments in the use of hyphenated multidimensional separation methods for polymer characterization. Divided into three sections, the book covers:

- general considerations
- light scattering and viscometry
- analysis of compositional heterogeneity and blends.

Among the chromatographic separation techniques discussed are: size-exclusion chromatography, liquid chromatography, and field-flow fractionation methods used in conjunction with information-rich detectors such as molecular size- or compositional-sensitive detectors and that are coupled in cross-fractionation modes.

Valuable reading for both academic and industrial scientists developing chromatographic methods for polymers or conducting polymer research.

Theodore Provdror, The Glidden Company, Editor

Howard G. Barth, DuPont, Editor

Marek W. Urban, North Dakota State University, Editor

Advances in Chemistry Series No. 247
314 pages (1993) Clothbound
ISBN 0-8412-3132-X
\$124.95

ORDER FROM

American Chemical Society
1155 Sixteenth Street, NW
Washington, DC 20036
Or CALL TOLL FREE

1-800-227-5558

(in Washington, DC 872-4363) and use your credit card!

FAX: 202-872-6067.

ACS Publications Catalog now available on Internet:

gopher acsinfo.acs.org or
URL <http://pubs.acs.org>

which the PAA was incorporated, but the PAA supplier would not (or could not) reveal the nature of the terminal groups. We performed an SFC separation of the PAA after formation of the *tert*-butyldimethylsilyl (TBDMS) derivative (41).

Figure 3 shows the NH_3 CI SFC/MS spectrum of one of the oligomers. Notice the successive losses of 186 Da, corresponding to TBDMS-derivatized acrylic acid, the oligomeric unit. (The most abundant isotope of the ammonium-adduct ion cluster is shifted by one mass unit because of the silicon isotopes.) Using data from the EI and CI SFC/MS separations, we postulated that the terminal groups were sulfonate and hydrogen, which was subsequently confirmed by the supplier.

Certain choices favor a more successful marriage between SFC and MS. SFC/MS has some distinct advantages, especially in applications where GC/MS and LC/MS are difficult. Complex mixtures, such as surfactants, emulsifiers, low molecular weight polymers, fats, oils, and waxes, that have relatively low volatility can benefit from the versatility offered by SFC/MS.

References

- (1) Arpino, P. J. *TrAC* **1982**, *1*, 154-58.
- (2) Milne, T. A. *Int. J. Mass Spectrom. Ion Phys.* **1969**, *3*, 153-55.
- (3) Giddings, J. C.; Myers, M. N.; Wahrhaftig, A. L. *Int. J. Mass Spectrom. Ion Phys.* **1970**, *4*, 9-20.
- (4) Smith, R. D.; Felix, W. D.; Fjeldsted, J. C.; Lee, M. L. *Anal. Chem.* **1982**, *54*, 1883-85.
- (5) Smith, R. D.; Kalinoski, H. T.; Udseth, H. R. *Mass Spectrom. Rev.* **1987**, *6*, 445-96.
- (6) Chester, T. L.; Pinkston, J. D.; Owens, G. D. *Carbohydr. Res.* **1989**, *194*, 273-79.
- (7) Schleimer, M.; Schurig, V. In *Analysis with Supercritical Fluids: Extraction and Chromatography*, Wenclawiak, B., Ed.; Springer-Verlag: Berlin, 1992; pp. 134-50.
- (8) Berger, T. A.; Wilson, W. H. *Anal. Chem.* **1993**, *65*, 1451-55.
- (9) Chester, T. L.; Innis, D. P. *Anal. Chem.* **1995**, *67*, 3057-63.
- (10) Ziegler, J. W.; Dorsey, J. G.; Chester, T. L.; Innis, D. P. *Anal. Chem.* **1995**, *67*, 456-61.
- (11) Cortes, H. J.; Pfeiffer, C. D.; Richter, B. E.; Stevens, T. S. U.S. Patent 4 793 920, 1988.
- (12) Guthrie, E. J.; Schwartz, H. E. *J. Chromatogr. Sci.* **1986**, *24*, 236-41.
- (13) Chester, T. L.; Innis, D. P.; Owens, G. D. *Anal. Chem.* **1985**, *57*, 2243-47.
- (14) Pinkston, J. D.; Hentschel, R. T. *J. High Resolut. Chromatogr.* **1993**, *16*, 269-74.
- (15) Pinkston, J. D.; Bowling, D. J. *Anal. Chem.* **1993**, *65*, 3534-39.
- (16) Huang, E. C.; Jackson, B. J.; Markides, K. E.; Lee, M. L. *Anal. Chem.* **1988**, *60*, 2715-19.
- (17) Pinkston, J. D. et al. *Anal. Chem.* **1988**, *60*, 962-66.
- (18) Berry, A. J.; Games, D. E.; Perkins, J. R. *J. Chromatogr.* **1986**, *363*, 147-58.
- (19) Edlund, P. O.; Henion, J. D. *J. Chromatogr. Sci.* **1989**, *27*, 274-82.
- (20) Jedrzejewski, P. T.; Taylor, L. T. *J. Chromatogr. A* **1995**, *703*, 489-501.
- (21) Holzer, G.; Deluca, S.; Voorhees, K. J. *HRCC* **1985**, *8*, 528-31.
- (22) Balsevich, J. et al. *J. Nat. Prod.* **1988**, *51*, 1173-77.
- (23) Saunders, C. W.; Taylor, L. T.; Wilkes, J.; Vestal, M. *Am. Lab.* **1990**, *22*, 46-53.
- (24) Huang, E. C.; Wachs, T.; Conboy, J. J.; Henion, J. D. *Anal. Chem.* **1990**, *62*, 713 A-724 A.
- (25) Tyrefors, L. N.; Moulder, R. X.; Markides, K. E. *Anal. Chem.* **1993**, *65*, 2835-40.
- (26) Sadoun, F.; Vrelizier, H.; Arpino, P. J. *J. Chromatogr.* **1993**, *647*, 351-59.
- (27) Smith, R. D.; Udseth, H. R. *Anal. Chem.* **1987**, *59*, 13-22.
- (28) Cousin, J.; Arpino, P. J. *J. Chromatogr.* **1987**, *398*, 125-41.
- (29) Kalinoski, H. T.; Udseth, H. R.; Chess, E. K.; Smith, R. D. *J. Chromatogr.* **1987**, *394*, 3-14.
- (30) Lee, E. D.; Henion, J. D.; Cody, R. B.; Kinsinger, J. A. *Anal. Chem.* **1987**, *59*, 1309-12.
- (31) Baumeister, E. R.; West, C. D.; Ijames, C. F.; Wilkins, C. L. *Anal. Chem.* **1991**, *63*, 251-55.
- (32) Todd, J. F. J. et al. *Rapid Commun. Mass Spectrom.* **1988**, *2*, 55-58.
- (33) Pinkston, J. D.; Delaney, T. E.; Morand, K. L.; Cooks, R. G. *Anal. Chem.* **1992**, *64*, 1571-77.
- (34) Sin, C.; Pang, H.; Lubman, D. M.; Zorn, J. *Anal. Chem.* **1986**, *58*, 487-90.
- (35) Schultz, G. A. et al. *J. Chromatogr.* **1992**, *590*, 329-39.
- (36) Houben, R. J.; Leclercq, P. A.; Cramers, C. A. *J. Chromatogr.* **1991**, *554*, 351-58.
- (37) Kalinoski, H. T.; Hargiss, L. O. *J. Chromatogr.* **1990**, *505*, 199-213.
- (38) Pinkston, J. D.; Baker, T. R. *Rapid Commun. Mass Spectrom.*, in press.
- (39) Pinkston, J. D.; Bowling, D. J.; Delaney, T. E. *J. Chromatogr.* **1989**, *474*, 97-111.
- (40) Pinkston, J. D. et al. *J. Chromatogr.* **1993**, *622*, 209-14.
- (41) Pinkston, J. D.; Delaney, T. E.; Bowling, D. J. *J. Microcol. Sep.* **1990**, *2*, 181-87.

J. David Pinkston, of Procter & Gamble's Corporate Research Division, focuses on SFC and coupling microcolumn separations to MS. Thomas L. Chester, head of Procter & Gamble's Separations and Optical Spectroscopy Section, focuses his work on analytical uses of supercritical fluids, high-resolution chromatography, and separations theory. Address correspondence about this article to Pinkston at Procter & Gamble, Corporate Research Division, Miami Valley Laboratories, P.O. Box 538707, Cincinnati, OH 45253-8707.

METROHM RAISES MOISTURE ANALYSIS TO A NEW LEVEL.



Brinkmann brings you two new Metrohm Karl Fischer Titrators for the highest levels of quality data and convenience.

NEW Coulometric Karl Fischer Model 737 for trace moisture analysis as low as 1 ppm. Titration cell has no diaphragm, allowing quick and easy cleaning and minimum downtime.

NEW Volumetric Karl Fischer Model 720 determines moisture quickly and accurately from 10 ppm to 100%. Store up to 60 titration methods. Perform direct or back titrations.

NOW have an economical, easy-to-use Karl Fischer workstation. Connect either instrument to a balance, printer, or your PC with *ready-to-use software* for an accurate automatic system.

For a demonstration, call 1-800-645-3050 (fax 1-516-334-7506).
In Canada, call 800-263-8715 (fax 905-826-5424).

BRINKMANN Quality products for research and control.

Brinkmann Instruments, Inc., One Cantiague Road, Westbury, NY 11590-0207
Brinkmann Instruments (Canada) Ltd., 8670 Campobello Road, Mississauga, Ont. L5N 2L8
Outside U.S. and Canada; Metrohm Ltd., Switzerland • Phone: 071/53 85 85 • Fax: 071/53 89 01

 **Metrohm**



0701-333-MET

CIRCLE 2 ON READER SERVICE CARD

Tracking Calibration Records



Calibration Manager

Blue Mountain Software
208 W. Hamilton Ave.
State College, PA 16801
814-234-2417; fax 814-234-7077
Version 1.1; \$1295

Performing accurate analytical testing requires calibration of the analytical instrumentation and apparatus involved. These records must be maintained and updated as needed to ensure accurate data reporting, to meet regulatory requirements of government and contractual commitments on QA/QC, to satisfy supplier and customer demands for documented QA performance, and to obtain ISO certification.

Most laboratories maintain written calibration records and scheduled times for recalibration. *Calibration Manager* is an effective tool for tracking calibration records, scheduling recalibrations, and documenting the findings. This DOS-based relational database software was easy to install on a 90-MHz Pentium (with a new Intel chip) running MS-DOS 6.22. It requires 1.5 MB of free hard drive disk space and an additional 420 KB for the tutorial program. About 560 KB of free RAM is required to run the program. Additional hard disk space is needed depending on the items whose calibration records are being tracked.

Users first establish a master equipment listing. Printout reports of equipment calibration due dates and corresponding forms prompt lab personnel to check the calibrations and record the results in the electronic database.

Password protection at authorization levels ranging from administrator to user to database viewer can be used to limit access. If activated, an audit trail feature automatically logs the user, date and time of all changes made to the equipment master list, calibration history, and measurement records. Both old and new values are recorded. Although it slightly slows the data entry process, this feature is useful for tracking how equipment records have been updated or modified. It is especially important for those who need to provide a high degree of assurance that records cannot be tampered with or changed unknowingly.

Menu-driven options were easy to follow, even if the program is only used occasionally. Most program features can be run from the main menu without memorizing special commands. This includes accessing equipment master or calibration

history files, generating reports of when calibrations are due, or customizing a number of other specialized report forms or summaries.

The master equipment file is the most critical. A separate file is established for each piece of equipment, and it includes a unique identification number that is assigned for each item along with specific information about the type of equipment, manufacturer, model and serial numbers, department and location, contact person, date of acquisition, and usage. Details can also be entered about the calibration procedure, standards to be used, and estimated cost and time needed to perform the task. The calibration history table allows users to record the calibration procedure and standard used, the target values and upper and lower acceptable limits, the values before and after recalibration, whether adjustments were needed, and

EQUIPMENT MASTER	
System ID: CALIPER	Current Due Date: 01/20/1995
Component ID: 001	Future Due Date: 02/20/1995
	Last Calibrated: 12/19/1994
Type: Dial Caliper Gage	
Description: Internal Dial Caliper	
Manufacturer: SPI	
Model: INTERTEST	Serial No.: 20-570-8
Department: Production	Location:
Contact Person: Matthew Aronson	Acquired: 01/04/1989
Calibrator: Mark Kauffman	Usage: Seldom
Status: Active	Status Date: 01/04/1989
Due Date Calculation	Special Dates
Base Date: 03/18/1992	Reminder Days: 00
Interval: Month	Reminder Date: 12/20/1994
Number: 1	Special Due Date: 02/31/1995
Basis for calculation of due dates: Current Due Date	
F1-Help F2-Pick F4-Select F5-Delete F6-Table F9-Prev F10-Next Esc-Exit	
Record: 4 of 13	VIEW/EDIT Page: 1 of 3

Calibration Manager's master equipment listing provides information about the specific piece of equipment as well as a calibration history.

other comments (e.g., whether the instrument was in or out of calibration).

Data sorting by lab location, individual owner, time when calibrations are due, or many other parameters was straightforward and logically laid out. Files that are no longer needed can be archived onto disk for storage, thus improving the overall performance of the program speed when conducting searches. Archived records can be reloaded if needed.

Both beginners and advanced users will appreciate the well-organized manual. The tutorial addresses all the initial questions a beginner would have in setting up the information for all the instrumentation to be tracked by the program. After spending a few hours learning the basics of the package, novice users should be able to customize the package for their individual lab. Examples in the tutorial, together with the templates, are excellent for hands-on demonstrations of all major features.

I encountered one software conflict when I tried to delete records while running *Calibration Manager* in a DOS window under Windows 3.1. I consider this a minor disadvantage in an otherwise good software package. Although many users may be able to use the package with minimal training, going through the tutorial is important, in part because some of the important features require certain commands that are not easily found in the help menus. The audit trail and password protection are especially valuable features.

All program functions performed well. Although entering all the data for each instrument takes time in setting up the files, labs that are aiming for ISO certification would have already assembled these records. Information on when instrumentation is due for recalibration and the records associated with performing the recalibrations are logically laid out in the series of pages for each piece of equipment.

Reviewed by F. C. McElroy, Exxon Research and Engineering Company

SOFTWARE RELEASED

ChemWeb

Softshell International
1600 Ute Ave.
Grand Junction, CO 81501-4614
970-242-7502; fax 800-240-6469
Version 1.0; free, or \$29 with phone support and manuals

ChemWeb is a chemistry drawing program intended to allow publication of chemistry files on the World Wide Web; these files can then be downloaded and edited by other users. The program, which can be downloaded from SoftShell Online (<http://www.softshell.com>), is similar to *ChemWindow* or *ChemIntosh* but cannot be used to copy and paste graphics to other applications or print. *ChemWindow* or *ChemIntosh* users can download a free patch that adds *ChemWeb* features to their existing software.

Accord for Access

Synopsis Scientific Systems
175 Woodhouse La.
Leeds LS2 3AR, UK
44-113-245-3339; fax 44-113-243-8733;
e-mail sales@synopsis.co.uk
Version 1.0; \$895, \$537 academic

Accord for Access is an add-in to the *Microsoft Access* desktop relational database designed to provide chemists with the ability to manage, analyze, and search chemistry and associated data directly within the *Access* environment. Databases containing thousands of chemical structures can be searched by substructure in seconds on a standard desktop PC, and both chemical and nonchemical data queries can be phrased in a single SQL string. The program offers full cut-and-paste compatibility with desktop chemical editors such as *ChemDraw*, *ISIS/Draw*, and *ChemWindow*, and individual structures or whole chemical data tables can be imported and exported in a variety of

standard formats, including SD, SMD, and SMILES. System requirements include *Microsoft Access 2.0* or higher and Windows 3.1 or higher.

Snap-Master General Analysis

HEM Data Corporation
17336 12-Mile Rd.
Southfield, MI 48076-2123
810-559-5607; fax 810-559-8008
Version 3.0; \$495

Snap-Master General Analysis provides powerful time-domain data analysis, including built-in event detection for intelligent calculations, Boolean logic, filter models, and more than 50 mathematical functions. The equation builder allows complex equations to be written using a simple point-and-click dialog interface and guides the user through each function. The number of data points that can be processed simultaneously is limited only by the computer's available memory or disk space. Data can be imported in ASCII, binary, or CSV formats or through dynamic data exchange. System requirements include an IBM PC or compatible with a 386 or faster processor and Windows 3.1 or higher.

Bookends Pro

Westing Software
134 Redwood Ave.
Corte Madera, CA 94925
415-945-3870; fax 415-945-3877; e-mail
westing@aol.com
Version 3.2; \$129, \$49 upgrade

This upgrade of *Bookends Pro* bibliography management software features a redesigned interface, improved Find and Replace capabilities, user-defined imports, expanded printing capabilities, and the abilities to attach any file (e.g., word processor file, spreadsheet, PDF file) to a reference and by double-clicking open it in the application that created it.

Predicting Retention in LC



Retention and Selectivity in Liquid Chromatography: Prediction, Standardisation and Phase Comparisons

Roger M. Smith, Ed.
 Elsevier Science Publishers
 655 Avenue of the Americas
 New York, NY 10010
 1995, 478 pp., \$265.75

One of the goals of the many efforts to predict retention is to relate physical and chemical factors to the observed changes in selectivity and retention with solvent and column type. These efforts overlap and parallel those that use chemometric methods such as factor analytical target prediction methods and heavily modeled formalisms based on linear, free-energy assumptions. The goal is both scholarly and practical.

From a scholarly view, the influence of molecular weight, size, structure, and functionality on retention is a fascinating topic. For the practicing scientist whose interest in any chemical separation method is the outcome, the goal is to minimize the effort involved in designing a new or modified separation method. Certainly, the vast majority of chromatography users fall into this category. They want quantitative answers or separate vials of compound A, B, C, and so on.

This book will fill a gap for the practicing scientist curious about progress in retention prediction based on chemical structure or chemically related parameters. The introductory chapter is especially well written. The majority of chapters relate some form of retention index

method to the prediction of behavior. Add to this the chapters by Sanders and Wise on their work in RPLC phase structure and selectivity for polyaromatic hydrocarbons, Pešek and Williamsen on novel phases, and a final chapter by Bolck and Smilde on multivariate methods, and you have a valuable tertiary reference.

This book discusses recent progress in transferring the Kováts method developed for GC to LC, and especially RPLC, an effort that began in the early days of modern HPLC. Retention indices help identify compounds, confirm the identity of anticipated compounds, and determine the influence of the branching of chains, changing functionality, and positional isomerism. Unfortunately, because there

is no simply defined void volume for RPLC, using retention indices is complicated. One of the reasons that compendial methods now specify a column type (e.g., USP Type L1) and then require the user to obtain at least a minimum set value of resolution between main component and common impurities is the difficulty of transferring methods between labs and/or columns.

The introductory paragraphs of Chapter 12 deal with the use of multivariate methods. This chapter also gives a good explanation of the techniques used and the "soft-model" nature of factor-analytical approaches, shows some examples of successes, and discusses some of the tools available. The very nature of factor analytical methods (that the observed variation can be explained by a progression of eigenvalues) makes it the least directly "molecular" in its results. But then these same methods are the basis of many of the commonly used molecular structure prediction programs now preferred by practicing chemists.

The reader should remember that correlation does not guarantee a causal relationship. Models such as topological shape and surface area correlate to molar volume, which correlates to polarizability and the London force contribution to sorption energetics in RPLC. Sorption is a free-energy change-described process. Linear free-energy relations prove little except that things related to the total free-energy change in a given process are proportional to each other and that they correlate. This does not imply that one factor causes the other. Hence, it is possible to relate octanol-water partition values (K_{ow}) to net retention in RPLC and to correlate octanol-water partition to hydrophobicity measured in other ways. One finds, however, that such correlations are only for compound classes in any precise sense. Families of straight lines are found in plots of many different compounds: K_{ow} values versus their RPLC retention values.

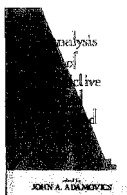
A good book, worth having at hand.
 Reviewed by C. H. Lochmüller, Duke University, Durham, NC

This book will fill a gap for the practicing scientist.

is no simply defined void volume for RPLC, using retention indices is complicated.

Many workers have demonstrated that each molecular type has its unique dead volume. However, as the total retention volume grows large and the net retention volume grows with respect to any range of void volumes, this becomes less of a problem, and it is possible to calibrate a given column with homologs of a given chemical class and then confirm the identity of one of those homologs relative to its behavior. But the dead volume is a function of solvent composition, the manufacturer of the column packing (all C_{18} columns are not the same), and other parameters. Therefore, the transfer of calibration methods, lab to lab or column source to column source, is rather diffi-

Determining Drugs of Abuse



Analysis of Addictive and Misused Drugs

John A. Adamovics, Ed.
Marcel Dekker
270 Madison Ave.
New York, NY 10016
1995, 660 pp., \$195

This book is a compilation of 10 chapters covering the determination of drugs, ranging from descriptions of assay systems for drugs of abuse (enzyme immunoassays, TLC, HPLC, CE, GC/MS), to testing athletes and forensic drug testing in South America. A major portion of the book, nearly half the printed pages, is an appendix. More than 400 drugs are presented in table form, along with a list of appropriate methods of determination and associated references. This appendix provides a quick start to becoming familiar with some of the available procedures.

The quality of the chapters varies dramatically. The chapter on enzyme immunoassays contains several errors and often refers to the parent drug when the metabolite should be discussed. In the listing of drugs tested under NIDA (more appropriately referred to as the Department of Health and Human Services' National Laboratory Certification Program), several that are mentioned are not actually part of that program.

For example, the screening test is actually the test for a cocaine metabolite and not for cocaine, and the test for marijuana

is for the Δ^9 -acid metabolite and not the Δ^8 -acid metabolite, as listed in the table. Although some immunoassays cross-react with some of the compounds listed, the text is not clear on what the program specifies for testing. It is unfortunate that these kinds of errors pervade an otherwise good description of how the immunoassays work.

Two chapters discuss resurging or emerging technology. The discussion of the potential use of biosensors is interesting, even though it describes an assay that is not used for drugs normally associated with abuse. The chapter on robotics describes an emerging area with the potential for some dramatic technological advances, taking robotics into the mainstream of drug testing.

Other chapters provide a good discussion on reversed-phase and unmodified silica HPLC. The book would be valuable to a wider audience, however, if there were a similarly well-written detailed chapter describing the determination of drugs in biological samples by HPLC. The chapter on South America not only provides useful information on determining drugs of abuse, it also presents the reader with some interesting insights into the processes and procedures used in another part of the world.

Reviewed by John T. Cody, Wilford Hall Medical Center, Lackland AFB, TX

BOOKS RECEIVED

Particle-Induced X-Ray Emission Spectrometry (PIXE)

Sven A. E. Johansson, John L. Campbell, and Klas G. Malmqvist, Eds.
John Wiley & Sons
605 Third Ave.
New York, NY 10158
1995, 451 pp., \$79.95

This book is intended as a complete handbook on PIXE. The chapter topics cover

basic instrumentation specimens; quantitative analysis; accuracy and detection limits; and applications in medicine, atmospheric chemistry, geochemistry, and art conservation. Each of its eight contributed chapters contains a bibliography, and a subject index is included at the end of the book.

Quality Assurance in Analytical Chemistry

W. Funk, V. Dammann,
and G. Donnevert.
VCH
220 East 23rd St.
New York, NY 10010
1995, 238 pp., \$80

This volume is a revised and updated English version of the original German edition first published in 1992. It presents a four-phase strategy for quality assurance (establishing new analytical procedures, preparatory QA, routine QA, and external analytical QA) and describes all of the necessary calculations as well as interpretations for quality parameters and statistical data.

Modern Practice of Gas Chromatography, 3rd ed.

Robert L. Grob, Ed.
John Wiley & Sons
605 Third Ave.
New York, NY 10158
1995, 888 pp., \$89.95

This book is intended both as a comprehensive treatise for experienced chromatographers and as a reference text for beginners. More than one-third of the book is new to this edition. Additions include detailed coverage of instrumentation, updated chapters on detectors and quantitative and qualitative analysis, new chapters on gas chromatography/mass spectrometry, and new applications in forensics and environmental monitoring. An extensive (25 pp.) subject index is included.

DISCOVER SOMETHING STUNNINGLY SMALL WITH OUR NEW LC/MS/MS...



...ITS PRICE.

You'll literally be amazed to discover that our new LCQ™ delivers MS/MS capability for just the cost of an MS-only instrument.

Now you can use the LCQ to solve problems such as drug metabolism, pharmaceutical quantitation, structural elucidation, natural products analysis, combinatorial libraries, protein and peptide analysis and QA/QC.

This power-packed benchtop detector offers MSⁿ, an LCQ exclusive, and it's absolutely the most sensitive full scan MS/MS mass spectrometer ever. LCQ's Windows NT® data system also makes all this power easy to use. For a quote on this stunning value, just fax us at 408-433-4823.



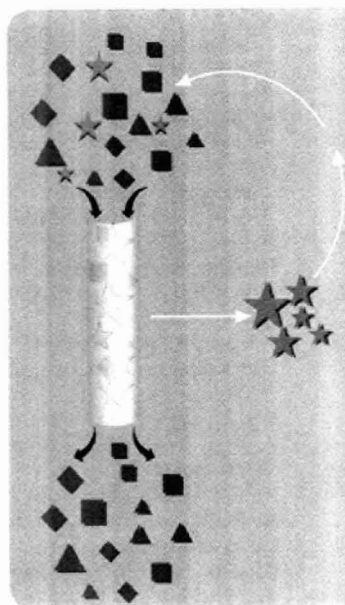
THE MASS SPECTROMETRY COMPANY



Australia Tel. (02) 646 2211 • France Tel. (1) 69 41 98 00 • Germany Tel. (0421) 54 930 • Italy Tel. (02) 66011742 • Japan Tel. (03) 3372 3001 • Netherlands Tel. (08385) 27266 • People's Republic of China Tel. (01) 8362441 • Sweden Tel. (08) 6800101 • United Kingdom Tel. (01442) 233555 • U.S.A. Tel. (408) 433-4800

Copyright 1996 by Finnigan Corporation, a subsidiary of Thermo Instrument Systems, Inc., a Thermo Electro Corporation. All rights reserved.
Windows NT is a registered trademark of Microsoft Corporation.

CIRCLE 14 ON READER SERVICE CARD



The Nucleic Acid Ligand

A New Tool for Molecular Recognition

Selective binding through molecular recognition is the basis of many important techniques in chemical analysis and separations, including those that employ enzymes, antibodies, or selective chelators. Reagents such as cyclodextrins that have preferential interaction with one isomer or enantiomer over another, often combined with selectivity based on size or shape, have been used to accomplish chiral or isomeric separations. Affinity-based separations depend on specific molecular recognition between immobilized ligands and their receptors, which are the target analytes. Chemical sensors often use selective binders that are immobilized at the sensor surface to generate an analyte-dependent signal.

**Linda B. McGown and
Melissa J. Joseph**
Duke University

**J. Bruce Pitner, Glenn P.
Vonk, and C. Preston Linn**
Becton Dickinson Research Center

Oligonucleotide ligands provide specific and high-affinity binding with selected target molecules

A recent entry in the field of selective binding and molecular recognition is the nucleic acid ligand, an oligonucleotide that exhibits high-affinity specific binding with selected target molecules (excluding hybridization interactions such as double-strand formation through base pairing). These ligands have ranged from 8 to 120 nucleotides in length, corresponding to a molecular weight range of ~ 3000–40,000. The ligands are typically truncated to a "consensus" region, which is the

minimal sequence needed for binding to the target and is usually 15–50 bases in length.

Individual sequences that have high binding affinities for a target analyte are selected from oligonucleotide libraries of as many as 10^{15} random sequences by a selective, iterative enrichment process (1, 2). The selective binding affinity toward the target is thought to arise from specific interactions such as hydrogen bonding or association with the phosphate groups of the ligand, or "aptamer" (2). These interactions are facilitated by the sequence-specific, 3-D structure of the ligand, which provides a rigid scaffold for the arrangement of functionalities of the ligand. Examples of 3-D structures (Figure 1) include the stem-loop/bulge (3), the pseudoknot (4), the helix (not shown), the hairpin (1), and the G-quartet (5–7) structure, which is characteristic of a thrombin-binding ligand.

Nucleic acid ligand selection
Because the probability that a given sequence will form a stable, 3-D structure

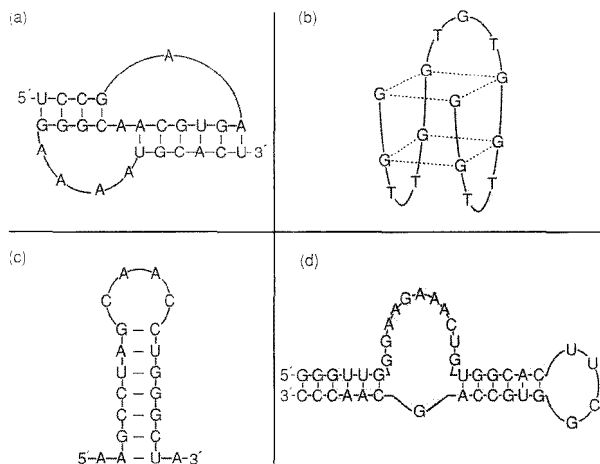


Figure 1. Structures of some nucleic acid ligands.

(a) Pseudoknot (RNA ligand for HIV-1 reverse transcriptase [4]), (b) G-quartet (DNA ligand for thrombin [5]), (c) hairpin (RNA ligand for Bacteriophage T4 polymerase [1]), and (d) stem-loop/bulge (RNA ligand for ATP [3]).

with a high binding affinity for a particular target molecule is very low, it is necessary to select ligands from a very large (10^{15} sequence) pool to maximize the chances of success. Consequently, the development of techniques to generate large, random DNA or RNA sequence libraries and to isolate molecules with specific binding affinities from these libraries is critical to the development of nucleic acid ligands as important binding reagents (1, 2).

For very short oligomers (15–25 nucleotides), all possible sequences may be included in the initial pool. However, such short strands may not fully represent the structure space needed to provide the desired binding properties. As the length of the oligonucleotide increases, the number of possible sequences increases exponentially by y^N , where y is the number of different oligonucleotides and N is the number of random positions.

With four different nucleotides (i.e., 4^N), it's not feasible to include all sequences with greater than ~ 25 random positions in the initial pool for a given selection process. Therefore, alternative strategies for generating the initial sequence pool are used, such as a "shotgun"

approach in which the entire range of possibilities is randomly sampled, or a more focused strategy in which the sequences are clustered about a particular sequence that has been identified as having the desirable binding properties (8, 9). Although the use of longer random oligonucleotides offers the advantages of easier generation of random sequence pools and more comprehensive spanning of the structural space, it also increases the likelihood of side reactions and of errors in the amplification process that may terminate strand replication.

Once the initial sequence pool has been generated, ligands with the desired binding characteristics are isolated by iterative *in vitro* processes that have variously been referred to as "systematic evolution of ligands by exponential enrichment" (SELEX) (1), *in vitro* selection (2), directed molecular evolution (10), or "evolution in a test tube" (11). Figure 2 summarizes the steps in these methods. The sequence pool is commonly passed over a support, such as an affinity column, to which the target molecule or macromolecule is attached. Numerous cycles of this partition procedure are repeated, each followed by polymerase chain reac-

tion amplification of the sequences that are highly retained on the support. If RNA is used, it is transcribed from the DNA template using a suitable promoter sequence and an RNA polymerase.

Table 1 (References 12–20) lists some of the ligands that have been isolated by ligand selection processes, with both RNA and DNA ligands represented. The targets include proteins and enzymes as well as a variety of small molecules. Some ligands exhibit stereoselectivity, such as the ligand that binds to agarose-bound D-tryptophan but not to L-tryptophan. Many of the ligands to macromolecules are notable for their ability to inhibit the action of their target macromolecule.

In contrast to methods such as SELEX, which screen entire libraries in parallel, alternative combinatorial methods successively fix positions in a biopolymer such as an oligonucleotide. Libraries are prepared in which the first position in the oligonucleotide chain is varied among the four possible bases. The rest of the positions in the polymer are allowed to vary randomly. The four different libraries, one for each base in the first position, are screened for binding activity. The identity of the first position is then fixed to that of the library exhibiting the tightest binding in the screening assays. The process is repeated at the second position, and so on progressively down the oligonucleotide chain. Generally, these methods screen a smaller number of molecules. However, the synthetic flexibility of these combinatorial methods permits a broader menu of structures uncompromised by the enzymatic requirements of permutational methods such as SELEX. Synthetic combinatorial methods have most recently yielded a DNA ligand that inhibits infection by HIV *in vitro* (21).

Chemical selectivity and stability

The binding of nucleic acid ligands to target molecules can be chemically selective as well as stereospecific. One selection experiment produced an RNA pool that bound to D-tryptophan rather than L-tryptophan, a molecule differing at only one stereocenter, by a greater than ninefold preference (13). One individual clone from this pool had 670-fold greater affinity for D-tryptophan than for L-trypto-

phan. Even greater degrees of selectivity can be achieved by incorporating target discrimination explicitly in the selection strategy. For example, to encourage selectivity of one molecule over another, another partition step can be added to the selection process shown in Figure 2 in which the column is "washed" with the undesired molecule prior to elution with the target. Such a counter-selection process has yielded an RNA ligand that has > 10,000-fold selectivity for theophylline over caffeine, molecules that differ by only one methyl group (12).

Limitations on the stability of nucleic acid ligands are an important consideration in their use as analytical reagents. This is particularly important for RNA, which is readily degraded by ribonucleases in samples of biological origin. Stability of DNA ligands is more of a concern when they are used as therapeutics and extended in vivo stability is needed. In practice, DNA may be handled routinely in most laboratories without exceptional precautions. However, RNA should be handled with gloves to limit contamination with nucleases present on the skin, and "nuclease-free" reagents should be used.

To increase the stability of nucleic acid ligands, they can be constructed from

chemically modified derivatives with structures similar to DNA or RNA. Because most enzymatic degradation of RNA occurs through intramolecular participation of the 2' hydroxyl on the ribose sugar of pyrimidine nucleotides, substitution of this functionality with fluorine, amino, or alkoxy substituents greatly enhances the stability of these oligomers (22). Other modifications include 2'-*O*-methyl derivatives, carbocyclic ribose analogues, thiophosphates, and modifications of the pyrimidine or purine bases. In one recent study, a 2'-amino pyrimidine modification extended the half-life of RNA in both serum and urine from a few minutes to several hours (23). DNA may also be stabilized through chemical modification (24).

Nucleic acid ligand structures

The structure of nucleic acid ligands can be studied by a number of techniques, including X-ray crystallography, NMR, circular dichroism (CD), UV-vis and IR absorption spectroscopies, and fluorescence probe. Comparisons can be made among different sequences as well as between the ligands and longer, double-stranded DNA or RNA. For example, Figure 3 shows the CD spectra of three different DNAs: a

thrombin-binding DNA ligand that contains the G-quartet structure (5'-GGTTG-GTGTGGTTGG-3'), a DNA oligomer with the same base content as the ligand in a "scrambled" sequence that does not promote intramolecular G-quartet formation (5'-GGTGGTGGTTGTGGT-3'), and duplex (double-stranded) DNA (dsDNA) (25). The CD spectrum of the thrombin-binding ligand is clearly distinct from the other two DNAs because of the unique intramolecular G-quartet. It is this G-quartet structure that underlies the unique high affinity of the thrombin-binding ligand for thrombin.

Interactions with nucleic acid indicator dyes

Indicator dyes that bind to double-stranded helical DNA or RNA may also bind to single-stranded ligands. For example, dyes such as oxazole yellow (YO), its homo dimer (YOYO) (26), and other related probes have been found to associate with the shorter, single-stranded ligands. These probes are essentially nonfluorescent in bulk aqueous solution, but they develop intense fluorescence upon association with double-stranded DNA or RNA. In the thrombin-binding ligand and the scrambled-sequence oligomer, YOYO and YO exhibit strong fluorescence, despite the absence of intercalation sites provided by dsDNA. Excitonic coupling leads to an induced CD spectrum of YOYO in the nucleic acids, which is further evidence of binding. At high dye loadings in dsDNA, intramolecular dimerization between surface-bound YO groups of a single, folded YOYO gives rise to a $-/+$ bisignate CD spectrum (27). In both the thrombin-binding ligand and the scrambled-sequence oligomer, a $+/-$ bisignate CD spectrum is observed for YOYO at a dye loading below the threshold that was reported for excitonic coupling in the dsDNA (25). This indicates differences between the binding of YOYO in the single-stranded and double-stranded DNAs.

We have found that the fluorescent dyes Hoechst 33324 and 33258 also bind to the single-stranded DNA ligands. These two dyes are similar compounds and minor groove binders in dsDNA. Their association with the single-stranded oligomers is weaker than was observed for the intercalating YO and YOYO dyes,

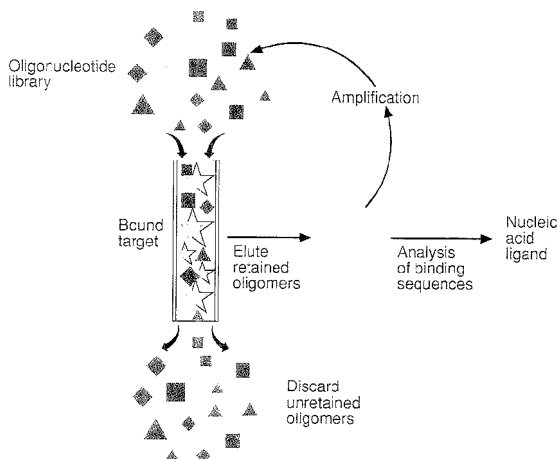


Figure 2. General summary of ligand selection processes.

Random sequence library undergoes partitioning for selection of binders for immobilized target; retained sequences are repetitively eluted and cycled through the selection and amplification processes to isolate families of nucleic acid ligands for the target.

Table 1. Some nucleic acid ligands and their target molecules

Target	Ligand type ^a	Ligand structure ^b	Reference
Small molecules			
Organic dyes	DNA		2
Theophylline	RNA	Hairpin with bulge	12
D-Tryptophan ^c	RNA		13
ATP	RNA	Stem-loop/bulge	3
L-Citrulline/ L-Arginine ^d	RNA		14
Arginine	RNA		15
Cyanocobalamin (vitamin B-12)	RNA	Pseudoknot	16
Biological cofactors (FAD, FMN, NAD ⁺ , NMN ⁺)	RNA	Hairpin/bulge	17
Macromolecules			
Human thrombin	DNA	G-quartet	5
Bacteriophage T4 polymerase	RNA	Hairpin	1
Antipeptide antibody	RNA	Hairpin	18
Basic fibroblast growth factor	RNA		19
HIV-1 reverse transcriptase	RNA	Pseudoknot	4
<i>E. coli</i> RhD factor	RNA	Hairpin	20

^a All are single strands.

^b If known.

^c The ligand was selective for D-trp-agarose over L-trp-agarose.

^d The L-arginine-binding ligand was evolved from the pool of L-citrulline-binding ligands and did not retain any affinity for L-citrulline.

which suggests the absence of an analogue to a minor groove-binding site or a suitable alternative in the single-stranded structures.

Further investigation of indicator dyes that bind to duplex nucleic acids will improve our understanding of the conformation and binding interactions of nucleic acid ligands and may lead to using these dyes as indicators of the ligands and their target analytes.

Nucleic acid ligands as analytical reagents

The application of nucleic acid ligands to chemical analysis is a new area of investigation with only a few specific examples to date, primarily in clinical diagnostics. Yet the possibility of generating stable structures with unique conformations offers enormous potential for chemical sensing and separations. This is analogous to the use of enzymes and antibodies in recent years but offers the advantages of smaller, less cumbersome molecules that, once identified, are simple to manufacture and manipulate. These are important factors, particularly for immobilization of these

reagents at surfaces of sensors or chromatographic supports because the smaller ligands will reduce steric hindrance and increase surface coverage and their conformational stability will help maintain their selectivity and activity upon attachment to a surface. Furthermore, using reversible attachment methods based on hybridization offers exciting possibilities for replacement or renewal of ligands at sensor or chromatographic surfaces.

A unique combination of stereoselectivity and chemical recognition is possible with nucleic acid ligands, which are in some respects similar to cyclodextrins but have greater structural variety and lack the size exclusion imposed by the rigid cyclodextrin cavity. The structural motifs that provide very specific sensing of designated target molecules may also show more general selectivity for a variety of unrelated molecules, which could be used to develop new methods for chemical and chiral separations. On the other hand, binding affinity for molecules unrelated to the target analyte may lead to unanticipated sources of interference that must be investigated.

Nucleic acid ligands and antibodies

A close analogy to the nucleic acid ligand is the antibody. Antibodies are proteins that develop molecular recognition by *in vivo* exposure of the unspecified immunoglobulin to the target (or target-carrier complex) through natural or artificially induced immunogenic response. In many ways, the evolution of molecular recognition in the immune response is analogous to the selection of nucleic acid ligands. In both cases, molecular recognition arises from the 3-D structure of the host (antibody or ligand) and its specific physicochemical interactions with the target analyte.

Antibodies, or antibody fragments, have binding constants on the order of 10^6 – 10^{12} . They are much larger than the nucleic acid ligands; molecular weights range from $\sim 160,000$ for the protein to 25,000 for SFV antibody fragments. They may be polyclonal, composed of a heterogeneous mixture of immunoglobulins with binding affinities for several determinant structures on the target molecule, or monoclonal, which is a homogeneous, pure species of immunoglobulin with selected specificity for a unique determinant on the target. Although homogeneity of monoclonal antibodies is advantageous for reproducibility and predictability, polyclonal antibodies are frequently more effective in immunoassays.

Nucleic acid ligands offer several potential advantages over traditional antibody-based reagents because they are not derived from living organisms and can be reproducibly and accurately synthesized in a short time by automated processes. Covalent attachment of dyes to nucleic acid ligands is relatively simple and may be done with high specificity at one or more locations on the ligand.

Other chemical modifications for stabilization, increased activity, or covalent attachment are also relatively simple. In traditional antibody production methods, the target molecule must be large enough to elicit an immune response (molecular weights of 1000 will provide marginal immunogenicity, and above 10,000, the response is usually strong); small molecular targets must be attached to a large carrier molecule, such as albumin, to generate antibodies to the target. Non- or

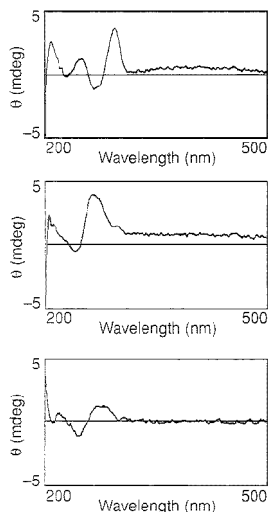


Figure 3. CD spectra of three different DNAs.

Thrombin-binding DNA ligand (top), a DNA oligomer of the same length and composition but different sequence (middle), and duplex DNA (bottom).

poorly immunogenic analytes that are problematic for antibody-based methods may be targeted by nucleic acid ligands, although the isolation of a highly selective ligand with a high binding affinity is by no means guaranteed for a given target analyte.

Like antibodies, nucleic acid ligands can be immobilized on electrodes or optical fibers for highly selective chemical sensing. Because the ligands are smaller and their 3-D structures are less complicated than those of antibodies, immobilization and subsequent binding interactions may encounter fewer steric hindrances and less degradation of binding activity. An important advantage of nucleic acid ligands as immobilized sensors is that they can easily be denatured to reverse binding and then regenerated simply by controlling buffer-ion concentrations. For example, the G-quartet structure can be controlled by altering the K^+ concentration. Antibody-based sensors generally require more drastic conditions, such as low pH, for regeneration, and they lose binding ability after repeated cycles.

Detection methods

The use of labeled nucleic acid ligands offers sensitive and simple methods for measuring binding to specific analytes. The techniques that have been developed for immunochemical analyses, including heterogeneous (separation based) and homogeneous (nonseparation) methods, are generally suitable for nucleic acid ligands as well. Detection can be accomplished with radiolabels in heterogeneous techniques, but using radioactive materials is generally discouraged because of their inherent danger and instability. Fluorescent labels are a less hazardous alternative that can be used in either heterogeneous or homogeneous analyses, through measurements of intensity, lifetime, anisotropy, or energy transfer. The use of fluorescent-labeled ligands allows direct signal generation without the need to separate bound from free labeled ligand.

One of the most successful homogeneous techniques is fluorescence polarization analysis. The change in signal upon binding of the analyte to the binding agent is related to the increase in size of the labeled moiety upon binding and results in a corresponding change in the effective rotational rate of the labeled moiety. Polarization analysis is an excellent example of a case in which nucleic acid ligands offer

important advantages over antibodies, as illustrated in Figure 4.

In immunoassay techniques, the change in size of the antibody upon binding of the analyte is often small because the antibody itself is large. Therefore, labeled analyte compound, rather than labeled antibody, is generally used. This necessitates a competitive determination scheme in which the unlabeled analyte competes with the labeled analyte reagent for antibody binding sites. In contrast, the relatively small nucleic acid ligands will experience a proportionally greater increase in effective size upon analyte binding, making it possible to label the ligands and measure the increase in their fluorescence polarization upon binding to the analyte in a direct, rather than a competitive, analysis (28).

The future

The exploration of nucleic acid ligands as reagents for chemical analysis will encompass a multitude of research objectives. New ligands for wide-ranging target analytes, both large and small, will continue to be identified through SELEX and other selection techniques. Innovations in the methodology for generating random libraries and identifying binding sequences will be pursued. Fundamental

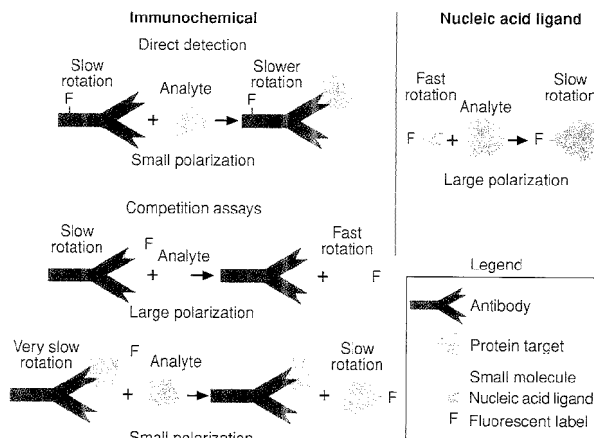
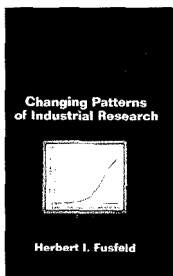


Figure 4. Comparison of polarization detection in immunochemical antibody-based methods and nucleic acid ligand-based methods.

For clarity, only one binding site interaction is shown for a given antibody.

Just Published!

Industry's Future: Changing Patterns of Industrial Research



This fascinating volume provides the readers with an understanding of the dynamic processes that make industrial research a principal driving force

in creating technical change, producing economic growth, and strengthening the technical institutions in society.

It describes and analyzes the major factors that shape the conduct and organization of industrial research, including the internationalization of R&D, restructuring of industry, declining defense expenditures and the pressure to develop access to sources of technical change outside the corporation.

The volume presents approaches for improved industry relations with government and academia, discusses complex conditions for conducting industrial research effectively and analyzes potential new conditions that can shape future industrial research. The experiences of specific corporations with modern management of technology are also described.

Herbert I. Fushfeld

384 pages (1994)
Clothbound: ISBN 0-8412-2983-X
\$39.95
Paperbound: ISBN 0-8412-2984-8
\$24.95

Order from

American Chemical Society
Distribution Office Dept. 74
1155 Sixteenth Street, NW
Washington, DC 20036

Or Call TOLL FREE 1-800-227-5558
(in Washington, D.C. 872-4363)
and use your credit card!
FAX: 202-872-6067.

ACS Publications Catalog now available on
internet: gopher.acsinfo.acs.org

ACS PUBLICATIONS
Essential Resources for the Chemical Sciences

Report

studies of the nature of molecular recognition by the ligands, and the dependence of binding strength and selectivity on the sequence, structure, and conformation of the ligands, will be investigated, as will the effects of experimental conditions and chemical modifications. Further identification and characterization of structural motifs and physicochemical interactions may lead to more rational and efficient approaches to the design of new ligands.

Applications of nucleic acid ligands will expand beyond clinical diagnostics and therapeutic monitoring to a broader arena of analytical chemistry. Immobilization chemistry, including reversible attachment and denaturation schemes, will facilitate the use of ligands as reagents at sensor or chromatographic support surfaces. Explorations of chiral recognition may lead to applications in the separation of enantiomers. Development of novel detection strategies will play a key role in the utilization of nucleic acid ligands to maximize the effectiveness of these reagents. Because methods for isolation, characterization, and modification of nucleic acid ligands are still at the embryonic stage, new properties and applications of these uniquely versatile reagents will unfold with further study.

The authors are grateful to Bob Hanson of Becton Dickinson for designing the figure graphics and to Larry Gold and Barry Polisky of NeXstar Pharmaceuticals for their helpful comments.

References

- (1) Tuerk, C.; Gold, L. *Science* **1990**, *249*, 505.
- (2) Ellington, A. D.; Szostak, J. W. *Nature* **1990**, *346*, 818.
- (3) Sassanfar, M.; Szostak, J. W. *Science* **1993**, *364*, 550.
- (4) Tuerk, C.; MacDougall, S.; Gold, L. *Proc. Natl. Acad. Sci. USA* **1992**, *89*, 6988.
- (5) Bock, L. C.; Griffin, L. C.; Latham, J. A.; Vermaes, E. H.; Toole, J. J. *Nature* **1992**, *355*, 564.
- (6) Wang, K. Y.; McCurdy, S.; Shea, R. G.; Swaminathan, S.; Bolton, P. H. *Biochemistry* **1993**, *32*, 1899.
- (7) Macaya, R. F.; Schultze, P.; Smith, F. W.; Roe, J. A.; Feigon, J. *Proc. Natl. Acad. Sci. USA* **1993**, *90*, 3745.
- (8) Wilson, C.; Szostak, J. W. *Nature* **1995**, *374*, 777.
- (9) Nieuwlandt, D.; Wecker, M.; Gold, L. *Biochemistry* **1995**, *34*, 5651.
- (10) Joyce, G. F. *Sci. Am.* **1992**, *269*, 90.
- (11) Schmidt, K. F. *Sci. News* **1993**, *144*, 90.
- (12) Jenison, R. D. et al. *Science* **1994**, *263*, 1425.
- (13) Famulok, M.; Szostak, J. W. *J. Am. Chem. Soc.* **1992**, *114*, 3990.
- (14) Famulok, M. *J. Am. Chem. Soc.* **1994**, *116*, 1698.
- (15) Connell, G. J.; Illangsekare, M.; Yarus, M. *Biochemistry* **1993**, *32*, 3497.
- (16) Lorsch, J. R.; Szostak, J. W. *Biochemistry* **1994**, *33*, 973.
- (17) Burgstaller, P.; Famulok, M. *Angew. Chem. Int. Ed. Engl.* **1994**, *33*, 1084.
- (18) Tsai, D. E.; Kenan, D. J.; Keene, J. D. *Proc. Natl. Acad. Sci. USA* **1992**, *89*, 8864.
- (19) Jelinek, D.; Lynott, C. K.; Rifkin, D. B.; Janjic, N. *Proc. Natl. Acad. Sci. USA* **1993**, *90*, 11227.
- (20) Schneider, D.; Gold, L.; Platt, T. *FASEB J.* **1993**, *7*, 201.
- (21) Wyatt, J. R. et al. *Proc. Natl. Acad. Sci. USA* **1994**, *91*, 1356.
- (22) Piecken, W. A.; Olsen, D. B.; Benseler, F.; Aarup, H.; Eckstein, F. *Science* **1991**, *253*, 314.
- (23) Lin, Y.; Qiu, Q.; Gill, S. C.; Jayasena, S. *Nucleic Acids Res.* **1994**, *22*, 5229.
- (24) Shaw, J. P.; Kent, K.; Fishbach, J.; Froehner, B. *Nucleic Acids Res.* **1991**, *19*, 747.
- (25) Joseph, M. J.; Taylor, J. C.; McGown, L. B.; Pitner, J. B.; Linn, C. P., submitted for publication in *J. Phys. Chem.*
- (26) Rye, H. S. et al. *Nucleic Acids Res.* **1992**, *20*, 2803.
- (27) Larsson, A.; Carlsson, C.; Jonsson, M.; Albinsson, B. *J. Am. Chem. Soc.* **1994**, *116*, 8459.
- (28) Hsieh, H. V. *Biophys. J.* **1995**, *68*, A298.

Suggested reading

- Edgington, S. M. *Bio/Technology* **1993**, *11*, 285.
- The RNA World*; Gesteira, R. F.; Atkins, J. F., Eds.; Cold Spring Harbor Laboratory Press: Cold Spring Harbor, NY, 1993; Chapters 19 and 20.
- Burke, J. M.; Berzal-Herranz, A. *FASEB J.* **1993**, *7*, 106-12.
- Ellington, A. D. *Curr. Biol.* **1994**, *4*, 427.
- Klug, S. J.; Famulok, M. *Mol. Biol. Rep.* **1994**, *20*, 97.

Linda B. McGown, professor of chemistry, performs research in fluorescence lifetime techniques, DNA detection and sequencing, molecular probe techniques, and organized media. Melissa J. Joseph recently completed her Ph.D. in chemistry at Duke University and is now a research chemist at Lorillard Tobacco Company in Greensboro, NC. Glenn P. Vonk uses organic chemistry to develop novel systems for biochemical analysis; J. Bruce Pitner performs research in bioconjugation, molecular recognition, and combinatorial chemistry; and C. Preston Linn develops novel chemical detection methods in the Molecular Biology Department at Becton Dickinson Research Center. Address comments to McGown at Department of Chemistry, Box 90346, Duke University, Durham, NC 27708-0346.

Introducing

VECTOR 22

FT-IR

Incomparable Optics. Very Comparable Price.



VECTOR 22

Compare today's routine FT-IR spectrometer and you'll discover that you often have to sacrifice either performance or affordability. We at Bruker believe that our superior optics should be available to all users. Look into VECTOR 22—a compact, high performance FT-IR system with extra-large sample compartment, ROCKSOLID™ alignment, notebook or PC operation with easy OPUS/LT software. An optional BeamBender™ makes multiple ports available for external accessories, such as GC, TGA or microscopes. And built-in diagnostics and auto-calibration keep it operating

reliably at optimum performance. So, why compromise at all? Look into VECTOR 22 and turn your FT-IR work into a high throughput pushbutton operation. For accurate, no-nonsense results. Ask for details on VECTOR 22 and compare to see how affordable Bruker quality has become.

Bruker Analytische Messtechnik GmbH
Wikingenstr. 13, D-76189 Karlsruhe
Tel. 0721/9528-0
Fax 0721/9528-712

CIRCLE 16 ON READER SERVICE CARD



Comprehensive Support for Innovative Systems

Biochemistry.

Critical research.

On time. On target.

On your must-read list!

Biochemistry is a must-read for researchers in chemistry, biochemistry, and molecular and cell biology. Every week (in over 12,000 pages a year), *Biochemistry* gives you fast-breaking, state-of-the-art research articles on a variety of important topics such as:

- Bioenergetics
- Carbohydrate chemistry
- Enzyme and protein biochemistry
- Gene structure and function
- Immunochemistry
- Lipid and cell membrane biochemistry
- Molecular and cell biology
- Virology

Before you begin your next research project or write your next proposal, subscribe to *Biochemistry* for the most relevant theories and methodologies in your field of endeavor.

Editor

Gordon G. Hammes
Duke University Medical Center

Associate Editors

Mary Barkley
Louisiana State University

Marc G. Caron
Duke University Medical Center

Earl W. Davie
University of Washington

Perry A. Frey
University of Wisconsin, Madison

Arno L. Greenleaf
Duke University Medical Center

Paul L. Modrich
Duke University Medical Center

William W. Parson
University of Washington

James F. Riordan
Harvard Medical School

Joseph J. Villafranca
Bristol-Myers Squibb Co.

Leslie Wilson
University of California, Santa Barbara

1995 Subscription Rates

	U.S.	Canada & Mexico	Europe*	All Other Countries*
ACS Members				
One Year	\$ 115	\$ 224	\$ 384	\$ 468
Two Years	\$ 207	\$ 425	\$ 745	\$ 913

Nonmembers				
One Year	\$1,517	\$1,626	\$1,786	\$1,870

*Air Service Included.

Call toll free 1-800-333-9511 today.
Outside the U.S., please call 614-447-3776.

Or mail or fax
your order to:
American
Chemical
Society,
Member &
Subscriber
Services,
P.O. Box 3337,
Columbus, OH
43210. FAX
614-447-3671.

Biochemistry

ACS  PUBLICATIONS
Essential Resources for the Chemical Sciences

Conferences

GENERAL

Eastern Analytical Symposium and Exposition

Nov. 12-17.
Somerset, NJ
Contact: Eastern Analytical Symposium, P.O. Box 633, Montchanin, DE

19710-0633 (302-738-6218; fax 202-738-5275)

5th International Conference on Automation, Robotics, and Artificial Intelligence Applied to Analytical Chemistry and Laboratory Medicine

Jan. 15-20, 1996. San Diego, CA
Contact: R. A. Felder, Dept. of Pathology, University of Virginia, Box 168, Charlottesville, VA 22908 (804-924-5151; fax 804-924-5718) or J. van der Greef, TNO and University of Leiden, P.O. Box 360, 3700 AJ Zeist, The Netherlands (31-3404-44144; fax 31-3404-57224)

Pittcon '96

March 3-8, 1996. Chicago, IL
Contact: Alma Johnson, The Pittsburgh Conference, Suite 332, 300 Penn Center Blvd., Pittsburgh, PA 15235-5503 (412-825-3226; fax 412-825-3224)

Materials Research Society 1996 Spring Meeting

April 8-12, 1996. San Francisco, CA
Contact: MRS, Meetings Dept., 9800 McKnight Rd., Pittsburgh, PA 15237 (412-367-3003; fax 412-367-4373)

26th International Symposium on Environmental Analytical Chemistry

April 9-12, 1996. Vienna, Austria
Contact: M. Grasserbauer, Institute for Analytical Chemistry, Vienna University of Technology, Getreidemarkt 9/151, A-1060 Wien, Austria (431-58801-4824; fax 431-5867813)

6th Symposium on Environmental Toxicology and Risk Assessment: Modeling and Risk Assessment

April 14-18, 1996. Orlando, FL
Contact: F. James Dwyer, National Biological Service, 4200 New Haven Rd., Columbia, MO 65201 (314-875-5399; fax 314-876-1896; e-mail: dwyerj@mail.fws.gov) or Thomas R. Doane, Battelle, 4114 Centerview, Suite 260, San Antonio, TX 78228 (210-738-8771, ext. 109; fax 210-737-5928; e-mail: doane@battelle.org)



8th Sanibel Conference on Mass Spectrometry

Jan. 20-23, 1996.
Sanibel Island, FL
Contact: American Society for Mass Spectrometry, 1201 Don Diego Ave., Santa Fe, NM 87505 (505-989-4517; fax 505-989-1073)



8th International Symposium on HPCE

Jan. 21-25, 1996.
Orlando, FL
Contact: Shirley Schlessinger, Suite 1015, 400 East Randolph Dr., Chicago, IL 60601 (312-527-2011)

7th International Symposium on SFC and SFE

March 31-April 4, 1996. Indianapolis, IN
Contact: Janet Cunningham, Barr Enterprises, 10120 Kelly Rd., Box 279, Walkersville, MD 21793 (301-898-3772; fax 301-898-5596)

18th International Symposium on Capillary Chromatography

May 20-24, 1996. Riva del Garda, Italy
Contact: P. Sandra, I.O.P.M.S., Kennedypark 20, B-8500 Kortrijk, Belgium (32-56-204-960; fax 32-56-204-859)

HPLC '96

June 16-21, 1996. San Francisco, CA
Contact: Janet Cunningham, Barr Enterprises, 10120 Kelly Rd., Box 279, Walkersville, MD 21793 (301-898-3772; fax 301-898-5596)



37th Experimental NMR Conference

March 17-22, 1996.
Pacific Grove, CA
Contact: Experimental NMR Conference, 1201 Don Diego Ave., Santa Fe, NM 87505 (505-989-4573; fax 505-989-1073)

EUROPT(R)ODE '96

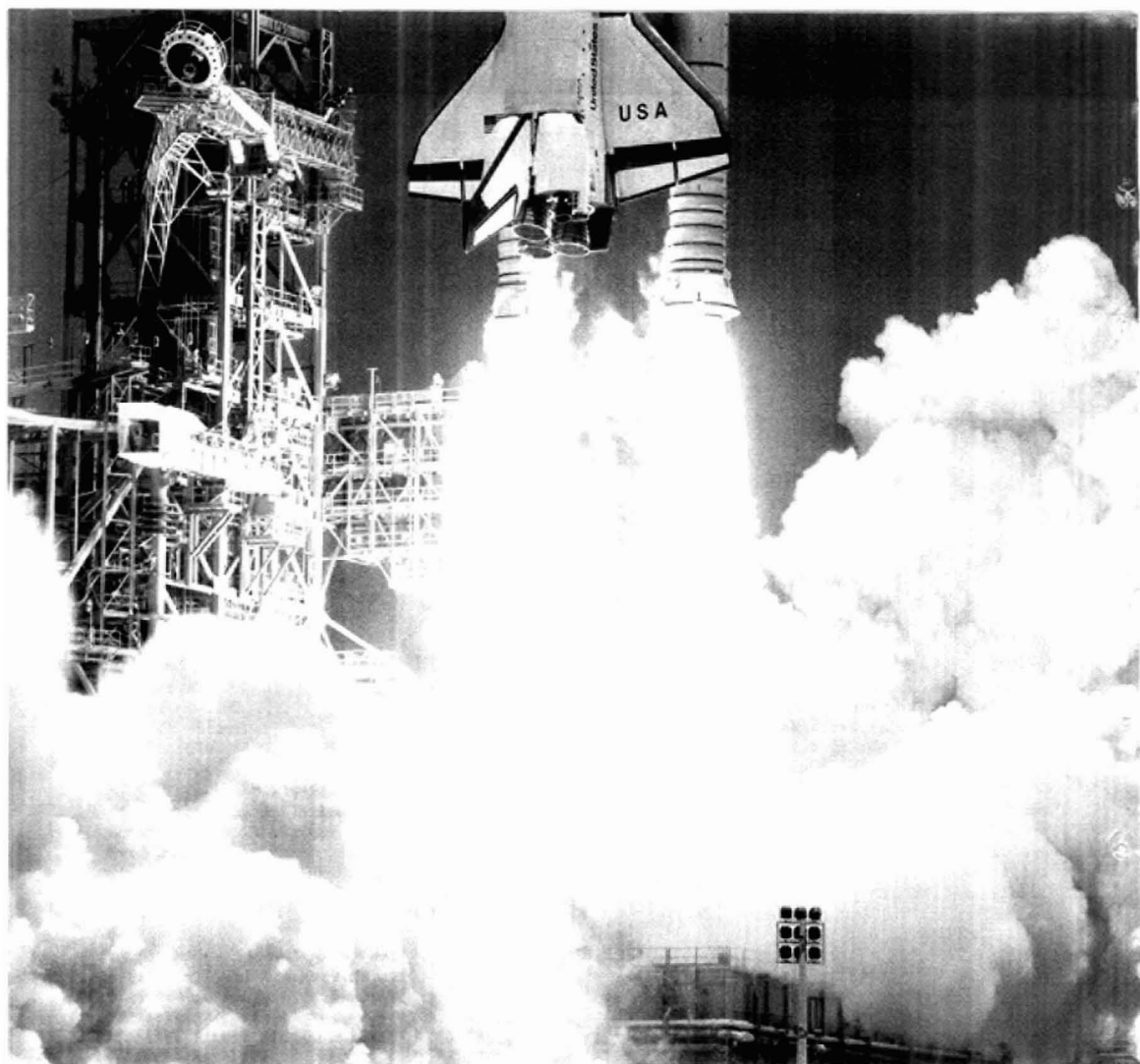
March 31-April 3, 1996. Zurich, Switzerland
Contact: Sergio Bellucci, Management and Technology Institute, Technopark Zurich, Pfingstweidstrasse 30, CH-8005 Zurich, Switzerland (41-1-445-1200; fax 41-1-445-1202)

7th International Symposium on Luminescence Spectrometry in Biomedical Analysis: Detection Techniques and Applications in Chromatography and CE

April 17-19, 1996. Sophia Antipolis, France
Contact: Willy R. G. Baeyens, University of Ghent, Pharmaceutical Institute, Dept. of Pharmaceutical Analysis, Laboratory of Drug Quality Control, Harelbekestraat 72, B-9000 Ghent, Belgium (32-9-221-8951; fax 32-9-221-4175; e-mail: willy.baeyens@rug.ac.be)

International Conference on Pharmaceutical Applications of Near-IR Spectroscopy

June 13-15, 1996. Stockholm, Sweden
Contact: The Swedish Chemical Society, Wallingatan 24, 3 tr, S-111 24 Stockholm, Sweden (46-8-411-5260; fax 46-8-106-678)



When you're going from zero to 17,000 mph,
the last thing you want is dirty fuel.

No wonder NASA scientists chose Scott to help them develop the standards for analyzing shuttle fuels.

After all, Scott has also established standards for automotive emissions, semi-volatile organic air pollutants, and the measurement of carbon dioxide in the atmosphere, to name a few. We've supplied the specialty gases and equipment needed to meet those standards, including parts-per-trillion mixtures and ultra-pure zero gases. And we have always supplied them quickly. Anywhere on earth. Overnight, if needed.

As to space shuttle launches, Scott gases have been "mission critical." Because NIST-traceable Scott gases are among those used to calibrate the spectrometer on the launch pad. The spectrometer checks the integrity of the shuttle's entire fuel system. And if it detects a fuel problem, the mission is cancelled.

When your mission is critical, depend on gases that set the standards for accuracy and performance: Scott specialty gases.

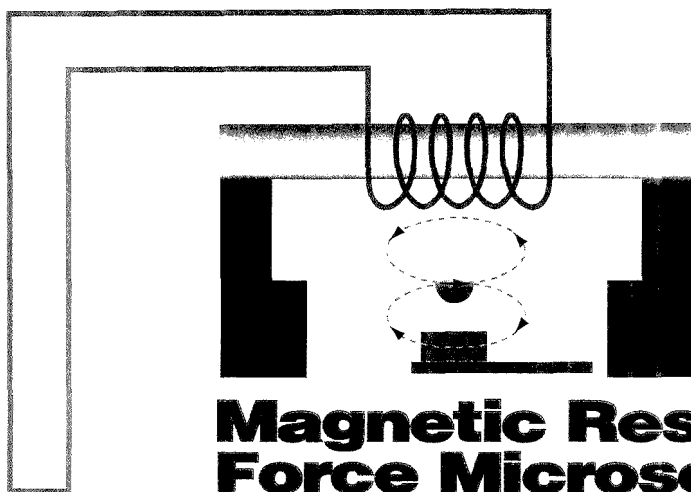
Call 1-800-21SCOTT for a complete catalog of our specialty gases and equipment.



Scott Specialty Gases

6141 Easton Road, P.O. Box 310, Plumsteadville, PA 18949-0310
Telephone: 215-786-8861 Fax: 215-786-0320





Magnetic Resonance Force Microscopy

Atomic force microscopy (AFM) offers a variety of complex microscale surface information about materials such as semiconductors, biological specimens, and magnetic media. In the past few years, AFM images with single-molecule resolution have begun to appear in numerous journals. Through optical measurement of the forces acting on a tiny cantilever/probe assembly as it scans across a sample, AFM and related techniques can now provide at least partial 3-D mapping of surface hardness, roughness, adhesiveness, temperature, and chemical and magnetic properties.

It seems natural to combine the advantages of AFM with those of more powerful chemical analysis techniques. AFM offers physical characterization and mapping at the single-molecule scale, which so far has been achieved by few other chemical methods. On the other hand, it lacks the chemical resolution needed for structural characterization of molecules

A hybrid of ESR or NMR with AFM could someday detect single spins

such as proteins and can't be used to detect subsurface structures. Its resolution certainly doesn't compare with that of macroscale protein characterization methods such as X-ray diffraction (XRD) or NMR spectroscopy.

Could NMR or something similar be combined with AFM and, if it were, could it provide full chemical structures of single molecules? John Sides of the University of Washington (UW) began asking these questions more than five years ago. Impressed by recent reports of genomic DNA sequencing, he says, "We have no similarly powerful instruments for microanalytical chemistry and structural

determination on that scale." Since 1991, he and his colleagues at UW, along with Dan Rugar and Nino Yannoni of IBM Almaden Research Center and their co-workers, have been developing and demonstrating instrumentation for a new force microscopy method that permits magnetic resonance measurements. Their goal for "magnetic resonance force microscopy" (MRFM) is to achieve nondestructive 3-D imaging with angstrom-scale resolution through the detection of single electronic or nuclear spins.

So far, most of the articles on MRFM have been published in physics journals rather than in the chemical literature. "The potential applications of this technology sometimes attract more publicity than is really appropriate at this early stage of development," Sides cautions. "Most of the issues at this point still have to do with design, noise, and cantilever relaxation." However, the two groups have made considerable progress with proof-of-concept experiments.

In 1991, using an adapted magnetic force microscope, Rugar and visiting scientist Othmar Züger performed ESR imaging with micrometer resolution. Since then, the groups have performed NMR imaging at the same resolution with a sensitivity of 10^{12} nuclei. "We've actually quite a long way to go before we can detect single spins, but the good news is, that's a thousandfold more sensitive than conventional NMR," says Rugar.

Squeezing NMR onto a cantilever tip

How do you put an NMR spectrometer on an AFM cantilever? Obviously, miniaturization is not the answer. Instead, MRFM is based on the magnetic field gradients used for magnetic resonance imaging and on the Stern-Gerlach effect (the idea that extremely small groups of spins are effectively self-polarizing). In current designs, the sample material is mounted on the cantilever with epoxy and placed close to a very small permanent magnet, which creates a field gradient. A radio frequency (rf) coil that modulates the sample magnetization at the resonant frequency of the cantilever sits nearby.

This configuration is the reverse of the one used for conventional AFM or magnetic force microscopy. In those methods, the cantilever contains the sensing instrumentation and rasters across a sample mounted on a stage. "Ultimately, we want to put the permanent magnet on the cantilever," Rugar explains, "but the magnetic tips that are suited to our current conditions are too large to fit. They have to be ~ 1 mm in diameter to develop gradients that are compatible with the current sensitivity of the instrument, but the cantilever is only 0.1 mm in length, so putting the sample on the cantilever is an expedient first step."

The gradient created by the permanent magnet provides the spatial resolution for imaging, says Yannoni. "A permanent magnet has a strong magnetic field that falls off rapidly. The smaller the magnet, the larger the gradient it will have." Current magnets generate gradients as large as 10 G/ μm to give a spatial resolution of ~ 2 μm . Eventually, very small magnets should be able to generate gradients of ~ 100 G/ \AA , which in principle could improve spatial resolution to 0.1 \AA .

MRFM exploits the gradient for "slice-selective" imaging of the sample in a manner similar to that of medical MRI but on a much smaller scale.

Because of the gradient created by the magnet, the field at various points surrounding the magnet tip is either too strong or too weak for resonance with the sample. Only a specific cross-section of the sample lies at the right distance from the magnet for its spin precession to be on resonance and to cause deflection in the cantilever tip. As the radio frequency is scanned in steps, the position of this resonance zone moves along the sample in the z direction and allows imaging of the entire sample in slices. "For each frequency step, the cantilever with the sample is physically raster scanned in x and y with respect to the permanent magnet to achieve full 3-D imaging," Rugar says.

*The gradient of
the permanent
magnet provides
high enough
spatial resolution
for imaging.*

Most of the rf modulation techniques being used for MRFM are analogous to continuous-wave (CW) NMR, says Yannoni. "In normal NMR and ESR [electron spin resonance], you have direct detection of spin precession at frequencies of a few hundred MHz or GHz, respectively. However, the cantilevers can't oscillate fast enough to keep up with the precession, so we have to match the spin frequencies by methods such as cyclic saturation for ESR and cyclic adiabatic inversion for NMR. We've also done some pulse experiments followed by CW measurement."

MRFM differs from conventional NMR, ESR, and MRI in that the rf coil is used only for manipulating the sample spins, not for detection. Based on current understanding, says Sidles, it appears that neither rf coils nor superconducting quantum interference detectors (SQUIDs),

another possibility he considered early on, are adaptable to detect spins at such a small scale. "I mention this to provoke the SQUID community to design one that can," he says. Optical detection of cantilever response to small forces is much more sensitive, he says. In this case, a fiber-optic interferometer registers the harmonic cantilever deflections after deconvolution produces images of the sample on the cantilever.

Forcing the issue

The main limitation to the use of MRFM is its force sensitivity. "It turns out that detecting a single spin requires a force sensitivity of $\sim 10^{-16}$ N for unpaired electrons and $\sim 10^{-19}$ N for protons," Sidles says. MRFM currently detects forces at $\sim 10^{-16}$ N, which he and Rugar point out is 10^4 – 10^6 times more sensitive than conventional AFM. It's just sensitive enough to try for single-spin ESR, the current focus of the IBM group's experiments, but it's still between 100-fold and 1000-fold less sensitive than it needs to be for single-spin NMR.

Increasing the force sensitivity of MRFM will require a decrease in noise picked up by the optical interferometer and increases in cantilever relaxation time and sensitivity. In practice, the experiments will probably have to be run at cryogenic temperatures (3–10 K) to reduce thermal noise. The current experiments are usually run at room temperature and at millitorr vacuum.

Increasing the cantilever sensitivity will also require ways to make the cantilever thinner and more flexible. "Commercial AFM cantilevers are 0.5–1 μm thick," says Rugar. "We've borrowed an integrated circuit fabrication technique where you lay down thin layers of silicon nitride in the shape of a cantilever on a silicon substrate and then etch the substrate out from under the cantilever. One of our post-docs, Storrs Hoen, has made cantilevers 0.09 μm thick for our NMR experiments. We've even made some cantilevers that are only 0.02 μm thick."

The thinner and more sensitive cantilevers should accommodate the use of higher magnetic field gradients as well as shorter distances between the cantilever and magnet for greater gradient resolution. Currently, the cantilever-magnet

distance is typically 0.1–1 mm, Rugar says. "For single-spin experiments, we'll need to decrease that to a few hundred angstroms."

Seeking out potential

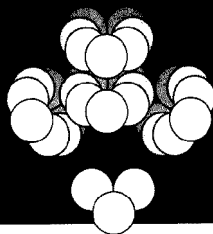
After five years and much publicity, the researchers at UW and IBM are cautious about making too many claims for MRFM. "There are so many competing imaging technologies and other good techniques for single-molecule detection that developing MRFM for those purposes alone makes no sense," Sidles says. On the other hand, Yannoni says, "We've already made a lot of progress. Because of the improvement in sensitivity, the NMR community is really following MRFM closely."

The ability to characterize individual protein structures in situ rather than purified in solution or in crystallized form for NMR or XRD would be extremely valuable, Sidles says, especially for transmembrane proteins that are highly lipophilic and hard to crystallize. These proteins tend to have active sites for hormone or drug reception or ion transport channels. "Force microscopes don't see into the channels and active sites, but NMR could," says Sidles.

Because electron spins are easier to detect than nuclear spins, ESR applications of MRFM might come first. "ESR is not as useful for structural determination as NMR," Rugar says, but it could be useful for spin-labeling techniques. Some of the suggested applications include the observation of receptor–ligand binding or the lattice structure of lipid membrane bilayers. Sidles adds that many metalloproteins have single electron spins and that the component subunits or strands of biological molecules such as DNA, RNA, and proteins could be spin labeled for observation of the self-assembly process. "I see these uses of MRFM as a key bridge technology that can lead to more difficult proton spin applications in the long term," he says. "Scanning probe microscopy in general is a fertile technology, and this adds one more wrinkle." *Deborah Noble*

Suggested reading

Sidles, J. A.; Garbini, J. L.; Bruland, K. J.; Rugar, D.; Züger, O.; Hoeh, S.; Yannoni, C. S. *Rev. Mod. Phys.* **1995**, *67*, 249–65.
Rugar, D.; Yannoni, C. S.; Sidles, J. A. *Nature* **1992**, *360*, 563–66.



The Future of Polymer Research

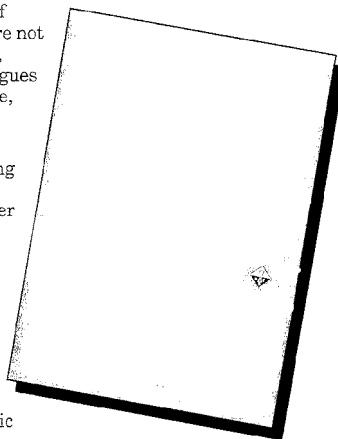
...Is Yours Today With MACROMOLECULES

In the ever changing field of polymer chemistry, if you're not reading **MACROMOLECULES**, you're missing what your colleagues regard as the most authoritative, in-depth coverage anywhere.

Each biweekly issue of **MACROMOLECULES** will bring you up-to-date, peer-reviewed coverage of all aspects of polymer chemistry including:

- ▲ synthesis
- ▲ polymerization mechanisms and kinetics
- ▲ chemical reactions
- ▲ solution characteristics
- ▲ bulk properties of organic polymers, inorganic polymers and biopolymers

For information you can trust to keep you on the cutting edge of the science of polymer chemistry, you simply cannot afford to do without a subscription to **MACROMOLECULES**.



1995 Subscription Rates

		U.S.	Canada & Mexico	Europe*	All Other Countries*
ACS Members	One Year	\$ 84	\$ 136	\$ 209	\$ 251
	Two Years	\$ 151	\$ 255	\$ 401	\$ 485
Nonmembers	One Year	\$1,145	\$1,197	\$1,270	\$1,312

(Member rates are for personal use only. Journal subscriptions start January 1995. For nonmember subscriptions in Japan, contact Maruzen Company, Ltd.)

To place your order simply call 1-800-333-9511 in the U.S.*, or send your order to:

ACS PUBLICATIONS

Essential Resources for the Chemical Sciences

American Chemical Society
Member and Subscriber Services
P.O. Box 3337
Columbus, OH 43210

* Outside the U.S. dial (614) 447-3776, or you may fax your order to 614-447-3671.

MACROMOLECULES

Editor: Robert W. Lenz — *University of Massachusetts*

**ACS
STUDENT
MEMBERS**

Access Your Future Success Today
with the leading scholarship advancing the chemical sciences

Print 1995	U.S.	Canada/ Mexico	Europe Air Svc.	All Others Air Svc.	Print 1995	U.S.	Canada/ Mexico	Europe Air Svc.	All Others Air Svc.
New editor!					Journal of Chemical Information and Computer Sciences (Bimonthly)				
<i>Accounts of Chemical Research</i> (Monthly)					Student Members	\$ 17.25	\$ 25.25	\$ 34.25	\$ 39.25
Student Members	\$ 14.50	\$ 23.50	\$ 27.50	\$ 31.50	Journal of Medicinal Chemistry (Biweekly)				
<i>Advance ACS Abstracts</i> (Semi-monthly) Co-published with CAS					Student Members				
Student Members	\$ 30.00	\$ 53.00	\$ 81.00	\$ 100.00	<i>The Journal of Organic Chemistry</i> (Biweekly)				
<i>Analytical Chemistry</i> (Semi-monthly)					Student Members				
Student Members	\$ 30.00	\$ 67.00	\$ 113.00	\$ 138.00	<i>The Journal of Physical Chemistry</i> (Weekly)				
<i>Biochemistry</i> (Weekly) Also available on CD-ROM*					Student Members				
Student Members	\$ 86.25	\$ 195.25	\$ 355.25	\$ 439.25	<i>Langmuir</i> (Monthly)				
<i>Bioconjugate Chemistry</i> (Bimonthly)					Student Members				
Student Members	\$ 23.25	\$ 32.25	\$ 38.25	\$ 42.25	New editor!				
More issues!					<i>Macromolecules</i> (Biweekly)				
<i>Chemical Research in Toxicology</i> (8 Issues/Year)					Student Members				
Student Members	\$ 35.25	\$ 44.25	\$ 53.25	\$ 57.25	<i>Organometallics</i> (Monthly)				
<i>Chemical Reviews</i> (8 Issues/Year)					Student Members				
Student Members	\$ 27.00	\$ 43.00	\$ 67.00	\$ 77.00	ALSO AVAILABLE AT ACS MEMBER RATES . . .				
<i>Chemistry of Materials</i> (Monthly)					<i>Angewandte Chemie</i> (Semi-monthly) A publication of the GDCh				
Student Members	\$ 37.50	\$ 56.50	\$ 76.50	\$ 88.50	First Class				
<i>CHEMTECH</i> (Monthly)					Student Members				
Student Members	\$ 21.00	\$ 31.00	\$ 38.00	\$ 43.00	Air Mail				
<i>Energy & Fuels</i> (Bimonthly)					ACS Members				
Student Members	\$ 36.75	\$ 45.75	\$ 53.75	\$ 58.75	<i>Biotechnology Progress</i> (Bimonthly) Co-published with AIChE				
<i>Environmental Science & Technology</i> (Monthly)					ACS Members				
Student Members	\$ 33.00	\$ 57.00	\$ 85.00	\$ 102.00	New!				
<i>Industrial & Engineering Chemistry Research</i> (Monthly)					<i>Chemical Health & Safety</i> (Bimonthly) Co-published with CHAS Division				
Student Members	\$ 48.75	\$ 72.75	\$ 100.75	\$ 114.75	ACS Members				
<i>Inorganic Chemistry</i> (Biweekly)					ACS Members				
Student Members	\$ 68.25	\$ 109.25	\$ 162.25	\$ 192.25	<i>Chemistry & Industry</i> (Semi-monthly)				
<i>Journal of Agricultural and Food Chemistry</i> (Monthly)					Published by the Society of Chemical Industry				
Student Members	\$ 26.25	\$ 45.25	\$ 68.25	\$ 82.25	ACS Members				
More issues!					<i>Journal of Pharmaceutical Sciences</i> (Monthly) Co-published with APHA				
<i>Journal of the American Chemical Society</i> (Weekly) Also available on CD-ROM*					ACS Members				
Student Members	\$ 80.25	\$ 149.25	\$ 261.25	\$ 321.25	<i>Journal of Physical and Chemical Reference Data</i> (Bimonthly)				
<i>Journal of Chemical & Engineering Data</i> (Bimonthly)					Jointly published by ACS, AIP and NIST				
Student Members	\$ 27.75	\$ 33.75	\$ 39.75	\$ 41.75	ACS Members				
					<i>Today's Chemist at Work</i> (Monthly)				
					ACS Members				

**ACS Student Members
SUBSCRIPTION ORDER FORM**

Start my one-year subscription to the ACS journals listed below at the special price indicated. My satisfaction's completely guaranteed with ACS's refund-in-full cancellation policy. (Please allow 45 days for delivery to begin.)

Title _____	Price _____	Title _____	Price _____
_____	_____	_____	_____

Name/Address _____

Enclosed is \$ _____ (Payable to American Chemical Society)

Bill me.

Charge my VISA/MasterCard.

Acct. # _____ Expires _____ Signature _____

I am a student member.

Please send me information on how to become a student member.

Order TOLL FREE 1-800-333-9511.
Outside the U.S. call 614-447-3776. FAX: 614-447-3671.

MAIL TO: American Chemical Society • Publications Marketing Department
1155 Sixteenth Street, N.W. • Washington, D.C. 20036

*Save \$\$\$
Work smarter.*

PUBLISHED BY THE CHEMICAL SOCIETY
OF JAPAN, AVAILABLE FROM ACS . . .

Bulletin of the Chemical Society of Japan (Monthly)
ACS Members/Nonmembers in North America:
\$ 552.00

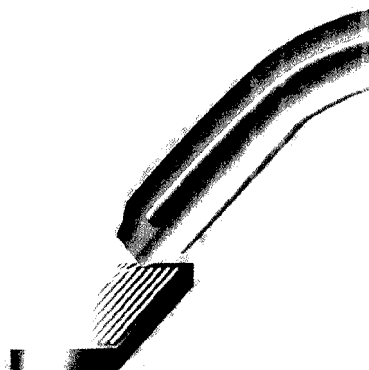
Chemistry Letters (Monthly)
ACS Members/Nonmembers in North America:
\$ 298.00

NOTE: Member rates are for personal use only. Journal subscriptions are based on a calendar year. Member subscriptions to *Advance ACS Abstracts*, *Analytical Chemistry*, *Chemical Health & Safety*, *CHEMTECH*, *Environmental Science & Technology*, *Journal of Pharmaceutical Sciences*, and *Today's Chemist at Work* may start any month and expire one year later. Please indicate starting month.

* To find out about ACS Publications on DISC call 1-800-333-9511 or 614-447-3776.

ACS PUBLICATIONS
Essential Resources for the Chemical Sciences

0954X



Scanning the new techniques for XPS

X-ray photoelectron spectroscopy (XPS), or electron spectroscopy for chemical analysis (ESCA), as it is also known, can be used to characterize the elemental and chemical composition of materials at their extreme surface, typically at depths no greater than 10 nm (100 Å), although with sputtering it can be used for depth profiling. Applications include quantitative surface analysis, stoichiometric determinations, detection of oxidation states, and the observation of layer growth, interface structures, and surface modifications. In the past 15 years, these applications have become increasingly important to the semiconductor, layered polymer, and magnetic materials industries.

All elements except hydrogen and helium are detectable by XPS. An X-ray tube or synchrotron beamline sends a beam of X-rays onto the sample surface, causing the ejection of core and valence-level electrons (photoelectrons). The photoelectrons are focused into an electron energy analyzer and then onto a detector, all under ultrahigh vacuum. The photon electron energy is characteristic not only of the element but also of the chemical en-

As new research uses for XPS emerge, so do new strategies for accomplishing them

vironment of the atoms from which the electrons were ejected.

Routine applications of XPS have been established to the point where XPS can be a modular add-on feature for a materials processing line. By contrast, research-grade instruments are becoming both more powerful and more diverse in their designs. In the past five years, newer capabilities such as imaging have been incorporated into most of the commercial research-grade instruments. However, different manufacturers use widely varying strategies and instrumentation to attain the same goals.

We asked Julia Fulghum of Kent State University for her comments on recent trends in XPS instrumentation and her advice for potential buyers. Table 1, although not intended to be comprehensive, features a selection of representative instruments. For more information, circle the appropriate number on the reader service card, use the Information Express page, or send an e-mail message to acprodrev@acs.org with a subject line containing one of the reflector keywords listed at the bottom of the table.

Sources

"Recently, some significant differences have developed in XPS source design," says Fulghum, whose laboratory has been a development site for some of the XPS instruments from Kratos Analytical. The most common X-ray sources for XPS are Mg and Al K α sources, with monochromatic Al K α sources becoming increasingly popular.

The monochromator decreases the X-ray linewidth for improved energy resolution and filters out the Bremsstrahlung and X-ray satellite background. Mono-

Table 1. Summary of representative products

Product	ESCALab 220i XL	Axis 165	Quantum 2000
Company	Fisons 55 Cherry Hill Dr. Beverly, MA 01915 508-524-1287	Kratos Analytical 535 East Crescent Ave. Ramsey, NJ 07446 201-825-7500	Physical Electronics 6509 Flying Cloud Dr. Eden Prairie, MN 55344 612-828-6100
Price range	\$500,000–\$900,000	\$350,000–\$800,000	\$600,000–\$700,000
Type	Research, multitechnique	Research, multitechnique	Research or routine
Source			
Type	Dual-anode Mg/Al; Al monochromator	Dual-anode Mg/Mg or Mg/Al; optional monochromator	Al monochromator
Focusing optics	Microfocusing monochromator	Optional 500-mm Rowland circle monochromator with quartz or toroidal crystals	10- μ m focused and scanning monochromator
Power	600 W dual anode; 200 W monochromator	450 W	100 W maximum
Sample chamber			
Sample size	4 in.	Choice of 15 mm. or 100 mm. diam. maximum	Up to 100 mm diam. or 75 mm \times 75 mm
Stage angle range	$\pm 90^\circ$	$\pm 180^\circ$ with manual control; $\pm 90^\circ$ automatic control	Tilt + 45 ; azimuthal > 360
Charge neutralization and electron energy range	Coaxial electron flood gun with selectable energy of 0–14 eV	Integral to base of analyzer input lens; uniform flood of electrons at ~ 0.1 eV	Electron flood source with energy range 0–20 eV
Electron energy analyzer			
Focusing optics	Magnetic and electrostatic lenses	165-mm hemispherical analyzer; electrostatic and magnetic lenses	High-transmission lens with dynamic emittance matching and dynamic dispersion compensation
Range	0–5000 eV	30–4800 eV standard, 10–1500 eV high resolution; programmable pass energy 5–260 eV with retard ratios of 2–20eV	0–3200 eV
Resolution	< 0.28 eV on Ag Fermi edge; < 0.46 eV on Ag 3d _{5/2} at fwhm	< 0.3 eV on Ag Fermi edge	< 0.3 eV on Ag Fermi edge; ≤ 0.5 eV on Ag 3d _{5/2} at fwhm
Detector			
Type	Channeltrons for spectroscopy; channel plates for imaging	Multichannel detector	Dual multichannel plates with multistrip detector array
Number of detectors	6 channeltrons	8 channeltrons	16
Imaging			
Method	Parallel imaging without scanning	Scanned focused analysis area; small-spot analysis area is electrostatically deflected in x and y	Scanning X-ray monochromator
Scan rate	NA	1 ms/point to > 10 s/point	0.5 μ s/pixel maximum
Resolution	< 5 μ m	< 30 μ m	< 10 μ m
Image area	120 μ m–8 mm diam.	100 μ m–2.5 mm diam. with magnetic lens; up to 10 mm without magnetic lens	Up to 1.5 mm \times 0.5 mm
Small-area analysis			
Sampling area range	20 μ m–8 mm diam.	From < 30 μ m to 3 mm \times 8 mm	≤ 10 μ m diam. – 1.5 mm \times 0.5 mm
Energy resolution	< 0.24 eV on Ag Fermi edge; < 0.42 eV on Ag 3d _{5/2} at fwhm	≤ 0.5 eV on Ag 3d _{5/2} fwhm over all analysis areas	≤ 0.5 eV on Ag 3d _{5/2} fwhm over all analysis areas
Data handling	Pentium PC with OS/2 platform and Eclipse control and data acquisition software	SunSparc workstation with UNIX platform and Vision software and graphical user interface	Online Sun SparcStation, offline Pentium PC with imbedded microprocessors for system control; online compass control software; offline Multipak data analysis software
Special features	Parallel imaging	Magnetic lens for imaging and charge neutralization	Scanning X-ray monochromator with "electronic rotating anode"; dynamic dispersion compensation; scanned X-ray image with secondary electrons
Options	Auger electron spectroscopy; SIMS; UV photoelectron spectroscopy; LEED; RHEED; EELS; ion-scattering spectroscopy; sample preparation accessories	Auger electron spectroscopy; SIMS; hot/cold sample stage; multiple sample parking; UV photoelectron spectroscopy	Hot/cold sample stage; < 2 μ m sample positioning with digital-encoded offline optical microscope; total in vacuo motorization with autosampling
Reader Service Number	401	402	403
E-mail reflector keyword	ac XPS622	ac XPS623	ac XPS624

NA = Not applicable

ESCA-200

Scientia-Xeion
P.O. Box 311
Short Hills, NJ 07078
201-564-8833
\$500,000–\$850,000
Research, multitechnique

A anode; monochromator

Multiarray of double-focusing quartz crystals

700 W

Standard, 3 in.; up to 8 in. optional

TiLl -5° to +185°; rotation ± 185

Electron flood gun with energy range
0–10 eV

200-mm radius hemispherical analyzer;
electrostatic lens

0–6000 eV

Ultimate, < 5 meV; XPS source-limited
resolution < 0.3 eV on Ag Fermi edge

2-D multichannel plate detector with CCD
camera readout

1

Electron energy analyzer retains spatial
distribution of electrons in x for E-x parallel
line imaging; sample is scanned in y for
E-x-y mapping

NA

< 7 μm ; ultimate, < 5 μm

E-x line imaging, (1–4 mm) \times (7–100 μm);

E-x-y mapping, (1–4 mm) \times 20 mm

Continuous from 7 μm \times 7 μm to 4 mm \times 100 μm
< 0.3 eV on the Fermi edge at ultimate spatial
resolution

Pentium PC with Windows-based control
and data acquisition software

On-axis sample monitoring; nondestructive
depth profiling with grazing polar angular
measurement at constant intensity and
energy resolution

Heating to 1000 °C; cooling to -180 °C; ion
etching and depth profiling; UV photoelectron
spectroscopy; angular-dispersed lens
mode; multi-analyte detection in angular
space with resolution < 0.5° with \pm 7° simultaneous recording range

404

ac: XPS625

chromatic sources are important in the analysis of delicate organic materials for which high-energy resolution and minimization of sample damage are necessary, Fulghum says. Several vendors now use a focused monochromatic X-ray source to decrease the analysis area on the sample surface, and one instrument (the Quantum 2000 from Physical Electronics) uses a scanning monochromatic X-ray source.

The choice of sources for optimization with a given sample type is still limited for most laboratories. However, most companies offer dual-anode X-ray sources that allow the user to choose the anode best suited to a particular application.

Recent advances in source capabilities include the construction of high-energy synchrotron facilities that produce tunable collimated X-ray beams with 1000-fold higher flux than in-lab sources. Much higher resolution and shorter data acquisition times are two of the benefits. But most of the synchrotron sites around the nation require researchers to apply for research time on a beamline and may allow only a few days or weeks of experiments per lab. "We all really want a tunable [in-lab] X-ray laser," Fulghum says.

Charge compensation

The availability of reliable monochromatic X-ray sources has increased the need for efficient charge neutralization methods. Neutralization is particularly important for strongly insulating samples, which can develop a positive surface charge as photoelectrons are ejected. Without a method for charge neutralization, photoelectron peaks tend to change shape and shift to higher binding energies, sometimes by as much as a few hundred electron volts. This problem becomes more important for small-area analyses and XPS imaging.

"The current standard method for neutralization is a source of low-energy electrons. The different spectrometers vary in the location of the source in the sample chamber, the energy of the electrons that are used, and the method used to get the electrons to the sample surface," says Fulghum. "In general, you're looking for the lowest energy electrons that can provide sufficient charge neutralization, so that you don't cause any damage to the sample in the process. The effort required to achieve good charge neutralization on different sample types varies from one instrument to another."

Sample type and analysis requirements are the most important factors in evaluating this feature, Fulghum says. "If some-

one mainly analyzes polymers, they need a monochromator and good charge neutralization, but for labs that analyze mainly conductive materials, other features such as high spatial resolution or sample handling may be more important."

Data acquisition

Currently, all commercial XPS instruments use a hemispherical electron energy analyzer and either channelplates or electron multiplier (channeltron) detectors. The most significant developments have occurred in the electron optics used to focus electrons from the sample surface into the energy analyzer.

Advances in lens systems have increased the flexibility of the instruments, allowing for small-area spectral analysis and imaging. For most instruments, the region on the sample for photoelectron collection can be adjusted from a few millimeters down to 10–50 μm on a side. Physical Electronics and Scientia accomplish this using electrostatic lenses; Kratos and Fisons use a combination of electrostatic and magnetic lenses. The use of a magnetic lens allows for a larger analyzer acceptance angle, higher magnification, and smaller spherical aberrations than are possible to achieve using electrostatic lenses alone.

The first successful commercial imaging XPS instrument appeared about 10 years ago, and in the past five years most of the vendors have developed image acquisition methods for their research instruments. "Imaging XPS is really new," says Fulghum. "The jury's still out on what it's best for. One of the most common uses of photoelectron imaging is to locate sites on a sample for small-area spectral acquisition. You can also use the images to show that a sample is heterogeneous or patterned as long as the surface features are compatible with the spatial resolution of the instrument. Current instruments have an ultimate spatial resolution of 2–20 μm ."

However, comparing one imaging system with another, solely on the basis of specifications, is nearly impossible, she cautions. "This is one of the areas where the instruments vary the most," she says. There are currently several different modes of image acquisition used in commercial instruments. These include physical rastering of the X-ray beam, parallel image acquisition, and point-by-point acquisition that is accomplished by varying the area on the surface from which photoelectrons are ejected.

The best method of comparison for these instruments is to see images acquired on a sample that is typical for the lab. "Comparing acquisition times and just looking at images may not tell you very much, since you don't know how much effort was required to set up the instrument to acquire the image and any small-area spectra," Fulghum notes. "The real trick is to find a good imaging instrument which can acquire small-area, high energy resolution spectra."

Other considerations

Information about elemental or chemical distributions with depth can be obtained using one of two depth profiling methods. An ion gun can be used either to clean the sample surface or to remove layers of sample for additional XPS analyses. Destructive depth profiling capabilities have been improved for some of the current research instruments through the use of small-area depth profiling and/or sample rotation during a depth profile. "Either of these methods has the potential to improve depth resolution significantly," Fulghum comments.

Angular-resolved XPS can be used to determine layer thicknesses or concentration gradients nondestructively in the first ~ 10 nm of the sample. This method is becoming increasingly important for microelectronics applications as gate oxides become thinner. The sample is tilted with respect to the analyzer to vary the angle at which photoelectrons are detected. Photoelectrons from the extreme surface atoms are emitted at glancing angles, whereas those from subsurface layers are emitted at angles approaching normal to the surface.

The drawback to this method, says Fulghum, lies in data handling and interpretation. "The problem is that there's no unique mathematical solution to determine how something is distributed over a surface using these data. It's a question of how well you can do using assumptions. The appropriate algorithms for data analysis are an area of current research.

She notes that multitechnique instruments that combine XPS with Auger electron spectroscopy or SIMS go in and out of style. "Six to eight years ago, the vendors' motto seemed to be 'You name it,

we can do it,' and multitechnique instruments were standard. Then there was a generation of stand-alone research-grade XPS instruments. Now we're seeing more multitechnique systems again, although generally just combining two techniques. The problem with combination instruments is that you can't optimize both methods. On the other hand, these instruments are usually less expensive than two stand-alone models would be."

Shopping around

Fulghum's general advice to potential buyers of research XPS instruments is to look for the features that are most important for their applications and sample types. "When evaluating instruments, be sure to take samples that are representative of your routine requirements as well as samples that are a real challenge. If at all possible, don't try to do science during your instrument demonstration. You'll learn a lot more about the instrument from running six very different sample types than you will by looking for subtle differences among six similar samples."

Deborah Noble

Just Published!

Understanding Medications: What the Label Doesn't Tell You

In this engaging new volume, Dr. Alfred Burger, founding editor of the journal *Medicinal Chemistry*, translates complex topics into clear and understandable terms for the nonexpert. The information he provides will both stimulate and satisfy readers' curiosity.

Covering the fate of chemical drugs, drugs of abuse, drug interactions, drug incompatibilities, the role of nutrition and diet in the control of diseases, and over-the-counter drugs, *Understanding Medications* answers many frequently asked questions. It explains the mode of action of most major drugs, discusses the action of hormones, vitamins, enzymes, and other biocatalysts, and explores the economic, ethical, and medical factors of drugs.

Dr. Burger also writes about the work of biologists, chemotherapists, and other medicinal researchers, and presents a compelling history of the discovery of drugs, including digitalis, aspirin, and sulfanilamides.

Valuable reading for anyone interested in the history, uses, and action of medications.

Alfred Burger, University of Virginia

206 pages (1995)

Clothbound ISBN 0-8412-3210-5

\$39.95

Paperbound ISBN 0-8112-3246-6

\$21.95

Contents

Drugs: Historical Beginnings
Early Modern Medicines
Naming Drugs
Biomedical Research
Modern Drug Discovery and Development
Molecular Modification of Prototype Drugs
Drug Use and Abuse
Neurohormones and Drugs That Affect the Central Nervous System
Drugs for the Relief from Pain
Local Anesthetics, Antispasmodics, and Antihistamines
Drugs That Act on the Blood Pressure and the Heart
Intestinal Tract Medications
Hormones and Vitamins
Drugs for the Treatment of Cancer
Drugs Affecting the Immune Response
Drugs for Infectious Diseases
Antiparasitic Drugs
Antiviral Drugs
Computer Assistance in Medicinal Research
Antiseptics and Disinfectants
What's Next?

ORDER FROM: American Chemical Society, 1155 Sixteenth Street, NW, Washington, DC 20036
Or CALL TOLL FREE **1-800-227-5558**

(in Washington, DC 872-4363) and use your credit card!

FAX: 202-872-6067.

ACS Publications Catalog now available on internet: gopher.acsinfo.acs.org or
URL <http://pubs.acs.org>

THE END OF INSCRUTABLE DISQUISITION.

The task of keeping up with the latest advances in chemical research can be daunting.

However, there is an easy way to gain a vital overview of basic research and applications in all areas of chemistry. Subscribe to *Accounts of Chemical Research* (ACR). ACR publishes leading researchers' reports of their own work. Concise, critical articles help end controversies,

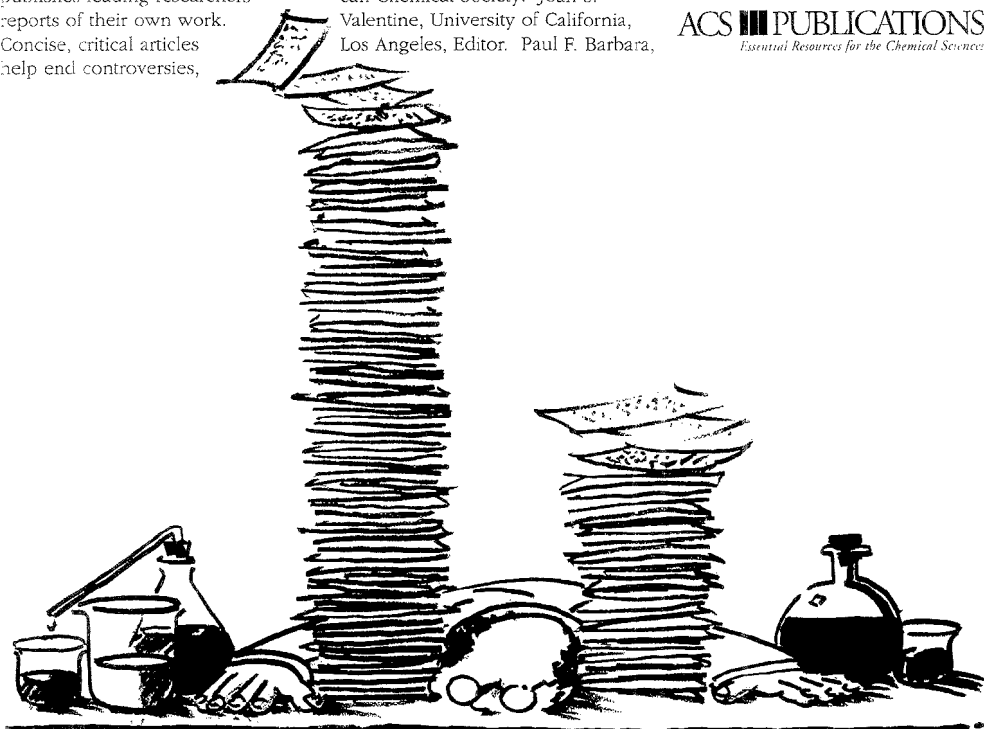
relate recent advances to earlier work, and project their future significance.

Place your order today by calling 1-800-333-9511. Outside the U.S. call 614-447-3776.

Accounts of Chemical Research is published monthly by the American Chemical Society. Joan S. Valentine, University of California, Los Angeles, Editor. Paul F. Barbara,

University of Minnesota, and Christopher S. Foote, University of California, Los Angeles, Associate Editors. Subscription rates in the U.S. for ACS Members are \$29 for one year, \$52 for two years. Nonmembers are \$204 for one year. Call for rates outside the U.S.

ACS PUBLICATIONS
Essential Resources for the Chemical Sciences

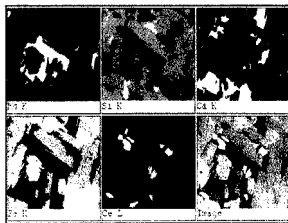


X-ray imaging for SEM

The IMIX-PTS is an energy-dispersive XRF module designed to provide pixel-by-pixel X-ray spectra of scanning electron microscope images. The instrument combines digital beam control with a digital pulse processor to perform "position-tagged spectrometry" in which the full XRF spectrum for each point in the SEM image is acquired in real time and tagged with the specimen *x* and *y* coordinates. The comprehensive data set is collected as a database and subsets are selected for specific imaging or chemical mapping applications.

The pulse processor contains a digital Si(Li) detector for enhanced sensitivity and energy resolution at high count rates and to reduce noise during the determination of lighter elements. The instrument detectors for the IMIX-PTS have an active area of 60 mm² as compared with the more conventional 30 mm² and can determine all elements down to boron.

Specific points, lines, or regions for analysis can be selected directly from a digital micrograph display on the Sun



workstation, and automated data collection can be performed using spot collection or variable-size rastering. The image analysis software features transforms, filters, and image optimization functions such as grain boundary reconstruction, particle cutting, and edge detection. Applications packages include feature analysis with chemical classification, stereo depth and true surface area measurement, coatings analysis, critical dimension measurement, grain sizing, and inclusion analysis. An optional automation package controls all electron microscope functions. **Princeton Gamma-Tech** ■ 406

INSTRUMENTATION

ELISA

Spectramax 340 is a tunable microplate reader for fluorescence-based immunoassays and similar microplate assays. A grating monochromator replaces conventional interference filters and allows tuning to the optimum wavelength for a particular assay. The microplate reader is controlled through software that performs data reduction and analysis and can be customized with user-programmed protocols, formulas, and report formats.

Molecular Devices ■ 405

RI detection

The ERC 7515A RI detector for LC permits the detection of sugars, carbohydrates, vitamins, organic acids, alcohols, and

other analytes that cannot be determined by a standard UV detector. Optical balance and recorder signals are displayed on an LCD panel. **Polymer Laboratories** ■ 407

Column selector

Scout software-controlled multicolumn switching device for perfusion chromatography systems is designed for automated multidimensional chromatography methods development and other applications. The selector features two biocompatible selection valves with seven ports each and up to six different columns can be attached at a given time. Column switching can be performed sequentially, with multiple runs on a given column before switching over, or with random access. Separations can be optimized by

screening columns with different selectivities or bed heights. Columns up to 24 mm in diameter and 30 cm long can be used with the selector. Column switching can also be used to perform automated batch column cleaning, testing, or conditioning. **PerSeptive Biosystems**

■ 408

Tablet dissolution

Model 2230A is a compact dissolution sampler for HPLC with external filtering capability that is designed to sample from up to 12 vessels. It accommodates sample volumes from 0.1–20 mL and can be programmed through keypad commands to calibrate all six pump channels simultaneously. The sampler operates in collect, collect and transfer, and transfer-only modes; up to seven dissolution protocols can be stored in memory. Options include media replacement and direct collection into most HPLC vials, and an injection valve and transfer pump allow on-line operation with HPLC. **Distek** ■ 409

LITERATURE

CCD

Guide to selecting electronic cameras for analytical application describes different types of CCD cameras, including intensified, integrating, and scientific video cameras, uncooled "megapixel" cameras, and high-performance cooled CCDs. Advantages and disadvantages, recommended applications, and price versus performance trade-offs are discussed for each type of camera. **Photometrics** ■ 410

FT-IR

"Complete Guide to FT-IR" describes FT-IR sampling accessories for liquid and solid transmission, diffuse reflectance, attenuated total reflectance, and specular reflectance as well as beam condensers, fiber optics, FT-IR microscopes, sampling kits, cells, windows, and software and spectral databases. New products include the InspectIR microsampling and videosampling accessory and the IR-Plan Advantage microscope.

Spectra-Tech ■ 411

CATALOGS

Chromatography

1995/1996 chromatography catalog lists vials, caps, seals, crimping tools, and sample racks. The catalog is illustrated with photographs and comparison charts and contains numerous tables on vial compatibility with commercial instruments.

Chromacol ■ 412

TOFMS

Catalog featuring time-of-flight mass spectrometers includes complete systems and subassemblies with flexible levels of system automation. Both EI- and MALDI-based instruments are featured, as are

unusual configurations and modules such as TOFMS combined with electrostatic energy analyzers for serial or parallel energy and mass analysis. The catalog includes selection guides for matching the appropriate instruments and components with user applications. **Comstock**

■ 413

Postcolumn derivatization

Catalog of postcolumn products for HPLC includes postcolumn reactors, column heaters, columns, mobile phases, and derivatization reagents. Product specifications and a guide to postcolumn derivatization methods are included. **Pickering**

■ 414

MS

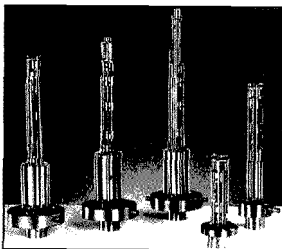
3F/PIC Series quadrupole mass spectrometers for low-mass compound characterization are designed for research applications ranging from fast-event UHV gas studies and thermal desorption to time-resolved measurements, radical analysis, and mass analysis of low-energy ions. The systems include a triple-stage quadrupole mass filter with a selection of integral electron impact ionization sources including radially symmetric and cross-beam designs, and an electron multiplier detector with 24-bit resolution and detector gating with resolution to 1 μ s.

The triple mass filter is designed to provide enhanced sensitivity for high-mass fragments in a 7-decade continuous dynamic range. Three versions are available for maximum masses of 300, 510, or 1000 Da. Short rf-only filter sections precede and follow the primary mass filter for control of electrostatic fringe fields and efficient high-mass transmission. The rf prefilter also guards the main mass filter from contamination for longer stability.

Windows-based software controls the ion source and mass filter scanning electronics for real-time tuning of filament voltage, mass selection, mass res-

olution, sensitivity, gain, scan times, and dwell times. Data are stored with the operating parameters on a scan-by-scan basis so that interactive tuning operations are saved throughout the experiment.

More than 100 mass channels can be monitored in multiple ion detection mode. Other modes include analog display and monitoring of user-definable mass peaks with respect to energy and other scanned parameters for applications such as radicals analysis via threshold ionization MS. The software provides interactive peak overlap warnings and suggests alternative mass numbers from the spectral library for analyses of complex mixtures. **Hidden Analytical ■ 415**



Multidispersive XRF

The MDX1000 is a compact XRF spectrometer designed for simultaneous measurement of both light and heavy elements in routine applications. It combines energy-dispersive and wavelength-dispersive XRF detection systems for optimization of both light and heavy-element determinations. Elements from fluorine to uranium are detectable at concentrations ranging from sub-part-per-million to 100%.

A 200-W end window Rh target X-ray tube is used for excitation. Wavelength-dispersive monochromators are available with flat or curved crystals for the fixed-element channels. The 2-channel energy-dispersive Si detector does not require liquid nitrogen cooling and the system can be configured for up to 10 detector channels.

The instrument can be controlled either manually or with full automation through Windows software. Preset parameters for common applications are included in the software, as is a spectral library for qualitative and semi-quantitative analysis. The spectrometer handles a variety of sample types including solids, liquids, granules, and powders, and an optional autosampler accommodates up to 72 samples.

Oxford ■ 416



**For more information,
please circle the appropriate
numbers on one of our
Reader Service Cards.**

ASSISTANT PROFESSOR POSITION IN ENVIRONMENTAL CHEMISTRY

The Department of Chemistry invites applications for a tenure-track faculty position at the Assistant Professor rank to commence **September 1, 1996**.

The Department seeks candidates with a background in environmental chemistry to promote an excellent teaching program in that area. The successful candidate will be expected to develop a vigorous research program in environmental chemistry, or in a closely related area, supported by external funding.

Applicants should send a complete resume, a proposal of research and a list of three individuals willing to act as referees with their addresses, telephone and/or fax numbers and, if possible, e-mail addresses to:

Professor Ralph Korteling
Chair, Department of Chemistry
SIMON FRASER UNIVERSITY
Burnaby, B.C. CANADA V5A 1S6
Fax: (604) 291-5424

Evaluation of applications will begin on **December 4, 1995**, but applications will be considered until the position is filled.

Simon Fraser University is an equal opportunity employer and strongly encourages applications from women and minorities. In accordance with Canadian immigration requirements, this advertisement is directed to Canadian citizens and permanent residents of Canada. The appointment is subject to final budgetary authorization.

HELP WANTED ADS

ROP display at ROP rates. Rate based on number of insertions within contract year. Cannot be combined for frequency.

Unit	1-Ti	6-Ti
1" (25 mm)	\$230	\$210
	12-Ti	24-Ti
	\$200	\$190

ANALYTICAL CHEMISTRY
1599 Post Road East
P.O. Box 231
Westport, CT 06881
203-256-8211/FAX: 203-256-8175



If this research succeeds, you'll be the next to know

But only if you subscribe to the *Journal of Medicinal Chemistry*! As the leading journal covering drug design and development, it's your best source for up-to-the-minute news about original research, early findings, and critical evaluations.

As a subscriber, you'll gain valuable access to landmark studies exploring the relationship between molecular structure and biological activity. And, cutting-edge information on drug design and allied activities will help you increase your research scope and efficiency. The *Journal of Medicinal Chemistry* spotlights the most significant primary research in the world today, and gives you new information with unprecedented speed!

Be the next in line for critical information.

Subscribe to the *Journal of Medicinal Chemistry* today!

Call Toll-Free 1-800-333-9511

ACS PUBLICATIONS
Essential Resources for the Chemical Sciences

American Chemical Society
 1155 Sixteenth Street, N.W.
 Washington, DC 20036

Laboratory Service Center

Laboratory Service Center (Equipment, Materials, Services, Instruments for Leasing). Maximum space — 4 inches per advertisement. Column width, 2-3/16"; two column width, 4-9/16". Artwork accepted. No combination of directory rates with ROP advertising. Rates based on number of inches used within 12 months from first date of first insertion. Per inch: 1" — \$200; 12" — \$195; 24" — \$190; 36" — \$185; 48" — \$180.

Call or write Jane Gatenby

ANALYTICAL CHEMISTRY
1599 Post Road East
P.O. Box 231
Westport, CT 06881
203-256-8211 / FAX: 203-256-8175

QUARTZ/PYREX®

• Material • Labware • Apparatus
We are veteran specialists in machining and fabrication, or repair and modification, of your custom lab apparatus.
Send for our latest catalog today.

TECHNICAL GLASS PRODUCTS
8720 Twimbrook • Mentor, OH 44060
216/974-2600 • FAX: 216/974-1292

FREE DATA, FAST

To quickly amass data on all of the products you need, consult the Lab Data Service Section on our *Analytical Chemistry* reader reply card insert.

Index to Advertisers

CIRCLE INQUIRY NO.	ADVERTISERS	PAGE NO.
13	*B&J, Inc.	IFC
2	Brinkmann Instruments, Inc. Lyons Lavey Nickel Swift, Inc.	657A
16	**Bruker Analytische Messtechnik GmbH Haller Werbemittlung	668B
1	*Chem Service, Inc. Bremble & Sewforth	638A
14	*Finnigan MAT, Inc. Communications West	662A
7	*Hamilton Company	0BC
9-12	*Isco, Inc. Farneaux Associates	639A
6	L.P.A. LaMotte Company	629A
8	*Mallinckrodt Baker, Inc. Suegler, Wolls & Brunswick, Inc.	647A
5	*Perkin-Elmer Corporation V3G	642A
15	Scott Specialty Gases, Inc. Backer/Jani, Inc.	670A
3	*Shimadzu Scientific Instruments, Inc. West & Brady, Inc.	632A

Classified section, see page 682A.

Directory section, page 683A.

**See ad in 1996 LabGuide Edition.*

***Companies so marked appear in Non-U.S. edition only.*

Advertising Management for the American Chemical Society Publications

CENTCOM, LTD.

President

James A. Byrne

Executive Vice President

Benjamin W. Jones

Joseph P. Stenza, Production Director

Laurence J. Doyle, Director of Marketing

1599 Post Road East
P.O. Box 231
Westport, Connecticut 06881-0231
(Area Code 203) 256-8211
Fax No. 203-256-8175

DIRECTOR, ADVERTISING SALES, LABORATORY PRODUCTS
Bruce E. Poorman

ADVERTISING PRODUCTION MANAGER

Jane F. Gatenby

SALES REPRESENTATIVES

Philadelphia, PA . . . CENTCOM, LTD., The Meadows, 485 Devon Park Drive, Suite 106, Wayne, PA 19087. Telephone: 610-964-8061, FAX: 610-964-807

New York/New Jersey . . . Dean A. Baldwin, John F. Rafferty, CENTCOM, LTD., Schoolhouse Plaza, 720 King Georges Post Road, Fords, NJ 08863. Telephone: 908-738-8200, FAX: 908-738-6128

Westport, CT/Boston, MA . . . Dean A. Baldwin, Michael J. Pak, CENTCOM, LTD., 1599 Post Road East, P.O. Box 231, Westport, CT 06881-0231. Telephone: 203-256-8211, FAX: 203-256-8175

Cleveland, OH . . . Bruce E. Poorman, Dean A. Baldwin, CENTCOM, LTD., 19035 Old Detroit Road, Suite 203, Rocky River, OH 44116. Telephone: 216-331-5151, FAX: 216-331-3432

Chicago, IL . . . Michael J. Pak, CENTCOM, LTD., 540 Frontage Rd., Northfield, IL 60093. Telephone: 708-441-6383, FAX: 708-441-6382

Houston, TX/Atlanta, GA . . . Edward M. Black, CENTCOM, LTD., P.O. Box 82096, Houston, TX 77082-0965. Telephone: 713-493-1560, FAX: 713-493-6673

West Coast . . . Bob LaPointe, CENTCOM, LTD., Suite 808, 2672 Bayshore Parkway, Mountain View, CA 94043-1010. Telephone: 415-969-4604, FAX: 415-969-2104

Denver, CO . . . Bob LaPointe, CENTCOM, LTD., Suite 808, 2672 Bayshore Parkway, Mountain View, CA 94043-1010. Telephone: 415-969-4604, FAX: 415-969-2104

United Kingdom, Scandinavia and Europe (Except: Germany, Switzerland, Austria, France, Italy, Spain) . . . Malcolm Thiele, Technomedia Ltd., Wood Cottage, Shurlock Row, Reading RG10 0QE, Berkshire, England. Telephone: 1734-343-302, FAX: 1734-343-948

Germany, Switzerland, Austria . . . IMP InterMediaPartners, GmbH, Deutscher Ring 40, 42327 Wuppertal, Germany. Telephone: (0202) 711091, FAX: (0202) 712431

France . . . Gerard Lecoeur, AIdmedia, 31-33 Grand rue de Saint-Rambert, 69009 Lyon, France. Telephone: 78-64-20-37, FAX: 78-83-56-67

Italy, Spain . . . Tess Serranti, Serranti Communications, 43 Van Sant Road, New Hope, PA 18938. Telephone: 610-598-0668, FAX: 610-598-0670

Hong Kong . . . SEAVEX, LIMITED, 503 Wilson House, 19 Wyndham Street, Central, Hong Kong. Telephone: 2868-2010, FAX: 2810-1283

Japan . . . Shigeyuki Yasui, Intercommunications (Japan), Inc., 2F Ginza ElwaBldg, 8-18-7 Ginza, Chuo-ku, Tokyo 104, Japan. Telephone: (03) 5565-0861, FAX: (03) 5565-0860

Korea . . . DooBee International Limited, Center Building (Byulgwan), 1-11 Jeong-dong, Choong-ku C.P.O. Box 4557, Seoul, Korea. Telephone: 822-776-2096, FAX: 822-755-9860

Singapore . . . SEAVEX, LIMITED, 400 Orchard Road, #10-01 Orchard Towers, Singapore 0923. Telephone: 734-9790, FAX: 732-5129

Taiwan . . . Epoch Limited, 2F No. 3, Lane 52, Nanking East Road, Section 4, P.O. Box 1642, Taipei, Taiwan, R.O.C. Telephone: 577-5441, FAX: 578-4308

South America . . . Bruce E. Poorman, CENTCOM, LTD., 19035 Old Detroit Road, Suite 203, Rocky River, OH 44116. Telephone: 216-331-5151, FAX: 216-331-3432

ANALYTICAL CHEMISTRY Information Express

Get the product data you need fast...

By Phone: Use the reference list below, and contact the companies to fill an immediate need, or...

By Fax: Use the fax form on the opposite page to send a direct written request.

Company	Page	Issue	RSN	Data+	Phone	Fax	Contact
AC Analytical Controls	623 A	10/1/95	415		215-639-7078	215-638-7096	Jim McCormack
Aldrich Chemical	1FC	10/15/95	none	●	414-273-3850	414-273-2095	Rich Gross
B&J	1FC	11/1/95	13	●	616-726-3171	616-728-8226	Kenneth L. Clark
Beckman Instruments	622 A	10/1/95	410	●	800-742-2345	714-773-8186	Amy Bratcher
Bioanalytical Systems	567 A	9/1/95	408	●	317-403-4572	317-497-1102	Craig Brumlett
Brinkmann Instruments	657 A	11/1/95	2	●	800-645-3050	516-334-7506	C. Shevchenko
Bruker Instruments	660 A	9/1/95	401	●	508-667-9580	508-66-3954	Mark Chaykovsky
Bruker Instruments	568 B*	11/1/95	16	●	0721/9528-0	0721/9528-712	
Carl Zeiss	565 A	9/1/95	415	●	800-356-1090	914-881-7443	Irv Toplin
Carl Zeiss Jena GmbH	623 A	10/1/95	417	●	49-3641-64-2500	49-3641-64-3311	Zeiss Gruppe
Chem Service	538 A	9/1/95	1	●	800-452-9894	610-692-8729	Ron Gray
Chem Service	839 A	11/1/95	1	●	800-452-9894	610-692-8729	Ron Gray
Chromacol	681 A	11/1/95	412	●	203-261-7582	203-261-7319	Donna Anthony
Comstock	681 A	11/1/95	413	●	615-483-7690	615-481-3884	Susan Zell
Ditek	680 A	11/1/95	409	●	908-422-7585	908-422-7310	Gerald Brinker
EG&G Instruments (Princeton)	610 A	10/1/95	10, 11	●	609-530-1000	609-863-7259	Ruth Rearick
Finnigan MAT	529 A	9/1/95	9	●	408-433-4800	408-433-4823	Gary Spear
Finnigan MAT	574 A	10/1/95	9	●	408-433-4800	408-433-4823	Gary Spear
Finnigan MAT	662 A	11/1/95	14	●	408-433-4800	408-433-4823	Gary Spear
Finnigan/Tremetrics	565 A	9/1/95	411	●	512-251-1555	512-251-1597	Elaine Moody
Fisons Instruments	622 A	10/1/95	413	●	508-524-1000	508-524-1100	Cathy Schaub
Fisons Instruments	618 A	10/1/95	401	●	508-524-1000	508-524-1100	Cathy Schaub
Fisons Instruments	676 A	11/1/95	401	●	508-524-1000	508-524-1100	Cathy Schaub
Fluka Chemie	509 A	9/1/95	5	●	41-81-7552511	41-81-7565449	
Fluka Chemie	57* A	10/1/95	1	●	41-81-7552511	41-81-7565449	
Hamilton	0BC	9/1/95	8	●	800-648-5950	702-856-7259	B. Milne/R. Beavers
Hamilton	0BC	11/1/95	7	●	800-648-5950	702-856-7259	B. Milne/R. Beavers
Hewlett-Packard	618 A	10/1/95	402	●	415-857-5603	415-857-8228	Doug Forsyth
Hidden Analytical	623 A	10/1/95	416	●	44-1925-445225	44-1925-416518	Ian D. Neale
Hidden Analytical	681 A	11/1/95	415	●	44-1925-445225	44-1925-416518	Ian D. Neale
Hinds Instruments	564 A	9/1/95	410	●	503-690-2000	503-690-3000	Ted Oakberg
Hi-Tech Scientific	564 A	9/1/95	409	●	44-722-323643	44-722-412153	David Mitchell
IN/US Systems	622 A	10/1/95	407	●	800-875-4687	813-620-3708	John Hinzdl
Isco	639 A	11/1/95	9-12	●	402-464-C231	402-464-0318	John R. Allington
Jeol USA	561 A	9/1/95	402	●	508-536-5900	508-536-2205	Robert DiPasquale
Jeol USA Inc.	0BC	10/1/95	7	●	508-536-5900	508-536-2205	Brian Musselrnan
John Wiley & Sons	591 A	10/1/95	5	●	212-850-6137	212-850-6264	S. Nelson
Kratos Analytical	676 A	11/1/95	402	●	201-825-7500	201-825-8659	David Surman
Labsphere	622 A	10/1/95	412	●	603-927-4266	603-927-4694	Joan A. Beaulieu
LPA	629 A	11/1/95	6	●	703-836-1360	703-836-6644	
Macrerey-Nagel	580 A	10/1/95	2	●	(02421) 969-0	(02421) 969-199	
Mallinckrodt Baker	647 A	11/1/95	8	●	800-582-2537	808-859-9318	William Broad
Melles Griot	622 A	10/1/95	409	●	800-835-2626	714-261-7589	Lynn Strickland
Metrohm	512 A	9/1/95	2	●	41-071-538-585	41-071-538-9041	R. Steiner
Metrohm	584 A	10/1/95	3	●	41-071-538-5	41-071-538-90	R. Steiner
Metrohm	6 C	10/1/95	none	●	41-071-538-5	41-071-538-90	R. Steiner
Mettler Toledo	565 A	9/1/95	412	●	800-639-6537	609-426-0121	Al Beronio
Molecular Devices	683 A	11/1/95	406	●	415-322-4790	415-322-2089	Kim Mulcahey
Oxford Instruments	681 A	11/1/95	417	●	508-371-5009	508-371-0204	Caroline Frankovich
Molecular Dynamics	564 A	9/1/95	408	●	800-333-5703	408-773-1493	Jim Bull
PE Nelson	618 A	10/1/95	403	●	408-577-2200	408-894-9307	Alycia Cortez-Frank
Perkin-Elmer	0BC	9/15/95	none	●	203-761-2574	203-762-6000	Mary Cooke-Kager
Perkin-Elmer	1BC	9/15/95	none	●	415-570-6667	415-638-6199	Valerie Tucker
Perkin-Elmer	589 A	10/1/95	6	●	415-570-6667	415-638-6199	Valerie Tucker
Perkin-Elmer	0BC	10/15/95	none	●	203-761-2574	203-762-6000	Mary Cooke-Kager
Perkin-Elmer	1BC	10/15/95	none	●	415-570-6667	415-638-6199	Valerie Tucker
Perkin-Elmer	642 A	11/1/95	5	●	415-570-6667	415-638-6199	Valerie Tucker
PerSeptive Biosystems	680 A	11/1/95	408	●	800-899-5858	508-393-7885	Charles Cuneo
Photometrics	564 A	9/1/95	405	●	602-889-9333	602-573-1944	Michelle Downs
Photometrics	680 A	11/1/95	410	●	602-889-9333	602-573-1944	Michelle Downs
Physical Electronics	676 A	11/1/95	403	●	612-828-6100	612-828-6109	John Hammond
Pickering Laboratories	681 A	11/1/95	414	●	415-694-6700	415-988-0749	John Deutschlander
Polymer Laboratories	680 A	11/1/95	407	●	413-253-5554	413-253-2476	Sheri Fetting
Princeton Gamma-Tech	680 A	11/1/95	406	●	609-924-7310	609-924-1729	Peter Quigley
Sapidyne Instruments	622 A	10/1/95	408	●	208-345-7677	208-392-4965	Steve Lackie
Scott Specialty Gases	1FC	9/1/95	7	●	215-766-6861	215-766-0320	Donna M. Vito
Scott Specialty Gases	599 A	10/1/95	8	●	215-766-6861	215-766-0320	Donna M. Vito
Scott Specialty Gases	670 A	11/1/95	15	●	215-766-6861	215-766-0320	Donna M. Vito
Shandon Lipshaw	565 A	9/1/95	413	●	800-547-7429	412-798-1138	Beverly Miller
Shimadzu Scientific Instruments	1FC	9/15/95	none	●	800-477-1227	410-381-1222	Roger Gresthead
Shimadzu Scientific Instruments	1FC	10/1/95	4	●	800-477-1227	410-381-1222	Roger Gresthead
Shimadzu Scientific Instruments	5 C	10/15/95	none	●	800-477-1227	410-381-1222	Roger Gresthead
Shimadzu Scientific Instruments	632 A	11/1/95	3	●	800-447-1227	410-381-1222	Roger Gresthead
Siemens Industrial Automation	622 A	10/1/95	411	●	404-740-3931	404-740-3998	Herbert Stuhler
Spectra-Tech	680 A	11/1/95	411	●	203-928-8998	203-928-8909	Debbie Esposito
Supelco	623 A	10/1/95	414	●	800-247-6628	800-247-3044	Michael Gray
Teledyne Electronic Technologies	521 A	9/1/95	3	●	415-962-6526	415-967-4353	Sharon Gomez
Thermo Separation Products	619 A	10/1/95	404	●	800-532-4752	408-526-9810	Brent Davis
Topac Scientific Instruments	565 A	9/1/95	414	●	617-740-8778	617-740-8779	Antoni Drybanski
Varian Associates	561 A	9/1/95	403, 404	●	415-424-6786	415-858-0480	Carl Hadjis
Varian Associates	619 A	10/1/95	405	●	415-242-6680	510-945-2335	Deborah Konnstrom
Varlen Instruments	564 A	9/1/95	406	●	800-729-4447	815-729-3700	Steve Klingler
Waters	619 A	10/1/95	406	●	800-252-4752	508-482-2674	Tony Lewis
Xelon	677 A	11/1/95	404	●	201-564-6833	201-564-8657	Jerry Rosenhal

Data+ Column: A bullet indicates that additional product and company information is available in the 1996 *Analytical Chemistry* LabGuide Edition.

RSN: Reader Service Number; *International Edition Only

PRODUCT DATA SERVICE

ANALYTICAL CHEMISTRY

NOVEMBER 7, 1995

Please circle the appropriate Reader Service Numbers to receive additional information.

Please help us determine your future laboratory buying trends. Which of the following products do you use, buy, specify, recommend or purchase? Circle all appropriate numbers on the attached reply card.

- 327 AA Spectroscopy
- 328 Analytical Services
- 329 Baths/Circulators
- 330 Biotechnology
- 331 Books/Periodicals
- 332 Centrifugation
- 333 Chemicals/Gases/Solvents
- 334 Computers/Software
- 335 Cooling/Freezing/Refrig.
- 336 Databases, Online
- 337 Densitometry
- 338 Detectors
- 339 Dryers/Evaporators
- 340 Electrochemistry
- 341 Elemental Analysis
- 342 Filtration
- 343 Flow Meters/Regulators
- 344 FT-IR Spectroscopy
- 345 Furnaces/Ovens
- 346 Gas Chromatography
- 347 General Lab Equipment
- 348 Heating/Temperature
- 349 Ion Chromatography
- 350 Lab Furniture/Hoods
- 351 Labware/Apparatus
- 352 Lasers/Fiber Optics
- 353 Liquid Chrom./HPLC
- 354 Mass Spectrometry
- 355 Microscopy
- 356 Capillary Electrophoresis
- 357 Mix/Stir/Blend/Grind
- 358 NMR Spectroscopy
- 359 Particle Size Analysis
- 360 Plasma Spectroscopy
- 361 pH/Ion Meters/Titrators
- 362 Pumping Monitoring
- 363 Recording/Integrating
- 364 Robotics/Automation
- 365 Sampling/Dispensing
- 366 Supercritical Fluid Chrom.
- 367 Spectrofluorometry
- 368 Stills/Purification
- 369 Surface Analysis
- 370 Thermal Analysis
- 371 Thin Layer Chrom.
- 372 UV-Vis Spectroscopy
- 373 Valves/Tubes/Fittings
- 374 Viscometry
- 375 Water/Moisture Analysis
- 376 Weighing/Balances
- 377 X-Ray Diffraction
- 378 X-Ray Spectroscopy

1	2	3	4	5	6	7	8	9	10	11	12	13	14	15	16	17
18	19	20	21	22	23	24	25	26	27	28	29	30	31	32	33	34
35	36	37	38	39	40	41	42	43	44	45	46	47	48	49	50	51
52	53	54	55	56	57	58	59	60	61	62	63	64	65	66	67	68
69	70	71	72	73	74	75	76	77	78	79	80	81	82	83	84	85
86	87	88	89	90	91	92	93	94	95	96	97	98	99	100	101	102
103	104	105	106	107	108	109	110	111	112	113	114	115	116	117	118	119
120	121	122	123	124	125	126	127	128	129	130	131	132	133	134	135	136
137	138	139	140	141	142	143	144	145	146	147	148	149	150	151	152	153
154	155	156	157	158	159	160	161	162	163	164	165	166	167	168	169	170
171	172	173	174	175	176	177	178	179	180	181	182	183	184	185	186	187
188	189	190	191	192	193	194	195	196	197	198	199	200	201	202	203	204

PRODUCT DATA SERVICE	327	328	329	330	331	332	333	334	335	336	337	338	339	340		
358	359	360	361	362	363	364	365	366	367	368	369	370	371	372	373	374
375	376	377	378													

NEW PRODUCTS	401	402	403	405	406	407	408	409	410	411	412	413	414	415		
416	417	418	419	420	421	422	423	424	425	426	427	428	429	430	431	432
433	434	435	436	437	438	439	440	441	442	443	444	445	446	447	448	449
450	451	452	453	454	455	456	457	458	459	460	461	462	463	464	465	466
467	468	469	470	471	472	473	474	475	476							

NAME (PLEASE PRINT) _____

TITLE _____

COMPANY _____

ADDRESS _____ MAIL STOP _____

CITY _____ STATE _____ ZIP _____

TELEPHONE _____ FAX _____

A. PRIMARY FIELD OF WORK

- 01 Energy
- 02 Environmental
- 03 Medical/Clinical
- 04 Drug/Toiletries
- 05 Forensic/Narcotic
- 06 Biotechnology
- 07 Metals
- 08 Pulp/Paper/Wood
- 09 Soaps/Cleaners
- 10 Paint/Coating/Inks
- 11 Electrical/Electronic
- 12 Instrument Dev./Design
- 13 Plastic/Polymer/Rubber
- 14 Agriculture/Food/Bev.
- 15 Inorganic Chemicals
- 16 Organic Chemicals

B. MY PRIMARY AREA OF EMPLOYMENT IS:

- INDUSTRIAL
- 17 Research & Development
- 18 Quality/Process Control
- MEDICAL/HOSPITAL
- 19 Research & Development
- 20 Clinical/Diagnostic
- GOVERNMENT
- 21 Research & Development
- COLLEGE/UNIVERSITY
- 22 Research & Development
- 23 Teaching
- INDEPENDENT/CONSULTING
- 24 Research & Development
- 25 Analysis/Testing

C. INTENSITY OF PRODUCT NEED

- 26 Purchasing Immediately
- 27 Within 3-6 months
- 28 Within 6-12 months
- 29 Future project

D. Is this your personal copy of Analytical Chemistry?

- Yes
- No



FOR FASTEST SERVICE, USE THIS CARD TO FAX YOUR REQUEST DIRECTLY TO THE ADVERTISER. PLEASE PHOTOCOPY THIS CARD FOR MULTIPLE USE.

TO: _____

FROM: _____

FAX: () _____ DATE: _____

MY NEED IS:

- Immediate
- 6 - 12 Mos.
- 12 + Mos.

I WANT TO KNOW MORE, PLEASE...

- Send Literature
- Have a Salesman Call
- Send Name of Nearest Dealer
- Send Me a Price Quote

Description: _____

Quantity: _____

I saw your... Advertisement Editorial Listing Regarding... on page _____ of the (date) _____ issue of AC

NAME: _____

TITLE: _____

COMPANY: _____

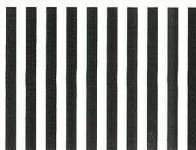
MAILSTOP: _____

STREET: _____

CITY: _____ STATE: _____ ZIP: _____

PHONE: _____ FAX: _____

NO POSTAGE
NECESSARY
IF MAILED
IN THE
UNITED STATES



BUSINESS REPLY MAIL
FIRST CLASS MAIL PERMIT NO 307 PITTSFIELD MA

POSTAGE WILL BE PAID BY ADDRESSEE

ANALYTICAL CHEMISTRY

PO BOX 5511
PITTSFIELD MA 01203-9384



PRODUCT DATA SERVICE

Please help us determine your future laboratory buying trends. Which of the following products do you use, buy, specify, recommend or purchase? Circle all appropriate numbers on the attached reply card.

- 327 AA Spectroscopy
- 328 Analytical Services
- 329 Baths/Circulators
- 330 Biotechnology
- 331 Books/Periodicals
- 332 Centrifugation
- 333 Chemicals/Gases/Solvents
- 334 Computers/Software
- 335 Cooling/Freezing/Refrig.
- 336 Databases, Online
- 337 Densitometry
- 338 Detectors
- 339 Dryers/Evaporators
- 340 Electrochemistry
- 341 Elemental Analysis
- 342 Filtration
- 343 Flow Meters/Regulators
- 344 FT-IR Spectroscopy
- 345 Furnaces/Ovens
- 346 Gas Chromatography
- 347 General Lab Equipment
- 348 Heating/Temperature
- 349 Ion Chromatography
- 350 Lab Furniture/Hoods
- 351 Labware/Apparatus
- 352 Lasers/Fiber Optics
- 353 Liquid Chrom./HPLC
- 354 Mass Spectrometry
- 355 Microscopy
- 356 Capillary Electrophoresis
- 357 Mix/Stir/Blend/Grind
- 358 NMR Spectroscopy
- 359 Particle Size Analysis
- 360 Plasma Spectroscopy
- 361 pH/Ion Meters/Titrators
- 362 Pumping Monitoring
- 363 Recording/Integrating
- 364 Robotics/Automation
- 365 Sampling/Dispensing
- 366 Supercritical Fluid Chrom.
- 367 Spectrofluorometry
- 368 Stills/Purification
- 369 Surface Analysis
- 370 Thermal Analysis
- 371 Thin Layer Chrom.
- 372 UV-Vis Spectroscopy
- 373 Valves/Tubes/Fittings
- 374 Viscometry
- 375 Water/Moisture Analysis
- 376 Weighing/Balances
- 377 X-Ray Diffraction
- 378 X-Ray Spectroscopy



FOR FASTEST SERVICE, USE THIS CARD TO FAX YOUR REQUEST DIRECTLY TO THE ADVERTISER.
PLEASE PHOTOCOPY THIS CARD FOR MULTIPLE USE.

TO: _____
FROM: _____
FAX: () _____ DATE: _____

- MY NEED IS:**
- Immediate
 - 6 - 12 Mos.
 - 12 + Mos.

- I WANT TO KNOW MORE, PLEASE...**
- Send Literature
 - Have a Salesman Call
 - Send Name of Nearest Dealer
 - Send Me a Price Quote

Description: _____
Quantity: _____

I saw your... Advertisement Editorial Listing Regarding...
on page _____ of the (date) _____ issue of AC

NAME: _____
TITLE: _____
COMPANY: _____
MAILSTOP: _____
STREET: _____
CITY: _____ **STATE:** _____ **ZIP:** _____
PHONE: _____ **FAX:** _____

ANCHAM 67(21) 3829-4032 (1995)
ISSN 0003-2700

Registered in the U.S. Patent
and Trademark Office

Copyright 1995 by the
American Chemical Society

ANALYTICAL CHEMISTRY®

NOVEMBER 1, 1995
Volume 67, Number 21

ACCELERATED ARTICLES

Ya-Wen Chiu, Robert E. Carlson,
Karen L. Marcus, and
Alexander E. Karu**

- 3829** A Monoclonal Immunoassay for the Coplanar Polychlorinated Biphenyls

Zaiyou Liu,
Donald G. Patterson, Jr., and
Milton L. Lee*

- 3840** Geometric Approach to Factor Analysis for the Estimation of Orthogonality and Practical Peak Capacity in Comprehensive Two-Dimensional Separations

Barry K. Lavine, Howard Mayfield,
Paul R. Kromann, and
Abdullah Faruque*

- 3846** Source Identification of Underground Fuel Spills by Pattern Recognition Analysis of High-Speed Gas Chromatograms

Purnendu K. Dasgupta and
Satyajit Kar*

- 3853** Measurement of Gases by a Suppressed Conductometric Capillary Electrophoresis Separation System

*Bhajendra N. Barman and
J. Calvin Giddings**

- 3861** Separation of Colloidal Latex Aggregates by Cluster Mass and Shape Using Sedimentation Field-Flow Fractionation with Steric Perturbations

*Wolfgang Schützner, Salvatore Fanali,
Andreas Rizzi,* and Ernst Kenndler*

- 3866** Separation of Diastereomers by Capillary Zone Electrophoresis with Polymer Additives: Effect of Polymer Type and Chain Length

C. M. John, R. W. Odom, L. Salvati,
A. Annapragada, and M. Y. Fu Lu*

- 3871** XPS and TOF-SIMS Microanalysis of a Peptide/Polymer Drug Delivery Device

*R. W. Peter Fairbank,
Yang Xiang, and Mary J. Wirth**

- 3879** Use of Methyl Spacers in a Mixed Horizontally Polymerized Stationary Phase

*Clayton McNeff and Peter W. Carr**

- 3886** Synthesis and Use of Quaternized Polyethylenimine-Coated Zirconia for High-Performance Anion-Exchange Chromatography

Colin G. Ong, Amresh Prasad, and
James O. Leckie*

- 3893** Effect of pH, NaCl, and Cocktail Selection on ²³²U Liquid Scintillation Spectra

Ming Fat Choi and Peter Hawkins*

- 3897** Novel Dye-Solvent Solutions for the Simultaneous Detection of Oxygen and Carbon Dioxide

ARTICLES

<i>Johannes T. van Elteren, Constant M. G. van den Berg,* Hao Zhang, Trevor D. Martin, and Eric P. Achterberg</i>	3903	Automated In-Line Extraction of Uranium(VI) from Raffinate Streams with On-Line Detection by Cathodic Stripping Voltammetry
<i>Johannes A. M. van Riel and Cornelis Olliman*</i>	3911	Selective Detection in RP-HPLC of Tyr-, Trp-, and Sulfur-Containing Peptides by Pulsed Amperometry at Platinum
<i>I. Papaefstathiou and M. D. Luque de Castro*</i>	3916	Integrated Pervaporation/Detection: Continuous and Discontinuous Approaches for Treatment/Determination of Fluoride in Liquid and Solid Samples
<i>Manus J. Dennison, Jennifer M. Hall, and Anthony P. F. Turner*</i>	3922	Gas-Phase Microbiosensor for Monitoring Phenol Vapor at ppb Levels
<i>Calum J. McNeil,* Dale Athey, Mark Ball, Wah On Ho, Steffi Krause, Ron D. Armstrong, J. Des Wright, and Keith Rawson</i>	3928	Electrochemical Sensors Based on Impedance Measurement of Enzyme-Catalyzed Polymer Dissolution: Theory and Applications
<i>F. Pariente, E. Lorenzo, F. Tobalina, and H. D. Abrúña*</i>	3936	Aldehyde Biosensor Based on the Determination of NADH Enzymatically Generated by Aldehyde Dehydrogenase
<i>Michael U. Kumke, Guang Li, Linda B. McGown,* G. Terrance Walker,* and C. Preston Linn</i>	3945	Hybridization of Fluorescein-Labeled DNA Oligomers Detected by Fluorescence Anisotropy with Protein Binding Enhancement
<i>Douglas J. Beussman, Paul R. Vlasak, Richard D. McLane, Mary A. Seeterlin, and Christie G. Enke*</i>	3952	Tandem Reflectron Time-of-Flight Mass Spectrometer Utilizing Photodissociation
<i>Gary J. Van Berkel* and Feimeng Zhou</i>	3958	Electrospray as a Controlled-Current Electrolytic Cell: Electrochemical Ionization of Neutral Analytes for Detection by Electrospray Mass Spectrometry
<i>Ron M. A. Heeren,* Chris G. de Koster, and Jaap J. Boon</i>	3965	Direct Temperature Resolved HRMS of Fire-Retarded Polymers by In-Source PyMS on an External Ion Source Fourier Transform Ion Cyclotron Resonance Mass Spectrometer
<i>Dale H. Patterson, George E. Tarr, Fred E. Regaier, and Stephen A. Martin*</i>	3971	C-Terminal Ladder Sequencing via Matrix-Assisted Laser Desorption Mass Spectrometry Coupled with Carboxypeptidase Y Time-Dependent and Concentration-Dependent Digestions
<i>Jarrod A. Marto, Forest M. White, Staci Seldomridge, and Alan G. Marshall*</i>	3979	Structural Characterization of Phospholipids by Matrix-Assisted Laser Desorption/Ionization Fourier Transform Ion Cyclotron Resonance Mass Spectrometry
<i>Richard B. van Breemen,* Chao-Ran Huang, Zhi-Zhen Lu, Agnes Rimando, Harry H. S. Fong, and John F. Fitzloff</i>	3985	Electrospray Liquid Chromatography/Mass Spectrometry of Ginsenosides
<i>Robert S. Brown* and John J. Lennon</i>	3990	Sequence-Specific Fragmentation of Matrix-Assisted Laser-Desorbed Protein/Peptide Ions

- Annabelle Dugay, Bien Dang-Vu,
Jean Christophe Moreau, and
François Guyon** **4000** Effect of Hydrogen Rearrangement on the Determination of the Enrichment of [¹⁵N]Leucine by GC/MS
- Michael E. Ketterer* and
Michael A. Fiorentino* **4004** Measurement of Ti(III/I) Electron Self-Exchange Rates Using Enriched Stable Isotope Labels and Inductively Coupled Plasma Mass Spectrometry
- Mei-Cheng Chen and
Hsuan-Jung Huang** **4010** An Electrochemical Cell for End-Column Amperometric Detection in Capillary Electrophoresis
- Jay W. Grate* and
R. Andrew McGill** **4015** Dewetting Effects on Polymer-Coated Surface Acoustic Wave Vapor Sensors
- P. Tschuncky and J. Heinze** **4020** An Improved Method for the Construction of Ultramicroelectrodes
- Rachael Barbour, Zhenghao Wang,
In Tae Bae, Yuriy V. Tolmachev, and
Daniel A. Scherson** **4024** Channel Flow Cell for Attenuated Total Reflection Fourier Transform Infrared Spectroelectrochemistry
- Ken-ichi Yoshino, Toshifumi Takao,*
Hiroshi Murata, and
Yasutsugu Shimonishi* **4028** Use of the Derivatizing Agent 4-Aminobenzoic Acid 2-(Diethylamino)ethyl Ester for High-Sensitivity Detection of Oligosaccharides by Electrospray Ionization Mass Spectrometry

TECHNICAL NOTES

There is no supporting information for this issue.

* In papers with more than one author, the asterisk indicates the name of the author to whom inquiries about the paper should be addressed.

*Accelerated Articles**Anal. Chem.* 1995, 67, 3829–3839**A Monoclonal Immunoassay for the Coplanar Polychlorinated Biphenyls**Ya-Wen Chiu,[†] Robert E. Carlson,^{*‡} Karen L. Marcus,[†] and Alexander E. Karu^{*†}*Hybridoma Facility, College of Natural Resources, University of California, Berkeley, 1050 San Pablo Avenue, Albany, California 94706, and ECOCHEM Research, Inc., Suite 510, 1107 Hazeltine Boulevard, Chaska, Minnesota 55318-1043*

Polychlorinated biphenyls (PCBs) are ubiquitous environmental pollutants with diverse toxic, teratogenic, reproductive, immunotoxic, and tumorigenic effects. Three of the least abundant of the 209 PCB isomers (congeners) are the most toxic and most difficult to quantify. These are 3,4,3',4'-tetrachlorobiphenyl, 3,4,3',4',5'-pentachlorobiphenyl, and 3,4,5,3',4',5'-hexachlorobiphenyl (IUPAC No. 77, 126, and 169, respectively). An immunizing hapten was designed to retain the 3,4,3',4' chlorine-substitution pattern and coplanarity characteristic of these toxic congeners. The optimal competitors for immunoassay were weaker binding distinctive single-ring fragments of the PCBs. A monoclonal antibody designated S2B1 was derived and used in direct (antibody-capture) competitive enzyme immunoassays (EIAs). The EIAs are highly specific for non-ortho-substituted congeners and do not recognize the more prevalent but much less toxic noncoplanar PCB congeners or 2,3,7,8-tetrachlorodibenzo-*p*-dioxin, 2,3,7,8-tetrachlorodibenzofuran, or dichlorobenzenes. Hapten and competitor design for this assay suggests a basis for development of sensitive EIAs for other classes of PCB congeners.

The polychlorinated biphenyls (PCBs) are among the most hazardous and ubiquitous man-made toxic compounds. They were in extremely wide use in numerous industrial applications from the 1930s until their toxicity, ability to bioaccumulate, and

carcinogenic potential were recognized. Their manufacture was discontinued in the 1970s. PCBs are distributed so widely that they have been classified as global chemical pollutants. This group of compounds has from 1 to 10 chlorines on the biphenyl nucleus, with a total of 209 possible combinations (congeners). The chemical and physical properties of PCBs make analysis difficult. They are highly persistent, they adsorb to soils and colloidal materials, they leach very slowly, and they bioaccumulate up the food chain. Large amounts of these compounds remain in the environment, in use or in waste.

The toxicology and the carcinogenic, mutagenic, teratogenic, and immunotoxic properties of various congeners are detailed in an extensive literature. Recent volumes published by the U.N.—World Health Organization International Program on Chemical Safety are particularly comprehensive summaries of the current understanding of the distribution and toxicology of PCBs and polybrominated biphenyls (PBBs).^{1,2} Some congeners and their metabolites have been implicated as estrogen mimics, with effects on postnatal development and reproductive ability.^{3–5} The coplanar and noncoplanar PCBs differ in their toxicological properties. [The terminology in the literature is not consistent with the nuclear magnetic resonance (NMR) data. Coplanarity implies a dihedral angle of 0° between the phenyl rings. All PCBs tend to be noncoplanar to some extent in solution. The congeners referred to as “coplanar” in the literature are coplanar in crystals used for X-ray crystallography. These congeners have minimal, but nonzero dihedral angles in solution.] The three most toxic congeners, 3,4,3',4'-tetrachlorobiphenyl (PCB 77), 3,4,3',4',5'-

* Corresponding authors. R.E.C.: telephone, 612-448-4337; FAX, 612-448-1651; e-mail, ecochem@aol.com. A.E.K.: telephone, 510-643-7746; FAX, 510-642-0875; e-mail, hyblab@violet.berkeley.edu.
† University of California, Berkeley.
‡ ECOCHEM Research, Inc.

(1) Dobson, S.; van Esch, G. J. *Polychlorinated biphenyls and terphenyls*, 2nd ed.; World Health Organization: Geneva, 1993.
(2) Gross, W.; Kielhorn, J.; Melber, C. *Polybrominated biphenyls*; World Health Organization: Geneva, 1993.

pentachlorobiphenyl (PCB 126), and 3,4,5,3',4',5'-hexachlorobiphenyl (PCB 169) are coplanar and structurally resemble dioxin.^{6,7} These congeners are minor mole fractions of commercial PCB formulations.¹ Their primary mode of action is binding to the aryl hydrocarbon (Ah) receptor, which leads to induction of cytochrome P450-associated enzyme activities.^{6,9} The much more abundant noncoplanar, ortho-chlorinated congeners have different mechanisms of toxicity that have not been well defined.

Analysis of PCBs is generally based on detecting the group of congeners that is most abundant in commercial formulations such as the Aroclors. There is increasing recognition that quantitation of the most toxic congeners is essential for evaluating the environmental impact of PCBs. However, gas chromatography of these congeners with electron capture detection (GC-ECD) or mass spectrometry (GC/MS) is particularly difficult because coeluting ortho-substituted congeners are typically present in much greater amounts.⁷ Instrumental toxic congener analysis may cost as much as \$1000 per sample. This greatly limits the scope of regulatory and research sampling.¹⁰

Congener-specific analysis has several advantages for regulatory as well as research applications. Commercial formulations each have relatively consistent mole fractions of certain congeners that provide a distinctive "signature". Draper¹¹ demonstrated that most of the Aroclor mixtures could be identified by capillary GC analysis of only 12 congeners. Nine congeners were classified as the most hazardous by McFarland and Clarke.⁹ Thirty to fifty congeners are found in various tissue samples, but fewer predominate.^{9,12} Canadian regulatory agencies use a reference mixture of 51 congeners for capillary GC analysis.¹³ A series of indicator congeners for contamination of foods has been proposed.¹⁴ The World Health Organization has emphasized the continuing need for long-term studies of the toxicity, epidemiology, and mechanisms of action of specific congeners and the value of identifying sensitive and specific biomarkers for some of the more subtle aspects of PCB toxicity.¹⁵ Monoclonal antibodies and an immunoassay specific for the toxic congeners could be particularly valuable for this type of research. They could be used as independent screening methods or in conjunction with instrumental analysis.

The molecular heterogeneity, low aqueous solubility, lack of functional groups for derivatization, and other chemical properties of PCBs make design of immunoassays a daunting problem. All of the published PCB immunoassays we are aware of were designed to detect "Aroclor equivalents" or the most abundant noncoplanar PCB congeners.¹⁶⁻²¹ To date we have not found any published reports of *monoclonal* antibodies for sensitive detection of PCB congeners or mixtures. The design and performance criteria for a toxic PCB congener immunoassay are exceptionally demanding. The assay must perform with sufficient sensitivity, accuracy, and precision despite the extremely low water solubility of the compounds. It must be specific for the coplanar congeners. There should be no significant cross-reaction with other halogenated biphenyls, dibenzofurans, dioxins, halowax (chlorinated naphthalene), or single-ring halogenated compounds, including chlorinated benzenes and phenols that may be present with PCBs in hazardous waste. Compounds such as DDT, DDE, and chlorophenoxy herbicides should not be recognized.

The immunizing hapten and competitor reagents for this project were synthesized expressly to derive a specific antibody and a sensitive assay for the most toxic PCB congeners. Our approach was based on the hypothesis that we could design an immunizing hapten to evoke high-affinity antibodies to the coplanar PCB structure, while molecules designed to mimic half of the PCB could serve as competitors of lower binding affinity in competition immunoassays. In the course of this work it became evident that polyclonal antisera would be unlikely to provide the specificity or sensitivity needed for single congener analysis and that monoclonal antibodies (MAbs) would be required.

This paper describes direct enzyme immunoassays (EIAs) that are highly selective for PCBs 77 and 126, utilizing one MAb developed with this strategy. An EIA using tubes coated with a capture antibody gives the most sensitive limit of detection. However, a format using streptavidin-coated microwells to capture biotinylated MAb is more reproducible for samples in more than 5% organic solvent. In 5% methanol, only PCBs 77 and 126 are recognized with a limit of detection at or below 1 ppb. Other congeners are less than 3% cross-reactive. In 10% DMSO, five ortho-substituted congeners are detected with I_{50} values less than 100 ppb, and five others including PCB 169 react with I_{50} values of 100–500 ppb. Mono-ortho-chlorination reduces or eliminates binding and di-ortho-chlorinated PCBs are not bound.

EXPERIMENTAL SECTION

Reagents and Materials. All reagents were purchased from Fisher Scientific, Aldrich Chemical Co., or Sigma Chemical Co. unless otherwise indicated. Only deionized, glass-distilled water was used, and Spectrograde methanol, DMSO, and 2-propanol were used as PCB solvents. PCB congeners >99% pure and all

- (3) Jacobsen, J. L.; Jacobsen, S. W. In *Prenatal exposure to toxicants: Developmental consequences*; Needleman, H. L., Bellinger, D., Eds.; The Johns Hopkins Press: Baltimore, MD, 1994; pp 130–147.
- (4) Colborn, T.; Clement, C. *Chemically induced alterations in sexual and functional development—the wildlife/human connection*; Advances in Modern Environmental Toxicology 21; Princeton Scientific Publishing Co.: Princeton NJ, 1992.
- (5) Korach, K. S.; Sarver, P.; Chae, K.; McLachlan, J. A.; McKinney, J. D. *Mol. Pharmacol.* **1988**, *33*, 120–126.
- (6) Safe, S. *CRC Crit. Rev. Toxicol.* **1984**, *13*, 319–396.
- (7) Creaser, C. S.; Krokos, F.; Startin, J. R. *Chemosphere* **1992**, *25*, 1981–2008.
- (8) Bandiera, S.; Safe, S.; Okey, A. B. *Chem. Biol. Interact.* **1982**, *39*, 259–277.
- (9) McFarland, V. A.; Clarke, J. U. *Environ. Health Perspect.* **1989**, *81*, 225–239.
- (10) Schwartz, T. R.; Stalling, D. L. *Arch. Environ. Contam. Toxicol.* **1991**, *20*, 195–219.
- (11) Draper, W. M. In *Proceedings of the EPA Sixth Annual Waste Testing and Quality Assurance Symposium*; American Chemical Society: Washington, D.C., 1990; pp II-124–II-138.
- (12) Mes, J.; Conacher, H. B. S.; Malcolm, S. *Int. J. Environ. Anal. Chem.* **1993**, *50*, 285–297.
- (13) National Research Council of Canada. Reference material no. CLB-1, Marine Analytical Standards Program, Atlantic Research Lab., Halifax Nova Scotia.
- (14) Jones, K. C. *Sci. Total Environ.* **1988**, *68*, 141–159.
- (15) World Health Organization. *Polychlorinated Biphenyls (PCBs) and Polychlorinated Terphenyls: Health and Safety Guide*; International Program on Chemical Safety (IPCS) Health and Safety Guide No. 68; World Health Organization: Geneva, 1992.

- (16) Fránek, M.; Hruska, K.; Sisák, M.; Diblíková, I. *J. Agric. Food Chem.* **1992**, *40*, 1559–1565.
- (17) Luster, M. I.; Albro, P. W.; Clark, G.; Chae, K.; Chaudhary, S. K.; Lawson, L. D.; Corbett, J. T.; McKinney, J. D. *Toxicol. Appl. Pharmacol.* **1979**, *50*, 147–155.
- (18) Newsome, W. H.; Shields, J. B. *Int. J. Environ. Anal. Chem.* **1981**, *10*, 295–304.
- (19) Goon, D. J. W.; Nagasawa, H. T.; Keyler, D. E.; Ross, C. A.; Pentel, P. R. *Bioconjugate Chem.* **1994**, *5*, 418–422.
- (20) Keyler, D. E.; Goon, D. J. W.; Shelver, W. L.; Ross, C. A.; Nagasawa, H. T.; St. Peter, J. V.; Pentel, P. R. *Biochem. Pharmacol.* **1994**, *48*, 767–773.
- (21) Mapes, J. P.; McKenzie, K.; Stewart, T. N.; McClelland, L. R.; Studabaker, W. B.; Manning, W. B.; Friedman, S. B. *Bull. Environ. Contam. Toxicol.* **1993**, *50*, 219–225.

other reference standards were purchased from AccuStandard, Inc. (New Haven, CT). Reference solutions of 200 ppm were prepared in 2-propanol and stored at 4 °C in glass vials with Teflon-lined screw caps.

Thin-layer chromatography (TLC) was performed on Analtech 250- μm silica gel GF Uniplates. Flash column chromatography was done with hand-packed 40 μm silica gel columns. Gas chromatography (GC) was performed on a Hewlett-Packard 5890 system equipped with an FID detector and a 30 m \times 0.32 mm i.d. Supelco SPB-5 (0.25- μm film of 5% diphenyl, 94% dimethyl-, 1% vinylpolysiloxane) column. The following GC conditions were used: initial temperature 100 °C; temperature hold 2 min, then 15 °C/min to 275 °C. NMR spectra were recorded with Nicolet NT-300 or IBM 200 MHz instrument. Mass spectra were typically obtained with an AEI-ms 30 spectrometer.

Swiss Webster mice were purchased from Simonsen Laboratories (Gilroy, CA), and Biozzi and B10.Q mice were from stock bred in the U.C. Berkeley Hybridoma Facility mouse colony. Titermax adjuvant was purchased from Vaxcel, Inc. (Norcross, GA), and Ribi MPL+TDM Emulsion was from Ribi Immunochem Research, Inc. (Hamilton, MT). Cell culture medium was purchased from Grand Island Biological Co. (GIBCO-BRL, Grand Island, NY), antibiotics and other additives were from Sigma Chemical Co., and fetal bovine serum was from Intergen, Inc. (Kankakee, IL).

Indirect ELAs were performed in Immulon 2 microplates (Dynatech, Inc., Chantilly, VA). The Immunosystems division of Millipore Corp. (Scarborough, ME) provided tubes, 12-well microwell strips coated with donkey anti-mouse immunoglobulin, and a diluent for the PCB hapten-horseradish peroxidase (HRP) conjugates used in some direct ELAs. The peroxidase substrate was a stabilized single-component tetramethylbenzidine (TMB) formulation (Catalog No. 50-76-05, Kirkegaard & Perry Laboratories, Inc., Gaithersburg, MD). Streptavidin-coated microwell strips were purchased from Labsystems Corp. (Needham Heights, MA). Bovine serum albumin (BSA) and alkaline phosphatase substrate tablets (*p*-nitrophenyl phosphate) for ELAs were purchased from Sigma Chemical Co. Alkaline phosphatase-antibody conjugates used for indirect ELAs were obtained from Boehringer-Mannheim Corp.

Safety Precautions. PCB reference standards were stored at 4 °C in glass vials with Teflon-lined screw caps. The vials were stored upright in a spill-proof steel box. All dilutions of PCBs were made in a chemical fume hood. PCBs were diluted into neat methanol in disposable glass tubes using a positive-displacement glass capillary pipettor with a Teflon plunger (Wheaton Corp., Millville, NJ). ELA steps involving solutions and rinses of microplates and tubes that contained PCBs were done in a stainless steel pan in a chemical fume hood lined with disposable paper. Solutions were aspirated into a glass waste container using a vacuum manifold (Nunc ImmunoWash 12). The vacuum line was protected with a glass trap and a Vacushield liquid-barrier filter. The analysts wore spill-resistant gowns and double nitrile gloves.

Chemical Syntheses. The immunizing hapten and competitor reagents used in this project are shown in Figure 1. The short names used in the text appear below the structures.

Hapten Synthesis. The immunizing hapten was synthesized by a Cadogan coupling of 3,4-dichloroaniline with 3-chloroanisole to form the three expected isomeric methoxytrichlorobiphenyls

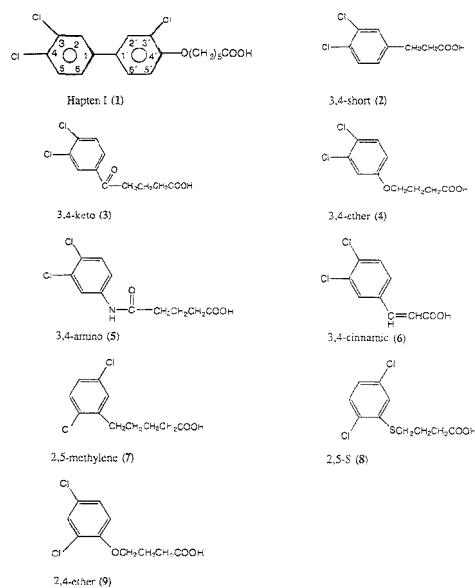


Figure 1. Immunizing hapten and competitors used in this study.

(10).²² These were distinguished by NMR and resolved by GC-FID. Isomer 10c was readily separated from the crude product by flash chromatography. Isomers 10a, 10b, and 10d, obtained as a difficult to resolve mixture, were carried into BBr_3 demethylation. The desired biphenyl (11) was obtained by flash chromatography. 11 was alkylated with ethyl 6-bromohexanoate to yield the ethyl ester 12. Upon isolation of the pure ester precursor, hapten I (13) was prepared by LiOH hydrolysis of 12 at room temperature (Figure 2). All intermediates and the hapten were characterized for purity by TLC and by gas chromatography with a flame ionization detector (GC-FID). Structures were verified by NMR and mass spectrometry (MS).

3,3',4'-Trichloro-4-hydroxybiphenyl. Isoamyl nitrite (2.69 mL, 20 mmol) was added portionwise over the course of 10 min to a mixture of 2-chloroanisole (10.7 mL, 80 mmol) and 3,4-dichloroaniline (1.62 g, 10 mmol) at 120 °C under nitrogen, and the reaction was allowed to stir for 18 h. The excess anisole was distilled under vacuum to give a residue which was purified by flash chromatography (silica gel, 95/5 petroleum ether/methylene chloride eluant). The major fraction (TLC R_f = 0.60; minor fraction R_f = 0.76) was concentrated to a residue by removal of the solvent on a rotary evaporator. The minor fraction had a GC retention time of 14.5 min; the major fraction, a GC retention time of 15.4, 16.0, 16.2 min. The major fraction residue was dissolved in 10 mL of methylene chloride, and 4 mL of 1 M BBr_3 in methylene chloride was added. The reaction was stirred under nitrogen at room temperature for 24 h and worked up by the addition of approximately 10 mL of saturated potassium dihydrogen phosphate followed by removal of the aqueous layer and addition of anhydrous sodium sulfate to the methylene chloride fraction. Flash chromatography (silica gel, 95/5 petroleum ether/

(22) Cadogan, J. I. G.; Roy, D. A.; Smith, D. M. J. *Chem. Soc. C* 1966, 1249-1250.

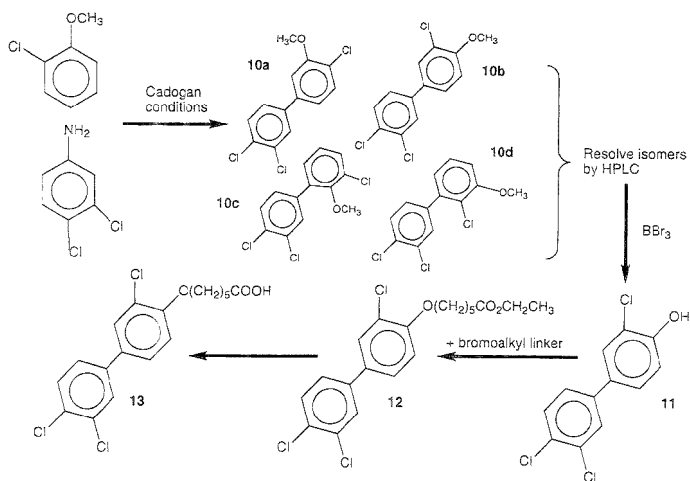


Figure 2. Synthesis scheme for the immunizing hapten.

ethyl acetate) of the residue obtained after removal of the solvent gave 91 mg (3.3% based on 3,4-dichloroaniline) of the desired compound (**11**) as a white solid: TLC (petroleum ether/ethyl acetate, 95/5) $R_f = 0.44$; $^1\text{H NMR}$ (200 MHz, CDCl_3) $\delta = 7.58$ (d, $J = 2.1$ Hz, H2'), 7.50 (d, $J = 2.3$ Hz, H2), 7.48 (d, $J = 8.5$ Hz, H5'), 7.35 (dd, $J = 8.5, 2.2$ Hz, H6'), 7.32 (dd, $J = 8.4, 2.3$ Hz, H6), 7.08 (d, $J = 8.4$ Hz, H5).

6-[(3,3',4'-Trichlorobiphenyl-4-yl)oxy]hexanoic Acid (13, Hapten I). Ethyl 6-bromohexanoate (65 μL , 0.36 mmol) was added to a solution of the biphenylol (**11**: 91 mg, 0.33 mmol) in 15 mL of acetone. Anhydrous potassium carbonate (55 mg, 0.40 mmol) and potassium iodide (5 mg) were added, and the mixture was refluxed for 18 h. The reaction solution was filtered and evaporated to dryness to yield a crude residue. To this residue was added 6 mL of absolute ethanol and 1.25 mL of 1 N LiOH. The reaction was stirred at room temperature overnight. On addition of 1.0 mL of 1 N HCl, the product was obtained as a microcrystalline powder (88 mg, 69%): TLC (petroleum ether/ethyl acetate, 95/5 with 0.1% acetic acid) $R_f = 0.57$; $^1\text{H NMR}$ (300 MHz, CD_3OD) $\delta = 7.66$ (d, $J = 2.1$ Hz, H2'), 7.59 (d, $J = 2.3$ Hz, H2), 7.52 (d, $J = 8.3$ Hz, H5'), 7.46 (dd, $J = 8.3, 2.1$ Hz H6'), 7.43 (dd, $J = 2.3, 8.6$ Hz, H6), 7.07 (d, $J = 8.6$ Hz, H5), 4.09 (t, $J = 6.2$ Hz, phenyl- OCH_2), 2.35 (t, $J = 7.1$ Hz, CH_2COOH), 1.93–1.83 (m, phenyl- OCH_2CH_2), 1.78–1.68 (m, $\text{CH}_2\text{CH}_2\text{COOH}$), 1.64–1.53 (m, $\text{CH}_2\text{CH}_2\text{CH}_2$); MS (EI, m/z (relative intensity)) 388 (11), 386 (M^+ , 12), 276 (29), 274 (94), 272 (100). High-resolution MS (EI, 70 eV), $\text{C}_{18}\text{H}_{17}\text{Cl}_3\text{O}_3$ requires 386.0231, found 386.0237.

Conjugation of Hapten I. Hapten I was conjugated to the carrier proteins keyhole limpet hemocyanin and bovine serum albumin by a standard activation of the hapten's carboxyl group with *N*-hydroxysuccinimide and carbodiimide in dimethylformamide.^{23,24} The activated hapten was conjugated to the carrier protein in a borate buffer at pH 9.2. Control reactions, which

contained hapten and protein without the activating agent, were used to evaluate the efficiency of the aqueous 2-propanol dialysis procedure for removal of noncovalent hapten from the conjugate solution (vide infra).

Hapten I, calculated to be a 200-fold molar excess over keyhole limpet hemocyanin (KLH) or a 100-fold molar excess over BSA, was dissolved in 400 μL of dimethylformamide (Aldrich, gold label) and activated to form the *N*-hydroxysuccinimide (NHS) ester. The activation was carried out using a 1.4-fold molar excess (calculated over the hapten) of 1-ethyl-3-[3-(dimethylamino)propyl]carbodiimide (EDC) and a 2-fold molar excess (calculated over the hapten) of NHS added dry to the hapten solution. The carrier protein was dissolved in borate buffer (0.1 M, pH 9.4) to a final concentration of 10 mg/mL. The protein solution was allowed to stir overnight at 0–5 $^\circ\text{C}$ to ensure that all of the protein was dissolved. Dimethylformamide (Aldrich, gold label) was added to a concentration of 5% (v/v). The activated hapten solution was added to the protein solution, 10 μL at a time, every 30–60 min, using a 10- μL pipettor. The conjugation mixtures were allowed to stir overnight at room temperature after the hapten solution had been added. The reaction solutions were transferred to wetted cellulose dialysis tubing (MW cutoff 12 000–14 000) and dialyzed vs two changes of 0.5–1.0-L volumes of 10% (v/v) 2-propanol in phosphate-buffered saline (PBS, pH 7.4) over 2 days. Controls with EDC omitted showed that this method removed all nonspecifically bound hapten from the carrier protein. The reaction solutions were then dialyzed vs two changes of 0.5–1.0-L volumes of PBS over 2 days to remove any traces of 2-propanol. After dialysis, the conjugate solutions were collected from the dialysis tubing.

Load Determination. The moles of carrier protein were determined by the Lowry method with the use of an appropriate standard curve.²⁵ The moles of hapten were determined using UV/visible spectroscopy of the conjugate and the UV/visible spectrum of the hapten. The conjugate load was determined by

(23) Kilbanov, A. L.; Slinkin, M. A.; Torchlin, V. P. *Appl. Biochem., Biotechnol.* **1989**, *22*, 45–58.

(24) Siaros, J. V.; Wright, R. W.; Swingle, D. M. *Anal. Biochem.* **1986**, *156*, 220–232.

(25) Lowry, O. H.; Rosebrough, N. J.; Farr, A. L.; Randall, R. J. *J. Biol. Chem.* **1954**, *193*, 265–275.

dividing the moles of hapten present by the moles of carrier protein (KLH, 300 000 daltons; BSA, 67 000 daltons).

The KLH conjugate used for immunization had an average of 89 mol of hapten I/mol of KLH. No hapten association with KLH was detected in a control reaction that omitted activating agent. The BSA conjugate used for indirect EIAs had approximately 48 mol of hapten I/mol of protein, with 2.2 mol/mol of nonspecific association in the absence of activating agent. Hapten I-KLH and hapten I-BSA both tended to aggregate when stored at 4 °C for several weeks, possibly due to the high hapten load. Aliquots were clarified by centrifugation (12 000g, 5 min), and only soluble conjugate was used for immunizations and EIAs.

Synthesis of Competitors. The syntheses involved addition of a linker moiety by alkylation or acylation to an appropriate chlorophenyl synthon, similar to the conversion of 11 to 13 in Figure 2. Competitor 2 (3,4-short) was purchased from Trans-World Chemicals (Kensington, MD). Preparation of the 3,4-keto competitor 3 utilized the Friedel-Crafts acylation of *o*-dichlorobenzene with glutaric anhydride, essentially as described by Rosowsky.²⁶ The precursor compounds were all commercially available. Competitor 4 (3,4-ether) was prepared as described by Tandon et al.²⁷ Competitor 5 (3,4-amino) was prepared as described by Rashid.²⁸ Competitor 6 (3,4-cinnamic) was purchased from Aldrich Chemical Co. (St. Louis, MO). Synthesis of competitor 7 (2,5-methylene) was described elsewhere.²⁹ Competitor 8 (2,5-S) was prepared as reported by Kukalenko,³⁰ and competitor 9 (2,4-ether) was purchased from Aldrich Chemical Co. Competitor structure and purity were determined by TLC, GC-FID, UV/visible spectrophotometry, NMR, and/or MS.

Synthesis of Competitor-BSA and Peroxidase Conjugates. Competitors 2-9 were conjugated to BSA or amino-modified HRP using the carbodiimide-mediated carboxyl activation procedure described above to couple hapten I to BSA and KLH. HRP conjugates of hapten I were also prepared. The HRP (Catalog No. P-6782, Sigma Chemical Co.) was modified as described by Hsiao³¹ to give 6-24 free amines. The conjugate stock solutions typically had a concentration of 5-10 mg/mL HRP, and they were stored at 4 °C.

Preparation of Biotinylated MAb. Immunoglobulin from MAb S2B1 (IgG) was purified to near-homogeneity by affinity chromatography of ascites fluid on protein A-Sepharose using a 1-mL HiTrap column (Pharmacia Biotech, Piscataway, NJ). The IgG was dialyzed overnight against three changes of 0.02 M KPO₄ (pH 7)/0.01 M EDTA/0.05 M NaCl. Protein concentration was determined by absorbance at 280 nm. A 1-mg sample of a biotin-spacer arm ester (NHS-XX-biotin; Calbiochem, La Jolla, CA) was dissolved in 0.5 mL of DMSO. Approximately 25 ng of ester was added in aliquots, with gentle shaking, to 1 mg of S2B1 IgG in 0.55 mL of 0.02 M Na₂CO₃/NaHCO₃ (pH 9) in a 1 mL glass vial. After 2 h at room temperature the solution was dialyzed against three changes of the KPO₄/EDTA/NaCl buffer overnight. Aliquots were stored at -70 °C or as a 50% glycerol solution at -20

°C. The extent of biotinylation and ability to bind PCB-HRP competitor were determined by EIA.

Immunization and Monitoring of Mice. Four mice each of three strains (Swiss Webster, Biozzi, B10.Q) were immunized with the hapten I-KLH conjugate. The immunizing doses consisting of approximately 50 µg of conjugate (as carrier protein) in 0.08 mL of physiological saline, emulsified with one mouse dose of Titermax adjuvant (Vaxcel, Inc.), were delivered subcutaneously in three or four sites on the back of the mouse. Identical doses were given 7, 22, 106, and 133 days after the initial injection, except that Ribi adjuvant was used instead of Titermax on days 106 and 133. The adjuvant was changed because the Titermax adjuvant used in the first three injections had accumulated at the injection sites, and Ribi adjuvant is cleared from the sites. Serum samples were taken from the tail vein on days 29, 120, and 137. Anti-hapten titers were determined on day 29 serum by indirect EIA on wells coated with hapten I-BSA. All 12 mice developed a strong anti-hapten response (signal at serum dilutions >50 000). At this stage, four B10.Q and three S/W mice had developed a weak competitive binding response to PCB 77 as measured by indirect EIA with 2,5-S-BSA (competitor 8). An indirect competition EIA with three of the sera taken on day 120 showed an improved competitive binding of 3,4,3',4'-tetrachlorobiphenyl vs 2,5-S-BSA. However, the day 137 sera from only one mouse, a S/W, showed competitive binding responses specific for PCBs 77 and 126 in this assay. On day 154, 3 days prior to cell fusion, this mouse was given a subcutaneous boost with 100 µg of hapten I-KLH in Ribi adjuvant. To lessen the risk of anaphylactic or delayed-type hypersensitivity responses, this mouse received a subcutaneous injection of antihistamine and antivasospasm drugs 1 h before the boost.³²

Hybridoma Production. All components of the cell culture media, electrical cell fusion procedures, and cryopreservation methods were as previously described.³³ Hybridoma colonies were screened by automated sampling between 12 and 18 days postfusion. Samples of 0.12 mL of supernate were transferred onto 96-well culture plates. Aliquots (0.05 mL) were transferred onto EIA plates coated with hapten I-BSA and plates coated with 2,5-S-BSA (competitor 8) conjugate. A total of 628 colonics were screened in three groups. Of these, 161 reacted only with hapten I-BSA and 123 reacted with both hapten I-BSA and 2,5-S-BSA. None of the MAbs bound exclusively to 2,5-S-BSA. All 284 cultures were expanded to 24-well culture dishes. Two aliquots of each cell line were frozen and stored in liquid nitrogen. Culture supernates that bound hapten were tested for competitive binding of PCB congeners in direct EIAs as described in Results and Discussion. Only one MAb, designated S2B1, gave the desired results. This cell line was subcloned by limiting dilution, and 11 stable subclones were expanded and frozen. One subclone was expanded to produce culture medium and ascites. The ascites was prepared in irradiated Swiss Webster mice as described previously.³³ Immunoglobulin subclass was determined by EIA using a commercial kit (Southern Biotechnology Associates, Birmingham, AL).

Enzyme Immunoassay Methods. Indirect (immobilized competitor conjugate) and direct (immobilized antibody) EIAs

(26) Rosowsky, A.; Chen, K. K. N.; Lin, M.; Nadel, M. E.; St. Armand, R.; Yeager, S. A. *J. Heterocycl. Chem.* 1971, 8, 789-795.

(27) Tandon, V. K.; Khanna, J. M.; Anand, N. *India J. Chem.* 1977, 15B, 264-266.

(28) Rashid, K. A.; Arjmand, M.; Sandermann, H.; Mumma, R. O. *J. Environ. Sci. Health* 1987, B22, 721-729.

(29) Carlson, R.; Chamerlik-Cooper, M.; Swanson, T.; Buirge, A., submitted for publication in *Anal. Chem.*

(30) Kukalenko, S. *Zh. Org. Khim.* 1970, 6, 680-684.

(31) Hsiao, R.; Royer, H. *Arch. Biochem. Biophys.* 1979, 198, 379-385.

(32) Karu, A. E. In *Hazard Assessment of Chemicals—Current Developments*; Saxena, J., Ed.; Taylor & Francis Intl. Publishers: Washington, DC, 1993; Vol. 8, pp 205-321.

(33) Karu, A. E.; Goodrow, M. H.; Schmidt, D. J.; Hammock, B. D.; Bigelow, M. W. *J. Agric. Food Chem.* 1994, 42, 301-309.

used for evaluating responses of mice and for primary screening of MABs utilized reagents and procedures of Voller *et al.*,³⁴ as modified in Karu *et al.*³³ Secondary screening and subsequent characterization of the MABs was done by direct EIA using plastic 12 × 75 mm tubes or microwells coated with donkey anti-mouse IgG (DAM). Where indicated, the direct EIA was done with biotinylated MAB S2B1 captured on streptavidin coated microwells. Tubes and plates containing PCBs were handled as described above in Safety Precautions.

Indirect competition EIAs were performed by coating wells with amounts of hapten-BSA or competitor-BSA conjugate that were determined to be subsaturating by a checkerboard EIA. Wells were blocked with PBST-BSA.³³ Mixtures for competition (0.1 mL) containing a limiting dilution of antiserum or hybridoma culture fluid and PCB standards (0.01–5000 ppb, diluted in PBST-BSA) were incubated overnight at room temperature in sealed glass tubes. The competition mixtures were added to the blocked plates for 2 h at room temperature, the wells were washed, alkaline phosphatase conjugated goat anti-mouse IgG was added, and the remainder of the assay was performed as previously described.

Direct EIAs (soluble competitor-enzyme conjugate; immobilized antibody) were performed in 12 × 75 mm polystyrene tubes or microwell strips coated with donkey anti-mouse IgG. The same procedures and incubation intervals were used for the coated tube and microwell EIAs. The PBST used in these EIAs contained only 0.01% (w/v) Tween 20 because higher concentrations of Tween 20 reduced the sensitivity. The blocking reagent was 1% (w/v) BSA/0.05 g/mL sucrose in PBS. All dilutions of PCBs were first made into neat methanol, in glass tubes. Aliquots of these were taken into an "assay diluent" consisting of 0.005% Tween 20 in glass distilled water and methanol to give a final methanol concentration of 5%. These dilutions were made directly in the antibody-coated tubes or made in a glass tube and added to coated wells. Transfers were made using a positive-displacement glass capillary pipettor with a Teflon plunger. The diluent for PCB competitor-HRP conjugates was a proprietary solution obtained from the Immunosegments division of Millipore Corp. Stopping solutions for end-point assays were 1% HCl for tube EIAs and 2.5% HCl for microwell EIAs. The volumes used in each EIA are summarized below:

step	volume added (mL)	
	tube	microwell
coating with MAB	0.5	0.2
blocking	0.6	0.25
analyte (standard or sample) solution	0.51	0.2
competitor-HRP conjugate	0.2	0.2
HRP substrate (chromogen)	0.5	0.2
stop solution	0.5	0.05

Aliquots of sera or hybridoma culture supernates diluted in PBST (1:100 to 1:40000) were allowed to stand in the tubes or wells overnight at room temperature. The antibody solution was decanted and the tubes or wells were washed four times with distilled water. Nonspecific binding was prevented by addition of blocking buffer for 3–4 h at room temperature or overnight at 4 °C. The blocking buffer was decanted, and the tubes or wells

could then be used immediately for EIA or they could be air-dried overnight at room temperature and stored for several weeks at 4 °C in Zip-lock bags.

The assay was performed by adding the PCB sample in assay diluent to the required number of antibody-coated tubes or wells and incubating 15 min at room temperature. The fluids were then aspirated into a waste reservoir, and the tubes/wells were rinsed four times with 0.5 mL of deionized water and shaken dry. Diluted PCB-HRP conjugate was then added for 5 min at room temperature. This solution was then aspirated and the tubes/wells were washed four times as before. Chromogen solution was then added to the tubes or wells. Color development was stopped by addition of HCl stopping solution. Aliquots of 0.1 mL were taken from tube EIAs into a microplate. Absorbance at 450 nm was recorded on a microplate reader. Nonspecific binding was determined using tubes or wells coated with nonimmune mouse serum or complete IMDM cell culture medium. Results were expressed as the ratio of B (A_{450} for the sample) to B_0 (that obtained with diluent containing no PCB). Competition EIA dose-response curves (B/B_0 vs log analyte concentration) were fitted using the four-parameter logistic model, and the data were analyzed as described previously.³⁵

Direct EIAs were also performed in microwells purchased with covalently attached streptavidin (160 ng/well). Dilutions (7.5 ng/well) of biotinyl-S2B1 IgG in PBST were allowed to bind for 1 h at room temperature. The wells were washed, blocked for 30 min with PBST/0.01% gelatin, and the remainder of the assay was conducted as described above. Where indicated, the assay diluent was adjusted to methanol concentrations up to 25% (v/v) to take advantage of this format's solvent tolerance.

RESULTS AND DISCUSSION

Immunizing Hapten and Competitors. Design of the immunizing hapten to evoke toxic congener-specific antibodies was based on three considerations. First, we retained the 3,3',4,4' chlorine-substitution pattern and coplanarity that are characteristic of the most toxic congeners. Second, an ether was used as a chlorine mimic for attachment of the spacer arm to the biphenyl. Third, the ether moiety spacer was attached to the biphenyl at the para position. Use of the ether linkage and para substitution was previously successful in deriving antibodies specific for the noncoplanar PCBs.²⁹ Most previously published PCB haptens used an amide spacer which was attached at the ortho position. The cross-reaction of antibodies raised by those haptens suggested that steric differences and noncoplanarity result from ortho placement of the amide spacer. Mattingly³⁶ used several para-substituted linkers, but none with the 3,3',4,4'-substitution pattern. Molecular models clearly showed that the para-substituted hapten used for this project (Figure 1) presents the coplanar biphenyl moiety extended distally from the linker. By contrast, ortho attachment places the linker moiety in a central position on the hapten.³⁷ Accordingly, we hypothesized that para orientation of the linker would lead to a combining site that would be more specific for the coplanar PCBs.

The competitors for EIA development were designed from different criteria. Our previous success developing an EIA for

(34) Voller, A.; Bidwell, D.; Bartlett, A. In *Manual of Clinical Immunology*; Rose, N., Friedman, H., Eds.; American Society for Microbiology: Washington, DC, 1976; pp 506–512.

(35) Schmidt, D. J.; Clarkson, C. E.; Swanson, T. A.; Egger, M. L.; Carlson, R. E.; Van Emon, J. M.; Karu, A. E. *J. Agric. Food Chem.* 1990, 38, 1763–1770.

(36) Mattingly, P. U.S. Patent 5,145,790, 1992.

(37) Carlson, R. E. In *Immunoanalysis of Agrochemicals: Emerging Technologies*; Nelson, J., Karu, A. E., Wong, R., Eds.; ACS Symposium Series 586; American Chemical Society: Washington DC, 1995; pp 140–152.

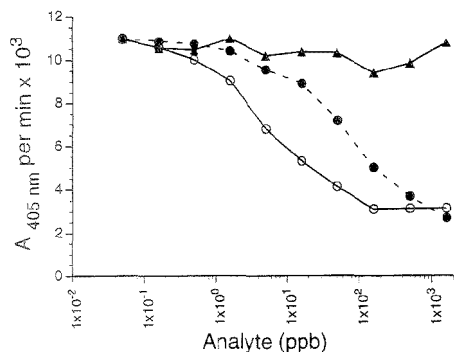


Figure 3. Indirect competition EIAs with mouse 2007-1 serum. Microwells were coated with 400 ng/well of the 2,5-S-BSA conjugate, and dilutions of the indicated PCBs were incubated with a 1/1667 dilution of 2007-1 serum from the third trial bleeding: (\blacktriangle) 2,4,5,2',4',5'-hexachlorobiphenyl (PCB 153); (\bullet) 3,4,3',4',5'-pentachlorobiphenyl (PCB 126); (\square) 3,4,3',4'-tetrachlorobiphenyl (PCB 77).

noncoplanar PCBs using PCB fragment-derived competitors suggested a similar approach for this assay.³⁷ However, we could not predict whether the most sensitive, congener-specific assay would result from antibody recognition of the most similar competitor or from less specific, lower affinity recognition of a dissimilar competitor. Differences in the pattern of competitor chlorination, linker placement relative to the chlorination pattern, and linker-to-aryl functional group produced different congener specificities in the EIA for noncoplanar PCBs (R. E. Carlson, unpublished). Consequently, in the present study we tested competitors with several different chlorination patterns, linker functional groups, and spacer lengths (Figure 1).

Responses of the Mice. By 29 days after the initial injection, all 12 mice produced sera with anti-hapten titers of >50 000. However, little or no competitive binding of PCB 77 was observed with the antisera at this stage. Sera taken from three of the mice 120 days after the initial dose showed competitive binding of PCBs 77 and 126 in EIAs using the 2,5-S competitor 8. Serum from the best-responding mouse (Swiss Webster No. 2007-1) gave competitive binding of PCB 77 with an I_{50} less than 10 ppb, approximately 10-fold more sensitive than sera from the other two mice. The day 120 serum from mouse 2007-1 had less than 1% cross-reaction with 2,4,5,2',4',5'-hexachlorobiphenyl (PCB 153), which is a prevalent but relatively nontoxic Aroclor constituent, in indirect and direct EIAs with the 2,5-S competitor (Figure 3). The shallow inhibition curves suggested a large ensemble of antibodies had developed with widely differing affinities and specificities for the different analytes and competitors. Sera from the three mice that gave the best competitive binding with the 3,4-short competitor 2 also bound competitors 3, 4, 7, and 8. However, only mouse 2007-1 serum competitively bound the toxic congeners below 10 ppb, with no competitive binding of PCB 153.

The direct EIA with mouse 2007-1 day 120 serum was used to compare the HRP conjugates of the immunizing hapten and four competitors with PCB 77 as the analyte. The fragment-based competitors improved the sensitivity by 5-fold to 27-fold over that obtained with hapten 1 as the competitor (Table 1). The 3,4-keto competitor 3 gave a more sensitive and reproducible competition with PCBs 77 and 126 than the 3,4-short competitor 2 that was

Table 1. Sensitivity of the Direct EIA for 3,3',4,4'-Tetrachlorobiphenyl Using Mouse 2007-1 Serum and Various HRP Conjugates^a

competitor (HRP conjugate)	I_{50} (ppb) for PCB 77
2,5-S (8)	1.5
3,4-keto (3)	3
3,4-ether (4)	3.5
2,5-methylene (7)	6-8
hapten 1 (1)	30-40

^a Numbers in parentheses refer to structures in Figure 1.

Table 2. Cross-Reactivity of PCB Congeners in the Direct EIA with Mouse 2007-1 Serum and the 3,4-Keto-HRP Competitor

IUPAC no.	congener	I_{50} (ppb)
77	3,4,3',4'-tetrachlorobiphenyl	3
70	2,5,3',4'-tetrachlorobiphenyl	50
118	2,4,5,3',4'-pentachlorobiphenyl	290
15	4,4'-dichlorobiphenyl	4300
52	2,5,2',5'-tetrachlorobiphenyl	>20000
153	2,4,5,2',4',5'-hexachlorobiphenyl	>20000

used in the earlier serum tests (data not shown). The results indicate that all of the fragment-based competitors improved the assay sensitivity. However, there was no clear relationship between the sensitivity and the competitor's chlorination pattern or linker moiety. The data in Table 2 demonstrate that direct EIA using the 3,4-keto competitor and 2007-1 antiserum showed preference for PCB 77 compared with congeners that are significantly more abundant components of the Aroclor mixtures. In a similar direct EIA with the mouse serum in antibody-coated tubes, 2,3,7,8-tetrachlorodibenzo-*p*-dioxin was not recognized in amounts up to 1 ppm.

Selection of Hybridomas. The fusion produced 628 hybridoma colonies from 3840 wells. On the basis of the results of the mouse serum testing, the culture supernatants were screened by indirect EIA for binding to hapten I-BSA or 2,5-S-BSA. A total of 284 cultures that produced hapten-binding antibodies were expanded to 24-well dishes. The secondary screening by direct EIA selected 69 MAbs able to bind hapten I-HRP, 2,5-S-HRP, or 3,4-keto-HRP. Only five of these competitively bound PCB 77 or showed relatively specific noncompetitive binding of the competitors. Of these, only one MAb, designated S2B1, proved to be specific for competitive binding of the toxic congeners PCB 77 and PCB 126. MAb S2B1 was an IgG_{2b} κ immunoglobulin, which allowed us to affinity purify it on protein A-Sepharose.

Optimization of the Direct EIA. The direct EIA was optimized with respect to dilutions of MAb S2B1 culture fluid using competitors 2-9 (checkerboard titrations). Nonspecific binding of the competitor-HRP conjugate preparations was measured with tubes or wells coated with dilutions of complete cell culture medium (Iscove's Modified Dulbecco's medium, IMDM) instead of MAb S2B1. Each conjugate had different amounts of nonspecific binding. Adventitious binding of the 3,4-keto-HRP and 3,4-amino-HRP competitors was negligible at dilutions of IMDM greater than 1/500. The 2,5-S-HRP and the 2,4-ether-HRP conjugates bound so weakly that B_0 values were low, and nonspecific binding was higher than that of 3,4-keto-HRP. The 3,4-cinnamic acid-HRP conjugate had significant nonspecific binding

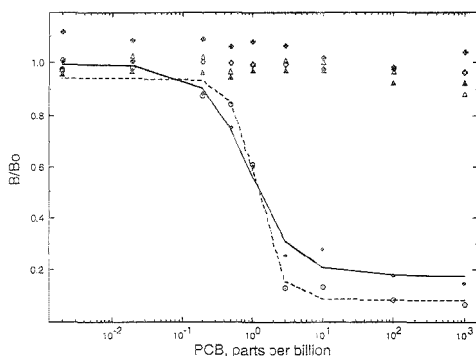


Figure 4. Direct competition EIA of six PCB congeners with MAb S2B1. Microwells coated with donkey anti-mouse IgG were allowed to bind S2B1 culture supernate (1/100 in PBS T). Dilutions of the PCB congeners in 0.01 mL were added to 0.2 mL of a 1/15000 dilution of the 3,4-keto-HRP conjugate as described in the Experimental Section. Color development was stopped after approximately 2 min by addition of 0.05 mL of 2.5% HCl to the 0.2 mL of substrate solution, and absorbance was read at 450 nm. B/B_0 is the ratio of the absorbance at the indicated concentration of analyte to the absorbance obtained with no added analyte: (solid cross) 2,4'-dichlorobiphenyl (PCB 8); (open cross) 2,5,2',5'-tetrachlorobiphenyl (PCB 52); (\blacktriangle) 2,4,5,2',4',5'-hexachlorobiphenyl (PCB 153); (\triangle) 2,4,4'-trichlorobiphenyl (PCB 28); (\bullet) 3,4,3',4'-tetrachlorobiphenyl (PCB 77); (\circ) 3,4,3',4',5'-pentachlorobiphenyl (PCB 126). The lines are four-parameter logistic fits of the data. The estimated I_{50} values were 0.9 and 1.2 ppb for PCBs 77 and 126, respectively.

at dilutions up to 1/10000, but it gave a similar I_{50} to the 3,4-keto-HRP conjugate. Direct competition EIAs using competitors 3-7 gave comparable I_{50} values for PCBs 77 and 126. These results suggest that the optimum competitors for MAb S2B1 have the same 3,4 chlorination pattern as the hapten, but a different linker moiety. The optimized direct EIA for competitive binding of the toxic congeners used microwells coated with a 1/300 dilution of S2B1 culture supernate and a 1/15000 dilution of 3,4-keto-HRP.

The specificity of the direct EIA in tubes and microwells was first tested with MAb S2B1 and the 3,4-keto-HRP conjugate using a sample diluent containing 5% methanol. Results for the microwell assay are illustrated in Figure 4. In two such experiments, the fitted I_{50} values were 0.9-2.7 ppb for PCB 77 and 1.2-3.7 ppb for PCB 126. None of the four noncoplanar, less toxic PCB congeners we tested bound competitively in amounts less than 2 ppm. The optimized coated tube EIA gave a similar result, with a minimum detection limit (I_{10}) of 0.2 ppb, an I_{50} of 1 ppb for PCB 77, and very similar values for PCB 126. None of the noncoplanar congeners that we tested were bound in amounts up to 1 ppm. Solvent tolerance experiments indicated that methanol concentrations less than 5% in the assay diluent may have been insufficient to keep more than 100 ppb of some congeners soluble. However, methanol concentrations of 7.5% or more increased outliers and error among replicates in the direct EIA using tubes and wells coated with donkey anti-mouse IgG.

Streptavidin-Biotin EIA. An alternate direct EIA format proved to be much more stable to organic solvents. Affinity-purified S2B1 IgG was labeled with biotin on a 14-carbon spacer arm. Optimal biotinylation was achieved with 25 ng of NHS-XX-biotin/mg of pure IgG. The optimum assay was obtained using wells with 160 ng of covalently attached streptavidin to bind 7.5

Table 3. Cross Section of MAb S2B1 with Various PCBs^a

IUPAC no.	CAS no.	common name	I_{50} ^b (ppb)	
			5% methanol	10% DMSO
77	32598-13-3	3,4,3',4'-tetrachloro	7-30	10-90
126	57465-28-8	3,4,5,3',4'-pentachloro	10-20	50
169	32774-16-6	3,4,5,3',4',5'-hexachloro	nc ^c	370
12	2974-92-7	3,4-dichloro	≥ 2000	235
35	37680-69-6	3,4,3'-trichloro	310	20
37	38444-90-5	3,4,4'-trichloro	$I_{50} \approx 2000$ ^d	135
70	32598-11-1	2,5,3',4'-tetrachloro	>2000	600
78	70362-49-1	3,4,3',5'-tetrachloro	520	40
79	41464-48-6	3,4,3',5'-tetrachloro	1500	65
81	70362-50-4	3,4,4',5'-tetrachloro	$I_{50} \approx 1000$ ^d	~ 320
118	31508-00-6	2,4,5,3',4'-pentachloro	1500	~ 5000

^a The biotin-streptavidin EIA was performed with the 3,4-keto-HRP competitor as described in the Experimental Section. ^b Half-maximal inhibition determined by four-parameter logistic fit, unless noted otherwise. Columns show data obtained in diluent containing the indicated solvent. ^c nc, no competition in amounts up to 5 ppm. ^d Percent inhibition observed at the highest concentration tested. A four-parameter fit could not be computed where a high-dose asymptote was not observed.

ng of biotin-S2B1/well, and 3,4-keto-HRP (diluted 1/100000) as competitor. The I_{50} values for PCBs 77 and 126 in this EIA were higher than those obtained in the direct EIA using capture antibody (7-30 ppb instead of 1 ppb), but they remained the same in 5, 10, and 25% methanol. The standard error of replicates was much lower in the biotin-streptavidin assay. This assay could also be performed using 10% DMSO rather than methanol in the diluent. This proved to be important for assays of dioxin, dibenzofuran, and other compounds that are poorly soluble in methanol. The specificity of MAb S2B1 for various congeners and other compounds and all experiments with Aroclors were done using the biotin-streptavidin EIA.

Assay Specificity. The cross-reactivity of several congeners was strongly influenced by the amount and type of organic solvent in the assay diluent. Measurements of the three most toxic coplanar congeners (PCBs 77, 126, and 169) and the noncoplanar 2,4,5,2',4',5'-hexachlorobiphenyl (PCB 153) were compared in diluent containing 5, 10, or 20% methanol, DMSO, and acetonitrile. The responses of PCBs 77 and 126 were very similar, although the I_{50} values tended to increase (the assay became less sensitive) with increasing organic solvent. PCB 169 did not react in amounts up to 1 ppm in 5% methanol or 5% DMSO, and shallow binding curves were obtained in 10 and 20% methanol. In 10 and 20% DMSO, PCB 169 reacted with detection limits (I_{10}) around 100 and 10 ppb, respectively. Detection of PCB 169 in acetonitrile was similar to that in methanol. Based on these results, cross-reaction of several other congeners and analogs was tested in the biotin-streptavidin assay using PBST-10% DMSO as the diluent.

Table 3 compares the half-maximal or limiting inhibition by all of the congeners that showed appreciable binding in the EIA. Reactivity for most congeners was increased; i.e., the assay became more sensitive in diluent containing 10% DMSO. The assay using 10% DMSO was about equally sensitive for PCBs 77 and 126, but it also detected several other coplanar congeners with 3,4,3' and 3,4,4' chlorination. Two mono-ortho-substituted congeners (PCBs 70 and 118) bound weakly. All of the congeners in Table 3 were soluble in 5% methanol to at least 5 ppm. It appeared that the differences in detection were due to effects of

Table 4. Compounds That Are Weakly Reactive or Do Not Cross-React in the EIA^a

IUPAC no.	CAS no.	common name	<i>I</i> ₅₀ ^b (ppb)	
			5% methanol	10% DMSO
PCBs				
2	2051-61-8	3-chlorobiphenylol	nc ^c	nt ^d
8	34883-43-7	2,4'-dichloro	nc	nt
13	2974-90-5	3,4'-dichloro	nc	nt
14	34883-41-5	3,5-dichloro	nc	nt
15	2050-68-2	4,4'-dichloro	nc	>3000
28	7012-37-5	2,4,4'-trichloro	nc	nt
52	35693-99-3	2,5,2',5'-tetrachloro	nc	nt
56	41464-43-1	2,3,3',4'-tetrachloro	nc	<i>I</i> ₇₀ ≈ 5000 ^f
76	70362-48-0	2',3,4,5-tetrachloro	nc	<i>I</i> ₆₀ ≈ 3000
80	33284-52-5	3,3',5,5'-tetrachloro	nc	<i>I</i> ₆₀ ≈ 3000
101	37680-73-2	2,4,5,2',5'-pentachloro	nc	nt
105	32598-14-4	2,3,3',4,4'-pentachloro	nc	<i>I</i> ₃₅ ≈ 5000
110	38380-03-9	2,3,6,3',4'-pentachloro	nc	nc
127	39635-33-1	3,3',4,5,5'-pentachloro	nc	415
153	35065-27-1	2,4,5,2',4',5'-hexachloro	nc	nc
156	38380-08-4	2,3,3',4,4',5-hexachloro	nc	<i>I</i> ₆₀ ≈ 5000
PBBs				
	77102-82-0	3,4,3',4'-tetrabromobiphenyl	<i>I</i> ₄₀ ≈ 1000	~300
	77607-09-1	3,4,5,3',4',5'-hexabromo	nc	nc
	59080-40-9	2,4,5,2',4',5'-hexabromo	nc	nc
Dibenzofurans and Dioxins				
	51207-31-9	2,3,7,8-tetrachlorodibenzofuran	<i>f</i>	<i>I</i> ₁₅ ≈ 5000
	1746-01-6	2,3,7,8-tetrachlorodibenzo- <i>p</i> -dioxin	<i>f</i>	<i>I</i> ₁₅ ≈ 5000
PCB Metabolites				
		3,4',5-trichloro-4-biphenylol	nc	nt
		3,3',5,5'-tetrachloro-4,4'-biphenyldiol	nc	nt
		3,4,3',4'-tetrachlorodiphenyl ether	<i>f</i>	<i>I</i> ₁₅ ≈ 1000
Other Compounds				
	95-50-1	1,2-dichlorobenzene	nc	nt
	541-73-1	1,3-dichlorobenzene	nc	nt
	106-46-7	1,4-dichlorobenzene	nc	nt
	120-82-1	1,2,4-trichlorobenzene	nc	nt
	95-76-1	3,4-dichloroaniline	nc	nt
	50-29-3	4,4'-DDT	nc	nt
	72-54-8	4,4'-DDD	nc	nt

^a The biotin-streptavidin EIA was performed with the 3,4'-keto-HRP competitor as described in the Experimental Section. ^b Half-maximal inhibition determined by four-parameter logistic fit, unless noted otherwise. Columns show data obtained in diluent containing the indicated solvent. ^c nc, no competition in amounts up to 5 ppm. ^d nt, not tested. ^e Percent inhibition observed at the highest concentration tested. A four-parameter fit could not be computed where a high-dose asymptote was not observed. ^f These compounds are not sufficiently soluble in PBST/5% methanol to conduct the assay.

DMSO on binding of the compounds by MAb S2B1 rather than to limited solubility of the congeners in methanol.

Table 4 lists compounds that were not reactive or reacted to weakly for practical detection. 3,4,3',4'-Tetrabromobiphenyl, the brominated analog of PCB 77, bound weakly, suggesting that bromine atoms with their larger radii are not accommodated well in the combining site. The most toxic dioxin (2,3,7,8-tetrachlorodibenzo-*p*-dioxin) and 2,3,7,8-tetrachlorodibenzofuran were not recognized in amounts up to 1 ppm; 5 ppm caused 15% inhibition at most. These compounds are approximate isostereomers of the PCBs.^{6,38,39} The coplanar biphenylols and 3,3',4,4'-tetrachlorodiphenyl ether are mammalian and microbial PCB metabolites with higher acute toxicity than the parent PCBs.^{40,41} They also did not react in the EIA. None of several single-ring chlorinated

compounds that may occur as PCB degradation products or are likely to be found with PCBs in hazardous waste were bound.

Similar selectivity but reduced sensitivity (higher *I*₅₀ value) for PCBs 77 and 126 was observed in EIAs using hapten I-HRP and competitor-HRP conjugates 4-6 and 8 shown in Figure 2. This indicated that the specificity for the toxic coplanar congeners is an intrinsic property of MAb S2B1, due primarily to the immunizing hapten and not the competitors. These results also support the notion that the hapten defines specificity while the competitor determines the sensitivity of the assay.³⁷

Detection of Aroclors. The Aroclors and related industrial PCB formulations vary greatly in their congener composition, including their content of the toxic coplanar tetra-, penta-, and hexachlorobiphenyls.¹ Several of the major Aroclors contained measurable amounts of congeners that are recognized in the assay. Direct EIAs were done with biotinyl-S2B1 in streptavidin-coated wells, to take advantage of the greater solvent tolerance. Aroclor stocks in neat methanol were diluted into PBST/25% methanol to give responses on the measurable range of a PCB 77 standard curve, based on published estimates of the mole

(38) Mason, G.; Farrell, K.; Keys, B.; Piskorska-Pliszczynska, J.; Safe, L.; Safe, S. *Toxicology* **1986**, *41*, 21-31.

(39) Stanker, L. H.; Watkins, B.; Rogers, N.; Vanderlaan, M. *Toxicology* **1987**, *45*, 229-243.

(40) Coulstor, F.; Korte, F.; Goto, M. *New Methods in Environmental Chemistry and Toxicology (Proceedings of the International Symposium)*; Susono, Japan, 1973.

(41) Safe, S. *RFR Res. Notes* **1977**, (March), 1-3.

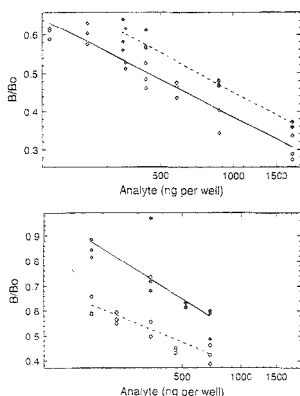


Figure 5. Measurement of immunoreactive material in Aroclors. The indicated amounts of Aroclor were added to the streptavidin–biotin EIA in diluent containing 25% methanol. Reference standards of PCB 77 had B_0 values of 12–20 ppb, corresponding to 1.2–2 ng/well: (top) Aroclor 1248 (◆) and Aroclor 1016 (◇); (bottom) Aroclor 1242 (●) and Aroclor 1254 (○). The lines are logarithmic fits as described in the text.

percent of PCBs 77, 126, and 35 (Tables 1 and 2 in ref 1). Measurable responses were obtained from 0.06 to 1.75 μg of Aroclors 1016, 1242, 1248, and 1254 (Figure 5). Aroclor 1260 gave a very weak response ($B/B_0 = 0.7\text{--}0.9$ at 0.5–1.75 μg /well) with large variation between replicates. Three industrial polychlorinated terphenyls (Aroclors 5442, 5460, and 5060) gave no responses up to 2 μg /mL, nor did the polybrominated biphenyl formulation Firemaster BP-6.

The B/B_0 responses of Aroclors 1016, 1242, 1248, and 1254 and the pure congeners were fitted to the model $y = m \ln(x) + b^{42}$ using an iterative nonlinear fitting routine (Passage II). The responses were roughly parallel to each other over this range of Aroclor dilutions, but they were not parallel to the working ranges of curves for PCBs 77 and 126. These results probably reflect differences in the amounts of congeners that cross-react differently in the EIA and/or different nonspecific interfering substances in the Aroclors. Thus, while MAb S2B1 can detect the toxic congeners in Aroclors, it would not be accurate to estimate amounts of individual congeners by interpolation from a single-congener standard curve.

CONCLUSIONS

In summary, we have developed a MAb-based immunoassay that is selective for the most toxic PCB congeners. The selectivity is due primarily to the immunizing hapten with its coplanar structure and ether-linked, para-substituted spacer arm, while the sensitivity results from use of the fragment-based competitor–HRP conjugates. Previous efforts by others were designed to evoke antibodies that would recognize many of the more abundant PCB congeners. Thus, nearly all of the previously reported haptens were ortho-substituted and used an amino or azo linkage to mimic a chlorine atom.^{16–18} Recently, PCB haptens with a glutaramyl- β -alanyl spacer arm were used to make an immunizing

antigen that evoked polyclonal antibodies to PCB 153.^{19,20} None of these assays were selective for the toxic coplanar congeners.

Most efforts at systematic hapten design have been based on the notion that both the immunizing hapten and the competitor should resemble the analyte as closely as possible.^{43–45} However, competitive-binding immunoassays are generally most sensitive when the antibody has a lower affinity for the competitor than it does for the target analyte.^{37,46} Accordingly, we designed our competitors to mimic half of the PCB molecule. The behavior of the mouse antisera as exemplified by Figure 3 indicated that our combination of immunizing and competing conjugates produced a congener-specific response. However, the results also suggested that the assay's performance might be limited by less selective or lower affinity antibodies in the repertoire. During hybridoma selection we also found that many antibodies in the repertoire bound to the immunizing hapten but did not competitively bind free PCB. Detection of individual PCB congeners appears to be an application for which MAbs are superior to whole antisera.

The limits of detection of PCBs 77 and 126 in our direct EIAs were 0.2–1.0 ppb, depending on the format. No immunoassay in the published literature reported a detection limit for these PCBs. The detection limit for these congeners in high-resolution capillary GC/MS is on the order of 10 ppb. Samples for GC/MS are generally concentrated 10 000-fold to give a detection limit around 1 (for extracts of fat) or 10–100 ppt (for extracts of sediments) in the original sample (Jianwen She and Kim Hooper, California Dept. of Health Services, personal communication). With similarly concentrated extracts, the EIA should thus be at least as sensitive as the instrumental method. Sample preparation for GC/MS also requires steps to eliminate noncoplanar PCBs that would coelute with the coplanar PCBs. These steps should not be necessary for the EIA.

Immunoanalysis could provide a more definitive and cost-effective way to identify and quantify the toxic congeners as an alternative to instrumental methods or in conjunction with them. The EIA is simple, fast, and amenable to automated sample processing. The negligible cross-reaction with 2,3,7,8-tetrachlorodibenzo-*p*-dioxin and 2,3,7,8-tetrachlorodibenzofuran makes it possible to independently measure the coplanar PCB congeners in the presence of dioxins and dibenzofurans. This would not be possible using, for example, an assay based on the aryl hydrocarbon receptor. Although the EIA responds to a subset of congeners in the Aroclors, additional experiments will be needed to develop a reliable quantitative correlation between the EIA response and the toxic congener content of Aroclor-contaminated samples. Congener-specific immunoassay is also potentially applicable to environmental toxicology and molecular epidemiology studies. MAb S2B1 may prove to be a useful antagonist or receptor mimic in studies of PCB binding by proteins such as the aryl hydrocarbon receptor. In addition, immunoaffinity methods with MAb S2B1 may be suitable for specifically recover-

(42) Brady, J. F. In *Immunoanalysis of Agrochemicals: Emerging Technologies*; Nelson, J., Karu, A. E., Wong, R., Eds.; ACS Symposium No. 586; American Chemical Society: Washington DC, 1995; pp 266–287.

(43) Jung, F.; Gee, S.; Harrison, R.; Goodrow, M.; Karu, A.; Braun, A.; Li, Q.; Hammock, B. *Pestic. Sci.* **1989**, *26*, 303–317.

(44) Harrison, R.; Goodrow, M.; Gee, S.; Hammock, B. In *Immunoassays for Trace Chemical Analysis*; Vanderlaan, M.; Stanker, L.; Watkins, E.; Roberts, D., Eds.; ACS Symposium Series 451; Washington, DC, 1990; pp 14–27.

(45) Goodrow, M. H.; Sanborn, J. R.; Stoutamire, D. W.; Gee, S. J.; Hammock, B. D. In *Immunoanalysis of Agrochemicals: Emerging Technologies*; Nelson, J., Karu, A. E., Wong, R., Eds.; ACS Symposium Series 586; American Chemical Society: Washington DC, 1995; pp 119–139.

(46) Jockers, R.; Bter, F. F.; Schmid, R. D. *J. Immunol. Methods* **1993**, *163*, 161–167.

ing residues of the toxic congeners from complex field samples. Our laboratories are presently exploring these and other applications.

ACKNOWLEDGMENT

This research was sponsored in part by NIH SBIR Phase I Grant 1R43 CA62679-01 to R.E.C. A.E.K. is an Investigator in the NIEHS Health Sciences Center at U.C. Berkeley (NIEHS Grant 2 P30 ES01896-16). A summary of this work was presented at

the 15th International Symposium on Chlorinated Dioxins and Related Compounds, Edmonton, Canada, August 21–25, 1995.

Received for review July 7, 1995. Accepted August 25, 1995.*

AC950675Y

* Abstract published in *Advance ACS Abstracts*, September 15, 1995.

Geometric Approach to Factor Analysis for the Estimation of Orthogonality and Practical Peak Capacity in Comprehensive Two-Dimensional Separations

Zaiyou Liu* and Donald G. Patterson, Jr.

U.S. Centers for Disease Control, National Center for Environmental Health, Division of Environmental Health Laboratory Sciences, Toxicology Branch, 4770 Buford Highway, NE, Atlanta, Georgia 30341-3724

Milton L. Lee

Department of Chemistry, Brigham Young University, Provo, Utah 84602

Procedures were developed for the estimation of orthogonality in two-dimensional (2D) separations. The parameters evaluated include peak spreading angle, retention correlation, and practical peak capacity. Solute retention parameters, such as retention times and capacity factors on both dimensions, were used to establish a correlation matrix, from which a peak spreading angle matrix was calculated using a geometric approach to factor analysis. The orthogonality is defined by the correlation matrix with correlation coefficients that vary from 0 (orthogonal) to 1 (perfect correlation). Equations were derived for the calculation of practical peak capacity in 2D separations. The calculations are based on the peak capacities obtained on each dimension and the peak spreading angle in an orthogonal, 2D retention space. The equations and the procedures can be used to evaluate the performance of a comprehensive 2D separation. Using experimental data from a 2D GC separation, it is demonstrated that the equations are very useful for the comparison, evaluation, and optimization of 2D separations.

Peak capacity, which is defined as the maximum number of peaks that can fit into an available retention space, is an important measure of the effectiveness of a separation process.¹ It is generally considered for a two-dimensional (2D) separation that the peak capacity is the product of the peak capacities obtained on each of the two dimensions.^{2,3} This multiplicative rule indicates

that a 2D separation should be substantially more powerful to resolve complex mixtures than its one-dimensional (1D) counterpart because of the large peak capacity. However, the multiplicative rule is only an estimation of the peak capacity in 2D separations because correlations of solute retention in two dimensions reduce the available retention space to a restricted region. Moreover, as already accepted in 1D separations, peak capacity represents the number of resolvable peaks with ideal spacing along the retention axis. The actual number of components that can be isolated in a separation is far less than the theoretical peak capacity due to statistical overlap of component zones.^{4,5} The statistical theory of zone overlap predicts that the ability to resolve zones in 2D separations does not increase in direct proportion to the increase in peak capacity.⁶

The expressions for peak capacity in 2D separations have been discussed in considerable detail.^{3,7} Most of the expressions are based on planar systems with orthogonal separations. In practice, the actual peak capacity is somewhat less than predicted because a truly orthogonal separation is seldom obtained. The concept of orthogonality in 2D separations has not been precisely defined, but it is generally understood that the separation is orthogonal if the two separation mechanisms are independent of each other, so that the distribution of component zones in one dimension is not correlated with the zone distribution in the other dimension. For example, the combination of liquid chromatography and electrophoresis should provide orthogonal separations because the two methods are based on quite different retention principles.⁸ However, orthogonality is dependent not only on the separation

* Current address: Ivorydale Technical Center, The Procter & Gamble Co., 5299 Spring Grove Ave., Cincinnati, OH 45217.

(1) Giddings, J. C. *Anal. Chem.* **1984**, *56*, 1258A.

(2) Giddings, J. C. *J. High. Resolut. Chromatogr. Chromatogr. Commun.* **1987**, *10*, 319.

(3) Giddings, J. C. In *Multidimensional Chromatography*; Cortes, H. J., Ed.; Marcel Dekker, Inc.: New York, 1990; Chapter 2.

(4) Davis, J. M.; Giddings, J. C. *Anal. Chem.* **1983**, *55*, 418.

(5) Oros, F. J.; Davis, J. M. *J. Chromatogr.* **1991**, *550*, 135.

(6) Davis, J. M. *Anal. Chem.* **1991**, *63*, 2141.

(7) Guiochon, G.; Beaver, L. A.; Gonnord, M. F.; Siouffi, A. M.; Zakaria, M. *J. Chromatogr.* **1983**, *255*, 415.

(8) Monnig, C. A.; Jorgenson, J. W. *Anal. Chem.* **1991**, *63*, 807.

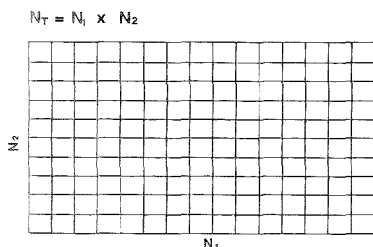


Figure 1. Orthogonal, 2D retention plane defined by the peak capacities, N_1 and N_2 .

mechanism but also on the properties of the solutes and the separation conditions. Orthogonal separations have been demonstrated even when the principal separation mechanisms are alike.⁹

It is necessary to establish a basis on which the performance of a comprehensive 2D separation can be evaluated and the analytical performance of different systems can be compared. Peak capacity and orthogonality are interrelated parameters describing the resolving power of 2D separations. The degree of orthogonality determines the available retention space in which the component zones spread. A procedure is developed in this paper to relate orthogonality and peak capacity in 2D separations. The procedure involves three steps: first, correlation and peak spreading angle matrices are computed using a set of 2D retention data; second, the peak capacities in each dimension are calculated, and the theoretical peak capacity is estimated; and third, the degree of orthogonality is used to calculate the practical peak capacity, which is the appropriate measure for the resolving power of 2D separation systems.

THEORY

Assumptions. In comprehensive 2D chromatographic separations, two sets of independent retention data (either in the form of k_R or k) are generated simultaneously. We assume that each set of retention data can be considered as an independent vector which represents the interactions between solutes and the stationary phase under a given set of conditions. This set of vectors can be manipulated mathematically for various calculations.

When more than one vector are generated in an analytical measurement, such as from gas chromatography/mass spectrometry or multichannel spectrometry, factor analysis has been used to determine the number of independent components within the set of measured vectors. We assume that there are two retention vectors associated with any given 2D chromatogram; then, as in other applications of factor analysis, correlations of the two retention vectors can be calculated.

To formulate the practical peak capacity, an orthogonal, 2D retention space is assumed in which a number of component zones spread. As illustrated in Figure 1, we assume that the peak capacity in the first dimension is N_1 and the peak capacity in the second dimension N_2 . On each retention coordinate, the peaks are evenly spaced with a Gaussian-shaped profile. The horizontal and vertical lines across the plane divide the retention space into resolution units with spacing approximately equal to the respective

peak widths. The small boxes represent resolution units in the 2D space. The theoretical or maximum peak capacity, therefore, is equal to the number of boxes in the plane, which is $N_1 \times N_2$. The area of the plane is then defined as the theoretical peak capacity,² N_T .

Retention correlations between dimensions shrink the retention space, which makes some of the area in Figure 1 inaccessible to component zones; therefore, the actual peak capacity, N_p , is smaller than N_T . An assumption is made here that the practical peak capacity, N_p , is equal to the available area determined by the retention correlation in the space.

Calculation of Correlation and Peak Spreading Angle Matrices.¹⁰ For simplicity, the following discussion is generalized for a multidimensional retention space, and so the procedures developed herein should be applicable to an n -dimensional retention space involving n independent retention vectors, where n is equal to or greater than 2.

For an i -dimensional separation, there are i sets of retention data generated from each run, which can be represented in a matrix form \mathbf{k} as

$$\mathbf{k} = \begin{pmatrix} k_{11} & k_{12} & \cdots & k_{1j} \\ k_{21} & k_{22} & \cdots & k_{2j} \\ \vdots & \vdots & \ddots & \vdots \\ k_{i1} & k_{i2} & \cdots & k_{ij} \end{pmatrix} \quad (1)$$

where the element k_{ij} is the retention value of the component j in the i th dimension. One of the main purposes of factor analysis is to provide a representation of data vectors in a space with a lower dimensionality, while preserving the original information content. Reducing the measurement dimensionality allows a better understanding of the phenomenon under consideration. Factor analysis could be useful in multidimensional separations because more than one retention vector and several solute property vectors could be involved. A geometric approach to factor analysis could be used to calculate correlations between a pair of vectors. Because the correlation between any two unit length vectors is the cosine of the angle between them, the entries in eq 1 must be scaled, such that their mean is zero and their variance is one. The scaled matrix can be calculated according to

$$k'_{ij} = \frac{k_{ij} - m_i}{s_i} \quad (2)$$

where m_i is the mean of the original entries of the i th vector, and s_i is the standard deviation of the original entries of the i th vector. The new scaled matrix is represented by \mathbf{k}' , and the transposed matrix is defined as \mathbf{k}'^T . The sample by sample correlation matrix is then given as

$$C = \left(\frac{1}{N-1} \right) \mathbf{k}'^T \mathbf{k}' \quad (3)$$

where N is the number of entries found in each data vector, which is also the number of components in a multidimensional chro-

(9) Liu, Z.; Phillips, J. E. *J. Chromatogr. Sci.* **1991**, *29*, 227.

(10) Sharf, M. A.; Ilman, D. L.; Kowalski, B. R. *Chemometrics*; John Wiley & Sons: New York, 1992.

matogram. The correlation matrix can be represented as

$$C = \begin{vmatrix} 1 & C_{12} & \dots & C_{1j} \\ C_{21} & 1 & \dots & C_{2j} \\ \vdots & \vdots & \ddots & \vdots \\ C_{i1} & C_{i2} & \dots & 1 \end{vmatrix} \quad (4)$$

where $C_{ij} = C_{ji}$ is the quantitative measure of the vector correlations. Equation 4 is significant because the degree of retention correlation between any two dimensions is defined. A perfect correlation is obtained when $C_{ij} = 1$, and truly orthogonal separation is obtained when $C_{ij} = 0$, because C_{ij} is the cosine of any two unit length vectors.

The peak spreading angle matrix between each two retention vectors can be calculated from eq 4 according to eq 5.

$$\beta_{ik} = \cos^{-1} C_{ik} \quad (5)$$

In the case of 2D chromatographic separations, the peak spreading angle matrix is given by eq 6, where $\beta_{12} = \beta_{21}$ is the correlation or spreading angle between the retention axis in the orthogonal retention space. Further calculations for eigenvalues

$$\beta = \begin{vmatrix} 0 & \beta_{12} \\ \beta_{21} & 0 \end{vmatrix} \quad (6)$$

and factors to retain are not necessary in this application, because only the correlation matrix (eq 4) and the peak spreading angle β (eq 5) will be used in the following calculations.

A data matrix can be expanded to include parameters of the solute, such as molecular weight and boiling point, as a vector. The correlation matrix generated using eqs 1-4 gives a measure of the interaction between the stationary phase and the chosen parameter for a group of solutes. Large correlation values between a retention vector and a solute parameter indicate a strong dependence of solute retention on that parameter for the dimension under consideration, and vice versa. Such information is useful in the selection of columns and in the optimization of particular column combinations for given separation problems.

Practical Peak Capacity in Two-Dimensional Chromatographic Separations. The theoretical peak capacity for truly orthogonal, comprehensive 2D chromatographic separations is estimated as in eq 7, where N_T is the theoretical peak capacity, and N_1 and N_2 are the peak capacities obtained in the first and second dimensions, respectively.

$$N_T = N_1 \times N_2 \quad (7)$$

In 2D chromatographic separations with a certain degree of retention correlations (more common than truly orthogonal), the actual peak capacity provided by the separation is less than N_T . The correlation requires that a zone appearing at one coordinate have a fixed value at the other coordinate. With a perfect correlation (identical separation mechanisms on both dimensions), all of the zones will lie on a straight line; therefore, the high degree of correlation will collapse the 2D space into a 1D line with a peak capacity close to the 1D value. Most separations lie between perfect correlation and perfect orthogonality. The peak capacity estimated using a 1D equation (eq 8) and that calculated with eq 7 are both incorrect in practical applications.

Figure 2 shows a 2D retention space with a peak spreading angle of β . Part of the area in the orthogonal retention space

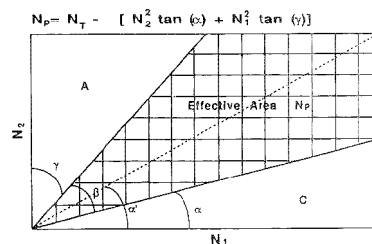


Figure 2. Effective nonorthogonal, 2D retention space when the peak spreading angle is β .

becomes unavailable because of correlation. The gridded area is the effective space in which zone spreading is allowed according to the correlation. Although the rectangular retention plane is immaterial, it is the most widely used form of representation for 2D chromatographic separations.^{11,12} This representation is used in this work because it is convenient for deriving equations to calculate the practical peak capacity.

The angles α , β , and γ shown in Figure 2 can be calculated using eqs 8-10, where α' is an angle determined by the shape of

$$\alpha = \alpha'(1 - 2\beta/\pi) \quad (8)$$

$$\alpha' = \tan^{-1}(N_2/N_1) \quad (9)$$

$$\gamma = \pi/2 - \alpha - \beta \quad (10)$$

the retention space, as given by eq 9. The peak spreading angle, β , is calculated using eqs 1-6. The effective area, or the practical peak capacity, is calculated as follows:

$$N_p = N_T - (A + C) \quad (11)$$

where A and C comprise the unavailable area in Figure 2 due to correlation, and they are given as

$$A = 1/2 N_2^2 \tan^2(\gamma) \quad (12)$$

$$C = 1/2 N_1^2 \tan^2(\alpha) \quad (13)$$

A more explicit form for N_p is given in eq 14, where N_1 and N_2 are the capacities in each dimension, and α and γ are the angles calculated from eqs 9 and 10.

$$N_p = N_1 N_2 - 1/2 [N_2^2 \tan^2(\gamma) + N_1^2 \tan^2(\alpha)] \quad (14)$$

When $N_1 = N_2$, $\alpha' = 45^\circ$, and $\alpha = \gamma$, eq 14 can be expressed as

$$N_p = N_T (1 - \tan(\alpha)) \quad (15)$$

A maximum peak capacity, N_T , is obtained when $\alpha = \gamma = 0$, which means that the 2D chromatographic separations are truly orthogonal. The 2D retention plane collapses to a straight line when $\alpha + \gamma = \pi/2$, which indicates a perfect correlation, and the separation is collapsed to a 1D separation. At this extreme, the calculated N_p is zero because the calculation of a 2D peak capacity

(11) Oros, O. J.; Davis, J. M. *J. Chromatogr.* 1992, 591, 1.

(12) Bushey, M. M.; Jorgenson, J. W. *Anal. Chem.* 1991, 62, 161.

Table 1. Characteristic and Retention Data for Various Compounds^a

solute	k_1	k_2	MW	bp (°C)
Alkanes				
hexane	0.02	0.59	86.18	69.0
heptane	0.05	1.05	100.21	98.0
octane	0.10	2.15	114.22	125.6
nonane	0.18	3.97	128.26	151.0
Aromatics				
benzene	0.24	0.87	78.11	80.0
toluene	0.44	1.65	92.14	111.0
<i>p</i> -xylene	0.77	3.14	106.17	138.1
<i>m</i> -xylene	1.03	3.74	106.17	144.0
styrene	1.44	3.64	104.15	154.4
Polar Compounds				
1,5-cyclooctadiene	0.89	4.92	108.18	150.0
cyclohexyl chloride	0.77	3.60	118.61	142.0
chlorobenzene	1.23	2.78	112.56	132.2
isobutanol	0.52	0.64	74.12	108.3
isoamyl alcohol	1.07	1.25	88.15	130.0

^a The first column was a 21-m \times 250- μ m-i.d. column with a 0.25- μ m stationary phase of Supelcowax-10 (Supelco). The second column was a 100-cm \times 100- μ m-i.d. column with a 0.5- μ m stationary phase film of 007 methylsilicone (Quadrex). The GC oven was kept at 93 °C isothermal. Detailed information is given in ref 9.

is meaningless. Such separations should be evaluated using the 1D formula.¹³

EXPERIMENTAL SECTION

Two-dimensional chromatograms were generated using a Varian 3700 GC system. The GC system was modified for comprehensive 2D chromatographic separations. Details of the instrumentation and procedures are given elsewhere.^{14,15} The columns and chromatographic conditions are given in Table 1.

Calculation of the correlation matrix and peak spreading angles was done within the SAS environment. Two sets of retention data were measured from each chromatogram. The retention data were normalized according to the retention mean in each dimension. The normalized data were calculated for the sample to sample correlation, from which the peak spreading angle, β , was obtained. The practical peak capacity was calculated using the peak spreading angle, β , and peak capacities estimated in each dimension. One-dimensional peak capacities were estimated from the ratio of total retention time to average peak width in that dimension.

RESULTS AND DISCUSSION

Figure 3 is a plot of practical peak capacity vs peak spreading angle calculated using eq 14. In this plot, N_T was kept constant at 100, while the ratio N_1/N_2 was varied. In Figure 3, the practical peak capacity reached the theoretical value when the peak spreading angle was $\pi/2$ (orthogonal). At this point, the 2D separations are truly orthogonal and retention correlation does not exist, and so the system can provide its maximum resolving power to a separation problem. The practical peak capacity decreases with a decrease in the peak spreading angle, but the rate of decrease varies according to the ratio N_1/N_2 . In general, N_p decreases at a lower rate when N_1/N_2 deviates from 1. The peak spreading angle has a reduced effect on N_p when the

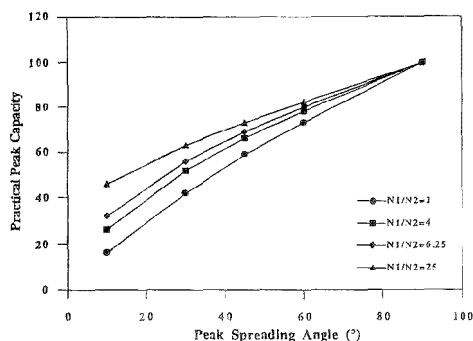


Figure 3. Relationship between the practical peak capacity, N_p , and peak spreading angle, β , at various N_1/N_2 ratios.

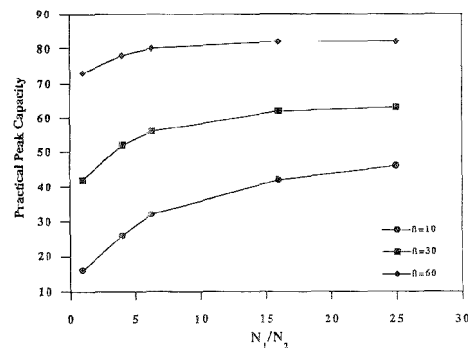


Figure 4. Relationship between practical peak capacity and N_1/N_2 ratios.

difference in peak capacities in the two dimensions increases. At $N_1/N_2 = 1$, a square-shaped retention plane is defined, and when $N_1 \neq N_2$, rectangular-shaped retention space is defined. At a given peak spreading angle, β , the effective retention space (N_p , see Figure 2) varies with the shape of the retention plane. This relationship is shown in Figure 4. The same conclusions are obtained when N_2/N_1 is used because this also defines the shape of the retention plane. Results in Figure 4 suggest that a better performance can be obtained when the peak capacities are different in different dimensions, at otherwise identical conditions.

Table 1 contains data obtained from a previous publication by the principal author.⁹ These data were reorganized for convenience. The molecular weights and boiling points of the solutes were added to this table for determination of the interactions between solutes and stationary phases. Each data column in the table was treated as an independent vector. The calculated correlation matrix and angle matrix using eqs 1–6 are given in Table 2.

The correlation matrix in Table 2 provides a measure of the solute–stationary phase interactions. For this sample mixture, solute retention on the second column was strongly correlated with molecular weight ($C_{ij} = 0.78642$) and boiling point ($C_{ij} =$

(13) Lee, M. L.; Yang, F. J.; Bartle, K. D. *Open Tubular Column Gas Chromatography*; John Wiley & Sons: New York, 1984; pp 14–49.

(14) Liu, Z.; Sirimanne, S.; Patterson, D. G., Jr.; Needham L. L.; Phillips, J. B. *Anal. Chem.* **1994**, *66*, 3086.

(15) Phillips, J. B.; Liu, Z. U.S. Patent 5,135,549, 1993.

Table 2.
Correlation (C_{ij}) and Angle (β) Matrix Values

	correlation				angle (deg)			
	k_1	k_2	MW	bp	k_1	k_2	MW	BP
k_1	1.000 00	0.505 39	0.154 46	0.660 19	0	60	81	49
k_2	0.505 39	1.000 00	0.786 42	0.876 18	60	0	38	29
MW	0.154 46	0.786 42	1.000 00	0.717 77	81	38	0	44
BP	0.660 19	0.876 18	0.717 77	1.000 00	49	29	44	0

Table 3. Correlation Matrix for Three Groups of Compounds

	k_1	k_2	MW	BP
		Alkanes		
k_1	1.000 00	0.998 67	0.978 34	0.971 75
k_2	0.998 67	1.000 00	0.966 51	0.958 45
MW	0.978 34	0.966 51	1.000 00	0.999 56
BP	0.971 75	0.958 45	0.999 56	1.000 00
		Aromatics		
k_1	1.000 00	0.909 23	0.805 75	0.927 91
k_2	0.909 23	1.000 00	0.960 29	0.976 01
MW	0.805 75	0.960 29	1.000 00	0.965 54
BP	0.927 91	0.976 01	0.965 54	1.000 00
		Polar Compounds		
k_1	1.000 00	0.340 66	0.482 61	0.549 23
k_2	0.340 66	1.000 00	0.987 67	0.877 54
MW	0.482 61	0.987 67	1.000 00	0.900 63
BP	0.549 23	0.877 54	0.900 63	1.000 00

0.876 18), while retention on the first column (k_1) was much less correlated with these parameters. This can be understood by considering the stationary phases in the two columns. The stationary phase used in the first column was polar so that solute retention was less correlated with molecular weight ($C_{ij} = 0.154 46$) and more correlated with boiling point ($C_{ij} = 0.660 19$). The strong correlation between k_2 and molecular weight and boiling point is a result of the nonpolar nature of the stationary phase used in the second column. Solute volatility is the dominating parameter for retention, which is in turn dependent on both molecular weight and boiling point.

From the angle matrix in Table 2, the calculated peak spreading angle in the orthogonal retention plane for this separation was 60°. The measured peak capacity was 15 on both columns, which defined a square-shaped retention space with $N_T = 225$. Using eqs 7 and 15, and the peak spreading angle, the estimated theoretical and practical peak capacities are 225 and 165, respectively. The correlation value between the two retention vectors is 0.505 39. A value of 26.7% of the theoretical peak capacity was lost due to this retention correlation. However, the peak capacity obtained from the 2D separation was more than 10 times higher than that from either of the two dimensions used alone. This result clearly shows the resolving power advantage of using 2D separations, even with a limited degree of correlation.

The solutes in Table 1 were categorized into three groups according to their interactions with the stationary phase. Correlation matrices and practical peak capacities were calculated for each group. The results are given in Table 3. The first group of compounds is comprised of alkanes. These compounds are nonpolar, and their retention on both columns is controlled mainly by solute volatility. This agrees very well with the results given in Table 3. Both k_1 and k_2 are strongly correlated with molecular weight and boiling point ($C_{ij} > 0.95$). Since the solute molecules

are nonpolar, stationary phase polarity is not a dominant factor affecting retention. In fact, a stronger correlation between k_1 and solute volatility was found for the polar column (first column) with C_{ij} values greater than 0.97. Because both retention vectors are strongly correlated with solute volatility, the 2D separation is close to perfect correlation, with $C_{ij} = 0.998 67$ (at perfect correlation, $C_{ij} = 1$). This 2D separation, therefore, is no better than a 1D separation. Using a multidimensional separation for this type of mixture is not recommended.

In this example, where the first column was polar and the second column was nonpolar, a low degree of correlation was expected for the separation of polar compounds because of strong solute interactions on the polar column. The calculated results in Table 3 illustrates this conclusion because the C_{ij} between k_1 and k_2 is only 0.340 66, which corresponds to only a slight correlation between retentions. The peak spreading angle was calculated to be 70°. At this level of correlation, the calculated practical peak capacity is 186, which is 82.7% of the theoretical peak capacity. The loss in resolving power by correlation is 17.3%. With such correlation, the resolving power for this type of mixture is 12 times better than that obtained using either one of the dimensions alone.

The resolving power for aromatic compounds using this column combination lies between the results for nonpolar and polar compounds discussed above. For aromatics, a practical peak capacity of 125 was calculated from eq 15. Close to half of the theoretical resolving power was lost due to the relatively strong correlation ($C_{ij} = 0.909 23$, $\beta = 25^\circ$).

The results in Table 3 reaffirm that the combination of a polar column and a nonpolar column in 2D separations is a powerful approach for the separation of mixtures containing various categories of compounds, especially if the components of the mixtures are polar compounds. However, the resolving power collapses to a 1D situation if a nonpolar, homogeneous mixture of compounds is subjected to the 2D separation. This suggests that if two components requiring resolution are closely related, their retention on different columns will be strongly correlated. In this case, multidimensional separations lose their advantage, and the separations are best accomplished by 1D separations with selective stationary phases.

CONCLUSIONS

Orthogonality in multidimensional separations is a very important measure for estimating resolving power. Previously, orthogonality was implied by the retention mechanisms involved. This study provides a method which allows quantitative evaluation of orthogonality in 2D separations. The retention correlation (C_{ij}) calculated using solute retention vectors is a measure of orthogonality between dimensions. A perfect correlation is represented by $C_{ij} = 1$, and a truly orthogonal separation is represented by $C_{ij} = 0$. Most practical applications fall between the two extremes, with C_{ij} values between 0 and 1. Therefore, the actual resolving power is somewhat less than that predicted from the multiplicative rule.

The equations derived in this study for the calculation of practical peak capacity are more accurate in describing resolving power than those calculated by the multiplicative rule. The practical peak capacity is defined as the actual peak capacity that can be obtained for a particular separation. This calculation is based on solute retention parameters, and therefore, the results are more specific.

The method is not only useful in the evaluation of the performance of multidimensional separations but also applicable to optimization methods, such as the selection of correct column combinations for a given separation problem. Work is presently underway to test the application of this method in the evaluation and optimization of multidimensional separations, including column selections for different separation problems, tuning of

separation conditions for a specific separation, and optimization for achieving maximum orthogonality.

Received for review December 21, 1994. Accepted June 20, 1995.*

AC9412286

* Abstract published in *Advance ACS Abstracts*, September 15, 1995.

Source Identification of Underground Fuel Spills by Pattern Recognition Analysis of High-Speed Gas Chromatograms

Barry K. Lavine*

Department of Chemistry, Box 5810, Clarkson University, Potsdam, New York 13699-5810

Howard Mayfield, Paul R. Kromann, and Abdullah Faruque

AL/EQ, 139 Barnes Drive, Suite 2, Tyndall AFB, Florida 32403-5323

Pattern recognition methods have been used to classify high-speed gas chromatograms of weathered and unweathered jet fuels. A total of 228 neat jet fuel samples representing common aviation fuels sold in the United States were characterized by 85-peak gas chromatograms. Discriminants were developed by parametric and non-parametric pattern recognition procedures that correctly classified the gas chromatograms of neat jet fuels according to fuel type (JP-4, Jet-A, JP-7, JP-5), and these discriminant functions were successfully used to classify gas chromatograms of jet fuels which had undergone weathering in a subsurface environment. This approach for identification of weathered fuels was taken because the physical and chemical interactions of jet fuel components with the subsurface environment are not yet fully understood.

More than half of the individual households and communities in the United States rely on groundwater as their primary potable water resource.¹ The possible contamination of this essential natural resource by fuels stored in leaking underground tanks or pipelines has prompted the U.S. Air Force (USAF) to develop new methods for the identification of fuel materials recovered from subsurface environments. Growing interest in techniques which can establish the type of fuel responsible for the contamination of an underground well or aquifer is motivated in part by the cleanup costs, legal fees, and fines incurred by the polluter. However, determining the type of fuel recovered from a subsurface site near an underground well or aquifer is not a simple task. A processed fuel is a highly complex mixture, and the action of the environment is another complicating factor that must be taken into account, since it can alter the composition of the fuel.

The potential of gas chromatography for correlating hydrocarbon spills to suspected fuel sources is recognized by many workers^{2,3} in the field of environmental chemistry. Typically, gas chromatograms of the fuel spill and a number of suspected sources are compared visually in order to obtain a best match. However, visual analysis of gas chromatograms can be subjective and usually cannot take into account the effects of weathering

on the overall GC profile of the fuel. Therefore, evidence based on visual analysis of gas chromatograms is not always persuasive in a court of law, especially in cases involving an unweathered fuel identified as the source of a fuel spill, because of the marked differences between gas chromatograms of weathered and unweathered jet fuels.

Due to the complexity of the mixture which constitutes a processed fuel, a systematic comparison of gas chromatograms is often necessary to ensure that differences in composition between various types of fuels are consistent,⁴ which is why pattern recognition methods offer a better approach to the problem of matching gas chromatograms of jet fuels than visual analysis. Pattern recognition methods can identify fingerprint patterns in the gas chromatographic (GC) data characteristic of fuel type even though the fuel samples in the training set have been subjected to a variety of conditions. Hence, classifiers can be developed from the GC data that are relatively insensitive to changes in the overall GC profile of the original fuel due to contamination, analytical error, or weathering. Furthermore, the discriminatory information that is sought in the chromatographic data often consists of subtle variations in relative peak intensities distributed across several peaks in the gas chromatograms. Pattern recognition methods are especially well suited for extracting this type of information from the large amounts of qualitative and quantitative data present in the gas chromatograms.

In this study, pattern recognition methods have been used to classify the gas chromatograms of weathered and unweathered jet fuels. A data base of 228 gas chromatograms of neat jet fuel samples representing common jet fuels found in the United States was developed. Employing pattern recognition methods, the gas chromatograms of jet fuels that had undergone weathering in a subsurface environment have been correctly classified by type using discriminants developed from the gas chromatograms of neat jet fuels. This approach has been taken because the physical and chemical interactions of jet fuel components with the subsurface environment are not yet fully understood. The study described here is a logical extension of an earlier effort^{5,6} which emphasized the development of graphical and statistical pattern recognition methods for interpretation of GC profile data.

(1) Cohen, S. Z.; Creeger, S. M.; Carsel, R. F.; Enfield, C. G. In *Treatment and Disposal of Pesticide Wastes*; Krueger, R. F., Seiber, J. N., Eds.; ACS Symposium Series 259; American Chemical Society: Washington, DC, 1984; pp 297-325.

(2) Kawahara, F. K. *J. Chromatogr. Sci.* **1972**, *10*, 629-635.

(3) Kawahara, F. K.; Yang, Y. *Anal. Chem.* **1976**, *48*, 651-656.

(4) Lavine, B. K.; Qin, X.; Stine, A.; Mayfield, H. T. *Process Control Qual.* **1992**, *2*, 347-355.

(5) Lavine, B. K.; Stine, A.; Mayfield, H. T. *Anal. Chim. Acta* **1993**, *227*, 357-367.

(6) Lavine, B. K. *Chemolab* **1992**, *15*, 219-230.

Table 1. Training Set

no. of samples	fuel type
54	JP-4 (fuel used by USAF fighters)
70	Jet-A (fuel used by civilian airliners)
32	JP-7 (fuel used by SR-71 Reconnaissance plane)
29	JPTS (fuel used by TR-1 and U-2 aircraft)
43	JP-5 (fuel used by Navy jets)

Table 2. Prediction Set

sample no.	identity	source
PF007	JP-4	a
PF008	JP-4	a
PF009	JP-4	a
PF010	JP-4	a
PF011	JP-4	a
PF012	JP-4	a
PF013	JP-4	a
KSE1M2	JP-4	b
KSE2M2	JP-4	b
KSE3M2	JP-4	b
KSE4M2	JP-4	b
KSE5M2	JP-4	b
KSE6M2	JP-4	b
KSE7M2	JP-4	b
STALE-1	JP-4	c
STALE-2	JP-4	c
STALE-3	JP-4	c
PIT1UNK	JP-5	d
PIT1UNK	JP-5	d
PIT2UNK	JP-5	d
PIT2UNK	JP-5	d

^a Sampling well at Tyndall AFB. The sampling well was near a previously functioning storage depot. Each well sample was collected on a different day. ^b Soil extract near sampling well at Tyndall AFB. Dug with a hand auger at various depths. Distance between sampling well and soil extract was approximately 80 yards. ^c Weathered in laboratory. Old JP-4 fuel samples which had undergone weathering in a laboratory refrigerator. ^d Sampling pit at Keywest Naval Air Station. Two pits were dug near a seawall to investigate a suspected JP-5 fuel leak.

EXPERIMENTAL SECTION

A total of 228 fuel samples representing five different types of jet fuels (JP-4, Jet-A, JP-7, JPTS, and JP-5) were obtained from Wright Patterson Air Force Base (Ohio) and Mukilteo Energy Management Laboratory (Washington). The fuel samples were splits from regular quality control standards used by these two laboratories to verify the authenticity of manufacturers' claims that purchased fuels meet designated specifications. The quality control standards were collected over a 3-year period and constituted a representative sampling of the fuels.

The fuel samples, after they arrived for the study, were immediately stored in sealed containers at -20°C prior to analysis by gas chromatography. The gas chromatograms of these neat jet fuel samples were used as the training set (see Table 1). The prediction set consisted of 21 gas chromatograms of weathered jet fuel (see Table 2). Eleven of the 21 weathered fuel samples were collected from sampling wells as a neat oily phase which was found floating on top of the well water. Seven of the 21 fuel samples were recovered fuels extracted from the soil near various fuel spills. (Methylene chloride was used to extract the fuel from the soil via a quick swirl extraction.) The other three fuel samples had been subjected to weathering in the laboratory.

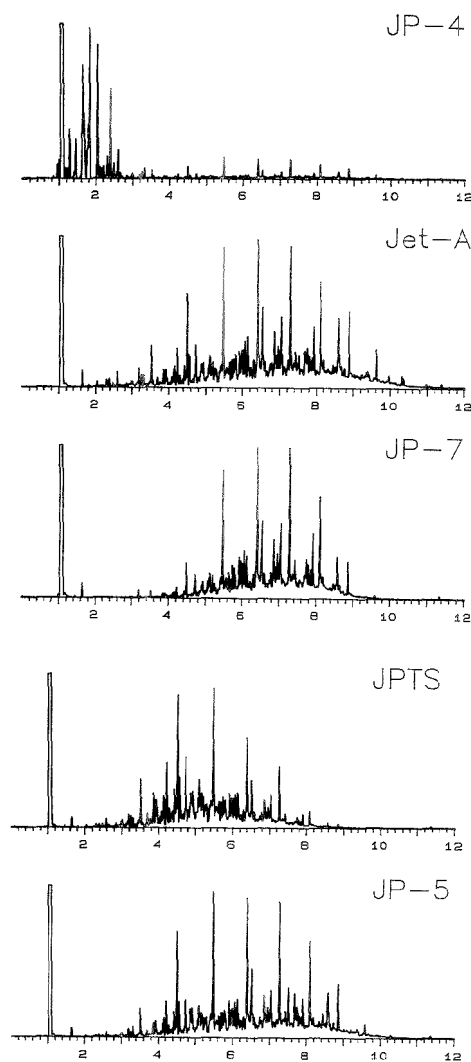


Figure 1. High-speed GC profiles of the five fuel types in this study: JP-4, Jet-A, JP-7, JPTS, and JP-5 fuels.

Prior to GC analysis, each fuel sample was diluted with methylene chloride, and the diluted fuel sample was then injected onto a GC capillary column using a split injection technique. High-speed GC profiles were obtained using a high-efficiency fused silica capillary column (Hewlett Packard, Analytical Products Group, San Fernando, CA) that was 10 m long with an internal diameter of 0.10 mm and coated with 0.34 μm of a bonded and cross-linked 5% phenyl-substituted poly(methylsiloxane) stationary phase. The column was temperature programmed from 60 to 270 $^{\circ}\text{C}$ at 18 deg/min using an HP-5890 gas chromatograph equipped with a flame ionization detector, a split/splitless injection port, and an HP-7673A autosampler. Gas chromatograms representative of the five fuel types in this study are shown in Figure 1.

DATA PREPROCESSING

The GC data were digitized and stored using an HP-3357 laboratory automation system implemented on an HP-1000-F minicomputer. A FORTRAN program was used to translate the integration reports into ASCII files formatted for entry into SETUP,⁷ a computer program for peak matching. SETUP correctly assigned the peaks by first computing the Kovat's retention index⁸ for the compounds eluting off the GC column. Since the *n*-alkane peaks are the most prominent features present in the gas chromatograms of these fuels,⁹ it was a simple matter to compute the Kovat's retention index for each GC peak. The peak-matching program then analyzed the GC data in three distinct steps. First, a template of peaks was developed by examining integration reports and adding features to the template which did not match the retention indices of previously observed features. Second, a preliminary data vector was produced for each gas chromatogram by matching the retention indices of GC peaks with the retention indices of the features in the template. A feature would be assigned a value corresponding to the normalized area of the GC peak in the chromatogram. Unmatched peaks were zeroed, whereas poorly resolved and tailing peaks were excluded from the analysis. Third, the frequency of each feature was computed, i.e., the number of times a particular feature is found to have a nonzero value was calculated, and features below a user-specified number of nonzero occurrences (which was set equal to 10% of the total number of fuel samples in the training set) were deleted from the data set, whereas features that passed the nonzero frequency criterion were retained. The peak-matching software yielded a final cumulative reference file containing 85 identities, though not all peaks were present in all chromatograms. Hence, for pattern recognition analysis, each gas chromatogram was initially represented as a 85-dimensional data vector, $x = (x_1, x_2, x_3, \dots, x_j, \dots, x_{85})$, where x_j is the area of the *j*th peak. The data vectors were normalized to constant sum, i.e., each x_j was divided by the total integrated peak area.

Because outliers have the potential to adversely affect the performance of statistical and pattern recognition methods, outlier analysis was performed on each fuel class in the training set prior to pattern recognition analysis using the generalized distance test¹⁰ implemented via SCOUT.¹¹ Three Jet-A and four JP-7 fuel samples were found to be outliers by both tests at the 0.01 level; therefore, these seven fuel samples were removed from the data base. Hence, the set of data—221 gas chromatograms of 85 peaks each—was transferred via floppy diskette from the USAF's SUN SPARC II workstation to Clarkson University's VAXstation 3100, where it was entered into the disk storage of FIP.¹² The data were standardized and autoscaled so that each variable (peak) had a mean of zero and a standard deviation of 1 within the entire set of 221 gas chromatograms. Thus, autoscaling ensured that each feature had equal weight in the analysis.

PATTERN RECOGNITION ANALYSIS

The pattern recognition analyses were directed toward three specific goals: (1) finding discriminants that can correctly classify

neat jet fuels on the basis of legitimate chemical differences between the different types of fuels, (2) studying the structure of the GC data to seek obscure relationships with mapping and display methods, and (3) developing the ability to predict the class membership of weathered fuels. Both principal component¹³ and statistical discriminant¹⁴ analysis were used to analyze the fuel data.

Principal Component Analysis. Principal component analysis (PCA) is a method for transforming the original measurement variables into new, uncorrelated variables called principal components. Each principal component is a linear combination of the original measurement variables. Using this procedure is analogous to finding a set of orthogonal axes that represent the directions of greatest variance in the data. Often, the two or three largest principal components of the data will capture the bulk of the variance or information; hence, we can use them to generate a plot that represents the structure of the *p*-dimensional measurement space. For data sets with a large number of interrelated variables, PCA is a powerful method for analyzing the structure of the data and reducing the dimensionality of the pattern vectors.

PCA is carried out via a decomposition of the data matrix X ($n \times p$) into a score matrix T ($n \times F$), a loading matrix P ($F \times p$), and a residual matrix E ($n \times p$), where *n* is the number of samples in the data set, *p* is the number of measurement variables, and *F* is the number of principal components necessary to represent a user-specified fraction of the total cumulative variance in the data, which is often 95%. Usually *F* is much smaller than *p* due to redundancies among the measurement variables.

The matrix equation for the decomposition is

$$X = (1 \times m) + TP + E \quad (1)$$

where 1 is a column vector ($n \times 1$) of ones and m is a ($1 \times p$) row vector representing the mean of the observations. The sample coordinates (or scores) in the principal component space are supplied by the score matrix, whereas the loading matrix supplies the necessary information for transforming the original measurement variables into principal components. By plotting the columns of T against each other, a plot representing the distribution of the data points in the *p*-dimensional multivariate space can be obtained. The number of principal components necessary to describe the signal in the data is equal to *F* or the number of columns in T , which in many studies is only two or three. The score and loading matrices describe the signal in the data, and the residual matrix describes the noise. Hence, dimensionality reduction and separation of signal from noise in the data matrix is possible via PCA.

Statistical Discriminant Analysis. Statistical discriminant analysis (SDA) generates classification surfaces or discriminants based upon the statistical properties of the data. Classifiers are developed from prior knowledge of class membership, from a priori assumptions about the distribution of the data, and from the mean vectors and covariance matrices of the classes. In SDA, the classes are assumed to possess a multivariate normal distribution, which is a reasonable assumption since most of the distribution functions encountered in fingerprinting problems possess elliptical probability contours and only differ in the rate at which the probability decreases away from the mean.

(7) Mayfield, H. T.; Bertsch, W. *Comput. Appl. Lab.* 1983, 1, 130–137.

(8) van den Doole, H.; Kratz, P. J. *Chromatogr. Sci.* 1963, 11, 463–471.

(9) Mayfield, H. T.; Henley, M. In *Monitoring Water in the 1990s: Meeting New Challenges*; Hall, J. R.; Glayson, G. D., Eds.; American Society for Testing and Materials: Philadelphia, PA, 1991; pp 578–597.

(10) Schwager, S. J.; Margolin, B. H. *Annu. Stat.* 1982, 10, 943–953.

(11) Stapanian, M. A.; Garner, F. C.; Fitzergerald, K. E.; Flatman, G. T.; Nocerino, J. M. *J. Chemom.* 1993, 7, 165–176.

(12) Lavine, B. K.; Faraque, A.; Mayfield, H. J. *Comput. Inf. Sci.*, submitted.

(13) Jolliffe, I. T. *Principal Component Analysis*; Springer Verlag: New York, 1986.

(14) James, M. *Classification*; John Wiley & Sons: New York, 1985.

In SDA, an observation is assigned to the class with the smallest discriminant score, $d_k(x)$ (eq 2). The first term in the

$$d_k(x) = \min[(x - m_k)^T C_k^{-1} (x - m_k) + \ln |C_k| - 2 \ln \pi_k] \quad (2)$$

equation is the Mahalanobis distance squared between the sample and the class center, the second term is the logarithm of the determinant of the class covariance matrix C_k (which is proportional to the scatter of the sample points about the class mean), and the third term is the class prior probability π_k . (k is the class index.) Equation 2 is the basis of quadratic discriminant analysis (QDA). In most applications of QDA, the class priors are assumed equal, so π_k is often deleted from eq 2, because it possesses the same value for each class. The assumption that each class possesses a similar correlation structure will often hold true as well. When all class covariance matrices are presumed equal, the second term can also be deleted from eq 2, which can then be rewritten as

$$d_k(x) = (x - m_k)^T C_k^{-1} (x - m_k) \quad (3)$$

Equation 3 is the basis of linear discriminant analysis (LDA). C_k^{-1} is computed by first estimating the variance covariance matrix of each class and then averaging the matrices to yield a pooled estimate of C_k .

QDA and LDA are guaranteed to produce an optimal classification surface. Nevertheless, QDA and LDA are seldom applied to problems in chemical pattern recognition because there are usually too few samples to reliably estimate C_k^{-1} .¹⁵ In 1976, Wold¹⁶ addressed the issue of covariance stabilization in discriminant analysis by developing a biased estimator for the covariance matrix. He called the method SIMCA, which can be viewed as a variation of quadratic discriminant analysis, where the inverse of the covariance matrix for each class is approximated by a principal component representation of the covariance matrix involving the so-called secondary eigenvectors.¹⁷ In other words, the inverse of the class k covariance matrix C_k^{-1} can be represented by the spectral decomposition

$$C_k^{-1} = \sum_{j=1}^p [v_{jk} v_{jk}^T / l_{jk}] \quad (4)$$

where v_{jk} is the j th principal component of C_k , l_{jk} is the corresponding eigenvalue, and p is the dimensionality of the multivariate data. When reconstructing C_k^{-1} , it is the smaller eigenvalues, not the larger ones, which are the most important. However, the smaller eigenvalues are difficult to reliably estimate in small sample/high dimensional settings. By taking the average of these smaller eigenvalues, Wold hoped to filter out the noise in them and hence obtain more reliable estimates of them:

(15) Frank, I. E.; Lanteri, S. *Chemolab* 1989, 5, 247-256.

(16) Wold, S. *Pattern, Recognit.* 1976, 8, 127-139.

(17) McLachlan, G. J. *Discriminant Analysis and Statistical Pattern Recognition*; John Wiley & Sons: New York, 1992; pp 129-167.

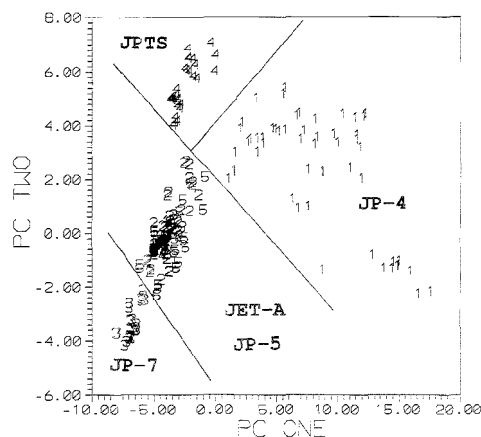


Figure 2. Plot of the two largest principal components of the 85 GC peaks for the 221 neat jet fuels. The map explains 72.3% of the total cumulative variance. 1, JP-4; 2, Jet-A; 3, JP-7; 4, JPTS; anc 5, JP-5.

$$C_k^{-1} = \left[\sum_{j=A+1}^p v_{jk} v_{jk}^T \right] / \left[\sum_{j=A+1}^p l_{jk} \right] \quad (5)$$

where A is the number of principal components necessary to describe class k , which is determined by cross validation.¹⁶ For problems with a low object to descriptor ratio, which generally is the rule in profile analysis, this biased estimate is usually a better approximation of the inverse of the covariance matrix than sample-based estimates, e.g., maximum likelihood.

RESULTS AND DISCUSSION

The first step in this study was to apply PCA to the analysis of the training set data, in order to obtain information about the overall trends present in the data. Figure 2 shows a plot of the scores of the two largest principal components of the 85 GC peaks obtained from the 221 neat jet fuel samples. Each fuel sample or gas chromatogram is represented as a point in the two-dimensional map. The JP-4, JP-7, and JPTS fuel samples are well separated from one another and from the gas chromatograms of Jet-A and JP-5 fuel samples in the map, suggesting that information characteristic of fuel type is present in the high-speed gas chromatograms of the neat jet fuels. Because this projection is made without the use of information about the class assignment of the fuel samples, the resulting separation is, therefore, a strong indication of real differences in the hydrocarbon composition of these fuels, as reflected in their gas chromatographic profiles.

The overlap of Jet-A and JP-5 fuel samples in the principal component map suggests that gas chromatograms of these two fuel materials share a common set of attributes, which is not surprising because of the similarity in their physical and chemical properties, e.g., flash point, freezing point, vapor pressure, and distillation curve.¹⁸ Mayfield and Henley⁹ observed that gas chromatograms of Jet-A and JP-5 fuels were more difficult to classify than gas chromatograms of other types of processed fuels because of the similarity in the overall hydrocarbon composition

(18) *Handbook of Aviation Fuel Properties*; Coordinating Research Council, Inc.: Atlanta, GA, 1983.

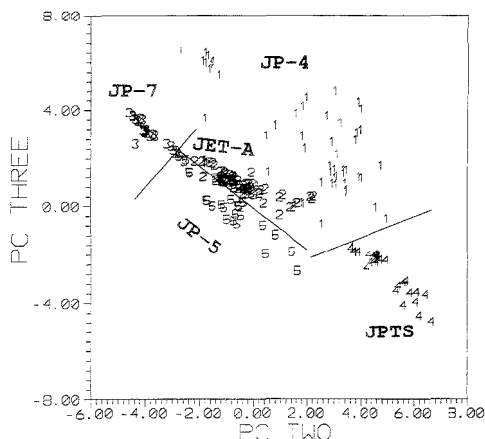


Figure 3. Plot of the second and third largest principal components of the 85 GC peaks for the 221 neat jet fuel samples. The map explains 23.1% of the total cumulative variance. 1, JP-4; 2, Jet-A; 3, JP-7; 4, JPTS; and 5, JP-5.

of these two fuel materials. Nevertheless, Mayfield and Henley also concluded that fingerprint patterns exist within the high-speed gas chromatograms of Jet-A and JP-5 fuels characteristic of fuel type, which is consistent with our score plot of the second and third largest principal components of the 85 GC peaks (see Figure 3), suggesting that differences do, indeed, exist between the hydrocarbon profiles of Jet-A and JP-5 fuels. Since the second and third largest principal components do not represent the directions of maximum variance in the data, we must conclude that most of the information contained within the 85 GC peaks is not about the differences between GC profiles of Jet-A and JP-5 fuels.

To better understand the problems associated with classifying gas chromatograms of Jet-A and JP-5 fuels, we found it necessary to reexamine this particular classification problem using PCA. Figure 4 is a score plot of the two largest principal components of the 85 GC peaks of the 110 Jet-A and JP-5 fuel samples. An examination of the principal component map reveals a very interesting result. Although the Jet-A and JP-5 fuel samples lie in different regions of the principal component map, the data points representing the JP-5 fuels form two distinct subgroups in the map, which could be a serious problem, since an important requirement in any successful pattern recognition study is that each class in the data set be represented by a homogeneous collection of objects. In other words, it will be difficult to adequately represent the gas chromatograms of the JP-5 fuels by a single prototypical class vector, which is necessary in order to successfully implement SDA or variations of it. Therefore, it is important that we identify and delete from the data set the GC peaks responsible for the subclustering of the JP-5 fuel samples in the 85-dimensional pattern space.

Hence, the following procedure was used to identify GC peaks strongly correlated with the subclustering. First, the JP-5 fuel samples were divided into two categories on the basis of the observed subclustering. Next, the variance weights^{19,20} were

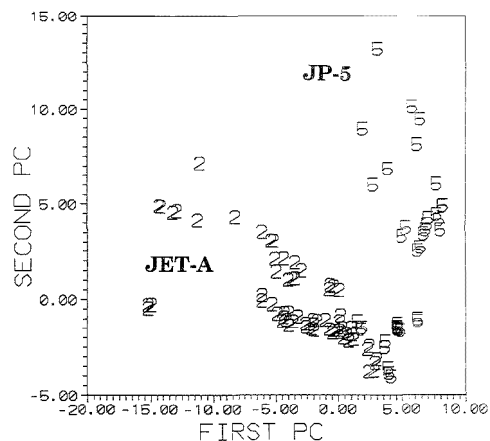


Figure 4. Principal component map of the 121 neat Jet-A and JP-5 fuel samples. (2, Jet-A, and 5, JP-5.) The map was developed from 85 GC peaks and explains 80% of the total cumulative variance. The JP-5 fuels can be divided into two distinct groups: fuel samples which lie close to the Jet-A fuels and fuel samples which are located in a region of the map distant from Jet-A fuels.

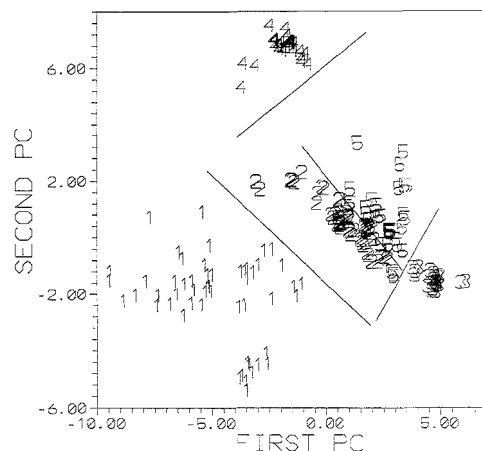


Figure 5. Principal component map of the training set. The map was developed from 27 GC peaks and represents 75% of the total cumulative variance. 1, JP-4; 2, Jet-A; 3, JP-7; 4, JPTS; and 5, JP-5.

computed for the GC peaks so that peaks strongly correlated with this subclustering could be identified. Variance weights were also computed for the following category pairs: JP-4 vs JP-5, Jet-A vs JP-5, JP-7 vs JP-5, and JPTS vs JP-5. A GC peak was retained for further analysis only if its variance weight for the subclustering dichotomy was lower than for any of the other category pairs. Twenty-seven GC peaks were retained for further study. Figure 5 shows a plot of the scores of the two largest principal

(19) Sharaf, M.; Illman, D.; Kowalski, B. R. *Chemometrics* John Wiley & Sons: New York, 1986; p 195.

(20) Harper, A. M.; Duewer, D. L.; Kowalski, B. R.; Fasching, J. L. ARTHUR and Experimental Data Analysis: the Heuristic Use of Polyalgorithms. In *Chemometrics: Theory & Application*; Kowalski, B. R., Ed.; ACS Symposium Series 52; American Chemical Society: Washington, DC, 1977.

Table 3. K-NN Classification Results

class	NIC	1-NN	3-NN	5-NN	7-NN
JP-4	54	54	54	54	54
JET-A	67	67	67	67	67
JP-7	28	28	28	28	28
JPTS	29	29	29	29	29
JP-5 ^a	43	43	41	36	37
total	221	221	219	214	215

^a Misclassified JP-5 fuel samples were categorized as JET-A. This result is not surprising because of the similarities in the hydrocarbon compositions of these two fuel materials (see ref 9).

components of these 27 GC peaks obtained from the 221 neat jet fuel samples. Since PCA does not directly utilize class information about the fuel samples in developing a map of the data, the eigenvector projection should be viewed in the context of this study as a conservative estimate of the differences in hydrocarbon composition of the fuels as reflected by their GC profiles. In other words, the fact that fuel samples in the principal component map cluster according to fuel type suggests that information is contained within the gas chromatograms of the fuels characteristic of fuel type.

Table 3 shows the results of the K-nearest neighbor method, i.e., K-NN,²¹ which was also used to analyze the data. (The K-NN method categorizes the data vectors in the training set according to their proximity to other objects of preassigned categories.) It is evident on the basis of K-NN and the PCA map that, in the 27-dimensional measurement space, the five fuel classes are well separated, and each fuel class is represented by a homogeneous collection of objects. (Evidence to justify the claim of class homogeneity, at least to a first approximation, is derived from the principal component map shown in Figure 5, which does not indicate the existence of subclustering within any fuel class.)

A five-way classification study involving the JP-4, Jet-A, JP-7, JPTS, and JP-5 fuel samples in the truncated pattern space was also undertaken using QDA, LDA, SIMCA, back propagation neural networks (BPN), discriminant analysis with shrunken covariance (DASCO), and regularized discriminant analysis (RDA). DASCO²² and RDA,²³ like SIMCA, also utilize nonsample-based methods to stabilize the inverse of the class covariance matrix, which is then substituted into the quadratic discriminant analysis rule. DASCO, like SIMCA, partitions the pattern space into a primary and secondary subspace. The contribution of the primary subspace to the inverse of the covariance matrix is estimated directly from the primary eigenvalues (see eq 4), whereas the eigenvalues associated with the secondary or complementary subspace are averaged like in SIMCA (see eq 5). (In SIMCA, the primary eigenvalues are ignored.) RDA employs a more complex scheme to obtain a biased estimate of the class covariance matrix. RDA shrinks the class covariance matrix toward the pooled covariance matrix, while simultaneously shrinking the eigenvalues of the class covariance matrix toward equality (by shrinking the resulting estimates toward multiples of the identity matrix). Optimum values of these shrinkage parameters are computed for a given data set by cross validating on the total number of misclassifications. (In other words, a vector of

Table 4. Training Set Results (%)

method	apparent ^a	bootstrap ^b	cross validation ^c
LDA	96.8	96.0	93.7
QDA	100	97.8	97.3
SIMCA ^d	99.5	98.3	96.4
DASCO ^e	100	99.2	97.7
RDA ^f	100	99.2	98.2
BPN	100	99.2	99.5

^a The ability of the discriminant to correctly classify those samples with which it was developed. ^b 60% of the samples were chosen at random from the training set, and a classification rule is developed from these fuel samples. The classification rule is validated using all of the fuel samples in the original training set, and the fraction of samples correctly classified in the validation set is computed. This procedure is repeated 10 times, and the recognition rate for the classifier is equal to the average classification success rate obtained for the validation set. ^c The classification rule is developed on one part of the training set, with the other part functioning as a mock test set. This process is repeated until all training set samples have been used as test set samples. The recognition rate is equal to the fraction of mock test set samples correctly classified. ^d An eight principal component model was developed for each fuel class. The number of principal components for each class model determined by cross validating on the total number of misclassifications. ^e The primary subspace was defined by the eight largest principal components. ^f γ was set equal to 0.0, and λ was set equal to 0.2.

Table 5. Prediction Set Results

method	error rate ^a	method	error rate ^a
LDA	14 (all JP-4)	DASCO ^b	0
QDA	4 (all JP-5)	RDA ^c	0
SIMCA ^b	0	BPN ^c	14

^a Number of samples misclassified. ^b Posterior probability for the samples correctly classified was > 75%. ^c Best results.

misclassifications as a function of the shrinkage parameter is generated, with the value of the evaluated parameter corresponding to the lowest error rate selected.)

Results from the five-way classification study involving the 221 neat jet fuel samples are shown in Table 4. The recognition rates for the discriminants developed from the 27 GC peaks using LDA, QDA, SIMCA, DASCO, RDA, or BPN are very high. Evidently, the gas chromatograms of the neat jet fuels contain information characteristic of fuel type.

To test the predictive ability of these GC peaks and the discriminants associated with them, a prediction set of 21 gas chromatograms was employed (see Table 2). The gas chromatograms in the prediction set were run a few months before the neat jet fuel gas chromatograms were run and thus constituted a true prediction set. Table 5 summarizes the results of this experiment. RDA, DASCO, and SIMCA correctly classified all of the weathered fuel samples in the prediction set, whereas LDA and BPN misclassified 14 of the 21 weathered fuel samples. QDA misclassified four of the 21 weathered fuels. The disparity between the recognition and classification success rates for the discriminants developed using LDA or BPN would suggest that both cross validated and bootstrapped estimates of the error rate can be overly optimistic figures of merit, despite claims made to the contrary by other workers.²⁴ (The apparent recognition rate is considered to be too optimistic by all workers in the field, because the samples used in the design of the classifier are the

(21) Kowalski, B. R.; Bender, C. F. *J. Am. Chem. Soc.* **1972**, *94*, 5632-5640.

(22) Frank, I. E. *Chemolab* **1988**, *4*, 215-222.

(23) Frank, I. E.; Friedman, J. H. *J. Chemom.* **1989**, *3*, 463-475.

(24) Efron, B.; Tibshirani, R. J. *An Introduction to the Bootstrap*; Chapman & Hall: New York, 1993.

same ones used for testing, so differences between this figure of merit and the classification success rate obtained for samples in the prediction set are not unexpected.) Evidently, a reliable estimate of the error rate for a classifier requires the use of an independent sample test set, i.e., samples that have not been used in the design of the classifier.

The fact that QDA out-performed LDA (see Table 5) comes as no surprise, because the assumption of equality between class covariance matrices is not justified in this problem, as evidenced by the unequal dispersion of the points representing the different fuels in the plot of the two largest principal components obtained from the 27 GC peaks (see Figure 4). With regard to BPN, we attribute its poor performance to overfitting of the training set data, which is a serious problem with certain types of artificial neural networks. The fact that SIMCA, DASCOS, and RDA out-performed QDA is also not surprising, since these methods were developed specifically for small sample/high dimensional settings. However, the fact that SIMCA, DASCOS, and RDA performed equally well in this study raises questions about the designation of either RDA or DASCOS as a so-called best method for pattern recognition problems involving data sets with a low object to descriptor ratio.²³ In all likelihood, these three methods perform equally well with real chemical data, so observed differences in performance between SIMCA, DASCOS, and RDA for a given problem are probably application specific.

Finally, the high classification success rate obtained for the weathered fuels suggests that information about fuel type is present in the gas chromatograms of weathered fuels. This is a significant result, since the changes in composition that occur after

a processed fuel is released into the environment constitute a major problem in fuel spill identification. These changes arise from evaporation of lower molecular weight alkanes, microbial degradation, and the loss of water-soluble compounds due to dissolution. However, the weathered fuel samples used in this study were recovered from a subsurface environment. Loss of lower alkanes due to evaporation is severely retarded in a subsurface environment,²⁵ and only a comparatively small number of jet fuel components are soluble in water.²⁶ (If the selective evaporation of lower alkanes had not been retarded in the subsurface environment, the weathered JP-4 fuel samples, which are high in volatiles, could not have been identified using discriminants developed from the gas chromatograms of the neat jet fuels.) Hence, the predominant weathering factor in subsurface fuel spills is probably biodegradation due to the action of microbial organisms, which does not appear to have a pronounced effect on the overall GC profile of the fuels. Therefore, the weathering process for aviation turbine fuels in subsurface environments is greatly retarded in comparison to surface spills, thereby preserving the fuel's identity for a longer period of time.

ACKNOWLEDGMENT

This study was supported by Contract F08635-90-C-0105 between Clarkson University and the USAF. The authors thank Ildiko Frank (Jerll Inc., Stanford, CA) and Charles Mann (Florida State University) for many helpful discussions.

Received for review May 16, 1995. Accepted August 18, 1995.*

AC950475M

(25) Spain, J. C.; Sommerville, C. C.; Butler, L. C.; Lee, T. J.; Bourquin, A. W. *Degradation of Jet Fuel Hydrocarbons in Aquatic Communities*; USAF Report ESL-TR-83-26; AFESC: Tyndall AFB, FL, 1983.

(26) Coleman, W. E.; Munch, J. W.; Streicher, R. P.; Ringhand, H. P.; Kopfler, W. F. *Arch. Environ. Contam. Toxicol.* **1984**, *13*, 171-180.

* Abstract published in *Advance ACS Abstracts*, September 15, 1995.

Measurement of Gases by a Suppressed Conductometric Capillary Electrophoresis Separation System

Purnendu K. Dasgupta* and Satyajit Kar

Department of Chemistry and Biochemistry, Texas Tech University, Lubbock, Texas 79409-1061

This paper describes the direct measurement of soluble ionogenic atmospheric gases by a suppressed conductometric capillary electrophoresis separation system (SuCCESS). A small circular wire loop is incorporated at the sampling end of a fused silica capillary located immediately at the tip in the same plane as the capillary. When the loop is dipped into a solution and withdrawn, a liquid film is formed on it. The film is in fluid communication with the capillary and acts as a microreservoir. When the film end is lifted relative to the destination side, all or part of the film contents can be injected into the capillary. To perform gas sampling, a series of automated operations are conducted with a commercial CE instrument modified in a minor fashion: the film-bearing loop is lowered into a sample chamber, and air is sampled for a preset period of time at a preselected flow rate (typically 1 min at 100 cm³/min). The capillary is then lifted to introduce an aliquot from the film for analysis and then dipped into the running electrolyte source vial, and electrophoresis is commenced. Under the above sampling conditions, 1 ppb SO₂ can be detected. The system should be applicable for use with other detection modes and nonaqueous electrolytes.

Capillary electrophoresis (CE) and the associated capillary scale technologies are rapidly and profoundly changing the way analytical separations and measurements are carried out.^{1–3} While the single most important area for these developments has undoubtedly been the separation and quantitation of large biomolecules,⁴ the separation/detection of small ions has also received attention.^{5–8} Separation of small ions has thus far been dominated by ion chromatography (IC).^{9,10} Recently, the most successful IC detection technique has also been shown to be applicable to CE, leading to suppressed conductometric capillary

electrophoresis separation systems (SuCCESS)^{11–13} that can produce low microgram per liter limits of detection (LODs) for a variety of small ions in a robust manner without special efforts toward preconcentration.

One of the earliest beneficiaries of IC was the analysis of atmospheric samples, an area that has been of continuing interest to this laboratory. CE-based analyses of atmospheric filter samples have now been reported,^{14,15} but in such cases, the analytical technology and the sample collection strategies are not necessarily optimally matched: extraction volumes of several milliliters are obligatorily produced with an atmospheric filter sample, while microliter scale samples are adequate for providing the nanoliter scale injections made in CE.

Recognizing that relative to particles, atmospheric gases can be sampled more directly and in a microscale, we previously described¹⁶ a technique in which a microscale membrane-based diffusion scrubber¹⁷ constitutes an integral part of the separation capillary. A small segment of a porous hydrophobic membrane capillary connected the fused silica separation capillary (FSC) to a small length of an "entrance" FSC. A jacket was built around the membrane and air sampled around it, whence analyte gases of interest diffused through the pores and were trapped by the internal electrolyte. Electrophoresis was then commenced. Indirect or direct optical detection was used. Although these detection methods are not as sensitive as suppressed conductometry, respectable LODs could be obtained. The major shortcomings of the technique, however, centered around the membrane itself: the fragility of the membrane, the change in the sample transfer function over prolonged use due to soiling, and the facile evaporation of the internal liquid through the membrane pores (which necessitated a "dry flush" ever during the analysis).

Recently, we have introduced a liquid droplet or a film as a gas sampling interface.^{18,19} Such an interface is not only indefinitely renewable, but it is best deployed in a microscale: due to the evaporative flux from the droplet/film, the approach of particles is greatly inhibited (cf. *diffusiophoresis* due to Stefan flow).²⁰ In the present paper, we show that a film is readily

(1) Wu, N.; Peck, T. L.; Webb, A. G.; Magin, R. L.; Sweedler, J. V. *Anal. Chem.* 1994, 66, 3849–3857.

(2) Jacobson, S. C.; Hergenroder, R.; Moore, A. W., Jr.; Ramsey, J. M. *Anal. Chem.* 1994, 66, 4127–4132.

(3) Schmalzing, D.; Nashabeh, W.; Yao, X.-W.; Mhatre, R.; Regnier, F. E.; Afeyan, N. B.; Fuchs, M. *Anal. Chem.* 1995, 67, 606–612.

(4) Monnig, C. A.; Kennedy, R. T. *Anal. Chem.* 1994, 66, 280R–314R.

(5) Jandik, P.; Bonn, G. K. *Capillary Electrophoresis of Small Molecules and Ions*; VCH: New York, 1993.

(6) Benz, N. J.; Fritz, J. S. *J. Chromatogr.* 1994, 671, 437–443.

(7) Salimi-Moosavi, H.; Cassidy, R. M. *Anal. Chem.* 1995, 67, 1067–1073.

(8) Lucy, C. A.; McDonald, T. L. *Anal. Chem.* 1995, 67, 1074–1078.

(9) Dasgupta, P. K. *Anal. Chem.* 1992, 64, 775A–783A.

(10) Noble, D. *Anal. Chem.* 1995, 67, 205A–208A.

(11) Dasgupta, P. K.; Bao, L. *Anal. Chem.* 1993, 65, 1003–1011.

(12) Avdalovic, N.; Pohl, C. A.; Rocklin, R. D.; Stillian, J. R. *Anal. Chem.* 1993, 65, 1470–1475.

(13) Dasgupta, P. K.; Bao, L. U.S. Patent 5,358,612, Oct 25, 1994.

(14) Dabek-Zlotorzynska, E.; Dlouhy, J. F. *J. Chromatogr.* 1994, 671, 389–395.

(15) Dabek-Zlotorzynska, E.; Dlouhy, J. F. *J. Chromatogr.* 1994, 685, 145–155.

(16) Bao, L.; Dasgupta, P. K. *Anal. Chem.* 1992, 64, 991–996.

(17) Dasgupta, P. K. *ACS Adv. Chem. Ser.* 1993, 232, 41–90.

(18) Liu, S.; Dasgupta, P. K. *Anal. Chem.* 1995, 67, 2110–2118.

(19) Cardoso, A. A.; Dasgupta, P. K. *Anal. Chem.* 1995, 67, 2562–2566.

(20) Hinds, W. C. *Aerosol Technology*; Wiley: New York, 1982; p 161.

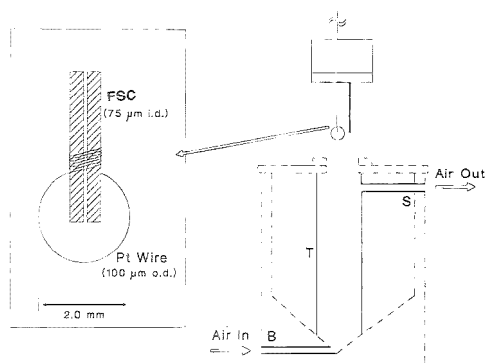


Figure 1. Schematic diagram of the gas sampling chamber (GSC) (modified "source vial" of Dionex CES-1): (B) gas sample inlet, (S) gas sample outlet, (T) polyethylene tube for reducing the chamber volume. Inset (not to scale) shows the expanded view of the Pt wire loop formed at the tip of the sampling end of the FSC.

coupled to a FSC as a sampling interface for gases. Using sulfur dioxide, an important atmospheric contaminant, as a test gas, we show that a film-coupled SuCESS can easily detect single digit part per billion (ppb) levels of this analyte in a 100 cm³ air sample.

EXPERIMENTAL SECTION

Equipment. The basic SuCESS is the same as that described previously.¹¹ A 45 cm long, 75 μm bore FSC equipped with a Nafion membrane suppressor, regenerated by 5 mM H₂SO₄, and a bifilar wire conductance cell¹² were used in conjunction with a Dionex CDM-I conductivity detector.

An wire loop of 2 mm diameter was formed at the tip of the sampling end of the FSC by using 100 μm o.d. Pt wire, as depicted in Figure 1 (inset). The sample/capillary transport capabilities and the high-voltage (HV) power supply of a Dionex Model CES-1 instrument was used for complete automation of the SuCESS-based gas sampling and analysis. This instrument maintains the sampling end of the capillary and the HV electrode affixed to a common head that can make limited but programmable movements in three dimensions. A typical "normal" sequence is to move the sampling end of the running electrolyte-filled FSC into a sample vial located in a programmable rotatable turret. The sampling head makes a gasket-based seal with the vial. The sample can be introduced either by (a) electromigration, (b) applying a pneumatic pressure pulse through a port in the head, or (c) grasping the vial, lifting the head along with it, and introducing the sample by gravity. The head is then returned to a "source vial" chamber where the head again makes a seal and dips into the running electrolyte; electrophoresis is then begun. The source vial contains connections that allow refilling with fresh running electrolyte or other wash liquids and pneumatic pressurization for flushing the FSC. In this work, the source vial was used as the gas sampling chamber. Minor changes were made to the source vial chamber to accommodate this, as shown in Figure 1. The bottom port (B) was enlarged and connected to a poly(tetrafluoroethylene) (PTFE) tube through which the sample

gas entered the poly(vinylidene fluoride) source vial. A polyethylene tube (T), 9.5 mm i.d., was installed to reduce the effective volume of the sampling chamber (the source vial itself is 41.5 mm i.d.). Approximately 7 mm from the top, a flexible poly(vinyl chloride) tube connected tube T to a side port (S) drilled on the side of the source vial as shown. This was connected to a sampling pump or other apparatus (vide infra).

For our experiments, the rotatable sample turret contained alternating vials of the liquid used for the sampling film (0.15% H₂O₂, 44 mM) and the running electrolyte used for the CE run (2 mM Na₂B₄O₇). The standard operating procedure consisted of dipping the sampling head into a Na₂B₄O₇ vial, pressurizing to flush the capillary with the running electrolyte, lifting the sampling head and dipping it into the film-making liquid, withdrawing it, and introducing it into the gas sampling chamber (formerly the source vial). Note that there is no significant hydrostatic difference between the film contents and the detector end of the capillary during sampling. Air was sampled immediately after the head sealed itself on the sampling chamber. Following the sampling period, the head was lifted to a height of 10 cm and maintained in that position for a fixed period of time to introduce an aliquot of the film contents into the capillary. The head was then returned to a fresh Na₂B₄O₇ vial and HV (+15 kV) applied to begin the electrophoretic run.

The calibrant gas generation arrangement is shown in Figure 2. House air was metered through a needle valve and flow meter (typically 70 cm³/min) through sequential columns (A–C) of activated charcoal, silica gel, and soda-lime and entered a thermal equilibration coil (EC) in a stirred (S) water bath (WB) maintained at 30 °C by a 100 W heater (H) and a mercury contact thermoregulator (TR) (Thomas Scientific) under control of relay (R). The thermally equilibrated air was admitted into the glass permeation chamber (U) containing a permeation wafer device (PW) emitting SO₂ at a gravimetrically calibrated rate of 0.27 ng/min. The SO₂-bearing air was diluted with dilution air (D) (typically 50–1500 cm³/min) metered through a needle valve and flow meter. It was split in two streams: one proceeded through a needle valve (N1) and the other through a water-filled bubbler (WFB) and a glass wool trap (G) (to remove any entrained water droplets before being recombined again as the dilution stream). By adjusting N1, the degree of humidification of the dilution air stream could be controlled. Part of the diluted SO₂ stream was vented to waste (W) controlled by another needle valve (N2). The rest proceeded through the gas sampling chamber (GSC). In some experiments, N2 was fully open, and the desired sampling flow rate was attained by a sampling pump (SP), equipped with its own flow control valve. In other experiments, a primary standard digital bubble meter (PS) (Gilibrator, Gilian Instrument Corp., West Caldwell, NJ) was placed at the exit of the GSC, and the sampling flow was adjusted by controlling the venting rate with N2. In some other experiments, a capacitance-type relative humidity probe (RH) was placed after the GSC to measure the RH of the sample air. All air flow rates cited in this paper are true volume flow rates at the ambient conditions of our experiments, 680 mmHg and 22 °C; these need to be multiplied by a factor of 0.828 for conversion into values at standard temperature and pressure.

Unless otherwise stated, gas sampling was conducted at 100 cm³/min for 1 min, and the hydrostatic sample introduction period was 20 s.

(21) Kar, S.; Dasgupta, P. K.; Liu, H.; Hwang, H. *Anal. Chem.* **1994**, *66*, 2537–2543.

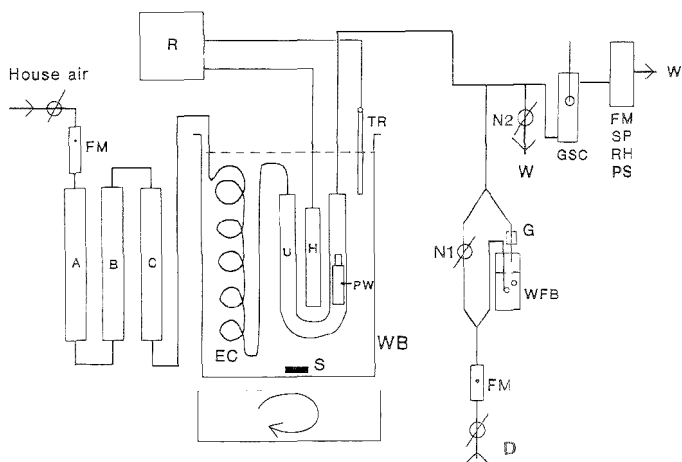


Figure 2. Schematic of SO₂ gas generation arrangement: (A–C) activated charcoal, silica gel, and soda-lime columns, respectively, (EC) thermal equilibration coil, (S) stir bar, (WB) water bath, (U) glass permeation wafer, (PW) SO₂ permeation wafer, (TR) thermoregulator, (R) relay controller, (D) dilution air, (N1 and N2) needle valves, (WFB) water-filled bubbler, (G) glass wool trap, (W) waste. (GSC) gas sampling chamber, (FM) flow meter, (SP) sampling pump, (RH) relative humidity probe, and (PS) primary standard bubble meter.

RESULTS AND DISCUSSION

Test Gas and Choice of Film-Forming Solution. We chose SO₂ as the test gas not only because of its importance as an atmospheric pollutant but also because the performance of the system with SO₂ in terms of LODs, etc., is likely to represent the lower limit. Positive polarity is used in SuCESS, and ions electromigrate opposite to the electroosmotic flow. Weaker acid gases like HCOOH have lower mobility anions that elute fast, resulting in more easily detectable peaks relative to sulfate resulting from SO₂. Other common acid gases like HONO or HCl have larger diffusion coefficient than SO₂ and should thus result in more efficient collection by the film, assuming that the film composition is chosen to be an effective sink for the gas.

Experiments with wet effluent diffusion denuders (WEDDs) have shown that H₂O₂ is an efficient absorbing liquid for capturing SO₂, wherein the collected gas is oxidized to sulfate.²² Initial experiments indicated, however, that 1 mM or lower H₂O₂ concentrations used with WEDDs are quite insufficient in the present case; the observed signal for 10–100 ppb SO₂ increases with increasing H₂O₂ concentrations in the range 1–35 mM. In the present case, the solution contained in the film is essentially stagnant. Only the reagent present on the surface is effective for capturing the analyte. Unlike the WEDD, where the absorber flows down a surface and convective/frictional/turbulent forces can bring new reagent to the surface, here the only motive force for replenishment of the surface reagent is diffusion, a slow process in the liquid phase. Consequently, the absorber reagent concentration used should be higher. However, reagent blank increases with increasing concentration as well; this is detrimental to any type of trace analysis. We have experimented with two different H₂O₂ stock reagents from two different manufacturers: one was 3% and the other 30% in concentration. The presence of sulfate as an impurity is particularly noticeable in the 3% H₂O₂ stock solutions that we have experimented with: after appropriate

dilution, impurity levels are significantly lower in 30% H₂O₂ solutions.

The minimum concentration of H₂O₂ necessary to function as a fully effective sink also depends on the concentration of SO₂ to be sampled and the sampling duration. Based on our experience related to ambient levels of SO₂, we decided on a maximum anticipated SO₂ concentration of 50 ppb and a sampling duration of 60 s. A concentration of 45 mM (~0.15%) H₂O₂ was found to be adequate for dealing with these maximum anticipated levels. If higher amounts must be determined, the concentration of H₂O₂ will need to be increased further. If LODs must also be maintained at previous levels, the H₂O₂ used may need to be cleaned to remove residual sulfate (vide infra).

Water by itself may serve as a suitable collection medium for some gases, but it is not ideal for collecting SO₂. Aside from lower sensitivity relative to the use of H₂O₂, in the absence of reactive uptake, the film becomes quickly surface saturated—strong nonlinearity is observed as a function of either sampling time or sample concentration. An alkaline medium, such as the borate solution used as the electrolyte, can also serve as an effective sink for an acidic analyte gas such as SO₂. However, in this case, it is analyzed as sulfite and detected as a monoprotic acid after suppression with consequent loss of sensitivity. Further, the sample can be partially oxidized to sulfate during electrophoresis, resulting in a broad peak that appears at a retention time intermediate for that of sulfite and sulfate, leading to difficulties in quantitation. An alkaline absorbent also absorbs CO₂ efficiently, and this results in a large carbonate peak. One other advantage with H₂O₂ as the collecting medium, relative to the use of the running electrolyte for the purpose, is electrostacking. This can effectively occur with a low-ionic-strength, low-conductance medium but not with an equal or higher conductance medium²³ (if an electrolyte is used for collection, some concentration is bound to occur during sampling due to evaporative losses of the solvent).

(22) Simon, P. K.; Dasgupta, P. K. *Anal. Chem.* **1993**, *65*, 1134–1139.

(23) Chien, R.-L.; Bargi, D. S. *Anal. Chem.* **1992**, *64*, 489A–496A.

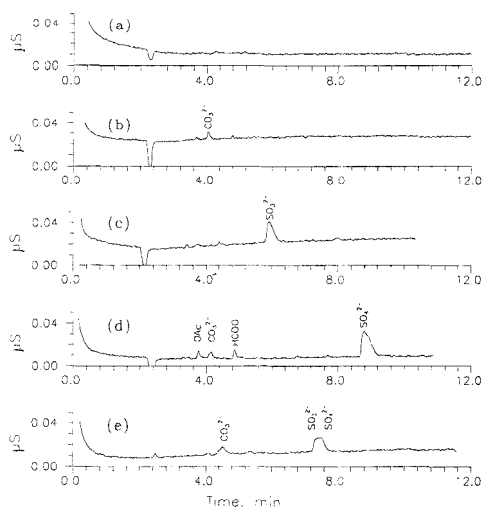


Figure 3. Electropherograms obtained by introducing sample from the film: (a) water blank, (b) H_2O_2 blank, (c–e) 20 ppbv SO_2 sampled with water, 45 mM H_2O_2 , and 2 mM $\text{Na}_2\text{B}_4\text{O}_7$ as absorber solution, respectively.



Figure 4. Photomicrograph of the liquid film formed on the loop. A thin film was made with an aqueous solution of 2.6 mM Malachite Green for easier visualization. The scale is indicated by the diameter of the wire, 100 μm .

The above issues are illustrated in Figure 3, which shows electropherograms of (a) pure water introduced from the film, (b) 45 mM H_2O_2 introduced from the film, without sampling SO_2 , (c) 20 ppb SO_2 sampled with the H_2O as absorber, (d) 20 ppb SO_2 sampled with the H_2O_2 absorber, and (e) 20 ppb SO_2 sampled with 2 mM $\text{Na}_2\text{B}_4\text{O}_7$ as absorber.

Loop Volume and Injection Techniques. Figure 4 shows a photomicrograph of the liquid-containing loop. The held-up liquid has the shape of a biconvex lens, bulging in the middle to just beyond the dimensions of the capillary. Based on microscopic

observations, we estimate that the radius of curvature is ~ 4 mm. The volume of a spherical cap, V_{cap} , of radius of curvature r and height h is given by

$$V_{\text{cap}} = \pi h^2(3r - h)/3 \quad (1)$$

while the volume occupied by the capillary, $V_{\text{capillary}}$, itself is

$$V_{\text{capillary}} = \pi r_c^2 L \quad (2)$$

where the outer radius of the capillary, r_c , is 0.18 mm and its length within the film, L , is 1.1 mm. The overall liquid volume in the film, V_{film} , is then estimated to be

$$V_{\text{film}} = 2V_{\text{cap}} - V_{\text{capillary}} \quad (3)$$

We measured the volume of the loop, by measuring the mass of water lost from a small tared water-filled vial upon the insertion and withdrawal of an initially empty wire loop, to be 880 ± 70 nL ($n = 12$). This is in excellent agreement with the value of calculated from eqn 3, where h is 0.2 mm.

When the loop is lifted with respect to the destination vial, hydrostatic introduction of the sample occurs. Several differences with respect to conventional hydrostatic injection need to be noted. Given the same hydrostatic head, the rate of sample introduction is different in the present case due to surface tension. The rate of sample introduction was evaluated by measuring the peak area resulting from introducing a 0.1% *N,N*-dimethylformamide solution for different periods of time and optical detection of the resulting signal. For a sample introduction period of up to 90 s, the signal was linearly related to the introduction time (uncertainty of linear slope, <3%; intercept indistinguishable from zero at the 95% confidence level; linear $r = 0.9933$; a total of 17 measurements at five separate introduction periods). At the end of 90 s, <25% of the original film volume has been introduced. The rate of liquid introduction does become slower at longer introduction times, and finally, the film breaks. As the liquid at the tip of the capillary is depleted, sample introduction stops altogether (unless an excessive hydrostatic head is applied, air actually never enters the hydrophilic capillary). A small amount of the original film contents are left on the wire loop and are never introduced. By constructing the loop differently, e.g., by placing the capillary on the periphery rather than at the center of the loop, it would be possible to inject virtually all of the loop contents into the capillary, especially for small loops. Nevertheless, without extraordinary measures toward electrostacking,²⁴ this is likely to be too large a sample volume to be used in its entirety. Since the total amount of sample introduced by conventional gravity injection is readily calculated,²⁵ the amount introduced from a film can be estimated by comparison of peak areas. The volume of the sample injected from the film during a 20 s period with a 10 cm hydrostatic head can be ascertained to be 37 ± 3 nL, $\sim 90\%$ of the value when the sample is introduced from a vial. The reproducibility of sample injection from the film by such hydrostatic means was examined by making the film from a standard sample solution containing ClO_3^- and SO_4^{2-} and performing a 40 s, 10 cm introduction. The

(24) Chien, R.-L.; Burgi, D. S. *Anal. Chem.* **1993**, *65*, 3726–3729.

(25) Grossman, P. D.; Colburn, J. C. *Capillary Electrophoresis: Theory and Practice*; Academic Press: San Diego, CA, 1992.

relative standard deviations (RSDs) for the two analytes were found to be 1.8–2.2%, not any worse than the RSD of 1.8–3.9% observed in this system with conventional hydrostatic injection of liquid samples. An aliquot from the film can also be introduced by bringing the head down on an empty vial and using a pneumatic pulse. The RSD for this approach, using a 2 s, 2.5 psi pressure pulse (this introduces an amount comparable to that from a 20 s 10 cm hydrostatic introduction), was 0.4–4.8%, also essentially the same as that observed for pressure injections made from vials.

Homogeneity of the Film at the Time of Sample Injection.

For NH_3 as an analyte gas diffusing into an acidic drop using a capillary format sequential injection analysis system, we have previously established the nature of the analyte distribution for a pendant drop at the tip of a capillary.¹⁸ The analyte concentration is much higher at the surface and is very low at the tip of the capillary—the first aliquot withdrawn into the capillary in that case contains almost no analyte. The situation is far more favorable in the present case. The film is much thinner than the drop, and mixing induced by surface circulation (brought about by the frictional drag of the moving gas)¹⁸ should be much more efficient. Even in the absence of such mixing, we can calculate the characteristic mixing time within the film. This can be approximated to be t^2/D , where t is half the maximum thickness of the film and D is the diffusion coefficient of the analyte (because it is not expected that a large fraction of the gas is removed, we can assume that the surface concentration is uniform; there is no significant dependence from the bottom to the top of the film). If we assume the average film thickness to be $\sim 250 \mu\text{m}$, D for SO_2 can be readily calculated from its equivalent conductance to be $2.45 \times 10^{-3} \text{ cm}^2/\text{s}$, and the radial mixing time is therefore only $\sim 6.3 \text{ s}$. The postsampling transport of the capillary to the sample introduction position requires 12–13 s, thus the film should be well mixed by that time. Comparative experimental data were obtained in which an additional waiting period of 30 s was added after sampling and before the capillary was raised to the sampling position. Statistically, there was no difference, either in the absolute value of the signals or in the RSD.

Effect of Sampling Period. The effect of the sampling period was determined for dry SO_2 gas at two different concentrations, 18 and 34 ppbv at six different nominal sampling periods ranging from 13 to 100 s at a constant sampling rate of $100 \text{ cm}^3/\text{min}$. The responses can be described by the linear equations

$$\text{peak ht} = 0.294 \pm 0.020(\text{sampling time}) + 4.25 \pm 1.36, \\ r = 0.9928 \quad (4)$$

and

$$\text{peak ht} = 0.528 \pm 0.008(\text{sampling time}) + 9.39 \pm 0.50, \\ r = 0.9995 \quad (5)$$

These data show that the ratio of the slopes is in the ratio of the sampled concentrations within experimental uncertainty. The finite positive intercepts are real and result from the fact that the film spends some time in the sampling chamber before and after the nominal sampling period. Since no attempts were made in these experiments to flush out the chamber between experiments, this essentially extends the sampling period beyond the nominal value, not accounted for in eqs 4 and 5. By dividing the intercept by the slope, this period can be calculated; within experimental

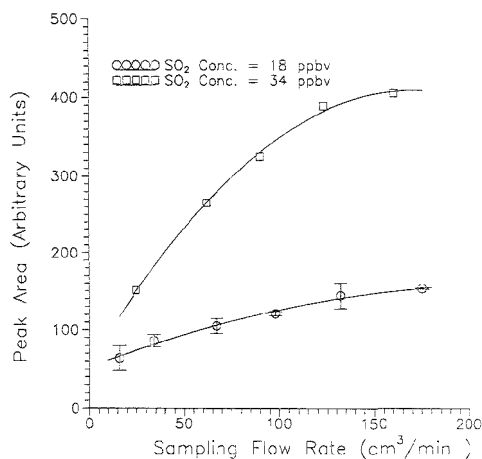


Figure 5. Influence of the sampling flow rate on the system response using a constant sampling time of 40 s at SO_2 concentrations of 13 and 34 ppbv. Error bars for the lower concentration data represent the standard deviations ($n = 3$).

uncertainty, these are identical for eqs 4 and 5, $16 \pm 2 \text{ s}$. If this time is included in the sampling period, eqs 4 and 5 can be expressed in terms of a zero intercept.

Another factor plays a role in these experiments that has not been considered above. Evaporation of the film takes place during sampling (especially with a dry, $\sim 10\% \text{ RH}$, sample), while the volume injected remains the same. However, since it is reasonable to expect that the evaporative loss is linearly dependent on the time, this factor gets incorporated in the linear relationship observed. Evaporation loss can be compensated for by using an internal standard, as described in a subsequent section; this is not essential to understand the dependence of the signal on the sampling period. Evaporative loss, however, sets an upper limit on the permissible sampling period. Dry sample gas naturally sets the most stringent limit. For the present loop/film, this is 120 s at a sampling rate of $100 \text{ cm}^3/\text{min}$.

Effect of Sampling Flow Rate and Collection Efficiency.

Figure 5 shows the dependence of the signal on the sampling flow rate in the range of 16–175 cm^3/min for a fixed sampling time of 40 s at SO_2 concentrations of 18 and 34 ppbv. The pattern, an initially steep dependence on the flow rate with a continued decrease in the flow rate dependence with increasing flow rate, culminating eventually to a situation where there is essentially no flow rate dependence, is quite typical of diffusion-based collection in the laminar flow regime.¹⁷ One particularly advantageous aspect of this dependence on sampling rate is that one can operate in the higher flow rate regime, where the effect of the flow rate is minimal, and expensive measures for flow control are not needed.

The fraction of the sample gas that is actually collected by the film decreases with increasing sample rate. Based on the known mass of SO_2 introduced into the sampling chamber and comparing the signal obtained with that resulting from an aqueous sulfate standard introduced from the loop, we find that under a typical experimental condition (45 mM H_2O_2 , $100 \text{ cm}^3/\text{min}$ sample for 60 s, 20 ppb SO_2), $\sim 10\%$ of the analyte gas is collected by the film. Since this value is far from quantitative, the parameters that

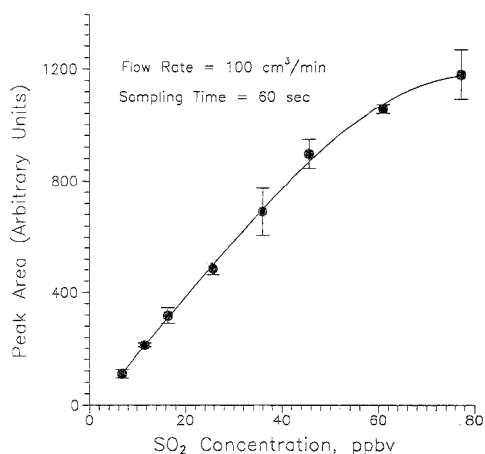


Figure 6. Calibration curve for SO₂ using 45 mM H₂O₂ as absorber solution.

affect the collection efficiency, most notably the temperature (which affects the diffusion coefficient of the sample gas), should be controlled. Since the flow rates and the size of the sampling system are small on an absolute scale, thermal mass is low, and the task of thermostating should be simple.

Calibration Behavior. A calibration plot for 6–80 ppbv SO₂ is shown in Figure 6, using 45 mM H₂O₂ as the absorber. While the response is linear up to about 50 ppbv under these conditions (60 s sample at 100 cm³/min), it clearly decreases at higher concentrations. For the large majority of ambient applications, this range and degree of linearity are adequate. The H₂O₂ concentration clearly plays a role in determining the applicable linear range. In the range of 0–50 ppb SO₂, the linear *r*² value for the concentration–peak area relationship increases from 0.9868 to 0.9962 as the H₂O₂ concentration is increased from 8.8 to 35 mM. However, H₂O₂ concentration is not the only factor in maintaining a constant collection efficiency as the sample concentration is varied. Since H₂SO₄ is formed on the surface of the film and is slow to diffuse into the interior, surface accumulation of acidity results in impaired uptake of SO₂. It is interesting to note in this context that the electropherogram shows both a sulfite and a sulfate peak *only* when the concentrations of sampled SO₂ and the H₂O₂ absorber concentration are *both* low; otherwise, sufficient H₂SO₄ is formed to preclude the significant presence of sulfite. It should also be pointed out that in the current age of data processing technology, an excessive emphasis of the linearity of calibration maybe is not fruitful: as long as there is sufficient slope, the analytical parameter of interest can be computed with equal ease from a nonlinear calibration plot stored in computer memory.

The above behavior is likely unique for the particular gas–absorber combination when a weak acid gas reacts to form a strong acid on the surface. In any case, the upper range of linearity can easily be manipulated by controlling the total amount of analyte collected, most easily by changing the sampling time.

Effect of Relative Humidity: Use of an Internal Standard for Compensating Evaporation Losses. All of the experiments

reported in the foregoing have been conducted under dry conditions. During sampling, the solvent in the film evaporates, the loss increasing with the sampling rate, sampling period, and decreased sample RH. Evaporation thus results in concentration of the analyte in the film. Thus, regardless of any intrinsic effect water vapor may have (e.g., forming water clusters in the gas phase with the analyte that decreases the diffusion coefficient and hence the collection efficiency of the analyte¹⁶), decreased sample RH will result in a greater concentration of the analyte injected, for the same total analyte mass collected by the film. This effect can be substantial: the best-fit linear calibration slope decreases by 45% as the sample RH increases from 10 to 80%. This concentration effect can be largely compensated for if a stable internal standard, one that is not likely to occur in the sample gas, is incorporated in the film-forming liquid at a constant concentration. For this purpose, we chose 1 mg/L chlorate. From 10 to 57% RH, the calibration slope decreases by 31%; with internal standard correction, the difference decreases to <12%. Use of an internal standard may also otherwise improve precision. We have not studied this in detail.

The residual effect of the influence of RH is real, however. In our experience, we have not generally encountered an RH dependence for SO₂ in other diffusion-based collection systems. The effect that we see is not insubstantial (the calibration slope decreases by 35% from 10 to 80% RH, even after internal standard correction). The overall flow in the test system is low, and we believe that we are encountering actual losses of SO₂ from the test stream because of adsorption of water vapor on the wall. Due to the low flow rates involved, the system never reaches adsorption equilibrium.

Because of the high sensitivity of the system, it may be practical to dilute the sample gas with highly humid air to keep the RH high. Interestingly, at 80% RH, sampling can be easily conducted for more than 10 min, as evaporation is low enough that the film remains intact for a very long period of time. By thus increasing the sampling time, it may actually be possible to improve on the concentration LOD, despite the fact that the sample is prediluted.

Reproducibility and LOD for the Measurement of Gaseous SO₂. The overall reproducibility of the gas sampling on a liquid film and measurement by an aliquot injection from it is obviously of interest. Precision data were as follows (reported as % RSD for peak area, % RSD for peak height, ppbv SO₂ sampled, *n* = 3 at each concentration level): 14.3, 8.3, 6.7 ppb; 3.1, 4.9, 11.6 ppb; 8.8, 4.0, 16.4 ppb; 4.3, 10.8, 25.7 ppb; 12.1, 8.5, 35.9 ppb; 5.7, 3.0, 45.5 ppb; 1.5, 5.6, 60.8 ppb; and 7.4, 5.5, 77 ppb. Considering the low parts per billion levels of these measurements and the attendant sources of error in the generation/transmission of the calibrant gas, dilution gas purity, and blank variability, these results are quite acceptable. We thus judged aliquot sampling from the film to be an acceptable process for sample introduction from the film.

The LOD for SO₂ is clearly dependent on a number of variables, including the sampling rate and the sampling duration. Electropherograms resulting from 1.5 ppbv SO₂ sampled for 1 and 2 min at 100 cm³/min are shown in traces a and b in Figure 7, respectively. Larger sampling periods will obviously be possible if the sample air is not completely dry. In any case, an LOD of 1 ppbv can be conservatively estimated for any sample RH. Elec-

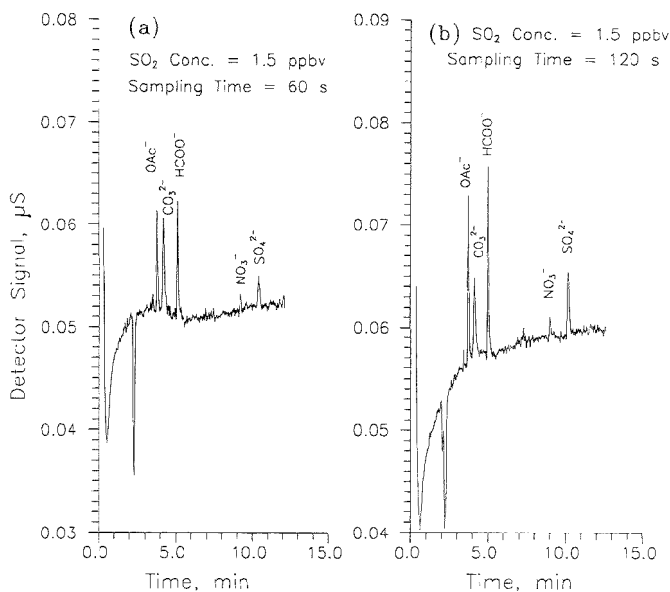


Figure 7. Performance near the detection limit: 1.5 ppbv SO₂ sampled for (a) 1 min and (b) 2 min. The air cleaning system does not adequately remove weak acid gases like HCOOH, CH₃COOH, and CO₂.

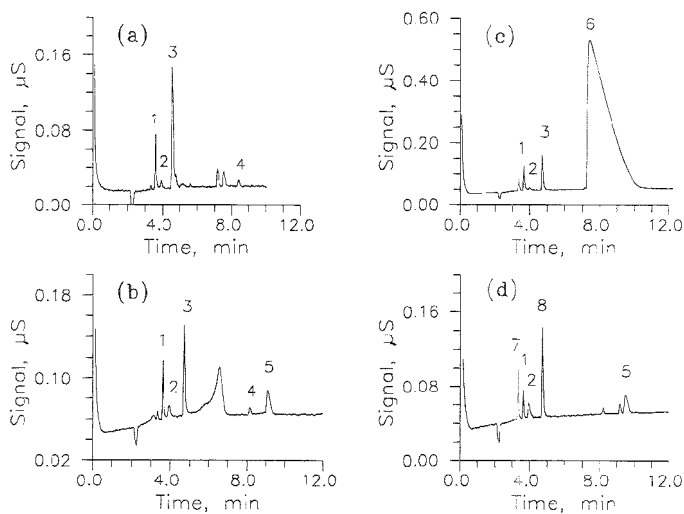


Figure 8. Electropherograms of (a) air outside of the TTU chemistry building, (b) vapors from a cut onion, (c) vapors from concentrated HClO₄ (15 s sampling), and (d) vapors from a half-filled diet cola can (half-full and mostly defizzed). Migration-based identifications: (1) acetate, (2) carbonate, (3) formate, (4) nitrate, (5) sulfate (probably originally sulfite), (6) perchlorate and chloride overlapped (can be resolved at lower concentrations), (7) benzoate, and (8) phosphate. Unlabeled peaks could not be identified.

tromigration is often practiced to improve LODs.²⁶ Electromigration is not easy to practice in SuCESS because EOF dominates electrophoretic movement, and the two oppose each other. However, if an indirect optical detection approach is used

with a cationic surfactant as a flow modifier and negative HV for operation,²⁷ we have found that it is easy, simple, and reproducible to practice electromigration by using the loop wire itself as the HV electrode. This approach would obviously be of value if such

(26) Gordon, M. J.; Huang, X.; Petoney, S. L.; Zare, R. N. *Science* **1988**, *242*, 224–228.

(27) Romano, J.; Jandik, P.; Jones, W. R.; Jackson, P. R. *J. Chromatogr.* **1991**, *546*, 411–421.

detection methods, rather than suppressed CE, are used for detection; a detailed account will be published subsequently.

Illustrative Applications. The present instrument could be useful for a variety of applications. Examples are shown in Figure 8 for (a) the significant occurrence of formic and acetic acids in the air outside the TTU chemistry building, (b) a sniff over a freshly cut onion, (c) volatile impurities over a concentrated HClO₄ bottle, and (d) CO₂ peak observed over a can of a carbonated beverage.

Future Possibilities. To our knowledge, this is the first example of direct determination of gases by capillary electrophoresis. The simple technique reported here opens the door of CE, possibly the most powerful and elegant separation technique of the decade, to gaseous analytes. It is likely that the horizon of applications for organic vapors, using micellar electrokinetic chromatography or nonaqueous electrophoretic media, will be much greater than what has been explored here. We also believe

that the concept of sampling from a film formed on a loop has many unique features. In the future, we expect to report on electromigrative injections from a loop and the use of the loop as a sample extraction interface in other biphasic systems.

ACKNOWLEDGMENT

This research was supported by the U.S. Environmental Protection Agency, Office of Exploratory Research, through R-8201117-01-1. This manuscript has not been subjected to review by the agency, and no official endorsement should be inferred. We thank Dr. Kazimierz Surowiec for the data on DMF introduction from the loop/film.

Received for review June 19, 1995. Accepted August 18, 1995.*

AC950622G

* Abstract published in *Advance ACS Abstracts*, October 1, 1995.

Separation of Colloidal Latex Aggregates by Cluster Mass and Shape Using Sedimentation Field-Flow Fractionation with Steric Perturbations

Bhajendra N. Barman[†] and J. Calvin Giddings*

Field-Flow Fractionation Research Center, Department of Chemistry, University of Utah, Salt Lake City, Utah 84112

Aggregated colloidal clusters consisting of different numbers of monodisperse latex spheres can be cleanly separated from one another on the basis of differences in cluster mass using the normal mode of sedimentation field-flow fractionation. However, steric effects perturb the experimental retention volumes and affect the spacing between cluster peaks. Most remarkably, the magnitude of the steric disturbance varies with the cluster shape, causing a shape-dependent shift in retention for clusters having the same number n of elementary spheres and thus having the same mass. The shape-dependent shift is verified by electron microscopy of fractions collected within individual cluster peaks; this shows a secondary fractionation within the peak according to cluster shape. The secondary fractionation is selective between compact and elongated clusters of equal aggregation number n . These and other steric perturbations are examined in some detail in this paper. In particular, the change in peak spacing with increasing n is discussed, and the factors affecting the transition from the normal mode to the steric mode are investigated. The theoretical concepts presented are verified using samples of aggregated PMMA colloidal latex.

Field-flow fractionation (FFF) techniques provide a broad spectrum of approaches for characterizing colloidal particles and associated colloidal phenomena.^{1,2} The unique capabilities of sedimentation field-flow fractionation (SdFFF) in studying particle aggregation by means of the separation and characterization of individual clusters of different mass were demonstrated first in the separation of viral rods³ and more recently in the separation of latex aggregates.^{4–7} As the separation process is described by well-defined theoretical principles, it is possible to establish resolution criteria for the separation of different cluster masses.⁴

It is also possible to determine the mass and polydispersity of aggregated clusters⁵ and the kinetics of their formation and breakup.^{5,7}

The "normal mode" of SdFFF has been used in the above studies of colloidal aggregates. In normal-mode SdFFF, a steady-state particle cloud or layer is formed when particle Brownian motion away from the accumulation wall is balanced against the centrifugal field. The layer thickness is smaller for the larger particles that are driven more strongly toward the accumulation wall. The particle diameter d is usually small (in the submicrometer range) compared to the average layer thickness l , the latter typically 2–20 μm . It is assumed that $d \ll l$ for unperturbed normal-mode SdFFF. However, steric perturbations (due to the physical size of the particles) become important with increasing cluster size as the increasing d approaches a decreasing l . Therefore, steric effects can become significant for higher order latex aggregates, those having a large number n of elementary particles in the cluster. Steric effects are obviously most important for clusters that have relatively extended conformations.^{4,6} Ultimately, the physical size determines the cluster retention after passing through a steric transition region.

The steric transition region refers to a range of particle sizes and corresponding elution volumes in which the dominant mechanism of retention is undergoing a transition from normal mode to steric mode. The elution order undergoes inversion in the steric transition region: for smaller particles, the retention volume increases with particle size, whereas for larger (steric mode) particles, the retention volume decreases with particle size. Steric transition phenomena have been characterized theoretically for both SdFFF and flow field-flow fractionation.⁸ The experimental verification of such phenomena in SdFFF has been carried out using polydisperse poly(vinyl chloride) latex beads as well as narrow polystyrene beads.⁹ The retention characteristics of irregularly shaped particles, which can be strongly influenced by steric effects, have also been studied by SdFFF.^{10,11} The most recent studies¹¹ have shown that steric effects, which are not yet fully characterized even for spherical particles, are quite complex and poorly understood for particles of nonspherical configuration. Because of the importance of nonspherical particles in many fields, it is important to better understand their steric behavior.

[†] Present address: Texaco Inc., P.O. Box 1608, Port Arthur, TX 77641.

(1) Giddings, J. C. *Science* **1993**, *260*, 1456–1465.

(2) Giddings, J. C. *Anal. Chem.*, in press.

(3) Caldwell, K. D.; Nguyen, T. T.; Giddings, J. C.; Mezzone, H. M. *J. Virol. Methods* **1980**, *1*, 241–256.

(4) Jones, H. X.; Barman, B. N.; Giddings, J. C. *J. Chromatogr.* **1988**, *455*, 1–15.

(5) Giddings, J. C.; Barman, B. N.; Li, H. J. *Colloid Interface Sci.* **1989**, *132*, 554–565.

(6) Barman, B. N.; Giddings, J. C. In *Particle Size Distribution II: Assessment and Characterization*; Prover, T., Ed.; ACS Symposium Series 472; American Chemical Society: Washington, DC, 1991; pp 217–228.

(7) Barman, B. N.; Giddings, J. C. *Langmuir* **1992**, *8*, 51–58.

(8) Giddings, J. C. *Analyst* **1993**, *118*, 1487–1494.

(9) Lee, S.; Giddings, J. C. *Anal. Chem.* **1988**, *60*, 2328–2333.

(10) Kirkland, J. J.; Schallinger, L. E.; Yau, W. W. *Anal. Chem.* **1985**, *57*, 2271–2275.

(11) Beckett, R.; Jiang, Y.; Liu, G.; Moon, M. H.; Giddings, J. C. *Part. Sci. Technol.* **1994**, *12*, 89–113.

Clusters of monodisperse spherical particles provide a good opportunity to further characterize steric effects and steric transition phenomena for nonspherical particles. Samples consisting of aggregated clusters are rather unique for such studies because particle mass, which controls normal-mode SdFFF and has a major role in the steric transition, varies in discrete units (given by the mass of a single sphere), while particle shape, and thus effective particle size, varies over a complex continuum. As will be shown in this report, clusters of fixed mass can be isolated from clusters of other discrete masses. Most importantly, the perturbations caused by shape variants within the constant mass population of a single peak can be examined and characterized.

In this report, the sample consists of aggregated poly(methyl methacrylate) (PMMA) latex beads with diameters in the range 0.2–0.25 μm . The retention of single latex spheres in this size range is usually governed by the normal mode of operation of FFF. As larger and larger clusters of such spheres are examined, steric effects increasingly perturb normal-mode behavior. The different levels of steric perturbations observed, first for clusters of different mass and second for variations in cluster shape within a fixed mass category, are examined here.

THEORY

The theory describing the normal-mode characterization and resolution of colloidal aggregates has been developed elsewhere.^{4,7} However, the following points are specifically relevant to this work.

The standard (normal-mode) retention equation in field-flow fractionation relates retention ratio R to experimental retention volume V_r and the channel void volume V^0 , and subsequently to the retention parameter λ :

$$R = V^0/V_r = 6\lambda[\coth(1/2\lambda) - 2\lambda] \quad (1)$$

Equation 1 can be modified to account for steric effects as follows:^{8,12}

$$R = 6\lambda(\alpha - \alpha^3) + 6\lambda(1 - 2\alpha)\left[\coth\left(\frac{1 - 2\alpha}{2\lambda}\right) - \frac{2\lambda}{1 - 2\alpha}\right] \quad (2)$$

where $\alpha = d'/2w$, w is the channel thickness, and γ is the dimensionless steric correction factor of order unity.⁹ In practice, the effective steric diameter d' can be roughly approximated by the longest dimension of the particle or particle cluster.⁸

The parameter λ in SdFFF is related to particle mass m or effective spherical diameter d by

$$\lambda = \frac{kT}{wG(\Delta\rho/\rho_p)m} = \frac{6kT}{\pi wG\Delta\rho d^3} \quad (3)$$

where k is Boltzmann's constant, T is absolute temperature, G is centrifugal acceleration, ρ_p is particle density, and $\Delta\rho$ is the difference in density between the particle and carrier liquid.

For well-retained colloidal particles (found when $V_r > 2V^0$), λ and α are small compared to unity. Under these conditions, with the substitution of λ from eq 3, eq 2 can be simplified and rearranged to obtain

$$\begin{aligned} V_r/V^0 &= \frac{1}{36kT/\pi wG\Delta\rho d^3 + 3\gamma d'/w} \\ &= \frac{1}{6kT/wG(\Delta\rho/\rho_p)m + 3\gamma d'/w} \end{aligned} \quad (4)$$

We note that d as used here represents the effective spherical diameter d_n of a cluster of n elementary particles of diameter d_1 and is thus given by $d_n = n^{1/3}d_1$.

The final equality of eq 4 can be rearranged to yield

$$V_r = AmG/(1 + B\gamma d'mG) \quad (5)$$

where A and B are constants.

EXPERIMENTAL SECTION

The two SdFFF systems used in this work were described elsewhere.⁶ The apparatus of system I was equipped with a channel 0.0254 cm thick, 89.4 cm long (tip-to-tip), and 1.90 cm in breadth. The distance between the channel and the axis of rotation is 15.1 cm. The channel void volume is 4.25 mL. For system II, the channel is of length 90.5 cm, thickness 0.0254 cm, and breadth 2.0 cm, and its radius of rotation is 15.3 cm. The void volume is 4.50 mL. A UV detector working at 254 nm was used to detect the elution of particles from the channel.

The carrier liquid was doubly distilled water with 0.05% (w/v) sodium dodecyl sulfate added as a suspending agent and 0.01% (w/v) sodium azide used as a bactericide. Two PMMA latex samples (latex density, 1.021 g/mL) were used in this study. A nominal 0.230 μm sphere diameter PMMA sample was obtained from Seradyn (Indianapolis, IN). The second sample, a nominal 0.207 μm PMMA, was obtained from Dr. T. Provder of The Glidden Co. (Strongsville, OH). The diameter-based polydispersity (σ_d/d) values of the nominal 0.207 and 0.230 μm primary latex beads measured by SdFFF are 0.040 and 0.023, respectively.⁴ Here, σ_d represents the standard deviation in mean particle diameter d .

RESULTS AND DISCUSSION

Steric Effects and Spacing of Clusters. In the absence of steric effects, the second term in the denominator of eq 5 vanishes. Under this situation, representing normal-mode elution, retention volume is proportional to mass at constant field strength or to field strength for a specific cluster mass. Since latex clusters in a sample population (having low-order aggregation) differ from one another by one elementary particle mass, SdFFF should provide a series of peaks with nearly equal spacing at constant field strength. These peaks correspond to singlets, doublets, triplets, and higher order clusters. Thus, a constant field operation (using constant G) can be used to obtain rather evenly resolved clusters in an aggregated latex population (see Figure 1).

For relatively strong field conditions and/or large cluster mass, the second term in the denominator of eq 5, reflecting steric effects, becomes significant. Under these conditions, the proportionality of retention volume V_r to mass (at constant field) is no longer valid. Similarly, V_r is not expected to be proportional to field strength for a particular cluster. Because of steric effects, the deviation from the proportionality of V_r to mass can be increasingly significant as the cluster size is increased. Thus, the spacing between successive peaks past the singlet is expected to

(12) Giddings, J. C. *Sep. Sci. Technol.* 1978, 13, 255–262.

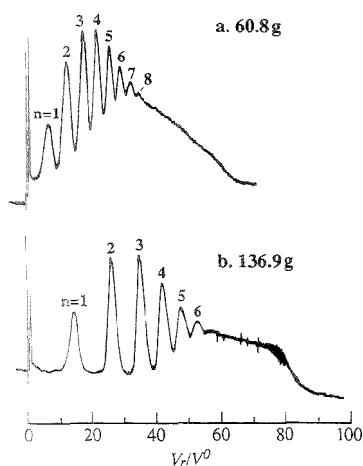


Figure 1. Fractograms of aggregates of the nominal $0.207\ \mu\text{m}$ PMMA latex obtained with system I at two different field strengths, (a) 60.8 and (b) 136.9 gravities, with a flow rate of 1.10 mL/min. The number of spheres per cluster is represented by n . Sample volume is $45\ \mu\text{L}$ (arbitrary concentration).

decrease continuously as the aggregation number n increases. Finally, the steric transition region (where the steric mode gains dominance over the normal mode) is reached and is associated with a sudden dropoff of the detector signal to baseline at a high retention level.⁹

The two fractograms in Figure 1 illustrate the diminishing spacing between successive cluster peaks for $0.207\ \mu\text{m}$ PMMA aggregated latex at field strengths of (a) 60.8 and (b) 136.9 gravities, respectively. These fractograms were obtained with system I using a carrier flow rate of 1.10 mL/min. The steric transition is apparent with the rapid dropoff of the signal in fractogram b at around 80 channel volumes. However, a rapid dropoff of signal is absent in fractogram a obtained at a lower field strength; in this case, the signal ramps down gradually to the baseline.

Another important difference between the two fractograms in Figure 1 arises from the number of observed peak maxima. Fractogram a displays eight peak maxima, in contrast to six in fractogram b. (Peak maxima are counted up to a point beyond which distinct and relatively narrow peaks are absent and the signal becomes featureless with higher level of noise and spikes.) Similar results can be found in ref 6, where fractograms of the same $0.207\ \mu\text{m}$ PMMA aggregates obtained at a flow rate of 1.10 mL/min but at three different field strengths are shown. These fractograms also show variations in the number of peak maxima. Specifically, eight, seven, and five peak maxima are observed in fractograms obtained at field strengths of 42.2, 108.1, and 204.5 gravities, respectively. This trend constitutes an apparent anomaly because normal-mode resolution is enhanced, not degraded, by increasing field strength.

Shape Effects. Values of V_r/V^0 corrected for steric effects can be obtained using eq 4. For a given cluster mass, two extreme limits of d' are considered. For the most compact conformation, the steric diameter can be approximated by that of an equivalent sphere: $d' = d_n = n^{1/3}d_1$. For a fully extended structure, $d'_{lc} = nd_1$, where the abbreviation "lc" indicates a linear chain.

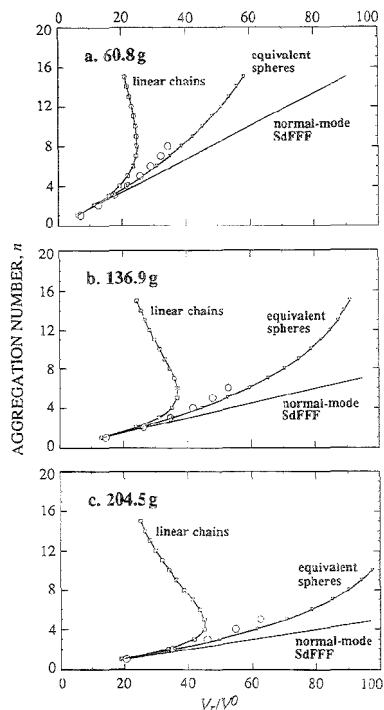


Figure 2. Plots of aggregation number n vs V_r/V^0 calculated for linear chains and equivalent spheres of the nominal $0.207\ \mu\text{m}$ PMMA beads. Experimental points (\circ) for observed cluster peaks are also shown. Plots a and b represent conditions pertaining to fractograms a and b in Figure 1, respectively. Plot c corresponds to a fractogram (not shown) obtained at 204.5 gravities with a flow rate of 1.10 mL/min.

Steric correction factor γ is a complex hydrodynamic parameter that varies with field strength, particle diameter, and flow rate.^{9,13} In typical cases, γ values fall between 0.5 and 2.0. Here, for simplicity, we assume $\gamma = 1$.

Since $d = d_n = n^{1/3}d_1$, all parameters in eq 4 are available, and V_r/V^0 values for the two extreme conformations of any individual cluster mass at a particular field strength G can be calculated. The resulting plots of aggregation number n vs V_r/V^0 are shown in Figure 2. Experimental values of V_r/V^0 for observed cluster peaks are shown for comparison. The points representing these measurements are limited in number, corresponding to the distinct peaks observed in each case. The experimental points lie between the curves for linear chains and equivalent spheres but are somewhat closer to the latter. This may reflect the lower relative stability of chainlike configurations, particularly with higher order aggregates and the consequent domination of the mean population, represented by each peak maximum, by more compact aggregates.

The plots in Figure 2a,b correspond to the experimental conditions for fractograms a and b in Figure 1, respectively. The plots in Figure 2c are based on the separation of $0.207\ \mu\text{m}$ PMMA

(13) Peterson, R. E., II; Myers, M. N.; Giddings, J. C. *Sep. Sci. Technol.* 1984, 19, 307-319.

Table 1. Calculated V_r/V^0 Values at Steric Inversion Point for Five Different Field Strengths

field strength (gravities)	$(V_r/V^0)_i$ (and corresponding n)		no. of obsd peaks
	linear chains	equivalent spheres	
42.2	20.6 (10)	74.0 (71)	8
60.8	24.7 (8)	81.1 (54)	8
108.1	33.0 (6)	93.6 (35)	7
136.9	37.0 (6)	99.3 (30)	6
204.5	45.1 (5)	109.7 (22)	5

aggregates at a higher field strength, 204.5 gravities, using the same flow rate, 1.10 mL/min. The curves for the linear chains show that the steric transition points (corresponding to the maximum values of V_r/V^0) occur at $n = 8$, $n = 6$, and $n = 5$ at field strengths 60.8, 136.9, and 204.5 gravities, respectively. On the other hand, the curves representing equivalent spheres display no such transition within the V_r/V^0 range covered in Figure 2.

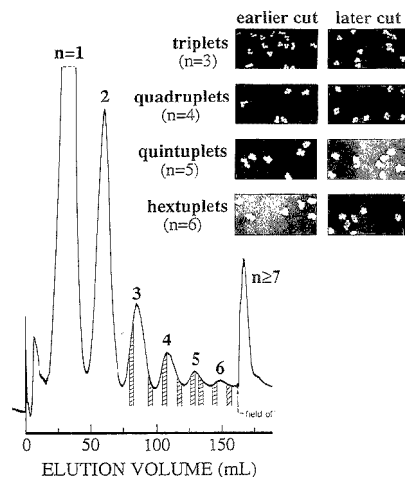
The values of V_r/V^0 at the inversion point, $(V_r/V^0)_i$, for both linear chains and equivalent spheres were determined for conditions under which five experimental fractograms of 0.207 μm PMMA latex aggregates were obtained. The aggregation number n corresponding to each steric transition point was also determined. These results are summarized in Table 1. The last column of Table 1 shows the numbers of experimentally observed peak maxima in the respective fractograms.

It is interesting to note that the number of observed peak maxima reported in Table 1 matches closely the aggregation number where the steric transition for the linear chains is predicted. This agreement is somewhat fortuitous; besides steric effects, other factors such as the polydispersity of the elementary latex beads,⁵ the variations in cluster shape (see below), and nonequilibrium effects^{4,5} contribute to peak broadening and consequently limit the number of observed peak maxima.

The plots in Figure 2 show that the steric transition for a linear chain is more abrupt at higher than at lower field strengths. The decrease in V_r/V^0 with aggregation number beyond the transition or inversion point is gradual at 60.8 gravities but becomes increasingly significant at 136.9 and at 204.5 gravities. As listed in Table 1, the steric inversion points for both linear chains and equivalent spheres move to higher V_r/V^0 values with an increase in field strength.

Figure 2 shows that the spread between V_r/V^0 curves for linear chains and equivalent spheres increases with n . The above spread will result in a loss of resolution between successive peaks because equal-mass clusters of different conformations will tend to spread out in the region between the two extreme limits of V_r/V^0 values. However, as mentioned above, latex clusters with conformations intermediate between the two extreme limits are expected to prevail, leading to the elution of distinct but somewhat broadened peaks at intermediate V_r/V^0 values. Since the spreading effect continues to increase with n , a total loss of resolution between successive clusters is eventually expected and is observed.

The above-noted spreading effect, and the associated resolution loss, will be greatest at high field strengths, as is apparent from Figure 2. This resolution loss at high field strengths is expected because equal-mass clusters with extended and compact conformations will have relatively larger differences in V_r/V^0 values at larger G values because of enhanced steric effects. Thus, there will be a more significant mixing (overlap) of clusters of different

**Figure 3.** Fractogram showing separated cluster populations of the nominal 0.230 μm PMMA latex beads. The eight electron micrographs show clusters found in successive fractions collected at the eight cross-marked intervals shown on the fractogram.

mass at high G . This mechanism of resolution loss at high G , which acts contrary to the normal trend (where shape differences are absent) of improved resolution at high G , is dominant in the present case, as confirmed by Figure 1.

Separation by Cluster Shape. Since clusters starting with triplets ($n = 3$) can have various conformations, their effective steric diameters would fall between the extremes d_e and d_c . We note that for low-order aggregates that elute before the onset of the steric transition, the cluster mass is still the primary factor governing the separation of aggregates, which leads to the near coelution of clusters of equal mass but of different shapes. However, eq 4 predicts that clusters with extended conformations (large d_e) will tend to elute in the early part of the peak (with lower V_r), followed by clusters having increasingly more compact conformations. These shape-induced differences in retention should become more pronounced for larger clusters subject to stronger steric perturbations.

To verify the differential elution stemming from cluster shape, it was necessary to eliminate higher order aggregates in the sample population. For a better resolution between cluster peaks, a population of aggregates formed from latex beads with low polydispersity was a preferred choice.⁵ It was also necessary to separate the aggregates using a low carrier flow rate to minimize nonequilibrium effects.^{4,5}

The nominal 0.230 μm PMMA latex sample was sonicated for a period of 1 h prior to its analysis by SdFFF. A fractogram of this PMMA sample was obtained using system II with a field strength of 61.6 gravities and a flow rate of 0.95 mL/min (see Figure 3). The experimental conditions are such that the steric transition for linear chains and equivalent spheres would occur for $n = 7$ and 39, respectively.

The micrographs shown in Figure 3 are in agreement with the above prediction. Two fractions were collected from the eluted peaks corresponding to the triplet ($n = 3$) through hexuplet ($n = 6$) clusters for microscopic examination. Scanning electron microscopy (SEM) was used to characterize the particles in each

fraction. The SEM micrographs of the above fractions (shown in Figure 3) indicate that for all four peaks examined, clusters with relatively extended conformations elute in the early part of the peak, and clusters with more compact conformations are found in the later cut. (Clusters with $n > 6$ did not form distinct peaks for reasons explained above. All higher order clusters were eluted as a single peak once the field was turned off. The size of this peak shows that the population of latex clusters with $n > 6$ was relatively small in the sonicated sample.)

The small number of aggregates shown in each micrograph of Figure 3 are representative of what was observed in a larger population of clusters with scanning electron microscopy. Many chainlike or relatively extended clusters were observed in the images obtained from the earlier cuts for triplets or quadruplets. The later cuts of triplets and quadruplets were found to contain tightly packed clusters. The marked difference in compactness in cluster configuration was less pronounced in the two-dimensional images of aggregates with five and six latex beads. Sonication may be responsible for the absence of chainlike (or relatively extended) clusters in the earlier cuts of quintuplets and hexuplets; a relatively larger proportion of extended (less stable) aggregates would likely be broken up during sonication of the sample.

CONCLUSIONS

While colloidal latex aggregates can be resolved by sedimentation FFF into separate peaks according to their mass or degree of aggregation, the peaks are broadened by a secondary fractionation caused by steric perturbations. The secondary fractionation depends on cluster shape. The ability to fractionate large clusters of equal mass according to differences in shape supports the possibility that FFF techniques might be adaptable to the characterization of colloidal particles by shape factors, which significantly influence the mechanical and optical properties of materials produced from the colloids.

The capability of sedimentation FFF to discriminate between different cluster masses as well as unlike cluster shapes for aggregated latexes is rather unique among instrumental systems. The generation of latex fractions differing in mass and shape has not been achieved by any other technique. The isolation of these major populations and subpopulations of latexes makes it possible to probe further details of colloidal structure by utilizing other analytical tools, such as electron microscopy and light scattering. Thus, the ability of sedimentation FFF to separate colloidal

fractions according to well-established principles not only has direct analytical applications but also makes possible powerful combinations of FFF with a host of other analytical techniques.

ACKNOWLEDGMENT

This work was supported by Grant CHE-9322472 from the National Science Foundation.

GLOSSARY

A	constant in eq 5
B	constant in eq 5
d	effective spherical diameter
d'	particle steric diameter
d'_{lc}	d' for linear chains
d_1	diameter of elementary sphere
d_n	effective spherical diameter of cluster of n particles
G	field strength measured as acceleration
k	Boltzmann's constant
l	average particle layer thickness
m	particle mass
n	aggregation number
R	retention parameter
T	absolute temperature
V_r	retention volume
V^0	channel void volume
w	channel thickness
Greeks	
α	$d'/2w$ in eq 2
γ	steric correction factor
$\Delta\rho$	density difference between particle and carrier
λ	retention parameter
ρ_p	particle density
σ_d	diameter-based polydispersity

Received for review March 2, 1995. Accepted August 18, 1995.*

AC950219+

* Abstract published in *Advance ACS Abstracts*, October 1, 1995.

Separation of Diastereomers by Capillary Zone Electrophoresis with Polymer Additives: Effect of Polymer Type and Chain Length

Wolfgang Schützner,[†] and Salvatore Fanali

Istituto di Cromatografia del CNR, Area della Ricerca di Roma, via Salaria km 29.300, C.P. 10, 00016 Monterotondo Scalo, Rome, Italy

Andreas Rizzi,* and Ernst Kenndler

Institute for Analytical Chemistry, University of Vienna, Währingerstrasse 38, A-1090 Vienna, Austria

Diastereomeric derivatives of enantiomers are separated by capillary zone electrophoresis in nonchiral separation systems in the presence of linear polymers. These polymers significantly influence the mobilities of the analytes as well as the stereoselectivity of the system. Three types of linear polymers, poly(vinylpyrrolidone), poly(ethylene glycol), and poly(acrylamide), are investigated to determine their influence on the stereoselective separation of diastereomeric derivatives of α -amino acids obtained by reaction with optically pure (+)-*O,O'*-dibenzoyl-L-tartaric anhydride. Differences are found in the strength of the polymer effect and the effected migration order. Polymer chain length had no impact on stereoselectivity.

In previous papers,^{1–3} the electrophoretic separation of diastereomeric derivatives of racemic amino acids has been reported, where the diastereomers were obtained by reaction with (+)-*O,O'*-dibenzoyl-L-tartaric anhydride (DBT anhydride). It was shown that in free solution using no further additives, many of the investigated compounds are resolved at appropriate pH conditions. It has been found that the presence of linear poly(vinylpyrrolidone) in the electrolyte solution significantly increases stereoselectivity and allows one to separate a larger number of diastereomeric analytes.^{1,2} This increased stereoselectivity is supposed to be based on intermolecular interactions between the analytes and the polymeric pseudophase. In aqueous electrolyte solutions, it can be assumed that the pseudophase acts predominantly on the basis of free energy contributions responsible for "hydrophobic" behavior, as well as on the basis of dipole and π - π interactions between appropriate structural moieties in analyte and polymer. Interactions between aromatic and π -electron-rich structural groups seem to be of special significance.⁴

In this paper, three different types of polymers are compared with respect to this observed effect on stereoselectivity: poly(vinylpyrrolidone) (PVP), poly(ethylene glycol) (PEG), and poly-

(acrylamide) (PAA). As stereorecognition might be affected by the conformation of the polymer, the parameter of chain length is investigated, too, using PVP and PEG with three different chain lengths. Test analytes were racemic α -amino and α -hydroxy acids converted to diastereomeric derivatives by reaction with DBT anhydride.

EXPERIMENTAL SECTION

Apparatus. The experiments were carried out using a laboratory-made apparatus as described in refs 1 and 5. The dimensions of the fused silica capillary used (Polymicro Technologies, Phoenix, AZ) were 56 cm \times 100 μ m i.d., with 39 cm length to the detector (UV absorption at 233 nm). A constant voltage of 12 kV was applied to the capillary during electrophoresis in the anionic mode. The capillary was coated to suppress the electroosmotic flow; it was kept at ambient temperature (24–25 °C) without thermostating. Sampling was done by the hydrodynamic method (5 s at a height of 10 cm).

For measurements of dynamic viscosities at three different temperatures, an automated microviscosimeter (AMV 200, A. Paar, Graz, Austria) was used.

Chemicals. Optically pure (optical purity >99.5%) and racemic α -amino acids, as well as buffering electrolytes and coating reagents, were purchased from Aldrich (Steinheim, Germany) in the purest obtainable quality. (+)-*O,O'*-diacetyl-L-tartaric anhydride (optical purity >99.5%) was obtained from Aldrich, and (–)-*O,O'*-dibenzoyl-L-tartaric anhydride was synthesized as described in refs 1 and 5, ending with an optical purity >99.5%.

PVP-15, PVP-25, and PVP-90, as well as PEG-200, PEG-20 000 and PEG 100 000, were obtained from Serva (Heidelberg, Germany). PAA was polymerized according to ref 6, with the given concentration of acrylamide.

Procedure. The derivatization of the racemic or optically pure analytes with DBT anhydride was performed as in refs 7 and 8; the poly(acrylamide)-type coating was made according to the procedure given in ref 6.

[†] Permanent address: Institute for Analytical Chemistry, University of Vienna.

(1) Schützner, W.; Caponecchi, G.; Fanali, S.; Rizzi, A.; Kenndler, E. *Electrophoresis* 1994, 15, 769.

(2) Schützner, W.; Fanali, S.; Rizzi, A.; Kenndler, E. *J. Chromatogr.* 1993, 639, 375.

(3) Schützner, W.; Fanali, S.; Rizzi, A.; Kenndler, E. *J. Chromatogr.*, in press.

(4) Blatny, P.; Fischer, H.-C.; Rizzi, A.; Kenndler, E. *J. Chromatogr.*, in press.

(5) Fanali, S.; Ossicini, L.; Foret, F.; Boček, P. *J. Microcolumn Sep.* 1989, 1, 190.

(6) Kilar, F.; Hjerten, S. *Electrophoresis* 1989, 10, 23.

(7) Zetzsche, F.; Hubacher, M. *Helv. Chim. Acta* 1926, 9, 291.

(8) Lindner, W.; Leitner, C.; Uray, G. *J. Chromatogr.* 1984, 316, 605.

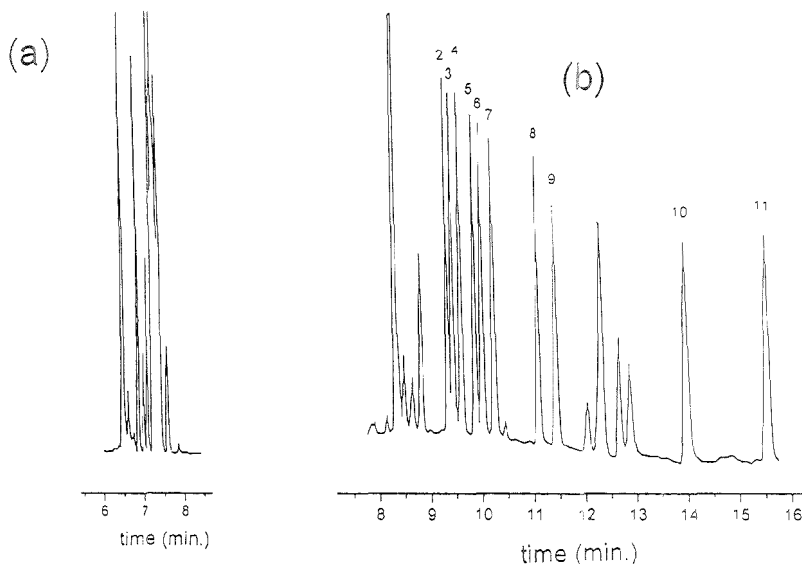


Figure 1. Electropherograms of a mixture of DBT-derivatized racemic amino acids without (a) and with PVP (b) added as pseudophase. (a) Sample: DBT-derivatized racemic Ser, Thr, Gln, Met, Leu, Phe, Phegly, and Trp. No polymer in the BGE. (b) Sample: DBT-derivatized D-Ser (2), L-Ser (3), D-Gln (4), L-Gln (5), D-Leu (6), L-Leu (7), L-Phe (8), D-Phe (9), L-Trp (10) and D-Trp (11). Peak 1 originates from DBT-acid. Additional peaks are byproducts of reaction. Electrophoretic conditions: coated fused silica capillary, dimensions 56 cm \times 100 μ m i.d., 39 cm length to the detector; voltage, 12 kV; ambient temperature; UV absorption at 233 nm. Composition of the BGE: aqueous buffer solution, 30 mM sodium phosphate, pH 5.8; 2.5% (w/v) PVP.

The BGE was composed of 30 mmol/L sodium dihydrogen phosphate, adjusted with NaOH to pH 5.8. The polymers were added to the BGE solution prior to pH adjustment in a concentration range from 0.5% to 3% (w/v) (PVP and PAA) and 5% (w/v) (PEG).

RESULTS AND DISCUSSION

Chemical Structure of Polymer and Analyte. The retardation of the analytes induced by interaction with the polymer network generates selectivity with respect to the chemical nature of the analytes, in particular the chemical structure of the amino acid side chains and their configuration.

Side-Chain-Related Selectivity. The retardation of the single DBT-derivatized amino acids by interaction with the different polymeric pseudophases is illustrated by the decrease in their effective mobilities given in Table 1. With PVP, aromatic amino acids are seen to be slightly more affected than aliphatic ones, and the hydrophilic groups in serine, threonine, and glutamine diminish the effect of PVP on mobility. The impact of PEG and PAA is generally of the same type, but weaker compared to PVP, and the side-chain-specific selectivity does not distinguish as clearly between aliphatic and aromatic moieties. The spreading of mobility values by interaction with the polymer is strongest with PVP. The thus-achieved broadening of the mobility window of a set of analytes allows us to enhance the number of separable components, as shown in Figure 1. Ten analytes are easily resolved in the presence of PVP which can hardly be separated in absence of the polymer.

Stereoselectivity. The impact of three different types of polymers on the stereoselectivity coefficients is shown in Figure 2 as

Table 1. Dependence of the Effective Mobilities of the DBT L-Analytes^a on Type and Concentration of Polymer^b

	no polymer	polymer type						
		PVP ^c			PEG ^c		PAA ^c	
		0.5	2.0	3.0	2.0	5.0	1.5	3.0
PheGly	39.5	36.2	27.1	25.9			35.3	33.8
Val	39.0	29.1	28.7	27.4				
Leu	38.8	32.4	28.0	27.5	31.5	24.8	35.1	30.6
Met	37.9	34.0	29.2	30.5				
Gln	37.4	34.0	32.0	30.0				
Phe	36.5	30.5	28.1	26.3	32.1	25.9	34.5	30.0
Trp	38.4	26.4	21.7		29.5	22.8	34.5	27.9
Ser	40.2	32.7	31.6	31.1	33.2	26.2	37.4	32.7
Thr	39.3	34.0	29.4	31.8	33.9	25.4	36.0	31.0
mandelic acid	36.0		25.6	24.3	31.5	24.0	35.7	32.2

^a $\mu_{\text{eff}}^{\text{L}} \times 10^9 \text{ cm}^2 \text{ V}^{-1} \text{ s}^{-1}$. ^b BGE as specified in the Experimental Section. ^c Polymer concentrations in % w/v.

a function of the polymer concentration. Stereoselectivity coefficients are calculated as the ratios of the effective mobilities, $\mu_{\text{D}}/\mu_{\text{L}}$, where D and L indicate the diastereomer carrying the D and L amino (or hydroxy) acid, respectively. The pH was adjusted to 5.8, where fairly complete dissociation of the carboxylic groups of the analytes can be assumed and where selectivity effects resulting from polymer-induced pK_{a} shift can widely be excluded. The results obtained with PVP have been discussed in a previous paper² and are repeated here to allow a direct comparison of polymer-type related effects. PVP (Figure 2a) affects the stereoselectivity coefficients of aliphatic and aromatic amino acid DBT

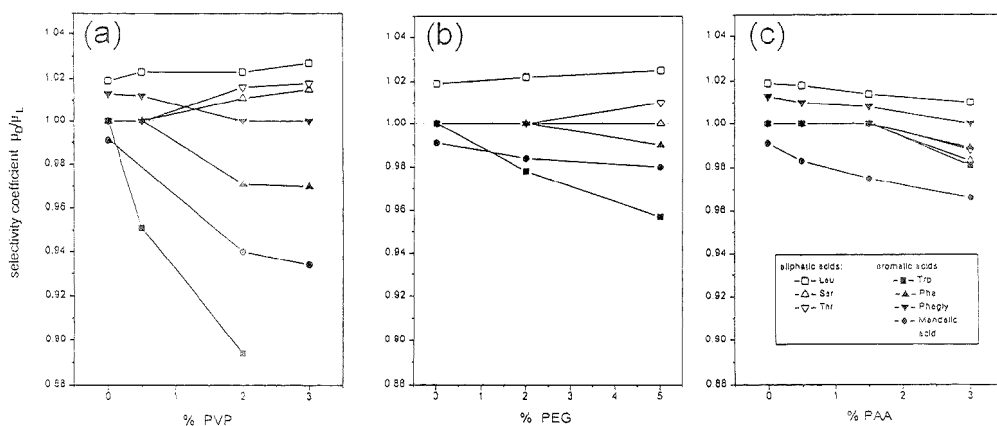


Figure 2. Stereoselectivity coefficients of various DBT-derivatized aliphatic and aromatic α -amino acids and mandelic acid as a function of the concentration (% w/v) of polymer in the BGE: (a) PVP-15, (b) PEG-20 000, and (c) PAA. Electrophoretic conditions as specified in the Experimental Section; pH 5.8.

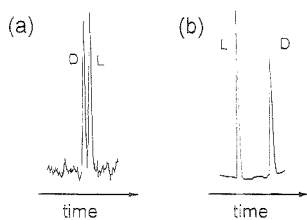


Figure 3. Electropherograms of (a) DAT-derivatized DL-Trp and (b) DBT-DL-Trp in the presence of PVP in the electrolyte solution. Composition of the BGE: aqueous buffer solution, 30 mM sodium phosphate, pH 5.8; (a) 6% and (b) 2% (w/v) PVP. Migration times: (a) 12.93 and 13.14 min; (b) 13.96 and 15.62 min. All other experimental conditions as in Figure 1.

derivatives in opposite direction. The D-analytes of the aromatic acids are more strongly retained by the polymer in all instances. The alteration of stereoselectivity is found to be considerably stronger for most of the aromatic acids than for aliphatic ones. With PEG (Figure 2b), essentially the same pattern is observed as with PVP, i.e., the stereoselectivity coefficients of aliphatic and aromatic amino acid derivatives are affected in opposite direction, although the strength of this effect is significantly less, even at a polymer concentration of 5% (w/v). With PAA (Figure 2c), however, stronger retardation of the D-analytes was found for aliphatic as well as aromatic amino (and hydroxy) acids. The strength of the polymer's effect on selectivity coefficients is comparable to that of PEG, i.e., less than PVP. Due to the differing stereospecificity of the polymer's effect, different migration order was found for racemic DBT-threonine depending on the type of polymer added to the BGE.

Separations carried out employing differently substituted derivatizing agents showed that the chemical structure of the *O,O'*-substituents attached to the L-tartaric acid decisively influences the separation factors and even the migration order of the diastereomers. The isomers of DL-tryptophan derivatized by di-*O,O'*-acetyl-L-tartaric anhydride (DAT derivative) showed the opposite migration order from those derivatized by di-*O,O'*-benzoyl-L-tartaric anhydride (DBT derivative), as documented in

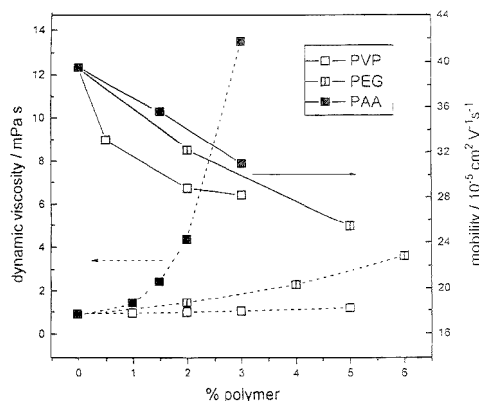


Figure 4. Dynamic viscosity of aqueous polymer solutions and effective mobilities of DBT-L-leucine as a function of polymer type and concentration. Polymers: PVP-15, PEG-20 000, and PAA in aqueous solution; temperature, 25 °C. Electrophoretic conditions as specified in the Experimental Section. Solid lines, effective mobility; broken lines, dynamic viscosity.

Figure 3. The magnitude of the separation factors was very different in these cases.

Viscosity of Polymer Solution and Retention Effect. Data for the dynamic viscosities of the BGE solution were measured at three different temperatures covering polymer concentrations of up to 3% (w/v) (for PAA), 5% (for PVP-15), and 6% (for PEG-20 000) in water. The viscosity data at 25 °C are shown in Figure 4, together with the mobility data of DBT-L-leucine. The increase in viscosity is small when PVP is added, considerably stronger for PEG, and drastic when PAA is added. The concave viscosity versus polymer concentration curves exhibit the steepest slope at higher polymer concentrations. Unlike these curves, the graphs displaying the decrease in the analytes' mobilities caused by the presence of the polymer are either approximately linear (PAA) or concave (PVP and PEG), with a stronger decrease at lower polymer concentrations. PVP, exhibiting the smallest increase

Table 2. Dependence of Stereoselectivity Coefficients^a on the Polymer Chain Lengths at Different Polymer Concentrations^b

	(a) PVP concn of PVP, % (w/v)					
	0	0.5			2.0	
		$M_w = 11\ 000$	$M_w = 25\ 000$	$M_w = 750\ 000$	$M_w = 11\ 000$	$M_w = 750\ 000$
PheGly	1.013	1.012	1.012	1.013	1.00	
Val	1.010	1.014	1.015	1.014	1.023	
Leu	1.019	1.023	1.022	1.022	1.023	
Trp	1.00	3.951	0.938	0.935	0.894	0.895
Ser	1.00	1.00	1.00	1.00	1.011	1.015
Phe	1.00				0.971	0.964
Thr	1.00				1.016	1.019
mandelic acid	0.991				0.940	0.931

	(b) PEG concn of PEG, % (w/v)					
	0	2			5	
		$M_w = 20\ 000$	$M_w = 100\ 000$	$M_w = 200$	$M_w = 20\ 000$	$M_w = 100\ 000$
Phe	1.00	1.00	1.00	1.00	0.990	0.987
Trp	1.00	0.978	0.974	1.00	0.957	0.958
Ser	1.00	1.00	1.00	1.00	1.00	1.00
Thr	1.00	1.00	1.00	1.005	1.010	1.009
mandelic acid	0.991	0.984	0.985	0.989	0.980	0.980

^a Selectivity coefficients are calculated as the ratio of effective mobilities, μ^e/μ^f . ^b BGE as specified in the experimental section.

in viscosity, showed the greatest impact on the mobilities. These data allow the following conclusions: (i) With the linear polymer networks employed, the changes in mobilities of the analytes do not reflect the changes in the solutions' viscosities. (ii) Specific selectivity effects as well as stereospecific effects make clear that analyte-polymer interactions are the cause of reduced mobility of the analytes.

Influence of the Chain Length. Stereoselectivity coefficients were measured at three different chain lengths of linear PVP and PEG polymers. The data are given in Table 2 for linear PVP of molecular masses 11 000 (PVP-15), 25 000 (PVP-25), and 750 000 (PVP-90) g/mol and for linear PEG of molecular masses 200 (PEG-200), 20 000 (PEG-20 000), and 100 000 (PEG-100 000) g/mol. (The corresponding mobility data are given in Table 3.) The molecular masses of the corresponding monomer units are 111 and 44 g/mol for PVP and PEG, respectively.

PVP polymers of different chain lengths exhibited very similar properties in terms of the resolution of the diastereomeric analytes. At a polymer concentration of 0.5% (w/v), DBT-Trp was the only analyte for which a small influence of chain length could be observed. With 2% PVP, this effect was slightly more pronounced but still small (up to about 1% for DBT-mandelic acid). Interestingly, at this polymer concentration, no dependence on chain length was seen for DBT-Trp.

Of particular interest, however, are the data of PEG-200, which is an oligomer with an average chain length of only 4.5 monomer units. It can thus serve as a reference additive, acting like a solvent rather than a polymer. The alterations of selectivity coefficients caused by PEG-200 compared to those of the polymer-free solution were found to be negligible; only for DBT-Thr and DBT-mandelic acid did the presence of 5% PEG-200 effect a small

Table 3. Dependence of Effective Mobilities^a on Polymer Chain Lengths at Different Polymer Concentrations^b

	(a) PVP concn of PVP, % (w/v)					
	0	0.5			2.0	
		$M_w = 11\ 000$	$M_w = 25\ 000$	$M_w = 750\ 000$	$M_w = 11\ 000$	$M_w = 750\ 000$
PheGly	39.5	33.8	31.5	32.7		
Val	39.0	32.2	34.4	35.6		
Leu	38.8	32.4	29.7	33.6		
Trp	38.3	26.4	26.1	26.8	21.7	21.7
Ser	40.2	32.7	36.3	34.3	31.5	34.1
Phe	36.5				26.1	28.9
Thr	39.3				29.4	30.4
mandelic acid	35.6				25.5	28.3

	(c) PEG concn of PEG, % (w/v)					
	0	2			5	
		$M_w = 20\ 000$	$M_w = 100\ 000$	$M_w = 200$	$M_w = 20\ 000$	$M_w = 100\ 000$
Phe	36.5	32.1	30.4	29.8	25.9	25.1
Trp	38.3	29.5	29.7	29.4	22.8	24.2
Ser	40.2	33.2	33.7	31.6	26.2	29.1
Thr	39.3	33.9	35.3	31.8	25.4	28.2
mandelic acid	35.6	31.6	33.0	30.1	24.0	24.1

^a $\mu^e \times 10^6$ cm² V⁻¹ s⁻¹. ^b BGE as specified in the Experimental Section.

change in resolution. With higher chain lengths, significant effects are seen. Apparently, a certain minimum polymer chain length is essential to affect the resolution of the diastereomers; however, significantly above this threshold value, polymer chain length has not much influence on steric resolution. Nonselective retardation of the analytes is found already with PEG-200 as documented in Table 3b.

CONCLUSION

The investigations employing different types of polymers show that retardation of analytes, and in a broad number of cases also stereospecific retardation of diastereomers, is a quite general phenomenon associated with polymeric additives. The data confirm the previous assumption that selectivity of the system is mainly based on free energy contributions responsible for "hydrophobic" behavior and on dipole-dipole as well as π - π and n - π interactions between polymer and analyte. The analogy to chromatographic stationary phases is evident, particularly to the reversed-phase type with certain affinity for aromatic and π -electron-rich structural groups. The retardation induced by the pseudophase allows us to enlarge the effective mobility window accessible for a set of analytes and thus to achieve separation of a much higher number of analytes. This was demonstrated for a sample of five pairs of diastereomeric amino acid derivatives.

The stereodiscriminating effect induced at a certain constant polymer concentration (e.g., 2%) is not equal for different polymers: PVP acts far stronger than PEG and PAA. The ring structures in the polymer thus seem to be advantageous for stereodiscrimination. The differences in migration order found for aliphatic versus aromatic amino acid derivatives with PVP is maintained with PEG, too, although the chemical structures of

the polymers differ widely. On the other hand, PAA does not exhibit such different migration order. The influence of polymer chain length on stereoselectivity is marginal. The aromatic moieties in the DBT group of the derivatization reagent lead to improved separation, accompanied by inversion of migration order, compared to the short aliphatic group in the corresponding DAT derivatives.

A comparison of the viscosity effects induced by the three different polymers again underlines that reduction of the analyte mobility is not a consequence of an increase in viscosity but rather a result of intermolecular interactions similar to "adsorption onto a pseudophase". The most pronounced effect related to the polymer was found for PVP, where the smallest viscosity increase was observed. This polymer can thus be favored in the practical use as the BGE additive that allows selectivity enhancement and

stereodiscrimination for diastereomeric analytes, particularly in those cases where aromatic moieties are present.

ACKNOWLEDGMENT

Financial support of this work by the Italian Ministry of Foreign Affairs and the Austrian Academic Exchange Service within the framework of the scientific technical agreement between Italy and Austria (project no. 89) is acknowledged. The authors thank G. Ribitsch, University Graz, Austria, and Rheocoll Co. for the kind permission to use the microviscosimeter.

Received for review March 28, 1995. Accepted August 18, 1995.*

AC950310D

* Abstract published in *Advance ACS Abstracts*, September 15, 1995.

XPS and TOF-SIMS Microanalysis of a Peptide/ Polymer Drug Delivery Device

C. M. John,[†] R. W. Odum,^{*†} L. Salvati,[§] A. Annappagada,[§] and M. Y. Fu Lu[§]

Department of Pharmaceutical Chemistry, School of Pharmacy, University of California, San Francisco, California 94143-0446, Charles Evans & Associates, Redwood City, California 94063, and Abbott Laboratories, Abbott Park, Illinois 60064-3500

The localization of a peptide drug dispersed in a solid matrix of hydroxypropyl cellulose (HPC) was determined at micrometer lateral resolution using secondary ion mass spectrometry (SIMS)/ion microscopy. Leuprolide formulated as a sustained release drug delivery device has been selected as a model compound for this investigation. One key facet of this study was to attempt to understand the distribution and ultimate bioavailability of the peptide dispersed in an inert polymer matrix. The results reported in this paper demonstrate that the lateral distribution of leuprolide along the surfaces of cross sections prepared from different polymer formulations is different. Ion microscopy directly measures the lateral distribution of protonated molecular ions as well as specific fragment peaks and provides a direct method of determining peptide distributions in polymers. Ion images of leuprolide dispersed in HPC demonstrate that the peptide distribution is critically dependent on polymer composition. The mass spectrometry results augment quantitative X-ray photoelectron (XPS) measurement of C and N levels in different polymer/peptide formulations. The combination of XPS and TOF-SIMS techniques provides a powerful method for determining the distribution of peptides in polymer matrices.

The localization of organic molecules in biological tissues and biopolymers is becoming increasingly important in pharmaceutical research and development.¹ For example, the ability to localize selected pharmaceutical compounds or metabolites within specific regions of a tissue or organ can provide tremendous advantages over existing methodologies for development and evaluation of drug delivery and efficacy.² Biomaterials utilized as artificial tissue, skin, prosthetic devices, and intraocular lens are typically synthetic polymers with some form of biocompatible surface layer.³ The ultimate acceptance or rejection of the artificial material by an organism depends on the compatibility of the implant surface with the cells with which it makes intimate contact.³

Another important, practical application of biopolymers is their use as solid media for innovative time-release pharmaceutical

formulations.⁴ For example, the development of protein and peptidic drugs that can regulate a number of physiological processes such as growth, immune responses, blood pressure, blood clotting, and bone calcification has been limited by the necessity of administering these drugs by injection since oral administration is generally ineffective.⁵ Polymer matrices containing peptidic drugs could provide a highly efficient method for drug administration. However, the polymer matrices must have well-characterized drug release rates, and of course, the polymers must be biocompatible.

The work reported in this paper illustrates one of the first examples of direct molecular microanalysis of a medicinal patch in which the distribution of a peptide is determined using molecular imaging secondary ion mass spectrometry. This study was performed on samples containing the drug leuprolide, dissolved in a matrix of hydroxypropyl cellulose (HPC). Leuprolide is an orally inactive synthetic nonapeptide analog of ovine or porcine gonadotropin-releasing hormone (GnRH), which is used as an antineoplastic agent in the treatment of endometriosis and precocious puberty. The structure of leuprolide is 5-oxoPro-His-Trp-Ser-Tyr-D-Leu-Leu-Arg-Pro-NHC₂H₅. Leuprolide is more potent than GnRH and differs from the naturally occurring hormone by the presence of the D isomer of leucine at position 6 and the ethylamide which replaces the glycine at position 10. A research effort was initiated to design a device that can be placed in direct contact with a biological membrane, and hence, the drug distribution in the polymer matrix is a critical parameter in these experimental devices.

Time-of-flight secondary ion mass spectrometry (TOF-SIMS) provided a direct method of determining the leuprolide distribution along cross sections of different peptide/polymer blends. TOF-SIMS localized the distribution of protonated molecular ions, (M + H)⁺, and fragment ions of leuprolide at lateral resolutions on the order of 3-5 μm along cross sections 100 μm or more thick. The cross-sectional distributions of the drug were found to be strongly dependant on the drug-to-polymer ratio. The addition of 12% oleic acid to the drug/HPC blend significantly changed the axial distribution of leuprolide compared to formulations that contained only leuprolide and HPC. X-ray photoelectron spectroscopy (XPS) was also employed in this study to measure the atomic concentrations and functional forms of C, O, and N on the sample surfaces.

[†]University of California,
[‡]Charles Evans & Associates,
[§]Abbott Laboratories.

(1) Kasedmo, B.; Lausmaa, J. In *Surface Characterization of Biomaterials*; Ratner, B. D., Ed.; Elsevier: New York, 1988; Chapter 1.
(2) Prescott, L. F. In *Novel Drug Delivery and Its Therapeutic Application*; Prescott, L. F., Nimmo, W. S., Eds.; John Wiley & Sons: New York, 1989; Chapter 1.
(3) Ratner, B. D. *J. Biomed. Mater. Res.* 1993, 27, 837.

(4) Kelly, P.; Atkins, T. W. In *Microencapsulation of Drugs*; Whately, T. L., Ed.; Harwood Academic Publishers: Chur, Switzerland, 1991; p 33.
(5) Aungst, B. J. in *Drug Permeation Enhancement: Theory and Applications*; Hsieh, D. S., Ed.; Marcel Dekker, Inc.: New York, 1991; p 323.

Table 1. Composition of Leuprolide/HPC Films

sample	leuprolide (mg)	HPC (mg)	oleic acid (mg)
A1	3.0	6.0	0.0
B1	1.0	6.0	0.0
C1	0.5	6.0	0.0
O1	1.0	6.0	1.0

EXPERIMENTAL SECTION

Table 1 lists the formulations of the leuprolide/HPC films investigated in this study. The films were prepared using 2% by weight HPC in methanol solutions, and all films contained 6 mg of HPC. The films were prepared by pipeting 100 μ L of the dispersions onto a clean PTFE substrate and air-drying at room temperature.

XPS analyses were performed on both air and substrate surfaces of the cast films. These latter surfaces were exposed by removing the films from the substrates. TOF-SIMS analyses were performed on both the air and substrate surfaces as well as cross sections of the polymer mixtures. Cross-sectional thickness ranged between 100 and 200 μ m, and cross sections were prepared by shock freezing the samples in liquid nitrogen followed by freeze fracturing. Frozen sections were warmed to room temperature prior to analysis. Reference data was acquired for both leuprolide and HPC. Leuprolide was dissolved in ethanol and solution cast onto an acid-etched Ag substrate. The reference HPC film was cast onto a PTFE substrate using the same procedure described above for the drug patches.

XPS spectra were collected on a Perkin-Elmer 5600 XPS/SIMS instrument. XPS scans were acquired using a monochromatic Al X-ray (Al K α = 1486.6 eV) source to minimize radiation damage to the sample and to optimize the instrumental energy resolution in the analysis. A low-energy electron gun was used to minimize sample charging. XPS data were acquired in both low-resolution survey scans (0–1100 eV) and high-resolution multiplex scans for each of the elements detected on the surface region.

TOF-SIMS spectra and ion images were acquired using the Charles Evans & Associates TFS time-of-flight secondary ion mass spectrometer. Secondary ions are produced by a pulsed primary ion beam and are accelerated to a fixed kinetic energy before entering the time-of-flight drift region of the mass spectrometer. TOF-SIMS mass analysis measures the time required for secondary ions to travel the distance between the sample surface and an ion detector.⁶ Low primary ion doses were used to minimize chemical alteration of the surface during the analysis. Typical primary ion doses were 10¹² ions/cm², which nominally consume 0.1% of the top monolayer. Low-dose conditions produce elemental, molecular, and/or structurally significant fragment ions from the near-surface region from essentially intact inorganic and organic solids.

TOF-SIMS mass spectra and ion images were acquired using an ion microprobe technique in which a pulsed, microfocused primary ion beam is rastered over the sample surface. Secondary ion images are acquired by synchronizing the ion arrival times (ion masses) with the position of the primary ion beam in the raster. This raster imaging technique is similar to those employed in scanning electron microscopy (SEM),⁷ and TOF-SIMS images

Table 2. Atomic Percent of O, N, and C Determined by XPS

sample	O (air)	O (sub)	N (air)	N (sub)	C (air)	C (sub)
HPC (control)	34.8	29.8	nd ^a	nd ^a	65.2	60.0
A1	23.0	33.8	12.6	0.6	64.1	62.1
B1	28.0	32.6	7.1	1.9	64.6	63.9
C1	29.9	31.8	4.9	2.2	63.1	65.2
O1	25.9	22.9	7.4	9.1	65.6	66.6

^a nd, not detected.

contain the distribution of mass-resolved secondary ions within the image field.⁸ A liquid metal ion gun (LMIG) employing a microfocused ⁶⁹Ga⁺ beam was used in these microbeam analyses. The ⁶⁹Ga⁺ beam used in these experiments was focused to a 0.5 μ m diameter spot size determined using a copper grid having 25 μ m diameter grid bars mounted on an aluminum substrate. Submicrometer image resolutions were validated from both the grid edges and small adventitious particles. The lateral resolution of SIMS ion images depend on the spot size of the primary ion beam and the topography of the sample surface. The image resolutions reported below ranged between 3 and 5 μ m and this factor of 6–10 decrease in image resolution with respect to the primary beam spot size is due primarily to sample topography.

Mass resolution in these experiments was typically >1000 measured at mass 41. Typical primary ion impact energies were 21.5 (+ions) and 28.5 keV (–ions). Sample surfaces were flooded with pulses of low-energy electrons (average impact energies, a few electronvolts) between primary ion pulses which minimized sample charging during the analysis.

All ion images were acquired into 256 \times 256 pixel areas at two different image magnifications corresponding to image areas of 150 \times 150 μ m² to 250 \times 250 μ m². These image fields contain 1.7 and 1.0 pixels per μ m, respectively. The secondary ion intensities within each image are the integrated secondary ion counts at each pixel location. Thus, the intensity scale in the images directly represents the number of ion counts in that image.

A positive ion fast atom bombardment (FAB) mass spectrum of leuprolide was recorded on a Finnigan MAT MAT95 mass spectrometer using a glycerol/thioglycerol matrix.

RESULTS AND DISCUSSION

XPS Results. Table 2 summarizes the atomic surface concentrations measured by XPS, and the two sets of values correspond to the polymer/air interface and polymer/substrate surfaces. The data show large variations in the nitrogen levels of the two surfaces, and since the peptide is the only significant source of N in the mixtures, the data indicate that the two surfaces have different peptide concentrations. In contrast to this behavior, drug/polymer films containing oleic acid show higher N concentrations at the substrate surface. For example, although samples O1 and B1 have similar N concentrations at the air surface; the N levels at the substrate surface of sample O1 is >4 times the value observed for sample B1. If the drug were uniformly distributed through the HPC matrix, the observed N concentrations would have been 7% for sample O1 and 10% for sample B1.

(6) John, C. M.; Chakel, J. A.; Odom, R. W. In *Secondary Ion Mass Spectrometry-SIMS VII*; Benninghoven, A., Janssen, K. T. F., Tumpner, J., Werner, H. W., Eds.; Wiley & Sons: New York, 1991; p 657.

(7) Goldstein, J. I.; Newbury, D. E.; Echlin, P.; Joy, D. C.; Fiori, C.; Lifshin, E. *Scanning Electron Microscopy and X-Ray Microanalysis*; Plenum Press: New York, 1984.

(8) Schueler, B. *Microsc. Microanal. Microstruct.* 1992, 3, 1.

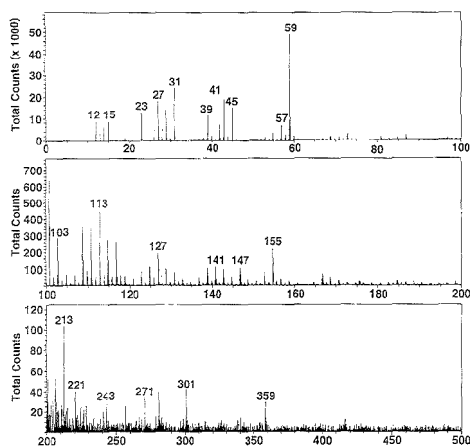


Figure 1. Positive ion TOF-SIMS spectrum of the polymer/air surface of pure HPC (control). Prominent Na^+ and K^+ ion peaks and apparent polymer fragment ion peaks, such as those at m/z 59, 155, 213, 301, 359, are detected. Some of these fragment ions are likely sodiated species.

The differences between the calculated and measured values suggest that leuprolide is nonuniformly distributed and the oleic acid significantly affects the drug distribution.

TOF-SIMS Mass Spectra. A positive ion TOF-SIMS spectrum of a HPC control sample shown in Figure 1 contains a number of peaks characteristic of hydroxypropyl cellulose including peaks at mass-to-charge ratios (m/z) 31 (CH_3O^+) and 45 ($\text{C}_2\text{H}_5\text{O}^+$) and a peak at m/z 59 corresponding to $\text{C}_5\text{H}_7\text{O}^+$. The spectrum is displayed out to m/z 500, and no peaks were observed above this mass. However, there are a number of low-intensity peaks between m/z 100 and 500 including peaks at 101, 113, 127, 141, 155, 213, 271, 301, and 359 Da. Several of the peaks in the m/z 100–200 range are separated by 14 Da, indicating probable loss of a methylene (CH_2) fragment. If these ions are fragments of hydroxypropyl cellulose, they are not produced by simple bond cleavages. In addition to these organic peaks, a series of peaks characteristic of siloxanes such as poly(dimethylsiloxane) are also detected in this spectrum. This siloxane has the general formula $[-(\text{CH}_3)_2\text{SiO}-]_n$, and positive ions produced from this organic silicone include peaks at 73, 147, 207, 221, and 281 Da.⁹ Siloxanes are commonly observed surface contaminants and are typically introduced by exposing the surface to materials containing silicones or silicone contamination.

Figure 2 is a positive ion TOF-SIMS spectrum produced from a solid residue of leuprolide dispersed on an Ag substrate. The protonated molecular ion, $(\text{M} + \text{H})^+$, is readily apparent at 1210 Da. Leuprolide molecular ions formed by cationization with Ag^+ produce peaks at m/z 1316 and 1318 corresponding to the molecular adduct with the two Ag isotopes. In addition, ions corresponding to $(\text{M} - \text{H} + \text{Ag})^{2+}$ are detected at m/z 1315 and 1317. The lower mass region of the spectrum also contains a number of peaks characteristic of fragments of leuprolide including peaks at m/z 353 and 466, which are discussed in more detail below.

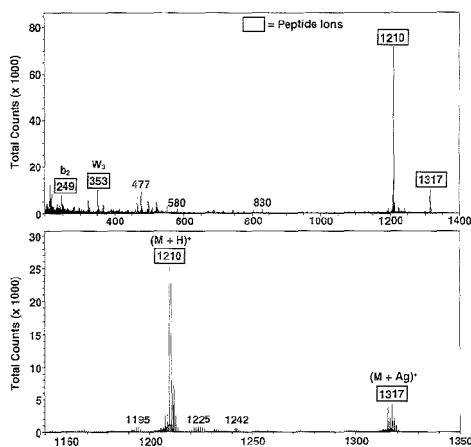


Figure 2. Positive ion TOF-SIMS spectrum of leuprolide on a gold substrate. Protonated molecular ions are apparent at m/z 1210 as are Ag cationized ions at m/z 1316 and 1318.

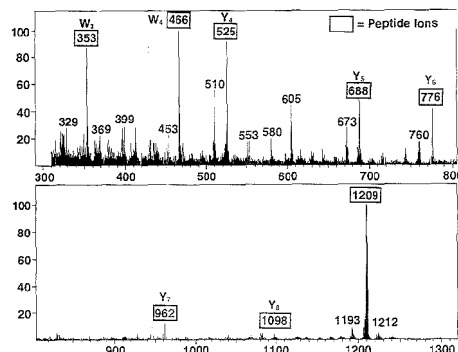


Figure 3. Positive ion FAB spectrum of leuprolide in glycerol. Matrix ion peaks can be observed at m/z 369, 461, and 553. A prominent protonated molecular at m/z 1210 and a series of y -ion fragments can be seen. Two w_n ion peaks are detected at m/z 353 and 466.

Figure 3 is a FAB spectrum of leuprolide dissolved in a glycerol/thioglycerol matrix. Molecular and protonated molecular ions detected at m/z 1209 and 1210 are the most intense peaks, and a series of C-terminal y_n ions are also detected at 525, 688, 776, 962, and 1098 Da corresponding to the series y_4 – y_8 , respectively.^{10,11} In addition, peptide molecules form w_n fragments by loss of substituents located on β carbons of amino acid residues,^{11,12} and the detection of w_n ions provides a direct method of distinguishing leucine and isoleucine residues. Two abundant leuprolide fragments formed as C-terminal w_n ions (w_3 and w_4) are observed at m/z 353 and 466 in this FAB spectrum. The presence of basic amino acid residues such as arginine near the C-terminus favor the formation of C-terminal ions in FAB and liquid secondary ion mass spectrometry (LSIMS) spectra.^{12,13}

(9) Briggs, D.; Brown, A.; Vickerman, J. C. *Handbook of Static Secondary Ion Mass Spectrometry*; John Wiley & Sons: Chichester, UK, 1989.

(10) Røpstorff, P.; Fohlman, J. *Biomed. Mass Spectrom.* **1984**, *11*, 601.

(11) Biemann, K. In *Methods in Enzymology*; McCloskey, J. A., Ed.; Academic Press: San Diego, 1990; Vol. 193, pp 455–479.

(12) Johnson, R. S.; Martin, S. A.; Biemann, K.; Stults, J. T.; Watson, J. T. *Anal. Chem.* **1987**, *59*, 2621.

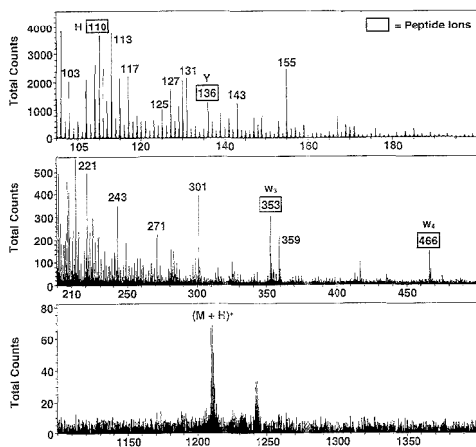


Figure 4. Positive ion TOF-SIMS spectrum of a cross section of a polymer film composed of 6 mg of HPC and 3 mg of leuprolide (sample A1). Peaks observed in TOF-SIMS spectra of the pure polymer are detected at m/z 101, 113, 127, 155, 213, 271, 301, and 359. A number of peptide fragment ions can also be observed as indicated along with protonated molecular ion at m/z 1210.

However, C-terminal w_x ions such as w_3 and w_4 are not generally observed in FAB or LSIMS spectra unless the molecular ion undergoes high-energy collision-induced dissociation (CID).^{11,12,14–16}

Positive ion TOF-SIMS spectra of cross sections through the polymer/air surfaces of films containing leuprolide only (sample A1) and leuprolide + oleic acid (sample O1) are illustrated in Figures 4 and 5, respectively. Protonated molecular ions are detected in both spectra along with several leuprolide fragment ions detected in FAB spectra of leuprolide/glycerol mixtures. Peaks for $(M + H)^+$ and $(M + Na)^+$ ions are detected at m/z 1210 and 1232, respectively, in Figure 5. A protonated molecular ion peak can also be observed in Figure 4 along with a higher mass adduct at 1242 Da. The identity of this adduct is not certain, but the ion mass is consistent with an oxidized species $(M + O_2 + H)^+$. Peaks are also detected in both TOF-SIMS spectra for the w_3 and w_4 ions observed in the FAB spectrum. The intensities of these two w_x ions are approximately equal to the molecular ion intensity. In addition, peaks for sodium adducts of the two w_x fragment ions are detected at m/z 375 and 488, respectively. Two z_n ion peaks are also detected in these spectra, z_2 at 284 Da and z_3 at 397 Da. Two peaks for N-terminal ions, the b_2 and possibly b_1 ions, are also observed at m/z 249 and 112 in the spectrum of the sample O1. Immonium ions having the general formula $(NH_2=CHR)^+$, where R is the amino acid side chain¹⁰ or immonium-like ions¹⁷ corresponding to His, Trp, Tyr, and Arg, are labeled with the single letter abbreviation for the amino acid residues. The peak at m/z 112 could be immonium-like ions from

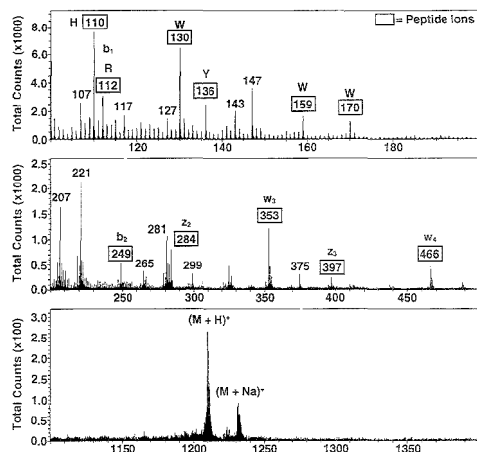


Figure 5. Positive ion TOF-SIMS spectrum of a cross section of a polymer film composed of 6 mg of HPC and 1 mg each of oleic acid and leuprolide (sample O1). The peaks associated with the HPC polymer are less intense and the peptide-related peaks are more intense relative to the spectrum of sample A1 shown in Figure 4. The protonated molecular ions of leuprolide are more abundant in the spectrum of sample O1 as well.

Arg¹⁷ or b_1 ions containing the N-terminal pyroglutamic (or 5-oxoproline) residue.

More intense peptide peaks are produced from TOF-SIMS spectra of leuprolide in mixtures of HPC and oleic acid. Figure 6 illustrates the normalized relative intensity, expressed as percent of the total ion intensity in the spectra, for the 12 most abundant peptide peaks produced from these two formulations. Two spectra were averaged for the leuprolide and HPC material while three spectra were averaged for the leuprolide + oleic acid sample.

The percent relative standard deviation (% RSD) for these data varied between 5 and 30% for most of the peaks. Interestingly, although the average total intensity in sample O1 spectra is only 50% higher than the average intensity in sample A1 spectra, the relative intensity of peptide peaks produced from the leuprolide + oleic acid samples is 3 times larger. This larger relative intensity is especially noteworthy since the bulk leuprolide concentration in the O1 samples is $1/3$ the bulk leuprolide concentration in the A1 samples. Thus, the addition of oleic acid to the HPC matrix has increased the ionization efficiency of the peptide molecular and fragment peaks by 1 order of magnitude. If the ion intensity is proportional to peptide surface concentration, the addition of oleic acid appears to have significantly increased the leuprolide concentration over the cross section of the polymer. The XPS data (Table 2) do not demonstrate an increase in leuprolide concentration for the mixture containing oleic acid. In fact, these data indicate that the surface concentration of leuprolide is higher on the A1 sample. The discrepancy between TOF-SIMS and XPS data is best explained in terms of the analytical zones for each analysis technique. XPS signals were produced from the top 10 nm of the air-exposed and substrate exposed surfaces of the mixtures while the TOF-SIMS mass spectra are produced from the top one to two monolayers of the polymers along cross sections of the samples. Thus, the differences in relative concentration of leuprolide between the XPS and TOF-SIMS data

(13) Johnson, R. S.; Martin, S. A.; Biemann, K. *Int. J. Mass Spectrom. Ion Processes* **1988**, *86*, 137.

(14) Martin, S. A.; Biemann, K. *Int. J. Mass Spectrom. Ion Processes* **1987**, *78*, 213.

(15) Naylor, S.; Moneti, G. *Rapid Commun. Mass Spectrom.* **1989**, *3*, 405.

(16) Stults, J. T. In *Biomedical Applications of Mass Spectrometry*; Suelter, C. J., Watson, J. T., Eds.; John Wiley & Sons: New York, 1990.

(17) McCormack, A. L.; Somogyi, A.; Dongr, A. R.; Wysocki, V. H. *Anal. Chem.* **1993**, *65*, 2859.

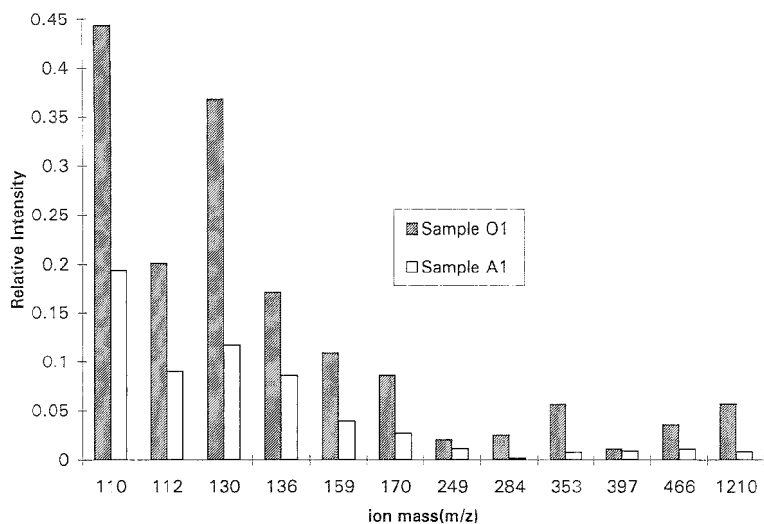


Figure 6. Graph of the intensities, normalized as a percent of the total ion intensity of the spectrum, of the peptide peaks for samples A1 and O1. The graph illustrates the greater prominence of the peptide peaks in the oleic acid-containing device, sample O1, compared to the spectrum of sample A1. The greater relative abundance of low-mass fragment ions such as those at m/z 110, 112, 130, and 136 compared to higher mass ions such as the molecular ions at m/z 1210 is also illustrated.

obviously relates to the differences in analysis locations and sampling depths from which the respective data were acquired. The most important observation in this research relates to the differences in relative concentration of leuprolide along cross sections of the two polymer blends.

Numerous peaks detected in the spectrum of the pure HPC polymer are also observed in the spectra of the polymer mixed with leuprolide. For example, spectra of the leuprolide/HPC mixture contain peaks at m/z 113, 127, 155, 243, 271, 301, and 359 which, although detected on sample O1, are not as prominent as those in the spectra of sample A1. The relative intensities of these low-mass HPC peaks are 5–10 times larger for sample A1 compared to sample O1. These observations strongly suggest that the near-surface chemistry of the two formulations is significantly different. For example, oleic acid could act as a surface coating if it migrated from the bulk polymer onto the surface and this coating could suppress the signals from HPC. Although oleic acid may be concentrated on the surface of sample O1, the surface is not highly enriched in oleic acid since negative ion spectra of the leuprolide + oleic acid samples have an $(M - H)^-$ ion for oleic acid at m/z 281.3 which constitutes only 0.1% of the total negative ion intensity.

The spectra of the leuprolide + oleic acid samples also contain $3\times$ higher intensities for the various PDMS peaks than the other HPC samples, indicating that the O1 samples have been exposed to siloxanes. The ions detected at m/z 221 could contain both siloxane and the a_2 fragment ions of leuprolide. A siloxane coating could suppress ionization of the HPC peaks, but this coating should also reduce the yield of leuprolide peaks. However, since the oleic acid samples produce larger relative abundances of peptide peaks, the data suggest that oleic acid has altered the surface chemistry of the solid. This change could simply be an increase in the surface density of H^+ from the acid, or it could be a more complex process involving selective migration of the

leuprolide to the polymer surface. Acid is commonly added to the liquid matrix in FAB analyses of peptides to enhance the molecular and fragment ion intensities, and hence, it is likely that the oleic acid simply increases the number of protons at the solid surface.

In summary, TOF-SIMS spectra of sample O1 have the most intense peptide peaks while spectra of the polymer mixed with only leuprolide produce intense peaks characteristic of HPC. Only a few of the peaks for the y_n ion series observed in FAB analysis of leuprolide are detected in TOF-SIMS analysis of leuprolide in HPC, and the relative intensities of protonated molecular ions of leuprolide are considerably lower in the TOF-SIMS spectra of the polymer/peptide mixture than in FAB spectra. The most dramatic differences between the FAB data of leuprolide dissolved in glycerol and the TOF-SIMS spectra of leuprolide in the solid matrices are the greater relative intensities of the w_n and w_1 ions in the TOF-SIMS. These peaks have intensities comparable to the protonated molecular ion. Side-chain cleavage to form w -type fragment ions was recently observed in collisions of peptide ions with solid surfaces,¹⁷ and the mechanisms of bond breakage in surface-induced dissociation are probably very similar to those induced by ion beam sputtering of a solid. Although the primary ion/solid surface impact energy in these TOF-SIMS analyses is much higher than the center of mass collision energies employed in the surface-induced dissociation study, a sputtering ion beam initiates a collision cascade (bond breakage zone) within the solid and the beam energy is rapidly dissipated.¹⁹ Thus, at distances several atomic diameters from the initial impact point, the average

(18) Falick, A. M.; Hines, W. M.; Medzihradsky, K. F.; Baldwin, M. A.; Gibson, B. W. *J. Am. Soc. Mass Spectrom.* 1993, 4, 882.

(19) Sigmund, P. In *Sputtering by Particle Bombardment*; Behrisch, R., Ed.; Springer-Verlag: Berlin, 1981; Vol. 1.

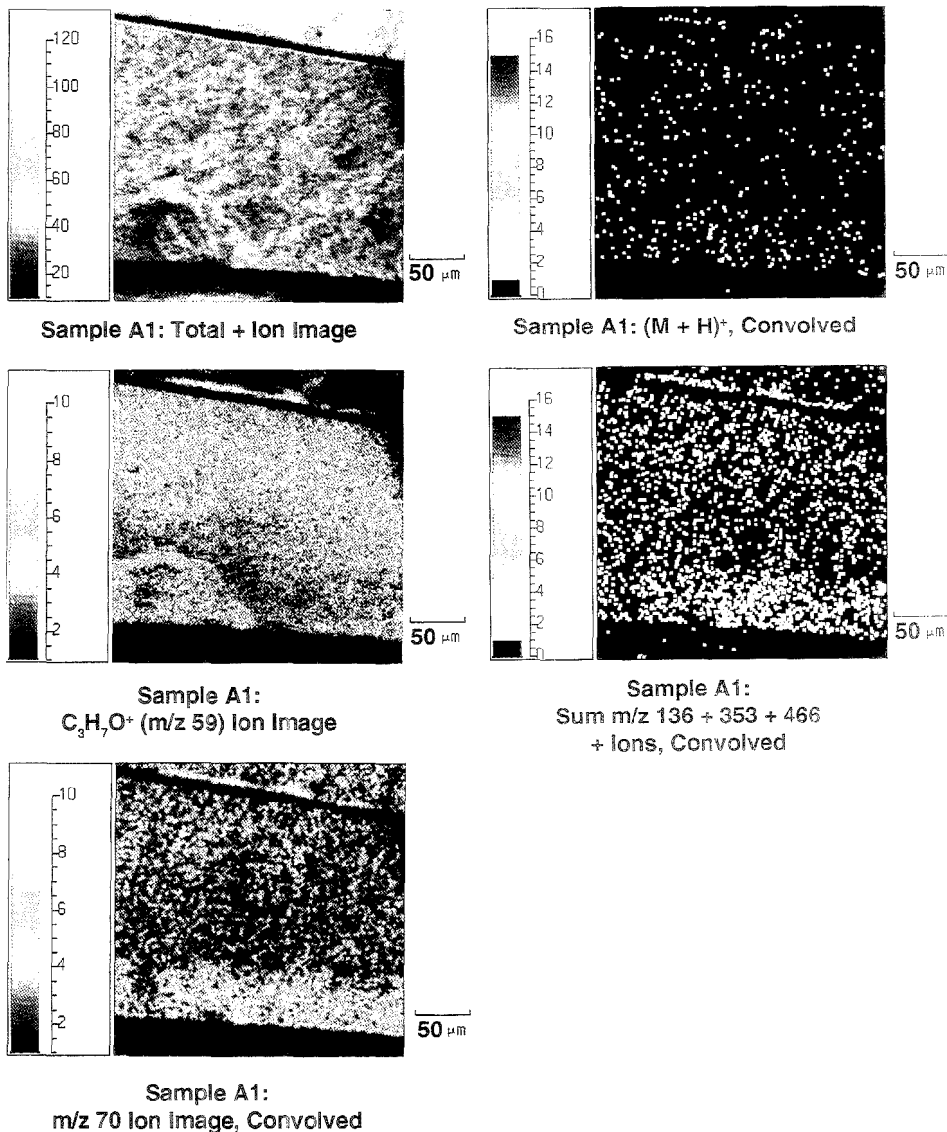


Figure 7. Five positive ion images acquired simultaneously from one region on a cross section of sample A1: a total ion image (A, top left); an image (B, middle left) of a polymer fragment ion, C₃H₇O⁺ at *m/z* 59; a convolved image (C, bottom left) of immonium-type¹⁸ arginine-derived C₄H₉N⁺ ions at *m/z* 70; a convolved image (D, top right) of the protonated molecular ions; and a convolved and summed image (E, middle right) of tyrosine-derived immonium ions at *m/z* 136 and w₃ and w₄ ions at *m/z* 353 and 466, respectively. These images clearly reveal the nonuniformity in the leuprolide distribution, which is more concentrated on the polymer/air side of the device on the bottom of the images. The dark regions at the top and bottom are gaps between the cross sections and the metal jaws of the cross-sectional holder. Some of the ion abundance at *m/z* 59 is likely due to immonium-related ions from arginine as are ions observed at *m/z* 100 and 112.¹⁸

kinetic energy of the recoiling target atoms is sufficiently low to permit desorption of intact molecular ions or large-mass fragment ions. A fraction of these sputtered or desorbed species could be ionized, thus giving rise to the secondary ion signals.²⁰

(20) Williams, P. *Appl. Surf. Sci.* 1982, 13, 241.

TOF-SIMS Ion Images. Ion images were acquired from cross sections of the two samples containing leuprolide. The cross sections were mounted in specially designed metal holders, and samples were positioned horizontally such that the Teflon side of the devices was at the top of the images. The orientation of these cross sections was confirmed by the localization of F⁻

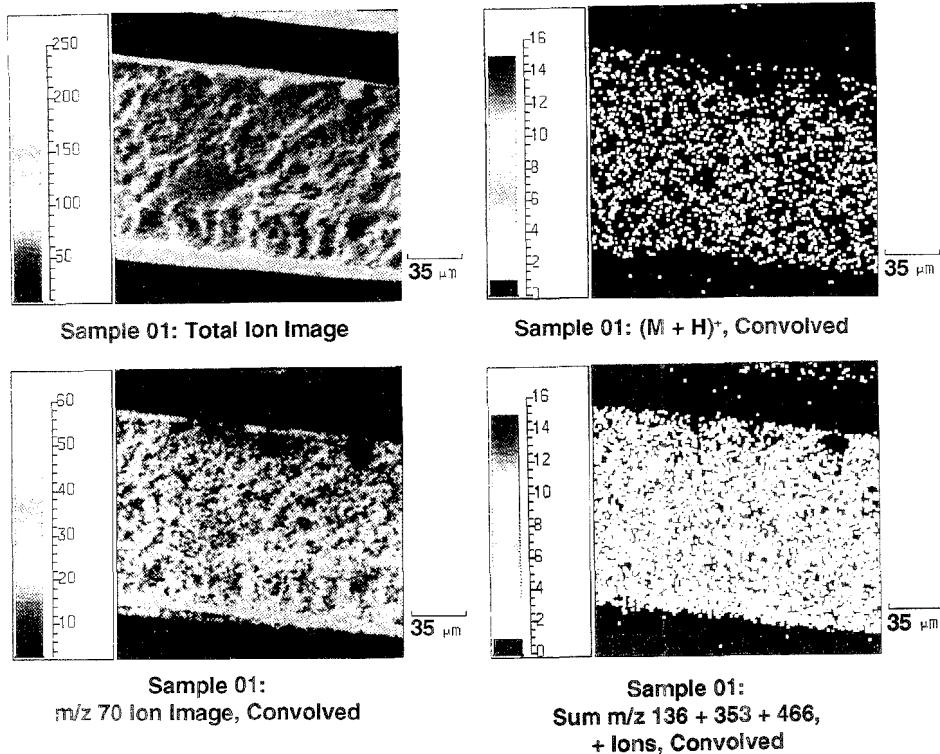


Figure 8. Four positive ion images acquired simultaneously from one region on a cross section of sample O1: A total ion image (A, top left); a convolved image of immonium-related ions from arginine (B, bottom left); a convolved image (C, top right) of protonated molecular ions; and a convolved image (D, bottom right) of summed tyrosine-derived immonium ions, w_3 ions at m/z 353 and w_4 ions at m/z 466 similar to that shown in Figure 7E. The relative uniformity of the distribution of leuprolide through the cross sections of sample O1 containing oleic acid is clearly illustrated (compare Figure 7E).

and other negative ions produced from the Teflon substrate.

Two different regions of sample A1 were analyzed in the positive ion mode, and one region was analyzed in the negative ion mode. Three different regions were analyzed on sample O1, and one of these regions was also analyzed in the negative ion mode. The different regions on each device produced very similar results. Images of five positive ions produced from sample A1 are illustrated in Figure 7; all of these images were acquired from a single region on the cross section. Four different ion images from sample O1 are presented in Figure 8, and these images were also acquired from one region on this sample.

Total secondary ion images of the cross sections illustrated in Figures 7A and 8A reveal the topographic features of the surfaces on a microscopic scale. The top regions of the images correspond to the polymer/substrate side, and the bottom regions are the polymer/air interface of the samples. The dark regions at the top and bottom are gaps between the cross sections and metal jaws of the cross section holder. Both images exhibit surface roughness approximately 2–4 μm in depth. This roughness is probably the result of the freeze-fracturing technique used to prepare the cross sections. The images also indicate that the sample thickness is slightly different for the two materials, where sample A1 is ~ 200 μm thick while sample O1 is 120 μm thick.

The relatively uniform intensity distributions across these samples indicate that the sample topography does not seriously effect ion emission. In addition, the total ion images suggest uniform composition of the major constituents (C, H, O) along the top monolayers of the cross sections. The total ion intensity in the image of sample A1 was 2.8×10^6 counts while the total intensity in sample O1 was 3.6×10^6 counts.

Images of the $\text{C}_3\text{H}_7\text{O}^+$ ions at m/z 59 (Figure 7B) are diagnostic for the hydroxypropyl cellulose polymer even though a fraction of the ions at this mass could be immonium-type ions produced from arginine residues of the peptide.¹⁸ Since other immonium-type ions from arginine (at m/z 87, 100, and 112¹⁸) have very low intensities in this spectrum, immonium ions probably make only a small contribution to the m/z 59 signal. The intensity distributions of $\text{C}_3\text{H}_7\text{O}^+$ are uniform along the surfaces of both samples and its intensity is a factor of ~ 10 higher for sample A1.

The relative distribution of leuprolide in the two cross sections is revealed in the convolved ion images shown in Figure 7C–E for sample A1 and Figure 8B–D for sample O1. These images have been convolved using a 3×3 pixel kernel at unit weighting for each element. Immonium and immonium-type ions from the

C-terminal proline and arginine residues of sample A1 are illustrated in Figure 7C. This image clearly shows a nonuniform ion intensity distribution with a greater relative concentration of the peptide at the polymer/air interface of the cross section, which corroborates the XPS results (Table 2). Nonuniform distributions of other peptide peaks on the sample A1 cross section are revealed in the protonated molecular ion image in Figure 7D and the summed ion image shown in Figure 7E. This latter image was created by summing the images of the immonium ion for tyrosine at m/z 136 with images of the w_3 (m/z 353) and w_4 (m/z 466) ions. The intensity distributions for each of these fragments were similar, and hence, summing the signals produces a more intense image, which better illustrates the distribution of the leuprolide. Imaging low-mass fragment ions could play a significant role in TOF-SIMS imaging of large peptides or proteins since these more massive structures often have low molecular ion yields which produce low contrast images. However, lower mass fragment ions of peptides or proteins are normally produced at adequate intensities for ion imaging, and these fragment ions can be used to determine the surface distribution of parent molecules.

Although the images clearly reveal the cross section of the sample, we also observe ion signals arising from regions above and below the actual sample. The total ion image of sample A1 in Figure 7E best illustrates this off-sample signal. These ions are most likely produced by inadvertent smearing of the sample surface onto the sides of the cross-sectional holder during sample mounting. The extent of this smearing is more noticeable in the images of sample A1.

The uniformity of leuprolide in the device formulated with oleic acid is clearly shown in the convolved images in Figure 8B–D, where the more uniform distribution of the leuprolide molecular and fragment ions is obvious. In particular, the protonated molecular ion image in Figure 8C shows almost uniform intensity

along the cross section as do the sum of tyrosine immonium ions with the w_3 and w_4 ions as illustrated in Figure 8D.

CONCLUSIONS

Molecular ion microscopy provides a sensitive method for determining the distribution of organic molecules in organic matrices. The determination of the drug distribution along the polymer device would be extremely difficult without the molecular visualization provided by this microscopic imaging technique. Ion microscopy also dramatically demonstrates that leuprolide dissolved in HPC, as represented in the cross-sectional surface, is clearly nonuniform and concentrates at the polymer/air interface. By contrast, images of leuprolide ions produced from polymer containing oleic acid demonstrate more uniform cross-sectional distribution of the leuprolide. These ion microscopy results are supported by XPS data, and the increased uniformity of leuprolide is definitely related to the presence of oleic acid although the exact nature of the interaction of the acid with the mixture is not known at this time. However, possible explanations for the detection of higher intensity and more uniform leuprolide peaks from the acid-treated polymer are the reduced surface free energy of leuprolide in the acidic solid or an increased degree of solvation of the peptide in the acidic matrix.

ACKNOWLEDGMENT

The authors thank Dr. Kenneth Matuszak for supplying the FAB mass spectrum of leuprolide.

Received for review May 8, 1995. Accepted July 27, 1995.*

AC950439N

* Abstract published in *Advance ACS Abstracts*, September 1, 1995.

Use of Methyl Spacers in a Mixed Horizontally Polymerized Stationary Phase

R. W. Peter Fairbank, Yang Xiang, and Mary J. Wirth*

Department of Chemistry and Biochemistry, University of Delaware, Newark, Delaware 19716

Studies of mixed horizontally polymerized monolayers of octadecyl- (C_{18}) and methyl- (C_1) trichlorosilanes show that C_1 groups are valuable as spacers in this type of chromatographic stationary phase. Molecular models are presented that predict C_1 spacers to have less steric hindrance than propyl (C_3) spacers, which aids in the cross-linking of the siloxane monolayer. ^{29}Si NMR measurements reveal significantly greater cross-linking in the polymerization of the C_{18}/C_1 mixed monolayer compared to the C_{18}/C_3 mixed monolayer. Contact angle measurements for a pure C_1 monolayer on a flat silica surface indicate that the methyl groups are predominantly directed away from the silica substrate. The chromatographic retention behavior of aniline shows that the C_{18}/C_1 monolayer has significantly less silanol activity than does the C_{18}/C_3 monolayer. As a critical test of silanol activity, the retention behavior of a set of cationic peptide standards shows that the C_{18}/C_1 monolayer has very low silanol activity and provides less peak asymmetry than does a monomeric phase made with the same high-quality silica gel (Zorbax-300RX-sil). The baseline resolution of a mixture of three cytochrome *c* genetic variants establishes that the C_{18}/C_1 stationary phase allows high column efficiency in addition to low silanol activity.

The separation of organic bases presents a problem for chromatographers using reverse-phase HPLC because organic bases adsorb to unreacted silanols, leading to peak tailing.^{1–5} Silanol activity can be reduced using a variety of techniques. Silica of a higher purity can be used, or a lower grade silica can be pretreated to minimize isolated silanols.^{6,7} The stationary phase can be exhaustively endcapped, or it can be synthesized from a silanizing reagent with bulky side groups on the silicon atom, resulting in a sterically protected surface.^{8,9} The mobile phase can be modified to reduce base adsorption by lowering the pH of the mobile phase with trifluoroacetic acid or by adding silanol blocking reagents, such as tetramethylammonium phosphate or tetrabutylammonium bisulfate.¹⁰ The lower pH typically hydro-

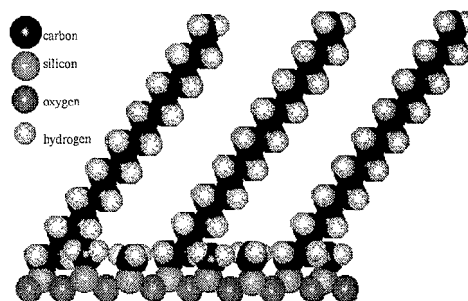


Figure 1. Depiction of ideal horizontal polymerization of C_{18} and C_1 trifunctional silanes using space-filling models. The C_{18} groups are indicated to constitute one-third of the monolayer, on the average. The spacings between C_{18} groups would ideally be random.

lyzes stationary phases. Various means have been introduced to increase hydrolytic stability, including the use of chlorodiisopropyl- and chlorodiisobutylalkylsilanes for steric protection of the surface,^{8,9} formation of Si–C bonds to the surface through Si–Cl bond formation, followed by a Grignard reaction to attach the organic ligand,^{11,12} and formation of Si–H bonds, followed by addition of a terminal olefin.¹³ Despite these advances, there is not yet a satisfactory stationary phase with adequately high hydrolytic stability and low silanol activity for the most demanding applications.

Recently, a new method has been introduced for potentially reducing the silanol activity while increasing the hydrolytic stability: horizontal polymerization of mixed trichlorosilanes into dense monolayers.^{14–18} Ideal horizontal polymerization would have highly dense bonding among reagent groups, forming an exoskeletal mesh to protect the unreacted silanols from base adsorption. Figure 1 illustrates what is intended for the structure of a mixed monolayer of C_{18}/C_1 , where the C_{18} functional group constitutes no more than one-third of the monolayer. This cross-sectional depiction shows the hydrocarbon groups directed away from the substrate and the siloxane backbone overlaying the silica substrate. The role of the short spacer groups is to control the coverage of the C_{18} groups while providing a barrier over the silica

(1) Shapiro, I.; Koltoff, I. M. *J. Am. Chem. Soc.* **1956**, *72*, 776.
 (2) Unger, K. K.; Becker, N.; Roumeliotis, P. *J. Chromatogr.* **1976**, *125*, 115.
 (3) Sadek, P.; Carr, P. W. *J. Chromatogr. Sci.* **1983**, *21*, 314.
 (4) Landy, J. S.; Ward, J. L.; Dorsey, J. G. *J. Chromatogr. Sci.* **1983**, *21*, 49.
 (5) Trushin, S.; Keve, J. J.; Vinogradova, L. V.; Belenki, B. G. *J. Microcolumn Sep.* **1991**, *3*, 185.
 (6) Kohler, J.; Chase, D. B.; Farlee, R. D.; Vega, A. J.; Kirkland, J. J. *J. Chromatogr.* **1986**, *352*, 275.
 (7) Kohler, J.; Kirkland, J. J. *J. Chromatogr.* **1987**, *385*, 125.
 (8) Kirkland, J. J.; Glajch, J. L.; Farlee, R. D. *Anal. Chem.* **1989**, *61*, 2.
 (9) Kirkland, J. J.; Dilts, C. H.; Henderson, J. E. *LC-GC* **1993**, *11*, 290.
 (10) Paesen, J.; Claeys, P.; Roels, E.; Hoogmartens, J. *J. Chromatogr.* **1993**, *630*, 117.

(11) Kocke, D. C.; Schmermund, J. T.; Banrer, B. *Anal. Chem.* **1972**, *44*, 90.
 (12) Pesek, J. J.; Swedberg, S. A. *J. Chromatogr.* **1989**, *361*, 2067.
 (13) Montcs, M. C.; van Amen, C.; Pesek, J. J.; Sandoval, J. E. *J. Chromatogr. A* **1994**, *688*, 31.
 (14) Fatunmbi, H. O.; Wirth, M. J. *Anal. Chem.* **1993**, *65*, 822.
 (15) Fatunmbi, H. O.; Wirth, M. J. *Anal. Chem.* **1992**, *64*, 2783.
 (16) Fatunmbi, H. O.; Wirth, M. J. U.S. Patent Appl. 900,215, June 17, 1992.
 (17) Wirth, M. J.; Fatunmbi, H. O. In *Chemically Modified Surfaces*; Pesek, J. J., Leigh, I. E., Eds.; Royal Society of Chemistry: Cambridge, U.K., 1994.
 (18) Wirth, M. J. *LC-GC* **1994**, *12*, 656.

substrate. ^{13}C NMR studies of a mixed C_{18}/C_3 monolayer showed that the C_{18} chains were randomly interspersed when the C_{18} chains constituted approximately one-third of the monolayer.¹⁹ Chromatographic studies are consistent with the random distribution of C_{18} chains: the mixed horizontally polymerized phase behaves chromatographically like a conventional monomeric stationary phase of the same C_{18} coverage.¹⁹ Improved hydrolytic stability over monomeric phases has also been demonstrated,¹⁵ presumably owing to multiple bonding and high density at the surface.

The space-filling view depicted in Figure 1 suggests the possibility that horizontal polymerization would provide very low silanol activity, because access to the silica would be blocked by the dense, two-dimensional siloxane polymer. However, previous work with C_{18}/C_3 mixed horizontally polymerized phases did not bear out this expectation.¹⁷ Comparing the C_{18}/C_3 phase with a conventional monomeric C_{18} phase synthesized on the same type of silica gel, aniline exhibited significantly longer retention on the C_{18}/C_3 phase: its capacity factor was nearly 4-fold larger.¹⁷ No C_{18}/C_3 phase has been reported to have efficiency comparable to that of monomeric C_{18} phases for organic bases. Quantitative ^{29}Si NMR data revealed that the C_{18}/C_3 monolayers are cross-linked only 20% as much as an ideal two-dimensional siloxane monolayer would be.¹⁹ These results indicate that the synthesized C_{18}/C_3 monolayers are too far from the ideal two-dimensional monolayer of Figure 1 to be advantageous for separations of organic bases.

The marked nonideality of the monolayer might be intrinsic to the C_{18} and C_3 functional groups because the Si-O-Si distance is not sufficiently large to accommodate long alkyl chains on adjacent Si atoms for a planar monolayer. While the actual structures of the trifunctional silane monolayers are not known, the densest, most completely cross-linked monolayer would be a lattice of 12 membered rings alternating in Si and O. A top view of a small section of such a monolayer is illustrated in Figure 2a for the case of the pure C_1 trifunctional silane. This structure was drawn using Hyperchem, with the siloxane bonds initially placed nearly in-plane. Molecular mechanics (MM+) was then used to optimize the geometry. Edge effects are evident, but the center of the structure shows that two-dimensional polymerization is sterically possible. The case of a C_2 monolayer is illustrated in Figure 2b. The MM+ optimization of the geometry quickly moves the silicon atoms out of plane to reduce the repulsive interactions among the ethyl chains. These models illustrate that any alkyl group longer than one carbon atom cannot be accommodated sterically in a completely cross-linked planar monolayer; however, methyl groups alleviate the steric restriction. Consequently, using C_1 groups as spacers in mixed monolayers might be advantageous chromatographically over C_3 spacers. In a mixed C_{18}/C_1 monolayer, the second carbon of the C_{18} chain could be accommodated sterically if its three neighbors were C_1 groups. Thus, in principle, a mixed C_{18}/C_1 monolayer could be planar and fully cross-linked if the ratio of C_{18} to C_1 were no more than 1:3. The relaxation of the steric restrictions for C_1 groups makes the use of these spacers worth exploring for mixed trifunctional siloxane monolayers. The use of C_1 as spacer groups has not previously been explored.

The purpose of this work is to investigate horizontally polymerized monolayers of C_{18}/C_1 with regard to structure and chromatographic performance. The extent of cross-linking is investigated with ^{29}Si NMR. Given the small size of methyl

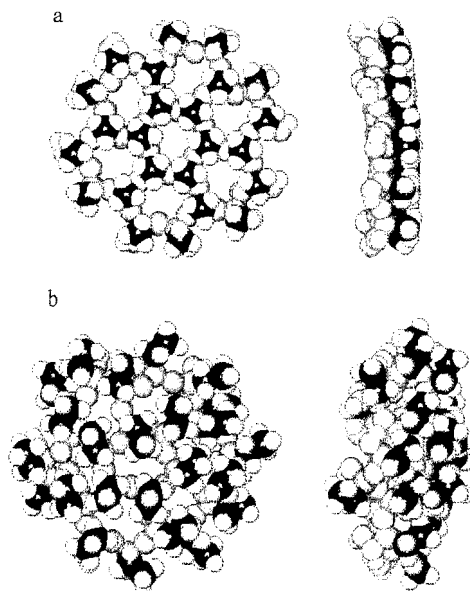


Figure 2. Molecular models for nearly two-dimensional siloxane polymers of maximum density: (a) pure C_1 , and (b) pure C_2 .

groups, it is possible that they will not orient in the desired way that is depicted in Figures 1 and 2, and this question is investigated by measurements of contact angles. For the chromatographic studies, Zorbax 300RX-sil is chosen as the silica substrate because, in the case of the conventional monomeric phase, low silanol activity is expected without encapping.^{6,7} The chromatographic performance of the C_{18}/C_1 phase is tested by three types of organic bases, and comparisons are made to a conventional monomeric C_{18} phase. The organic bases include aniline, a set of cationic peptide standards, and a mixture of cytochrome c genetic variants.

EXPERIMENTAL SECTION

Chemicals and Sample Preparation. *n*-Octadecyltrichlorosilane, methyltrichlorosilane, and dimethyloctadecylchlorosilane were purchased from Hüls America (Piscataway, NJ) and were used as received. Aniline was purchased from Aldrich (Milwaukee, WI). Cationic peptide standards were purchased from Alberta Peptides (Edmonton, Canada). The cytochrome c mixture contained a combination of samples from the hearts of canines, bovines, and equines and was purchased from Sigma (St. Louis, MO).

The silica used in these experiments was Zorbax 300RX-sil (5.3 μm diameter, 300 Å pore size, 45 m^2/g surface area). The synthesis of the horizontally polymerized phase was the same as described previously¹⁴ and is summarized briefly here. The silica was boiled in concentrated nitric acid for 24 h to remove any atmospheric contaminants adsorbed to the silica surface. The silica was then rinsed with pure water until the pH of the filtrate reached neutrality and was dried at 100 °C under a continuous flow of N_2 using a Sybron Thermolyne Type 21100 tube furnace. The dried silica was placed in a humidification chamber at room temperature, where moist nitrogen at 50% relative humidity was

(19) Fatunmbi, H. O.; Bruch, M. D.; Wirth, M. J. *Anal. Chem.* **1993**, *65*, 2048.

Table 1. Experimental Conditions for Each of the Samples Run on the HPLC

sample	mobile phase	gradient	stop time (min)	post time (min)	wave-length (nm)	injection volume (μ L)
aniline	A, 85% ACN+H ₂ O	none	3	NA	210	10
cationic peptides	A, H ₂ O + 0.1% TFA; B, ACN + 0.1% TFA	initial, 0% B; increase 1% B/min	30	5	210	10
cytochrome c genetic variants	A, H ₂ O + 0.1% TFA; B, ACN + 0.1% TFA	initial: 25% B; increase 1% B/min	20	5	220	3

flowed through the silica gel until the humidity of the effluent reached 50%. It has been shown that a reproducible amount of water on the order of a monolayer adsorbs to silica surfaces at this humidity level.²⁰ In preparation for derivatization, *n*-heptane was passed through a dried silica column to remove polar surfactants which might impede the horizontal polymerization. Under a nitrogen blanket, 4 mL of *n*-octadecyltrichlorosilane and 1 mL of methyltrichlorosilane were added to 50 mL of filtered *n*-heptane. This composition was shown to provide a 1:3 ratio of C₁₈/C₃ in the mixed monolayer.^{17,19} After mixing, the solution was poured into a flask containing the humidified silica and a small stirring bar. The hydrolysis of the silanizing reagents was observed by the immediate evolution of HCl gas from the flask. The reaction was allowed to continue for 24 h at room temperature with stirring. The derivatized silica was then rinsed with 200 mL each of heptane, toluene, tetrahydrofuran, methylene chloride, and acetone and dried for 2 h at 120 °C.

The pure C monolayer was made on a flat silica plate (Esco Products). The silica plate was pretreated in the same way as the silica gel and then exposed to nitrogen at 50% relative humidity and finally immersed in *n*-heptane. Under a nitrogen blanket, the methyltrichlorosilane reagent was added to the container holding the *n*-heptane and silica plate. The reaction was allowed to proceed for 24 h. No sign of a film due to excess water was observed. The plate was cleaned with the same types of solvents as were used for cleaning the chromatographic silica sample.

For preparation of the monomeric C₁₈ phase, the silica was pretreated the same way as it was for the horizontally polymerized phase, except that it was not humidified. A 5 g silica sample was refluxed with 2 mL of dimethyloctadecylchlorosilane and 50 mL of toluene, with 1 mL of pyridine added as a catalyst. After 24 h, the silica was filtered with 200 mL of fresh heptane, toluene, and acetone and then dried for 2 h at 120 °C.

Each chromatographic silica sample was packed into a 15 cm x 4.6 mm column using a Haskel pump, Model MCP 110. Silica (2.5 g) was added to a 50:50 mixture of cyclohexanol and acetone for a total volume of 30 mL. The resulting slurry was sonicated for 20 min and then poured into the slurry chamber. Methanol was used as the packing liquid. The columns were repeatedly repacked after chromatographic runs to ensure that differences in the column efficiency were not due to irreproducible packing irregularities.

For preparation of the cationic peptide standards, 0.5 mL of HPLC grade water was added to the sample vial. To prepare the cytochrome *c* sample, 5 mg of the bovine, canine, and equine genetic variants were added to an HPLC vial and dissolved in 1% acetic acid in water. These samples were kept in a -20 °C freezer to prevent degradation. A 10⁻⁴ M solution of aniline was prepared fresh on the day of use in 85% acetonitrile in water.

(20) Gee, M. L.; Hsaly, T. W.; White, L. R. *J. Colloid Interface Sci.* **1990**, *40*, 450.

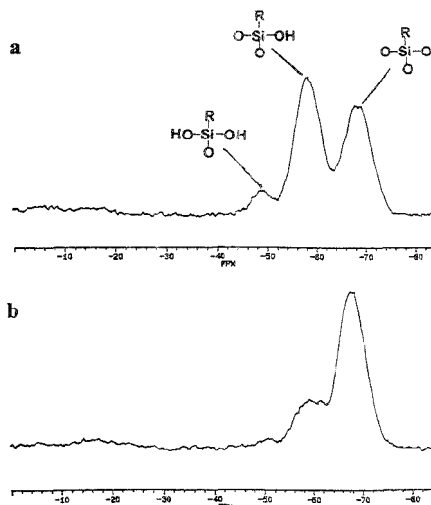


Figure 3. ²⁹Si NMR spectra of the horizontally polymerized packing materials. The peaks corresponding to unterminated (R-Si-O₃), terminated (RSi(O₂)OH), and doubly terminated (RSi(O)(OH)₂) reagent groups are labeled on the spectra: (a) C₁₈/C₃ and (b) C₁₈/C₁.

Equipment. A Hewlett Packard 1090 HPLC was used in these experiments. Table 1 contains information regarding initial conditions, use of gradients, mobile phases, and stop times for each sample. The flow of the mobile phase was 1 mL/min, and the detector response time was 1 ms. Each sample was injected three times to confirm reproducibility. A Bruker 300 ML NMR spectrometer was used to obtain the ²⁹Si NMR spectrum. As in previous reports, cross-polarization and magic angle spinning techniques were used to obtain the spectra reported.¹⁹ A contact time of 5 ms was used in all experiments. A Mattson Galaxy 5020 Fourier transform infrared spectrometer, equipped with a mercury-cadmium-telluride detector cooled by liquid N₂, was used to obtain infrared spectra for the silica plates. The molar absorptivity of the methyl stretch was determined using tetramethylsilane in CCl₄. Contact angle measurements were made on an apparatus built in-house.

RESULTS AND DISCUSSION

NMR Spectroscopy. ¹³C NMR spectroscopy confirmed that the ratio of C₁₈/C₁ was less than 1:3. ²⁹Si NMR spectroscopy was used to investigate the siloxane bonding of the C₁₈/C₁ monolayer, and the spectra for the horizontally polymerized C₁₈/C₂ and the C₁₈/C₁ phases are shown in Figure 3. For the C₁₈/C₃ case, which had been detailed previously, the spectrum shows that there are three types of reagent silicon atoms bonded to the surface.¹⁹ The peaks at -58 and -50 ppm correspond to reagent silicon atoms

having one terminal hydroxy group and two terminal hydroxy groups, respectively. Both of these peaks are considered to be due to defects in the monolayer because these groups terminate rather than propagate the two-dimensional polymer. The peak at -68 ppm is due to reagent silicon atoms having no terminal hydroxy groups. This type of silicon atom would be the only type in the spectrum if there were ideal two-dimensional polymerization, with all silicon atoms attached through oxygens to other silicon atoms. Previous work revealed that the C_{18}/C_3 monolayer is structured as linear polymer chains with most reagent silicon atoms attached to a terminal hydroxy group, and only 20% of the reagent silicon atoms cross-linked to reagent silicon atoms in adjacent chains.¹⁹ Since these terminal hydroxy sites amount to defects, it is likely that aniline tailed when eluted from this phase, because the silica substrate is exposed between the polymer chains.

For the C_{18}/C_1 case, the -68 ppm peak, due to the unterminated reagent silicon atoms, is much larger than either of the other two peaks. Qualitatively, this is consistent with the idea that C_1 spacers allow two-dimensional polymerization. Quantitatively, one must account for occasional bonding of the reagent silicon atoms to the silica substrate, which would be spectrally indistinguishable. Analogous to the C_{18}/C_3 study,¹⁹ the ^{29}Si NMR spectrum of the underivatized silica gel was obtained to account for the number of reacted surface silanol groups. Quantitative results were obtained as detailed before,¹⁹ where the buildup and decay of the magnetization from the cross-polarization was measured for each type of silicon atom. The primary source of error was the slow relaxation of the Si atoms of the bare silica gel. The results revealed that no more than 15% of the peak intensity at -68 ppm is due to attachment to the surface. Accounting for the small intensity of the peak at -60 ppm, at least 60% of the reagent silicon atoms are cross-linked, which is three times higher than for the C_{18}/C_3 case. The C_{18}/C_1 monolayer thus approaches the two-dimensional monolayer more closely than does the C_{18}/C_3 monolayer. This agrees with the predictions from the molecular models that the C_1 spacers allow formation of a denser barrier monolayer over the silica substrate.

Contact Angle Measurements. The C_1 spacers allow for extensive cross-linking, but their sizes may not be large enough to force them to orient away from the substrate. The orientations of the methyl groups in the C_{18}/C_1 monolayer are important for assessing its prospects in chromatography, and these orientations can be inferred from measurements of contact angles. The hydrophobicity of the surface is expected to be higher if the methyl groups are oriented away from the substrate. Surface hydrophobicity is fundamentally related to the interfacial tension between the surface and the water droplet, γ_{sv} . The contact angle, θ , between a surface and a drop of water is related to γ_{sv} through Young's equation,

$$\gamma_{lv} \cos \theta = \gamma_{sv} - \gamma_{sl} \quad (1)$$

The terms γ_{sv} and γ_{sl} are the interfacial tensions of the surface-vapor and liquid-vapor interfaces. In general, the contact angle is large ($>90^\circ$) for a hydrophobic surface and small ($\sim 0^\circ$) for a hydrophilic surface.

For the flat silica plate, infrared spectroscopy revealed a coverage of $11 \pm 2 \mu\text{mol}/\text{m}^2$ of C_1 groups, which is in agreement with the model of Figure 2a that predicts $10 \mu\text{mol}/\text{m}^2$. The contact

angle was measured to be $77^\circ \pm 1^\circ$, which is in agreement with a previous report.²¹ By way of comparison, for methanethiol on gold, it is known that the methyl groups are oriented away from the substrate, because a gold-sulfur bond is formed. The contact angle for methanethiol on gold was reported to be 78° ,²² which is virtually the same as that for the C_1 monolayer on silica. The methyl coverages are comparable for the two surfaces; therefore, the similarity in contact angles suggests that the methyl groups are oriented away from the substrate for the silica case. Contact angles for C_{18} were reported to be 110° for both octadecyltrichlorosilane on silica²¹ and octadecanethiol on gold.²² The C_{18} monolayer is expected to have a higher contact angle because the chain lengths are longer. The contact angle data are thus consistent with the methyl groups being oriented away from the substrate for C_1 on silica.

As a check, it would be valuable to know what the contact angle would be if the methyl groups were directed toward the substrate and the siloxane backbone was in contact with the water droplet. To approximate this case, a clean, bare silica plate (contact angle, 0°) was heated at 600°C for 2 h. This is sufficient to dehydrate 70% of the surface SiOH groups, forming siloxane (Si-O-Si) linkages,²³ leaving an SiOH concentration of $1.5 \mu\text{mol}/\text{m}^2$. This is lower than the estimated $2.5 \mu\text{mol}/\text{m}^2$ SiOH concentration in the pure C_1 monolayer, based on 25% OH groups in a $10 \mu\text{mol}/\text{m}^2$ monolayer. However, the bare siloxane surface was measured to have a contact angle of only $21^\circ \pm 1^\circ$, which is significantly more hydrophilic than the surface coated with the C_1 monolayer. The contact angle data thus support strongly the notion that the methyl groups are predominantly directed away from the substrate, and this is promising for the use of C_1 spacers in chromatographic stationary phases.

It may at first seem surprising that the methyl groups orient away from the substrate, because methyl groups are expected to be too short to self-assemble at room temperature, based on investigations of longer chain lengths.²⁴ Rather than being due to a cooperative effect, such as self-assembly, the orientation is likely due to orientation of the reactants at the heptane/water interface during the reaction. The heptane/water interface is created by the thin layer of water adsorbed to the silica surface upon humidification, and this water layer is in contact with the heptane that is used as the solvent for the horizontal polymerization. The methyl groups would tend to orient toward the heptane at this interface, resulting in an oriented monolayer without requiring the cooperativity of alkyl chains that is involved in self-assembly.

Chromatography. While the structural features of the C_{18}/C_1 monolayer, as revealed by the NMR and contact angle measurements, portend a favorable chromatographic phase, the chromatographic study of base retention is required as a final test. For each chromatographic measurement, the C_{18}/C_1 phase was compared with a monomeric phase prepared on the same silica gel. The monomeric C_{18} phase synthesized for this work on Zorbax-300RX-sil was determined by microanalysis to have a C_{18} coverage of $3.3 \pm 0.1 \mu\text{mol}/\text{m}^2$, which is the same as the coverage for the commercial phase. However, this monomeric phase is not the same as the commercial product, Zorbax-RX-C18, because

- (21) Wasserman, S. R.; Tao, Y.-T.; Whitesides, G. M. *Langmuir* 1989, 5, 1074.
 (22) Bain, C. D.; Troughton, E. B.; Tao, Y.-T.; Ewail, J.; Whitesides, G. M.; Nuzzo, R. G. *J. Am. Chem. Soc.* 1989, 111, 321.
 (23) Zhuraviev, L. T. *Langmuir* 1987, 3, 316.
 (24) Brzoska, J. B.; Shahidzadeh, N.; Rondelez, F. *Nature* 1992, 360, 719.

Table 2. Chromatographic Data: (a) Horizontally Polymerized Phase and (b) Monomeric Phase

analyte		t_0 (min)	t_r (min)	N	asymmetry
hexanophenone	(a)	1.2	2.09	1500	2.0
	(b)	1.2	1.98	1680	2.3
aniline	(a)	1.3	1.52	1728	2.1
	(b)	1.3	1.82	876	3.8
cationic peptide (peak 3)	(a)	1.1	21.4	71 190	1.9
	(b)	1.6	26.4	41 190	3.5

both the pretreatment of the silica and the silanization are not the same as the proprietary treatments used for the commercial product. These treatments can affect silanol activity. Results for the commercial product are excluded from this report to avoid conflicts. The silica gel was pretreated the same way for the monomeric C_{18} and the horizontally polymerized C_{18}/C_1 to allow fair comparison.

Chromatograms of aniline at neutral pH are shown in Figure 4 on an expanded scale for both the horizontally polymerized C_{18}/C_1 and the monomeric C_{18} phases. Both phases provide good performance, despite the absence of trifluoroacetic acid. The asymmetry factor was calculated as the ratio of trailing to leading half-widths at 10% above the baseline. Efficiency, N , was calculated from the Jeansonne and Foley relation,²⁵ which applies to asymmetric bands. Table 2 shows that the retention time of aniline is 15% less, the efficiency is twice as high, and the asymmetry factor is half as much for the horizontally polymerized phase compared to the monomeric phase. For the case of C_{18}/C_3 , the capacity factor of aniline was measured to be 4-fold larger than that obtained here for C_{18}/C_1 .¹⁵ The C_3 spacers thus resulted in a stationary phase that was uncompetitive with the monomeric phase. The superior performance of the C_{18}/C_1 phase over the C_{18}/C_3 phase agrees with the expectations from the structural models and the NMR spectra: polymerization of C_1 groups forms a better barrier over the silica substrate than does that of C_3 groups.

The comparison between the C_{18}/C_1 phase and the conventional monomeric phase is complicated by the fact that aniline is a very early eluting compound for both columns, which enables effects other than adsorption to silanols to contribute to both peak width and asymmetry. Hexanophenone, which is an early eluting compound that is inert toward silanols, was studied to assess broadening effects other than adsorption to silanols. The chromatographic data for hexanophenone are presented in Table 2. The low column efficiency and peak asymmetry for this early eluting compound are likely due to extracolumn broadening. The essential information is that the retention times, column efficiencies, and asymmetry factors of this non-silanol-active analyte, hexanophenone, are comparable for the horizontally polymerized and monomeric phases. The differences for aniline are thus attributed to lesser interaction with silanols in the case of the horizontally polymerized phase.

While the elution behavior of aniline shows that the C_1 horizontally polymerized phase is quite competitive with the monomeric C_{18} phase, compounds having stronger interactions with silanols are required to judge base elution more critically. A set of cationic peptides has been reported to be a very sensitive

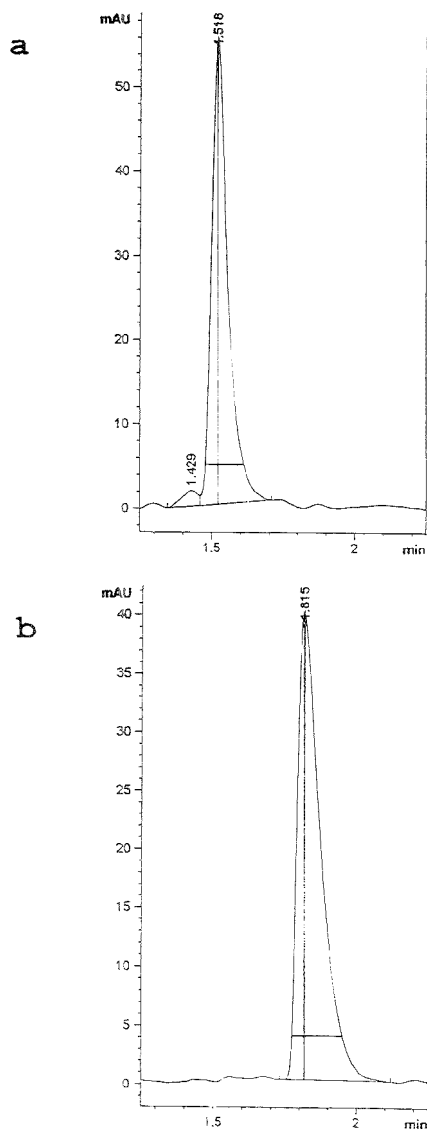


Figure 4. Chromatograms of aniline at neutral pH using (a) the horizontally polymerized C_{18}/C_1 stationary phase and (b) the conventional C_{18} stationary phase.

probe of silanol activity by virtue of strong coulombic interactions between protonated lysine groups and the surface $Si-O^-$ groups.^{26,27} The four cationic peptides are retained in order of increasing number of lysine groups, which increases from 1 to 4. The chromatograms for the cationic peptides at pH 2 are shown in Figure 5. The chromatograms obtained for both phases are

(25) Jeansonne, M. S.; Foley, J. P. *J. Chromatogr. Sci.* **1991**, *29*, 258.

(26) Mant, C. T.; Hodges, R. S. *Chromatographia* **1987**, *24*, 805.

(27) Sander, L. C. *J. Chromatogr. Sci.* **1988**, *26*, 380.

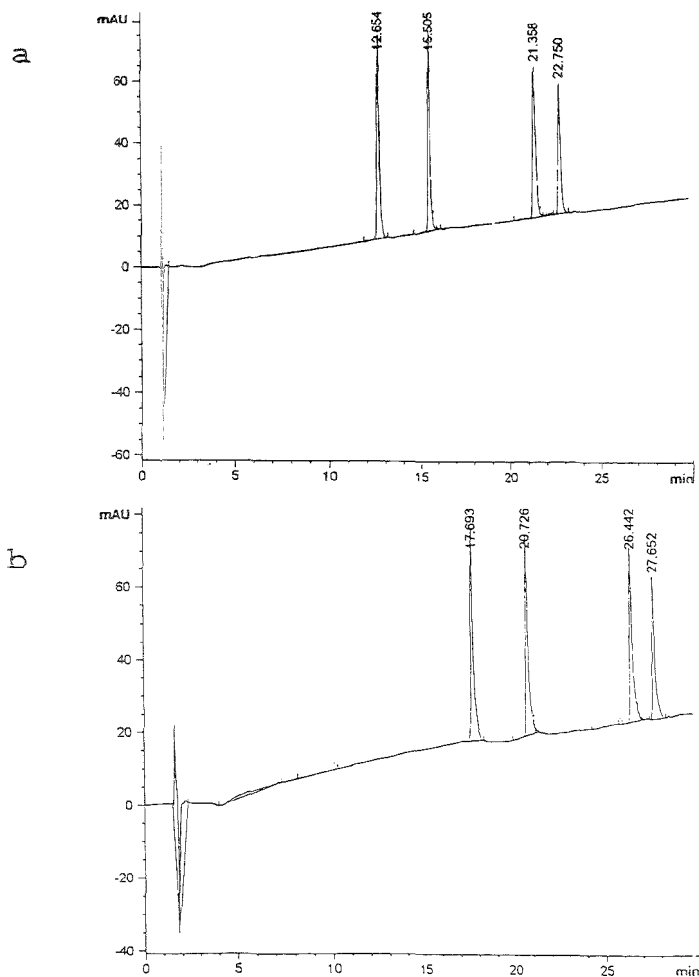


Figure 5. Chromatograms of cationic peptide standards with trifluoroacetic acid in the mobile phase for (a) the horizontally polymerized C_{18}/C_1 stationary phase and (b) the conventional C_{18} stationary phase.

considerably better than those reported earlier in the literature for C_{18} phases.^{26,27} It is evident that the horizontally polymerized phase has higher column efficiency than the monomeric phase. Figure 6 shows the third peak on an expanded scale, and Table 2 lists the retention times and asymmetry factor for the third peak. The retention time is 20% shorter for the horizontally polymerized phase, indicating decreased interaction with $Si-O^-$ groups. The column efficiency is 2-fold higher, and the peak asymmetry is almost half as much, further indicating less interaction with silanols. These results are consistent with the expectation from the molecular models and the ^{29}Si NMR spectra: C_1 spacers enable an effective barrier to be formed between the mobile phase and the substrate silanols.

A fundamental issue in assessing the prospects for practical use of horizontally polymerized phases is column efficiency, which is critical for the most demanding separations. Heterogeneous

polymerization over the silica gel sample would constitute another source of band broadening. Alteration of the pore structure from excess polymer would make the separation of proteins difficult. To test these aspects of column efficiency, the genetic variants of cytochrome *c* are used, which are separable only with wide-pore silica for columns having high efficiency and low silanol activity. Figure 7 shows chromatograms of the protein mixture for the two stationary phases. Baseline resolution is achieved for the horizontally polymerized C_{18}/C_1 phase, while tailing is evident for the monomeric phase. Since none of the peaks is isolated for the monomeric case, the asymmetry factor was not calculated. The shorter retention times and lesser tailing are again indicative of lower silanol activity for the horizontally polymerized phase. The baseline resolution indicates that the pore structure of the silica remains intact after polymerization and that the stationary phase is homogeneous.

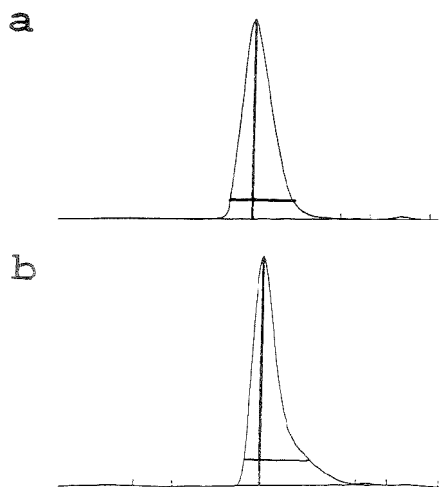


Figure 6. Chromatograms on an expanded scale for the third peak of the cationic peptides: (a) the horizontally polymerized C_{18}/C_1 stationary phase and (b) the conventional C_{18} stationary phase.

In conclusion, for the elution of organic bases, the use of methyltrichlorosilane (C_1) as a spacer group appears to allow the dense, two-dimensional horizontal polymerization needed for blocking access from the mobile phase to the substrate silanol groups. As a result, mixed horizontally polymerized monolayers of C_{18}/C_1 provide improved separations of aniline, cationic peptide standards, and cytochrome *c* genetic variants, as indicated by short retention times, high efficiency, and low asymmetry factors.

ACKNOWLEDGMENT

We are grateful to Dr. Joseph J. DeStefano of Rockland Technologies for generously donating the silica gel, to Dr. Martha D. Bruch of the University of Delaware for obtaining the ^{29}Si NMR

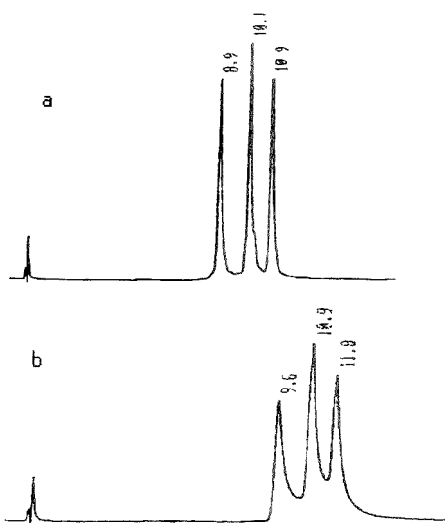


Figure 7. Chromatograms of cytochrome *c* genetic variants with trifluoroacetic acid in the mobile phase for (a) the horizontally polymerized C_{18}/C_1 stationary phase and (b) the conventional C_{18} stationary phase.

spectra, and to Dr. Faizy Ahmed of Phenomenex, Inc., for suggesting the peptide standards and genetic variants of cytochrome *c*. This work was supported by Dow Chemical Co., and by the National Science Foundation under Grant CHE-9113544.

Received for review May 23, 1995. Accepted August 4, 1995.[®]

AC9504934

[®] Abstract published in *Advance ACS Abstracts*, October 1, 1995.

Synthesis and Use of Quaternized Polyethylenimine-Coated Zirconia for High-Performance Anion-Exchange Chromatography

Clayton McNeff and Peter W. Carr*

Department of Chemistry, University of Minnesota, 207 Pleasant Street SE, Minneapolis, Minnesota 55455

The synthesis of an alkali-stable strong anion-exchange stationary phase by deposition of polyethylenimine (PEI), followed by cross-linking and quaternization, onto porous zirconia particles is described. Physical characterization of quaternized PEI-zirconia and PEI-zirconia shows that 50% and 24% of the amine groups are cross-linked, respectively. A plot of $\log k'$ versus \log (competing ion concentration) is linear for three homopeptides, suggesting that ion exchange is the primary mechanism of retention on quaternized PEI-zirconia. Column efficiency for two 2,4-dinitrophenyl amino acids increased by 80% upon increasing the temperature from 50 °C to 100 °C. The hydrophobicity of quaternized PEI-zirconia was studied using a homologous series of *p*-alkoxybenzoic acids. For quaternized PEI-zirconia and PEI-zirconia, we found that the free energy of transfer of a methylene unit from the mobile phase to the stationary phase was -2.0 and -0.90 kJ/mol, respectively. The free energy of transfer of a methylene unit on quaternized PEI-zirconia is similar to that of a typical ODS phase (-2.4 kJ/mol). A van't Hoff plot for the above two 2,4-dinitrophenyl amino acids showed that the enthalpies of transfer are exothermic and fairly large (~ -14 kJ/mol). Isocratic separations on quaternized PEI-zirconia of inorganic and organic anions are presented. Quaternized PEI-zirconia, quaternary amine-functionalized silica, and PEI-zirconia are compared chromatographically. Quaternized PEI-zirconia is more efficient than the silica-based phase in the separation of benzoic acid derivatives but slightly less efficient than PEI-zirconia. The major virtue of quaternized PEI-zirconia is that it is chemically stable in the pH range of 1-13 and is also stable at temperatures up to 100 °C.

Anion-exchange chromatography is a powerful technique for the separation of inorganic and organic anions as well as biomolecules.¹⁻⁵ Previously we described the synthesis of polyethylenimine (PEI)-coated porous zirconia for use as an anion-exchanger.⁶ Although polymeric supports are chemically stable,⁷ they can shrink and swell as a function of the organic modifier

content of the mobile phase,⁸ ionic strength, and pH.⁷ This results in loss of efficiency or unacceptable pressure drops across the column. Zirconia exhibits extraordinary chemical, mechanical, and thermal stability and does not swell or shrink as a function of mobile phase changes.⁹ PEI has been widely used¹⁰⁻¹⁴ as a coating for a variety of substrates¹⁵⁻¹⁸ including silica, titania, alumina, zirconia-clad silica, and porous polystyrene-divinylbenzene beads to produce stationary phases useful for the chromatography of biomolecules. PEI-zirconia has been useful for the separation of proteins.¹⁹ Silica-based supports and bonded-phase silica supports, while attractive because of their mechanical properties, are recognized as being chemically stable only in the range of pH 2-9.²⁰⁻²¹ Polymer coating of silica has been used to extend its working pH range, with some success, but it is still unstable at extreme pHs.²² We report here the synthesis of an acid- (pH 1) and alkali- (pH 13) stable quaternized PEI-coated zirconia stationary phase for use in high-performance anion-exchange chromatography.

EXPERIMENTAL SECTION

All chemicals were reagent grade or better. Polyethylenimine (PEI), average molecular weight 1800, was obtained from Polysciences (Warrington, PA). A 50% sodium hydroxide solution, 3,5-dinitrobenzoic acid, and sodium acetate were obtained from Fisher Scientific (Fairlawn, NJ). Aniline, *p*-nitrotoluene, *p*-cyanobenzoic acid, *p*-iodobenzoic acid, *p*-hydroxybenzoic acid, and *p*-ethylbenzoic acid were obtained from Aldrich (Milwaukee, WI). *p*-Toluenesulfonic acid, *p*-aminobenzoic acid, and *p*-nitrobenzoic acid were from Eastman (Rochester, NY). Sodium bromate and concentrated phosphoric acid were purchased from J. T. Baker

- (7) Helfferich, F. *Ion Exchange*; McGraw-Hill: New York, 1962.
- (8) Arshady, R. *J. Chromatogr.* 1991, 586, 199-219.
- (9) Weber, T. P.; Funkenbush, E. F.; Carr, P. W. *J. Chromatogr.* 1990, 519, 31-52.
- (10) Pearson, J. D.; Regnier, F. E. *J. Chromatogr.* 1983, 255, 137-149.
- (11) Takayanaagi, T. I.; Kubo, Y.; Kusano, H. *Chromatographia* 1988, 25 (7), 647-651.
- (12) Lawson, T. G.; Regnier, F. E.; Wenth, H. L. *Anal. Biochem.* 1983, 133, 85.
- (13) Rassi, Z. E.; Horvath, Cs. *Chromatographia* 1982, 19, 290-299.
- (14) Kitagawa, N. *LCGC* 1988, 6 (3), 260-262.
- (15) Strega, M. A.; Legu, A. L. *J. Chromatogr.* 1991, 555, 109-124.
- (16) Drager, R. R.; Regnier, F. E. *Anal. Biochem.* 1985, 145, 47-56.
- (17) Chicz, R. M.; Shi, Z.; Regnier, F. E. *J. Chromatogr.* 1986, 339, 121-130.
- (18) Kennedy, L. A.; Kopiciewicz, W.; Regnier, F. E. *J. Chromatogr.* 1986, 359, 73-84.
- (19) Regnier, F. E. *Methods Enzymol.* 1984, 104, 170-189.
- (20) Tanaka, N.; Kimata, K.; Mikawa, Y.; Hosoya, K.; Araki, T.; Ohtsu, Y.; Shiojima, Y.; Tsuboi, R.; Tsuchiya, H. *J. Chromatogr.* 1990, 535, 13-31.
- (21) Soderquist, M. E.; Walton, A. G. *J. Colloid Interface Sci.* 1980, 75, 386-397.
- (22) Andrew, A. J.; Regnier, F. E. *J. Chromatogr.* 1979, 185, 375-392.

- (1) Thompson, J. A. *Biochromatography* 1986, 1 (1), 15-20.
- (2) Thompson, J. A. *Biochromatography* 1986, 1 (1), 22-31.
- (3) Smith, R. E. *Ion Chromatography Applications*; CRC Press Inc.: Boca Raton, FL, 1951.
- (4) Rocklin, R. D.; Pohl, C. A.; Schibler, J. A. *J. Chromatogr.* 1987, 411, 107-119.
- (5) Gjerde, D.; Fritz, J.; Schmuckler, G. *J. Chromatogr.* 1979, 186, 509.
- (6) McNeff, C.; Zhao, Q.; Carr, P. W. *J. Chromatogr.*, in press.

(Phillipsburg, NJ). Sodium nitrite, benzoic acid, and sodium nitrate were from Mallinckrodt (St. Louis, MO). The quaternary amine-functionalized strong anion-exchange silica-based stationary phase was produced by Macherey-Nagel (Düren, Germany) and obtained from Phenomenex (Torrance, CA).

All chromatograms were collected on a Hewlett-Packard 1090 (Palo Alto, CA) chromatograph with a photodiode array detector (PDA) and a Hewlett-Packard ChemStation for data collection. The alkali stability study was done using an Altex pump, a Hitachi Model 100-010 UV spectrophotometric detector, an Alltech pressure gauge (Deerfield, IL), and a Rheodyne 7125 injector valve equipped with a 10 μ L fixed sample loop. The acid stability study was done using the Altex pump. All zirconia-based phases were packed into either 5 cm \times 4.6 mm i.d. or 15 cm \times 4.6 mm i.d. stainless steel columns by the stirred upward slurry method at 5000 PSI in 2-propanol. The silica-based phase was packed into a 5 cm \times 4.6 mm i.d. stainless steel column at 4000 PSI in 2-propanol. Water was obtained from a Barnstead Nano-Pure system with an "organic-free" final cartridge and boiled to remove dissolved carbon dioxide. All buffer solutions were filtered using Millipore (type HA) 0.45- μ m membrane filters.

The dead volume marker used for all chromatographic investigations was the negative peak obtained upon injection of pure water. The dead volume was checked for each mobile phase used and was found to deviate less than 3% over the course of this work.

The PEI-coated zirconia stationary phase, previously described,⁶ was produced by an adsorption method using a 2% (w/v) solution of PEI solution in methanol and a 5% (w/v) 1,4-butanediol diglycidyl ether (BUDGE) solution in methanol for cross-linking.

Zirconia Substrate Particles. Porous zirconia particles (batch Coac 15), produced by the polymerization-induced colloid aggregation^{23,24} method, were used as the substrate material for this work. The particles have an average diameter of 6 μ m, a surface area of 29 m²/g, and an average pore size of 220 Å, as analyzed by SEM and BET nitrogen adsorption. An energetically more homogeneous surface was obtained by washing in acid and base: 85 g of zirconia was suspended in 300 mL of 0.5 M hydrochloric acid and sonicated under vacuum for 5 min. The slurry was further sonicated for 45 min and then allowed to stand for 4 h with occasional mixing. The particles were allowed to settle, and the liquid was decanted. The particles were collected on a sintered glass funnel and rinsed with 500 mL of water until neutral. This procedure was repeated using 0.5 M sodium hydroxide, and then the particles were rinsed with another 500 mL of water, dried at 150 °C overnight in a vacuum oven, and stored in a vacuum desiccator.

Synthesis of Quaternized PEI-Zirconia Particles. Synthesis of quaternized PEI-coated zirconia was carried out by a modification of the procedure developed by Kennedy et al.¹⁸ Nine grams of dry zirconia was placed in 45 mL of 2% (w/v) PEI in methanol. The mixture was then sonicated under vacuum for 5 min, capped, and allowed to stand for 2 h. The product was isolated on a sintered glass funnel and cross-linked with 45 mL of 5% (v/v) 1,10-diododecane in 2-propanol, and then 1 mL of 1,2,2,6,6-pentamethylpiperidine was added. This mixture was

(23) Sun, L.; Annen, M. J.; Lorenzano-Porras, C. F.; Carr, P. W.; McCormick, A. V. *J. Colloid Interface Sci.*, in press.

(24) Navrochil, J.; Rigney, M. P.; McCormick, A.; Carr, P. W. *J. Chromatogr.* 1993, 657, 229–232.

Table 1. Chemical Characterization of Supports

phase	Elemental Analysis versus IPC coverage			
	elemental ^a	IPC ^b		
QPEI-ZrO ₂	13.0	4.68		
PEI-ZrO ₂	11.0	7.24		
silica-based bare ZrO ₂	1.44	0.26		
phase	Elemental Analysis coverage			
	C ^c	H ^d	PEI ^e	C/N ratio ^f
QPEI-ZrO ₂	31.6	86.2	0.310	3.21
PEI-ZrO ₂	50.3	113	0.260	4.52
silica-based	18.5	36.3		12.9

^a Micromoles of nitrogen per square meter on the support by elemental analysis. ^b Micromoles of nitrogen per square meter on the zirconia by picric acid assay. ^c Micromoles of carbon per square meter on the support by elemental analysis. ^d Micromoles of hydrogen per square meter on the support by elemental analysis. ^e Micromoles of PEI per square meter on the zirconia by elemental analysis (assuming 42 nitrogens per PEI molecule). ^f Carbon to nitrogen mole ratio by elemental analysis.

heated at 65 °C in an oil bath overnight. The amine groups on the stationary phase were quaternized the next day by addition of 6 mL of iodomethane and heated at 65 °C for an additional 6 h. The coated and cross-linked particles were collected on a sintered glass funnel.

Washing Procedure for Quaternized PEI-Zirconia Particles. The quaternized PEI-zirconia particles were washed in acid and base solutions. First, the particles were suspended in 50 mL of 0.5 M hydrochloric acid and sonicated for 10 min. The particles were then allowed to stand for 4 h. The particles were collected on a sintered glass funnel and washed with 50 mL of 0.5 M hydrochloric acid, 100 mL of water, and 100 mL of methanol. The above procedure was repeated using 0.5 M sodium hydroxide instead of 0.5 M hydrochloric acid. The particles were collected, washed as above, dried at 120 °C at atmospheric pressure for 6 h, and stored in a vacuum desiccator.

Physical Characterization of Stationary Phases. The PEI-zirconia and quaternized PEI-zirconia phases were characterized by elemental analysis (C, H, and N) and small-molecule ion-exchange capacity (IEC). The elemental composition of the coatings was determined by M-H-W laboratories (Phoenix, AZ). The ion-exchange capacity was determined by a small-molecule binding assay as previously described.⁶

RESULTS AND DISCUSSION

Stationary Phase Characterizations. Quaternized PEI-zirconia, PEI-zirconia,⁶ and a commercial silica-based quaternary amine-functionalized phase were characterized by elemental analysis and by the picric acid assay.¹⁸ The picric acid assay is sensitive to nonionized primary, secondary, and tertiary amines. Bare zirconia was also subjected to the picric acid assay to ensure that interactions with bare zirconia sites would not bias test results. The results are given in Table 1. Bare zirconia has an ion-exchange capacity of 0.26 μ mol/m² by the picric acid assay. According to the results of the elemental analysis, the PEI loadings of both the quaternized PEI-zirconia and PEI-zirconia are very similar: 13.0 and 11.0 μ mol/m² of nitrogen, respectively. The

Table 2. Capacity Factor and Reduced Plate Height Comparison of Inorganic and Organic Anions on Quaternized PEI-Zirconia, Silica-Based, and PEI-Zirconia Anion Exchangers^a

solute	$k'_{\text{QPEI-zirc}}$	$\frac{k'_{\text{PEI-zirc}}}{k'_{\text{QPEI-zirc}}}$	$\frac{k'_{\text{silica-based}}}{k'_{\text{QPEI-zirc}}}$	$h_{\text{QPEI-zirc}}$	$\frac{h_{\text{silica-based}}}{h_{\text{QPEI-zirc}}}$	$\frac{h_{\text{PEI-zirc}}}{h_{\text{QPEI-zirc}}}$
water	0.00					
benzylamine	0.32	2.2	5.0	7.9	1.2	0.7
benzamide	0.44	1.7	3.8	6.4	2.1	0.7
sodium nitrite	0.50	1.5	1.1	4.7	0.6	0.6
<i>p</i> -aminobenzoic acid	0.66	1.4	3.4	8.4	0.6	0.5
benzoic acid	0.88	1.0	3.1	6.5	1.4	0.7
<i>o</i> -iodobenzoic acid	1.25	0.7	2.8	7.4	1.1	0.6
sodium nitrate	1.48	0.6	0.6	5.0	0.7	0.6
<i>m</i> -toluic acid	1.49	0.6	3.1	7.3	2.3	0.6
<i>p</i> -ethoxybenzoic acid	1.94	0.5	5.0	7.9	0.8	0.6
<i>p</i> -cyanobenzoic acid	2.20	0.4	1.2	8.2	1.2	0.9
<i>p</i> -hydroxybenzoic acid	2.47	0.5	1.1	8.0	0.9	0.7
<i>p</i> -ethylbenzoic acid	2.55	0.4	3.3	8.4	2.0	0.6
<i>p</i> -toluenesulfonic acid	3.09	0.3	2.0	7.6	2.8	0.6
<i>p</i> -nitrobenzoic acid	4.00	0.2	0.9	8.6	1.8	0.5
<i>p</i> -chlorobenzoic acid	4.67	0.3	1.6	8.2	0.9	0.6

^a Columns, 5 cm × 0.46 cm i.d.; mobile phase A, 100 mM potassium phosphate dibasic at pH 7.4, 40 mM sodium chloride; flow rate, 1.0 mL/min; column temperature, 35 °C; injection volume, 5 μL; solute concentration, 10 mM; detection at 240 nm.

silica-based phase had a nitrogen coverage of 1.44 μmol/m² by elemental analysis. The silica-based phase had a surface area of 350 m²/g, whereas the zirconia supports had a surface area of 29 m²/g, but zirconia's density is approximately twice that of silica gel,²⁴ giving the zirconia-based stationary phases a much higher overall ion-exchange capacity per column. The picric acid assay results for quaternized PEI-zirconia and PEI-zirconia were 4.68 and 7.24 μmol/m² of nitrogen, respectively. Because the picric acid assay is not sensitive to quaternized amine sites, the capacities obtained by its use represent the amount of unquaternized (that is, residual) primary, secondary, and tertiary amines.

Cross-Linking of Quaternized PEI-Zirconia and PEI-Zirconia. Two different cross-linking agents were used for the synthesis of quaternized PEI-zirconia and PEI-zirconia, namely BUDGE and 1,10-diiododecane, respectively. As will be seen, the resulting phases differ markedly in stability and chemical properties. BUDGE and 1,10-diiododecane have elemental formulas of C₁₀H₁₈O₄ and C₁₀H₂₀I₂, respectively. The theoretical molar ratio of carbon to nitrogen (C/N) for PEI is 2.0, so values greater than 2.0 provide information about the amount of cross-linking. As shown in Table 1, the C/N ratios of quaternized PEI-zirconia and PEI-zirconia were 3.2 and 4.5, respectively. If we assume that PEI has a formula (C₂H₅N)_{*n*} and both ends of the cross-linker are linked with PEI, then 50% and 24% of the amine groups on the surface are cross-linked for each respective phase. This estimate of cross-linking for the quaternized PEI-zirconia phase may be somewhat high, as more than one cross-linking agent molecule may react with a single amine site. For instance, in the case of a primary amine, three molecules of 1,10-diiododecane can, in principle, react with a single primary nitrogen.

Comparison of Quaternized PEI-Zirconia, PEI-Zirconia, and a Silica-Based Strong Anion-Exchanger in the Chromatography of Inorganic and Organic Anions. Quaternized PEI-zirconia, PEI-zirconia, and a silica-based quaternary amine functionalized stationary phase were compared chromatographically using some carefully selected inorganic and organic anions. Retention and column efficiency data are shown in Table 2. The capacity factors on the PEI-coated zirconia ranged from 0.7 to 1.4.

The same solutes were much more retained on both the quaternized PEI-zirconia and the silica-based anion-exchangers. Inspection of Table 2 shows that the capacity factors of all well-retained ($k' > 1$) solutes on PEI-zirconia are systematically lower than those on quaternized PEI-zirconia. In contrast, the ratio of capacity factors of the silica-based support to the quaternized PEI-zirconia support shows no systematic variation with capacity factor. There was no observable correlation between the p*K*_a values of the *p*-benzoic acid derivatives and retention on any of the three phases. This is in contrast to a strong dependence on p*K*_a of the retention of *p*-benzoic acids on bare zirconia.²⁵ These retention ratio results suggest that retention on quaternized PEI-zirconia is due to a "mixed-mode" process and is not purely an ion-exchange process. If the only mechanism of retention on the three phases were ion-exchange, then we would expect the ratio of capacity factors on the two columns to be the same for all probe solutes. Furthermore, we would expect the ratio of capacity factors to be directly proportional to the ratio of phase ratios. This is clearly not the case for the data shown in Table 2.

Comparison of Column Efficiency for Quaternized PEI-Zirconia, PEI-Zirconia and a Silica-Based Strong Anion-Exchanger. The column efficiency for small anions on quaternized PEI-zirconia, PEI-zirconia, and the silica-based phase is also shown in Table 2. The height/area method was used to calculate the number of theoretical plates and reduced plate heights:

$$N = 2\pi(Ht_R/A)^2 \quad (1)$$

$$h = L/(Nd_p) \quad (2)$$

where *N* is the number of theoretical plates, *H* is the height of the peak, *t_R* is the retention time, *A* is the peak area, *h* is the reduced plate height, *L* is the column length, and *d_p* is the average particle diameter. In general, quaternized PEI-zirconia was somewhat more efficient than the silica-based support and slightly

(25) Blackwell, J. A. Ph.D. Thesis, University of Minnesota, Minneapolis, MN, 1991.

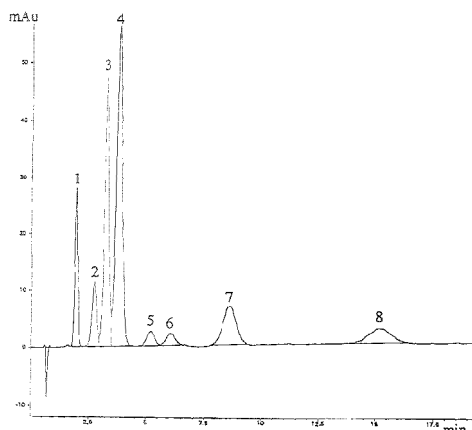


Figure 1. Separation of eight: benzoic acid; 2, methoxybenzoic acid; 3, *p*-cyanobenzoic acid; 4, ethylbenzoic acid; 5, *p*-nitrobenzoic acid; 6, *p*-chlorobenzoic acid; 7, *p*-bromobenzoic acid; 8, *p*-iodobenzoic acid. Column, 5 cm \times 0.46 cm i.d.; mobile phase, 100 mM dibasic potassium phosphate, 400 mM sodium chloride at pH 7.39 adjusted by HCl; flow rate, 1.0 mL/min; column temperature, 35 °C; injection volume, 5 μ L; solute concentration, 10 mM; detection at 254 nm.

less efficient than the PEI-zirconia phase. The average ratio of reduced plate height for the 15 probe solutes for the silica-based and quaternized PEI-zirconia phases ($h_{\text{silica-based}}/h_{\text{QPEI-zirc}}$) was 1.4. The difference in efficiency between the silica-based and quaternized PEI-zirconia phases was particularly evident for benzoic acid derivatives such as *p*-nitrobenzoic acid and 3,5-dinitrobenzoic acid, which had reduced plate heights of 15.2 and 21.7, respectively, on the silica-based phase and 8.6 and 10.3, respectively, on the quaternized PEI-zirconia support. The average ratio of the reduced plate height for the probe solutes on the PEI-zirconia phase to the quaternized PEI-zirconia phase ($h_{\text{PEI-zirc}}/h_{\text{QPEI}}$) was 0.6. The separation of a mixture of eight benzoic acid derivatives on quaternized PEI-zirconia is shown in Figure 1. Good resolution of all eight benzoic acid derivatives was obtained in less than 20 min.

Ion-Exchange Mechanism of Retention on Quaternized PEI-Zirconia. It has been widely observed that plots of $\log k'$ versus \log (competing ion concentration) are linear when ion exchange is the primary mechanism of retention.^{26–29} The theoretical basis for this experimental relationship has been a point of recent discussion.³⁰ According to Haddad et al.,²⁷ on the basis of mass action arguments, the capacity factor of a solute ion is related to the competing ion concentration as follows:

$$\log k' = C - \frac{x}{y} \log [E_m^{y-}] \quad (3)$$

where k' is the capacity factor, x is the charge on a solute ion, y

(26) Gje-de, D. T.; Schmuckler, G.; Fritz, J. S. *J. Chromatogr.* **1980**, *187*, 35.

(27) Haddad, P. R.; Jackson, P. E. *Ion Chromatography*; Elsevier: Amsterdam, 1990.

(28) Haddad, P. R.; Cowie, C. E. *J. Chromatogr.* **1984**, *303*, 321.

(29) Rooklin, R. L.; Pohl, C. A.; Schibler, J. A. *J. Chromatogr.* **1987**, *411*, 107.

(30) Ståhlberg, J. *Anal. Chem.* **1994**, *66*, 440–448.

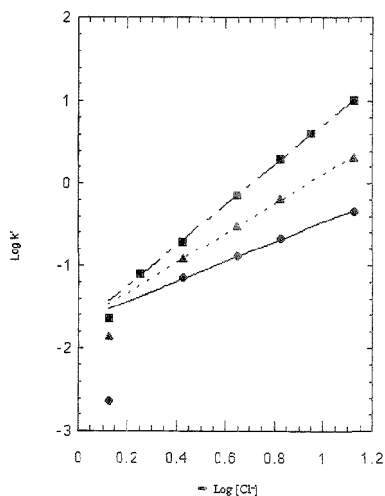


Figure 2. Study of the ion-exchange mechanism on quaternized PEI-zirconia using homopeptides: ■, Asp-Asp-Asp-Asp; ▲, Asp-Asp-Asp; ●, Asp-Asp; column, 15 cm \times 0.46 cm i.d.; mobile phase, 0.02 M dibasic potassium phosphate, 0.75 M NaCl, adjusted to pH 7 with HCl; flow rate, 1.0 mL/min; injection volume, 20 μ L; detection at 220 nm.

is the charge on the competing ion, C is a constant, and $[E_m^{y-}]$ is the mobile phase concentration of the competing ion. The observed relationship between capacity factor and competing ion concentration has also been derived by Ståhlberg,³⁰ who based his model for retention on the Gouy–Chapman double-layer theory. His model includes specific interactions between the solute ions and the counterions with the charged surface. Within Ståhlberg's model, a mass action equation is used to allow for specific adsorption of ions. This model is appealing in that it does not resort to unrealistic assumptions about the activity coefficients of ions in the mobile and stationary phases, as is done in the stoichiometric model. Ståhlberg's model also results in a linear relationship between $\log k'$ and $\log [E_m^{y-}]$ (competing ion concentration), where the slope is close but not necessarily exactly equal to $-x/y$ (the net charges on the solute ion and competing ion, respectively) and depends only slightly on the nature of the solute ion and stationary phase.

The ion-exchange mechanism on quaternized PEI-zirconia was studied using homopeptides of aspartic acid with 2–4 aspartic acid residues. If we assume complete ionization of the carboxylic acid groups, the peptides have net charges of -2 , -3 , and -4 , respectively. A constant amount of phosphate was maintained in the mobile phase to moderate Lewis acid–base interactions between the solutes and bare zirconia sites. The concentration of chloride ion in the mobile phase was varied. Plots of $\log k'$ versus $-\log [Cl^-]$ for the three peptides are shown in Figure 2. The three plots in Figure 2 are linear up to 0.75 M chloride. However, the capacity factors at 0.75 M chloride are much less than 0.1, and all solutes are virtually unretained. When the data at this high concentration of chloride ion are excluded, the least-squares slopes for the di-, tri-, and tetrapeptides are 1.21 ± 0.02 , 1.80 ± 0.02 , and 2.45 ± 0.03 , with correlation coefficients of 0.9987, 0.9995, and 0.9995, respectively. All three slopes are definitely

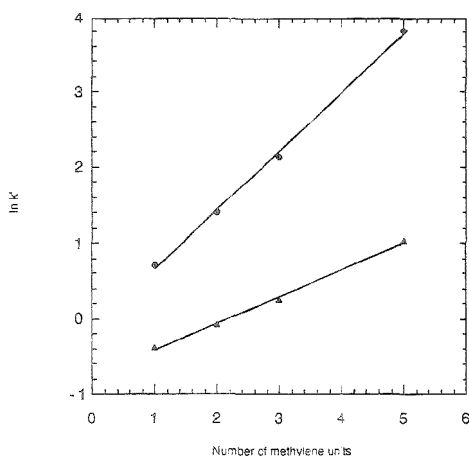


Figure 3. Study of the hydrophobic interactions on PEI-zirconia and quaternized PEI-zirconia stationary phases: ●, quaternized-PEI zirconia phase; ▲, PEI-zirconia phase; column, 5 cm × 0.46 cm i.d.; mobile phase, 100 mM dibasic potassium phosphate, 400 mM sodium chloride at pH 7.00, adjusted by HCl; flow rate, 1.0 mL/min; column temperature, 35 °C; injection volume, 25 μ L; detection at 254 nm.

less than those predicted on the basis of the stoichiometric model and our assumption as to the net charge on the solutes. This could also be due to the neglect of variations in the activity coefficient²⁷ in the mobile phase and stationary phase or to the existence of non-Coulombic interactions that are not accounted for in the model, such as hydrophobic interactions and Lewis acid–base interactions.

Hydrophobic Interaction Comparison of Quaternized PEI-Zirconia and PEI-Zirconia Stationary Phases. Since the ratios of capacity factors in Table 2 and the slopes of the data in Figure 2 suggest a complex mechanism of retention, the possibility that the quaternized PEI-zirconia and PEI-zirconia participate in hydrophobic interaction with solutes was studied by using a homologous series of *p*-alkoxybenzoic acids. A plot of the natural logarithm of the capacity factor versus the number of methylene units in the homologue for the two zirconia-based phases is shown in Figure 3. The quaternized PEI-zirconia phase proved to be much more hydrophobic than the PEI-zirconia phase. Its regression line is shifted to larger capacity factors for a given solute, and the slope of the line was larger. This can be explained on the basis of the self-evident greater hydrophobicity of 1,10-diiodododecane used to prepare the quaternized PEI-zirconia in contrast to the BUDGE used to prepare the unquaternized phase. Quaternization with iodomethane adds additional hydrocarbon. The slopes of the regression lines of $\ln k'$ versus the number of methylene units for quaternized PEI-zirconia and PEI-zirconia phases were 0.78 ± 0.03 and 0.36 ± 0.01 with $R^2 = 0.998$ and 0.997 , respectively. Capacity factors can be related to the free energy of transfer (ΔG°) of a solute³¹ as follows:

$$\Delta G^\circ = -RT \ln(k'/\phi) \quad (4)$$

where R is the gas constant, T is the temperature in kelvins, and

(31) Carr, P. W. *Microchem. J.* 1993, 48, 4–28.

ϕ is the phase ratio. The slopes of the linear regression lines in Figure 3 are proportional to the free energy of transfer of a methylene group from the mobile phase to the stationary phase:

$$\Delta G_{\text{retn,CH}_2}^\circ = -RT \ln(k'_{n+1}/k'_n) \quad (5)$$

where k'_n and k'_{n+1} denote capacity factors of the n th and $n+1$ homologues. The corresponding free energies of transfer of a methylene unit from the mobile phase to the stationary phase are -2.0 and -0.90 kJ/mol, respectively. The free energy of transfer of a methylene unit for a typical ODS silica-based phase from a pure water mobile phase to the stationary phase is -2.4 kJ/mol.³² This value for an ODS phase was estimated by linearly extrapolating $\log k'$ values in methanol–water mixtures versus ϕ (percent organic in the mobile phase) to pure water. The value for free energy of transfer of a methylene unit from the mobile phase to the stationary phase for quaternized PEI-zirconia indicates that it is almost as hydrophobic as an ODS phase in terms of its affinity for a methylene unit. This large difference in hydrophobicity between the two zirconia-based stationary phases helps explain why solutes are, in general, more retained and more selectively separated on quaternized PEI-zirconia compared to PEI-zirconia.

van't Hoff Plot of 2,4-DNP Amino Acids on Quaternized PEI-Zirconia. In order to quantify the enthalpic contribution to retention on quaternized PEI-zirconia, the effect of temperature on the retention of 2,4-DNP amino acids was studied. The resulting van't Hoff plot was nicely linear (data not shown), as predicted by the following equation,³³ which assumes a temperature-invariant enthalpy of transfer:

$$\ln k' = -\Delta H/RT + \Delta S/R - \ln \phi \quad (6)$$

From the slope of the van't Hoff plot, the enthalpic contributions to the retention of 2,4-DNP-DL-methionine sulfoxide and 2,4-DNP- β -alanine were evaluated at -14.2 and -13.8 kJ/mol, respectively. This negative value of ΔH is similar to that which has been reported for reversed-phase separations,^{34,35} where an increase in temperature causes a decrease in retention. In reversed-phase chromatography in pure methanol, a typical value of the enthalpy of transfer is -10 to -17 kJ/mol.³⁶ Thus, the effect of temperature on k' for quaternized PEI-zirconia is a moderate one for these solutes. Furthermore, the mechanism of the process is invariant over the temperature range investigated.^{35,36}

Effect of Temperature on the Efficiency of 2,4-DNP Amino Acids. Figure 4 shows that column temperature has a dramatic effect on the column efficiency for 2,4-dinitrophenyl amino acids. Raising the temperature from 50 °C to 100 °C increased the number of theoretical plates by 80%–90% for both solutes. This beneficial effect of temperature on the reduced plate height may be understood to a first approximation in terms of its effect on the diffusion coefficient of solutes and the viscosity of the mobile phase. In general, the reduced plate height in liquid chromatog-

(32) Park, J. H.; Carr, P. W. Submitted to *J. Chromatogr.*

(33) Poole, C. F.; Poole, S. K. *Chromatography Today*; Elsevier: Amsterdam, 1991.

(34) Hancock, W. S.; Chloupek, R. C.; Kirkland, J. J.; Snyder, L. R. *J. Chromatogr. A* 1994, 686, 31.

(35) Melander, W.; Campbell, D. E.; Horváth, C. J. *Chromatogr.* 1978, 158, 215.

(36) Coin, H.; Diez-Masa, J. C.; Guiochon, G.; Czajkowska, T.; Miedziak, I. J. *Chromatogr.* 1978, 187, 41.

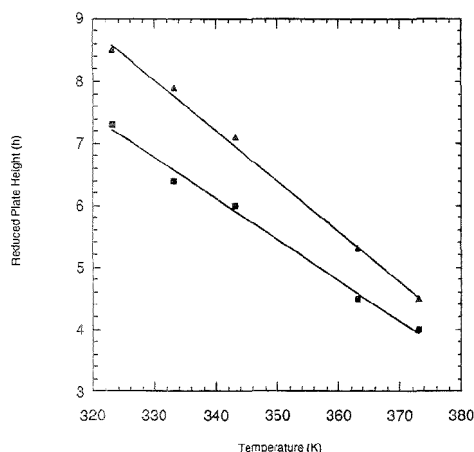


Figure 4. Study of the effect of temperature on reduced plate height for 2,4-dinitrophenyl amino acids: ▲, 2,4-DNP-DL-methionine sulfoxide; ■, 2,4-DNP- β -alanine; column, 5 cm \times 0.46 cm i.d.; mobile phase, A, 10 mM potassium phosphate dibasic, 40 mM sodium chloride at pH 7.4, 20% acetonitrile, B, 100 mM cibasic potassium phosphate, 400 mM sodium chloride at pH 7.4, 20% acetonitrile, gradient, 10% B to 90% B over 25 min; flow rate, 1.0 mL/min; column temperature, 50 °C to 100 °C; injection volume, 5 μ L; detection at 240 nm.

raphy may be related to the reduced flow velocity by the Knox equation:³⁷

$$h = B/\nu + A\nu^{1/3} + C\nu \quad (7)$$

where h is the reduced plate height, ν is the reduced flow velocity, and A , B , and C are the fitting coefficients. Typical coefficient values for a good column are $A < 1$, $B \approx 2$, and $C < 0.2$.³⁸ A is related to the goodness of column packing, B to longitudinal diffusion, and C to the mass transfer of a solute. At higher reduced flow velocity, the C term of the above equation dominates the magnitude of the reduced plate height. If we make this simplifying assumption, then the reduced plate height is roughly related to the inverse of the diffusion coefficient of a solute:

$$\nu = ud_p/D_m \quad (8)$$

where u is the linear velocity, d_p is the stationary phase particle size, and D_m is the diffusion coefficient of a solute in the mobile phase. The diffusion coefficient of molecules can be estimated from the Stokes-Einstein relationship:

$$D = RT/6\pi\eta N \quad (9)$$

where r is the radius of the molecule, η is the solution viscosity, and N is Avogadro's number.

In Figure 4, the regression line for 2,4-DNP-DL-methionine sulfoxide has a slope of -0.082 ± 0.004 and a constant of 12.7 ± 0.3 , with $R^2 = 0.992$. 2,4-DNP- β -alanine has a slope of $-0.066 \pm$

(37) Bristow, P. A.; Knox, J. H. *Chromatographia* 1977, 10 (6), 279-298.

(38) Knox, J. H. *High Performance Liquid Chromatography*; Edinburgh University Press: Edinburgh, Great Britain, 1982.

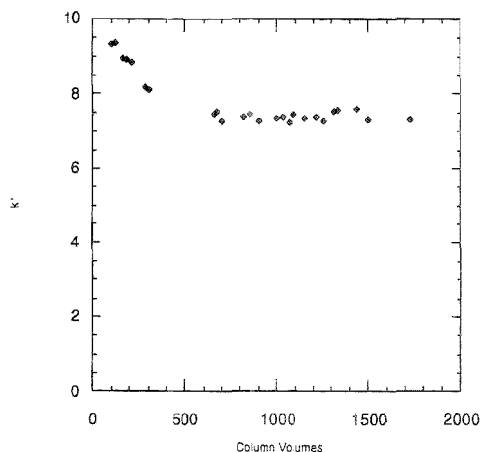


Figure 5. Base stability study of quaternized PEI-zirconia: column, 5 cm \times 0.46 cm i.d.; mobile phase, 100 mM sodium hydroxide, 400 mM sodium acetate at pH 13; flow rate, 1.0 mL/min; column temperature, 35 °C; injection volume, 5 μ L; solute concentration, 10 mM; detection at 240 nm.

0.003 and a constant of 10.6 ± 0.3 , with $R^2 = 0.990$. As shown in eq 9, the diffusion coefficient is directly proportional to the kelvin temperature and inversely related to the viscosity of the mobile phase. The viscosity of pure water at 50 °C is 0.5468 cP, and at 100 °C it is 0.2818 cP.³⁹ Thus, the primary effect of raising the temperature is to lower the viscosity of the mobile phase. The calculated ratio of diffusion coefficients at 100 °C versus those at 50 °C is 2.3, which should result in a proportional improvement in the reduced plate height. Experimentally, 1.9- and 1.8-fold decreases in reduced plate heights were observed from 50 °C to 100 °C for 2,4-DNP-DL-methionine sulfoxide and 2,4-DNP- β -alanine, respectively.

Chemical Stability of Quaternized PEI-Zirconia. The acid and base stability of quaternized PEI-zirconia, which we believe to be a major advantage of zirconia-based over silica-based phases, was assessed chromatographically using sodium nitrite as the test solute. The base stability was tested at pH 13 by measuring the k' of the probe solute over repeated injections. A plot of the capacity factor for nitrite for a particular injection had passed the number of column volumes of mobile phase that had passed through the column by that time is shown in Figure 5. The capacity factor initially dropped from 9.3 to 7.5 (a 19% change) over the first 650 column volumes, but it then stabilized. This initial drop in retention upon the first aggressive treatment with base is rather typical behavior of our materials, even those which are coated with polybutadiene.⁴⁰ A total loss of capacity factor of 21% over 1700 column volumes was observed. The initial loss in capacity factor likely resulted from elution of un-cross-linked or lightly cross-linked PEI polymer that was not removed in the washing steps when the phase was first prepared. The acid stability was also tested by using nitrite as a probe solute. The capacity factor for nitrite was checked initially at neutral pH using

(39) *CRC Handbook of Chemistry and Physics*, 66th ed.; CRC Press: Boca Raton, FL, 1986.

(40) Sun, L. Ph.D. Thesis, University of Minnesota, Minneapolis, MN, 1994.

0.1 M dibasic potassium phosphate with 10% acetonitrile as the mobile phase. Five injections were made, with an average capacity factor of 2.23 ± 0.02 . Then, 1600 column volumes of 0.1 M nitric acid were run through the column at 25 °C. After the acid treatment, the column was flushed with water for 30 min at 1 mL/min, and then the capacity factor for nitrite was measured again using the previous mobile phase. Five injections were performed, with an average capacity factor of 2.15 ± 0.02 , corresponding to only a 3.5% change.

CONCLUSIONS

Quaternized PEI-zirconia is an alkali- and acid-stable stationary phase useful for high-performance anion-exchange chromatography of both inorganic and organic anions. The thermal stability, chemical stability, and "mixed-mode" of retention on quaternized PEI-zirconia are of great utility. For instance, thermal stability allows for column operation at elevated temperatures, which results in significant gains in column efficiency and reduction in the ionic strength necessary to elute solutes. Chemical stability over a pH range of 1–13 allows for the possibility of separations based on differences in solute ionization state over a wide pH range. The major mixed-mode solute–surface interactions include electrostatic, hydrophobic, and Lewis acid–base interactions. Quaternized PEI-zirconia does not shrink or swell appreciably upon addition of organic modifiers to the mobile phase. Thus, a variety of organic modifiers may be used in order to attenuate hydrophobic interactions with solutes or to effect a change in column selectivity. This is a distinct advantage over polymeric stationary phases, which may shrink or swell as a function of organic modifier concentration. Quaternized PEI-zirconia is comparable in efficiency to a silica-based strong anion-exchanger in the separation of inorganic anions and proved to be more efficient in the chromatography of benzoic acid derivatives.

Physical characterization of quaternized PEI-zirconia and PEI-zirconia showed that 50% and 24% of the amine groups on the surface are involved in cross-linking, respectively. A plot of $\log k'$ versus \log (competing ion concentration) for three selected homopeptides showed that one mechanism of retention on quaternized PEI-zirconia is ion exchange. A study of the effect of temperature on quaternized PEI-zirconia column efficiency showed that from 50 °C to 100 °C, the number of theoretical plates was increased by at least 80% for selected probe amino acids. Quaternized PEI-zirconia cross-linked with 1,10-diiododecane is more hydrophobic than PEI-zirconia cross-linked with BUDGE. The free energies of transfer of a methylene group from the mobile phase to the stationary phase for quaternized PEI-zirconia and PEI-zirconia are -2.0 and -0.90 kJ/mol, respectively. The free energy of transfer of a methylene unit on quaternized PEI-zirconia is similar to that of a typical ODS phase (-2.4 kJ/mol). A van't Hoff plot for two 2,4-dinitrophenyl amino acids showed an average enthalpy of transfer of -14 kJ/mol, indicating that temperature has only a moderate effect on the capacity factor for these solutes on quaternized PEI-zirconia.

ACKNOWLEDGMENT

This research was supported by SarTec Corp. (Anoka, MN), the National Science Foundation, and the National Institutes of Health.

Received for review March 20, 1995. Accepted July 26, 1995.*

AC950278N

* Abstract published in *Advance ACS Abstracts*, September 15, 1995.

Effect of pH, NaCl, and Cocktail Selection on ^{232}U Liquid Scintillation Spectra

Colin G. Ong,* Amresh Prasad, and James O. Leckie

Environmental Engineering & Science, Department of Civil Engineering, Stanford University, Stanford, California 94305

The liquid scintillation energy spectra from the analysis of the radioisotope ^{232}U were obtained for ranges of pH and NaCl concentration, using a variety of scintillation cocktails. Shifts in peak position, as well as variation in peak widths and total counts, were observed for the variables studied. The results suggest that ^{232}U , a narrow energy band α -particle emitter, can be analyzed with an energy window significantly more narrow than the instrument full scale. This results in the elimination of much of the incidental background counts associated with additive instrument detection errors in the high-energy region, as well as α - and β -activity of daughter products.

The artificial radionuclide ^{232}U is being used as the radiotracer in the isotope dilution analysis¹ (IDA) of inorganic uranyl ion. IDA methods have commonly been developed for compounds of organic and biochemical interest.² The system of interest for which this ^{232}U IDA procedure is being developed involves mineral suspensions in which partitioning of the uranyl ion between solid and solution phases is being determined. This work is related to the study of radioactive waste containment in underground repositories.³ Partition ratios are determined under a range of pH and ionic strength conditions. Similar experiments with other sorbing species and mineral substrates have employed radiochemical IDA techniques. For example, IDA procedures associated with ^{45}Ca , ^{80}Se , and ^{109}Cd have been used for uptake studies on CaCO_3 .^{4–6} ^{63}Ni and ^{57}Co have also been used as radiotracers in sorption experiments.^{7,8} ICP emission spectroscopy has been used for direct quantitation of the interaction of U(VI) with calcite.⁹ IDA procedures employing other uranium radioisotopes for environmental analysis have been used in tandem with mass spectrometry,^{10–12} secondary ion mass spectrometry,¹³ thermal

ionization mass spectrometry, spark source mass spectrometry,¹⁴ inductively coupled plasma mass spectrometry,^{15–17} and α -spectrometry.¹⁸

Quantitation of the α -particle activity of the ^{232}U source can be achieved via liquid scintillation analysis, which calls for the use of complex organic mixtures called scintillation cocktails.¹⁹ Cocktail composition varies according to application and can affect the sample load capacity. The load capacities for water, NaOH, HCl, and NaCl are of particular concern in this ^{232}U IDA procedure. Exceeding load capacities results in heterogeneity of the sample-cocktail mixture, which may be a problem for liquid scintillation detectors which are in geometrically fixed positions around sample scintillation vials in a detection chamber.

^{232}U emits α -particles predominantly at 5.32 and 5.26 MeV (69 and 31% intensity, respectively),²⁰ toward the low end of α -particle energies. Use of liquid scintillation analysis results in photon production of lower energy suitable for detection with a photomultiplier tube (PMT). The response may differ according to interaction with the sample matrix and the efficiency of energy transfers. In this study, liquid scintillation spectra of ^{232}U are collected for samples adjusted to a range of NaCl concentrations and pH. Further motivation for this study is derived from the benefit of using a narrow energy window for peak integration. The α -particle energy full scale is far broader than needed for capture of the ^{232}U peak, and background counts may be critical to low activity sample analysis. In addition, ^{232}U has a half-life of 68.9 years in which ingrowth of daughter products can be rapidly established to become significant interferences within the order of weeks. Interference from the ingrowth manifests as a shoulder to the right of the ^{232}U peak and β -particle activity to the left.

EXPERIMENTAL SECTION

Materials. ^{232}U not in equilibrium with daughter products was purchased from Isotope Products Laboratories (Burbank, CA). The analyte of interest, ^{232}U , was isolated from ingrowths of

* To whom correspondence should be addressed. FAX: 415-725-3162. E-mail: cgon@leland.stanford.edu.

- (1) Ehmann, W. D.; Vance, D. E. *Radiochemistry and Nuclear Methods of Analysis*; Wiley-Interscience: New York, 1991; Chapter 10.
- (2) Skoog, D. A. *Principles of Instrumental Analysis*, 3rd ed.; Saunders College Publishing: Philadelphia, PA, 1985; Chapter 17.
- (3) Krauskopf, K. *Radioactive Waste Disposal and Geology*; Chapman and Hall: New York, 1988; Chapter 4.
- (4) Zachara, J. M.; Cowan, C. E.; Resch, C. T. *Geochim. Cosmochim. Acta* **1991**, *55*, 1549–1562.
- (5) Cowan, C. E.; Zachara, J. M.; Resch, C. T. *Geochim. Cosmochim. Acta* **1990**, *54*, 2223–2234.
- (6) Davis, J. A.; Fuller, C. C.; Cook, A. D. *Geochim. Cosmochim. Acta* **1987**, *51*, 1477–1490.
- (7) Bryce, A. L.; Kornicker, W. A.; Elzerman, A. W. *Environ. Sci. Technol.* **1994**, *28*, 2353–2359.
- (8) Zachara, J. M.; Resch, C. T.; Smith, S. C. *Geochim. Cosmochim. Acta* **1994**, *58*, 553–566.
- (9) Carroll, S. A.; Bruno, J. *Radiochim. Acta* **1991**, *52*, 187–193.
- (10) Li, S.; Hou, S. *Yuanzineng Kexue Jishi* **1991**, *25*, 68–70.
- (11) Pan, W.; Jin, J.; Zhang, X. *Sichuan Daxue Xuebao, Ziran Kexueban* **1991**, *28*, 186–190.

- (12) Shihomatsu, H. M.; Kakazu, M. H.; Iyer, S. S. *Isotopepraxis* **1987**, *23*, 35–37.
- (13) Adriens, A. G.; Fassett, J. D.; Kelly, W. R.; Simons, D. S.; Adams, F. C. *Anal. Chem.* **1992**, *64*, 2945–2950.
- (14) Jochum, K. P.; Seufert, H. M.; Midinet, B. S.; Rettmann, E.; Schoenberger, K.; Zimmer, M. *Fresenius' Z. Anal. Chem.* **1988**, *331*, 104–110.
- (15) Toole, J.; McKay, K.; Baxter, M. *Anal. Chim. Acta* **1991**, *245*, 83–88.
- (16) McLaren, J. W.; Beauchemin, D.; Berman, S. S. *Anal. Chem.* **1987**, *59*, 610–613.
- (17) Pin, C.; Lacombe, S.; Telouk, P.; Imbert, J. L. *Anal. Chim. Acta* **1992**, *256*, 153–161.
- (18) Shihomatsu, H. M.; Iyer, S. S. *J. Radioanal. Nucl. Chem.* **1988**, *128*, 393–401.
- (19) Ehmann, W. D.; Vance, D. E. *Radiochemistry and Nuclear Methods of Analysis*; Wiley-Interscience: New York, 1991; Chapter 8.
- (20) Heath, R. L. In *CRC Handbook of Chemistry and Physics*, 63rd ed.; Weast, R. C., Astle, M. J., Eds.; CRC Press: Boca Raton, FL, 1982.

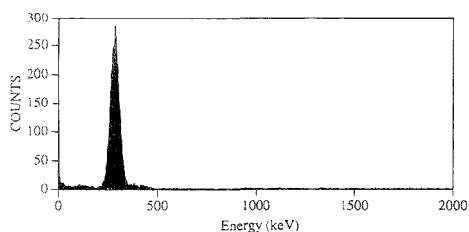


Figure 1. Liquid scintillation spectrum of ^{232}U in 0.1 M NaCl using Ultima Gold XR scintillation cocktail.

daughter products by preparative chromatography on AG1-X8 anion exchange resin from Bio-Rad (Richmond, CA), using concentrated HCl for retention and 0.1 M HCl for elution. Scintillation cocktails, including Ecolite from ICN Biomedicals (Irvine, CA) and Ultima Gold (UG), Ultima Gold AB (UGAB), and Ultima Gold XR (UGXR) from Packard (Downer Grove, IL), were obtained from reliable sources. Reagent grade chemicals were used to prepare a stock 5 M NaCl solution. Acculute standard solutions were used to prepare stock solutions of 1 N NaOH and 1 N HCl. Traceable pH buffers were used to calibrate pH measurement instrumentation.

Apparatus. A TR2500/AB liquid scintillation analyzer (Packard Instruments, Meriden, CT) was used for α -particle counting. Instrument control, data acquisition, and processing were done from an IBM PS/2 Model 60 computer.

Sample Preparation and Analysis. A stock 5 M NaCl solution was used to prepare 3, 2, 1, 0.5, and 0.1 M concentrations of the salt solution by successive dilution with distilled-deionized water. Solutions with measured pH of 8.9 and 11.0 were prepared from the stock base solution by dilution with distilled-deionized water. Solutions with measured pH of 1.0, 3.0, 4.8, and 6.1 were prepared from the stock acid solution by dilution with distilled-deionized water. A linear response over the range of sample pH values was assumed in the calibration of the pH measurement equipment with pH 4 and 10 buffers.

Samples were prepared by combining 3 mL of NaCl, NaOH, or HCl solution with 50 μL of ^{232}U solution and 15 mL of scintillation cocktail. The samples were manually shaken to thoroughly mix the contents. The samples were analyzed by liquid scintillation analysis (LSA) using a 60 min count time with no other termination parameter. The luminescence correction and high sensitivity count mode features were used. The instrument was also set to use the tSIE/AEC (transformed Spectral Index of the External standard coupled with Automatic Efficiency Correction²¹) quench indicator and a coincidence time of 18 ns.

Safety Considerations. Radioactive reagents should be transported, stored, handled, and disposed according to site-specific laws and regulations.

RESULTS AND DISCUSSION

A representative liquid scintillation spectrum of a sample containing ^{232}U is shown in Figure 1. Relatively low level interference resulting from daughter product ingrowth can be

(21) *Tri-Carb Liquid Scintillation Analyzers Model 2500TR Series Reference Manual*; Publication No. 169-4093 Rev. B; Packard Instrument Co.; Meriden, CT, 1992; Chapter 2.

Table 1. ^{232}U Peak Position and Half-Height Peak Width (in keV) for Samples of Various NaCl Concentrations

[NaCl] (M)	Ultima Gold		Ultima Gold AB		Ultima Gold XR		Ecolite(+)	
	posi- tion ^a	width ^b	posi- tion ^a	width ^b	posi- tion ^a	width ^b	posi- tion ^a	width ^b
0.1	180.0	38.5	261.5	47.0	283.5	49.5	230.5	43.0
0.5	175.0	40.0	261.5	46.0	287.5	52.5	225.5	43.0
1.0	174.5	38.5	260.5	44.5	307.5	53.5	243.0	41.0
2.0	172.5	39.0	294.5	50.0	327.5	54.5	266.0	44.0
3.0	178.0	56.5	315.0	55.5	343.0	56.0	276.0	43.5
5.0	207.5	59.0	343.0	55.5	355.0	56.0	285.0	41.5

^a Peak positions are points on the energy scale at which 10-value running sum is maximum. ^b Peak widths are reported as width at peak half-height.

Table 2. ^{232}U Peak Position and Half-Height Peak Width (in keV) for Samples of Various pH

pH	Ultima Gold		Ultima Gold AB		Ultima Gold XR		Ecolite(+)	
	posi- tion ^a	width ^b	posi- tion ^a	width ^b	posi- tion ^a	width ^b	posi- tion ^a	width ^b
1.0	265.5	50.5	235.0	45.5	185.0	40.0	217.0	41.5
3.0	262.5	49.5	257.0	48.5	176.5	38.5	226.5	42.0
4.7	263.5	48.0	258.5	47.0	186.5	39.5	226.5	42.0
6.1	267.0	50.0	257.0	47.5	185.0	39.5	227.0	42.0
8.9	265.5	51.0	250.5	48.5	178.0	37.5	221.0	41.0
11.0	267.5	48.5	258.0	48.5	186.5	40.0	223.5	42.5

^a Peak positions are points on the energy scale at which 10-value running mean sum is maximum. ^b Peak widths are reported as width at peak half-height.

observed adjacent to the peak. The baseline was essentially zero when samples containing recently purified ^{232}U were analyzed. Lower levels of counts arising from detector noise can also be observed scattered in the higher energy channels. The energy distribution peak for ^{232}U is characterizable as singular and symmetrical in the lower α -particle energy region.

Tables 1 and 2 contain the peak positions and widths at half-height for NaCl concentration- and pH-adjusted samples, respectively. Peak positions were determined using a 10-value running total average to smooth out the peak and selecting the channel in which this value was maximum. Variability in peak position was observed in the order UG < Ecolite < UGXR < UGAB for the NaCl-containing samples and UG < Ecolite \approx UGXR < UGAB for the pH-adjusted samples. However, no clear trends were observed except in the case of UGXR under varying NaCl concentration, where the peaks shifted to higher energies with increasing electrolyte concentration. The greatest shifts toward higher energy were typically observed at the high end of the pH and NaCl concentration ranges. Peak widths over all samples were fairly constant, with minimum variability in this characteristic found with the Ecolite cocktail. Peak widths varied more under the range of NaCl concentrations than in the pH series.

The observed peak heights are shown in Table 3 for the NaCl-containing samples. UG performed poorly in the 5.0 M NaCl case, and Ecolite performed poorly at 2.0 M NaCl and above. Increasing NaCl concentration appears to gradually lower the peak height in samples using UGXR. Peak heights were scattered in a narrow range when UGAB was used.

Table 3. ²³²U Peak Height for Samples of Various NaCl Concentrations

[NaCl] (M)	peak height (counts)			
	Ultima Gold	Ultima Gold AB	Ultima Gold XR	Ecolite(+)
0.1	186.0	234.8	254.2	341.9
0.5	182.5	215.8	225.1	341.1
1.0	170.4	232.0	213.7	336.2
2.0	120.9	194.2	196.5	266.6
3.0	195.5	180.7	187.0	255.3
5.0	364.8	172.5	178.5	248.2

Table 4. ²³²U Peak Height for Samples of Various pH

pH	peak height (counts)			
	Ultima Gold	Ultima Gold AB	Ultima Gold XR	Ecolite(+)
1.0	212.1	275.3	300.2	316.0
3.0	160.3	221.6	296.5	296.7
4.7	161.1	228.8	287.1	293.9
6.1	168.2	226.9	283.1	298.9
8.9	260.3	226.2	310.2	336.7
11.0	156.8	221.3	259.7	321.1

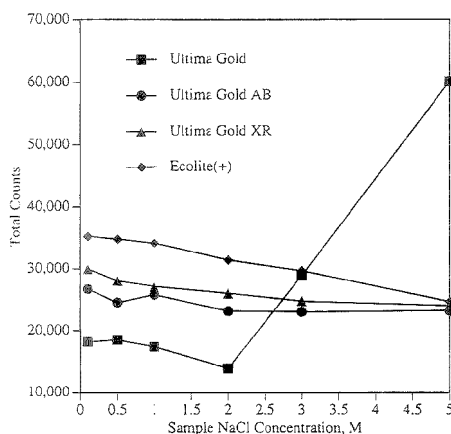


Figure 2. Effect of NaCl concentration on total integrated counts for various scintillation cocktails.

The observed peak heights are shown in Table 4 for the pH-adjusted samples. All the cocktails appear to have performed well in the intermediate-pH range. However, Ecolite, UG, and UGAB had higher peak heights at pH 1.0. Peak heights were elevated at pH 8.9 using UGXR, and at pH 8.9 and 11.0 using Ecolite.

For the routine quantitation of the ²³²U isotope in the IDA procedure, the counts are integrated over all energy channels. The quantitative response as represented by total counts is shown in Figure 2 for the NaCl series of samples, and in Figure 3 for the pH-adjusted series of samples. The uncertainty in the gross count values with 95% confidence limits is based on the accumulated counts²² and ranged from 1 to 2% 2σ. Over the ranges studied, UG obviously is an unsuitable choice. Ecolite provided

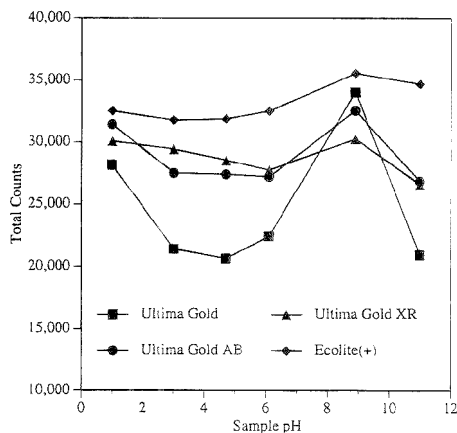


Figure 3. Effect of pH on total integrated counts for various scintillation cocktails.

the most attenuated level response but is appreciably above the count levels obtained by using UGXR and UGAB. A slightly broader range was seen in the UGAB response in the pH series. UGXR therefore appears to be the cocktail least affected by variations in pH and NaCl concentration. Samples using Ecolite were observed to experience phase separation in the form of either two liquid phases or a liquid phase and a solid phase which quickly settles. In either situation, the sample becomes heterogeneous and appears likely to have concentrated in the lower part of the vial in closest proximity to the photomultiplier sensors.

From the above results, it appears that UGXR is the most suitable scintillation cocktail for the quantitation of ²³²U in the IDA procedure applied to the chemical systems of interest. To estimate a suitable count integration window across the energy scale using UGXR, the range of peak positions and baseline widths can be used. Since the peaks are generally symmetrical and triangular, the baseline widths can be assumed to be twice the width at half-height, $W_{1/2}$. Therefore, the lower end of the window can be calculated from subtracting the maximum $W_{1/2}$ observed from the lowest peak position. Similarly, the upper end of the window is obtained by adding the maximum $W_{1/2}$ to the highest peak position. Such an approach yields a lower window limit of 156.5 keV and an upper window limit of 383 keV. Although this study does not experimentally address the composite effect of pH and NaCl concentration on peak positions, it has been found in practice that a window from 100 to 400 keV is an adequate bracket. Since a series of samples from a partition study is typically of constant NaCl concentration, the window can be narrowed further for each NaCl concentration, allowing about 10 keV leeway for the effect of pH. If interference from daughter products is significant in the analysis, integration may be performed only after establishing the energy channels making up a sample's peak base.

CONCLUSIONS

The liquid scintillation spectrum from ²³²U α-particle activity yields a symmetrical peak at the lower end of α-particle energies. Compared to instrument full scale of energy channels, the window bracketing different peak energy positions resulting from

(22) *Tri-Carb Liquid Scintillation Analyzers Model 2500TR Series Reference Manual*; Publication No. 169-4093 Rev. B; Packard Instrument Co., Meriden, CT, 1992; Chapter 6.

variations in pH or NaCl concentration is small. Use of a narrow integration window may improve the quantitation of the analyte.

The pH of samples has a relatively small effect on the position of the analyte peak in the liquid scintillation spectrum of ^{232}U . In contrast, NaCl concentration has a large effect but this does not pose a serious problem since the series of samples from any individual experimental run have uniform electrolyte concentration.

Phase separation can result from exceeding the sample loading capacities of scintillation cocktails. Although this can be ameliorated by increasing the ratio of cocktail to sample, it may require the use of larger volumes or longer count times to accumulate a statistically adequate number of counts.

ACKNOWLEDGMENT

The authors gratefully acknowledge funding from Sandia National Laboratories operated for the United States Department of Energy under Contract DE-AC04-94AL85000. The manuscript has not been subjected to official funding agency review, and no official endorsement by the agency should be inferred.

Received for review May 24, 1995. Accepted August 4, 1995.*

AC950504T

* Abstract published in *Advance ACS Abstracts*, September 15, 1995.

Novel Dye-Solvent Solutions for the Simultaneous Detection of Oxygen and Carbon Dioxide

Ming Fat Choi* and Peter Hawkins

Faculty of Applied Sciences, University of the West of England, Coldharbour Lane, Frenchay, Bristol BS16 1QY, U.K.

The effects of the compositions of *N,N*-dimethyl-*p*-toluidine/*N,N*-dimethylformamide (DMT/DMF) solvent mixtures, the types of bases, the initial base concentrations, and the water content on the performance of alkaline fluorescein (FL)-DMT/DMF (dye-solvent) solutions in determining oxygen (O₂) and carbon dioxide (CO₂) have been investigated. Increased [O₂] causes the absorbance of dye-solvent solutions at 400 nm to increase because of a contact charge transfer existing between DMT and O₂ molecules, and increased [CO₂] produces a nonlinear decrease in absorbance at 520 nm as the color of FL changes from its orange dianion (FL²⁻) to the colorless, neutral, lactic forms. The sensitivity to O₂ can be enhanced by increasing [DMT] in the DMT/DMF solvent mixture. A linear equation (i.e., $\log(A_0 - A)/A = 2\beta \log[\text{CO}_2] + \log(\alpha^2/K)$, where A_0 and A are the absorbances of dye-solvent solutions with nitrogen and CO₂ standards passing through, respectively, α and β are constants, and K is the dissociation constant for FL) is derived to relate the change of absorbance and applied [CO₂]. The sensitivity of dye-solvent solutions to O₂ is independent of the types of bases, but the sensitivity to CO₂ is not. Increased base concentration causes a change in the sensitivity to CO₂ but has no effect on O₂. The higher water concentration in dye-solvent solutions has two effects. First, dye-solvent solutions are more sensitive to CO₂. Second, there is a hypsochromic shift of FL²⁻ ions in DMT/DMF solvent mixture. A fiber-optic detecting system based on a solution of 10 μM FL and 336 μM tetrabutylammonium hydroxide in 1:1 (v/v) DMT/DMF has been developed for the determination of O₂ and CO₂. Their responses are reversible and independent. This solution can be used for future development of a single fiber-optic-based O₂/CO₂ sensor.

Oxygen (O₂) and carbon dioxide (CO₂) are the two most important gases in our environment, being found as either reactants or products in vast numbers of chemical and biochemical reactions. Considerable effort has been devoted to the development of analytical techniques for qualitative and quantitative determination of these two gases. The oldest standard method of analysis for dissolved O₂ is probably the Winkler method,¹ which is based on the colorimetric titration of liberated iodine in reaction mixtures with thiosulfate. This analytical method is time-consuming and cannot be used for in situ measurements or continuous monitoring. Another commonly used method for O₂ employs the Clark-type amperometric electrode, which is based

on the electroreduction of O₂ on a polarized cathode. It is a moderately fast, simple, and convenient technique. However, it suffers from several drawbacks, such as the flow dependence of the O₂ response and interferences from easily reducible species like hydrogen sulfide.² Potentiometric O₂ sensors are based on the Nernstian response of some solid oxide ion conducting electrolytes operating at high temperatures.³⁻⁵ Paramagnetic quantitation of gaseous O₂ suffers from interference by other paramagnetic species, such as nitric oxide or free radicals.⁶ The fluorescence quenching effect of O₂ on some fluorophores, analyzed by the Stern-Volmer equation,⁷ is another promising approach for O₂, but this method suffers from competitive quenching by other interferents.

There are fewer CO₂ detection techniques, due to its relative chemical inertness. Indirect detection is often used, based on the pH modulation of a detecting system upon exposure to CO₂. pH changes can be measured and related to the [CO₂]⁸ or indirectly detected by absorbance or fluorescence changes of some pH-sensitive dyes. Direct detection of CO₂ can be based on its intense infrared (IR) absorption band at 4.2 μm , which is particularly useful for its determination.^{9,10} However, this technique also suffers from interference from other absorbing species, such as water (H₂O) vapor and carbon monoxide. Potentiometric CO₂ sensors based on the Nernstian response of a solid metal carbonate electrolyte were employed by other workers,^{11,12} but the sensors required high operation temperatures. Sawyer et al.^{13,14} employed an amperometric technique for CO₂ based on the electroreduction of CO₂ at a stationary electrode in dimethyl sulfoxide. However, it is essential to exclude O₂, because O₂ is more easily reduced than CO₂, which becomes a serious drawback to this design.

With the advent of modern optic and electronic technologies, there is now a growing interest in multianalyte sensors for biomedical and environmental fields. O₂, CO₂, and pH are three clinical target analytes desired for simultaneous determinations.

(2) Hitchman, M. L. *Measurement of Dissolved Oxygen*; John Wiley & Sons: New York, 1978; pp 132-133.

(3) Heyne, L. *Electrochim. Acta* 1970, 15, 1251-1266.

(4) Agrawal, Y. K.; Short, D. W.; Gruenke, R.; Rapp, R. A. *J. Electrochem. Soc.* 1974, 121, 354-360.

(5) Lukaszewicz, J. P.; Mitura, N.; Yamazoe, N. *Sens. Actuators B* 1990, 1, 195-198.

(6) Reference 2, pp 178-182.

(7) Stern, O.; Volmer, M. *Phys. Z.* 1919, 20, 183.

(8) Severinghaus, J. W.; Bradley, A. F. *J. Appl. Physiol.* 1958, 13, 515-520.

(9) Ammann, E. C. B.; Galvin, R. D. *J. Appl. Physiol.* 1968, 25, 333-335.

(10) Ellis, R. E.; Schurin, B. *Appl. Opt.* 1969, 8, 2265-2268.

(11) Imanaka, N.; Kawasato, T.; Adachi, G. *Chem. Lett.* 1990, 4, 497-500.

(12) Yao, S.; Shimizu, Y.; Miura, N.; Yamazoe, N. *Chem. Lett.* 1990, 11, 2033-2036.

(13) Roberts, J. L.; Sawyer, D. T. *J. Electroanal. Chem.* 1965, 9, 1-7.

(14) Haynes, L. V.; Sawyer, D. T. *Anal. Chem.* 1967, 39, 332-338.

(1) Winkler, L. W. *Ber. Dtsch. Chem. Ges.* 1888, 21, 2843.

Few publications on multianalyte detection have appeared so far. Severinghaus^{8,15,16} used separate electrodes and compartments for individual amperometric determination of O₂ and potentiometric determination of CO₂. Albery and Barron¹⁷ applied similar techniques by employing an isolated aqueous electrolyte for electroreduction of O₂ and a nonaqueous electrolyte for electroreduction of CO₂. In addition, separate O₂, CO₂, and pH electrochemical microsensors were fabricated and integrated on a silicon chip for blood gas monitoring.^{18,19} Arnould et al.²⁰ designed a breath-by-breath instrument for O₂ and CO₂ detection based on nondispersive absorption of O₂ at 147 nm and CO₂ at 4.3 μm. However, there is some cross-interference of O₂ from CO₂, and a wavelength in the vacuum ultraviolet region is required for monitoring O₂.

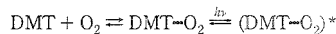
In the last decade, considerable research effort has been expended on optical fibers owing to their advantages of ease of miniaturization, immunity to electric interference, relatively low cost, high information carrying capacity. Fiber-optic-based sensors for O₂, CO₂, and pH have already been reported in the literature. For instance, three individual optical fibers with analyte-sensitive dyes attached to their ends were positioned in a probe for measuring O₂, CO₂, and pH.^{21,22} Wolfbeis et al.²³ and Yim et al.²⁴ applied a similar approach by entrapping both O₂- and CO₂-sensitive dyes to the distal end of a single fiber for detection of O₂ and CO₂. In these techniques, separate analyte-sensitive dyes were often used for each gas determination; however, no single detecting medium has been reported for sensing both analytes. There is a need to develop a simple, single detecting medium for both analytes which can be further developed into a multianalyte fiber-optic-based sensor.

Contact charge transfer (CCT) absorption of some organic solvents with O₂ has been known for over 40 years,²⁵ and the CCT absorption is proportional to the applied O₂ of the solvent.²⁶ We have reported the potential applications of some organic solvents for fiber-optic detection of gaseous O₂.²⁷ Recently, we found that, with the incorporation of a pH-sensitive dye in some aniline derivatives, a single dye-solvent solution is able to sense both gaseous O₂ and CO₂ reversibly and independently.^{28,29} In this paper, we further investigate in detail the compositions of the solvent mixtures, the types of bases, the initial base concentra-

tions, and the H₂O content, which can affect the performance of dye-solvent solution sensors for O₂ and CO₂. The results are important for optimization of a dye-solvent solution to sense O₂ and CO₂ independently, simultaneously, and reversibly.

THEORY

The response of our dye-solvent solutions to O₂ is based on the CCT absorption of molecular O₂ with *N,N*-dimethyl-*p*-toluidine (DMT). A donor molecule, such as DMT, reacts with an O₂ molecule to form a CCT complex, DMT···O₂, which is responsible for the CCT absorption.²⁷ If the absorbance of the



DMT···O₂ complex, A_{O₂}, follows the Beer-Lambert law, the following equation can be obtained:

$$A_{\text{O}_2} = k[\text{DMT}]P_{\text{O}_2} \quad (1)$$

where *k*, [DMT], and P_{O₂} are a constant, DMT concentration, and partial pressure of applied O₂, respectively. It was observed that DMT gives a strong CCT absorption spectrum with O₂ in the ultraviolet/visible (UV/vis) region. The reactions are completely reversible, and the change in absorbance is directly proportional to [DMT] and the applied gaseous O₂. Thus, it is possible that DMT can act as a sensing medium for O₂.

It has also been reported that some pH-sensitive dyes change color when exposed to gaseous CO₂. The color change (absorbance/fluorescence change) of the dye is sensitive to the pH of its surrounding environment. Fluorescein (FL) dye was successfully used for the fabrication of a fiber-optic CO₂ sensor.³⁰ We observed that there was an absorbance change of a highly alkaline solution of FL in *N,N*-dimethylformamide (DMF) upon exposure to CO₂. The neutral form of fluorescein (H₂FL) can exist in three tautomers, i.e., zwitterion, quinoid, and lactone. The colorless lactonic form of H₂FL is usually the dominant tautomer present in organic solvents.³¹ H₂FL in a highly alkaline DMF medium will completely deprotonate into fluorescein dianion (FL²⁻) ions. However, the orange FL²⁻ ions are easily converted into the colorless H₂FL form upon exposure to CO₂.

The pH in an aqueous solution of base or hydrogen carbonate should be directly proportional to applied pCO₂,⁶ however, we found that this was not the case in an alkaline DMF solution. To process our experimental results, the following equation was derived:

$$\log[(A_0 - A)/A] = 2\beta \log [\text{CO}_2] + \log(\alpha^2/K) \quad (2)$$

where A₀ and A are the absorbances of FL in alkaline DMF with nitrogen (N₂) bubbling (i.e., [CO₂] = 0) and [CO₂] standards passing through, respectively, α and β are constants, and K is the acid dissociation constant of FL in DMF/DMT solvent mixture. From eq 2, a dye-solvent solution will be in its half-way absorbance change at the applied CO₂ ([CO₂]_{1/2}) when [H₂FL] is equal to [FL²⁻]. The [CO₂]_{1/2} value can provide an indication of the sensitivity of a dye-solvent solution to CO₂.

- (15) Severinghaus, J. W. *Ann. N. Y. Acad. Sci.* **1968**, *148*, 115–132.
 (16) Severinghaus, J. W. *J. Appl. Physiol.* **1981**, *51*, 1027–1032.
 (17) Albery, W. J.; Barron, P. *J. Electroanal. Chem.* **1982**, *138*, 79–87.
 (18) Arquint, Ph.; van den Berg, A.; van der Schoot, E. H.; de Rooij, N. F.; Bühler, H.; Morf, W. E.; Dürselen, L. F. *J. Sens. Actuators B* **1993**, *13–14*, 340–344.
 (19) Gumbrecht, W.; Peters, D.; Scheiter, W.; Erhardt, W.; Henke, J.; Steil, J.; Sykora, U. *Sens. Actuators B* **1994**, *18–19*, 704–708.
 (20) Arnould, P. B.; Pardue, H. L.; Bourliand, J. D.; Miller, R.; Geddes, L. A.; *Anal. Chem.* **1992**, *64*, 200–204.
 (21) Gehrich, J. L.; Lübbers, D. W.; Optiz, N.; Hansmann, D. R.; Miller, W. W.; Tusa, J. K.; Yafuso, M. *IEEE Trans. Biomed. Eng.* **1986**, *BME-33*, 117–132.
 (22) Miller, W. W.; Yafuso, M.; Yan, C. F.; Hui, H. K.; Arick, S. *Clin. Chem. (Winston-Salem, NC)* **1987**, *33*, 1538–1542.
 (23) Wolfbeis, O. S.; Weis, L. J.; Leiner, M. J. P.; Ziegler, W. E. *Anal. Chem.* **1988**, *60*, 2028–2030.
 (24) Yim, J. B.; Khalil, G. E.; Pihl, R. J.; Huss, B. D.; Vurek, G. G. U.S. Patent 5098659, 1992.
 (25) Evans, D. F. *J. Chem. Soc.* **1953**, 345–347.
 (26) Munck, A. U.; Scott, J. F. *Nature* **1956**, 587.
 (27) Choi, M. F.; Hawkins, P. *Talanta*, in press.
 (28) Choi, M. F.; Hawkins, P. In *Frontiers in Analytical Spectroscopy*; Andrews, D. L.; Davies, A. M. C., Eds.; Royal Society of Chemistry: Cambridge, U.K., 1995; pp 189–195.
 (29) Choi, M. F.; Hawkins, P. *Talanta* **1995**, *42*, 483–492.

(30) Munkholm, C.; Walt, D. R. *Talanta* **1988**, *35*, 109–112.

(31) McEedlov-Petrosyan, N. O.; Rubtsov, M. I.; Lukatskaya, L. L. *Dyes Pigm.* **1992**, *18*, 179–198.

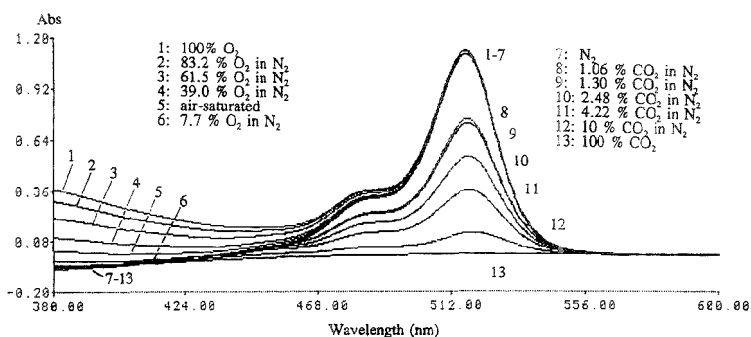


Figure 1. Effect of O₂ and CO₂ on the absorption spectra of 10 μM FL and 168 μM TBUAOH in 2:3 (v/v) DMT/DMF solvent mixture. References: air-saturated 168 μM TBUAOH in 2:3 (v/v) DMT/DMF solvent mixture. Path length, 10 mm.

With the combination of FL in alkaline DMF and DMT, it is possible to prepare a dye-solvent solution to determine both gaseous O₂ (based on the CCT absorption of DMT with O₂) and CO₂ (based on the color change of the FL²⁻ ions).

EXPERIMENTAL SECTION

Reagents. DMT (99%), DMF (>99.9%, HPLC grade), methanol (MeOH, >99% HPLC grade), FL dye (98%), tetrabutylammonium hydroxide (TBUAOH, 1.0 mol dm⁻³ solution in MeOH), tetrapentylammonium bromide (TPeABr, >99%), tetrahexylammonium bromide (99%), tetraheptylammonium bromide (99%) and tetraoctylammonium bromide (98%) were obtained from Aldrich Chemical Co. Potassium hydroxide (KOH, 85.0%, AnalaR grade) was from BDH Chemical Co. Approximately 0.10 mol dm⁻³ methanolic tetrapentylammonium hydroxide (TPeAOH) solution was prepared from a solution of TPeABr treated with KOH in MeOH, and the insoluble potassium bromide was removed by filtration.³² Methanolic solutions of tetrahexylammonium hydroxide (THxAOH), tetraheptylammonium hydroxide (THpAOH), and tetraoctylammonium hydroxide (TOcAOH) were prepared similarly. The concentrations of all the methanolic base solutions were determined by a standard acid-base titration method,³³ whereas the concentration of the FL dye was determined spectrophotometrically by employing the molar absorptivity of FL²⁻ ions.³⁴ Water used was deionized by the Purite RO200-Stillplus HP system. Nitrogen gas, O₂ gas, 10% (v/v) CO₂ in a N₂/CO₂ gas mixture and CO₂ were supplied by Distillers MG. All other gas mixtures were generated by controlling the flow rates of either O₂ gas or 10% CO₂ in a N₂ gas mixture and the diluent N₂ gas entering a home-made gas blender. The O₂ and CO₂ concentrations in the gas mixture were determined with an O₂ meter (Oxywarn 100I, Draeger Manufacturing) and a CO₂ detector (LFG 10 landfill gas analyser from Analytical Development Co. Ltd).

Instrumentation. UV/vis absorption spectra were recorded with a Perkin-Elmer Lambda 15 spectrophotometer (Buckinghamshire, U.K.) equipped with an Epson FX-850 dot-matrix printer (Epson Telford Ltd.). Fluorescence excitation and emission spectra were obtained with a Perkin-Elmer LS-5 luminescence

spectrometer in conjunction with a Perkin-Elmer GR100 graphics printer. The fiber-optic sensing system for O₂ and CO₂ comprised a laboratory-made optical arrangement as previously described.²⁹ Briefly, a modulated beam of incident light [provided from a 100 W quartz halogen lamp, a current-stabilized filament power supply, an optical chopper, and a monochromator (Bentham Instruments Ltd.)] guided by a 1 m long plastic optical fiber (core/cladding diameter, 1.00 mm; NA, 0.47 from RS Components) irradiated the investigating dye-solvent solution in a 10 mm quartz cuvette with gaseous O₂ and CO₂ standards passing through. The transmitted light was collected by another similar 0.5 m long plastic optical fiber and led onto a 100 mm² photovoltaic detector (RS Components). The output signal was amplified by a lock-in amplifier (Bentham Instruments) and recorded on a BBC Goerz Metrawatt SE120 chart recorder or shown on a light-emitting diode display unit (Bentham 217 digital unit).

Dye-Solvent Solutions. Dye-solvent solutions were prepared by adding 70 μL of a concentrated FL solution in DMF solution and 5–40 μL of a concentrated methanolic base solution in a solvent mixture of DMT/DMF. For the fluorescence measurement, the concentration of FL in the dye-solvent solution was 100-fold lower than that in the dye-solvent solution for absorbance measurement.

RESULTS AND DISCUSSION

Effect of Compositions of Solvent Mixtures. A strong absorption band of FL²⁻ ions in the visible region was found for an alkaline solution of FL in DMF. When DMT is added into this solution with O₂ standards passing through it, another absorption band emerges in the near UV region (due to the CCT absorption of DMT with O₂), its absorption edge overlapped with the FL²⁻ ions absorption band (Figure 1). The absorbance change of the band in the near-UV region responds to different [O₂] whereas the FL²⁻ ions absorption band in the visible region is sensitive to different [CO₂]. Using eq 1, plots of A₀₂ vs [O₂] at 400 nm for the different solvent mixtures of DMT/DMF are obtained (Figure 2a). It is clearly seen that the absorbance change of dye-solvent solutions is directly proportional to the applied [O₂], and the sensitivity to O₂ increases as [DMT] in dye-solvent solutions increases. The absorbance change of dye-solvent solutions at 520 nm to CO₂ is nonlinear; however, applying eq 2, straight lines can be obtained by plotting log(A₀₂ - A)/A vs log [CO₂] (Figure 2b).

(32) Miller, I. T.; Springall, H. D. *Sidwick's Organic Chemistry of Nitrogen*, 3rd ed.; Clarendon Press: Oxford, U.K., 1966; p 117.

(33) Vogel, A. I. *Quantitative Inorganic Analysis*, 3rd ed.; Longmans, Green: London, U.K., 1961; p 243.

(34) Diehl, H. *Talanta* 1989, 36, 413–415.

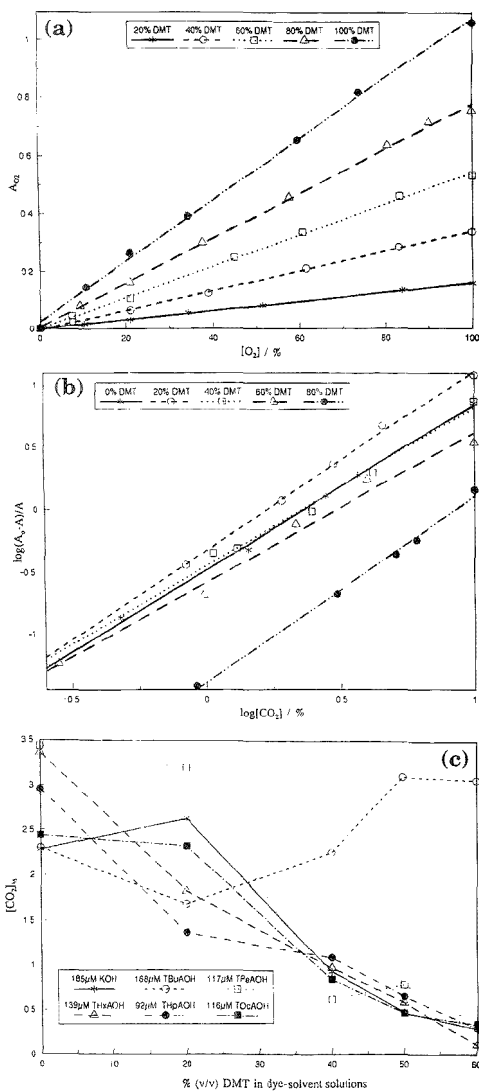


Figure 2. (a) Plot of A_{400} vs $[O_2]$ at 400 nm. (b) Plot of $\log(A_{520} - A)/A$ vs $\log[CO_2]$ at 520 nm. (c) Plot of $[CO_2]_{1/2}$ vs percentage (v/v) of DMT in dye-solvent solutions.

Different types of bases dissolved in various [DMT] and [DMF] of dye-solvent solutions have been tested for their response to O_2 and CO_2 . It was found that the absorption spectra of these solutions (not shown in this paper) are similar to those shown in Figure 1. The response of dye-solvent solutions to O_2 is independent of the types of bases, and the sensitivity to O_2 is directly proportional to [DMT] and the applied $[O_2]$ in dye-solvent solutions. As long as some base is present, regardless of type, dye-solvent solutions respond well to CO_2 . However, the sensitivity to CO_2 varies slightly with different types of bases, as indicated by the $[CO_2]_{1/2}$ value and shown in Figure 2c. The

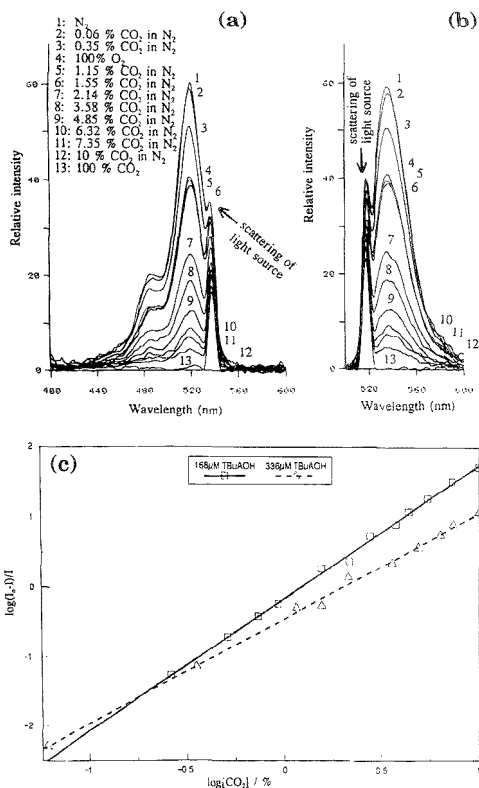


Figure 3. Effect of CO_2 on the fluorescence excitation and emission spectra of a solution of $0.10 \mu M$ FL and $336 \mu M$ TBuAOH in 1:1 (v/v) DMT/DMF solvent mixture. Path length, 10 mm. (a) Excitation spectra with emission wavelength at 536 nm. (b) Emission spectra with excitation wavelength at 520 nm. (c) Plot of $\log(I_0 - I)/I$ vs $\log[CO_2]$. Solutions of 168 and $336 \mu M$ TBuAOH were used.

general trend is that as [DMT] increases, the sensitivity increases (or $[CO_2]_{1/2}$ decreases), except for the TBuAOH. We do not know why TBuAOH behaves differently from other types of bases. With a further increase of DMT ([DMT] > 60% (v/v)), the color of the dye-solvent solutions is unstable and the response to CO_2 is irreversible. Thus, we are unable to obtain accurate values of $[CO_2]_{1/2}$ in the range of [DMT] > 60% (v/v). The acid dissociation constant of FL in DMT/DMF solvent mixtures decreases as dye-solvent solutions change from low to high [DMT]. Comparing DMT and DMF, DMT is a more hydrophobic or nonpolar solvent than DMF. We expect the neutral lactonic form of H_2FL (nonpolar) to be more soluble in DMT than in DMF. Similarly, FL^{2-} ions are more soluble in DMF than in DMT. As a result, more FL^{2-} ions are converted into H_2FL as [DMT] increases in dye-solvent solutions. In theory, different quaternary ammonium hydroxides (QAOHs) can act as a buffer in dye-solvent solutions. However, KOH has a limited solubility in DMT/DMF solvent mixtures, and the syntheses of other QAOHs are time-consuming. Therefore, we used TBuAOH in most of our experiments because it is easily available commercially and requires no further purification and synthesis.

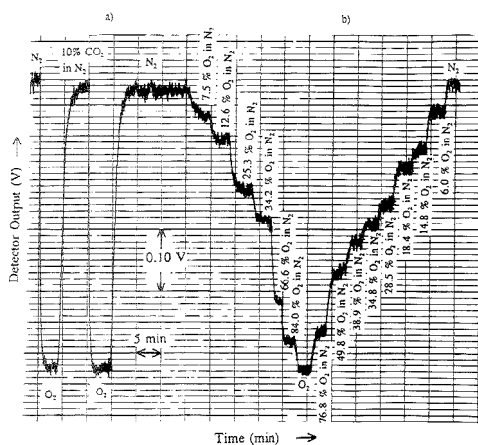


Figure 4. (a) Response time, reproducibility, and total signal change of the fiber-optic sensing system subjected to changes between $N_2 \rightarrow O_2 \rightarrow 10\% CO_2$ in $N_2 \rightarrow O_2 \rightarrow N_2$. A 0.75 mL portion of a solution of $10 \mu M$ FL and $336 \mu M$ TBuAOH in 1:1 (v/v) DMT/DMF solvent mixture was used. Path length, 10 mm. (b) Response of the fiber-optic sensing system to different $[CO_2]$.

Effect of Concentration of Bases. The variation in concentration of bases $[OH^-]$ in dye-solvent solutions does not affect the sensitivity to O_2 (not shown in this paper), and the sensitivity to CO_2 varies only a little with different $[OH^-]$. The effect of [TBuAOH] on sensitivity to CO_2 is greater than that of the other QAOHs. The general trend is that as $[OH^-]$ increases, the sensitivity decreases ($[CO_2]_{1/2}$ increases). This can be explained by the fact that more dissolved CO_2 is consumed by the OH^- ions when $[OH^-]$ increases.

Effect of Water Content. The effect of water content in FL-TBuAOH-DMT/DMF solutions was investigated. As the $[H_2O]$ increases, the $[CO_2]_{1/2}$ value decreases. H_2O has a higher tendency to dissociate into H^+ and OH^- ions as the $[H_2O]$ increases, with a concomitant effect of converting the FL^{2-} ions into H_2FL . It is also found that there is a hypsochromic shift of the FL^{2-} ions absorption band for DMT/DMF solvent mixtures when $[H_2O]$ increases. This observation is consistent with the results reported by Martin.³⁵ The electronic ground (S_0) state of FL^{2-} ions is more stabilized than its first excited (S_1) state by the hydrogen-bonding effect of FL^{2-} ions with the surrounding H_2O molecules.

Fluorescence Studies. The response of dye-solvent solutions to CO_2 can also be determined by fluorescence measurement since FL^{2-} ions are strongly fluorescent; but the neutral lactonic form of H_2FL is not (Figure 3a,b). Emission spectra obtained at excitation (EX) wavelengths of 488 and 520 nm are similar but different in intensity, indicating that internal conversion from the second excited (S_2) state to the S_1 state is efficient after EX from the S_0 state to the S_2 state, with subsequent fluorescence occurring when electrons fall from the S_1 state back to the S_0 state. The fluorescence intensity decreases with increased applied $[CO_2]$. The change of the intensity (I) is nonlinear with $[CO_2]$ and decreases as [TBuAOH] increases. Using eq 2, with substitution of A by I ,

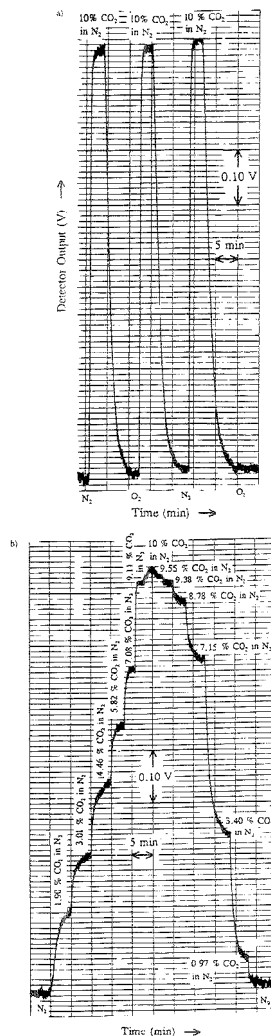


Figure 5. (a) Response time, reproducibility, and total signal change of the fiber-optic sensing system subjected to changes between $N_2 \rightarrow 10\% CO_2$ in $N_2 \rightarrow O_2 \rightarrow 10\% CO_2$ in $N_2 \rightarrow O_2 \rightarrow N_2$. A 0.75 mL portion of a solution of $10 \mu M$ FL and $336 \mu M$ TBuAOH in 1:1 (v/v) DMT/DMF solvent mixture was used. Path length, 10 mm. (b) Response of the fiber-optic sensing system to different $[CO_2]$.

straight lines (Figure 3c) can be obtained by plotting $\log[(I_0 - I)/I]$ vs $\log[CO_2]$, where I_0 and I are the fluorescence intensities with N_2 and different $[CO_2]$ standards passing through dye-solvent solutions, respectively.

Fiber-Optic Sensing System for O_2 and CO_2 . The experimental results show that FL dye dissolved in an alkaline DMF/DMT solvent mixture can sense gaseous O_2 and CO_2 . A solution of $336 \mu M$ TBuAOH and $10 \mu M$ FL in 1:1 (v/v) DMT/DMF was used to develop a sensing system for both O_2 and CO_2 . Absorbance changes at 400 and 520 nm were monitored to detect O_2

(35) Martin, M. M. *Chem. Phys. Lett.* 1975, 35, 105-111.

and CO₂, respectively. Although fluorescence measurement of FL²⁻ ions, in principle, can be adapted to sense CO₂, we found that there was a cross-interference on CO₂ from O₂ due to the fluorescent quenching effect of molecular O₂ on FL²⁻ ions (Figure 3a, line 4). Thus, all the studies were based on absorption spectroscopy. Using the experimental setup described earlier, the response time, reproducibility, and total signal change of the sensing system for O₂ and CO₂ were investigated.

Figure 4a shows the response of the sensing system monitored at 400 nm to step changes in gas concentration from 100% N₂ to 100% O₂ and from 100% O₂ to 10% CO₂ in N₂. The reversibility is good, and there is no cross-interference from CO₂. The response times are 0.67 and 1.75 min for a 90% signal change from N₂ to O₂ and from O₂ to N₂, respectively. The response to different levels of O₂ was investigated (Figure 4b), and the decrease in signal level with increasing [O₂] is nonlinear but obeys the Beer-Lambert law in a plotting of $\log(I_{N_2}/I_{O_2})$ vs [O₂], where I_{N_2} and I_{O_2} are the signal levels recorded in N₂ only and O₂, respectively. Figure 5a shows the response of the sensing system at 520 nm to step changes in gas concentration from 100% N₂ to 10% CO₂ in N₂ and from 10% CO₂ in N₂ to O₂. The reversibility is good, and there is no cross-interference from O₂. The response times are 0.35 and 4.75 min for a 90% signal change from N₂ to 10% CO₂ in N₂ and from 10% CO₂ in N₂ to O₂, respectively. The response to different levels of CO₂ was investigated (Figure 5b), and the decrease in signal level with increasing [CO₂] was found to be nonlinear, but a straight line can be obtained by plotting $\log(A_0 - A)/A$ vs $\log[CO_2]$, where $A_0 = \log(I_b/I_{N_2})$ and $A = \log(I_b/I_{CO_2})$. I_b is the signal level obtained by using a solution of 336 μ M TBuAOH in 1:1 (v/v) DMT/DMF, whereas I_{N_2} and I_{CO_2} are signal levels recorded with N₂ and CO₂ passing through a solution of 336 μ M TBuAOH and 10 μ M FL in 1:1 (v/v) DMT/DMF, respectively.

The precision of the detecting system is 1.59% ($n = 5$) in a gas mixture of 40.1% O₂ in N₂ and 0.89% ($n = 5$) in a gas mixture of 6.95% CO₂ in N₂. The stability is good, having 0.83–2.92% signal drift per hour of operation. This dye-solvent solution is fairly

stable for over a period of 6 months at ambient conditions, having only 1.98% loss in sensitivity to O₂ and 5.03% loss in FL due to photobleaching of FL.

CONCLUSIONS

The sensitivity of dye-solvent solutions to O₂ and CO₂ can be tuned by adjusting the composition of the DMT/DMF solvent mixture, the initial base concentration, and the water content. There are several advantages to using these dye-solvent solutions to determine O₂ and CO₂. There is no cross-interference between the two gases. Preparation of dye-solvent solutions is simple and fast. The two absorption bands in the visible region allow the use of plastic optical fibers. The chemicals used are cheap and easily available commercially.

Finally, to avoid a slight signal drift caused by a small evaporation of the solvents, the dye-solvent solution can be replaced with a fresh one at ~2 h intervals. Alternatively, the reagent can be confined behind a small-pore-size gas-permeable hydrophobic [poly(tetrafluoroethylene)] membrane so as to prevent any solvent loss and water contamination. The stability of the output signal can be further improved by ratioing the intensities at an analytical wavelength to a reference wavelength (e.g., above ~550 nm, free from O₂ and CO₂ interferences). The dye-solvent solution can possibly be used as a sensing medium for the development of a fiber-optic O₂/CO₂ sensor in the future.

ACKNOWLEDGMENT

The authors express their thanks to Dr. A. Tubb (University of the West of England) for the loan of the oxygen and carbon dioxide detectors and to the University of the West of England for financial support.

Received for review October 5, 1994. Accepted August 4, 1995.*

AC9409849

* Abstract published in *Advance ACS Abstracts*, October 1, 1995.

Automated In-Line Extraction of Uranium(VI) from Raffinate Streams with On-Line Detection by Cathodic Stripping Voltammetry

Johannes T. van Elteren,[†] Constant M. G. van den Berg,^{*†} Hao Zhang,^{†,§} Trevor D. Martin,[‡] and Eric P. Achterberg[†]

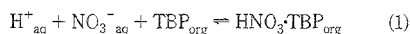
Oceanography Laboratories, University of Liverpool, P.O. Box 147, Liverpool L69 3BX, U.K., and Analytical Services Technical Department B229, Chemical Analysis, BNFL, Sellafield Seascale, Cumbria CA 20 1PG, U.K.

An automated method for on-site monitoring of uranium(VI) in raffinate streams originating from nuclear fuel reprocessing plants is described. An in-line stripping procedure (based on liquid/liquid extraction) was developed to extract U(VI) from this stream, a solvent mixture of 20% tributyl phosphate and nitric acid in kerosene, into an aqueous sodium sulfate solution. Degradation products in the solvent mixture, especially dibutyl phosphate, give rise to very strong complexes and are responsible for moderate but constant U(VI) recoveries (~50%). Optimal conditions for in-line stripping comprise a mixing ratio of extractant (0.5 M sodium sulfate in water)/solvent mixture of ~3 and a pumping rate of ~0.4 mL min⁻¹ of the solvent mixture. The determination of U(VI) was by on-line cathodic stripping voltammetry (CSV), preceded by adsorptive collection of the U(VI) as an oxine complex onto a hanging mercury drop electrode. Quantities of 1–2 mL of the aqueous extract were pumped into the voltammetric cell and diluted (1/5 to 1/10) with a background electrolyte containing 0.1 M PIPES buffer, 2 × 10⁻⁴ M oxine, 10⁻⁴ M EDTA, and 0.2 M hydrazine hydrate (pH 9.0). The CSV peak for U(VI) was obtained at -0.68 V with a detection limit of 20 nM in the raffinate stream using an adsorption time of 120 s. Both the in-line stripping procedure and the on-line measurement were fully automated, with a relative standard deviation in the measurements of <5%.

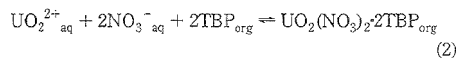
This study describes a method for the determination of hexavalent uranium (U(VI)) in mixtures of tributyl phosphate (TBP) and kerosene. These solvents are used in the reprocessing of nuclear fuels. In this process, the "unburnt" uranium is separated from plutonium and other radioactive fission products. To this end, the "spent" fuel elements are dissolved in concentrated nitric acid, and the U(VI) in the resulting solution is extracted, purified, and preconcentrated with a TBP/kerosene mixture (usually ~20% TBP in kerosene) in a three-step procedure:¹ In the first step, uranium(VI) and plutonium(IV) are separated together from the fission products; uranium(VI) and plutonium(IV) are extracted into the organic phase, and the fission

products remain in the aqueous phase. In the second step, plutonium(IV) is transferred to the aqueous phase by reducing it to the trivalent state, while uranium(VI) remains in the organic phase. In the third step, the uranium(VI) is stripped from the organic phase by washing with dilute nitric acid. Although most of the uranium is back-extracted into the aqueous nitric acid phase, trace amounts remain in the organic phase. Insight into the remaining uranium in this phase is of eminent importance in the reprocessing of nuclear fuels.

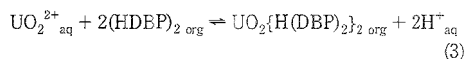
The chemistry of the uranium(VI)-nitric acid-TBP system has been reviewed by De et al.² The extraction is generally formulated as an ion exchange reaction, the extractant being regarded as a liquid ion exchanger. The extraction reactions (side reactions are ignored) are



and



In nuclear fuel reprocessing, several beneficial decomposition effects have been observed in the extraction of U(VI) with TBP in kerosene. Due to radiolytic and hydrolytic decomposition, the extractant partially decomposes to mono- and dibutyl phosphoric acids, which complex and extract U(VI) as well. Even small amounts of dibutyl phosphate (DBP) can alter the extraction properties of the TBP solvent. DBP (protonated and dimerized under the given conditions) extracts U(VI) with high distribution ratios even at low pH values of the aqueous phase according to the reaction³



Under comparable conditions the extraction coefficient for reaction 3 is a factor of 10³–10⁴ greater than that for reaction 2. Synergistic effects from a combination of TBP and DBP further enhance the extraction of U(VI).⁴

[†] University of Liverpool.

[‡] BNFL.

[§] Current address: Environmental Science Department, Lancaster University, Lancaster LA1 4YQ, U.K.

(1) Collins, J. C. *Radioactive Wastes, Their Treatment and Disposal*; Wiley: New York, 1960; Chapter 2.

(2) De, A. K.; Khopkar, S. M.; Chalmers, R. A. *Solvent Extraction of Metals*; Van Nostrand Reinhold Co.: London, 1970.

(3) Baes, C. F.; Zingaro, R. A.; Coleman, C. F. *J. Phys. Chem.* 1958, 62, 129.

(4) Hahn, H. T.; Van der Wall, E. M. *J. Inorg. Nucl. Chem.* 1964, 26, 191.

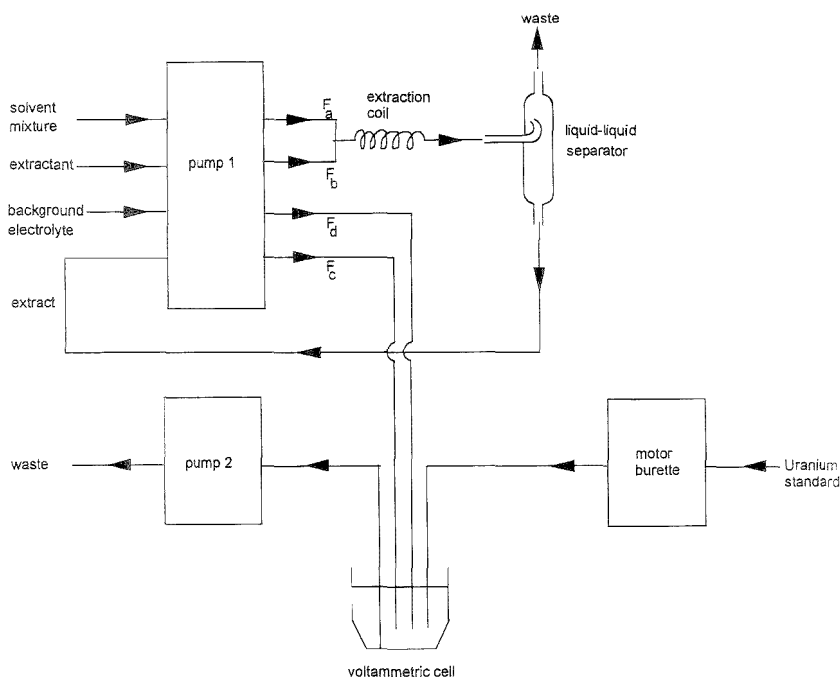
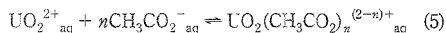
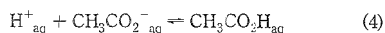


Figure 1. Flow chart of automated system for in-line extraction and on-line voltammetric analysis.

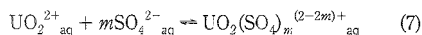
Solvent extraction methods, combined with spectrometric techniques, have been reported² for determination of U(VI) in mixtures of kerosene/TBP. In this work, a method is presented for the determination of U(VI) in such mixtures using in-line extraction into an aqueous phase, where the uranium is determined with high sensitivity by on-line CSV.

The extraction of uranium into the aqueous phase is facilitated by anions which form hydrophilic complexes with U(VI), such as sulfates, fluorides, phosphates, oxalates, fluorosilicates, sulfites, formates, acetates, and citrates. Acetate and sulfate are known⁵ to form relatively strong complexes with U(VI) and were thus selected for this work.

The relevant complexation reactions between U(VI) and acetate or sulfate are



and



with n and m equal to 1 or 2.

The extractants were used in an in-line extraction system comprising a setup for mixing of solvent mixtures and extractants combined with separation in a liquid/liquid separator. The extract was analyzed with voltammetric detection using accumulation of a uranium(VI) oxine complex on the hanging mercury drop electrode (HMDE), followed by square wave cathodic stripping voltammetry (CSV); the voltammetric detection method was adapted from an existing method⁶ to determine uranium in seawater. This paper describes the optimization of the inline extraction procedure and the voltammetric detection. The detection was performed in off-line mode during the preliminary optimization experiments, whereas on-line detection in a flow cell was used in the automated system.

EXPERIMENTAL SECTION

A. Instrumentation. In-Line Extraction Device. In Figure 1, a schematic outline for the in-line extraction of uranium(VI) from solvent mixtures (kerosene/TBP) into aqueous solutions is given. Pump 1 (Gilson Minipuls 2, four channels) is used to pump the solutions to and from the separator as indicated. The flow rates of the channels are denoted as F_a (solvent mixture), F_b (extractant), and F_c (extract). The solvent mixture and the extractant are mixed in a glass T-junction (2 mm i.d.), and subsequent extraction of uranium(VI) into the aqueous phase takes place in a Teflon coil (length, 1.6 m; internal tubing diameter, 0.81 mm; windings, 34). In the separator (a CO₂ trap purchased from ChemLab Instruments Ltd.), the aqueous phase is separated from the solvent phase. The aqueous phase is pumped away with

(5) Kragten, J. *Atlas of Metal-Ligand Equilibria in Aqueous Solution*; Ellis Horwood Ltd.: Chichester, U.K., 1978.

(6) Van den Berg, C. M. G.; Nimmo, M. *Anal. Chem.* **1987**, *59*, 924.

a flow rate F_c , which is smaller than the combined flow rates F_a and F_b of the incoming solutions. This gives an excess of solution in the separator, resulting in a waste flow rate (of solvent and aqueous phase) of $F_c + F_b - F_a$. The pumped aqueous phase is collected (off-line measurements) or pumped into the voltammetric cell (on-line measurements). The internal diameters of the pump tubing (PVC) were 0.64 mm for the solvent mixture, 1.14 mm for the extractant, and 1.02 (off-line) or 0.64 mm (on-line) for the aqueous extract. PVC tubing was used throughout, as the compatibility of the kerosene/TBP mixture with other types of tubing is unpredictable.

Electrochemical Equipment. An Autolab polarograph (Eco Chemie BV) with a Metrohm Model 663 hanging mercury drop electrode was used for the on- and off-line voltammetric uranium determinations. Potentials are given with respect to an Ag/AgCl, saturated AgCl in 3 M KCl reference electrode (SSCE). For off-line measurements, the computer program General Purpose Electrochemical System 3.1 (Eco Chemie BV) was used. For on-line measurements, the software for automated analysis (Electro Analytical System 1.0; Eco Chemie BV) was modified with features previously used for automated seawater analysis.⁷ The modifications made it possible to control the pumps for automated flow cell measurements. Pump 1 delivers the extract to the voltammetric cell (see above) and also pumps the cell buffer (flow rate F_b) using PVC pump tubing with an internal diameter of 1.85 mm. Pump 2 (Metrohm 683 pump Unit) is a high-capacity pump for emptying the cell. A Metrohm 665 Dosimat autoburet was used to perform standard additions to the cell, generally a constant volume of 100 μL of a uranium working solution (10 μM , see below).

B. Materials. A Milli-Ro system and a Milli-Q system (Millipore) were used in tandem to produce pure water (MQW) for preparation of the reagents. All chemicals used were of analytical reagent grade. An aqueous stock solution of 0.02 M oxine (8-hydroxyquinoline, BDH) was prepared in 0.05 M HCl. An aqueous stock solution of 0.1 M EDTA (ethylenediaminetetraacetic acid, sodium salt, BDH) was prepared in MQW, and the pH was adjusted to 7 using NaOH. An aqueous pH buffer stock solution was prepared containing 0.1 M PIPES (1,4-piperazinediethanesulfonic acid, monosodium salt, BDH) with a pH adjusted to 7 with NaOH. Aqueous stock solutions of 0.1 M acetate and 0.5 M sulfate were prepared by dissolving sodium acetate (BDH) and sodium sulfate (BDH) in MQW. Hydrazine hydrate solution (99.0%) was from BDH. Kerosene (low odor), tributyl phosphate (99%), and ammonia solution (about 30% NH_3) were from Aldrich. Dibutyl phosphate (DBP) was from Fluka. The cell buffer for automated measurements contained 250 mL of 0.1 M PIPES buffer (pH 7), 2.5 mL of 0.02 M oxine stock solution, 2.5 mL of hydrazine hydrate (99%), and 0.5 mL of 0.1 M EDTA stock solution.

An aqueous U(VI) working solution containing 10 μM U in dilute HCl (0.035%) was prepared from a commercially available standard solution (Aldrich, 975 $\mu\text{g}/\text{mL}$ (4.1 mM) U in 1% HNO_3). A synthetic U(VI) solution in a solvent mixture (20% TBP/kerosene) was prepared as follows: a mixture containing 10 mL of water, 4 mL of 70% HNO_3 , 8 mL of kerosene, and 2 mL of TBP was shaken in a separation funnel for about 1 min; after settling of the phases, the upper layer was separated and spiked with U(VI) on the 1 μM level. The aqueous spike was ultrasonically mixed

with the sample for 15 min. It can be calculated that >99.5% of the U(VI) is transferred to the solvent as a result of complexation by TBP.

A degraded raffinate was obtained from BNFL (British Nuclear Fuels plc) to test the system. This simulated sample contained kerosene (80%), TBP (~20%), nitric acid (0.2–0.3 M), RNO_2 (0.9%), RNO_3 (0.5%), $\text{R}_2\text{R}_2\text{CO}$ (0.5%), RCOOH (<0.2%), and DBP (1000 $\mu\text{g}/\text{mL}$). The sample had a bright yellow color. Most experiments were carried out with this sample. For optimization of the method, the solution was spiked with U(VI) on the 2 μM level. Here, too, the aqueous spike was ultrasonically mixed with the sample for 15 min.

C. Procedures. In-Line Extraction Procedure. The uranium in the sample solvent is extracted into sodium acetate or sulfate solutions using flow rates of 0.44 (F_a), 1.32 (F_b), and 1.07 (off-line) or 0.44 mL min^{-1} (on-line) (F_c) according to the scheme set out in Figure 1. The mixing ratio R (F_b/F_a) is 3. The flow rates are average values, as the day-to-day variation was ~5%. The solvent mixtures were thus extracted in-line, and an extract was collected continuously (for off-line measurements) or delivered to the voltammetric cell (for on-line measurements). The void volume of the liquid/liquid separator (~1 mL) made it necessary to flush with the solvent mixtures between measurements.

Off-Line Voltammetric Procedure. One milliliter of the extract was pipetted into the voltammetric cell, to which 8.8 mL 0.1 M PIPES buffer, 100 μL of the oxine stock solution (final concentration, 2×10^{-5} M), 100 μL of 99% hydrazine hydrate (final concentration, 20 μM), and 20 μL of the EDTA stock solution (final concentration 0.1 mM) were added; the final pH of this solution was 9.0, and the total volume of the solution in the cell was 10.0 mL. After deaeration of the solution by purging with water-saturated nitrogen for 5 min, the CSV cycle was started. A new mercury drop was extruded (drop size setting, 3), and adsorption at a potential of -0.5 V for 30–120 s (depending on the U concentration) was performed under continuous stirring (stirrer setting, 5), followed by a period of quiescence of 10 s. The potential scan was carried out using a square wave modulation at 50 Hz and a scan rate of 25 mV s^{-1} . Usually, the potential scanning range was from -0.5 to -0.85 V. The peak appeared at a potential of -0.68 V. The measurement was repeated after standard addition of uranium to quantify the uranium concentration in the voltammetric cell.

On-Line Voltammetric Procedure. The pumping time of pump 1 was set to deliver 10.0 mL of a solution with a ratio of background electrolyte/extract of 5 : 10 to the voltammetric cell. The flow rate (F_b) of the background electrolyte was 2.71 mL min^{-1} . The pumping time (to empty the cell) of pump 2 was set to 60 s. The sequence of the automated procedure was as follows: empty the cell, rinse with the background electrolyte/extract solution, empty again, and fill with the same solution for the measurement. The voltammetric measurement is the same as for the off-line procedure but is now performed automatically, including the standard addition.

D. Calculations. Uranium Extraction Efficiency from Solvent. In order to establish the extraction of uranium from solvent mixtures, an amount of sample was spiked with U(VI) to yield an additional concentration of A . Assuming original U concentrations of x_s and x_{s+A} for sample and spiked sample, respectively, the measured concentrations in the voltammetric cell,

(7) Achte-bernt, E. P.; van den Berg, C. M. G. *Anal. Chim. Acta* 1994, 284, 453.

Table 1. Compilation of Published Formation Constants for the Uranium(VI)–Nitric Acid/Sulfate/Acetate–TBP/DBP System

complex	eq no.	log <i>K</i>	ref
HNO ₃ ·TBP _{org}	1	−0.7	8
UO ₂ (NO ₃) ₂ ·2TBP _{org}	2	1.507	4
UO ₂ {H(DBP) ₂ } _{2org}	3	15.6	9
CH ₃ CO ₂ H _{aq}	4	4.57	10
UO ₂ CH ₃ CO ₂ ⁺ _{aq}	5	2.44	10
UO ₂ (CH ₃ CO ₂) ₂ [−] _{aq}	5, <i>n</i> = 1	4.42	10
HSO ₄ [−] _{aq}	6, <i>n</i> = 2	1.10	11
UO ₂ SO ₄ ^{aq}	7, <i>m</i> = 1	1.81	11
UO ₂ SO ₄ ^{2−} _{aq}	7, <i>m</i> = 2	2.5	11

m_s and m_{s+A} , are given by (see also Figure 1)

$$m_s = (x_s E) / (100RD) \quad (8)$$

and

$$m_{s+A} = (x_{s+A} E) / (100RD) \quad (9)$$

with

$$x_{s+A} - x_s = A \quad (10)$$

where R is mixing ratio (F_b/F_a), E is extraction efficiency (in %), and D is the dilution factor of extract in the cell (10 for off-line measurement and $(F_c + F_d)/F_c$ for on-line measurement).

Subtraction of eq 8 from eq 9 and substitution of eq 10 in the resulting equation gives the following expression for the extraction efficiency:

$$E = 100 \times (m_{s+A} - m_s)RD/A \quad (11)$$

Uranium Concentration in Solvent. If the extraction efficiency is known, the U concentration in solvent can be calculated from eq 8 as

$$x_s = 100 \times m_s / RD/E \quad (12)$$

Modeling. Calculations of individual species were made by mass balance and distribution coefficient equations, together with constants from Table 1. Computations were made using the Mathcad 4.0 software package (MathSoft Inc.).

RESULTS AND DISCUSSION

Optimization of Extraction Conditions. Preliminary experiments were carried out in an attempt to determine uranium by voltammetry directly in the kerosene mixture. However, no response was obtained, even at high (μ M) uranium concentrations. For this reason, the uranium was extracted into an aqueous electrolyte, in which it can be determined by CSV in the presence

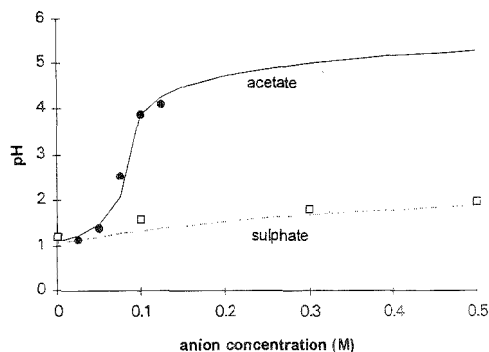


Figure 2. Influence of the concentrations of acetate and sulfate in the extractant solutions on the pH of the degraded raffinate extract using in-line stripping. The solid lines represent the calculated pH, and the symbols denote experimental data points. The theoretical curves were calculated using an estimated initial concentration of HNO₃ of 0.25 M in 20% TBP/kerosene.

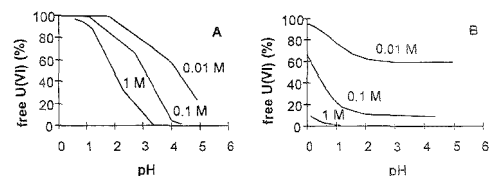


Figure 3. Calculated complex formation of acetate (A) and sulfate (B) with U(VI) in water as a function of the pH at different concentrations. Initial U(VI) concentration set at 300 nM. The free U(VI) is representative of the uncomplexed uranium. Stability constants used for the calculations are tabulated in Table 1.

of oxine.⁵ The extraction was complicated by the acidic nature of the kerosene/TBP mixture which caused the pH of the aqueous extract to drop to ~ 1 at a 3:1 ratio of water/solvent mixture. The variation of the pH as a function of the concentrations of sulfate and acetate in the extractant used to strip the uranium from the degraded raffinate is shown in Figure 2. It can be seen that the pH of the extract rises above 4 when concentrated acetate (>0.1 M) is used. Although these conditions favor the uranium extraction because of the increased stability of the U(VI) complexes with acetate and sulfate (Figure 3), experiments using degraded raffinate showed that the extraction of interfering substances (mainly surfactants interfering with the voltammetric detection) was also much enhanced. This was visually apparent in terms of an increasingly yellow color at increasing acetate concentrations (and therefore higher pH values) in the extracts. Uranium sulfate complexes are more stable than the acetate complexes at low pH (Figure 3). Extractions at lower pH using sulfate showed much reduced coextraction of the voltammetric interferences (no coloration was observed in the extract, and the CSV determination could be made free of interfering background currents by optimization), so sulfate was more suitable to extract the uranium from the degraded raffinate.

The extraction efficiency of uranium from raffinate using acetate or sulfate extractants is shown in Figure 4A. It can be seen that the maximum attainable extraction efficiency was $\sim 50\%$. Only low concentrations of acetate could be used to minimize the coextraction of the voltammetric interference, so the recovery was

(8) Alcock, K.; Grimley, S. S.; Healy, T. V.; Kennedy, J.; McKay, H. A. C. *Trans. Faraday Soc.* **1956**, *52*, 39.

(9) Dyrssen, D.; Kuca, L. *Acta Chem. Scand.* **1960**, *14*, 1945.

(10) Martell, E. M.; Smith, R. M. *Critical Stability Constants, Volume 3: Other Ligands*; Plenum Press: New York, 1977.

(11) Martell, E. M.; Smith, R. M. *Critical Stability Constants, Volume 4: Inorganic Complexes*; Plenum Press: New York, 1981.

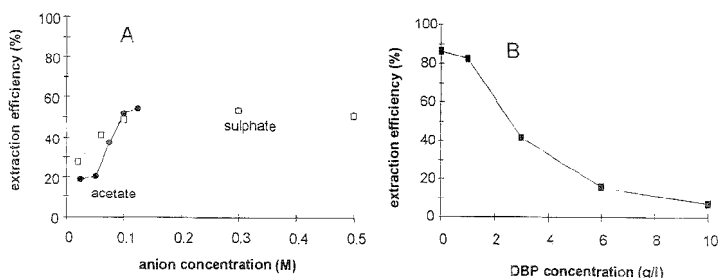


Figure 4. (A) Extraction of U(VI) from a degraded raffinate (containing ~20% TBP and ~0.01% DBP in kerosene) with sulfate and acetate. Effect of varying the concentrations of acetate and sulfate. The ratio R was 3. (B) Influence of DBP on the uranium extraction from a simulated solvent mixture containing 20% TBP in kerosene. The ratio R was 3.

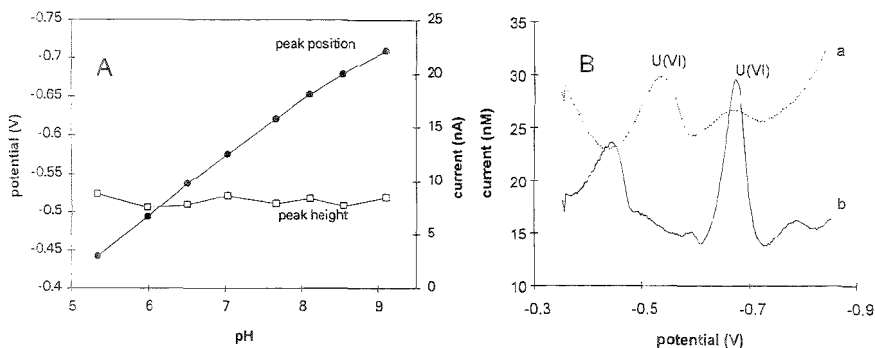


Figure 5. (A) Peak height and peak potential as a function of the pH in a solution containing 20 nM U(VI), 0.1 M PIPES, 2×10^{-5} M oxine, and 10^{-4} M EDTA; pH adjustments were carried out with NaOH and HNO₃ solutions. (B) Voltammetric measurement of U(VI) in degraded raffinate at two pH values. One milliliter of the aqueous extract was added to 9 mL of cell solution containing 0.1 M PIPES, 2×10^{-5} M oxine, and 10^{-4} M EDTA in the absence (scan a) and presence (scan b) of hydrazine (0.2 M). The pH values of the respective solutions are 7.0 (scan a) and 9.0 (scan b).

poorly reproducible. The extraction efficiency increased with the sulfate concentration until ~0.3–0.5 M, where it stabilized, so a 0.5 M sulfate solution was used in the subsequent experiments.

The low (~50%) uranium recovery from the degraded raffinate even at high sulfate concentrations is less than expected in view of the comparative stability of the sulfate and TBP complexes with uranium (Table 1). However, the degraded raffinate contained significant amounts of DBP, which forms much more stable complexes with uranium (Table 1) and probably caused the comparably low recovery of uranium from these samples. The influence of the DBP on the extraction efficiency of uranium was evaluated by extractions from a synthetic solvent (20% TBP/kerosene) to which DBP was added (Figure 4B). It can be seen that at DBP concentrations higher than 1 g L^{-1} , the extraction efficiency drops significantly. In the absence of the DBP, the extraction efficiency was 87% and therefore more consistent with expectation (Figure 3B and Table 1).

Optimization of Voltammetric Conditions. *Effect of pH, Hydrazine Hydrate, Oxine, and EDTA.* The pH of the cell solution was varied to investigate the influence of the hydrogen ion concentration on the peak height and peak potential of U(VI). The results are shown in Figure 5A. The peak potential was found to shift almost linearly with increasing pH from -0.44 V at pH 5.3 to -0.68 V at pH 8.5, which reflects the increasing complex stability due to diminished proton competition. This is in

agreement with CSV of uranium in seawater.⁶ The sensitivity for uranium remained more or less constant in the pH range from 5.3 to 8.5, indicating a consistent adsorption mechanism in this range. The constant sensitivity over this pH range is in contrast with CSV of uranium in seawater, where the sensitivity decreases with increasing pH between 7 and 9 due to U(VI) complexation by carbonate present in the seawater.⁶

Traces of coextracted interfering material were found to produce a broad voltammetric peak overlapping with and suppressing the uranium peak. It was found that this interference could be largely eliminated by increasing the pH. Comparative additions of ammonia and hydrazine hydrate to adjust the pH showed, interestingly, that the hydrazine hydrate enhanced the U(VI) peak height (no peak was obtained on addition of hydrazine in the absence of uranium, so the effect was to increase the CSV sensitivity for uranium). Addition of 0.2 M hydrazine hydrate (99%) to the 0.1 M PIPES buffer increased the initial pH of 7 to pH 9, causing the uranium peak to shift to a more negative potential and increasing the peak current from 7 to 16 nA (Figure 5B). Thus, the CSV scan of uranium was apparently free of the unknown organic interference coextracted from the degraded raffinate, and the sensitivity was improved. Increasing the hydrazine hydrate concentration to 0.2 M at a constant pH of 7 resulted in unchanging sensitivities, while the sensitivity increased by a factor of ~2 when the pH was raised to 9. This indicates

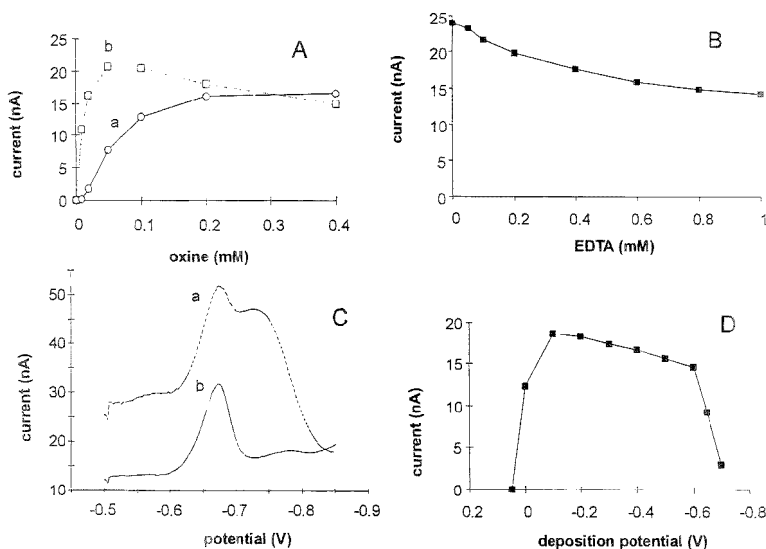


Figure 6. Optimization of the voltammetric determination of uranium in diluted (1/10) raffinate extract in background electrolyte. The cell solution contained 0.088 M PIPES, 10^{-4} M EDTA, 2×10^{-5} M oxine, and 0.2 M hydrazine hydrate at a pH of 9.0. (A) Effect of varying the concentration of oxine on the peak height of 20 nM U(VI) in the presence (a) and absence (b) of the raffinate extract. (B) Influence of varying the concentration of EDTA on the peak height of 20 nM U(VI) in the voltammetric cell. (C) Voltammetric scans in the absence (a) and presence (b) of EDTA. (D) Influence of varying the deposition potential on the peak height for U(VI); CSV scans were started at -0.5 V.

that hydrazine hydrate was responsible for the increase in sensitivity, but only when the pH increased as well. A possible (hypothetical) explanation for this effect could be the formation of a mixed complex with uranium. Repeating the experiments with an ammonia solution ($\sim 30\%$ NH_3) instead of hydrazine showed a less pronounced influence; the peak shift was similar, but the sensitivity increase was a factor of 1.3 when the pH changed from 7 to 9 as a result of the addition of ammonia. An optimal hydrazine hydrate concentration in the cell solution of 0.2 M was chosen.

Oxine influences the peak height of U(VI) positively due to the adsorption of the U(VI) oxine complex on the mercury drop. The peak height, therefore, increases with the oxine concentration until all U(VI) is complexed, as can be seen from Figure 6A (curve b). The presence of interfering compounds from a degraded raffinate were found to compete with the oxine, and therefore, more oxine had to be added to the "real" sample solution to reach highest sensitivity (Figure 6A, curve a). A concentration of 2×10^{-5} M oxine in the cell solution was selected to optimize the peak height in samples containing degraded raffinate extract.

Remaining interferences in the voltammetric scans (a peak more negative than the uranium peak) were found to be due to other metals coextracted with the uranium. Addition of EDTA resulted in suppression of this peak as a result of preferential complexation of several interfering metal ions, which otherwise are complexed by the oxine. The CSV peak height was reduced somewhat as a result of complexation of U(VI) with the EDTA, but this effect was small at EDTA concentrations below 0.1 mM (Figure 6B). Metal ion interferences from degraded raffinate were suppressed well in this condition, giving a voltammetric scan largely free of interfering peaks (Figure 6C, scan b is in the presence

of EDTA). An optimal EDTA concentration of 0.1 mM was selected for further experiments.

Effect of Varying the Deposition Potential and Accumulation Time. The peak potential for the reduction of U(VI) is at -0.68 V in the presence of 0.1 M PIPES buffer, 0.2 M hydrazine hydrate, 2×10^{-5} M oxine, and 10^{-4} M EDTA. Variation of the deposition potential showed that the peak height was comparatively constant at deposition potentials between -0.6 and -0.1 V (Figure 6D). The peak height diminished at deposition potentials more negative than -0.6 V, probably because of reduction of U(VI) to U(V) and the inability of U(V) to form adsorptive complexes with oxine. Also at deposition potentials more positive than -0.1 V, the U(VI) oxine complex was found to adsorb poorly onto the mercury drop. When measuring degraded raffinate extracts, it is advisable to use a deposition potential as close as possible to the peak potential to diminish the influence of organic interferences, which show a strong tendency for adsorption onto the mercury drop at more negative deposition potentials. A deposition potential of -0.5 V was therefore selected for uranium determinations in the degraded raffinate.

Variation of the accumulation time showed that the peak height increased linearly with the accumulation time up to about 500 s (from a stirred solution containing 0.088 M PIPES, 2×10^{-5} M oxine, 0.2 M hydrazine hydrate, 10^{-4} M EDTA, and 1 mL of degraded raffinate extract, giving a total volume of 10 mL at pH 9.0 and containing ~ 35 nM U(VI)). The peak height increased nonlinearly thereafter, presumably as a result of saturation of the surface of the mercury drop with uranium complexes with oxine. For a lower uranium concentration and fewer interfering compounds present, the curve can be expected to show an extended linearity.

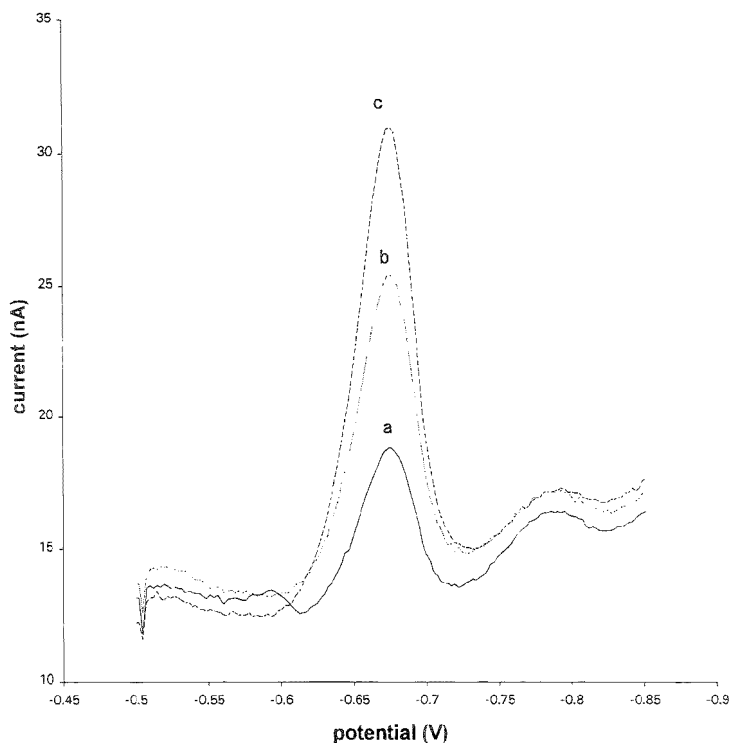


Figure 7. Determination of U(VI) in a degraded raffinate. Mixing ratio R was 3.2. Solution composition in voltammetric cell: 0.088 M PIPES, 2×10^{-5} M oxine, 0.2 M hydrazine hydrate, 10^{-4} M EDTA, 1 mL of degraded raffinate extract (total volume 10 mL, pH 9.0). Scan a: 5.97 nM U(VI) in cell (191 nM in raffinate). Scan b: standard addition of 5 nM U(VI) to the solution in scan a. Scan c: standard addition of 10 nM U(VI) to the solution in scan a. Accumulation time, 120 s.

Sensitivity and Limit of Detection. The calibration curve of peak height as a function of the uranium concentration shows a linear relationship up to ~ 100 nM U(VI) and nonlinearly at higher uranium concentrations (in a solution containing 0.088 M PIPES, 2×10^{-5} M oxine, 0.2 M hydrazine hydrate, 10^{-4} M EDTA, and 1 mL of degraded raffinate extract, giving a total volume of 10 mL at pH 9.0; accumulation time, 120 s). The linear range could be extended by reducing the accumulation time, resulting in less absorption of complex on the electrode surface.

The sensitivity of the CSV measurement is influenced by the concentration of interfering surface active compounds and is therefore directly proportional to the amount of extract in the cell. However, using 0.5, 1, or 2 mL extracts of the degraded raffinate in the cell (final volume, 10 mL) showed no notably different sensitivities (arbitrary peak heights were 42 ± 3 , 100 ± 6 , and 206 ± 10 for addition of 0.5, 1, and 2 mL to the cell, respectively). This indicates that the amount of interferences stripped from the degraded raffinate extract into the aqueous solution was not significant at these ratios. The buffering capacity of the cell buffer was sufficient to keep the pH constant at 9.0 on addition of these acidic aliquots.

Using the optimized extraction/measurement conditions, CSV scans as presented in Figure 7 are obtained. Replicate in-line extraction with off-line measurement of this sample resulted in

an extraction efficiency of 48.6% and a U(VI) concentration in the solvent of 393 ± 40 nM (average and standard deviation, $n = 5$). Increasing the dilution factor shows that the minimum detectable U(VI) concentration in solvents is 20 nM.

Automated Measurements. The uranium measurement in kerosene was fully automated by interfacing the in-line extraction with automated voltammetric detection. Small volumes (0.5–2 mL) of the extract were thereto pumped directly into a T-junction (see Figure 1), where they were mixed with the background electrolyte before going into the voltammetric cell. The pumping time was set to deliver a total volume of 10 mL to the voltammetric cell. The voltammetric analysis (including deaeration and repeated scans) was then carried out automatically; the standard deviation of the peak height for uranium was evaluated from three scans, and two further scans were carried out if the standard deviation was greater than a preset value (typically 5%). A standard addition of uranium was then made to the cell (by computer-controlled autoburet) to calibrate the CSV sensitivity, and the scans were repeated. Sufficient uranium was added to at least double the initial peak height; more uranium was added if the peak height was less than double the initial one. The uranium concentration in the extract was then calculated from the sensitivity, and the extraction efficiency was evaluated from analysis of an aliquot of degraded raffinate to which a spike of uranium was

added. An extraction efficiency of 88.5% and a U(VI) concentration in the solvent of 35.24 ± 1.69 nM (average and standard deviation) was obtained using the automated on-line voltammetric method with the optimized conditions for automated in-line extraction of U(VI) (1 μ M) from a synthetic solvent mixture (20% TBP/kerosene containing 1 g L⁻¹ DBP). This is consistent with expectation in view of the complexation of uranium by sulfate (Figure 3B) and the preceding experiments in which the extracted fractions were collected. The mixing ratio R was 3.44, and the dilution factor D in the cell was 7.29.

CONCLUSIONS

A successful automated method has been developed to determine U(VI) in mixtures of tributyl phosphate and kerosene using an in-line extraction into an aqueous phase, combined with on-line electrochemical determination. Traces of degradation products as a result of radiolytic and hydrolytic decomposition in degraded raffinate were found to interfere with the on-line extraction and measurement. Dibutyl phosphate was found to be responsible for the reduced extraction of uranium from the raffinate since it forms very strong complexes with U(VI) in the organic phase. The maximum attainable extraction efficiency was therefore ~50% when acetate or sulfate extractants were used. An extractant containing 0.5 M sulfate was found to be optimal to extract the uranium, giving a maximum attainable extraction

efficiency of ~50%, which was constant. Acetate was found to give rise to the extraction of an excess of electrochemically interfering compounds. Residual interferences from the extraction using sulfate were suppressed by addition of EDTA (to complex interfering metal ions) and hydrazine hydrate (to suppress the interference of surfactants). The latter compound was found to enhance the sensitivity by a factor of ~2. The detection limit of the method (including extraction and voltammetric analysis) was 20 nM uranium in the degraded raffinate using extractant/solvent ratios of 3, dilution factors of extract in the cell of 5–10, and an adsorption time of 120 s. Important advantages of this method are the small sample size required for each analysis (0.5–2 mL), leading to very small waste product volumes, which could be recycled back into the system, and the full automation, which requires little supervision.

ACKNOWLEDGMENT

This investigation was financially supported by British Nuclear Fuels plc.

Received for review January 23, 1995. Accepted August 2, 1995.[®]

AC950071U

[®] Abstract published in *Advance ACS Abstracts*, September 1, 1995.

Selective Detection in RP-HPLC of Tyr-, Trp-, and Sulfur-Containing Peptides by Pulsed Amperometry at Platinum

Johannes A. M. van Riel and Cornelis Olieman*

Department of Analytical Chemistry, Netherlands Institute of Dairy Research, P.O. Box 20, 6710 BA Ede, The Netherlands

A technique for electrochemical detection of Trp-, Tyr-, and sulfur-containing peptides, using a two-step potential waveform at a platinum wall-jet electrode, has been developed. The detection is fully compatible with reversed-phase HPLC employing gradients of acetonitrile in water/trifluoroacetic acid. At $\sim +1.2$ V (first potential) versus Ag/AgCl, Trp-, Tyr-, and Cys-containing peptides are predominantly detected, while at $+1.4$ – 1.6 V, Met- and (Cys)₂-containing peptides are additionally detected. The electrode surface is cleaned by the second potential ($+2.0$ V). The linearity is at least 2 orders of magnitude. The sensitivity is in the picomole range. By using postcolumn electrochemical conversion, the selectivity toward Met- and Cys-containing peptides can be enhanced. Applications are shown for the determination of caseinomacropeptide (6.6 kDa) and a tryptic map of β -casein.

In the European Community, the subsidized utilization of milk and buttermilk powders for animal feed requires the absence of rennet whey solids.¹ The characteristic component of rennet whey is caseinomacropeptide (CMP), which is formed in the milk-clotting process by the enzymatic cleavage of the Phe¹⁰⁵–Met¹⁰⁶ peptide bond of κ -casein. Para- κ -casein (1–105) remains in the precipitated caseins, while CMP (106–169, 6.6 kDa) is recovered in the rennet whey. In a fermented milk product, such as buttermilk, proteolytic enzymes of the starter culture cause protein degradation. On rare occasions, κ -casein is split at position 106–107, resulting in the formation of pseudo-CMP,² lacking the N-terminal Met. The (fraudulent) addition of rennet whey to milk and milk products can be detected by the determination of CMP with reversed-phase HPLC (RP-HPLC).² This method employs an extremely flat gradient of acetonitrile (ACN), which generates just enough resolution between CMP and pseudo-CMP to prevent false positive results; however, under certain conditions, false negative results cannot be excluded. In principle, there are two possibilities for improving the analysis: (1) increase the resolution of the separation system and (2) apply selective detection.

Capillary electrophoresis (CE) fulfilled the first option.³ This paper deals with the second option.

Electrochemical detection of amino acids, peptides, and proteins has been reviewed by Krull et al.^{4,5} Glassy carbon electrodes afford reasonable sensitivities for easily oxidized amino

acids, like Tyr and Trp. The compatibility with gradients of ACN in water is poor. In combination with postcolumn photolytic derivatization, peptides and proteins containing Phe, Tyr, Trp, Met, and Cys can be detected⁶ at glassy carbon; however, ACN should be replaced with a mixture of alcohols to ensure durable operation of the photolytic reactor. Modification of a glassy carbon electrode with a film of Ru(III,IV) oxide stabilized with cyano crosslinks permits the amperometric detection of Cys, (Cys)₂, and Met at pH 2.⁷ The preparation of the electrode and its limited life of about 2 weeks hamper application for routine analyses. A similar electrode was used in the simultaneous detection of several thiols and disulfides after separation by CE.⁸

Conventional voltammetric and amperometric techniques at Pt or Au electrodes have not been considered applicable for quantitative detection of most sulfur compounds, because of the observed loss of electrode activity due to accumulation of sulfurous adsorbates. Pulsed electrochemical detection (PED) at noble metal electrodes was recently reviewed by LaCourse⁹ and Johnson et al.¹⁰ Sulfur-containing pesticides could be detected in the presence of ACN at pH 5.0 at a Au electrode using a two-step potential waveform.¹¹ Evidence was given that the mechanism involved adsorption of the analytes at the oxide-free surface during cathodic polarization and subsequent amperometric detection catalyzed by oxide formation following anodic polarization. The same mechanism was proposed for the detection of sulfur-containing analytes at Pt electrodes in alkaline solutions.¹²

Glutathione, (Cys)₂, Cys, and Met were detected at a Au electrode in acidic medium using integrated PED.^{13,14} The current is integrated during a fast scan from 0 to $+1.6$ to 0 V, thereby eliminating the current originating from the formation of the Au oxide. Subsequently, the surface is reactivated by an anodic polarization of $+1.9$ V and a cathodic polarization of -0.6 V.

We have investigated the possibility of oxidative PED of sulfur-containing amino acids at a Pt electrode at low pH.

EXPERIMENTAL SECTION

Chemicals. All amino acids, dipeptides, and trypsin (TPCK treated, type XIII, bovine pancreas) were received from Sigma (St. Louis, MO). ACN (HPLC Ultra Gradient Grade) and trifluo-

(1) Regulation 1725/79 of the Committee. *Off. J. Eur. Communities* **1979**, *L228*, 9–14.

(2) Olieman, C.; van Riel, J. A. M. *Neth. Milk Dairy J.* **1989**, *43*, 171–84.

(3) van Riel, J. A. M.; Olieman, C. *Electrophoresis* **1995**, *16*, 529–33.

(4) Dou, L.; Mazzeo, J.; Krull, I. S. *BioChromatography* **1990**, *5*, 74–96.

(5) Chen, L.; Krull, I. S. *Electroanalysis* **1994**, *6*, 1–8.

(6) Dou, L.; Krull, I. S. *Anal. Chem.* **1990**, *62*, 2559–606.

(7) Cox, J. A.; Dabek-Zlotorzynska, E. *J. Chromatogr.* **1991**, *543*, 226–32.

(8) Zhou, J.; O'Shea, T. J.; Lunte, S. M. *J. Chromatogr. A* **1994**, *680*, 271–7.

(9) LaCourse, W. R. *Analysis* **1993**, *21*, 181–95.

(10) Johnson, D. C.; Döbberpohl, D.; Roberts, R.; Vandenberg, P. *J. Chromatogr.* **1993**, *640*, 79–96.

(11) Ngovivatchai, A.; Johnson, D. C. *Anal. Chim. Acta* **1988**, *215*, 1–12.

(12) Polta, T. Z.; Johnson, D. C. *J. Electroanal. Chem.* **1986**, *209*, 159–69.

(13) Vandenberg, P. J.; Johnson, D. C. *Anal. Chem.* **1993**, *65*, 2713–8.

(14) Vandenberg, P. J.; Johnson, D. C. *Anal. Chim. Acta* **1994**, *290*, 317–27.

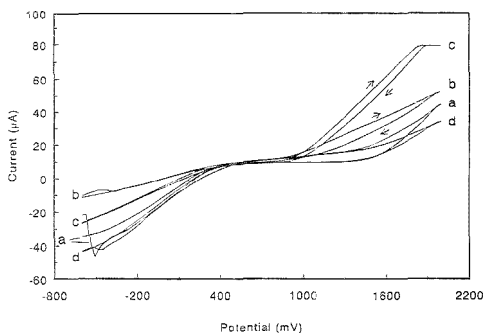


Figure 1. Cyclic voltammetry at a Pt wall-jet electrode of solvent (a) (water/ACN/TFA 85:15:0.1), 10 mM Met (b), 2 mM Tyr (c), and 10 mM Ser (d). Scan rate, 50 mV/s; flow rate, 0.5 mL/min.

roacetic acid (TFA, HPLC/Spectro Grade) were obtained from J.T. Baker (Deventer, NL) and Pierce (Rockford, IL), respectively.

HPLC. Separations were carried out with a M600 quaternary gradient pumping system with a built-in column oven in combination with a Model 717 plus autosampler (Millipore-Waters, Milford, MA). All solvents were sparged with helium (15 min) and stored in closed, pressurized vessels (ESM, Millipore-Waters). The analytes were detected with a Model 783A UV detector (Applied Biosystems, Foster City, CA) or, in the case of peptide maps, with a diode array detector (Model 2140, LKB, Bromma, Sweden) in series with a wall-jet (spacer 50 μm) Pt electrode (Antec, Leiden, NL), equipped with an Ag/AgCl [saturated KCl] reference electrode, connected with a Model 400 pulsed amperometric detector (EG&G Princeton Applied Research, Princeton, NJ). Unless otherwise indicated, $E_{\text{det}} = -1.4$ V, $t_{\text{det}} = 0.8$ s, $E_{\text{ox}} = +2.0$ V, $t_{\text{ox}} = 0.2$ s. A porous graphite electrode (Model 5020 Guard Cell, ESA, Inc., Bedford, MA), controlled by the EG&G detector and placed between the UV detector and the wall-jet electrode, was used for postcolumn electrochemical conversion (PCEC). The separations were performed on a reversed-phase resin-based column (PLRP-S, 5 μm , 300 \AA , 150 mm \times 4.6 mm i.d., Polymer Laboratories, Shropshire, U.K.) or on reversed-phase silica columns (Zorbax 300 SB-C8, 5 μm , 250 mm \times 4.6 mm i.d., Rockland Technologies, Inc., Newport, DE, or Nova-Pak C₁₈ cartridge, 4 μm , 100 mm \times 5.0 mm i.d., Millipore-Waters). Columns were operated at room temperature, except for peptide maps, which were obtained at 50 $^{\circ}\text{C}$.

Cyclic Voltammetry. The HPLC setup was used without a column. A manual injector equipped with a 2 mL loop replaced the autosampler. The flow rate was 0.5 mL/min, and the scan rate was 50 mV/s. Met, Ser, and Tyr were dissolved in ACN/water/TFA (15:85:0.1) at concentrations of 10, 10, and 2 mM, respectively.

Sample Preparation. Milk powder (2.00 g) was dissolved in 20.0 g of water at 50 $^{\circ}\text{C}$. The solution was heated for 6 min at 90 $^{\circ}\text{C}$. After the solution was cooled to 25 $^{\circ}\text{C}$, 5.00 mL of a solution of trichloroacetic acid (200 g/L) was added over 2 min at constant speed, with vigorous stirring. After the solution was left to stand for 60 min at 25 $^{\circ}\text{C}$, the precipitate was filtered off, the first 5 mL of the filtrate was discarded, and the remaining solution was used for HPLC analysis.

The tryptic map of β -casein was obtained by dissolving the protein (2 mg/mL) in a 0.2 M Tris/HCl buffer (pH 8). Trypsin

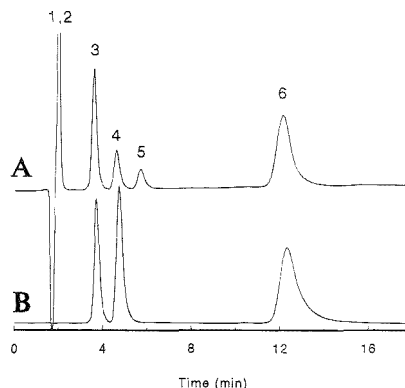


Figure 2. Isocratic RP-HPLC of Leu-Arg (1), Leu-Ser (2), Leu-Tyr (3), Met-Leu (4), Leu-Leu (5), and Leu-Trp (6), detected by UV at 205 nm (A) and by PED at $E_{\text{det}} = 1.4$ V and $E_{\text{ox}} = 2.0$ V (B). Column, Nova-Pak C₁₈; eluent, water/ACN/TFA 82:18:0.1; flow rate, 2.0 mL/min.

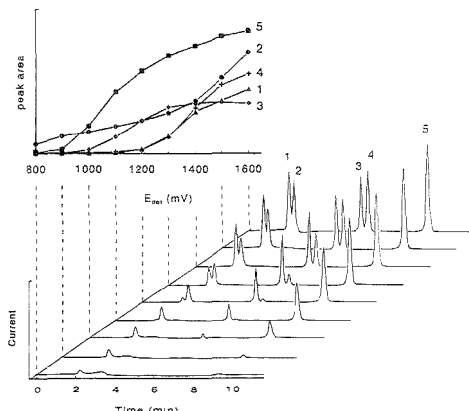


Figure 3. Gradient RP-HPLC of (Cys)₂ (1), Cys (2), Leu-Tyr (3), Met-Leu (4), and Leu-Trp (5) detected at various E_{det} values (indicated by the dashed lines dropping from the voltammogram (top)). Column, PLRP-S; eluent A, water/TFA 99.9:0.1, eluent B, water/ACN/TFA 70:30:0.1; gradient 0% B to 80% B linear in 10 min; injection 7 min after start of the gradient; flow rate, 1.0 mL/min.

(2% (m/m)) was added, and the solution was incubated at 25 $^{\circ}\text{C}$ for 24 h.

RESULTS AND DISCUSSION

Preliminary experiments with cyclic voltammetry using Au or Pt electrodes revealed that Pt showed a suitable response for Met at low pH (Figure 1). Apparently, Pt is not oxidized in ACN/water/TFA at potentials up to +2.0 V. In the presence of perchloric acid we obtained a response roughly comparable to the one obtained by Johnson et al.,¹⁵ indicating the formation of platinum oxide. The useful potential range in TFA is -0.6 to $+2.0$ V, which is extended compared to -0.2 to $+1.2$ V in 0.1 M perchloric acid. Initially, we used a triple waveform, similar to

(15) Johnson, D. C.; LaCourse, W. R. *Electroanalysis* 1992, 4, 367-80.

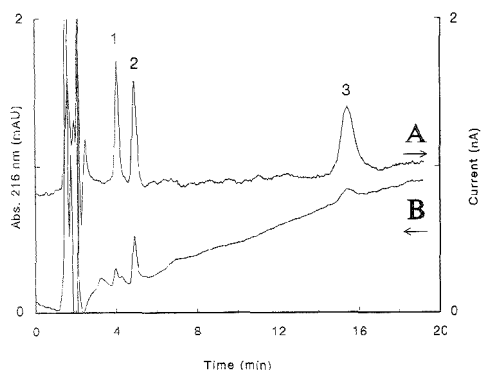


Figure 4. High-sensitivity PED of Leu-Tyr (1), Met-Leu (2), and Leu-Trp (3), each 20 pmol injected. Isocratic RP-HPLC with PED at $E_{\text{det}} = 1.4$ V and $E_{\text{ox}} = 2.0$ V (A) and UV detection at 216 nm (B). Column, PLRP-S; eluent, water/ACN/TFA 85:15:0.1; flow rate, 1.0 mL/min.

Table 1. Linear Regression Statistics for PED Response of Leu-Tyr, Leu-Trp, and Met-Leu in the range of 0.8–100 μM ($n = 15$, 25 μL injection) at 1 μA Full Scale (Other Conditions as in Figure 4)

	Leu-Tyr	Leu-Trp	Met-Leu
slope ^a (area/ μM)	1590 \pm 46	3760 \pm 58	2390 \pm 27
intercept ^a (area $\times 10^{-3}$)	0.4 \pm 0.2	1.1 \pm 0.3	1.5 \pm 0.8
error at 80 μM ^b	0.4, 0.5	0.21, 0.3	1.6, 2.0
error at 15 μM ^b	0.18, 1.2	0.12, 0.8	0.5, 3
error at 3 μM ^b	0.22, 7	0.14, 5	0.6, 21

^a The uncertainty is reported at the 95% confidence interval. ^b The error (95% confidence) of the concentration is obtained at a mean area count corresponding to the given concentration of analyte. The first number represents the absolute error, in μM ; the second number represents the relative error, in %.

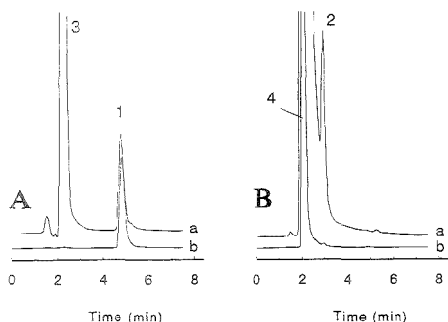


Figure 5. Analysis of Met-Leu (1) dissolved in 1% TFA (3) in water (A) and 20 min after the addition of 0.5% hydrogen peroxide (4) (B), forming Met(O)-Leu (2). Detection by UV at 205 nm (a) and by PED at $E_{\text{det}} = 1.4$ V and $E_{\text{ox}} = 2.0$ V (b). Column, PLRP-S; eluent, water/ACN/TFA 85:15:0.1; flow rate, 1.0 mL/min.

that for the detection of alcohols,¹⁵ with $E_{\text{det}} = +1.2$ V, $E_{\text{ox}} = +1.4$ V, and $E_{\text{red}} = -0.4$ V. During the stepwise optimization of the waveform, we found that there was no need for E_{red} . The optimum value for E_{ox} was 2.0 V, while E_{det} should be between 1.1 and 1.6 V, depending on the desired selectivity. At these settings, no response was obtained for aliphatic alcohols in 0.1% TFA, even

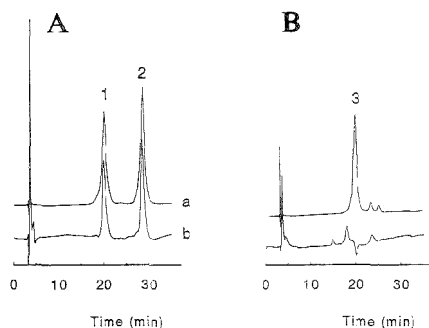


Figure 6. UV (a, 205 nm) and PED (b, $E_{\text{det}} = 1.4$ V and $E_{\text{ox}} = 2.0$ V) detection of CMP_A (1), CMP_B (2), and pseudo- CMP_A (3). Column, Zorbax 300 SB-8; eluent A, water/ACN/TFA 85:15:0.1, eluent B, water/ACN/TFA 45:55:0.1; gradient, 24% B to 47% B linear in 27 min, 47% B to 90% B linear in 2 min, 90% B isocratic for 5 min, 90% B to 24% B linear in 3 min; flow rate, 1.0 mL/min.

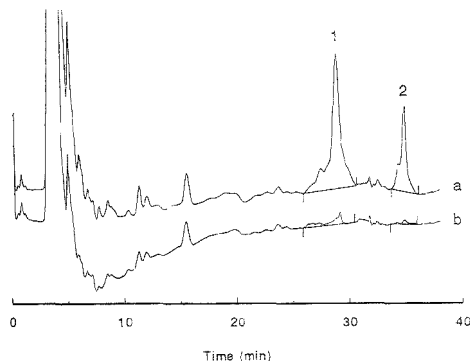


Figure 7. Analysis of skim milk powder with (a) and without (b) 5% rennet whey solids. PED ($E_{\text{det}} = 1.4$ V and $E_{\text{ox}} = 2.0$ V) of CMP_A (1) and CMP_B (2). Column, Zorbax 300 SB-8; eluent A, water/ACN/TFA 85:15:0.1, eluent B, water/ACN/TFA 45:55:0.1; gradient, 24% B to 34% B nonlinear (curve 8) in 20 min, 34% B to 42% B linear in 5 min, isocratic for 5 min, 42% B to 100% B linear in 2 min, isocratic for 10 min, 100% B to 24% linear in 2 min; flow rate, 1.0 mL/min.

when a cathodic polarization of -600 mV was included. This indicates that the oxidation mechanism in the presence of TFA is completely different from that in perchloric acid, where aliphatic alcohols are easily detected.¹⁵

The absence of cathodic polarization results in a relatively small charging current during E_{pot} , effecting a low background current (~ 30 – 80 nA) and thus low noise levels. A full-scale sensitivity of 1 nA is possible, which is unusually sensitive for pulsed amperometric detection. The relative high voltage of $+2.0$ V for E_{ox} is needed to oxidatively clean the electrode. Omitting E_{ox} results in a diminishing response and tailing peaks. The signal-to-noise ratio increases on increasing t_{pot} ; a value of 0.8 s, together with a t_{ox} of 0.2 s (the minimum value possible on our instrument), results in a 1 Hz sampling frequency, sufficient for normal HPLC. The EG&G detector does not allow a setting of the current sampling time: it is a fixed fraction of t_{det} . Figure 2 shows the detection of some selected dipeptides. No response is obtained for amino, guanidosyl (Arg), and alkylhydroxyl (Ser) groups, whereas thio-

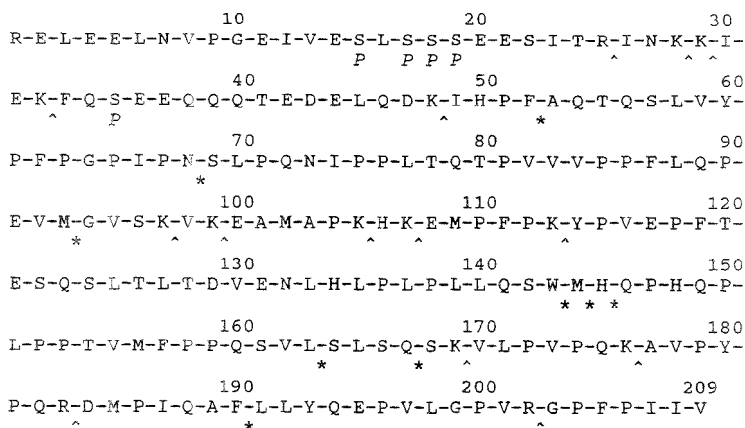


Figure 8. Amino acid sequence of bovine β -casein A₂. Positions of enzymic cleavage¹⁴ are indicated (\wedge for regular tryptic and * for atypical cleavage sites); P denotes a phosphorylated residue.

ether (Met), hydroxybenzyl (Tyr), and indole (Trp) groups show electroactivity. This selectivity is also observed in the absence of ACN, even for simple alcohols like 2-propanol. The chromatograms, obtained with a gradient of ACN in water/TFA, and the voltammogram (Figure 3) show the selectivity and the distinct waves of the electroactive amino acid residues, respectively. For instance, at +1.2 V, only Trp, Tyr, and Cys are detected, while at +1.4–1.6 V, Met and (Cys)₂ are additionally detected. The sensitivity of the detector is shown in Figure 4 for the isocratic separation of some selected dipeptides. The detection limit for these dipeptides is about 7 pmol on-column (S/N = 3), comparable to that obtained with UV detection at low wavelength; however, PED shows less drift and better selectivity. The linearity was determined for the dipeptides (0.8–100 μ M) at a detector sensitivity of 1 μ A full scale (Table 1). Leu-Tyr and Leu-Trp showed a linear response. The response of Met-Leu showed above 25 μ M a slight (5%) negative deviation from linearity. Moreover, the limited (14 bit) resolution of the D/A converter of the detector dictates the lower limit of the dynamic range, resulting in a maximum dynamic range of 2 orders of magnitude.

Oxidation of Met-Leu with hydrogen peroxide in acid medium (1% TFA) results in the formation of the corresponding sulfoxide, which shows no electroactivity (Figure 5). The PED is, as expected, not sensitive to TFA (Figure 5A), but hydrogen peroxide is easily detected (Figure 5B).

The selective detection of CMP (A and B genetic variants) versus pseudo-CMP, using an ACN gradient in water/TFA, is demonstrated in Figure 5. Pseudo-CMP generates a slightly negative peak, which is due to its adsorption on the electrode, reducing the background current. Compared to a normal thin-layer cell, equipped with a 100 μ m spacer (EG&G), the wall-jet cell improves the S/N ratio for CMP by an order of magnitude and affords less peak tailing and a more stable baseline. Although it is tempting to ascribe this to the wall-jet principle, only 0.7% of the electrode surface is operating as a wall-jet, the remaining surface functions as a normal thin-layer cell.¹⁶ The different spacers used (50 and 100 μ m) cannot fully explain this phenom-

enon. Possibly, the purity of Pt is important. A practical application is shown in Figure 7 for the determination of 5% rennet whey solids in skim milk powder. Some minor peaks, with an area equivalent to ~0.3% rennet whey solids, are detected in authentic skim milk powder; however, the addition of 1% of rennet whey solids can be easily detected.

Peptide Mapping. The versatility of this type of PED prompted us to investigate other application areas, like tryptic mapping of proteins. β -Casein A₂¹⁷ (Figure 8) contains six Met residues, thus making it an interesting protein for selective detection of sulfur-containing peptides in a tryptic digest. Figure 9 shows the peptide map obtained by RP-HPLC, together with a tentative assignment of the majority of the peaks^{18,19} (fragment 114–169 and intact β -casein A₂ is not eluted with the gradient used). A positive response of the EC detector, in combination with the absence of UV absorption at 230 nm, indicates the presence of a sulfur-containing amino acid in the peptide. The voltammogram (Figure 3) shows that a decrease of E_{det} from +1.4 to +1.2 V selectively reduces the response of sulfur-containing peptides (Figure 9, trace d) of the tryptic map of β -casein. Intact proteins like β -casein, α -lactalbumin, and β -lactoglobulin show an attenuated response, due to the limited accessibility of the electroactive groups. In contrast, postcolumn photolytic derivatization,⁶ in combination with detection at glassy carbon, gives an acceptable response for intact proteins. Proteins undergo photolysis reactions, resulting in fragments, which can more easily interact with the electrode surface. At glassy carbon, Phe-, Met-, or Cys-containing peptides gave a response only when the UV lamp was on.

Postcolumn Electrochemical Conversion (PCEC). The selectivity of the PED can be increased by using PCEC. Easily oxidized residues like Tyr and Trp are converted to oxidized species, for which PED at Pt is not sensitive. A porous graphite electrode, having a large surface area and thus operating in the coulometric mode, was tested with dipeptides (Figure 10). The

(17) Yan, S. B.; Wold, F. *Biochemistry* 1984, 23, 3759–65.

(18) Visser, S.; Slangen, Ch. J.; Lagerwerf, F. M.; van Dongen, W. D.; Haverkamp, J. J. *Chromatogr.*, in press.

(19) Briand, L.; Chobert, J.-M.; Heertle, T. *Milchwissenschaft* 1994, 7, 367–71.

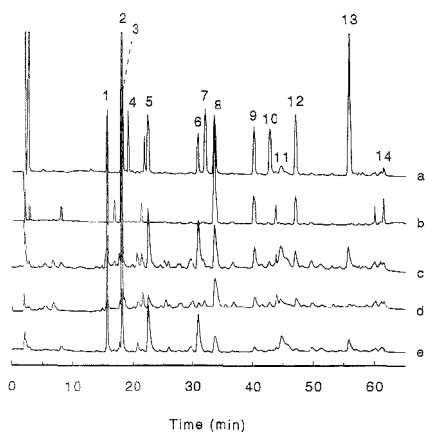


Figure 9. RP-HPLC of tryptic peptides of β -casein A_2 detected by UV at 216 nm (a), UV at 278 nm (b), PED at $E_{\text{set}} = 1.4$ V (c), PED at $E_{\text{set}} = 1.2$ V (d), and PCEC at 1.2 V with PED at $E_{\text{set}} = 1.4$ V (e). Peak assignment (tentative): 100–105 (1), 177–183 (2), 33–48 (3), 170–176 (4), 108–113 (5), 184–190 (6), 1–25 (7), 191–202 (8), 49- or 53–97 (9), 203–209 (10), 144(5)–169 (11), 53- or 49–97 (12), 69–97 (13), and 184–202 (14). Column, PLRP-S eluted at 50 °C; eluent A, water/TFA 100:0.1; eluent B, water/ACN/TFA 40:60:0.1; gradient 0% B to 100% B linear in 62 min; flow rate, 1.0 mL/min.

peaks containing Tyr or Trp are markedly reduced in size, depending on the potential applied to the electrode; optimum results were obtained at -1.3 V. In principle, the selectivity could differ from that observed with Pt, due to the difference between graphite and Pt. Moreover, the actual potential might be different, because the reference electrode in the coulometric cell is a Pd wire.

A practical application of PCEC is shown for the tryptic map of β -casein in Figure 9 (trace e). The optimum voltage is a function of the solvent composition or the analyte structure, or both. In this case, the optimum potential of the graphite electrode was $+1.2$ V. At higher settings, new peaks appeared in the chromatogram, indicating that electroinactive residues were converted to electroactive ones. The chromatogram obtained with PCEC looks like the difference of the ones obtained at E_{det} of $+1.4$

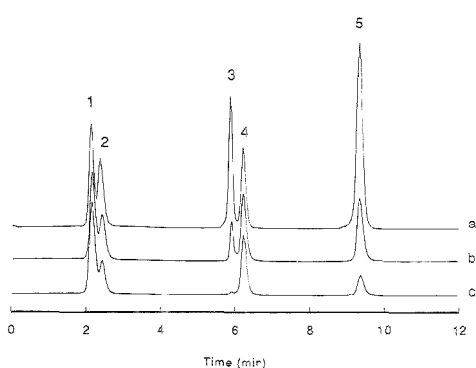


Figure 10. Detection of dipeptides and cystine by PED ($E_{\text{set}} = 1.4$ V and $E_{\text{ox}} = 2.0$ V) without PCEC (a) and with PCEC at 1.2 (b) and 1.3 V (c). Peak assignment and conditions as in Figure 3.

and $+1.2$ V (Figure 9, traces c and d). The selectivity of graphite is, apparently, not very different from that of Pt. The application of PCEC makes the identification of sulfur-containing peptides more straightforward.

CONCLUSIONS

PED at Pt under typical RP-HPLC conditions seems to take place at an oxide-free surface. It has been demonstrated to be a reliable detector,²⁰ showing high stability, which is quickly attained after switching on. The only maintenance required is to replace the electrolyte in the reference electrode regularly; the Pt electrode did not need any form of maintenance during 6 months of operation, and the electrode retained its highly polished surface. PED at Au has been used in combination with CE for the detection of carbohydrates.^{21,22} Peptide maps were obtained with CE using acidic buffers.^{23,24} In principle, PED at Pt could be applied in combination with CE in peptide mapping. Furthermore, PED at Pt seems promising for the HPLC (or CE) analysis, after, e.g., enzymic cleavage, of sulfur-containing proteins (e.g., *N*-methionyl proteins obtained by recombinant DNA techniques) and other sulfur-containing organics (e.g., antibiotics, pesticides).

ACKNOWLEDGMENT

This work was supported in part by a grant of the Program Measurement and Testing (BCR, DG XII, Commission of the European Union).

Received for review February 6, 1995. Accepted August 2, 1995.[®]

AC950127K

[®] Abstract published in *Advance ACS Abstracts*, September 1, 1995.

(20) The quality of ACN might be crucial, as we noted for the PED at Au of bile acids [Dekker, R.; van der Meer, R.; Olieman, C. *Chromatographia* **1991**, *31*, 549–55]. Several makes of ACN, all labeled as Gradient HPLC or Spectroscopic Quality, prohibited the PED of bile acids.

(21) Lu, W. Z.; Cassidy, R. M. *Anal. Chem.* **1993**, *65*, 2678–81.

(22) O'Shea, T. J.; Lumie, S. M.; LaCourse, W. R. *Anal. Chem.* **1993**, *65*, 948–51.

(23) Cobb, K. A.; Novotny, M. V. *Anal. Chem.* **1992**, *64*, 879–86.

(24) Rudnick, S. E.; Hilser, V. J.; Worosila, G. D. *J. Chromatogr. A* **1994**, *672*, 219–23.

Integrated Pervaporation/Detection: Continuous and Discontinuous Approaches for Treatment/Determination of Fluoride in Liquid and Solid Samples

I. Papaefstathiou and M. D. Luque de Castro*

Department of Analytical Chemistry, Faculty of Sciences, University of Córdoba, E-14004 Córdoba, Spain

Methods based on integration of pervaporation and potentiometric detection in a laboratory-made module are proposed for the determination of fluoride in liquid and solid samples by formation of a volatile product with hexamethyldisiloxane. The method for liquid samples is developed in a continuous system either by injection or by aspiration of the in-line-formed derivative and features linear determination between 2.5 and 500 $\mu\text{g/mL}$ (detection limit of 1.5 $\mu\text{g/mL}$) with good precision and a sample throughput of 20 samples/h. It has been validated and applied to tap water, ceramic industry wastewater, and dissolved fertilizers. The method for solid samples integrates leaching of the target analyte, formation of the volatile derivative, separation, and detection in the laboratory-made module and shows figures of merit similar to those of the method for liquid samples, but the sample throughput is 2 samples/h. It has been successfully applied to the determination of fluoride in orange tree leaves.

Miniaturization is one of the great endeavors of analytical chemists,¹ to which considerable efforts in research and development are being and are likely to continue to be devoted at the beginning of the 21st century. Two approaches can be adopted to achieve this aim: (a) reduction of the size of the apparatus and instruments involved in a step or process and (b) integration of several steps in a single module. The first approach gives rise to a concomitant reduction in the consumption of the sample and reagents, which can be crucial in the development of methods involving valuable or scarce samples and expensive reagents, but which also involves the shortcomings associated with both microsystems and complex and little-known physics and chemistry. The integration of steps is a less complex task which endows the overall process with abundant features and allows the use of easily designed and produced modules, with minimal changes to the physical and chemical features of the conventionally developed system.

We have adopted the latter approach to develop methods for the determination of fluoride which can be easily extended to other volatile or readily converted into volatile analytes, applicable to both liquid and solid samples, and based on integration of pervaporation and detection. Pervaporation is a membrane-based separation technique in which the sample never enters into contact with the membrane, since the volatile analyte or its volatile

reaction product evaporates to a space between the donor solution and the membrane and then diffuses through this to a static or flowing acceptor solution. For liquid samples, a conventional continuous manifold² has been developed, into which the sample can be either injected or aspirated for transport to the separation unit, which consists of a laboratory-made module for development of pervaporation.^{3,4} A potentiometric sensor for fluoride is placed in the acceptor chamber of the unit and above the membrane, thus allowing the monitoring of the kinetics of the mass transfer through the membrane and the determination of the target analyte. The determination of fluoride in solid samples is developed in a discontinuous approach with all the steps involved occurring in the separation unit, where the sample is weighed and the reagents added. The leaching, formation of the volatile derivative, separation, and detection all take place simultaneously.

EXPERIMENTAL SECTION

Instruments and Apparatus. A four-channel Gilson Minipuls-3 peristaltic pump fitted with a rate selector, three Rheodyne 5041 low-pressure injection valves (two of them used as selection valves), and Teflon tubing of 0.7 mm i.d. were used to build the hydrodynamic manifold. The fluoride-selective electrode (Metrohm 6.0502.150) was fitted in the upper part of the pervaporation module. A Ag/AgCl reference electrode (Metrohm 6.0726.100) was also used and was located in a flow cell made in the laboratory from a standard 10 mL disposable plastic syringe body with a 15 mm i.d. and 2 mm drain holes drilled at 0.5 cm from the bottom. The tip of the syringe was cut, and the hole left was sealed with silicone.⁵ A Crison micro-pH 2001 potentiometer, coupled to a Knauer recorder, was used to monitor the potential.

The pervaporation cell (Figure 1), designed in our laboratory, consisted of two chambers: a donor chamber (lower part of the separation unit, 11) and an acceptor chamber (upper part of the unit, 6), both fitted with inlet and outlet orifices for connectors (5) of the corresponding streams and a membrane support (8). The volume of both chambers can be changed by placing spacers (9, 10) between the membrane support (7, 8) and the chamber. The upper chamber was fitted with a central orifice at the top to accommodate the sensor (ISE) by adaptors (2, 3). Both chambers and the membrane support were aligned by inserting rods in the

(1) Guardia, M. de la; Ruzicka, J. *Analyst* 1995, 120, 17N.

(2) Valcárcel, M.; Luque de Castro, M. D. *Flow Injection Analysis: Principles and Applications*; Ellis Horwood: Chichester, U.K., 1987.

(3) Mattos, I. L.; Luque de Castro, M. D. *Anal. Chim. Acta* 1994, 298, 159–165.

(4) Mattos, I. L.; Luque de Castro, M. D.; Valcárcel, M. *Talanta*, in press.

(5) Douglas, J. G. *Anal. Chem.* 1989, 61, 922–924.

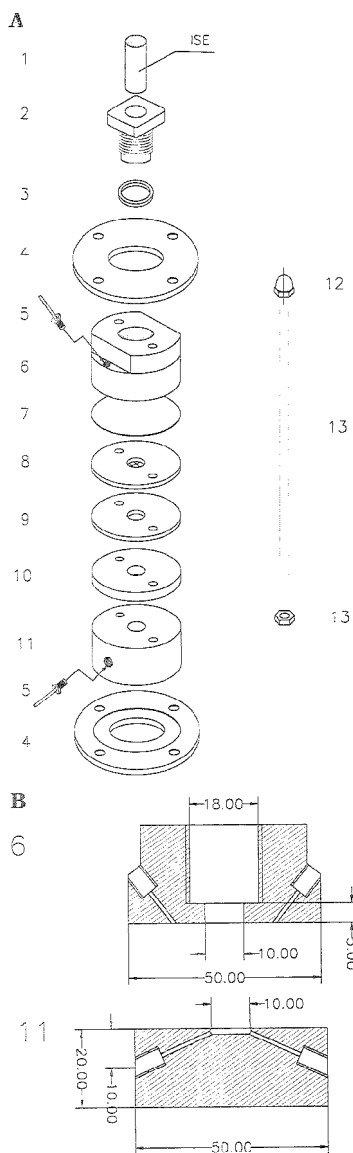


Figure 1. (A) Parts of the pervaporation cell: 1. ion selective electrode; 2. adaptor; 3. rubber ring; 4. aluminum supports; 5. connectors; 6. receptor chamber; 7. membrane; 8. membrane support; 9 and 10, spacers of 2 and 5 mm; 11. donor chamber; 12 and 13, screws. (B) Cross-sectional views and dimensions, in mm, of the receptor (6) and donor (11) chambers.

orifices, and a closer contact was achieved by fixing them with four screws (12, 13) between two aluminum supports (4). The cross-sectional views in Figure 1B show the dimensions and shape of the module, which was made of methacrylate.

Reagents. Sodium fluoride (extra pure, Merck) was dried at 130 °C for ~1 h, and 5.528 g of the dried product was dissolved

in 250 mL of Milli-Q purified water to make a 10 g/L fluoride stock solution. All standard solutions within the working range were prepared by appropriate dilution of the stock solution. A 1.5% (v/v) hexamethyldisiloxane (HMDSA) solution was prepared whenever required by measuring out 25 mL of 2 M H₂SO₄ into a flask, adding the appropriate volume of HMDSA (organic solution, Aldrich), and stirring for 5 min. After the solution was left to stand for ~15 min, the upper organic layer was aspirated off. The 1 and 2 M H₂SO₄ solutions were prepared by diluting the appropriate volume of concentrated acid (96% purissimum, Pan-reac) in Milli-Q water. The acceptor buffer, 0.2 M Na₂HPO₄ (pro analysi, Merck)/0.1 M citric acid (pro analysi, Merck)/1 M KCl (pro analysi, Merck) of pH 7.8, was also prepared in Milli-Q water. Stock aqueous solutions of Fe(III) and Al(III), used in the study of interferences, were prepared from their nitrate salts. A 0.5 M sodium citrate solution, used for the masking of Al(III) and Fe(III), was also prepared by dissolving the appropriate amount of the salt in Milli-Q water. Poly(vinylidene fluoride) (PVDF) and poly(tetrafluoroethylene) (PTFE) membranes of 5.0 μm and 47 mm diameter, respectively, purchased from Millipore, were also used.

Sample Treatment. Liquid Samples. Fluoride was determined in tap water, fertilizers, and ceramic industry wastewater. Tap water was directly introduced into the flow injection (FI) system. For fertilizers, 50 g of each sample was dissolved in 200 mL of Milli-Q water. The remaining solids were removed by filtration with a double filter (Whatman qualitative filter paper) in order to avoid clogging the system. Solids were also removed from the ceramic industry wastewater as described above.

Solid Samples. Leaves from orange trees were washed with doubly distilled water and then with a 0.05% v/v detergent/0.05% w/v EDTA solution by stirring for ~1 min. The leaves were thoroughly rinsed with doubly distilled water and oven-dried at 60–80 °C for 48 h. Higher temperatures were not recommended, as these could result in losses of the volatile fluoride. The dried leaves were ground to a very fine powder using a Sorvall Omni-Mixer 17106 (DuPont Instruments), and the desired amount of fluoride standard solution was added. The samples were then dried at 60–80 °C for 24 h and kept in plastic bottles previously washed with 1:3 HCl/H₂O solution and rinsed thoroughly with doubly distilled water. All the samples were stored in a desiccator.^{6,7} Solid standards were prepared in the same way as solid samples, but the standard solution of fluoride was added directly to the sample chamber after the ground leaves were weighed.

Manifold and Procedure for Liquid Samples. The samples were introduced into the dynamic manifold shown in Figure 2A, either by injection or by aspiration. Using the sample injection procedure, the sample or standard solution is mixed with HMDSA in an acidic medium in which the volatile product (trimethylfluorosilane, TMFS) is formed in a 300 cm coil at 80 °C. This TMFS is then injected into a H₂SO₄ stream and led to the donor chamber, also thermostated at 80 °C. During the evaporation and diffusion of the TMFS through the PTFE membrane, the acceptor buffer stream is halted, and the decrease in the potential due to the accumulation of fluoride by hydrolysis of the volatile product is monitored. For direct aspiration, the sample or standard solution is mixed with HMDSA as in the former method, but both the channel of acid solution and the injection valve are removed by

(6) Cooke, J. A.; Johnson, M. S.; Davison, A. W. *Environ. Pollut.* 1976, 11, 257–268.

(7) *Official Methods of Analysis of the Association of Official Analytical Chemists*, 15th ed.; Helrich, K., Ed.; AOAC: Arlington, VA, 1990; pp 51–56.

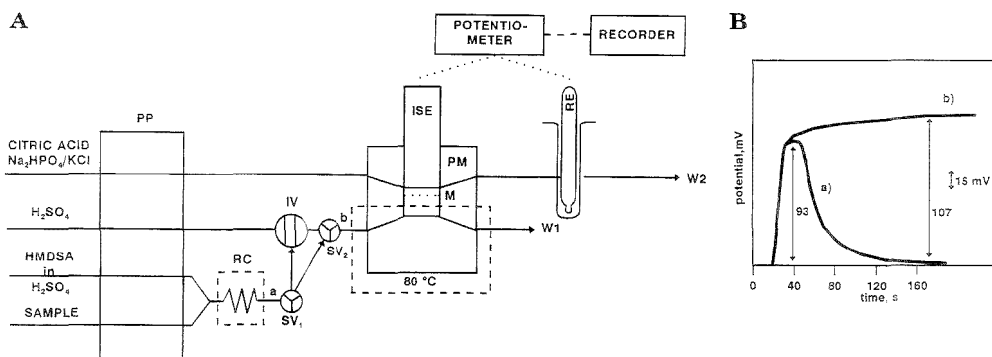


Figure 2. (A) Flow injection pervaporation/detection arrangement for the determination of fluoride in liquid samples: PP, peristaltic pump; RC, reaction coil; IV, injection valve; SV₁ and SV₂, switching valves to select between the injection and aspiration modes; PM, pervaporation module; ISE, ion-selective electrode; RE, reference electrode; M, membrane; W₁, waste. The dashed lines indicate thermostated zones. (B) Recordings obtained by sample injection (a) and continuous aspiration (b). $[F^-] = 100 \mu\text{g/mL}$.

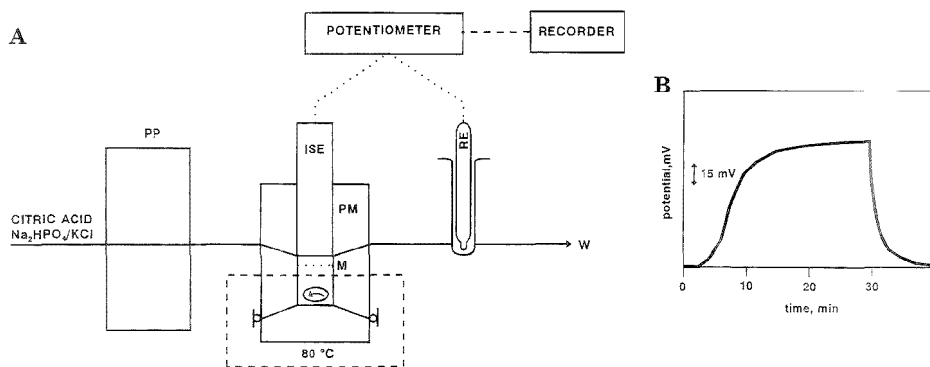


Figure 3. (A) Discontinuous approach for the determination of fluoride in solid samples: PP, peristaltic pump; ISE, ion-selective electrode; RE, reference electrode; PM, pervaporation module; M, membrane; w, waste. (B) Recording obtained by integration of separation and detection. $[F^-] = 50 \mu\text{g/mL}$.

switching the selection valves, so the points a and b in Figure 2A are connected. The volatile product, formed along RC, reaches the donor chamber, and the pervaporation/detection step occurs as described earlier. The potential versus time recordings obtained with both sample introduction procedures are shown in Figure 2B.

Manifold and Procedure for Solid Samples. The operational setup for the determination of fluoride in solid samples is a hybrid between static and flow systems, as shown in Figure 3A. Approximately 0.1000 g of sample is accurately weighed in the lower chamber, and a spacer is located between this chamber and the membrane support in order to increase the volume of the chamber and maintain constant the free volume between the sample surface and the membrane. The cell is shut after positioning the membrane and the acceptor chamber together with the fluoride electrode, and the acceptor buffer stream is introduced into the upper chamber by a peristaltic pump and then stopped in order to obtain the baseline. The appropriate volumes of the reagents necessary for the extraction of fluoride and its conversion into the volatile derivative are added through the inlet or outlet of the donor chamber, which are then closed with screws,

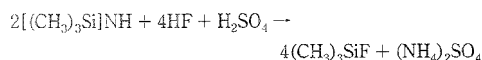
and the pervaporation/detection module is located in a thermostated magnetic stirrer. The extraction of the analyte from the solid samples, its reaction with the HMDSA, the evaporation of the volatile product, its transfer through the membrane to the acceptor buffer solution, and continuous monitoring of the fluoride released all then take place. The potential versus time recording provided by the system is shown in Figure 3B.

RESULTS AND DISCUSSION

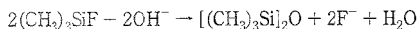
What the two approaches designed for the determination of fluoride in liquid and solid samples have in common is the integration of the pervaporation process with the detection step. An additional step of leaching of the analyte is mandatory when solid samples are involved. The two chemical steps of the overall process are as follows.⁸

The analyte reacts in an acidic medium with hexamethyldisiloxane to yield the volatile product, according to the reaction

(8) Cardwell, T. J.; Catrall, R. W.; Mitri, M. *Talanta* 1994, 41, 115-123.



which evaporates and diffuses through the hydrophobic membrane to be absorbed into the buffer solution, as follows:



The fluoride released is monitored by a fluoride-selective electrode.

Integration of Separation and Detection for the Determination of Fluoride in Liquid Samples. *Optimization of Variables.* The chemical, physical, and hydrodynamic variables affecting the formation of the volatile product and its evaporation-diffusion through the membrane were studied and optimized in a previous paper, in which the potentiometric detection of the released analyte was performed in a flow cell, on-line with the acceptor chamber of the pervaporation unit.⁹ In that method, a basic stream was used for collection of the volatile product and release of the fluoride, while a merging point of the basic stream with an acetate buffer solution provided the optimal medium for the functioning of the working electrode. The integration of the transfer of the volatile product through the membrane, with its absorption into the acceptor solution, and also the release of the analyte and its detection, makes it essential to adopt a compromise pH for the acceptor solution in order to obtain optimal absorption, hydrolysis, and performance of the ion-selective electrode (optimal working pH of the sensor between 5.0 and 8.0). A buffer solution of $\text{Na}_2\text{HPO}_4/\text{citric acid}/\text{KCl}$ with pH values between 7.2 and 8.1 provided an accurate working zone, in which the analytical signal remained constant for a given concentration of the analyte in the samples.

In order to choose the appropriate buffering system, the following solutions were checked: 0.2 M $\text{Na}_2\text{HPO}_4/0.1$ M citric acid/1 M KCl, 0.2 M $\text{Na}_2\text{HPO}_4/0.2$ M $\text{NaH}_2\text{PO}_4/1$ M KCl, and 0.05 M $\text{Na}_2\text{B}_4\text{O}_7/0.2$ M $\text{H}_3\text{BO}_3/1$ M KCl, all adjusted to pH 7.3. A slightly higher analytical signal was obtained when the first buffer solution was used; therefore, it was selected for further experiments.

A key variable for manipulating sensitivity was the length of the tubing from the donor chamber to waste, as it affected the pressure in the module and therefore the free volume between the membrane and the surface of the liquid in the donor chamber. For relatively short tubing lengths (60 cm), the signal appeared to be low and wide. For longer lengths (100–220 cm), sharper peaks were obtained, whereas the increased pressure in the system resulted in a slight movement of the upper acceptor stream. In this way, the signal started to return to the baseline after obtaining its maximum value, even before restarting the flow of the buffer stream (the latter step was mandatory after monitoring in order to reestablish the baseline; see Figure 2B). A 220 cm length of waste tubing was chosen as optimum since longer lengths resulted in a loss of sensitivity, probably due to the deterioration of the membrane by contact with the sulfuric mixture in the donor chamber. All the variables studied and their optimum values are listed in Table 1.

Halting the donor flow when the sample/reagent mixture reached the separation module was checked as a way of enhancing the analytical signal when the sample injection mode is used. No

Table 1. Optimization of the Variables Affecting the Determination of Fluoride in Liquid Samples

parameter	range studied	optimum value
[KCl] (in the acceptor stream), M ^a	1.0–3.0	1.0
HMDSA, % ^a	1.0–2.0	1.5
[H ₂ SO ₄] (derivatizing medium), M ^a	1.0–4.0	2.0
[H ₂ SO ₄] (carrier), M ^a	0.5–2.0	1.0
temperature, ^b °C ^a	60–90	80
temperature, ^c °C ^a	40–80	80
loop, μL ^c	100–1000	1000
reaction coil length, cm ^a	100–560	300
donor flow rate, mL/min ^a	0.6–2.7	1.3
acceptor flow rate, mL/min ^a	0.6–2.4	1.3
flow rate of the combined stream for the formation of TMFS, mL/min ^a	0.5–1.8	0.5
pH of the acceptor stream ^d	5.0–8.15	7.8
waste length of the donor chamber, cm ^d	60–410	220

^a Variables optimized in the previous work. ^b Temperature for the formation of the volatile compound. ^c Temperature for pervaporation of the volatile compound. ^d Variables optimized in this work.

signal increase was observed by halting the flow for 1, 2, or 5 min. This result demonstrated both the fast removal of the volatile product and its transfer to the detection chamber, which was corroborated by using the continuous sample introduction mode. As shown in Figure 2B, the sharp slope of the initial rising portion of the signal is identical for both sample introduction modes, and the increase in the signal for the additional amount of volatile product is slight. This behavior proved the close-to-equilibrium state attained in the separation process when the first portion of sample reached the donor chamber and the fact that the injected volume is sufficient to fill the donor chamber without dispersion.

As the increase in the signal with use of continuous sample introduction was negligible, the injection mode was used for characterization of the method.

Features of the Method. The calibration curve showed two linear ranges: from 2.5 to 100 μg/mL and from 100 to 500 μg/mL, with correlation coefficients better than 0.99 in both cases. The detection limit was 1.5 μg/mL. Other figures of merit are listed in Table 2.

Only two cationic species, Al(III) and Fe(III), caused interference in the determination of fluoride by the proposed method. Aluminum decreased the signal by 52% when present in a 1:5 F⁻/Al(III) ratio. A decrease of 7.6% in the signal was observed for a 1:10 F⁻/Fe(III) ratio. The interferences for other analyte/foreign species ratios are listed in Table 3. The presence of 0.5 M citrate ion in the reagent solution lowered the interference from these species: Fe(III) did not interfere at concentrations 100 times higher than that of the analyte, and a 1:10 F⁻/Al(III) caused a decrease of only 7.1% in the analytical signal (see Table 3).

Determination of Fluoride in Liquid Samples. The proposed method was applied to the determination of fluoride in tap water, fertilizers, and ceramic industry wastewater after the treatment described in the Experimental Section. The recovery in these samples ranged between 95.15 and 113.16% for a 5 μg/mL addition of fluoride and between 88.85 and 108.64% for a 20 μg/mL addition of fluoride, with RSD values, for $n = 5$, of 2.65–4.48 and 2.42–4.39, respectively. The concentration found, recovery, and RSD for each sample are listed in Table 4.

Integration of Leaching, Derivatization, Pervaporation, and Potentiometric Detection for the Determination of Fluoride in Solid

⁽⁹⁾ Papacifstathiou, I.; Tena, M. T.; Luque de Castro, M. D. *Anal. Chim. Acta* 1995, 308, 246–252.

Table 2. Features of the Methods

sample	equation ^a	correln coeff	linear range, mg/mL	RSD, % (n = 9)	detection limit, µg/mL	sampling frequency, h ⁻¹
liquid	y = 43.55x + 5.64	0.9954	2.5–100	2.49 ^b	1.5	20
solid	y = 74.46x - 56.41	0.9996	100–500			
	y = 38.42x + 16.88	0.9993	2.5–100	3.96 ^c	1.3	2

^a y is the potential in mV; x is the logarithm of fluoride concentration in µg/mL. ^b 100 µg/mL. ^c 20 µg/mL.

Table 3. Decrease (%) in the Analytical Signal Caused by Interferents

ion added		analyte-to-foreign species ratio				
		1:1	1:5	1:10	1:100	1:500
Al(III) ^a	c	52.7	66.4	91.1	na ^d	
Fe(III) ^a	c	c	7.6	39.4	na ^d	
Al(III) ^b	c	c	7.09	11.02	26.77	
Fe(III) ^b	c	c	c	c	8.33	

^a Concentration of fluoride, 60 µg/mL; without the addition of sodium citrate. ^b Concentration of fluoride, 20 µg/mL; with the addition of sodium citrate. ^c Within the confidence limits. ^d Not assayed.

Table 4. Determination of Fluoride in Liquid Samples

sample	fluoride found, µg/mL	mean recovery, % (RSD, %; n = 5)	
		addn of 5 µg/mL	addn of 20 µg/mL
tap water		95.15 (2.69)	99.08 (2.42)
fertilizer 1	22.90	98.27 (3.62)	96.00 (2.60)
fertilizer 2	26.15	104.60 (4.48)	98.57 (2.62)
fertilizer 3	30.90	113.60 (2.67)	108.64 (3.25)
ceramic industry wastewater 1	4.31	98.77 (3.69)	95.07 (4.39)
ceramic industry wastewater 2	8.51	105.00 (4.33)	88.85 (3.92)

Samples. The fluoride content of vegetation is used in the diagnosis of plant injury because plants are more sensitive to fluoride (that is, the element fluorine in any combined form¹⁰) than to most other air pollutants,¹¹ while grazing animals can be adversely affected by consuming contaminated forage. This evaluation can also be used in monitoring sources of pollution and therefore as an air quality standard. As a result, the accurate quantitative determination of fluoride is necessary. Methods for the determination of this analyte include the decomposition of organic material and the conversion of fluoride into inorganic forms by ashing, fusion, and pyrohydrolysis, followed by the separation of the analyte, usually by either steam distillation or diffusion.^{12–18} Fluoride is finally monitored by titrimetric,^{17,18} spectrophotometric,^{14,19,20} or potentiometric methods using an ion-selective electrode.^{21–24} When non-acid-labile compounds (e.g., fluorosilicates, organofluorides) are absent, extraction of fluoride with an acid can be used in conjunction with the fluoride electrode without prior ashing, fusion, or separation.^{7,25} The fluoride content in leaves is up to a little over 30 µg of F/g of dry weight in rural

areas,²⁶ but it can reach a level of several thousand micrograms of fluoride per gram of dry weight in polluted areas, whereas dense tissues such as cereal grains, straw, and wood have much lower concentrations.

Fluoride-spiked orange tree leaves have been the target samples in this study to be treated in a hybrid system, where solid-liquid extraction (leaching) of the analyte with sulfuric acid, conversion into TMFS, and detection by a fluoride electrode occur simultaneously.

Optimization of Variables. Using the pervaporation cell for the development of all the steps involved in the method, from weighing to detection, the study of variables was performed by maintaining the optimal values of the previous method for the common variables, namely the pH of the acceptor stream, concentrations of KCl and HMDSA, temperature, and acceptor flow rate. The variables to be optimized were those involved in the leaching step in conjunction with the formation of the volatile derivative, since both steps have to be developed in the same medium.

Although different acid solutions have been used for the leaching of fluoride from plants,^{7,13–16,25} H₂SO₄ was selected for development of the method, as this is the medium for optimal formation of the fluoride derivative. The concentrations of sulfuric acid studied ranged between 0.5 and 3.0 M, and the optimum value was 2.0 M, which yielded a signal 73% higher than that obtained for 0.5 M and 45% higher than that for 3.0 M. The influence of the volume of H₂SO₄ added to 0.1 g of sample, with 400 µL of HMDSA (1.5% in 2 M H₂SO₄) and 100 µL of 0.5 M trisodium citrate always present for masking of Al(III) and Fe(III), was also studied. When more sulfuric acid than that contained in the reagent solution was present, the analytical signal was smaller. This can be attributed to higher dilution of both sample and reagent.

The optimization of the volume of HMDSA was demonstrated to be necessary. Volumes higher than 100 µL gave rise to gradually smaller signals, probably because more efficient extraction of the analyte and its transformation into the volatile product

- (10) NAS. *Biological Effects of Atmospheric Pollutants: Fluorides*; National Academy of Sciences: Washington, DC, 1971.
- (11) Jacobson, J. S.; Weinstein, L. H.; McCune, D. C.; Hitchcock, A. E. *J. Air Pollut. Control Assoc.* **1966**, *16*, 412–417.
- (12) Jacobson, J. S.; McCune, D. C. *J. Assoc. Off. Anal. Chem.* **1972**, *55*, 991–998.
- (13) Debiard, R.; Dupraz, M. L. *Chim. Anal.* **1966**, *48*, 384–387.
- (14) Hall, R. J. *Analyst* **1960**, *85*, 560–563.
- (15) Hall, R. J. *Analyst* **1963**, *88*, 76–83.
- (16) Hall, R. J. *New Phytol.* **1972**, *71*, 855–871.
- (17) Willard, H. H.; Horton, C. A. *Anal. Chem.* **1950**, *22*, 1190–1194.
- (18) McDonald, A. M. G. In *Handbuch der Experimentellen Pharmakologie*; Eichler, O., Farah, A., Harben, H., Welch, A. D., Eds.; Springer-Verlag: Berlin, 1970; Vol. 22, pp 1–47.
- (19) Hall, R. J. *Analyst* **1968**, *93*, 461–468.
- (20) Newman, E. J. *Analyst* **1971**, *96*, 384–392.
- (21) Frant, M. S.; Ross, J. W. *Anal. Chem.* **1968**, *40*, 1169–1171.
- (22) Durst, R. A., Ed. *Ion-selective electrodes, proceedings*; National Bureau of Standards Special Publication 314; U.S. Government Printing Office: Washington, DC, 1969.
- (23) Harwood, J. E. *Water Res.* **1969**, *3*, 273–280.
- (24) Buck, R. P. *Anal. Chem.* **1972**, *44*, 270R–295R.
- (25) Cooke, J. A.; Johnson, M. S.; Davison, A. W.; Bradshaw, A. D. *Environ. Pollut.* **1976**, *11*, 9–23.

- (26) Suttie, J. W. *J. Agric. Food Chem.* **1969**, *17*, 1350–1352.

were surpassed by its dilution. Consequently, the volumes added to ~0.1000 g of samples were 100 μL of HMDSA (1.5% in 2 M sulfuric acid) and 100 μL of 0.5 M trisodium citrate. A higher or lower weight of solid sample, followed by the positioning or removal of suitable spacers and addition of proportional volumes of reagent and masking solutions, was checked. Greater or smaller signals, respectively, were obtained, but they were not proportional to the amount of sample, due to the difficulty in keeping the volume between the sample surface and the membrane constant. Thus, an amount of sample similar to the amount of matrix for calibration must be always used.

After the absence of fluoride in unspiked leaves was verified, this material was used as a blank in order to estimate the strength of the retention of the analyte by the organic matrix and thus the facility for calibration. Three different experiments were performed with the same amount of fluoride used for (1) spiking ground leaves, which were then oven-dried at 60–80 °C for ~24 h before the method was applied, (2) spiking the dried leaves, which were then oven-dried as above and ground, and (3) adding the spike directly to the ground and dried leaves previously weighed in the donor chamber of the separation/detection module. Identical results obtained in experiments 1 and 3 proved the quantitiveness of the leaching step. The lower recoveries achieved by experiment 2 were foreseeable because of the lack of homogeneity of the leaves/ F^- mixture.

Features of the Method. The similarity of the results obtained by spiking the ground leaves and determining the spiked analyte with or without a drying step made it easier to carry out the calibration by the latter procedure. Therefore, the calibration curve was prepared by weighing 0.1000 g of the solid matrix in the pervaporation cell and adding the appropriate amount of fluoride standard solution, followed by that of the reagents. The calibration graph showed a linear range between 2.5 and 100 $\mu\text{g}/\text{mL}$. The equations describing this behavior and other significant figures are listed in Table 2.

As was expected, the potential interferences from Fe(III) and Al(III) showed the same behavior as in the liquid samples method (see Table 3).

Determination of Fluoride in Solid Samples. The applicability of the proposed method was evaluated by determining the target analyte in leaves from orange trees. The recovery ranged from 97.22 to 102.43% and from 92.86 to 103.30% for addition of 10 and 20 $\mu\text{g}/\text{mL}$ of fluoride, respectively. All the results obtained in the determination of fluoride in these samples are listed in Table 5.

Table 5. Determination of Fluoride in Solid Samples

sample	fluoride found, $\mu\text{g}/\text{mL}$	mean recovery, % (RSD, %, $n = 3$)	
		addn of 10 $\mu\text{g}/\text{mL}$	addn of 20 $\mu\text{g}/\text{mL}$
orange tree leaves 1	10.60	98.54 (2.54)	100.96 (3.67)
orange tree leaves 2	14.96	97.22 (2.02)	92.86 (0.99)
orange tree leaves 3	35.48	102.48 (2.57)	98.84 (0.83)
orange tree leaves 4	50.12	98.86 (2.44)	103.30 (1.52)

CONCLUSIONS

Continuous and discontinuous methods for the determination of fluoride in liquid and solid samples, respectively, involving the integration of separation with potentiometric detection in both cases, are proposed.

The response time is shortened as compared to the conventional location of the sensor after the separation module,⁹ since the transport of the target species from the separation module to the detector is avoided. In addition, the monitoring of the kinetics of the mass transfer through the membrane is feasible, thus allowing a better understanding of the separation step and an easier and in-depth optimization.

The danger of clogging the separation membrane is avoided by using pervaporation rather than gas-diffusion for the separation of the volatile compound formed from the analyte.

Miniaturization of the setup for the determination of an analyte easily convertible into a volatile derivative in solid samples is achieved by integration of the leaching, derivatization, separation, and detection steps.

The approach can be applied to the determination of any volatile or any easily formed volatile species for which ion-selective electrodes exist (e.g., NH_3 , CO_2 , halogenides, etc.). In addition, both species with redox properties can be monitored voltammetrically, while colored or luminescent species or derivatization products can be monitored via optical fiber-assisted molecular detectors.

ACKNOWLEDGMENT

Dirección Interministerial de Ciencia y Tecnología is thanked for financial support (Project PB-93/0827). I.P. expresses gratitude to the Human Capital and Mobility Programme (EU).

Received for review April 10, 1995. Accepted August 7, 1995.*

AC950357Z

* Abstract published in *Advance ACS Abstracts*, September 15, 1995.

Gas-Phase Microbiosensor for Monitoring Phenol Vapor at ppb Levels

Manus J. Dennison, Jennifer M. Hall, and Anthony P. F. Turner*

Cranfield Biotechnology Centre, Cranfield University, Cranfield, Bedfordshire MK43 0AL, U.K.

A microbiosensor capable of measuring very low levels of phenol vapor directly in the gas phase has been constructed. The microbiosensor is based on the enzyme polyphenol oxidase, which catalyzes the oxidation of phenols to catechols and then to quinones. Polyphenol oxidase was immobilized in a glycerol-based gel which did not dehydrate significantly over time. An interdigitated microelectrode array was used as transducer. Phenol vapor partitioned into the glycerol gel, where it was enzymatically oxidized to quinone. Signal amplification was achieved by redox recycling of the quinone/catechol couple. This redox recycling produced a biosensor capable of measuring phenol vapor concentrations of 30 ppb. The biosensor produced a constant signal after 5 days of continuous use at room temperature and has potential application in the field of health and safety monitoring, where its ease of use, selectivity, and real-time monitoring would provide personnel with accurate data.

Gas-phase sensing has been dominated by nonbiological sensors, such as electrochemical, semiconducting, and pellister-type sensors. Commercial semiconducting sensors exist for many gases,¹ while chemical sensors based on colorimetric principles are commercially available for over 100 different gases.² There is a great variety of applications for sensors which can detect the presence of hazardous gases in industrial environments, and current equipment suffers from a lack of portability and the inability to determine cumulative exposure.³ Potentiometric and amperometric gas sensors are, in general, limited to a narrow range of electroactive gases.⁴ Semiconducting gas sensors, while able to detect a wide range of gases, have high power consumption and suffer from a serious lack of specificity. Pellister-type sensors are used for volatile organic carbons and cannot effectively distinguish between different gases. There exists a need for gas sensors with low power consumption and which are selective for unreactive gases or vapors, gas-phase biosensors could fulfill a niche requirement here.

Biological recognition proteins, such as enzymes and antibodies, have high inherent selectivity. These proteins, when incorporated into sensors, confer this property of selectivity on the biosensor. Biosensors have been developed for a large range of

analytes, including glucose,⁵ cholesterol,⁶ alcohol,⁷ and lactate,⁸ and have made their mark mainly in the field of clinical analysis, although recently many have been developed for environmental analysis.⁹ Biosensors can also operate in certain organic phases,¹⁰ provided that some water is available to the enzyme.

Certain problems are involved with applying biosensors for gas-phase sensing. As all enzymes need water for activity, and as the gas phase is usually a drier environment than the aqueous phase, water from the biosensor will evaporate to the gas phase. This loss of water will eventually affect enzyme activity and will also change the concentrations of the substrates and products. Hence, biosensor response, stability, and lifetime will be affected by the relative humidity. The fact that enzyme activity is dependent on the availability of water has been the largest limitation on the advancement of biosensors into the field of gas monitoring.

Early gas-phase biosensors were essentially bioreactors containing the sensing element (usually bacteria or enzymes) in an aqueous phase, into which was pumped the gas in question. The gas then dissolved in the aqueous phase, where it was detected by the sensing element. Using a bioreactor format overcomes the problem of water evaporation by avoiding direct interfacing with the gas phase. Biosensors based on this principle include the earliest reported gas-phase biosensor.¹¹ This biosensor was based on a methane oxidizing bacterium, *Methylomonas flagellata*, dissolved in buffer which, when exposed to methane in solution, oxidized the gas, reducing aqueous levels of O₂, which were detected by a Clark-type oxygen electrode. A similar biosensor has also been constructed for nitrogen dioxide.¹² A carbon monoxide sensor incorporating CO oxidoreductase similarly involved dissolution of the analyte in a layer retained in a reactor or as a probe.¹³ A mediator was used to effect electron transfer from the enzyme to the electrode. Guilbault¹⁴ produced a biosensor for formaldehyde based on formaldehyde dehydrogenase immobilized on a piezoelectric crystal detector which could

(1) Bott, B.; Thorpe, S. C. In *Techniques and mechanisms in gas sensing*; Moseley, P. T., Norris, J. O. W., Williams, D. E., Eds.; Adam Hilger: Bristol, UK, 1991; pp 139–160.
(2) *Draeger tube handbook*, 8th ed.; Draeger Ltd.: Lübeck, Germany, 1992.
(3) Hollingum, J. *Sens. Rev.* 1993, 13, 32–33.
(4) Hobbs, B. S.; Tantram, A. D. S.; Chan-Henry, R. In *Techniques and mechanisms in gas sensing*; Moseley, P. T., Norris, J. O. W., Williams, D. E., Eds.; Adam Hilger: Bristol, UK, 1991; pp 161–181.

(5) Cass, A. E. G.; Davis, G.; Francis, G. D.; Hill, H. A. O.; Aston, W. J.; Higgins, I. J.; Plotkin, E. V.; Scott, L. D. L.; Turner, A. P. F. *Anal. Chem.* 1984, 56, 667–671.
(6) Ball, M. R.; Frew, J. E.; Green, M. J.; Hill, H. A. O. *Proc. Electrochem. Soc.* 1986, 86, 14–25.
(7) Wang, J.; Romero, E. G.; Reviejo, A. J. *J. Electroanal. Chem.* 1993, 352, 113–120.
(8) Mullen, W. H.; Churchouse, S. J.; Freedy, F. H.; Vadgama, P. M. *Clin. Chim. Acta* 1986, 157, 191–198.
(9) Dennison, M. J.; Turner, A. P. F. *Biotechnol. Adv.* 1995, 13, 1–12.
(10) Hall, G.; Best, D.; Turner, A. *Enzyme Microb. Technol.* 1988, 10, 543–546.
(11) Karube, I.; Okada, T.; Suzuki, S. *Anal. Chim. Acta* 1982, 135, 61–67.
(12) Okada, T.; Karube, I.; Suzuki, S. *Biotechnol. Bioeng.* 1983, 25 (6), 1641–1651.
(13) Turner, A. P. F.; Aston, W. J.; Higgins, I. J.; Bell, J. M.; Colby, J.; Davis, G.; Hill, H. A. O. *Anal. Chem. Acta* 1984, 163, 161–174.
(14) Guilbault, G. G. *Anal. Chem.* 1983, 455, 1682–1684.

detect 10 ppm formaldehyde. Guilbault did not report investigating the effect of humidity on sensor response. Further gas-phase biosensors include a potentiometric biosensor for CO₂¹⁵ based on the enzyme carbonic anhydrase dissolved in a commercial hydrogel. The stability and response of this biosensor were dependent on the relative humidity of the test gas. A gas-phase biosensor for ethanol¹⁶ was based on immobilized alcohol oxidase with an oxygen electrode. A circulating buffer system was necessary to prevent dehydration of the enzyme. Spectral changes observed on binding of HCN to hemoglobin were used as the basis for a gas-phase HCN biosensor.¹⁷ Air humidity was found to have a significant effect on response, but the authors found they could compensate for it by measurement at a third wavelength.

Biosensors offer a number of important advantages over conventional analytical techniques: specificity, low cost, and portability. Their biological base also makes them exquisitely sensitive to toxins and ideal for health and safety applications, and also for pollution monitoring. Biosensors are unsuitable for use at high temperatures (due to biological inactivation) or at low temperatures. These high- and low-temperature areas will probably remain the domain of chemical sensors. Gas-phase biosensors could function admirably in the areas of health and safety monitoring and clinical sensing. Monitoring of clinically significant gases and vapors in the breath in a noninvasive fashion is particularly appealing.

Phenol is one of the most important and most widely used industrial chemicals,¹⁸ being used in the manufacture of products ranging from plastic resins to pesticides. Studies have shown the existence of phenols as pollutants of air, water, and soil.^{19–21} Studies in factories using phenol have shown the presence of low levels of background phenol vapor.^{19,22} Phenol is easily adsorbed by humans, regardless of the type of exposure, and high levels of phenols have been shown to have detrimental effects on animal health.²³ The effect of long-term exposure to low levels of phenols in the atmosphere is as yet unclear. However, natural phenols present in plants have been shown to have estrogenic properties.^{23,24} A phenol present in certain plastics, *p*-nonylphenol, has also been shown to have estrogenic properties,²⁵ as have alkylphenols.²⁶

Highly sensitive biosensors for monitoring phenols using the enzyme polyphenol oxidase have been described for organic solutions²⁷ and for aqueous solutions.²⁸ Polyphenol oxidase catalyzes the oxidation of phenol to catechol and then to quinone

using molecular oxygen. Quinones can be electrochemically reduced at approximately -150 mV (vs Ag/AgCl). To date, no gas-phase biosensor for phenol vapor has been reported. As phenol is very volatile (mp 41 °C) and one of the most widely used industrial chemicals, and legislation requires a maximum exposure limit of no more than 5 ppm over 8 h,²⁹ there exists a need for a selective, sensitive phenol vapor sensor providing real-time results. This paper reports on the development of a microbiosensor that uses polyphenol oxidase incorporated in a water-retaining gel with a microelectrode functioning as transducer for measurement of phenol directly in the vapor phase.

EXPERIMENTAL SECTION

Reagents. Chemicals. Analar grade chemicals were employed without further purification. Sodium dihydrogen orthophosphate and potassium chloride were supplied by BDH (Poole, UK). Disodium hydrogen orthophosphate was supplied by Fisons (Loughborough, UK).

Enzyme "Gel". Mushroom polyphenol oxidase (EC 1.14.18.1) (1 mg) with an activity of 6300 units/mg from Sigma (Poole, UK) was dissolved in a "gel" of 80% (v/v) glycerol (BDH) and 20% 0.1 M sodium phosphate buffer, pH 7, containing 0.1 M potassium chloride. Although a solution of glycerol is not technically a gel, but rather a viscous solution, for brevity the viscous glycerol solution will be referred to as a gel.

Biosensor Construction. Enzyme gel (4 μ L) was deposited onto the interdigitated area of a SAW-302 interdigitated microelectrode (Microsensor Systems Inc., Bowling Green, KY) (Figure 1, inset). The SAW-302 interdigitated microelectrode is a gold two-electrode system with arrays of 50 microelectrodes each (15 μ m \times 4 mm). The macrosections of the electrodes were insulated with red conformal coating (RS Components, Corby, UK), leaving the microelectrode area and the electrical contact area free of insulation. Each biosensor was based on one interdigitated microelectrode in which one microelectrode array acted as a working electrode and the other array acted as a combined counter and quasi-reference electrode (CC+QRE). SAW-302 interdigitated microelectrodes were used unless otherwise stated. Gold microdisk electrodes with a combined Ag/AgCl reference and counter electrode incorporated into the electrode design were used in certain experiments and were kindly supplied by Ecosensors Ltd. (Long Hanborough, UK).

Gas Rig. A gas rig capable of generating phenol vapor under different humidity conditions was constructed (Figure 1). Phenol high-emission permeation tubes (Vici Metronics Inc., Santa Clara, CA), which penetrates phenol at a rate which is temperature dependent, were sealed in air-tight glass U-tube and immersed in an oil bath. Low relative humidity air was then passed through the U-tube over the permeation tubes at a known flow rate. This yielded low relative humidity air containing phenol vapor, which was then mixed with air which had been humidified by passing through a Dreschel bottle containing water, generating air containing phenol vapor at the required concentration and relative humidity.

(15) Tierney, J. J.; Kim, H. L. *Anal. Chem.* **1993**, *65*, 3435–3440.

(16) Mitsubayashi, K.; Yokoyama, K.; Takeuchi, T.; Karube, I. *Anal. Chem.* **1994**, *66*, 3297–3302.

(17) Moss, D. A.; Sans, J.; Acfe, H. J. *Abstracts from the World Congress on Biosensors*, New Orleans, LA, 1994; p 3.12

(18) Gilbert, J. *Sci. Tot. Environ.* **1994**, *143*, 103–111.

(19) Drugov, Y. S.; Murav'eva, G. V. *Zh. Anal. Khim.* **1991**, *46*, 2014–2020.

(20) Shah, J. J.; Singh, H. B. *Environ. Sci. Technol.* **1988**, *22*, 1381–1388.

(21) Ciccoli, P.; Cecinato, A.; Brancaloni, E.; Frattoni, M. *Fresenius Environ. Bull.* **1992**, *1*, 73–78.

(22) Cleghorn, H. P.; Fellin, P. *Toxic. Environ. Chem.* **1992**, *34*, 85–98.

(23) VarOettingen. *Phenol and its derivatives: The relationship between their chemical constitution and their effect on the organism*; National Institute of Health: The Netherlands, 1949.

(24) StoB, M. *Handbook of naturally occurring food toxicants*; CRC Press Ltd.: Boca Raton, FL, 1983.

(25) Soto, A. M.; Justica, H.; Wray, J. W.; Sonnenschein, C. *Environ. Health Persp.* **1991**, *92*, 167–173.

(26) Colborn, T.; vonSaal, F. S.; Soto, A. M. *Environ. Health Perspect.* **1993**, *101*, 378–384.

(27) Wang, J.; Lin, Y.; Chen, L. *Analyst* **1993**, *118*, 277–280.

(28) Ortega, F.; Dominguez, E.; Jonsson-Pettersson, G.; Gorton, L. *J. Bioelectrochem.* **1993**, *31*, 289–300.

(29) Lenta, R. E. *Library of chemical safety data*, 2 ed.; Sigma-Aldrich Corp.: Milwaukee, WI, 1988.

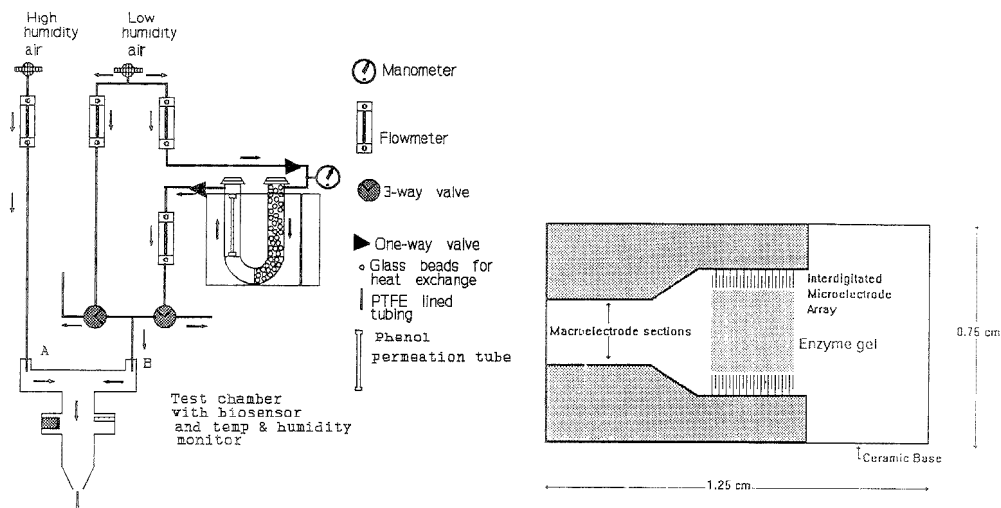


Figure 1. Schematic diagram of gas rig constructed for generating different concentrations of phenol vapor at different humidities. Arrows refer to direction of air flow. Left-hand side shows schematic diagram of biosensor.

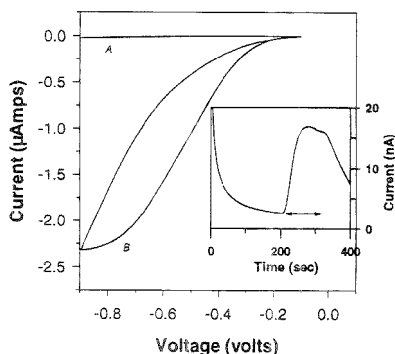


Figure 2. Cyclic voltammogram of phenol biosensor in the absence (A) and presence (B) of ~ 8.5 ppm phenol vapor at 75% RH and 25 °C. Scan rate, 0.005 V/s vs CC+QRE. Inset shows an amperometric response of the phenol biosensor on exposure to 1.6 ppm phenol vapor for 100 s at 40% RH, 25 °C. Poise potential, -700 mV vs CC+QRE.

The phenol permeation rate of the gas rig was measured using the method of Lahmann.³⁰ An impinger was used to trap the phenol vapor in 0.1 N NaOH at point B (Figure 2). The phenol was then determined spectrophotometrically (UV-visible spectrophotometer) with *p*-nitroaniline at 530 nm. The permeation rate was then back calculated. This measured phenol permeation rate agreed closely with the estimated permeation rates calculated from data provided by Vici Metronics Inc. It was not possible to use the entrapment method to measure phenol vapor concentrations in the ppb range due to time limitations, and concentrations in this range were estimated using data supplied by Vici Metronics Inc. Actual phenol vapor concentrations were calculated using

(30) Leithe, W. *Analysis of air pollutants*; Ann Arbor-Humphrey Science Publishers: Ann Arbor, MI, 1970; p 247.

the measured phenol permeation rate at the set temperature and the input flow rates of the low-humidity air containing phenol vapor and the dilutant humidified air. Concentrations were calculated as parts per million by volume (ppm) or parts per billion by volume (ppb). Two three-way valves were used so that the low relative humidity input air could be switched between clean air and air containing phenol vapor without affecting humidity or flow rate. This prevented fluctuations in the flow rate and relative humidity. All interconnecting tubing on the gas rig was composed of short length PTFE-lined tubing (Aldrich, Poole, UK). All work was carried out in a fume hood.

Apparatus and Measurements. All electrochemical measurements were carried out using an Autolab Pstat 10 electrochemical analyzer (EcoChemie, Utrecht, the Netherlands).

Procedures. The biosensor was inserted in a flow-through chamber (Aldrich) which was thermostated at 25 °C by a circulating water bath. A poised potential of -700 mV was applied between the working electrode and the CC+QRE. A steady base line current was established in air of the appropriate humidity with no phenol vapor, and the biosensor was then exposed to air containing phenol vapor for a measured time period (100 s unless otherwise stated) using the two three-way valve control system. The input air was then switched back to non-phenol air. Temperature and humidity measurements were made by a Vaisala HM34 relative humidity and temperature meter (RS Components), inserted into the test chamber near the biosensor. The response to phenol vapor was evaluated by calculating the difference between the base line current and the amperometric response. The activity of the biosensor was defined as the amperometric response (minus background current) recorded after 100 s of exposure to phenol vapor and was measured in nanoamperes per 100 s. The maximum amperometric response was defined as the level (minus background current) the current reached after the biosensor had been exposed to phenol vapor for 100 s. This is similar to peak response. This measurement was independent

Table 1. Response Times and Maximum Amperometric Responses of Phenol Biosensors as a Function of Gel Thickness^a

gel thickness (mm)	response time ^b	maximum response ^c (nA)
0.14 ± 0.025	135 ± 13	68.5 ± 5.4
0.23 ± 0.039	143 ± 40	41.3 ± 10
0.34 ± 0.059	191 ± 37	9.7 ± 2.8
0.45 ± 0.079	253 ± 36	2.4 ± 1

^a In column 1, ± figures are the limits of measurement; in columns 2 and 3, ± figures are 1 standard deviation. Biosensors were exposed to 0.53 ppm phenol vapor for 100 s at 40% RH, 25 °C. ^b Time to reach maximum amperometric response. ^c Average of four measurements.

of time and was measured in nanoamperes. The response time was defined as the time taken for the biosensor to reach its maximum amperometric response, with $T = 0$ when phenol exposure had just begun. As phenol exposure was normally 100 s, the response time cannot be less than 100 s.

RESULTS AND DISCUSSION

Cyclic Voltammetry. Cyclic voltammograms of the biosensor system in the presence and absence of phenol vapor (Figure 2) were recorded. A large increase in cathodic current at approximately -700 mV (vs CC+QRE) was observed when the biosensor was exposed to phenol vapor (8.5 ppm). When a gold microdisk electrode with a Ag/AgCl reference electrode was used as the transducer instead of the gold two-electrode microband array, a large increase in current at -150 mV (vs Ag/AgCl) was observed. This reduction potential for benzoquinone agrees with previously published values,³¹⁻³³ indicating that benzoquinone is being reduced at -700 mV (vs CC+QRE) on the interdigitated gold microband electrode. This would seem to indicate that the QRE is operating at -550 mV vs Ag/AgCl when measuring quinones.

Amperometric Response. The Figure 2 inset shows a typical amperometric response of the biosensor on exposure to phenol vapor. The biosensor showed no response to exposure to a range of solvent vapors including isopropyl alcohol, chloroform, and acetone. The response time and magnitude of the amperometric response depend on the gel thickness (Table 1), relative humidity (RH), and phenol vapor concentration. The response time is shortest for a thin gel and a high relative humidity. As glycerol is hygroscopic,³⁴ a high relative humidity would increase the water content in the gel, increasing diffusion coefficients and decreasing the response time.

Calibration. The sensor was calibrated over a range of phenol vapor concentrations at three different humidities. Figure 3 shows a calibration curve at 40% RH, and Table 2 summarizes details of the biosensor response at different humidities. The biosensor response to phenol vapor is dependent on the relative humidity. This is not a limitation, because as the background current is also dependent on the relative humidity (Table 2), the biosensor is able to measure the relative humidity and take its affect into account. Many commercial humidity sensors are based on a similar principle: that the conductivity of electrolyte in a hy-

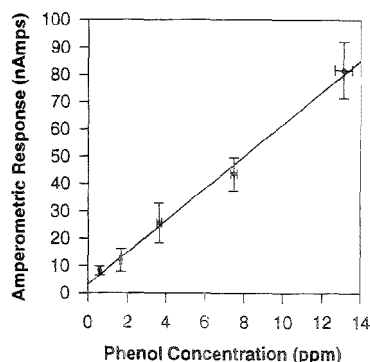


Figure 3. Amperometric response of phenol biosensors on exposure to a range of phenol vapor concentrations. A minimum of five measurements were recorded at each phenol vapor concentration. Error bars are ±1 standard deviation. Conditions: 40% RH, 25 °C; poised potential, -700 mV vs CC+QRE.

Table 2. Effect of Relative Humidity on Phenol Biosensor Sensitivity and Background Current^a

RH (%)	sensitivity (nA/ppm)	correlation coefficient	background current (nA)
64	28.5	0.977	9.0
44	5.85	0.994	3.5
27	2.39	0.950	1.6

^a Each sensitivity value is the slope of a line through 5 × 5 measurements over the phenol vapor range 0.5–14 ppm. Temperature, 25 °C.

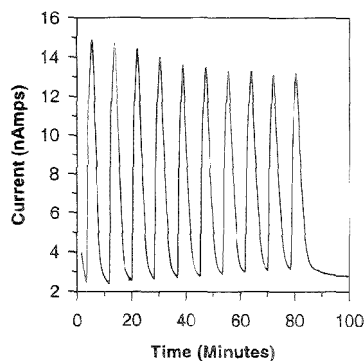


Figure 4. Amperometric response of phenol biosensors on repeated to 1.4 ppm phenol vapor. Exposure time was 100 s. Conditions: 40%–47% RH, 22–26.5 °C; poised potential, -700 mV vs CC+QRE.

scopic medium will be directly dependent on the relative humidity of the atmosphere.²⁵

Repeatability. The biosensor could be used for successive measurements of phenol vapor (Figure 4). The maximum amperometric response declined in direct proportion to the assay number. This is thought to be due to the fact that repeat exposures to phenol vapor were performed before the biosensor current had reached its original background level, indicating that

(31) Skladal, P. *Collect. Czech. Chem. Commun.* **1990**, *56*, 1427–1433.

(32) Cosnier, S.; Innocent, C. J. *Electroanal. Chem.* **1992**, *328*, 361–366.

(33) Cosnier, S.; Innocent, C. *Bioelectrochem. Bioenerg.* **1993**, *31*, 147–160.

(34) *The Merck Index*, 9th ed.; Merck & Co., Inc.: Rahway, NJ, 1976.

(35) Yamoaze, N. *Sens. Actuators* **1986**, *10*, 379–398.

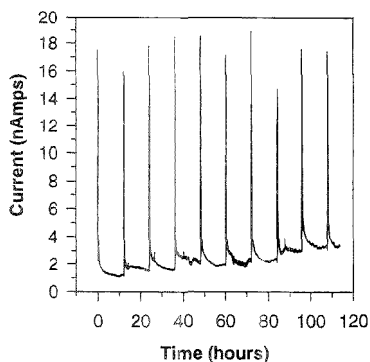


Figure 5. Amperometric response of phenol biosensors on exposure to 0.5 ppm phenol vapor over a continuous 5 day period. Exposure time was 100 s. Conditions: 43% RH, 25 °C; poise potential, -700 mV vs CC+QRE.

the electrode was still reducing quinones at the electrode surface. Quinone polymers are thought to result in enzyme inactivation³⁶⁻³⁸ and could react with phenol and catechol to form complexes. Darkening of the biosensor gel (indicative of melanin formation) after exposure to phenol vapor was apparent. The presence of quinone polymers could affect activity and electrode surface activity (by adsorption), which could account for the 17.5% decline in maximum amperometric response after nine consecutive exposures. However, if the biosensor is repeatedly exposed to phenol vapor, but with a time period between subsequent exposures long enough to ensure complete reduction of quinone species (Figure 5), then little or no decline in the maximum amperometric response occurs. A time period sufficient to allow complete or near complete reduction of quinone species to inert melanin polymers would avoid enzyme inactivation due to quinone species or cross reactions between quinone species and phenol or catechol. Adsorption of quinone species is thought to account for the increase in background current apparent in Figure 4.

Stability. The maximum amperometric response to 0.5 ppm phenol vapor remained approximately constant over the 5 day period (Figure 6). Fluctuations in peak height corresponded to uncontrollable fluctuations in temperature and relative humidity over the course of the experiment. The time required for the current to reach its maximum amperometric response (the response time) increased over the course of the experiment. The water content of the gel remained constant over a 5 day period, so the increase in response time is most likely due to enzyme inactivation. As enzyme inactivation proceeds, the rate of product (benzoquinone) production decreases, corresponding to a decrease in activity (as shown in Figure 6). However, the final amount of benzoquinone produced for a given quantity of phenol is not affected by enzyme inactivation; hence, the maximum amperometric response does not change with time. Only the rate of production of product and not the concentration of product is affected by enzyme inactivation. Hence, for the phenol vapor

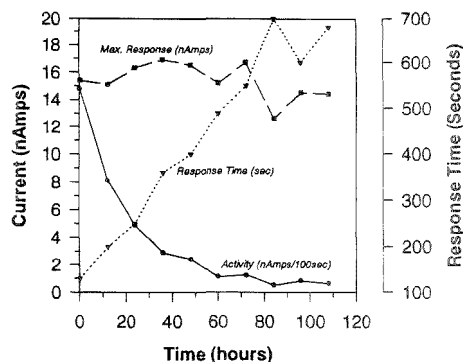


Figure 6. Profiles of the maximum amperometric response, response time, and activity on exposure to 0.5 ppm phenol vapor for 100 s over a 5 day period. Conditions as in Figure 5.

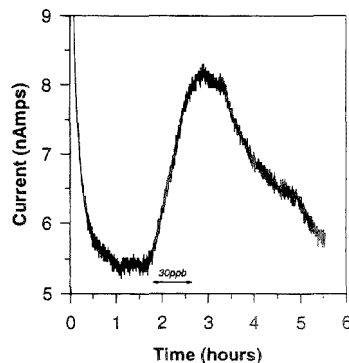


Figure 7. Amperometric response of a phenol biosensor to 30 ppb phenol vapor. Exposure time, 45 min. Conditions as in Figure 5.

biosensor, although enzyme activity apparently declines over time and results in a slower conversion of phenol to catechol, the magnitude of the maximum amperometric response is not affected.

Limit of Detection. The limit of detection (LOD) depends on the relative humidity and the exposure time to phenol vapor. At 40%RH, the LOD was calculated to be 29 ppb phenol for an initial exposure time of 100 s (a signal-to-noise ratio of 3). For repeated exposures, the LOD would be somewhat less, as the drift in background current observable on multiple exposures (Figure 4) would affect the LOD. If the exposure time is increased, then the LOD will depend mainly on the exposure time, as the glycerol gel will concentrate the phenol vapor until sufficient phenol has been trapped to generate a signal. Experiments showed that phenol is very soluble in glycerol, more so than water: glycerol will dissolve up to 50% of its own weight in phenol, compared to 10% for water. Time is the main limiting factor. Figure 7 shows the response of the phenol biosensor on exposure to 30 ppb phenol for a period of 45 min. Although 30 ppb phenol is the lowest vapor level generatable at present, it is possible that the sensor will measure phenol at lower concentrations if sufficient time is allowed.

(36) Ingraham, L. L.; Corse, J.; Makower, B. *J. Am. Chem. Soc.* **1952**, *74*, 2623-2630.

(37) Asimov, A.; Dawson, C. R. *Anal. Chem.* **1950**, *72*, 820-828.

(38) Vanneste, W. H.; Zuberbuhler, Z. In *Molecular mechanisms of oxygen activation*; Hayaishi, O., Ed.; Academic Press: New York, 1974; pp 371-404.

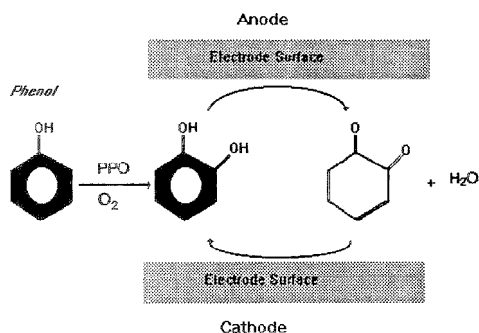


Figure 8. Redox recycling of the catechol/quinone couple at the electrode surface.

CONCLUSIONS

The sensitivity of the microbiosensor to phenol is postulated to be due to redox recycling. Redox recycling has been reported in the literature at microband arrays³⁹ and has been specifically reported for the catechol/quinone redox couple.⁴⁰ The oxidation of catechol to quinone at an anodic microelectrode is followed by diffusion of the quinone to the neighboring cathodic microelectrode, where it is reduced back to the catechol (Figure 8). This recycling probably continues until quinone polymerization products are formed. The fact that both microelectrode arrays are

involved in redox recycling suggests that the potential of the QRE will change as the catechol/quinone couple replaces the original species. We believe that this transition period is very short and that the catechol/quinone couple reaches equilibrium quickly. Cyclic voltammograms at different times show very little change in peak potential, indicating that either the catechol/quinone couple establishes itself very quickly or the shift in potential of the QRE is small. Although the use of a QRE is somewhat unorthodox, there are many reports of their use in electrochemistry.^{41–45} Redox recycling amplifies the signal considerably. In one report, it was calculated that the signal was amplified by a factor of 30 for benzoquinone redox recycling,⁴⁰ although a strict comparison is not possible here, as the authors controlled the potentials of their microelectrode relative to a Ag/AgCl reference in this report. This amplification system, in conjunction with a hydrogel which can concentrate phenol from the vapor phase, results in a biosensor capable of measuring low levels of phenol vapor which could function admirably in the field of health and safety applications.

ACKNOWLEDGMENT

The authors are grateful to the European Commission Directorate-General XII, Science, Research and Development Environmental Research program for generous sponsorship of this project. Many thanks to Dr. W. J. Aston and Dr. B. Hobbs of City Technology Ltd., to Dr. J. MacAleer of Ecosensors Ltd., and to Miss C. O'Sullivan, Dr. S. Lafis, Dr. S. Saini, and Dr. G. Pilidis of ELVIEEX for their very helpful advice and assistance.

Received for review May 9, 1995. Accepted August 4, 1995.*

AC950443Z

* Abstract published in *Advance ACS Abstracts*, September 15, 1995.

- (39) Johnson, D. C.; Ryan, M. D.; Wilson, G. S. *Anal. Chem.* **1988**, *60*, 147R–162R.
- (40) Hinsche, R.; Paeschke, M.; Wollenberger, U.; Schnakenberg, U.; Wagner, B.; Lisee, T. *Biosens. Bioelectron.* **1994**, *9*, 697–705.
- (41) Bond, A. M.; Feldberg, S. W.; Greenhill, H. B.; Mahon, P. J.; Colton, R.; Whyte, T. *Anal. Chem.* **1992**, *64*, 1014–1021.
- (42) Dressman, S. F.; Michael, A. C. *Anal. Chem.* **1955**, *67*, 1339–1345.
- (43) Michael, A. C.; Wrightman, R. M. *Anal. Chem.* **1989**, *61*, 272–275.
- (44) Sullenberger, E. F.; Michael, A. C. *Anal. Chem.* **1993**, *65*, 2304–2310.
- (45) Bond, A. M.; Lay, P. A. *J. Electroanal. Chem.* **1986**, *199*, 285–295.

Electrochemical Sensors Based on Impedance Measurement of Enzyme-Catalyzed Polymer Dissolution: Theory and Applications

Calum J. McNeil,*† Dale Athey,^{†,§} Mark Ball,[†] Wah On Ho,[‡] Steffi Krause,[†] Ron D. Armstrong,[‡] J. Des Wright,[§] and Keith Rawson[§]

Department of Clinical Biochemistry, The Medical School, University of Newcastle upon Tyne, Framlington Place, Newcastle upon Tyne, NE2 4HH UK, Department of Chemistry, Bedson Building, University of Newcastle upon Tyne, Newcastle upon Tyne, NE1 7RU UK, and Cambridge Life Sciences plc, Cambridgeshire Business Park, Angel Drive, Ely, Cambs, CB7 4DT UK

A novel sensor approach based on ac impedance measurement of capacitance changes produced during enzyme-catalyzed dissolution of polymer coatings on electrodes, leading to a 4 orders of magnitude change in capacitance, is described. Electrodes were coated with an enteric polymer material, Eudragit S 100, which is based on methyl methacrylate, and dissolution was exemplified by utilizing the catalytic action of the enzyme urease. The resulting alkaline pH change caused dissolution of the polymer film with a consequent large increase in capacitance. A mechanism for polymer breakdown is proposed which has been validated experimentally using both ac impedance measurements and electron microscopy. The large changes in capacitance that are apparent using this technique allow much greater sensitivity of measurement than, for example, potentiometric electrodes. The potential broad clinical analytical application of this technique is demonstrated in this report by application to urea measurement and to enzyme immunoassay. Urea measurement between 2 and 100 mM has been achieved with a change in response over this concentration range by over 4 orders of magnitude. We have taken account of both the effect of protein adsorption on the surface of the polymer-coated and bare electrodes and the effect of buffer capacity when carrying out these measurements in buffered solutions containing 8% (w/v) protein and have demonstrated that the method should allow simple, interference-free measurement of urea in serum and whole blood. In addition, both competitive and noncompetitive enzyme immunoassays for human IgG based on the use of urease-antibody conjugates are reported. Human IgG, or goat anti-human IgG (Fab specific), were immobilized covalently onto cellulosic membranes via a diamine spacer group and the membranes placed over enteric polymer-coated electrodes. Specific measurement of IgG in both formats was achieved over the concentration range 0.0001–100 $\mu\text{g mL}^{-1}$. The performances of the impedance-based enzyme immunoassays were compared directly with identical assays employing spectrophotometric detection.

The concept of sensors based on an electrochemical transducer sensitized with a biological moiety is both simple and elegant and

offers the prospect of reagentless clinical analysis with minimum sample preparation. The major advantage of this approach for medical use is ease of operation, thus allowing deployment of sensors in decentralized laboratories and facilitating a more rapid return of clinical information, the net benefit being an earlier institution of appropriate therapy.¹ In efforts to decrease overall analysis time and to produce methods suitable for decentralized laboratory measurement, attempts have been made to produce electrochemical sensors for clinically important analytes. To date, these have mainly been based on amperometric or potentiometric measurement using enzyme electrodes which for certain analytes have drawbacks for biosensor exploitation. The purpose of this report is to introduce a new electrochemical approach to circumvent these problems and to produce a specific, sensitive technique suitable for interference-free clinical measurement of analytes such as urea and creatinine and for application to immunoassay. In the method described in this report, we have investigated the feasibility of constructing sensors based on enteric polymer coatings which dissolve in the presence of analyte leading to highly sensitive impedance changes at underlying electrodes. Relatively little effort has been directed at the exploitation of electrode impedance measurements which have, potentially, distinct advantages for analysis including a dynamic range extending over 4 orders of magnitude and the lack of an absolute requirement for a reference electrode.

Principle of the Proposed Method. The impedance of an electrode is determined by applying a sinusoidal potential of small peak-to-peak amplitude to the electrode and measuring the resultant sinusoidal current. The frequency range used for measurement of electrode impedance is typically between 10^5 and 10^{-3} Hz. There is generally a phase difference (θ) between the potential and current so that the ratio of potential to current is essentially a vector quantity (Z) which has magnitude ($|Z|$) and direction (θ). The impedance of an electrode can be changed in many ways. For example, the adsorption of protein to an electrode will cause the electrode impedance to change.² However, in order to be useful as a sensor, the change of impedance must be highly specific to the substance being measured and give high sensitivity. The capacitance of the electrical double layer at an electrode can

* Cambridge Life Sciences plc.

† Department of Chemistry, University of Newcastle upon Tyne.

(1) Alberti, K. G. M. M., Price, C. P., Eds. *Recent Advances in Clinical Chemistry*; Churchill Livingstone: Edinburgh, 1985; Vol. 3.

(2) Bernabeu, P.; Tamisier, L.; De Cesare, A.; Caprani, A. *Electrochim. Acta* 1988, 33, 1129–1136.

§ Department of Clinical Biochemistry, University of Newcastle upon Tyne.

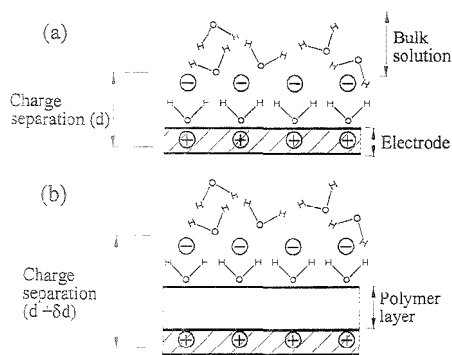


Figure 1. Schematic diagram of (a) an uncoated electrode in contact with electrolyte and (b) a polymer-coated electrode. The polymer layer increases the distance between the electrode and electrolyte by δd , thus decreasing the capacitance.

be calculated from the equation

$$C_{\text{dl}} = \epsilon_0 \epsilon_r A / d$$

ϵ_0 is equal to the permittivity of free space, ϵ_r is the dielectric constant of the material that separates the electrode from the mobile charges. A is the surface area, and d is the distance of closest approach of the mobile charges to the electrode surface. For a planar electrode in direct contact with an aqueous solution (Figure 1a), the double-layer capacitance value is $\sim 20 \mu\text{F cm}^{-2}$. If the surface of an electrode is coated with an electrically insulating layer of known dielectric constant, a dielectric, then the distance d is increased, ions are forced further from the surface of the electrode, and the capacitance value decreases (Figure 1b). The value of ϵ_r is generally also reduced, which further reduces the capacitance. This effect is small, however, in comparison to the large change produced by the increased charge separation. If a planar electrode is covered with $1 \mu\text{m}$ of an insulating polymer, the capacitance due to the double layer would be expected to change by ~ 4 orders of magnitude. Upon removal or partial degradation of the polymer film, a return to the original capacitance value would be observed. By coupling such large changes in capacitance values to a sensor format by using enzymes to catalyze the formation of polymer-degrading products, it is envisaged that metabolite assays and immunoassays with extended dynamic ranges and improved sensitivities in comparison to other sensor formats may be produced. We have chosen to demonstrate the application of this principle to metabolite assay and immunoassay by examining the effect of immobilized urease, in the presence of urea, on enteric polymer-coated electrodes.

Enteric Polymers. By definition, enteric coatings are polymers used in the coating of dosage forms for orally administered drugs, with the purpose of delivering the drug to specific regions of the gastrointestinal tract. These pH-sensitive coatings are moisture resistant and are known to be stable as polymer layers in contact with aqueous solutions provided that the solution acidity is high, e.g., in the acid environment of the stomach, but dissolve at higher pH, in most cases as a result of the loss of a proton

from a carboxyl group, e.g., in the alkaline environment of the small intestine.³ The pH sensitivity of enteric polymers depends on the hydrophobicity of the backbone polymer, the coating thickness, and the degree of derivatization within the acidic functional group.⁴ The degree of derivatization is of vital importance to enteric polymer design, as it is the presence of ionizable groups that determines the exact dissolution pH. A sufficient portion of these acidic groups $\sim 10\%$, must be ionized for water solubility to be achieved. This degree of ionization corresponds to the point at which pH rises to within one pH unit of the pK_a value. A development in enteric polymer technology are the methyl methacrylate copolymers, known by the trade name Eudragit (Röhm Pharma, Germany). The particular material used in this study, Eudragit S 100, begins to dissolve at pH 7 and is resistant to water absorption below the dissolution pH. Eudragit S 100 becomes highly soluble at pH values above 7.⁵⁻⁷ In contrast, other Eudragit polymers, such as Eudragit RL, which incorporate quaternary ammonium groups, are designed for use as delayed release coatings and, instead of dissolving, swell and become permeable in aqueous solution (independent of the solution pH).^{5,7}

Enteric polymers can be deposited on an electrode by solvent evaporation, and by generating OH^- ions adjacent to a polymer-coated electrode as a result of immobilization of an enzyme in intimate contact with the electrode, it should therefore be possible to sense low levels of an analyte, since 50% of the locally generated OH^- ions will react with the polymer, whereas if the OH^- ions were generated homogeneously in solution, a much smaller proportion would diffuse to, and react at, the polymer-coated electrode.

Measurement of Urea. Urea is one of the most requested analytes in the central hospital diagnostic laboratory in both routine and emergency situations. Indirect methods based on the determination of NH_3 released by the action of urease (EC 3.5.1.5) are now established as the methods of choice.⁸

Electrochemical sensors for urea have concentrated mainly on the use of urease in combination with ion-selective electrodes to produce potentiometric sensors for ammonium ions and ammonia gas.⁹⁻¹¹ Ammonium ion-sensitive electrodes may suffer from interference from Na^+ and K^+ , while ammonia gas electrodes are prone to error due to the background levels of endogenous ammonia nitrogen. There are few reports of practical amperometric sensors for urea,¹²⁻¹⁴ but only one method, based on the

- (3) McGinity, J. W.; Cameron, C. G.; Cuff, G. W. *Drug Dev. Ind. Pharm.* **1983**, *8*, 1409-1427.
- (4) Dressman, J. B.; Ridout, G.; Guy, R. H. In *Comprehensive medicinal chemistry: The rational design, mechanistic study and therapeutic application of chemical compounds*. Volume 5, *Biopharmaceutics*; Hansch, C.; Sammes, P. G., Taylor, J. P., Eds.; Pergamon Press: Oxford, UK, 1988; pp 537-539.
- (5) Eudragit Technical Information. Röhm Pharma GmbH, Weiterstadt, Germany.
- (6) Dew, M. J.; Hughes, P. J.; Lee, M. G.; Evans, B. K.; Rhodes, J. *Br. J. Clin. Pharmacol.* **1982**, *14*, 405-408.
- (7) Lehmann, K.; Rothgang, G.; Bossler, H. M.; Dreher, D.; Peterreit, H. U.; Liddiard, C.; Weisbrod, W. *Practical course in lacquer coating*; Röhm Pharma GmbH, Weiterstadt, Germany, 1989.
- (8) Sampson, E. J.; Baird, M. A.; Burtis, C. A.; Smith, E. M.; Witte, D. L.; Bayse, D. D. *Clin. Chem.* **1980**, *26*, 815.
- (9) Guibault, G. G.; Hraňankova, E. *Anal. Chim. Acta* **1970**, *52*, 287-294.
- (10) Hansen, E. H.; Ruzicka, J. *Anal. Chim. Acta* **1974**, *72*, 353-364.
- (11) Papastathopoulos, D. S.; Rechiniz, G. A. *Anal. Chim. Acta* **1975**, *79*, 17-26.
- (12) Senda, M.; Yamamoto, Y. *Electroanalysis* **1993**, *5*, 775-779.
- (13) Okada, T.; Karube, I.; Suzuki, S. *Eur. J. Appl. Microbiol. Biotechnol.* **1982**, *14*, 149.
- (14) Kirstein, L.; Kirstein, D.; Scheller, F. W. *Biosensors* **1985**, *1*, 117.

use of oxygen detection via horseradish peroxidase, is used commercially.

Enzyme Immunoassay. Theoretically, urease has advantages over both horseradish peroxidase (HRP) and alkaline phosphatase (AP) in enzyme immunoassay as it has considerably higher activity on a molar basis,¹⁵ therefore allowing a greater turnover of substrate to measurable product, and thus potentially creating assays with improved limits of detection and sensitivity. This should be particularly true when used in combination with the electrode impedance measurement system described in this report.

A number of urease-labeled immunoassays have been developed which utilize pH-sensitive chromogens as indicators.¹⁶⁻¹⁸ Typically, urease has been used in semiquantitative, yes/no, immunoassays, due to the sharp and unequivocal color change produced. Potentiometric immunoassays based upon urease conjugates have also been produced.^{19,20} Meyerhoff and Reznitz¹⁹ reported the use of urease conjugates with potentiometric detection, using an ammonium ion-selective electrode, in a model immunoassay for BSA and a fully optimized competitive immunoassay for cAMP. Such sensors suffered from the drawbacks usually associated with potentiometric measurement, i.e., interference from sample components and poor sensitivity.

Relatively recently, urease-based sensors based on the measurement of conductance have been produced.²¹⁻²³ An immunoassay based on this principle has been developed by Thompson et al.,²⁴ using a steel rod electrode, which could be lowered into standard polystyrene microtiter wells in which a two-site immunoassay, using a urease-labeled second antibody, for human chorionic gonadotrophin (hCG) had been performed.

Immunosensors not based on enzyme labels have also been developed which measure the change in the dielectric properties of an electrode as a direct result of a specific binding interaction between antibody and antigen.²⁵⁻²⁸ It was shown by Gardies and Martelet²⁷ using silicon/silicon dioxide electrodes to which anti- α -fetoprotein had been covalently coupled, that after exposure to serum containing α -fetoprotein, concentration-dependent changes in electrode capacitance could be measured. However, the direct binding of protein on an electrode surface produced impedance changes of typically less than 15%,²⁹ a change considered too small to be of practical use in a commercial device. In addition,

nonspecific binding is a major problem when such small changes in signal are considered.

In this paper we report preliminary studies of both competitive and noncompetitive enzyme immunoassay formats for human IgG based on the use of urease conjugates and impedance measurement of enteric polymer dissolution.

EXPERIMENTAL SECTION

Reagents. Jack bean urease (Type VI), β -NADH (disodium salt), α -ketoglutarate (disodium salt), L-glutamate dehydrogenase (FC 1.4.1.3, Type III from bovine liver), human immunoglobulin G (h-IgG, technical grade), goat anti-h-IgG (Fab specific), bovine serum albumin (BSA, Fraction V), glutaraldehyde (Grade II, 25%), Tween 20, putrescine (tetramethylethylenediamine, 98%) and 1,1'-carbonyldiimidazole were obtained from the Sigma Chemical Co. (Dorset, UK). Goat anti-h-IgG-urease conjugate (heavy- and light-chain specific) was obtained from Biogenesis (Bournemouth, UK). Urea was obtained from BDH Chemicals Ltd. (Dorset, UK). Dibutyl phthalate and bromocresol purple (indicator grade, sodium salt) were obtained from Aldrich (Dorset, UK). Regenerated cellulose membranes (0.2- μ m pore size) were obtained from Sartorius AG (Göttingen, Germany). Eudragit S 100 polymer was obtained from Dumas (UK) Ltd. (Kent, UK). Acetone was obtained from Fisons Scientific Equipment (Loughborough, UK). Buffer solutions were prepared using AnalaR grade reagents from BDH Ltd. All buffers and solutions were prepared using distilled water passed through a Milli-Q purification system (Millipore).

Apparatus. Impedance measurements were performed using a Schlumberger Solartron 1253 gain-phase analyzer and Schlumberger Solartron 1286 electrochemical interface (Schlumberger Technologies, Hampshire, UK). The Schlumberger Solartron equipment was interfaced to an IBM-compatible personal computer via an IEEE card obtained from National Instruments UK (Berkshire, UK). Instrument operation and data acquisition was controlled using "in-house" software. All impedance measurements were performed in the two-electrode mode. The counter electrode was a 4-mm-diameter glassy carbon disk sealed in a 10-cm-long PTFE tube. This was placed directly opposite and parallel to the gold ink working electrode in the template with a separation of \sim 3 mm. All impedance measurements were performed at zero dc potential, with respect to the counter electrode, with an ac peak-to-peak amplitude of 30 mV using a 5-s integration time. Electrodes for impedance measurements were manufactured by Gwent Electronic Materials Ltd. (Wales, UK) using a gold organometallic ink screen printed onto a ceramic substrate. The electrodes were fitted into a 10-well Perspex template containing silicone O rings, which exposed a 6-mm-diameter (0.28 cm²) working area at the bottom of a well to applied solutions. The total capacity of each well was 1 mL. Electrodes were spray-coated with Eudragit S 100 polymer solution using an air brush system (BioDot Ltd., Cambridgeshire, UK). Spectrophotometric measurement of urease activity was carried out using a Titertek Multiscan MCC/340 microtiter plate reader (IQ Systems, Cambridge, UK).

Spray Coating of Electrodes with Eudragit S 100. A 1.1-g sample of Eudragit S 100 polymer was dissolved in 13.7 g of acetone containing 0.25 g of dibutyl phthalate. A total of three layers (three spray passes) were sprayed over the working area of the gold ink electrodes, with each layer being allowed to dry for \sim 20 min before the next layer was applied. To ensure effective drying of the polymer film the electrodes were left for at least 24 h at room temperature before use.

(15) Zerner, B. *Bioorg. Chem.* **1992**, *19*, 116-131.

(16) Chandler, H. M.; Cox, J. C.; Healey, K.; MacGregor, A.; Premier, R. R.; Hurrell, J. G. R. *J. Immunol. Methods* **1982**, *53*, 187-194.

(17) Bradley, M. P.; Ebersperger, C.; Wilberg, U. H. *Hum. Genet.* **1987**, *76*, 352.

(18) Lo, C. Y.; Notemboom, R. H.; Kayioka, R. J. *Immunol. Methods* **1988**, *114*, 127-137.

(19) Meyerhoff, M. E.; Reznitz, G. A. *Methods Enzymol.* **1980**, *70*, 439-454.

(20) Olsen, J. D.; Panfili, P. R.; Armenia, R.; Femmel, M. B.; Merrick, H.; Gumpertz, J.; Goltz, M.; Zuk, R. F. *J. Immunol. Methods* **1990**, *134*, 71-79.

(21) Billowski, U.; Drewes, W.; Schmid, R. D. *Sens. Actuators B* **1992**, *7*, 321-326.

(22) Lawton, B. A.; Lu, Z. H.; Pethig, R.; Wei, Y. J. *Mol. Liq.* **1989**, *42*, 83-89.

(23) Pethig, R. *Biochem. Soc. Trans.* **1991**, *19*, 21-25.

(24) Thompson, J. C.; Mazah, J. A.; Hochberg, A.; Tserg, S. Y.; Seago, J. L. *Anal. Biochem.* **1991**, *194*, 295-301.

(25) Bruno, C.; Mandrand, B.; Martelet, C.; Jaffrezic, N. European patent application 0 244 326, 1987.

(26) Billard, V.; Martelet, C.; Binder, P.; Therasse, J. *Anal. Chim. Acta* **1991**, *249*, 367-372.

(27) Gardies, F.; Martelet, C. *Sens. Actuators* **1989**, *17*, 461-464.

(28) Bataillard, P.; Gardies, F.; Jaffrezic, N.; Martelet, C.; Bruno, C.; Mandrand, B. *Anal. Chem.* **1988**, *60*, 2374-2379.

(29) Lacour, F.; Torresi, R.; Gabrieli, C.; Caprani, A. *J. Electrochem. Soc.* **1992**, *139*, 1619-1622.

Polymer Dissolution Mechanism. Initial impedance measurements were carried out in 2 mM phosphate buffer (pH 5.2) containing 1 M NaCl. The dissolution of the polymer was then initiated by removing the measuring solution and adding 100 μ L of 0.1 M phosphate buffer (pH 7.8) over the electrodes in the template described previously. In order to halt polymer dissolution at different stages during the breakdown, the experiment was interrupted by removing the pH 7.8 phosphate buffer, rinsing the template well with deionized water and adding the same electrolyte as for the initial measurements. Electron micrographs of the polymer film-coated gold ink electrodes were taken at the same stages of dissolution.

Immobilization of Urease on Membranes. A 450-mg aliquot of 1,1'-carbonyldiimidazole (CDI) was dissolved in 10 mL of acetone (total 4.5% w/v), and 100 6-mm-diameter disks of regenerated cellulose membrane were placed into the solution. The contents were gently mixed by rotation for 16 h at room temperature. The disks were then removed and washed several times with acetone. The CDI-activated membranes were stored in acetone at room temperature until required. Urease was dissolved in 0.1 M sodium carbonate buffer (pH 9.6) to a concentration of 10 mg mL⁻¹. CDI-activated membranes were removed from the acetone, blotted dry on tissue paper, and placed into the enzyme solution. The membranes were incubated with agitation for 16 h at 4 °C. The membranes were then removed, rinsed, and stored in 140 mM sodium chloride solution (pH 6.5) containing 0.2 mM EDTA at 4 °C until required. The activity of the urease-loaded membranes was measured using a coupled enzyme reaction employing glutamate dehydrogenase.⁸ The rate of NADH consumption was followed by measuring the change in absorbance at 340 nm. A standard curve with soluble urease was used to estimate the amount of urease activity immobilized onto the membrane disks.

Urea Assay Based on Impedance Measurement. A 6-mm-diameter urease-loaded membrane disk was placed over the working area of an Eudragit S 100-coated gold ink electrode. The membrane was gently pressed down and the electrode loaded into the template. A silicone O ring was placed on top of the membrane and used to ensure a leak-proof seal between the electrode and the template. A solution consisting of 140 mM NaCl and 0.2 mM EDTA, adjusted to pH 6.5 using 0.1 N HCl, was used as the electrolyte from impedance measurements and for the preparation of urea standard solutions. The template well was filled with 200 μ L of urea standard solution (1–100 mM), the counter electrode was placed in position, and impedance measurements were carried out at a fixed frequency of 20 kHz using an external measuring resistor of 10 k Ω . In addition, to investigate the effect of buffer capacity and protein in a simulated serum matrix, urea solutions in 10 mM phosphate buffer (pH 6.5) containing 8% (w/v) BSA, 0.2 mM EDTA, and 0.14 M NaCl were prepared and used as described above.

Immobilization of h-IgG. Fifty regenerated cellulose membranes (6-mm diameter) were activated with CDI as described previously. After activation, the membranes were placed into 10 mL of 0.5 M sodium carbonate buffer (pH 9.6) containing 0.3 M putrescine and mixed by rotation for 16 h at room temperature. The membranes were then removed and washed several times with distilled water before addition to 10 mL of a 25% (w/v) solution of glutaraldehyde. Thereafter, the membranes were mixed by rotation for 30 min. The disks were then washed several

times with distilled water before placing the membranes in 3 mL of a 3 mg mL⁻¹ solution of h-IgG in 0.5 M sodium borate buffer (pH 10). The membranes were then mixed by rotation for 4 h at room temperature, then placed in 5 mL of 0.1 M Tris-HCl buffer (pH 7.5) containing 1 mM EDTA and 1% (w/v) glycine to neutralize any unreacted glutaraldehyde. After mixing for 30 min, the membranes were removed and washed several times with 0.1 M Tris-HCl buffer (pH 7.5) prior to storage at 4 °C in this buffer until required. Prior to use in a competitive immunoassay format, potential protein binding sites on the membranes were blocked using 5 mL of 0.1 M Tris-HCl buffer (pH 7.5) containing 1% (w/v) BSA.

Impedimetric Competitive Immunoassay. A range of h-IgG standards were prepared in 0.1 M Tris-HCl buffer (pH 7.5) containing 1% BSA, and 100 μ L of each standard competed against 100 μ L of a 1:250 dilution of anti-IgG-urease conjugate for IgG-binding sites on regenerated cellulose membranes for 1 h. Thereafter the membranes were removed and washed several times with 0.1 M Tris-HCl buffer (pH 7.5) containing 0.1% (v/v) Tween 20. They were then rinsed with deionized water and the urease activity of the membranes, after competitive binding of anti-IgG-urease conjugate, was assessed by impedance measurement. Individual membranes were placed over the working surface of polymer-coated gold ink electrodes. The electrodes were inserted into the template, and each template well filled with 90 μ L of 0.2 mM EDTA containing 140 mM NaCl (pH 6.5). The initial impedance of each electrode at 20 kHz was measured, using an external measuring resistor of 10 k Ω and then 10 μ L of 1 M urea in EDTA/NaCl solution added. The impedance was then monitored over a 1 h period. Final capacitance values were calculated and the ratio of final to initial capacitance (C_f/C_i) taken. In addition, for comparative purposes, the urease activity of each membrane was measured spectrophotometrically at 540 nm using bromocresol purple color reagent⁹ according to the following procedure. After the immunological reaction had been carried out and the membranes washed, each membrane was immersed in 200 μ L of substrate solution. This was prepared by dissolving 8 mg of bromocresol purple in 1.5 mL of sodium hydroxide and diluting with 100 mL of water to which 100 mg of urea and 7 mg of EDTA were added. The pH of this solution was adjusted to 4.8 with dilute sodium hydroxide. Optical density measurements after a fixed time were made in microtiter plate wells after removing a 50- μ L aliquot of substrate solution.

Immobilization of Anti-h-IgG. Regenerated cellulose membranes were activated with CDI, putrescine, and glutaraldehyde exactly as described previously. A 10- μ L aliquot of a 2.3 mg mL⁻¹ solution of goat anti-h-IgG in phosphate-buffered saline (pH 7.4) was then spotted onto the activated membranes. The spotted membranes were then stored in Tris-HCl buffer at 4 °C until required. Prior to the use in a two-site noncompetitive immunoassay format, potential protein binding sites on the membranes were blocked in 5 mL of a 0.1 M Tris-HCl buffer (pH 7.5) solution containing 1% (w/v) BSA.

Impedimetric Sandwich Immunoassay. Individual anti-h-IgG-coated membranes were incubated in 100 μ L of a range of h-IgG standards in 0.1 M Tris-HCl/1% BSA buffer (pH 7.5) for 1 h at room temperature. The membranes were washed several times with Tris-HCl/0.1% Tween 20 and then individually incubated with 100 μ L of anti-h-IgG-urease conjugate solution diluted 1:500 with 0.1 M Tris-HCl/1% BSA buffer for 1 h at room

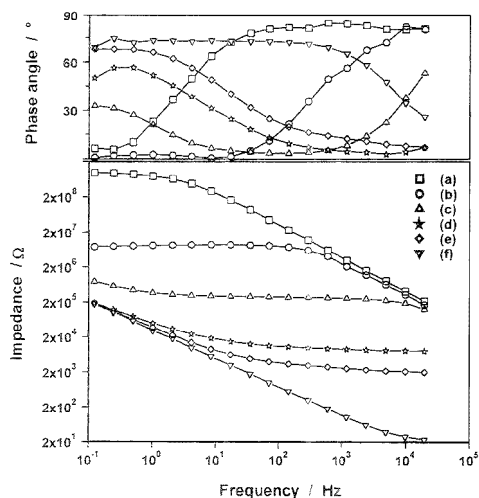


Figure 2. Bode plots of (a) a polymer-coated electrode prior to breakdown, (b–e) partially degraded polymer films, and (f) a bare electrode.

temperature. This was followed by washing several times with Tris-HCl/0.1% Tween 20. The amount of urease labeled bound to the membranes was assessed by both impedance and spectrophotometric measurement exactly as described previously.

RESULTS AND DISCUSSION

Mechanism of Polymer Breakdown. We have carried out simple qualitative experiments to demonstrate that Eudragit S 100 dissolves completely at pH values greater than 7. This involved titrating a suspension of the polymer (1 g in 50 mL of distilled, deionized water, pH 4.5) with 0.1 M NaOH and observing the formation of a homogeneous solution above pH 7. The mechanism of dissolution of the enteric polymer coated on gold ink electrodes was then investigated using impedance spectroscopy. Basically, three different states of the Eudragit S 100-coated gold ink electrodes were examined, the initial film, bare gold electrode, and intermediate stages of partial dissolution of the polymer.

The impedance spectrum of the initial film showed capacitive behavior over a large frequency region (spectrum a in Figure 2); i.e., the phase angle was close to 90°. This indicated that the Eudragit S 100 films provided good insulating properties. The geometric capacitance calculated from a fit of the spectrum was 177 pF cm⁻² and corresponded to a dielectric constant of $\epsilon_r = 7$. From the spectrum of a bare electrode (Figure 2, spectrum f), a double-layer capacitance for the gold/electrolyte interface of $\sim 25 \mu\text{F cm}^{-2}$ was determined, as would be predicted from theoretical considerations.

Impedance spectra of partially dissolved films are represented in spectra b–e in Figure 2. Interestingly, polymer dissolution from the electrode surface could be observed visually during the course of these experiments. For the first stage of breakdown (spectrum b), the geometric capacitance of the polymer was 188 pF cm⁻², i.e., nearly the same as for the initial state (spectrum a). The low-frequency region of the spectrum showed a resistive behavior, which can be ascribed to the formation of pores in the polymer

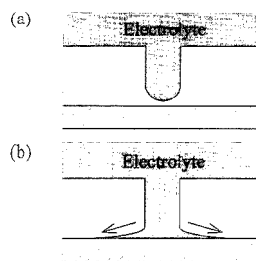


Figure 3. Schematic diagram showing the proposed mechanism of pore formation in the polymer film in alkaline solution: (a) Electrolyte begins to penetrate the polymer; (b) electrolyte penetrates the polymer to the gold electrode and spreads across the surface beneath the polymer.

layer. The resistance reflected the conductivity of the electrolyte in the pores and allowed an estimate of the relative porosity of the film. For this purpose, the resistance calculated from the impedance data was divided by the resistance of an electrolyte layer that would occupy the same space as the initial polymer (0.034 $\Omega \text{ cm}^2$). For spectrum b, a porosity of 1.7×10^{-8} was obtained. In the frequency range used for the measurements, the limiting low-frequency behavior of spectrum b was purely resistive. Therefore, in this instance the electrolyte did not penetrate the polymer and contact the gold surface (Figure 3a). At later stages of breakdown, as shown in Figure 2, spectra c–e, where the electrolyte had penetrated the polymer film to contact the electrode surface, the low-frequency impedance was capacitive and represented the wetted area of the gold electrode. For these partially dissolved films, the ratio of the double-layer capacitance of a polymer-covered electrode to a bare electrode gave the fraction of the gold surface wetted with electrolyte.³⁰

At the second stage of breakdown (Figure 2, spectrum c), the geometric capacitance of the polymer was still the same (138 pF cm⁻²). However, the porosity of the film had increased to 4.9×10^{-7} and the double-layer capacitance, by comparison with that of a bare electrode, showed that $\sim 8.5\%$ of the gold surface was wetted with electrolyte. The relatively high fraction of wetted electrode surface in combination with the small porosity of the film can only be explained by spreading of the electrolyte on the gold surface beneath the Eudragit S 100 polymer layer (Figure 3b).

These results were confirmed by the impedance spectra of films which had been broken down further. For spectrum d in Figure 2, a geometric capacitance of 425 pF cm⁻² and a porosity of 1.5×10^{-5} were calculated, while $\sim 90\%$ of the surface area was wetted. At the next stage of breakdown, spectrum e, the geometric capacitance could no longer be measured. From the electrolyte resistance in the pores, a relative porosity of 5.6×10^{-5} was estimated. Since the double-layer capacitance obtained from spectrum e was identical to the capacitance of a bare electrode, essentially 100% of the gold surface was covered with electrolyte.

From the results described, a probable mechanism for polymer dissolution on the electrode surface can be derived. When the polymer film is exposed to a pH higher than 7.0, initially partial pores are formed. This was confirmed by electron micrographs (Figure 4), which showed the formation and growth of holes in

(30) Armstrong, R. D.; Wright, D. *Electrochim. Acta* 1993, 38, 1799–1801.

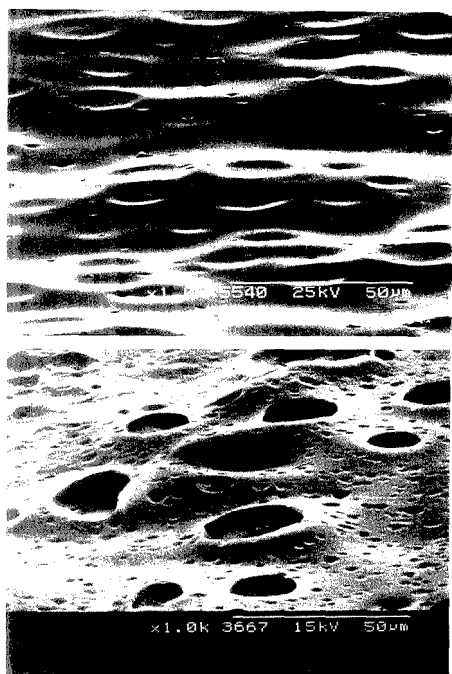


Figure 4. Electron micrographs of (a, top) a polymer-coated electrode prior to breakdown and (b, bottom) a partially broken down polymer film on the electrode showing pore formation.

the film that, in cross section, was $\sim 36 \mu\text{m}$ thick. Further dissolution resulted in the penetration of the electrolyte to the gold electrode where it spread across the surface (Figure 3b). Further investigations are in progress which will provide a more detailed explanation of the dissolution mechanism.

Urea Measurement. The polymer-coated electrodes with urease membranes in place initially exhibited capacitive behavior at a frequency of 20 kHz. This enabled the initial capacitance of the electrode to be calculated (C_0). The initial C_0 values of electrodes prepared in an identical fashion showed some degree of variation ($0.4 \pm 0.1 \text{ nF cm}^{-2}$, $n = 11$).

Using the coupled enzyme assay method, the activity of the membrane-bound urease was determined to be 0.135 unit/disk based on a specific activity of the urease preparation of 13.5 units mg^{-1} . Incubation of an uncoated membrane disk with the assay reagents gave no significant changes in absorbance.

The impedance of the electrodes was measured as a function of incubation time with urea standard solutions over the range 1–100 mM. The imaginary impedance component (Z'') at 20 kHz was used to calculate the electrode capacitance (C) at all times. The time-dependent values of C/C_0 as a function of urea concentration are shown in Figure 5. By using the ratio C/C_0 we should be able to account, to a large extent, for the initial variability in capacitance. For example, after 10 min the coefficient of variation of the C/C_0 ratio for five replicate measurements of 10 mM urea was 3.6%. Using the data generated after a 10-min incubation, it was apparent from C/C_0 vs log [urea] calibration curves that, over the range of urea concentrations from 2 to 100

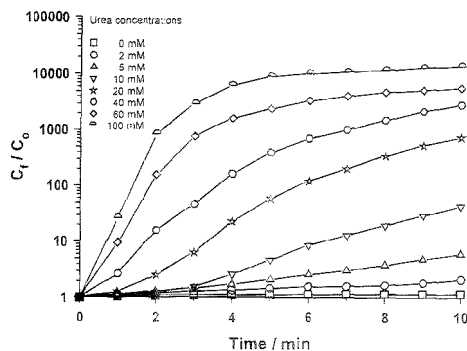


Figure 5. Effect of urea concentration in 140 mM NaCl and 0.2 mM EDTA (pH 6.5) on the time-dependent change in C/C_0 ratio using a urease-active cellulose membrane laid over an Eudragit S 100 polymer-coated electrode. A calibration curve of $\ln C/C_0$ vs $\ln [\text{urea}]$ generated using the 10-min incubation data gave a linear response over the range 2–100 mM ($y = 2.21x - 0.88$, $r = 0.99$).

mM, this ratio changed by over 4 orders of magnitude. However, due to the complex mechanism of polymer removal, the capacitance ratio increased nonlinearly with urea concentration. The mean value ($n = 10$) of C/C_0 after a 10-min incubation in the absence of urea was 1.1 ± 0.1 , indicating that the use of the capacitance ratio did significantly improve the signal variation. Thus these results and the data shown in Figure 5 demonstrate clearly that the full potential of the method could be achieved in these measurements. Obviously a prime future concern is the development of methodology that would provide highly reproducible values of C_0 , and to this end we are currently investigating the use of spin-coating of the polymer onto the electrodes.

When considering changes in capacitance at electrode surfaces in biological samples for the ultimate development of sensors capable of measurement in undiluted serum or whole blood, it is obviously important to take account of both the effect of protein adsorption on the surface of the polymer-coated and bare electrodes and the effect of buffer capacity. Adsorption of proteins is known to cause impedance changes at electrodes. For example, Lacour et al.²⁹ have shown that the capacitance of a gold electrode will decrease by 15–20% when exposed to a solution of bovine serum albumin (BSA) for 30 min. However, at a polymer-coated electrode, protein adsorption will not appreciably change the effective thickness of the insulating dielectric layer and therefore will not give rise to a measurable change in capacitance. We have verified experimentally that this is the case by measuring the capacitance of Eudragit S 100-coated gold ink electrodes in a 10 mM phosphate buffer solution containing 10 mM urea, 0.2 mM EDTA, and 0.14 M NaCl in the presence and absence of 8% (w/v) BSA. This buffer and protein concentration was used to simulate the situation that would be encountered in serum samples since although the major buffering system in serum is related to the balance between bicarbonate and dissolved CO_2 /carbonic acid, proteins also significantly contribute to the buffer capacity. The capacitance of a polymer-coated electrode after a 30-min exposure to BSA was 0.38 nF cm^{-2} . This was identical to the value measured in the absence of BSA after the same time. Therefore, protein binding to the intact polymer should not be a source of interference in this method. Removal of the polymer film using

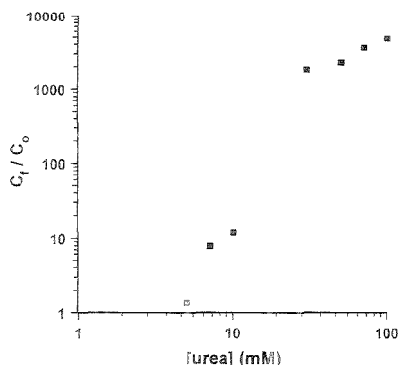


Figure 6. Calibration curve (10-min incubation) for urea assay in a simulated serum matrix [10 mM phosphate buffer (pH 6.5) containing 8% (w/v) BSA, 0.2 mM EDTA, and 0.14 M NaCl] using a urease-active cellulose membrane laid over an Eudragit S 100 polymer-coated electrode.

a urease membrane located over the electrode caused the capacitance to change to a final value of $5.7 \mu\text{F cm}^{-2}$ in both cases, although it was noticed that the rate of polymer breakdown was slowed by $\sim 20\%$ in the presence of protein. In parallel with these experiments, the change in potential due to the pH change upon the action of a urease membrane with the same 10 mM buffered urea solution was monitored. An overall change in potential of ~ 120 mV was observed (equivalent to a 2 order of magnitude change in H^+ concentration) compared with a simultaneous 4 order of magnitude change in capacitance. This demonstrated the potential sensitivity of impedance analysis compared with simple pH measurement.

To investigate further the effect of buffer capacity and protein during urea-catalyzed polymer dissolution, we generated calibration curves after a 10-min incubation with urea standard solutions prepared in 10 mM phosphate buffer (pH 6.5) containing 8% (w/v) BSA, 0.2 mM EDTA, and 0.14 M NaCl (Figure 6). It was apparent that although the presence of buffer and protein decreased the rate of polymer dissolution, such that the detection limit after 10 min was increased from 2 to 5 mM (cf. Figure 5), the system still displayed a 4 order of magnitude change in impedance. It is thought that the decrease in dissolution rate was probably caused to some extent by protein entering the pores during formation; however, since the polymer acts by dissolving rather than swelling this does not cause serious nonspecific interference.

The experiments carried out have shown clearly that the method described in this report can operate in protein-containing buffered solutions. While it is recognized that protein may bind to the bare metal after complete removal of the polymer film, by making measurements at a particular time when the polymer is being removed, this source of potential interference will be avoided. It should also be stressed that protein binding directly to the electrode surface may alter the capacitance by $\sim 15\%$ ²³ while removal of the dielectric enteric polymer will cause a 4 order of magnitude change.

Work is currently in progress to increase the rate of polymer dissolution in the presence of protein and buffer by use of wicking materials³¹ and also to produce prototype instrumentation based

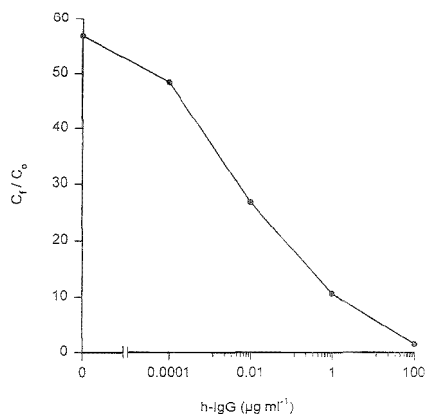


Figure 7. Calibration curve for impedimetric competitive immunoassay for h-IgG.

on single-frequency capacitance measurement for urea determination in whole blood or serum. To achieve this, the synthesis of enteric polymers that are stable at the pH of these matrices is being undertaken. Heller et al.³² reported that for a series *n*-butyl and *n*-pentyl half-esters, depending on the degree of esterification, the dissolution pH can be controlled to occur anywhere in the region pH 5–7.5. Further, they described that esterification of *n*-hexyl and *n*-heptyl half-esters to $\sim 60\%$ will produce polymers with dissolution pH's between 7.5 and 8.

Impedimetric Immunoassay. A competitive immunoassay for h-IgG was carried out using h-IgG and a limiting amount of membrane-bound h-IgG competing for goat anti-h-IgG–urease conjugate in solution. Figure 7 shows a typical competitive assay response curve produced using capacitance measurement. As would be expected, similar behavior was observed when colorimetric detection using bromocresol purple was employed. Membranes that had no h-IgG immobilized to the surface but that were blocked using BSA showed no significant responses in either the capacitance or colorimetric measurement formats when exposed to the goat anti-h-IgG–urease conjugate. Thus, the degree of nonspecific binding to the cellulose membrane surface was minimal.

Colorimetric detection demonstrated poor sensitivity at low h-IgG concentrations ($< 0.01 \mu\text{g mL}^{-1}$) due to the sharp and unequivocal color change of the pH indicator dye, bromocresol purple. Optical density values, at 540 nm, of the low standards reached a plateau after 15 min of incubation (data not shown). In contrast, no such "saturation" effect was observed using capacitance measurement. The curve shown in Figure 7 was obtained 1 h after the addition of 100 mM urea, and discernible concentration-dependent responses could also be obtained after 15 min.

The two-site assay format, with F_{ab} -specific anti-h-IgG immobilized at the surface of regenerated cellulose membranes, produced typical noncompetitive immunoassay standard curves using capacitance measurement (Figure 8). Colorimetric detec-

(31) Zuk, R. F.; Ginsberg, V. K.; Houts, T.; Rabbie, J.; Merrick, H.; Ullman, E. F.; Fischer, M. M.; Chung Sizto, C.; Stiso, S. N.; Litman, D. J. *Clin. Chem.* **1985**, *31*, 1144–1150.

(32) Heller, J.; Baker, R. W.; Gale, R. M.; Rodin, J. O. J. *Appl. Polym. Sci.* **1978**, *22*, 1991–2009.

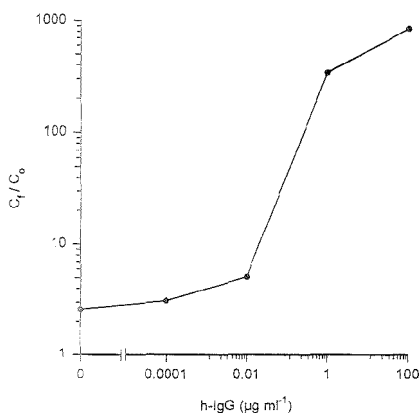


Figure 8. Calibration curve for impedimetric noncompetitive immunoassay for h-IgG.

tion using bromocresol purple once again proved to have limitations since the optical density measurements at 540 nm for h-IgG standards above $0.1 \mu\text{g mL}^{-1}$ reached a plateau value after a 30-min incubation (data not shown). Using capacitance measurement, the standard curve shown (Figure 8) was obtained after a 1-h incubation with 100 mM urea, although it was possible to measure concentration-dependent responses after a 20-min incubation with substrate (data not shown).

The capacitance ratios (C_1/C_0) shown for both the competitive and two-site assays were once again used to minimize the effect of the degree of interelectrode initial capacitance value irreproducibility. It was apparent that in both h-IgG immunoassay formats capacitance measurement produced an increased dynamic range compared with spectrophotometric detection. Further

optimization of both immunoassay formats, in terms of electrochemical cell design and the possible use of wicking systems as the immunological capture phase,³¹ should allow a significant decrease in substrate incubation time for capacitance measurement.

In summary, we have demonstrated the feasibility of a new concept for electrochemical sensors based on the measurement of the change in electrode impedance upon the degradation of polymer coatings as a result of specific interactions. We are currently extending this approach to the interference-free measurement in blood of other clinically important analytes such as creatinine. The major advantages of this technique for such analytes are the wide dynamic range available and the inherent sensitivity of the method. In addition, we are examining the use of alternative approaches to polymer breakdown such as Fenton chemistry based upon free radical attack on electrode coatings such as *cis*-polyisoprene.^{33,36}

ACKNOWLEDGMENT

This work was supported by a grant from the Biotechnology and Biological Sciences Research Council (GR/J90954) and by the European Union through a EUREKA project grant (EU 568 Medisens) to Cambridge Life Sciences plc. S.K. is grateful to the Deutscher Akademischer Austauschdienst for a postdoctoral research fellowship. We thank Mr. Roy Erwood of Dumas UK Ltd. for the gift of Eudragit S 100.

Received for review April 19, 1995. Accepted August 4, 1995.*

AC950386+

(33) McNeil, C. J.; Athey, D.; Mullen, W. H. United Kingdom Patent Application 9311206.8, 1993.

(34) McNeil, C. J.; Athey, D.; Armstrong, R. D.; Mullen, W. H. United Kingdom Patent Application 9325398.6, 1994.

* Abstract published in *Advance ACS Abstracts*, September 15, 1995.

Aldehyde Biosensor Based on the Determination of NADH Enzymatically Generated by Aldehyde Dehydrogenase

F. Pariente,[†] E. Lorenzo,[†] F. Tobalina,[†] and H. D. Abruña^{*‡}

Departamento de Química Analítica y Análisis Instrumental, Universidad Autónoma de Madrid, Cantos Blanco 28049, Madrid, Spain, and Baker Laboratory, Department of Chemistry, Cornell University, Ithaca, New York 14853-1301

We describe the preparation, characterization, and performance of an aldehyde biosensor based on the determination of NADH generated by the enzymatic activity of immobilized (on a nylon mesh membrane) aldehyde dehydrogenase. The enzymatically generated NADH is, in turn, electrocatalytically oxidized at a glassy carbon electrode modified with an electropolymerized film of 3,4-dihydroxybenzaldehyde (3,4-DHB). We have characterized the response of the biosensor in terms of the effects of the immobilization procedure, enzyme loading, pH of the solution, and the presence of anionic species with particular emphasis on the role of phosphate anions. In addition, we have carried out studies of the kinetics of the catalytic reaction, as well as permeability studies. The sensor exhibits high sensitivity and a limit of detection in the micromolar regime (5.0 μM), as well as rapid response (60 s to reach 90% of its steady state value). We have also carried out analytical determinations of aliphatic and aromatic aldehydes and consistently find that aromatic aldehydes give superior results.

There continues to be a great deal of interest in the development of materials capable of the electrocatalytic oxidation of NADH, in order to diminish the typically large overpotentials encountered in its direct oxidation at most electrode surfaces. Particular interest has centered on materials that can be immobilized onto electrode surfaces. This interest derives, in part, because of the very large number (over 300) of dehydrogenases that employ NADH as a cofactor.^{1,2} In addition, because dehydrogenase activity can be employed in biosensor design, the coupling of such enzymatic activity with the ability to catalyze the product of such reactions (NADH) opens numerous possibilities in sensor design and development.

Numerous materials and procedures as well as several modified electrodes^{3–5} have been identified for the electrocatalytic oxidation of NADH. Although most of these can react with NADH added to a solution, examples where the mediator or modifier

reacts with enzymatically generated NADH are less common. In one of the more recent examples where enzymatically generated co-factors were detected, Willner and Riklin⁶ reported on an amperometric biosensor utilizing the NAD⁺ cofactor-dependent enzyme, malic enzyme, using a quinone–enzyme monolayer-modified electrode. In this work, they were able to detect enzymatically generated products. If enzyme activity, coupled to other cofactors, is to be exploited in biosensor design and development, new approaches for coupling these need to be developed.

We recently⁷ reported that the electrooxidation of 3,4-dihydroxybenzaldehyde (3,4-DHB) on glassy carbon electrodes gives rise to stable redox-active electropolymerized films. These films exhibited very high and persistent electrocatalytic activity for the oxidation of NADH.

We have now combined the electrocatalytic activity of glassy carbon electrodes modified with electropolymerized films of 3,4-DHB with the enzymatic activity of immobilized (on a nylon mesh) aldehyde dehydrogenase (ALDH) to develop an aldehyde biosensor. ALDH, with a molecular weight of about 200 000 and composed of four subunits, catalyzes the oxidation of a broad range of aromatic and aliphatic aldehydes to the corresponding carboxylic acids with the concomitant reduction of NAD⁺ to NADH.⁸ The sensor we describe herein is based on the determination of NADH enzymatically generated by the reaction of aldehyde dehydrogenase. We describe the preparation, characterization, and utility of such a sensor. The approach described here can, in principle, be extended to the use of other dehydrogenase enzymes, including alcohol and glutamate dehydrogenase, among others.

EXPERIMENTAL SECTION

A. Materials. Aldehyde dehydrogenase (ALDH; EC 1.2.1.5, from baker's yeast) was obtained from Sigma Chemical Co. as a lyophilized powder containing 7.7 units of enzyme activity per milligram of protein or as an ammonium sulfate-stabilized solution containing 12.0 units/mg of protein. Both preparations were stored below 0 °C. Under these conditions, no loss of enzyme activity was observed for several months. 3,4-Dihydroxybenzaldehyde (3,4-DHB; 97% purity) from Aldrich Chemical Co. was

[†] Universidad Autónoma de Madrid.

[‡] Cornell University.

- (1) (a) Chenault, H. K.; Whitesides, G. M. *Appl. Biochem. Biotechnol.* **1987**, *14*, 147. (b) Dugas, H.; Penney, C. In *Bioorganic Chemistry*; Cantor, C. R., Ed.; Springer Verlag: New York, 1981; p 395.
- (2) Willner, I.; Mandler, D. *Enzyme Microb. Technol.* **1989**, *11*, 467.
- (3) Laval, J. M.; Bourdillon, C.; Moiroux, J. *J. Am. Chem. Soc.* **1984**, *106*, 4701.
- (4) (a) Gorton, L. *J. Chem. Soc., Faraday Trans. 1* **1986**, *82*, 1245. (b) Persson, B. *J. Electroanal. Chem.* **1990**, *286*, 51.

- (5) Gorton, L.; Persson, B.; Hale, P. D.; Bouguslavsky, L. I.; Karan, H. I.; Lee, H. S.; Skotheim, T.; Lan, H. L.; Okamoto, Y. In *Biosensors and Chemical Sensors*; Edelman, P. G., Wang, J., Eds.; ACS Symposium Series 487; American Chemical Society: Washington, DC, 1992; Chapter 6, p 56.
- (6) Willner, I.; Riklin, A. *Anal. Chem.* **1994**, *66*, 1535.
- (7) Pariente, F.; Lorenzo, E.; Abruña, H. D. *Anal. Chem.* **1994**, *66*, 4337.
- (8) Clark, J. F.; Jacob, W. B. *J. Biol. Chem.* **1970**, *245*, 6072.

recrystallized twice from water using activated charcoal. Oxidized and reduced forms of nicotinic adenine dinucleotide (NAD^+ and NADH, grade III), glutaraldehyde (grade I, 50% aqueous solution), and bovine serum albumin (BSA, fraction V, 96% purity) were obtained from Sigma Chemical Co. and used as received. Benzaldehyde, 4-pyridinecarboxaldehyde, formaldehyde, acetaldehyde, and heptaldehyde used as substrates of ALDH were high-purity reagents (>99%) obtained from Aldrich Chemical Co. All other reagents were of at least analytical grade and were used as received. Tris and phosphate buffers (0.1 M) with 0.1 M KNO_3 were employed. Nylon mesh (Nytal) with $50 \times 50 \mu\text{m}$ pores and $70 \mu\text{m}$ in thickness were employed for enzyme immobilization. Water was purified with a Millipore Milli-Q system. All solutions were prepared just prior to use.

B. Apparatus. Cyclic voltammetric and chronoamperometric studies were carried out with a BAS CV-27 potentiostat and a Linseys X-Y recorder or a Nicolet digital oscilloscope. Teflon-shrouded glassy carbon electrodes (geometric area, 0.071 cm^2) were used as working electrodes. A coiled platinum wire served as the auxiliary electrode. All potentials are reported against a sodium saturated calomel electrode (SSCE) without regard for the liquid junction. A Pine Instruments rotating disk electrode system with a glassy carbon disk electrode (geometric area, 0.26 cm^2) was employed in rotating disk electrode experiments.

C. Procedures. **1. Electrode Activation and Modification with 3,4-DHB.** Prior to each experiment, glassy carbon electrodes were polished and activated as described previously.⁷ For modification, the activated electrodes were placed in a 0.5 mM solution of 3,4-DHB in Tris/0.1 M KNO_3 or phosphate buffer (pH 7.0 or 8.0), and the potential was held at about +0.20 V (depending on pH: *vide infra*) for 3 min. Subsequently, the modified electrode was rinsed with water and placed in fresh buffer solution. The potential was scanned for 3 min at 100 mV/s over the range of -0.20 to +0.25 V so as to obtain a stable redox response for the surface-immobilized film of 3,4-DHB. Surface coverages were determined from integration of the charge under the voltammetric wave.

2. Enzymatic Immobilization on Nylon Meshes. The solubilized ALDH preparation was used as received, whereas the ALDH available as a lyophilized powder was dissolved, prior to immobilization, in buffer containing at least 50% glycerol. In the absence of glycerol, we observed a complete loss of activity after the immobilization process. The presence of ammonium sulfate in the solubilized ALDH preparation did not appear to affect the immobilization procedure with glutaraldehyde. Nylon meshes were cut into 5.0 mm diameter disks, dipped in methanol, rinsed with water, and dried in an air stream prior to use. For enzyme immobilization, the following solutions were added to each disk: 2.0 μL of glutaraldehyde (2.5% v/v), 2.5 μL of BSA (1% w/v), and 5.0 μL of ALDH (0.1–0.5 unit in 50 mM phosphate buffer containing 50% (v/v) glycerol). The mixture was carefully homogenized on the surface of the disk. Gelification of glutaraldehyde and the protein was carried out at room temperature for 30 min and afterward at -4 °C overnight. The unreacted carboxaldehyde groups were inactivated by immersing the disks in 50 mL of 0.10 M phosphate buffer (pH 7.0) containing 0.10 M glycine for 15 min at room temperature. The disks were washed three times with 25 mL of fresh phosphate buffer (pH 7.0). After use, the disks were washed with phosphate buffer and stored at -4 °C in 50% (v/v) glycerol/0.10 M phosphate buffer solution.

3. Electrocatalytic Oxidation of NADH. Cyclic voltammetric studies of NADH oxidation at glassy carbon electrodes modified with electropolymerized films of 3,4-DHB were carried out at different sweep rates and in the presence of various anions. In these studies, the solutions employed were either 0.10 M Tris/0.10 M NaNO_3 or 0.10 M phosphate buffer (pH 8.0), and the sweep rate was varied from 5 to 625 mV/s over the range from -0.20 to +0.25 V. The pH value of 8 was chosen as it falls within the range over which the enzyme exhibits maximal activity. In addition, rotating disk electrode (RDE) and potential step chronoamperometric experiments were carried out in order to investigate permeability and other transport effects. RDE experiments were carried out by sweeping the potential at 5 mV/s from -0.20 to +0.25 V. The rotation rate (ω) was varied from 0 to 4000 rpm. In the chronoamperometric experiments, the potential was stepped from -0.20 (where no electrochemical activity was observed for 3,4-DHB layers) to +0.25 V. In some instances (see below), the potential was stepped to a value beyond the direct oxidation of NADH. The resulting current/time transients were recorded on a digital oscilloscope and transferred to a personal computer for further analysis.

4. Biosensor Preparation and Response. The biosensor was assembled by securing, with a holed cap, an enzyme-modified nylon mesh disk (prepared as described above) over a glassy carbon electrode previously modified with a film of 3,4-DHB. The assembled biosensor was placed in buffer solution for 1–2 min prior to use to ensure solvent equilibration.

The biosensor response was assayed in buffer solution containing 2.0 mM EDTA. Control voltammograms were carried out in the absence of either NAD^+ or substrate (see results). For substrate (aldehydes) determinations, the sensor was placed in 3.0 mL of buffer solution, containing 2.0 mM EDTA, at an applied potential of +0.25 V. After the background current had decayed to a steady value, aliquots (typically microliter) of a stock solution of substrate (typically 50 mM) in buffer were added. After the mixture was stirred for 30 s and allowed 2 min for equilibration, the steady-state current (typically achieved in less than 60 s) in the unstirred solution was recorded.

RESULTS AND DISCUSSION

A. Biosensor Description. The biosensor used in this work is schematically depicted in Figure 1. It consists of a 6 mm diameter nylon mesh disk modified with ALDH as described earlier. The disk is held over a glassy carbon electrode previously modified with an electropolymerized film of 3,4-DHB with a plastic cap with a 4 mm hole which defined the active area of the sensor. From optical microscopy studies (not shown), we have found that enzyme immobilization takes place preferentially on the fibers of the mesh, without occlusion of the pores. Under these conditions, transport to the electrode surface is not impeded, making this immobilization procedure superior to direct protein immobilization over the electrode surface as we have reported previously.⁵ Moreover, in this assembly, the enzyme component is physically separated, thus allowing for its ready reuse with other electrodes.

The immobilized enzyme (ALDH) oxidizes aldehydes to the corresponding carboxylic acids in the presence of NAD^+ . This cofactor acts as an acceptor of electrons generated in the enzymatic reaction and is transformed to its reduced form, NADH.

(9) Pariente, F.; Hernandez, L.; Lorenzo, E. *Bioelectrochem. Bioenerg.* 1992, 27, 73.

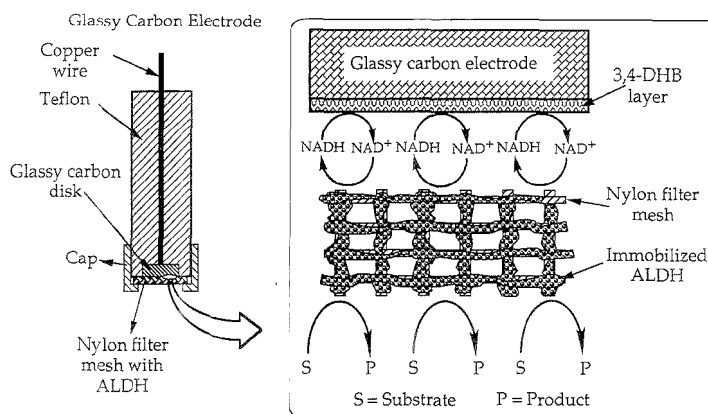


Figure 1. Schematic depiction of biosensor.

This, in turn, diffuses to the electrode, where it is catalytically reoxidized back to NAD^+ by the layer of electropolymerized 3,4-DHB (Figure 1). The 3,4-DHB-modified electrode serves as a secondary acceptor of electrons able to regenerate the cofactor (NAD^+) used in the enzymatic reaction so that the magnitude of this catalytic current can be employed as the analytical signal in the determination of the substrate (aldehyde) concentration.

To demonstrate that the NAD^+ generated by the catalytic oxidation of NADH by the electrodeposited film of 3,4-DHB is enzymatically active, we compared the currents for NADH oxidation at an electrode modified with 3,4-DHB only with the response for a biosensor in the presence of benzaldehyde. The current density for a biosensor with an NAD^+ concentration of 0.5 mM and 3.5 mM benzaldehyde is significantly larger than that for an electrode modified with 3,4-DHB alone in the presence of 0.5 mM NADH. The significantly larger current density for the biosensor indicates that the NADH generated (and which is subsequently oxidized to NAD^+) is enzymatically active and thus gives rise to the much larger catalytic currents. If the generated NAD^+ were not enzymatically active, such high catalytic currents would not be observed. In addition, we have carried out an experiment where a biosensor was removed from a solution containing NAD^+ and placed in one containing benzaldehyde but no NAD^+ in solution. A catalytic current is observed, and although it decreases with time (ostensibly due to diffusion of NADH/NAD^+ into the solution), the fact that a catalytic response is observed implies that the NAD^+ generated is enzymatically active.

B. Electrochemical Characterization of NADH Oxidation at Electrodes Modified with an Electropolymerized Film of 3,4-DHB. As we previously reported,⁷ glassy carbon electrodes modified with an electropolymerized film of 3,4-DHB show the behavior anticipated for a surface-immobilized redox couple. As shown in Figure 2A, the voltammetric response had the expected wave shape for a surface-confined redox center with a small (although not zero) ΔE_p value. In addition, the current was directly proportional to the rate of potential sweep over the range of 25–500 mV/s, suggesting facile charge transfer kinetics. Virtually the same results were obtained in Tris/ KNO_3 or phosphate buffers. As we have previously reported,⁷ these films are quite stable as long as the applied potential does not exceed +0.40 V, where film degradation appears to take place. The

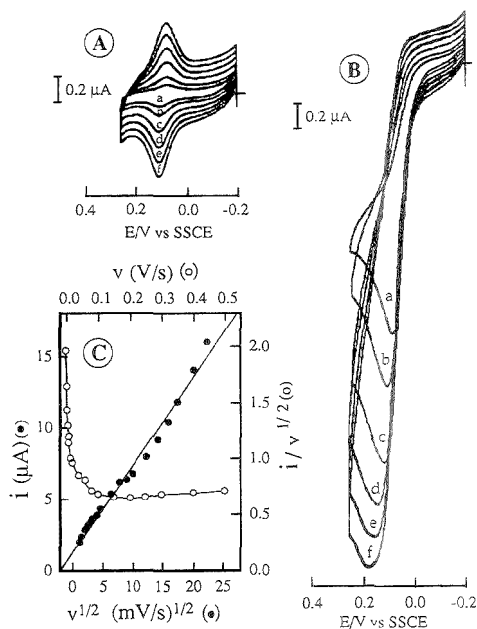
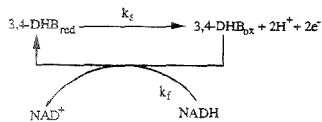


Figure 2. (A and B) Dependence of cyclic voltammetric response on sweep rate for a glassy carbon electrode modified with an electropolymerized film of 3,4-DHB in 0.1 M phosphate buffer (pH 7.0) in the absence (A) or in the presence (B) of 0.9 mM NADH. Sweep rates: a, 1.0; b, 2.0; c, 4.0; d, 6.0; e, 8.0; and f, 10.0 mV/s. (C) Variation of the catalytic current (i) with the square root of sweep rate (\bullet) and variation of the sweep rate-normalized current $i/v^{1/2}$ with the sweep rate (\circ) for 3,4-DHB-modified electrodes in 0.1 M phosphate buffer (pH 7.0) in the presence of 0.9 mM NADH.

addition of NADH to the solution (Figure 2B) resulted in a dramatic change in the voltammogram, with a large enhancement of the anodic current and virtually no current in the reverse (cathodic) sweep. It can also be noted in Figure 2B that the peak potential for the catalytic oxidation of NADH shifts to more positive potentials as the sweep rate is increased, suggesting a kinetic

Scheme 1



limitation in the reaction between the electropolymerized film of 3,4-DHB and NADH. However, a plot of the catalytic peak current vs the square root of the sweep rate is linear (Figure 2C(●)), suggesting that at sufficient overpotentials the reaction is transport limited.

A plot of the sweep rate-normalized current ($i/v^{1/2}$) vs sweep rate (Figure 2C (○)) exhibits the characteristic shape typical of an EC_{cat} process, as depicted in Scheme 1, where k_s is the heterogeneous charge transfer rate constant and k_f is the pseudo-first-order rate constant. Andrieux and Saveant¹⁰ developed a theoretical model for such a mechanism and derived a relation (eq 1) between the peak current and the concentration of the

$$i_{\text{cat}} = 0.496nFAD_s^{1/2}v^{1/2}C_s^*(nF/RT)^{1/2} \quad (1)$$

substrate for the case of slow sweep rate (v) and large k_s , where D_s and C_s^* are the diffusion coefficient (cm^2/s) and the bulk concentration (mol/cm^3) of the substrate (NADH in this case), respectively, and the other symbols have their usual meanings. Low values of k_f result in values lower than 0.496 for the constant. For low sweep rates (1.0–10.0 mV/s), we find the average value of this constant to be 0.35 for a 3,4-DHB-modified electrode with a coverage of $\Gamma = 3.3 \times 10^{-10} \text{ mol}/\text{cm}^2$ in the presence of 0.93 mM NADH. According to the approach of Andrieux and Saveant and using Figure 1 in their theoretical paper,¹⁰ we calculate a value of $k_f = 2.6 \times 10^3 \text{ M}^{-1} \text{ s}^{-1}$. This value is of the same order of magnitude as those previously reported by several authors for electrooxidation of NADH at graphite electrodes modified with catechol functionalities.^{11,12} Since in all of these cases the active component is an *o*-quinone moiety, the similarity of these values suggests that the measured rate constant is inherent to the reaction.

C. Rotating Disk Electrode Experiments. Kinetic parameters were also obtained from RDE measurements. The catalytic current, i , for NADH oxidation at 3,4-DHB-modified electrodes was measured in 0.1 M phosphate buffer solutions (pH 8.0) containing 0.10 mM NADH. The results for an electrode with a coverage of $2.0 \times 10^{-10} \text{ mol}/\text{cm}^2$ are shown in Figure 3. The current increased with increasing rate of rotation, ω , up to about 500 rpm and then leveled off. Also, a plot of i vs $\omega^{1/2}$ (i.e., a Levich plot) was found to be nonlinear, suggesting kinetic limitations. In addition, at lower NADH concentrations, the current was proportional to $\omega^{1/2}$ over a larger range of rotation rates, although at sufficiently large values, they all leveled off. These are the anticipated results for a system that is under kinetic control.^{13,14}

- (10) Andrieux, C. P.; Savéant, J.-M. *J. Electroanal. Chem.* **1978**, *93*, 163.
 (11) Jaegfeldt, H.; Torstensson, A. B. C.; Gurton, L. G.; Johansson, G. *Anal. Chem.* **1981**, *53*, 1979.
 (12) Jaegfeldt, H.; Kuwana, T.; Johansson, G. *J. Am. Chem. Soc.* **1983**, *105*, 1805.
 (13) Andrieux, C. P.; Dumas-Bouchiat, J. M.; Savéant, J.-M. *J. Electroanal. Chem.* **1980**, *114*, 159.
 (14) Andrieux, C. P.; Dumas-Bouchiat, J. M.; Savéant, J.-M. *J. Electroanal. Chem.* **1984**, *169*, 9.

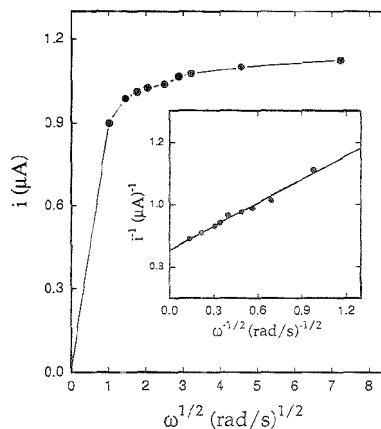


Figure 3. Electrochemical current, at an applied potential of +0.25 V, vs $\omega^{1/2}$ for 0.1 mM NADH oxidation at a 3,4-DHB-modified glassy carbon rotating disk electrode in 0.1 M phosphate buffer (pH 8.0). The coverage was $2.0 \times 10^{-10} \text{ mol}/\text{cm}^2$. (Inset) Plot of i/v vs $1/\omega^{1/2}$ (Koutecky–Levich plot).

Since at +0.20 V the rate of oxidation of the electropolymerized film of 3,4-DHB on the electrode can be considered fast, this would suggest that the oxidation of the NADH (Scheme 1) is the rate-determining step. Under these conditions, the Koutecky–Levich equation can be used to determine the rate constant for the process. The Koutecky–Levich equation can be formulated as follows:

$$1/i_{\text{lim}} = 1/(nFAk\Gamma C_b) + 1/(0.62nFA\nu^{-1/6}D^{2/3}\omega^{1/2}C_b) \quad (2)$$

where C_b is the bulk concentration of the reactant (NADH) in solution, Γ is the total surface coverage, ν is the kinematic viscosity, ω is the rate of rotation and k is the rate constant, with all other symbols having their conventional meanings. From eq 2, it is apparent that the value of k can be determined from the intercept of a plot of $1/i_{\text{lim}}$ vs $1/\omega^{1/2}$ (or a so-called Koutecky–Levich plot). Such a plot (Figure 3, inset), obtained from the experimental data in the main panel in Figure 3, shows the anticipated linear dependence. From the value of the intercept, k_f was found to be $2.7 \times 10^3 \text{ M}^{-1} \text{ s}^{-1}$, which is virtually identical to that determined from cyclic voltammetric measurements.

D. Permeability of NADH. Using potential step chronoamperometry, we have determined the diffusion coefficient of NADH at glassy carbon electrodes modified with an electropolymerized film of 3,4-DHB and in the presence or absence of the nylon filter mesh which was modified as previously described. In chronoamperometric studies, the current, i , for the electrochemical reaction (at a mass transport-limited rate) of an electroactive material (NADH in this case) that diffuses to an electrode through a film barrier with a diffusion coefficient, D (which maybe different from the value in solution), is described by the Cottrell equation,

$$i = \frac{nFAD^{1/2}C_{\text{NADH}}^*}{\pi^{1/2}t^{1/2}} \quad (3)$$

where D is the diffusion coefficient and C^* is the bulk concentration

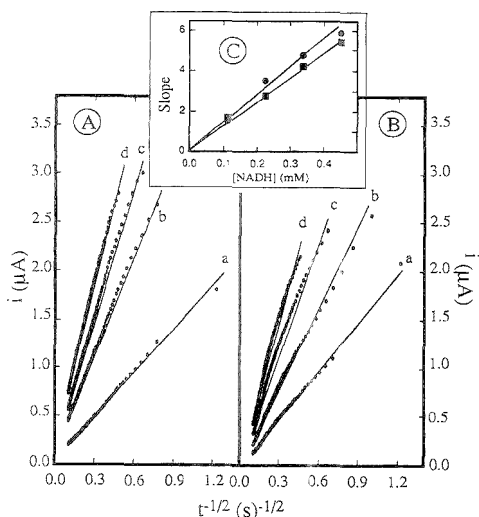


Figure 4. (A and B) Plots of i vs $t^{-1/2}$ obtained from chronoamperometric experiments for a 3,4-DHB-modified electrode (A) or for a 3,4-DHB/ALDH biosensor (B) in 0.1 M phosphate buffer solutions (pH 8.0) containing NADH at concentrations of a, 0.113; b, 0.226; c, 0.34; and d, 0.45 mM. Lines are the best fits to the data. (C) Plot of the slopes of the straight lines from A and B against the NADH concentration for the 3,4-DHB-modified electrode (●) and for the 3,4-DHB/ALDH biosensor (■).

in mol/cm^3 .¹⁵ Under diffusion (mass transport) control, a plot of i vs $t^{1/2}$ will be linear, and from the slope, the value of D can be obtained. We have carried out such studies at various NADH concentrations, for glassy carbon electrodes modified with electropolymerized films of 3,4-DHB in the absence (Figure 4A) and in the presence (Figure 4B) of the modified nylon filter mesh in phosphate buffer (pH 8.0). Parts A and B of Figure 4 show the experimental plots along with the best fits for the different concentrations of NADH employed. The slopes of the resulting straight lines were then plotted vs the NADH concentration (Figure 4C), from whose slopes we calculated diffusion coefficients of 2.67×10^{-6} and 2.14×10^{-6} cm^2/s for NADH in the absence and presence of the nylon filter mesh, respectively. In order to unambiguously establish that the oxidation of NADH is transport limited, we also carried out experiments where the potential was stepped to values where the direct oxidation of NADH was transport limited. The results obtained were virtually identical to those where the potential was stepped beyond the value for the surface-immobilized film of 3,4-DHB, suggesting that under those conditions, the process was indeed transport limited. These results indicate that the presence of the filter mesh results in a diminution in the transport of NADH of about 20%, so the present procedure for enzyme immobilization is very well suited for biosensor applications because of the relatively small decrease in transport rates.

E. Optimal Conditions for Catalytic Oxidation of NADH at 3,4-DHB-Modified Glassy Carbon Electrodes. Since this biosensor combines two kinetic reactions (enzymatic and electrochemical), experimental conditions compatible with both

(15) Bard, A. J.; Faulkner, L. R. *Electrochemical Methods*; Wiley: New York, 1980.

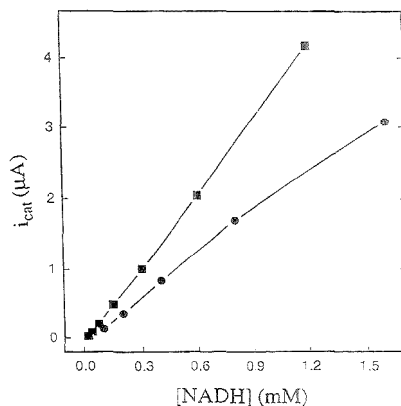


Figure 5. Calibration curves (i vs [NADH]) for a 3,4-DHB-modified glassy carbon electrode in 0.1 M phosphate (■) or 0.1 M Tris/0.1 M NaNO_3 (●) buffer solutions (pH 8.0).

processes are required. Of particular importance are the optimal conditions for the enzymatic reaction, which is a key component of the sensor. ALDH requires the presence of relatively high concentrations of potassium ions for its activity.¹⁶ Heavy metals, especially Cu^{2+} , strongly inhibit its activity.¹⁷ In addition, the enzyme is active from pH 7.0 to 9.0, although pH 8.75 has been reported to be optimal.¹⁶ For these reasons, in all studies of the biosensor, we employed buffers containing 0.1 M potassium ions and 2.0 mM EDTA (so as to complex any trace Cu^{2+} ions). In addition, the pH studies were restricted to a range around the optimal pH described for this enzyme.

Tris or phosphate buffers gave the best results in terms of levels of activity for NADH in solution. To determine the optimal buffer for the experiments, we carried out a comparative study of the oxidation of NADH, at different concentrations, at glassy carbon electrodes modified with electropolymerized films of 3,4-DHB over the pH range of 7.0 to 9.0. When phosphate buffers were employed, the catalytic activity of the films was 20% higher than in the presence of Tris buffers, and the linear range of the response was wider (Figure 5). These effects were observed over the entire pH range studied. We have previously observed similar effects of the nature of the supporting electrolyte anions on the electrochemical response of a self-assembling quinone derivative used as a surface-immobilized material for the catalytic electrooxidation of NADH.¹⁸ In that study, we observed that the addition of phosphate or acetate buffers resulted in better defined waves as well as an apparent enhancement of the surface coverage in addition to an enhancement in the electrocatalytic current. Although we are, at this time, uncertain as to the origin of these effects, they might be due to an enhancement in the charge transport properties of the film. Based on these results, phosphate buffers were employed in all further experiments.

As we reported previously,⁷ the electropolymerization of 3,4-DHB and the redox response of the resulting electropolymerized

(16) Black, S. In *Methods in Enzymology*, Vol. 1; Colowic, S. P., Kaplan, N. O., Eds.; Academic Press: New York, 1955; p 508.

(17) Jacobsen, M. K.; Bernofsky, C. *Biochim. Biophys. Acta* 1974, 350, 277.

(18) Lorenzo, E.; Sánchez, L.; Pariente, F.; Tirado, J.; Abruña, H. D. *Anal. Chim. Acta* 1995, 309, 79.

Table 1. Variations in the Properties of Electropolymerized Films of 3,4-DHB in Phosphate Buffers as a Function of Deposition Potential and pH

pH	E_{dep}^a	I_{pa}^b	I_{pc}^b	E_{pa}^c	E_{pc}^c	ΔE_p^d	$E_{s'}^e$	Γ^f
7.0	+0.25	4.7	4.7	+0.150	+0.100	50	+0.125	3.60
7.5	+0.23	4.4	4.4	+0.115	+0.080	35	+0.100	3.46
8.0	+0.20	4.2	4.0	+0.100	+0.075	25	+0.088	3.30
8.5	+0.15	3.9	3.8	+0.060	+0.030	30	+0.045	2.71
9.0	+0.13	3.6	3.2	+0.040	+0.015	25	+0.028	2.52

^a Deposition potential in volts vs SSCE. ^b Anodic (a) and cathodic (c) peak currents in microamperes. ^c Anodic (a) and cathodic (c) peak potentials in volts vs SSCE. ^d Defined as $E_{pa} - E_{pc}$, in millivolts. ^e Formal potential defined as $(E_{pa} + E_{pc})/2$ in volts vs SSCE. ^f Surface coverages in $\text{mol}/\text{cm}^2 \times 10^{10}$.

material are strongly pH dependent in Tris/nitrate buffers. To determine if such effects were also present here, we studied, in phosphate buffers, the effects of the deposition potential and pH over the range of 7.0–9.0 on the voltammetric response and the properties of the 3,4-DHB-modified electrodes. Table 1 shows representative data. In general, for pH values above 7.0, a decrease in the apparent surface coverage is observed. Since the pK_a for 3,4-dihydroxybenzaldehyde is 7.21,¹⁹ above this pH value the material will be present in its deprotonated form, and this might be responsible for the observed effect. However, this apparent decrease in the surface coverage observed at pH values above 7.0 (Figure 6B) does not involve a dramatic decrease in the sensitivity of the modified electrode for the catalysis of NADH oxidation, as can be ascertained from the calibration curves presented in Figure 6A. Although the slopes of the calibration curves decrease with increasing pH, the changes are not dramatic. In addition, the linear range of the response remained virtually unchanged and reached values of up to 1.2–1.5 mM (Figure 6A).

Moreover, the coverage-normalized response (i/Γ) actually increases at pH values above 8 (Figure 6C), suggesting that whereas the apparent coverage decreases, the material has a higher activity. These results suggest a more effective interaction of the NADH with the *o*-quinone groups of the 3,4-DHB film at slightly basic pH as opposed to neutral or acidic pH.

We have also carried out a series of experiments intended to address potential interferences by ascorbate, uric acid, and acetaminophen by determining the current response of glassy carbon electrodes modified with 3,4-DHB in the presence of 1 mM NADH and in the presence or absence of potential interferences at varying concentrations. Whereas uric acid and acetaminophen presented no interference effects at concentrations up to 10-fold higher than the NADH concentration, ascorbate did present interference effects which were concentration dependent. At NADH/ascorbate concentration ratios of 10:1, the interference due to ascorbate was of the order of 1.5%. However, at comparable concentrations, the interference effects were more marked (80% at 1.0 mM ascorbate concentration). We have carried out some preliminary experiments where the electrode assembly is coated with a thin film of Nafion, and it appears that this might suppress these interference effects.

F. 3,4-DHB/ALDH Biosensor Response. One of the objectives of these investigations was the development of biosensors based on dehydrogenase activity. To test for the potential utility in biosensors of glassy carbon electrodes modified with

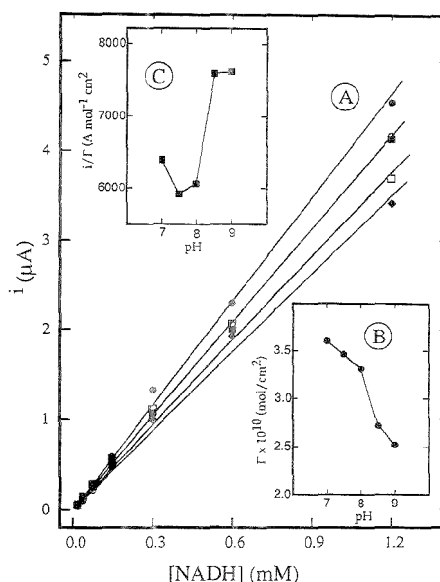


Figure 6. (A) Effect of pH (0.10 M phosphate buffer) on the electrocatalytic oxidation of NADH at 3,4-DHB-modified glassy carbon electrodes. pH values were (●) 7.0, (○) 7.5, (■) 8.0, (□) 8.5, and (◆) 9.0. (B) Effect of pH on the apparent coverage of 3,4-DHB. (C) Variation of the coverage-normalized current (i/Γ) with pH in 0.10 M phosphate buffer solutions containing 0.6 mM NADH.

electropolymerized films of 3,4-DHB, we employed them in conjunction with immobilized (on a nylon filter mesh) aldehyde dehydrogenase (ALDH). The intent was to couple the enzymatic activity (toward aldehydes) of ALDH with the electrocatalytic activity of the 3,4-DHB films toward NADH oxidation. Initial studies were performed with benzaldehyde as substrate. The cyclic voltammetric response (at slow sweep rate) of the biosensor in the presence and absence of benzaldehyde was used to assess the activity of the biosensor.

Figure 7A, trace a, shows the cyclic voltammetric response at 5 mV/s for a biosensor incorporating 0.5 unit of immobilized ALDH and in contact with a pH 8 phosphate buffer solution containing 2 mM EDTA and 1 mM NAD⁺ but in the absence of benzaldehyde. The characteristic and well-behaved redox response for the 3,4-DHB polymer film on the electrode is readily apparent. Upon the addition of benzaldehyde to a concentration of 50 μM , an enhancement of the anodic current (Figure 7A, trace b) is clearly noted. Additional increases in the concentration of benzaldehyde to 100 (c), 200 (d), 300 (e), 400 (f), 500 (g), and 600 μM (h) resulted in concomitant increases in the anodic peak current. At NADH concentrations of 300 μM and above, there is no current in the return (cathodic) sweep, consistent with a high degree of electrocatalytic activity for the enzymatically generated NADH. In addition, the biosensor response was linear from 50 to 400 μM benzaldehyde. Over this concentration range, the response was very similar to that obtained for NADH added to the solution (see Figure 5), suggesting that the biosensor response is under mass transport control and that virtually all of the NADH generated by the enzymatic reaction is immediately reoxidized

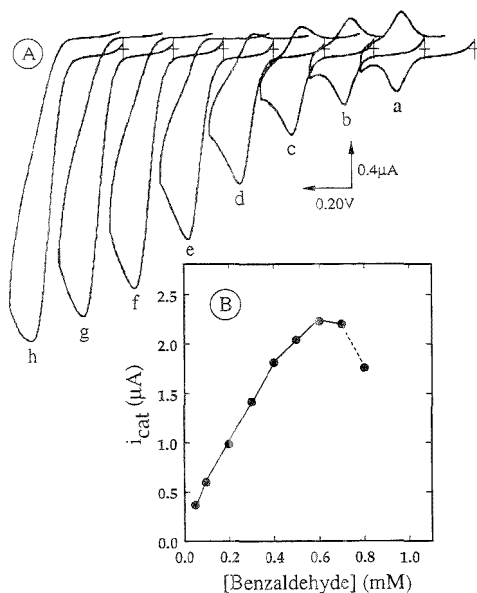


Figure 7. (A) Cyclic voltammetric response at 5 mV/s for a 3,4-DHB/ALDH biosensor with 0.5 unit of immobilized ALDH in 0.1 M phosphate buffer (pH 8.0), 2.0 mM EDTA, and 1.0 mM NAD^+ as a function of benzaldehyde concentration: (a) none, (b) 50.0, (c) 100, (d) 200, (e) 300, (f) 400, (g) 500, and (h) 600 μM . (B) Catalytic current (i_{cat}) vs benzaldehyde concentration.

by the 3,4-DHB layer on the glassy carbon electrode. Concentrations of benzaldehyde higher than 0.6 mM (Figure 7B) caused a dramatic decrease in the response, probably due to an inhibitory effect of the ALDH activity by excess substrate. A similar inhibitory effect has been reported for this enzyme in solution when acetaldehyde was used as substrate.¹⁷

For immobilized enzymes used in amperometric biosensors, the observed electrochemical response may be either mass transport limited or kinetically controlled.²⁰ Mell and Malloy suggested that for an immobilized enzyme reaction that is kinetically controlled, the steady state current, i_{ss} , is proportional to the initial rate of the enzymatic process. In this case, a plot of i_{ss} vs the substrate concentration, C_s , gives a typical Michaelis–Menten-type response. In addition, a linear double reciprocal plot (or a so-called Lineweaver–Burk plot) of $1/i_{\text{ss}}$ vs $1/C_s$ will be diagnostic of kinetic control of the electrochemical response. Figure 8 shows the steady state currents obtained at +0.25 V for increasing concentrations of benzaldehyde employing a biosensor with 0.5 units of ALDH immobilized on the nylon mesh. The i_{ss} vs C plot exhibits the typical Michaelis–Menten shape with a saturation response being reached for benzaldehyde concentrations above 0.5 mM. The double reciprocal plot (inset) is linear over the benzaldehyde concentration range studied. These results suggest control by the enzymatic reaction, and the apparent Michaelis–Menten constant, K'_m , was calculated to be 0.55 mM.

G. Effect of pH on the Biosensor Response. As was mentioned before and as depicted in Figure 6C for the catalytic

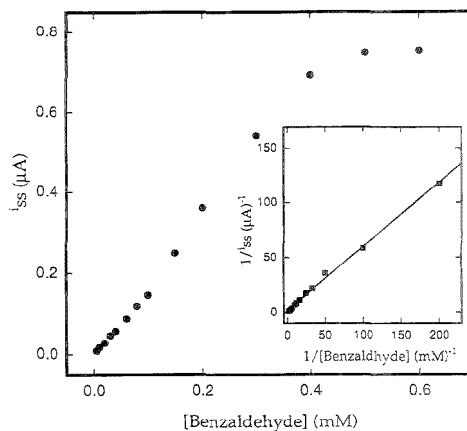


Figure 8. Steady state current at +0.25 V and double reciprocal (Lineweaver–Burk) plot (inset) for a 3,4-DHB/ALDH biosensor containing 0.5 unit of immobilized ALDH in the presence of increasing concentrations of benzaldehyde. Other experimental conditions as in Figure 7.

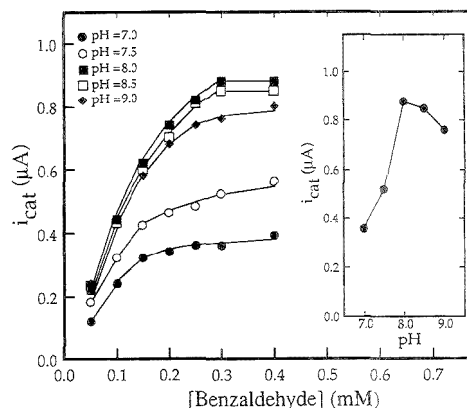


Figure 9. Voltammetric response, at various pH values, of the 3,4-DHB/ALDH biosensor containing 0.5 unit of immobilized ALDH as a function of benzaldehyde concentration. Other experimental conditions as in Figure 7. (Inset) Current vs pH response for a 3,4-DHB/ALDH biosensor containing 0.5 unit of immobilized ALDH at a benzaldehyde concentration of 300 μM . Other experimental conditions as in Figure 7.

oxidation of NADH at 3,4-DHB-modified electrodes, the best normalized current response (i/I) was obtained in the interval of pH between 8.0 and 9.0. To determine the pH dependence of the biosensor response, we monitored the current (at +0.25 V) at different pH values and for noninhibitory concentrations of benzaldehyde, and the results are presented in Figure 9.

The biosensor exhibits a marked increase in response above pH 7.5, with the highest response being achieved from pH 8 to 8.5 (Figure 9). Above pH 9.0, there is a significant decrease in response. The inset to Figure 9 depicts the biosensor response as a function of pH at a benzaldehyde concentration of 300 μM . From this plot, it is evident that the optimal response is attained at a pH of 8, so further studies were carried out at this pH value.

(20) Mell, L. D.; Malloy, J. T. *Anal. Chem.* 1975, 47, 299.

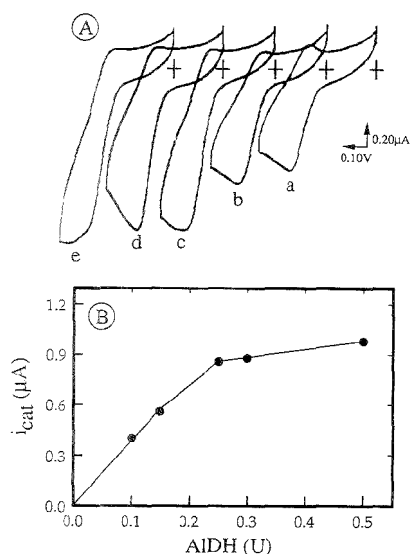


Figure 10. (A) Effect of ALDH loading on the voltammetric response to substrate (0.3 mM benzaldehyde) of 3,4-DHB/ALDH biosensors performed with filter meshes containing (a) 0.1, (b) 0.15, (c) 0.25, (d) 0.3, and (e) 0.5 unit of immobilized ALDH. (B) Plot of peak current against the ALDH units loaded in each biosensor. Other experimental conditions as in Figure 7.

H. Effect of Enzyme Loading and NAD^+ Concentration on Biosensor Response. The response of the 3,4-DHB/ALDH biosensor will be dependent on the amount of active ALDH immobilized. Figure 10A shows the voltammetric response for biosensors prepared with increasing amounts of immobilized ALDH, to a constant concentration (0.3 mM) of benzaldehyde in solution. At loadings below 0.25 unit (traces a and b), an increase in response with enzyme loading is evident, but at higher loadings (d and e), the response levels off, suggesting a saturation response. Figure 10B shows a plot of catalytic current as a function of enzyme loading where the above-mentioned trends are clear, with the response increasing linearly at low loadings and reaching a saturation response for enzyme loadings above 0.25 units. In order to obtain a sensor with a long lifetime and to account for possible losses of enzymatic activity, which would affect reproducibility, an enzyme loading level of 0.5 unit was deemed optimal and was thus employed in all further studies.

The effect of NAD^+ concentration on the response was studied using a biosensor with 0.5 unit of immobilized ALDH and at a benzaldehyde concentration of 300 μM ; the results are presented in Figure 11. In the main panel are presented the current-time profiles after the application of a potential of +0.25 V under the above-mentioned conditions and for increasing concentrations of NAD^+ . It is evident that there is an increase in the steady state current plots for increasing concentrations of NAD^+ . The inset to Figure 11 shows a plot of the steady state current as a function of NAD^+ concentration, where it is apparent that for concentrations below 0.3 mM there is an increase in the response with concentration, whereas the response levels off for concentrations above 0.35 mM. Based on these results and in order to ensure

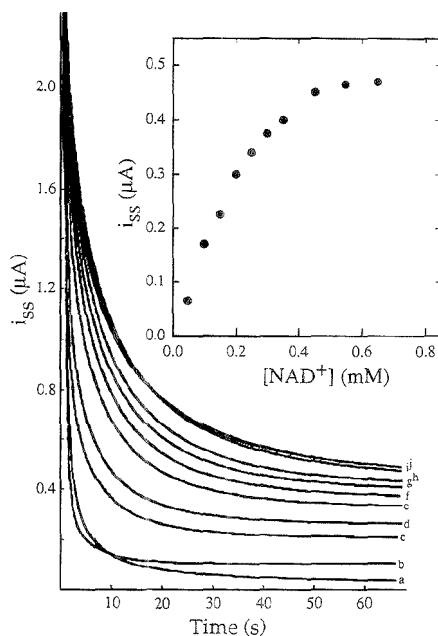


Figure 11. Current-time transients for the oxidation of 0.35 mM benzaldehyde at a 3,4-DHB/ALDH biosensor containing 0.5 unit of immobilized ALDH in the presence of NAD^+ at concentrations of (a) 50, (b) 100, (c) 150, (d) 200, (e) 250, (f) 300, (g) 350, (h) 450, (i) 550, and (j) 650 μM . (Inset) Plot of steady state current as a function of NAD^+ concentration.

that the response of the biosensor was independent of NAD^+ concentration, a value of 1 mM was employed in analytical determinations.

Another point to be considered from the data in Figure 11 is the response time for the sensor. In the family of current-time response curves, it is clear that in all cases a steady state response is reached within 60 s. Since the benzaldehyde concentration used in these studies (300 μM) was at the onset of a saturation response for the enzyme, it implies that the biosensor will have, in general, rapid response times which is a very valuable aspect in analytical determinations.

I. Analytical Determinations of Various Aldehydes with the 3,4-DHB/ALDH Biosensor. Amperometric enzyme biosensors are systems that combine the specificity of enzyme catalysis with the high sensitivity of electrochemical methods. To test for substrate sensitivity effects, various aldehydes were used as substrate for the 3,4-DHB/ALDH biosensor. The specific substrates employed were benzaldehyde, 4-pyridinecarboxaldehyde, heptaldehyde, formaldehyde, and acetaldehyde. These substrates were chosen so that comparisons could be made between the responses for aromatic vs aliphatic aldehydes and, in the latter, in terms of short (formaldehyde, acetaldehyde) vs long (heptaldehyde) aliphatic chains. In these studies, the optimized parameters previously established were employed. The catalytic peak currents obtained at different substrate concentrations were used in constructing response curves, and the results are presented in Figure 12. As is evident from the figure, the

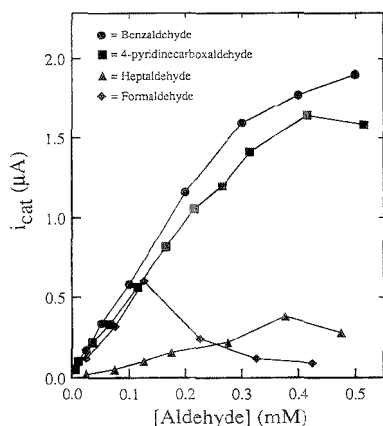


Figure 12. Catalytic current in 0.1 M phosphate buffer (pH 8.0) of 3,4-DHB/ALDH biosensors containing 0.5 unit of immobilized ALDH when different aldehydes were used as substrate. Other experimental conditions as in Figure 7.

best responses were obtained for aromatic aldehydes such as 4-pyridinecarboxaldehyde and benzaldehyde. In addition, inhibiting effects were apparent for all aldehydes, but the effects were more pronounced for the aliphatic ones. Moreover, heptaldehyde, with the longest aliphatic chain, had the lowest response of all substrates tested. Formaldehyde and acetaldehyde (the latter not shown in Figure 12) showed virtually identical responses, suggesting that for short-chain aliphatic aldehydes, the chain length does not appear to strongly affect the response.

Although ALDH from baker's yeast, as used in this work, has been reported to have a low affinity in solution for formaldehyde and acetaldehyde relative to ALDH from liver,¹⁷ changes in the enzyme environment generated during the immobilization process and possible slight modifications of the active center could also be responsible, at least in part, for the decrease in the affinity for these aldehydes. As mentioned above, heptaldehyde exhibited the lowest response. This material has a very low solubility in aqueous media and can, furthermore, generate micelles which would be anticipated to have a very low affinity for the enzyme's active center, and this could, in part, be responsible for the very

low response observed for this aldehyde. Perhaps the use of nonaqueous systems or surfactant solutions could enhance the response by minimizing micelle formation, and we are currently exploring such approaches.

It is clear that this approach to biosensor design can, in principle, be extended to other dehydrogenases, and we are currently involved in the development of biosensors based on the enzymatic activity of alcohol and lactate dehydrogenases. The results of these investigations will be reported elsewhere.

CONCLUSIONS

We have prepared and characterized the performance of an aldehyde biosensor based on the determination of NADH generated by the enzymatic activity (toward aldehydes) of aldehyde dehydrogenase immobilized on a nylon mesh membrane. The analytical signal is based on the electrocatalytic oxidation, at a glassy carbon electrode modified with an electropolymerized film of 3,4-dihydroxybenzaldehyde, of the enzymatically generated NADH. We have characterized the response of the biosensor in terms of the effects of the immobilization procedure, enzyme loading, pH of the solution, and the presence of anionic species. We find that the immobilization procedure gives rise to only a small decrease (~20%) in transport rates, making it very appealing for biosensor applications. An enzyme loading of 0.5 unit and a pH of 8 gave the best performance. Phosphate anions enhance the response, and we believe this to be due to improved charge propagation. The sensor exhibits high sensitivity and a limit of detection in the micromolar regime (5.0 μ M), as well as rapid response (60 s to reach 90% of its steady state value). We have also carried out analytical determinations of aliphatic and aromatic aldehydes and consistently find that aromatic aldehydes give superior results relative to aliphatic aldehydes, with long-chain aldehydes (heptaldehyde) giving the lowest response.

ACKNOWLEDGMENT

This work was supported by the DGICYT of Spain through Grants BIO 93-0660C04-02 (E.L., F.P.F.T.) and PB92-0167 (H.D.A.), the National Science Foundation (DMR-9107116; H.D.A.) and a NATO Collaborative Research Grant (91-0047; H.D.A., E.L.).

Received for review February 27, 1995. Accepted August 18, 1995.*

AC950207O

* Abstract published in *Advance ACS Abstracts*, October 1, 1995.

Hybridization of Fluorescein-Labeled DNA Oligomers Detected by Fluorescence Anisotropy with Protein Binding Enhancement

Michael U. Kumke, Guang Li, and Linda B. McGown*

P. M. Gross Chemical Laboratory, Department of Chemistry, Duke University, Box 90346, Durham, North Carolina 27708-0346

G. Terrance Walker* and C. Preston Linn

Becton Dickinson and Company Research Center, Research Triangle Park, North Carolina 27709

Fundamental aspects of the application of fluorescence anisotropy to detect the hybridization of fluorescein-labeled DNA oligomers were explored. The oligomers included a binding site for the *EcoRI* restriction enzyme, which binds to double-stranded DNA and is used in this work to enhance the difference between the anisotropies of the single-stranded and double-stranded oligomers by increasing the effective volume of the latter. The fluorescence anisotropy increases upon hybridization and further upon binding of *EcoRI* to the double strand. By varying the length of the tether used to attach the fluorescein to the 5' end of the oligonucleotide, it was found that a 6-carbon tether was optimal, providing the most dramatic increases in anisotropy in the presence of *EcoRI*. Dynamic fluorescence anisotropy (DFA) provided insight into the increases in steady-state anisotropy. In most cases, the best fits to the DFA data were obtained using a biexponential decay model, which describes an anisotropic rotator. Upon hybridization, the faster rotational motion is more hindered, and the contribution of the slower rotational component is increased. This effect is enhanced by binding of *EcoRI* to the double strand, especially when the *EcoRI* binding site is near the fluorescein at the 5' end and the tether length is in the optimal range. Because the rotational correlation time of the slower anisotropy decay component is much longer than the fluorescence lifetime, it is possible in some cases to reduce the anisotropic rotator model to the special limiting case of a hindered rotator.

Detection of DNA sequences has important applications in clinical diagnostics. A simple and direct approach is to probe the unknown DNA specimen with probe DNA of a known sequence and monitor the occurrence of hybridization using separation techniques. These separation techniques, however, are time consuming and sensitive to experimental conditions. A big improvement would be the ability to monitor the hybridization process in situ without a physical separation.¹⁻⁶

Fluorescence spectroscopic methods offer high sensitivity and selectivity, combined with the potential for nonseparation, in situ applications. Among these methods, steady-state and dynamic fluorescence anisotropy have proven to be particularly useful for monitoring molecular motions, such as rotations of proteins and reorientations of molecules in membranes or macromolecular structures.⁷⁻¹⁰ Due to the dependence of these molecular motions on molecular size, fluorescence anisotropy offers the potential for monitoring DNA hybridization.

This paper describes the detection of DNA hybridization through measurements of the fluorescence anisotropy of fluorescein that is covalently tethered to the oligomers. By applying steady-state fluorescence anisotropy, we were able to monitor the DNA hybridization in situ without a prior separation step. The incorporation of a binding site for the *EcoRI* restriction enzyme into the oligomers provided a mechanism for enhanced detection of hybridization, since *EcoRI* binds only to the double-stranded DNA. Thus, the increase in anisotropy observed when the fluorescein-labeled oligomer undergoes hybridization is enhanced by the binding of *EcoRI* to the double strand. The hybridization and *EcoRI* binding are depicted in Figure 1.

Dynamic fluorescence anisotropy (DFA) provided further insight into the mechanisms that are responsible for the increases in anisotropy that occur upon hybridization and *EcoRI* binding, through measurements of oligomers with different tether lengths and different positions for the *EcoRI* binding site relative to the tethered fluorescein. Results of fluorescence lifetime measurements, which are necessary for the DFA analysis, are described as well.

EXPERIMENTAL SECTION

Materials. DNA33-4C-5', DNA33-9C-5', and DNA33-12C-5' were synthesized and purified by Molecular Probes (Eugene, OR).

- (3) Schwartz, H. E.; Ulfelder, K. J. *Anal. Chem.* **1992**, *64*, 1737.
- (4) Seeger, S.; Galla, K.; Arden-Jacob, J.; Deltau, G.; Drexhage, K. H.; Martin, M.; Sauer, M.; Wolfrum, J. *J. Fluoresc.* **1994**, *4*, 111.
- (5) Seeger, S.; Sauer, M.; Han, K.-T.; Mueller, R.; Schulz, A.; Tadday, R.; Wolfrum, J.; Arden-Jacob, J.; Deltau, G.; Marx, N. J.; Drexhage, K. H. *J. Fluoresc.* **1993**, *3*, 131.
- (6) Vo-Dinh, T.; Houck, K.; Stokes, D. L. *Anal. Chem.* **1994**, *66*, 3379.
- (7) Fleming, G. R.; Petrich, J. W.; Longworth, J. W. *Biochemistry* **1987**, *26*, 2711.
- (8) Lakowicz, J. R.; Gryczynski, I. *J. Fluoresc.* **1992**, *2*, 117.
- (9) Lakowicz, J. R.; Buccell, F.; Gryczynski, Z.; Fronticelli, C.; Gryczynski, I. *J. Fluoresc.* **1992**, *2*, 29.
- (10) Stryer, L.; Munro, I.; Pedit, I. *Proc. Natl. Acad. Sci. U.S.A.* **1979**, *76*, 56.

(1) Mathies, R. A.; Zhu, H.; Clark, S. M.; Benson, S. C.; Rye, H. S.; Glazer, A. N. *Anal. Chem.* **1994**, *66*, 1941.
(2) Netzel, T. L.; Telsler, J.; Cruickshank, K. A.; Morrison, L. E. *J. Am. Chem. Soc.* **1989**, *111*, 6966.

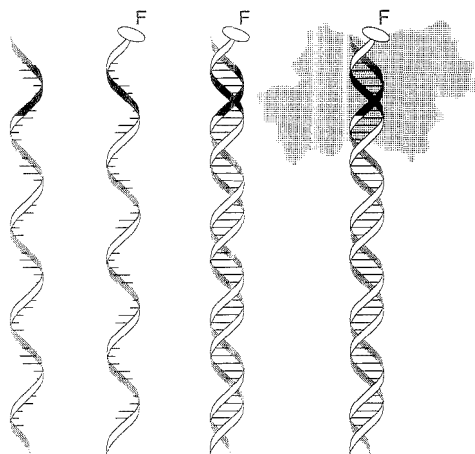


Figure 1. Depiction of (left to right) a single-stranded oligomer, hybridization to form a double strand, and *EcoRI* binding to the double strand at the 5' end. The schematic representation of *EcoRI* bound to the fluorescein-labeled DNA oligomer is based on the X-ray crystal structure of *EcoRI* bound to DNA²³ as deposited in the Protein Data Bank (PDB).^{24,25} F denotes the fluorescein that is tethered to the 5' end.

Set I (location of binding site varied)

DNA28-6C-3': ⁵F-TGAAAGACGTTGAATTCATACGGATAG

DNA28-6C-5': ⁵F-GGAAATTCAGTTATCCACCATACGGATAG

DNA28-6C-mid: ⁵F-TGAAAGAATTCATCCACCATACGGATAG

Set II (tether length varied)

DNA33-4C-5': ⁵F-GGAAATTCATCCGGATCGTGATAACGTCITTTCA

DNA33-6C-5': ⁵F-GGAAATTCATCCGGATCGTGATAACGTCITTTCA

DNA33-9C-5': ⁵F-GGAAATTCATCCGGATCGTGATAACGTCITTTCA

DNA33-12C-5': ⁵F-GGAAATTCATCCGGATCGTGATAACGTCITTTCA

Figure 2. Sequences of the DNA oligomers. The *EcoRI* binding site (GAATTC) is underlined.

The other oligodeoxynucleotides were synthesized by an ABI Model 380B synthesizer (Applied Biosystems Division, Perkin Elmer, Norwalk, CT) and purified by denaturing gel electrophoresis. The oligodeoxynucleotides are described in Figure 2 and Table 1. Homogeneous preparations of the oligonucleotides were confirmed by observation of a single band upon gel electrophoresis analysis. 5'-Fluorescein-labeled oligodeoxynucleotides were prepared by standard procedures using the reagent 6-FAM Amidite from Applied Biosystems Inc. (P/N 401527) according to the product insert protocols. Chemical structures of the various tethers used to link the fluorescein label (F) to the DNA oligomers are as follows: 4C, F-CONH(CH₂)₃-OPO₂-DNA(5'-3'); 6C, F-CONH(CH₂)₅OPO₂-DNA(5'-3'); 9C, F-CONH(CH₂)₅CNH-(CH₂)₃OPO₂-DNA(5'-3'); 12C, F-CONH(CH₂)₅CNH(CH₂)₅OPO₂-DNA(5'-3'). The samples were purified by oligonucleotide purification cartridge and standard gel purification. Oligomer concentrations were determined using the molar absorptivity at 260 nm. The absorbances of the labeled oligomers were corrected for fluorescein contributions at 260 nm by subtraction of one-fifth

Table 1. Summary of the DNA Oligomers Used in This Work^a

sample	no. of nucleotides	tether length	location of <i>EcoRI</i> binding site
		Set I	
DNA28-6C-5'	28	6	1 nucleotide from tether
DNA28-6C-mid	28	6	6 nucleotides from tether
DNA28-6C-3	28	6	11 nucleotides from tether
		Set II	
DNA33-4C-5	33	4	1 nucleotide from tether
DNA33-6C-5	33	6	1 nucleotide from tether
DNA33-9C-5	33	9	1 nucleotide from tether
DNA33-12C-5	33	12	1 nucleotide from tether

^a Set I consists of 28-mers with a 6-carbon tether to fluorescein; the *EcoRI* binding site is varied. Set II consists of 33-mers in which the binding site is one nucleotide removed from the 5' end; the tether length is varied.

of the fluorescein absorbance at 496 nm. Unless otherwise stated, the concentration of oligomer in the samples was 5×10^{-8} M.

The *EcoRI* restriction enzyme (*EcoRI* 101 CXL, New England BioLabs) was purchased at a concentration of 100 000 units/mL. The experiments with *EcoRI* were performed at a concentration of 2500 units/mL. All experiments were performed in a buffer solution containing 100 mM Tris-HCl (pH 7.5), 0.6 mM K₂PO₄ (pH 7.5), 50 mM NaCl, 6% glycerol, 1 mM EDTA, 24 μg/mL bovine serum albumin (BSA), 0.02% Triton X-100, and 0.6 mM β-mercaptoethanol. The K₂PO₄, glycerol, BSA, Triton X-100, and β-mercaptoethanol were contributed by the stock *EcoRI* solution. Experiments lacking *EcoRI* also contained these reagents. The *EcoRI* cleavage of the DNA upon hybridization is inhibited by inclusion of EDTA, which chelates the cofactor Mg²⁺.

Methods. Steady-State Anisotropy Measurements. Steady-state anisotropy measurements were performed using a phase-modulation spectrofluorometer (Model 4800S, SLM instruments, Inc.) in the steady-state mode, in the L-format configuration. Excitation at 488 nm was provided by passing the output of a 450 W xenon arc lamp through a monochromator with the entrance and exit slits set to a bandpass of 4 nm.

Fluorescence anisotropy was measured with the same instrument using the L-format configuration,¹¹ in which the anisotropy (*r*) is calculated from measurements of the emission intensity, *I*, according to

$$r = \frac{I_{vv} - I_{vh}G}{I_{vv} + 2I_{vh}G} \quad (1)$$

where the subscripts v and h refer to the orientation (vertical or horizontal) of the polarizers in the excitation beam (first subscript) and the emission beam (second subscript) for that intensity measurement. The instrumental correction factor, *G*, is equal to the ratio of *I_{hv}* to *I_{hh}*.

Fluorescence Lifetime and Dynamic Anisotropy Measurements. Fluorescence lifetime and dynamic anisotropy measurements were performed in the frequency domain,¹¹ using a multiharmonic Fourier transform spectrofluorometer (Model 4850 MHF, SLM

(11) Lakowicz, J. R. *Principles of Fluorescence Spectroscopy*; Plenum Press: New York, 1983.

Instruments Inc.).¹² A base frequency of 4.1 MHz and a correlation frequency of 7.292 Hz were used in all experiments. Data at 50 modulation frequencies ranging from the base frequency up to 205 MHz were used in the analyses. Each measurement consisted of 15 (or, in some cases, 10) pairs of sample-reference measurements, each of which was the internal average of 100 samplings. An air-cooled argon laser (Model 543, Omnichrome) was used to provide excitation at 488 nm. The laser output power was set to 50 mW (~40% of maximal output power) and was controlled by an internal laser power meter. The sample compartment was maintained at 25 ± 0.1 °C with a water circulating thermostat. Emission wavelength selection was achieved using a combination of a 520 nm long-pass filter (Oriol) and a 560 nm short-pass filter (CVI Laser Corp.). In the dynamic anisotropy measurements, this filter combination was used in both detection channels in the T-format configuration.

All of the dynamic data were fitted by nonlinear least-squares (NLLS) analysis to various models, as discussed below. The best fits were judged on the basis of the χ^2 goodness-of-fit parameter, the randomness of the fitting residuals, and visual inspection of the fitting curve.

In the fluorescence lifetime determinations, the multifrequency phase and modulation data were fitted to a multiexponential decay law,

$$I(t) = \sum_{i=1}^n A_i \exp(-t/\tau_i) \quad (2)$$

using a Marquardt-Levenberg NLLS algorithm.¹³ In eq 2, A_i and τ_i are the amplitude and the fluorescence decay time of the i th component, respectively. A solution of fluorescein (pH 7.5 phosphate buffer) served as the reference fluorophore. Under our experimental conditions, the fluorescence lifetime of the fluorescein reference was determined to be 4.02 ± 0.05 ns.

In the dynamic anisotropy measurements, the time-dependent anisotropy decay, $r(t)$, was calculated as

$$r(t) = \frac{I(t)_v - I(t)_h}{I(t)_v + 2I(t)_h} \quad (3)$$

where $I(t)_v$ and $I(t)_h$ represent the fluorescence intensity decays of the vertical and horizontal components of the emission beam that is excited with vertically polarized light. In the frequency domain, two measured quantities, phase angle difference (Δ) between the horizontal and the parallel components of the modulated emission,

$$\Delta = \phi_h - \phi_v \quad (4)$$

and the ratio (Λ) of the amplitudes of the modulated emission,

(12) Mitchell, G.; Swift, K. In *Time-Resolved Laser Spectroscopy in Biochemistry*; Lakowicz, J. R., Ed.; SPIE 1204; SPIE—The International Society for Optical Engineering: Bellingham, WA, 1990; Part 1, pp 270–274.

(13) *Globals Unlimited*, Technical reference manual; Laboratory for Fluorescence Dynamics, Department of Physics, University of Illinois, 1110 W. Green St., Urbana, IL 61801; 1990.

$$\Lambda = m_v/m_h \quad (5)$$

are used in the calculation of $r(t)$.^{9,11,14}

The anisotropy data were fitted, using NLLS routines in software that was supplied with the instrument, to three different models, as described below.

(1) Isotropic rotator:

$$r(t) = r_0 \exp(-t/\Phi) \quad (6)$$

where Φ is the rotational correlation time and r_0 represents a limiting anisotropy for $t = 0$. An isotropic, or monoexponential, decay is expected for a spherical molecule when only one rotational motion contributes to the loss of polarization. Fluorescein free in solution is assumed to be pseudospherical and is considered to be an ideal isotropic rotator (r_i) because its absorption and emission dipole moments are parallel and only the rotation around one of the molecular axes will result in anisotropy loss.

(2) Anisotropic rotator:

$$r(t) = r_0 \sum_{i=1}^n \alpha_i \exp(-t/\Phi_i), \quad n = 2 \quad (7)$$

where Φ_i and α_i are the rotational correlation time and the associated amplitude of each of the decay components. The anisotropic rotator model is used to describe the multiexponential anisotropy decay of a molecule which does not exhibit equal rotational rates in all directions.^{11,14–18}

(3) Hindered rotator:

$$r(t) = (r_0 - R_\infty) \sum_{i=1}^n \alpha_i \exp(-t/\Phi_i) + R_\infty, \quad n = 1 \quad (8)$$

The hindered rotator model, which is a monoexponential decay function with a constant factor, may be used to represent a limiting case of the more general model for an anisotropic rotator.¹⁹ The term R_∞ describes a limiting anisotropy observed at times which are long compared to the fluorescence lifetime. If one of the rotational correlation times is much longer than the fluorescence lifetime, the contribution of the slow motion to the anisotropy loss becomes significant only when the anisotropy is not fully decayed by the fast component because of hindered rotation. Attempts have been made to connect the quantity R_∞ with a cone angle δ or an order parameter to describe the probe.^{7,11}

For the determination of the anisotropy decay, the measured data were fitted to each of the three models. In most cases, only the rotational correlation times and the amplitudes were allowed to vary in the fits; the limiting anisotropy (r_0) of fluorescein was

(14) Lakowicz, J. R.; Cherek, H.; Kusba, J.; Gryczynski, I.; Johnson, M. J. *J. Fluoresc.* **1993**, *3*, 103.

(15) Lakowicz, J. R.; Gryczynski, I.; Johnson, M. L. *Biophys. Chem.* **1994**, *52*, 1.

(16) Weber, G. *J. Chem. Phys.* **1971**, *55*, 2399.

(17) Weber, G.; Belford, G. C.; Belford, R. L. *Proc. Natl. Acad. Sci. U.S.A.* **1972**, *69*, 1392.

(18) Zannoni, C. *Mol. Phys.* **1981**, *42*, 1303.

(19) Lakowicz, J. R.; Maliwal, B. P.; Cherek, H.; Ba'ter, A. *Biochemistry* **22**, **1983**, 1741.

Table 2. Steady-State Fluorescence Anisotropy Results for Set I and Set II Oligomers

sample	fluorescence anisotropy		
	ss	ds	ds+EcoRI
	Set I		
DNA28-6C-5'	0.037	0.056	0.073
DNA28-6C-mid	0.034	0.053	0.067
DNA28-6C-3'	0.040	0.044	0.053
	Set II		
DNA33-4C-5'	0.061	0.091	0.100
DNA33-6C-5'	0.049	0.076	0.106
DNA33-9C-5'	0.040	0.048	0.073
DNA33-12C-5'	0.038	0.060	0.055

fixed to a value of 0.40,²⁰ and the fluorescence lifetime was fixed to the experimentally determined value. In the few cases in which τ_1 was allowed to vary, a limiting anisotropy of 0.40 was recovered from the fit.

RESULTS

Oligomer Samples. Two different sets of fluorescein-labeled DNA oligomers were used in the experiments. These are summarized in Table 1, which also gives the abbreviations used in this paper for the different oligomers. The sequences of the two sets are shown in Figure 2. Set I consists of 28-base oligomers (28-mers) in which the fluorescein was attached by a 6-carbon tether. In this sample set, the location of the binding site of the *EcoRI* enzyme was varied. Three different binding locations were investigated: 1 base from the 5' end of the DNA strand (referred to as the 5' binding site), 5 bases from the 5' end (referred to as the middle binding site), and 11 bases from the 5' end (referred to as the 3' binding site). The second set of oligomers, set II, consists of 33-base oligomers (33-mers) in which the *EcoRI* binding site is located one base from the 5' end and the length of the tether was varied. Oligomers with 4-, 6-, 9-, and 12-carbon tethers were used to attach the fluorescein to the oligomer. For each oligomer, four different samples were prepared: single-stranded DNA (ss), single-stranded DNA + *EcoRI* (ss+EcoRI), double-stranded DNA (ds), and double-stranded DNA + *EcoRI* (ds+EcoRI).

Steady-State Anisotropy. The steady-state anisotropy results are shown in Table 2. For the single strands, the anisotropy is greatest for the 4-carbon tether and decreases with increasing tether length. Anisotropy increases upon hybridization and again upon *EcoRI* binding to the double strand. The greatest increase is observed for the oligomers with the 6-carbon tether and the *EcoRI* binding site at the 5' end, which is closest to the fluorescein label. The increase becomes smaller as the tether length is increased or as the *EcoRI* binding site is moved toward the 3' end.

Fluorescence Lifetime Measurements. In order to perform DFA experiments, it is necessary to first analyze the fluorescence lifetime characteristics of the labeled oligomers. The fluorescence lifetime results are shown in Table 3 for set I (the oligomers with the *EcoRI* binding site in various positions) and in Table 4 for set II (the oligomers with different tether lengths). For most of the samples, the data were best fit by biexponential decays. In the other cases, monoexponential decays were indicated. For the

Table 3. Fluorescence Lifetime Results for Set I Oligomers^a

	τ_1	A_1	τ_2	A_2	χ^2
	DNA28-6C-5'				
ss	3.83	0.98	0	0.02	4.2
ds	4.00	0.98	0	0.02	1.2
ss+EcoRI	3.87	0.97	0.43	0.03	1.2
ds+EcoRI	4.06	0.98	0.30	0.02	6.2
	DNA28-6C-mid				
ss	4.07	0.98	0.67	0.02	1.7
ds	4.26	0.97	1.36	0.03	2.3
ss+EcoRI	4.06	0.98	0.44	0.02	1.8
ds+EcoRI	4.26	0.97	1.28	0.03	2.4
	DNA28-6C-3'				
ss ^b	4.15	0.81	3.56	0.19	1.4
	4.03	1			1.7
ds	4.04	0.98	0.60	0.02	1.7
ss+EcoRI	4.09	0.98	1.50	0.02	0.8
ds+EcoRI	4.08	0.98	1.34	0.02	1.1

^a In cases where the biexponential fit revealed a second component with a fluorescence lifetime comparable to that of the main lifetime component, the results of a monoexponential fit are also shown. Standard deviations of triplicate determinations of τ_1 were <3%. τ is the fluorescence lifetime (ns), A is the fractional intensity contribution, and χ^2 is a goodness-of-fit parameter. ^b Fits to both two-component and one-component models are shown.

Table 4. Fluorescence Lifetime Results for Set II Oligomers^a

	τ_1	A_1	τ_2	A_2	χ^2
	DNA33-4C-5'				
ss	3.92	0.94	1.46	0.06	1.1
ds	3.86	0.84	1.06	0.16	4.5
ss+EcoRI	3.90	0.95	1.36	0.05	1.5
ds+EcoRI	3.87	0.84	0.96	0.16	3.0
	DNA33-6C-5'				
ss	3.97	0.97	0.49	0.03	2.3
ds	4.05	0.99	0.18	0.01	1.2
ss+EcoRI	3.95	0.97	0.53	0.03	1.4
ds+EcoRI	4.13	0.98	1.40	0.02	1.4
	DNA33-9C-5'				
ss	4.05	0.99	0.13	0.01	1.3
ds	4.01	0.99	0.19	0.01	0.8
ss+EcoRI	4.07	0.98	0.23	0.02	1.0
ds+EcoRI	4.05	0.97	0.32	0.03	1.2
	DNA33-12C-5'				
ss ^b	4.12	0.89	2.74	0.11	1.0
	3.95	1			3.8
ds	3.97	0.99	0.19	0.01	0.9
ss+EcoRI ^b	4.07	0.95	2.42	0.05	0.9
	3.97	1			4.4
ds+EcoRI	4.04	0.97	0.39	0.03	1.1

^a In cases where the biexponential fit revealed a second component with a fluorescence lifetime comparable to the main lifetime component, the results of a monoexponential fit are also shown. Standard deviations of triplicate determinations of τ_1 were <3%. τ is the fluorescence lifetime (ns), A is the fractional intensity contribution, and χ^2 is a goodness-of-fit parameter. ^b Fits to both two-component and one-component models are shown.

biexponential decays, the shorter lifetime component generally contributed <5% of the total intensity and showed poor run-to-run reproducibility. Similar results for the dominant lifetime component, which is in the range of 3.3–4.3 ns, were obtained when the second lifetime component was allowed to float, as in the results presented in Tables 3 and 4, and when it was fixed to 0 ns to account for scattered light (results not shown). Therefore,

(20) Fleming, G. R.; Morris, J. M.; Robinson, G. W. *Chem. Phys.* 1976, 17, 91.

Table 5. Dynamic Fluorescence Anisotropy Results for Set I Oligomers^a

	isotropic		anisotropic				hindered			
	Φ	χ^2	Φ_1	α_1	Φ_2	α_2	χ^2	Φ	R_∞	χ^2
DNA28-6C-5'										
ss	0.61	82.2	0.51	0.97	∞	0.03	3.6	0.51	0.012	3.3
ds	0.87	258.9	0.63	0.92	25	0.08	9.0	0.66	0.026	9.9
ss+EcoRI	0.63	69.2	0.53	0.96	∞	0.04	8.6	0.53	0.013	5.1
ds+EcoRI	0.97	681.5	0.57	0.88	23	0.12	4.9	0.62	0.038	8.9
DNA28-6C-mid										
ss	0.51	142.9	0.38	0.95	23	0.05	1.7	0.40	0.015	2.6
ds	0.68	395.4	0.41	0.86	13	0.11	1.7	0.46	0.028	9.5
ss+EcoRI	0.56	99.6	0.46	0.96	59	0.04	4.2	0.46	0.015	4.1
ds+EcoRI	0.76	411.6	0.47	0.90	16	0.10	2.4	0.52	0.029	7.9
DNA28-6C-3'										
ss	0.37	3.5	0.37	1			4.4	0.37	-0.002	3.6
ds	0.62	148.5	0.36	0.84	4	0.16	1.9	0.49	0.021	23.4
ss+EcoRI	0.39	2.7	0.39	1			2.9	0.39	-0.001	2.6
ds+EcoRI	0.69	141.9	0.44	0.86	5	0.14	2.4	0.55	0.018	12.2

^a Fits are shown to three decay models: the isotropic rotator, the biexponential anisotropic rotator, and the hindered rotator. For each sample, a single fluorescence lifetime (from Table 3) was used in the DFA analysis. Φ is the rotational correlation time (ns), α is the fractional intensity contribution, χ^2 is a goodness-of-fit parameter, and R_∞ is the limiting anisotropy at "infinity". Standard deviations of triplicate determinations of Φ_1 or Φ_2 were $<10\%$, and standard deviations of the fractional intensities of Φ_1 were $<5\%$.

it is most likely that the second lifetime component is an artifact caused by small amounts of scattered light and noise. A possible exception is the hybridized oligomer with the 4-carbon tether, which may have a significant second decay component. Further studies would be needed to verify such biexponential decay. In this work, only the dominant lifetime was used in the analysis of the DFA data for all samples.

For the single strands, slight increases in lifetime were observed when the EcoRI binding site was moved away from the 5' end or when the tether length was increased. Hybridization causes small but reproducible increases in lifetime for the oligomers that have a 6-carbon tether and in which the EcoRI binding site is in the 5' or middle position, but it has no effect on the other oligomers. Addition of EcoRI has no significant effect on the lifetimes in any of the samples.

Dynamic Fluorescence Anisotropy. The DFA results are shown in Tables 5 and 6 for the set I and set II oligomers, respectively. The data for both sets of samples were evaluated by three different models: the isotropic rotator, the anisotropic rotator with two rotational correlation times (Φ_1 , Φ_2), and the hindered rotator. Fits to an isotropic rotator with three rotational correlation times (not shown) gave no improvement over the two-component anisotropic rotator model and recovered a zero fractional intensity for the third correlation time.

In most cases, the experimental data could be reasonably fit (based on the random residual distribution and the χ^2 values) by either the biexponential anisotropic rotator or the hindered rotator model, yielding similar values for the rotational correlation time Φ_1 of the anisotropic rotator model and rotational correlation time Φ of the hindered rotator model. There is, however, an interesting relationship between the goodness-of-fit to the different models and the length of the fluorescein tether. For the shortest (4-carbon) tether, the biexponential anisotropic rotator gives the best fit, while for the long (9- and 12-carbon) tethers, the hindered rotator model generally gives the best fits (in a few cases for the

Table 6. Dynamic Fluorescence Anisotropy Results for Set II Oligomers^a

	isotropic		anisotropic				hindered			
	Φ	χ^2	Φ_1	α_1	Φ_2	α_2	χ^2	Φ	R_∞	χ^2
DNA33-4C-5'										
ss	0.62	1238	0.41	0.87	12.3	0.13	1.8	0.47	0.035	27.2
ds	1.14	522	0.72	0.83	10.9	0.17	6.5	0.83	0.042	21.9
ss+EcoRI	0.86	71	0.45	0.78	4.0	0.22	1.2	0.65	0.026	11.9
ds+EcoRI	1.02	192	0.52	0.72	5.5	0.29	0.5	0.77	0.049	11.9
DNA33-6C-5'										
ss	0.74	73	0.62	0.96	∞	0.04	6.9	0.62	0.018	6.3
ds	0.92	270	0.68	0.91	25	0.09	8.4	0.71	0.027	9.0
ss+EcoRI	0.89	150	0.69	0.94	∞	0.06	13.5	0.68	0.023	12.0
ds+EcoRI	1.24	727	0.70	0.85	37	0.15	8.6	0.74	0.052	10.2
DNA33-9C-5'										
ss	0.33	22	0.31	0.99	99.2	0.01	26.0	0.38	-0.011	1.9
ds	0.39	11	0.39	1			11.3	0.43	-0.008	2.3
ss+EcoRI	0.38	31	0.38	1			31.8	0.43	-0.011	2.9
ds+EcoRI	0.53	7	0.48	0.97	5.5	0.03	3.3	0.5	0.005	3.7
DNA33-12C-5'										
ss	0.32	18	0.32	0.99	99.2	0.01	18.9	0.36	-0.011	0.7
ds	0.36	9	0.36	0.99	99.1	0.01	9.2	0.39	-0.006	4.0
ss+EcoRI	0.36	2	0.36	1			1.7	0.36	0.000	1.7
ds+EcoRI	0.49	4	0.48	0.99	95	0.01	3.4	0.48	0.001	3.4

^a Fits are shown to three decay models: the isotropic rotator, the biexponential anisotropic rotator, and the hindered rotator. For each sample, a single fluorescence lifetime (from Table 4) was used in the DFA analysis. Φ is the rotational correlation time (ns), α is the fractional intensity contribution, χ^2 is a goodness-of-fit parameter, and R_∞ is the limiting anisotropy at "infinity". Standard deviations of triplicate determinations of Φ_1 or Φ_2 were $<10\%$, and standard deviations of the fractional intensities of Φ_1 were $<5\%$.

long tethers, the isotropic model gave results that were comparable to one or both of the other models). For the 6-carbon tether, the data are fit equally well by the anisotropic rotator and the hindered rotator models. This trend from biexponential anisotropic behavior for short tethers to hindered rotator behavior for long tethers is discussed later.

In the anisotropic rotator model, Φ_1 is largest for the single strand when the EcoRI binding site is at the 5' position and when the tether length is 6 carbons. Similar trends are observed for Φ in the hindered rotator model. The fractional intensity contribution of Φ_2 is small ($<6\%$), except for the 4-carbon tether. In the anisotropic rotator model, hybridization generally causes increases in both Φ_1 and the fractional intensity of Φ_2 . In the hindered rotator model, hybridization similarly increases both Φ and R_∞ . This effect is largest for the shorter tether lengths. For the oligomers with the binding site at the 5' end and a tether length of 4 or 6 carbons, there is an additional increase in the contribution of Φ_2 upon addition of EcoRI. For the longer tethers, the fractional contribution of Φ_2 is negligible, and in some cases, the isotropic model is sufficient to describe the data; much less hindrance is observed in these samples compared to the shorter tethers.

DISCUSSION

Under the experimental conditions of these studies (pH = 7.5), the dianionic form of fluorescein predominates. It is known that fluorescein does not intercalate in DNA,²¹ and its fluorescence characteristics are relatively insensitive to environmental conditions other than pH. In experiments with free fluorescein in the presence of unlabeled oligomers (results not shown), both single-

(21) Murakami, A.; Nakaura, M.; Nakatsuji, Y.; Nagahara, S.; Tran-Cong, Q.; Makino, K. *Nucleic Acids Res* 1991, 19, 4097.

stranded and double-stranded, no changes in the fluorescence lifetime or anisotropy decay were detected.

The fluorescence decay of the covalently tethered fluorescein is essentially monoexponential. A small increase in lifetime is observed upon hybridization for oligomers with the 6-carbon tether. For the other oligomers, the lifetimes remained essentially constant. *EcoRI* binding had no effect on the lifetimes of any of the oligomers. The unique sensitivity of the fluorescence lifetimes of the 6-carbon tether oligomers to hybridization, as well as the observation of maximum increases in anisotropy for these oligomers upon hybridization and *EcoRI* binding, clearly indicates that the 6-carbon tether length is particularly well-suited to detection of hybridization and *EcoRI* enhanced detection.

For all of the oligomers, the main anisotropy decay can be attributed to a fast rotational motion that is evident in all of the models used to fit the DFA data. This rotation occurs on the time scale of a few hundred picoseconds (~350–700 ps). This is only slightly longer than the rotational correlation time of $\sim 0.2 \pm 0.05$ ns which was determined for free fluorescein in solution under similar conditions of pH and viscosity.

For the oligomers with the long tethers (9 and 12 carbons), the motion of the fluorescein is not coupled to the motion of the oligomer because of the large freedom of motion afforded by the long tether. This nearly independent motion results in rotation that is essentially isotropic. For the shorter tethers (4 and 6 carbons), the fluorescein rotational motion is more influenced by the attached oligomer, and the biexponential anisotropy decay model provides good representation of the rotational motion. The rotational correlation time of the second, slow motion varies from 10 ns to "infinity". Thus, although two rotational decay components were clearly indicated for the oligomers with shorter tethers, recovery of a value for the second correlation time (Φ_2) was markedly unstable. This is because the fluorescence lifetime is much shorter than Φ_2 .

To further examine the instability of Φ_2 , a simulation of an anisotropic rotator was conducted in which the rotational correlation times were similar to the ones found in our experiments ($\Phi_1 = 0.5$ ns, $\Phi_2 = 20$ ns). These simulated data sets were used to monitor the dependence of the goodness of fit (expressed as the χ^2 values) on the long rotational correlation time Φ_2 . As shown in Figure 3, it is difficult even for this simulation to recover an exact value for Φ_2 , especially for the case in which Φ_2 is much longer than τ_1 and has only a small fractional intensity. For comparison, a third data set was simulated with the same parameter settings as for the previous simulations except that Φ_2 was set to 4 ns. In this case, the fits are much more sensitive to the value of Φ_2 .

Despite the uncertainties in the actual magnitude of Φ_2 , its existence can be used to explain the significant increases in the steady-state anisotropy that are observed upon hybridization of some oligomers, just as the absence of a significant Φ_2 can explain the absence of a significant increase in steady-state anisotropy for other oligomers. This effect is illustrated in Figure 4 using a modified form of the Perrin equation to describe the dependence of the steady-state anisotropy (r) on Φ_2 and the ratio of the fractional intensities¹⁹ of Φ_1 and Φ_2 :

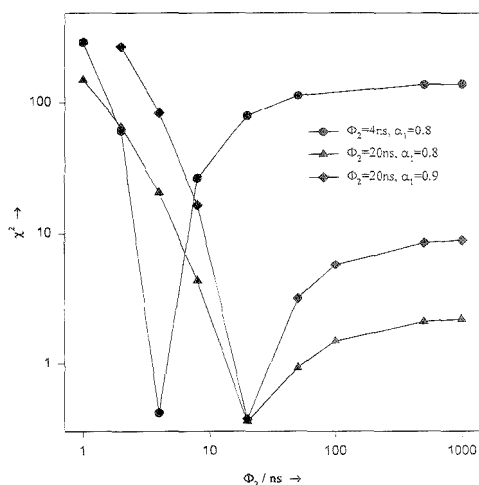


Figure 3. Simulated χ^2 for an anisotropic rotator with two rotational correlation times. Three initial data sets were simulated and used for the χ^2 calculations (for all, $r_0 = 0.4$, $\tau_1 = 4$ ns, $\Phi_1 = 0.5$ ns): (\blacktriangle) $\Phi_2 = 20$ ns, $\alpha_1 = 0.8$, $\alpha_2 = 0.2$; (\blacklozenge) $\Phi_2 = 20$ ns, $\alpha_1 = 0.9$, $\alpha_2 = 0.1$; and (\bullet) $\Phi_2 = 4$ ns, $\alpha_1 = 0.8$, $\alpha_2 = 0.2$. A constant phase error of 0.5° and a constant modulation error of 0.005 were assumed.

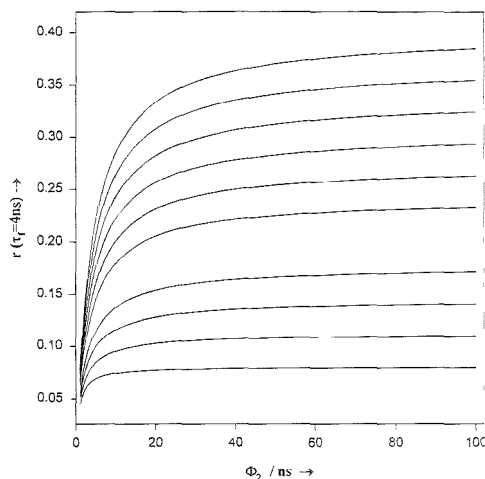


Figure 4. Steady-state anisotropy (r) simulated for an anisotropic rotator with two rotational correlation times ($\Phi_1 = 1$ ns) for different fractional contributions of Φ_2 ($\alpha_2 = 0.001, 0.1, 0.2, 0.3, 0.5, 0.6, 0.7, 0.8, 0.9$, and 0.999 , from bottom to top).

$$r = \frac{\alpha r_0}{1 + (1/\Phi_1 + 1/\Phi_2)\tau_1} + \frac{(1 - \alpha)r_0}{1 + (\tau_1/\Phi_2)} \quad (9)$$

As stated above, it is difficult to determine a reliable value for Φ_2 because it is much longer than the fluorescence lifetime. On the other hand, this allows us to reduce the number of fitting parameters and thereby simplify the model used to fit the data. It is reasonable to assume that during the fluorescence lifetime, the fast component is primarily responsible for the anisotropy decay, and because of a hindrance, the anisotropy does not decay to zero.

The longer decay component can be represented in a first approximation by a constant term, R_{∞} . This can be modeled as a hindered rotator. Application of this model to the DFA data produced results that were similar to the steady-state anisotropy results. R_{∞} increases upon hybridization and increases further upon *EcoRI* binding to the double strand if the binding site is near the 5' end. Similar increases in R_{∞} are observed for the 4C and 6C tether lengths. This tendency is less pronounced for the 9C and 12C tethers.

CONCLUSIONS

The results demonstrate the detection of DNA hybridization by fluorescence anisotropy. The detection can be improved by including a binding site for the enzyme *EcoRI* on the oligomer probe. *EcoRI*, which binds only to double-stranded DNA, increases the effective volume of the double strand complex and thereby amplifies the difference between the anisotropies of the single strand and the double strand. *EcoRI* enhancement of polarization can be applied to the detection of any sequence when used in conjunction with a nucleic acid amplification method such as polymerase chain reaction (PCR) or strand displacement amplification (SDA). The approach involves the use of an amplification primer or detector probe that contains the specific target sequence at its 3'-end and the *EcoRI* site at its 5'-end. The primer or detector probe is converted from a single strand to a double-stranded form that binds *EcoRI* during amplification of the target sequence.²²

(22) Walker, G. T.; et al. unpublished results.

(23) Kim, Y.; Grable, J. C.; Love, R.; Greene, P. J.; Rosenberg, J. M. *Science* **1990**, *249*, 1307.

(24) Bernstein, F. C.; Koetzle, T. F.; Williams, G. J. B.; Meyer, E. F., Jr.; Brice, M. D.; Rodgers, J. R.; Kennard, O.; Shimanouchi, T.; Tasumi, M. *J. Mol. Biol.* **1977**, *112*, 533.

(25) Abola, E. E.; Bernstein, F. C.; Bryant, S. H.; Koetzle, T. F.; Weng, J. In *Scientific Applications*; Allen, F. H., Bergerhoff, G., Sievers, R., Eds; Data Commission of the International Union of Crystallography: Bonn/Cambridge/Chester, 1987; pp 107-132.

The results show that the *EcoRI*-enhanced polarization detection scheme is effective only if (1) the fluorescein tether is short (~6 carbons or less) and (2) the *EcoRI* binding site is near the fluorescein attachment site at the 5' end. The 6C tether is the optimal length for the particular system investigated here, yielding the largest anisotropy differences upon hybridization in both the absence and the presence of *EcoRI* binding. Further investigations are needed to determine the dependence of the optimum tether length on the sequence and length of the probe, the dye used for detection, and the location of the *EcoRI* binding site.

The anisotropy decay in the single strand is dominated by the very fast motion of the fluorescein molecule about the tether. Only a very small portion, if any, of the anisotropy decay is caused by motion of the whole molecular unit (oligomer + fluorescein). For the oligomers with a short (4 or 6 carbons) tether, the contribution of the slow rotational component to the anisotropy decay increases upon hybridization and further upon binding of *EcoRI* to the double strand near the 5' end, due to hindrance of the fast fluorescein motion, and the anisotropy does not decay to zero. When the tether length is increased, the motion of the fluorescein is less influenced by hybridization and *EcoRI* binding, and anisotropy decay is due to the fast motion of the fluorescein only.

ACKNOWLEDGMENT

The authors are grateful to Michael Mitchell of Becton Dickinson and Co. Research Center for performing the molecular modeling of the *EcoRI* bound to the fluorescein-labeled DNA oligomer and providing the graphical depiction of this system that is shown in Figure 1.

Received for review May 17, 1995. Accepted August 13, 1995.*

AC950478Z

* Abstract published in *Advance ACS Abstracts*, September 15, 1995.

Tandem Reflectron Time-of-Flight Mass Spectrometer Utilizing Photodissociation

Douglas J. Beussman, Paul R. Vlasak, Richard D. McLane,[†] Mary A. Seeterlin, and Christie G. Enke*

Department of Chemistry, Michigan State University, East Lansing, Michigan 48824

A tandem time-of-flight (TOF) mass spectrometer has been designed to obtain complete MS/MS spectra from compounds eluting from a gas chromatograph. This application requires high spectral generation rate, unit mass resolution for both precursor selection and product spectra, and efficient ion utilization. These objectives are achieved by reflectron TOF mass separation in both stages and laser photoinduced dissociation as the ion fragmentation method. Careful timing of the laser pulse relative to ion extraction allows ions of a single m/z value up to m/z 1000 to be photodissociated while ions with adjacent m/z values are essentially unaffected. The convergent foci of the ion packet and laser pulse results in ion fragmentation efficiencies as high as 79%. An ion gate prevents the nonselected precursor ions from convoluting the product spectra. Product spectra can be generated at the maximum laser repetition rate (currently 200 Hz). To achieve unit mass resolution for all product m/z values simultaneously, a novel reflectron was designed for the second TOF stage.

Tandem mass spectrometers have the capability of providing substantial improvements over single-stage mass spectrometers in both chemical selectivity and the amount of structural information obtained about an analyte. The complete tandem mass spectrometry (MS/MS) characterization of an analyte requires obtaining the product mass spectrum for each of the m/z values of interest in the primary mass spectrum. One of the most severely felt limitations is the amount of MS/MS data that can be collected on a compound introduced to the mass spectrometer after chromatographic separation, due to the requirement that the analyte partial pressure remain relatively constant in the source during the analysis time. For this application, it is desirable to be able to collect 100 or more product spectra per second. The high sensitivity desired for such an application also requires that at least the second mass analysis be performed by array detection rather than by scanning a mass filter. The existing true array detection mass spectrometric techniques include magnetic sector with spatial array detection and Fourier transform mass spectrometry, while time-of-flight (TOF) with time array detection and the ion trap are batch array detection techniques.

In this paper, the design and performance of an instrument intended to obtain MS/MS spectra on the chromatographic time scale is described. The emphasis is on design considerations and

initial performance characterizations. This instrument (see Figure 1) utilizes TOF separation in both stages of mass analysis and a laser pulse to provide unit resolution selection of the precursor ion packet of interest, achieve high-efficiency photoinduced dissociation (PID), and yield a complete, unit-resolved product ion spectrum for each laser pulse.¹

Photon-induced fragmentation by pulsed laser beam allows precursor ion selection by laser timing and provides efficient fragmentation in a manner that does not compromise the TOF analysis of the products. The high degree of photon-ion overlap at the interaction region, resulting from a focused ion packet and a focused laser pulse, results in the excitation of a large fraction of the selected ions and thus high fragmentation efficiencies. Because a useful normal or product spectrum can be obtained from each source extraction, it is practical to generate product spectra at the maximum laser repetition frequency (e.g., 200 Hz for pulsed excimer lasers). Since this rate of extraction is quite slow for TOF mass analysis, the generation of normal or primary spectra can be interspersed with product spectrum generation.

Several other researchers have designed tandem mass spectrometers which use photodissociation as the fragmentation method. Duncan et al. performed photodissociation in a single reflectron TOF mass spectrometer by intersecting a laser pulse and an ion packet at the turnaround point of the reflectron.² Schlag and co-workers also used a single reflectron TOF instrument to photodissociate benzene.³ This was accomplished by focusing a laser pulse at the space focus plane outside the ion source and timing the laser pulse such that it intersected the isomass ion packet of choice. While demonstrating the practicality of PID in TOF instruments, these designs have not achieved our goal of unit mass resolution to m/z 1000 for both precursor and product ions.

Another related instrument is that of Cotter and Cornish.⁴ They have constructed a tandem reflectron TOF mass spectrometer and used it to collect MS/MS data. Instead of using a laser for photodissociation in the fragmentation process, a gas pulse was used to perform collision-induced dissociation (CID) experiments.

EXPERIMENTAL SECTION

The instrument chamber has inner dimensions of 60 in. long \times 11 in. wide \times 9 in. tall with three removable access panels (\sim 20

* Address reprint requests to Christie G. Enke, Department of Chemistry, 103 Clark Hall, University of New Mexico, Albuquerque, NM 87131. E-mail: enke@unm.edu.

[†] Current address: The Procter and Gamble Co., Sharon Woods Technical Center, 11450 Grooms Rd., Cincinnati, OH 45241.

- (1) Seeterlin, M. A.; Vlasak, P. R.; Beussman, D. J.; McLane, R. D.; Enke, C. G. *J. Am. Soc. Mass Spectrom.* **1993**, *4*, 751-754.
- (2) LaiHing, K.; Cheng, P. Y.; Taylor, T. G.; Willey, K. F.; Peschke, M.; Duncan, M. A. *Anal. Chem.* **1989**, *61*, 1458-1460.
- (3) Boesl, U.; Weinkauff, R.; Walter, K.; Weickhardt, C.; Schlag, E. W. *Ber. Bunsenges. Phys. Chem.* **1990**, *94*, 1357-1362.
- (4) Cornish, T.; Cotter, R. J. *Rapid Commun. Mass Spectrom.* **1992**, *6*, 242-248.

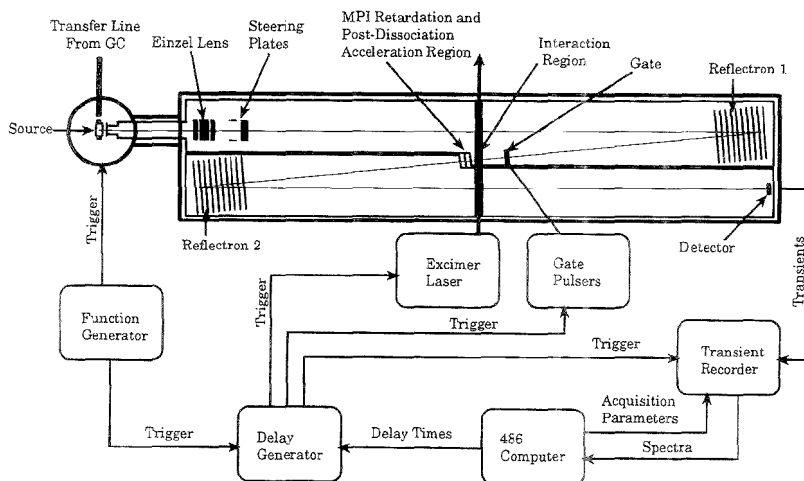


Figure 1. Schematic diagram of the tandem reflectron TOF mass spectrometer designed for photoinduced dissociation.

in. \times 12 in.) in the top of the chamber to allow easy access to all areas of the instrument. The source housing is a six-way cross mounted on the end of the instrument chamber. A viewport is attached to the top of the source housing, and a heated GC transfer line (Finnigan, San Jose, CA) from a gas chromatograph (Model 5890, Hewlett-Packard, Palo Alto, CA) enters the source housing orthogonal to the ion flight path. The GC column terminates just inside the source region. The gaseous molecules resulting from continuous or injected sample introduction are allowed to spray into the source region, where electron impact ionization occurs continuously. One turbomolecular pump is mounted directly underneath the source, while a second is mounted on the underside of the chamber itself. The normal working pressure of the main chamber is between 3×10^{-7} and 6×10^{-7} Torr.

During ion extraction, a potential drop from the center of the source to the field-free region of 650 V is created. An Einzel lens is used to collimate the ion beam, while steering plates allow minor steering of the ion packets toward the first reflectron. High-voltage shields, constructed from stainless steel wire mesh (Newark Wire Cloth Co., Newark, NJ), line the inside of the instrument to create field-free flight paths. The shields for the first and second field-free regions are electrically isolated from the instrument chamber and from each other by $\frac{3}{8}$ in. ceramic spacers (NTT, Meadville, PA) attached to the mesh. The first reflectron consists of nine stainless steel electrodes and a stainless steel backplate. Each electrode is a 1 mm thick stainless steel ring with an outer diameter of 10.2 cm and an inner diameter of 6.3 cm.

The ion-deflection gate is constructed from two electrically isolated interleaved 0.003 in. diameter stainless steel wires. These wires are strung back and forth through alternate holes in two Vespel (E.I. du Pont de Nemours, Wilmington, DE) blocks, located on the top and bottom of the gate, such that they form a plane of 26 wire segments separated from each other by ~ 1 mm. The total dimensions of the wire gate are ~ 25 mm wide \times 65 mm high.

Since the laser beam is of sufficient power to ablate metal, holes have been cut in the shield material to create an unimpeded path for the laser beam. To prevent field leakage through these holes, a tube has been constructed and placed through the holes such that the focused laser beam can pass through the tube without interacting with the shields or any other metal component inside the instrument. This tube is held at the potential of the first field-free region (-550 V). A second, shorter tube is slid over the first tube. This second tube just spans the width of the second field-free region and is at the same potential as the second field-free region shield (-2500 V). The two tubes are electrically isolated from each other by a thin sheet of Kapton (E.I. du Pont de Nemours, Wilmington, DE). Two 22 mm high \times 34 mm wide holes have been cut out of opposite sides of the light tube where it intersects the ion flight path. In order to ensure that ion packets interact with photons only once along the flight path, the plane in which the z-shaped ion trajectory lies is tilted with respect to the laser beam path.

Three 5 cm \times 5 cm grids, constructed from 88% ion transmission grid material (Buckbee-Mears, St. Paul, MN), are located just after the interaction region, with the first grid ~ 2 cm from the interaction region. The first grid is set at the field-free voltage of the first TOF stage (-550 V). The second grid has an applied potential ~ 20 – 30 V more positive than the first grid, which creates a retardation field to eliminate multiphoton ionization (MPI) products from reaching the detector. The potential applied to the third grid is that of the second field-free region. This creates an acceleration field after the interaction region. The grids which define the retardation and acceleration fields are separated by ~ 1 cm. The second reflectron in this instrument employs first two grids to provide a rapid deceleration region with a field strength of ~ 1565 V/cm and then a series of 10 gridless electrodes to produce a nonlinearly increasing field with a continuously decreasing field strength. This field shape was determined using a novel method for wide-energy-range reflectron design.⁵ The electrodes are the same size and of the same material as those used in the first reflectron.

(5) Vlasak, P. R.; Beusman, D. J.; Ji, Q.; Enke, C. G. Manuscript in preparation.

Detection of the ions at the end of the second mass analyzer is achieved through the use of a dual 40 mm microchannel plate, chevron-type detector (modified Model TOF-2003, Galileo, Sturbridge, MA). The detector anode is connected to the input of the digital storage oscilloscope (described below) through a terminated 50 Ω BNC cable. A second, removable detector with 25 mm microchannel plates has been constructed and mounted on a sliding carrier such that it can be placed anywhere along the rail beyond the interaction region. This allows detection and verification of ions after the interaction region components, ion focusing at the interaction region, and collection of crude spectra just beyond the interaction region in order to test the photodissociation process.

In the photodissociation experiments, a high-power Questek 2580 v β excimer laser (Lambda-Physik, Acton, MA) is used to provide the necessary photons. This laser provides 150 mJ at 20 Hz using the ArF line (193 nm). The pulse width of the laser is \sim 15 ns. A cylindrical plano-convex fused silica (Dynasil 1100) lens (Newport, Irvine, CA) of 300 mm focal length is used to focus the laser beam to \sim 2 cm high \times 1 mm wide at the interaction region inside the mass spectrometer. Two fused silica interferometer flats (Newport, Irvine, CA) are positioned on flanges mounted to the outside of the mass spectrometer in order to allow the photons to pass into the instrument and exit the other side, where they are collected in a beam dump device.

The electronics for all instrument components were designed and built in this lab, except for the high-voltage gate pulsers (Model GRX-1.5K-E, Directed Energy Inc., Fort Collins, CO). The timing sequence of the experiment is started by a square wave pulse from a function generator (Datapulse, Culver City, CA). This wave simultaneously triggers the pulser for the source backplate, a delay generator (Model 4222, LeCroy, Chestnut Ridge, NY), and a digital storage oscilloscope (Model 9450, LeCroy, Chestnut Ridge, NY). The source pulser then pulses the backplate from 0 to 200 V in order to extract the ions contained in the source volume. The four-channel delay generator provides timing, to within 1 ns, for the gate pulsers and the laser trigger. The delay generator and the digital oscilloscope are controlled through a general purpose interface bus connection (National Instruments, Austin TX) by a 486/33 computer (Zenith, St. Joseph, MI) running a control program written for LabWindows (National Instruments, Austin, TX).⁶

RESULTS AND DISCUSSION

Ion Source Considerations. Essential to the achievement of high sensitivity is the ability of the source to accumulate a significant fraction of the ions that are produced between the extraction pulses. This requires continuous ionization and some mechanism for retention of the ions produced. To this end, we have implemented a well-focused electron beam which produces a potential well between the backplate and the first grid.⁷ This source design is similar to that of Wollnik and co-workers.⁸ These sources have been shown to store ions between extraction pulses, thus increasing sensitivity.⁹

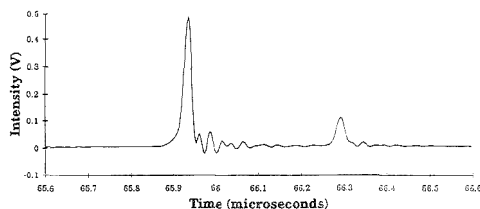


Figure 2. Normal EI spectrum of the molecular ion region of toluene (m/z 91–92), indicating a resolution of 1500 (fwhm) obtained at the interaction region (100 transients averaged). Peak width of 22 ns (fwhm) for m/z 91 (peak at 65.935 μ s).

Precursor Ion Selection. Mamyrin et al. demonstrated a method of improving resolution using a reflectron.¹⁰ Wollnik and Przewlaka improved upon the Mamyrin reflectron TOF instrument by using grid-free reflectrons.¹¹ The grid-free devices do not suffer from ion transmission losses due to collisions with the grid material or loss of resolution associated with the field perturbations in the vicinity of the wire mesh;¹² they also serve to radially focus the ion packets. The first stage of mass analysis in the tandem TOF instrument was designed and constructed using a combination of the above technologies. As shown in Figure 2, a mass resolution of 1500 (fwhm) is obtained in the first TOF analyzer, as determined by placing a temporary detector at the interaction region.

To eliminate normal mass spectrum ions from the product spectrum, we have implemented an interleaved-comb ion deflection gate which can be quickly switched between ion deflection and ion transmission.¹³ The ion gate is fashioned after a device first proposed by Loeb and studied theoretically by Lusk.¹⁴ This device was further developed and used by Cravath,¹⁵ as well as by Bradbury and Nielsen as an electron filter.¹⁶ Later, Schlag et al.¹⁷ adapted their design for use as an ion gate. When 250 and -250 V potentials, with respect to the field-free voltage, are applied to the alternate wires of the gate, the gate is "closed". In this state, each ion is deflected to the right or left. The gate is "open" when all the wires are set at the field-free voltage. A precursor ion packet is isolated by leaving the gate closed until the precursor ion packet is about to enter its field, at which time the gate is pulsed open until the precursor ion packet has passed through the space that the deflection field normally occupies. At this point, the gate is closed again, thereby deflecting all ions of higher m/z than the precursor ion packet and achieving precursor ion isolation.

The molecular ion region of bromobenzene (m/z 156–159) has been used to perform initial characterization of the ion gate. Figure 3A shows the normal molecular ion region of bromobenzene using a wide gate pulse, indicated by the gray box, to select

(6) McLane, R. D. Ph.D. Thesis, Michigan State University, East Lansing, MI, 1993.

(7) Studier, M. H. *Rev. Sci. Instrum.* **1963**, *34*, 1367–1370.

(8) Grix, R.; Grüner, U.; Li, G.; Stroth, H.; Wollnik, H. *Int. J. Mass Spectrom. Ion Phys.* **1989**, *93*, 323–330.

(9) Puzycki, M. A.; Gardner, B. D.; Allison, J.; Enke, C. G.; Grix, R.; Holland, J. F.; Yelchak, G. E. *Proceedings of the 39th ASMS Conference on Mass Spectrometry and Allied Topics*; Nashville, TN, May 19, 1991; p 156.

(10) Mamyrin, B. A.; Karataev, V. I.; Shmikk, D. V.; Zagulin, V. A. *Pis'ma Zh. Eksp. Teor. Fiz.* **1973**, *37*, 45–48.

(11) Wollnik, H.; Przewlaka, M. *Int. J. Mass Spectrom. Ion Processes* **1990**, *96*, 267–274.

(12) Bergmann, T.; Martin, T. P.; Schaber, H. *Rev. Sci. Instrum.* **1989**, *60*, 347–349.

(13) Vlasak, P. R.; Beussman, D. J.; Davenport, M. R.; Enke, C. G. Manuscript in preparation.

(14) Loeb, L. B. *Basic Processes of Gaseous Electronics*; University of California Press: Berkeley, CA, 1961.

(15) Cravath, A. M. *Phys. Rev.* **1929**, *33*, 605–613.

(16) Bradbury, N. E.; Nielsen, R. A. *Phys. Rev.* **1936**, *49*, 368–393.

(17) Weinkauff, R.; Walter, K.; Weickhardt, C.; Boesi, U.; Schlag, E. W. *Z. Naturforsch.* **1989**, *44a*, 1219–1225.

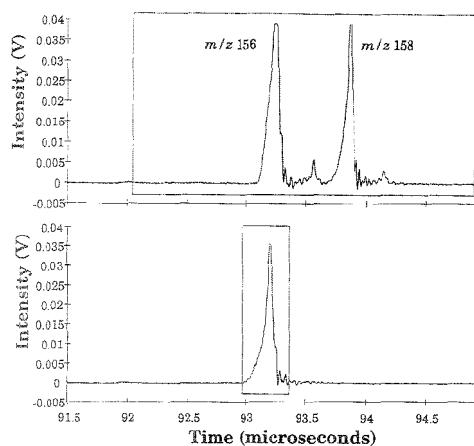


Figure 3. Spectra of the molecular ion region of bromobenzene, showing the ability to selectively gate an ion packet. The shaded regions indicate the gate "open" time window. Spectrum A shows a wide gate pulse, allowing m/z 153–161 to pass through. Spectrum B shows a narrow gate pulse used to selectively pass m/z 156 while deflecting all other m/z values.

the entire molecular ion region. In Figure 3B, the gate pulse is narrow and has been timed such that the m/z 156 ion packet has been selectively allowed to pass through the gate, while m/z 157–159 ions have been deflected away from the detector. The principal function of the gate in this instrument is to keep source ions of lower m/z value than the desired precursor ion packet out of the product spectrum. The actual precursor ion packet selection is determined by the coincidence of the laser photons and the precursor ion packet in the interaction region.

The focusing of the laser beam allows photons to interact with ions of only a single m/z value. Using the resolution for m/z 156 of bromobenzene obtained at the interaction region, the 1 mm spatial width of the laser beam, the 15 ns temporal width of the laser pulse, and the calculated ion velocity for each m/z value, the ability to selectively photodissociate a single m/z ion packet can be calculated. If the laser pulse is timed such that the photons at the midpoint of the laser pulse reach the interaction region at the same time as the midpoint of the ion packet, ~98% of the selected ion packet at m/z 156 is overlapped by the laser pulse, with no overlap or interference of neighboring m/z ion packets. At higher masses, the ability to selectively dissociate a single m/z ion packet is degraded due to the fact that the separation between adjacent m/z ion packets decreases, while the laser pulse dimensions remain the same. Also, since higher m/z ions have lower velocities than lower m/z ions, the higher m/z ions travel a shorter distance over the duration of the laser pulse, and thus a smaller fraction of a high m/z ion packet interacts with photons. At m/z 1000, the laser pulse interacts with 92% of the selected ion packet, but now 8% of the adjacent m/z ion packets also interact with the photons. The interference will be decreased if the mass resolution of the spectrum at the interaction region is increased, if the time between adjacent m/z ion packets is increased, or if the laser beam is focused to <1 mm. Critical to the achievement of this high level of precursor selectivity is the very small (~2 ns) jitter in the laser pulse timing.

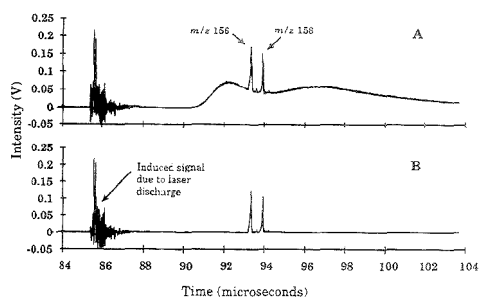


Figure 4. Spectra of the molecular ion region of bromobenzene (m/z 156–159) with laser discharge (indicated by sharp signal at ~86 μ s) timed prior to ion arrival at the interaction region. Spectrum A shows the detection of MPI products causing interference with the EI spectrum. Spectrum B shows the use of the MPI retardation field, eliminating MPI interferences.

We have previously demonstrated experimentally the ability to selectively photodissociate a single m/z ion peak with this instrument.¹ Due to the linear relationship of flight time and square root of mass-to-charge ratio of ions in TOF mass spectrometry, the calibration of laser delay time is readily accomplished. The flight time to the temporary detector for a given m/z ion packet can be used to approximate the flight time of the ion packet to the interaction region in order to set an approximate laser delay time. Once the actual delay times required for ion-photon overlap for two m/z values have been determined, the flight time to the interaction region of any m/z ion packet can be calculated for the same instrument tune. This allows the laser delay time to easily be set so that the pulse interacts with any m/z ion packet of choice.

Pulsed Laser Photodissociation. The maximum fragmentation efficiency for photodissociation will be achieved at the maximum ion-photon overlap. The ion bunching nature of TOF mass spectrometry, as well as the fact that the ion packets are spatially focused to a narrow slice within the beam cross section at the interaction region, ensures a high ion density in this region. The photon beam is optically shaped to a beam 2 cm high \times 1 mm wide to intercept the ion packet edge on. The very high photon and ion temporal and spatial overlap at the interaction region provides a maximum likelihood of photon and ion interaction. With this system, we have previously demonstrated efficiencies of 27%–79% for the photodissociation of various ions using 193 nm photons.¹

The high photon flux also results in MPI of the background gas molecules present in our instrument. Unless discriminated against, these ions can then drift down the flight path and become accelerated by the postdissociation acceleration field. The resulting ion current due to these MPI products can convolute the mass spectrum. Figure 4A shows the resulting ion signal for the molecular ion region of bromobenzene with the detector placed ~20 cm past the interaction region. The sharp, noisy signal on the left is the induced signal in the detector due to the 30 kV discharge of the laser thyatron. The laser was timed such that the photons reached the interaction region just prior to molecular ions of bromobenzene; therefore, no PID products of bromobenzene ions were produced. The sharp peaks near the center of the spectrum are the undissociated molecular ions of bromobenzene (m/z 156 and 158). The broad peaks are due to the MPI

products reaching the detector and thus interfering with the normal mass spectrum of bromobenzene.

The MPI products in the interaction region have only the thermal kinetic energy that the background gas molecules have, while the PID products have a substantial fraction of the original precursor ion energy. To prevent the motion of the MPI products toward the analyzer, a slightly positive field (20–30 V) was introduced. Figure 4B shows a spectrum of the molecular ion region of bromobenzene, but with the addition of the MPI retardation field so that interference from the MPI products is eliminated. The laser discharge signal can again be seen, indicating that the laser has been fired and that ions are being created by MPI.

Product Ion Dispersion and Focusing. While the average velocity of the precursor ions of a particular m/z is mass-dependent, the velocity of the product ions formed by PID is approximately the same as that of their precursors. Some electric field gradient is required after the interaction region to separate the product ions in time. This is accomplished with the postdissociation acceleration field after the interaction region in order to impart mass-dependent velocities to the product ions. In order to maximize the product spectrum resolution, a temporal focusing system must compensate for the energy distribution of the isomass precursor ion packet that was focused at the interaction region (plus the additional kinetic energy distribution from the PID process), and it must do this for product ions whose average initial kinetic energies vary from a few percent to 100% of the average precursor ion energy.

All designs to date for achieving temporal focusing of mass-dispersed product ions involve the use of a reflectron. Scanning the reflectron voltage profile has been used to obtain focused product spectra,¹⁷ but this solution is not consistent with our goal of achieving a complete product spectrum from each PID event. To avoid scanning the reflectron field strength, a curved-field reflectron has been implemented by Cornish and Cotter which serves both to time-disperse the product ions and to provide reasonable ion focus over the entire product ion m/z range.¹⁸

In our instrument, we have chosen to use an acceleration field of 1950 eV after the interaction region to provide mass-dependent product ion velocities. Since the product ions will retain some fraction of their initial 650 eV energy, the energy range of the accelerated product ions will be from 1950 to 2600 eV. This reduces the relative kinetic energy range of the product ions from nearly 100% to ~25% (defined as the energy range divided by the maximal energy).

Since the acceleration field provides the flight time dispersion of the various product ion masses, the second reflectron is used in its more traditional mode of focusing the different energies of the isomass product ions. Because the mean energy is different for each product ion m/z value, some field curvature in the reflectron is required to provide the correct field gradient at each turnaround point. The method by which we determined the optimum field shape and electrode voltages is described elsewhere.⁵

Figure 5 is the normal mass spectrum of toluene recorded at the final detector position. The resolution of this spectrum is ~1000, indicating that the resolution of a normal mass spectrum through the second reflectron is not severely degraded as

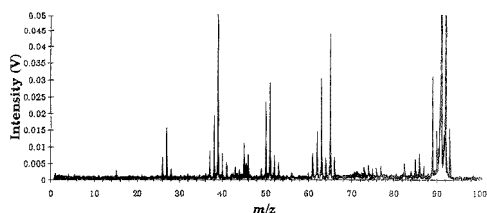


Figure 5. Normal EI spectrum of toluene (m/z 92), indicating a resolution of 1000 (fwhm) obtained at the final detector position (100 transients averaged). Peak intensities at m/z 91 and 92 are off-scale.

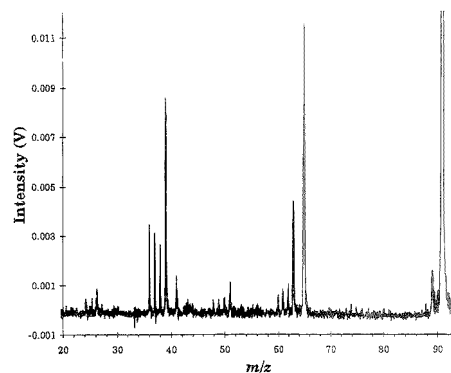


Figure 6. Product spectrum for m/z 91 of toluene, indicating a resolution of 300 (fwhm) obtained at the final detector position (200 transients averaged). Peaks due to the normal spectrum prior to m/z 91 have been eliminated by the ion gate.

compared to that from a spectrum recorded using the temporary detector placed in front of the second reflectron. Despite the longer path length, no increase in resolution is observed at the final detector. We believe this is primarily due to the increased number of grids that the ions must pass through, each of which degrades the resolution.¹⁹ The resulting product spectrum from the photodissociation of m/z 91 from toluene is shown in Figure 6. The resolution of the spectrum is ~300 ($m/\Delta m$, fwhm). This spectrum represents a kinetic energy range of ~2035–2600 eV, or a 22% relative range. The resolution for the product spectrum is lower than that for a normal mass spectrum, but this is expected since in the normal spectrum isomass ion packets begin separating from one another just outside of the source, while the product isomass ion packets begin separating from each other only after the postdissociation acceleration. This leads to a time-compressed spectrum and therefore decreased resolution.

The mass axis of the product spectrum has been calibrated using the m/z values and flight times for the precursor ion and two product ions. Once a calibration has been determined, it can be used to calibrate product spectra from any precursor m/z , using the same instrument tune.

Overall Instrument Performance and Applications. Fragmentation efficiencies of up to 79% (for bromobenzene) have been obtained in our tandem TOF instrument. This represents a significant increase in the PID fragmentation efficiency compared

(18) Cornish, T. J.; Cotter, R. J. *Rapid Commun. Mass Spectrom.* 1993, 7, 1037–1040.

(19) Bergmann, T.; Martin, T. P.; Schaber, H. *Rev. Sci. Instrum.* 1989, 60 (3), 347–349.

with earlier results obtained in an ion cyclotron mass spectrometer.²⁰ The efficiencies obtained in this instrument are comparable to those obtained using CID in a triple quadrupole mass spectrometer.²¹

Unit mass resolution to at least m/z 300 has been demonstrated for all components of the tandem TOF mass spectrometer. This is not a theoretical limit, but one that can be improved with further design refinements. Even the current resolution allows for both the selection of a single m/z ion packet for further fragmentation and the collection of resolved product spectra over the entire mass range. Since the instrument voltages do not need to be adjusted during an experiment, and since the photodissociation process is efficient, a full product spectrum of any m/z can be obtained for each ion extraction from the source.

In the analytical application of this instrument, a laser with a repetition rate of 200 Hz will be used, allowing up to 200 product spectra to be produced each second. With the incorporation of an integrating transient recorder like that developed at Michigan State University,²² the continuous acquisition and storage of these spectra will be feasible. This will allow full MS/MS data to be collected on the time scale of a component elution from a gas chromatograph.

This instrument is also proving to be an ideal platform for studying the photodissociation of small ions. Laser wavelength and pulse energy can be varied to determine the effects on the fragmentation process. Also, the structural usefulness of the product ions can be determined and compared with those obtained using CID in other tandem mass spectrometers. This will allow for a determination of the analytical utility of photodissociation as a fragmentation method in MS/MS.

We intend also to increase the mass range of ions introduced into our tandem mass spectrometer by either replacing the EI source with a MALDI source²³ or using a novel ion trap source, being built by our group,²⁴ to attach an electrospray source to a TOF mass spectrometer. Since the energy imparted to an ion by a photon is independent of the ion's mass (unlike in CID, where the imparted energy decreases with increasing ion mass), PID may prove to be an advantageous fragmentation technique for high-mass ions. The implementation of the above sources will allow this to be investigated.

ACKNOWLEDGMENT

We gratefully acknowledge the National Institutes of Health for supporting this work (NIH GM 44077). H. Wollnik made several valuable suggestions during the initial design phase of this work. M. Rabb did much of the electronics system design and construction.

Received for review March 23, 1995. Accepted August 10, 1995.*

AC950288O

* Abstract published in *Advance ACS Abstracts*, September 15, 1995.

-
- (20) Bowers, W. D.; Delbert, S. S.; McIver, R. T., Jr. *Anal. Chem.* **1986**, *58*, 969-972.
- (21) Yost, R. A.; Enke, C. G.; McGilvery, D. C.; Smith, D.; Morrison, J. D. *Int. J. Mass Spectrom. Ion Phys.* **1979**, *50*, 127-136.
- (22) Holland, J. F.; Newcombe, B.; Teckenburg, R. E., Jr.; Davenport, M.; Allison, J.; Watson, J. T.; Enke, C. G. *Rev. Sci. Instrum.* **1991**, *62*, 69-75.
- (23) Gardner, B. D.; Vlasak, P. R.; Beussman, D. J.; Enke, C. G.; Watson, J. T. *Proceedings of the 42nd ASMS Conference on Mass Spectrometry and Allied Topics*; Chicago, IL, June 2, 1993; p 1037.
- (24) Ji, Q.; Vlasak, P. R.; Holland, J. F.; Enke, C. G. *Proceedings of the 42nd ASMS Conference on Mass Spectrometry and Allied Topics*; Chicago, IL, June 2, 1993; p 1042.

Electrospray as a Controlled-Current Electrolytic Cell: Electrochemical Ionization of Neutral Analytes for Detection by Electrospray Mass Spectrometry

Gary J. Van Berkel* and Feimeng Zhou†

Chemical and Analytical Sciences Division, Oak Ridge National Laboratory, Oak Ridge, Tennessee 37831-6365

In this paper an electrospray ion source is shown to be a controlled-current electrolytic flow cell which, when operated so that three key requirements are met, can be used for efficient neutral analyte ionization (i.e., complete analyte electrolysis) and sensitive gas-phase detection (i.e., minimized gas-phase signal suppression) in electrospray mass spectrometry (ES-MS). These three requirements are as follows: (1) the magnitude of the ES current, i_{ES} , must be sufficient for the oxidation of the molar equivalent of all species available for reaction in the ES capillary that are as easily or more easily oxidized than the targeted analyte, including all of the analyte; (2) the analyte must be available for reaction at the metal/solution interface in the ES capillary; and (3) the steps taken to ensure the first two requirements must not inhibit the formation of gas-phase ions from the ions generated electrolytically in solution. The means to meet these requirements are discussed, including the addition of an appropriate electrolyte to the electrosprayed solutions (e.g., lithium triflate), the use of slower flow rates (e.g., 5.0 vs 40 $\mu\text{L}/\text{min}$), and the use of a platinum capillary in the ES device, rather than the more commonly used stainless steel capillary. Neutral metallocenes, metalloporphyrins, and polycyclic aromatic hydrocarbons are used as the model compounds. Operation of the ES ion source in the manner described expands the neutral compound types amenable to low level detection by ES-MS to include even those that are relatively difficult to oxidize (i.e., $E > 1.0 \text{ V}$ vs SCE) and, therefore, also expands the universality of ES as an ionization source. From the electrochemical point of view, this operation of the ES ion source might be viewed as a means to provide molecular weight information, and possibly the structure, for the ionic products formed during a controlled-current electrolysis experiment.

As a means to further the analytical utility of electrospray mass spectrometry (ES-MS),¹ many recent fundamental investigations have been aimed at obtaining definitive descriptions of the various processes in ES that lead ultimately to the generation of gas-phase ions.^{2–16} Along these lines, we have focused on understanding

the electrolytic process,^{17–19} originally described by Kebarle and co-workers,²³ that is inherent to the operation of the ES ion source. This electrolytic process maintains charge balance in the ES device, necessitated by the selective loss of one ion polarity in the charged ES droplets, via oxidation/reduction of the excess ions in the ES capillary or via creation of ions of the appropriate polarity, or both.

Our study of the electrolytic nature of ES has been motivated, in part, by the desire to exploit the process for analytical purposes. In particular, we have focused on determining the means by which the electrolysis process could be used to oxidize (positive ion mode) or reduce (negative ion mode) certain types of neutral analytes (e.g., aromatics and other highly conjugated systems), thereby forming their respective ES-active cations or anions.^{17–19} Reports from our group^{17–21} and a few other groups^{22–25} have demonstrated that the electrolysis process in ES can be used to ionize neutral analytes in solution and that these ionized analytes (if relatively long-lived in solution) can be detected in the gas

- (3) Blades, A. T.; Ikononou, M. G.; Kebarle, P. *Anal. Chem.* 1991, 63, 2109–2114.
- (4) Tang, L.; Kebarle, P. *Anal. Chem.* 1991, 63, 2709–2715.
- (5) Raffaelli, A.; Bruins, A. P. *Rapid Commun. Mass Spectrom.* 1991, 5, 269–275.
- (6) Guevremont, R.; Siu, K. W. M.; Le Blanc, J. C. Y.; Berman, S. S. *J. Am. Soc. Mass Spectrom.* 1992, 3, 216–224.
- (7) Fenn, J. B. *J. Am. Soc. Mass Spectrom.* 1993, 4, 524–535.
- (8) Tang, L.; Kebarle, P. *Anal. Chem.* 1993, 65, 3654–3663.
- (9) Siu, K. W. M.; Guevremont, R.; Le Blanc, J. C. Y.; O'Brien, R. T.; Berman, S. S. *Org. Mass Spectrom.* 1993, 28, 579–584.
- (10) Fenn, J. B. *J. Am. Soc. Mass Spectrom.* 1993, 4, 524–535.
- (11) Kostainen, R.; Bruins, A. P. *Rapid Commun. Mass Spectrom.* 1994, 8, 549–558.
- (12) Wang, G.; Cole, R. B. *Anal. Chem.* 1994, 66, 3702–3708.
- (13) Le Blanc, J. C. Y.; Wang, J.; Guevremont, R.; Siu, K. W. M. *Org. Mass Spectrom.* 1994, 29, 587–593.
- (14) Gatlin, C. L.; Tureček, F. *Anal. Chem.* 1994, 66, 712–718.
- (15) Hagar, D. B.; Dovichi, N. J.; Klassen, J.; Kebarle, P. *Anal. Chem.* 1994, 66, 3944–3949.
- (16) Wiim, M. S.; Mann, M. *Int. J. Mass Spectrom. Ion Processes* 1994, 135, 167–180.
- (17) Van Berkel, G. J.; McLuckey, S. A.; Glish, G. L. *Anal. Chem.* 1992, 64, 1586–1593.
- (18) Van Berkel, G. J.; Zhou, F. *Anal. Chem.* 1995, 67, 2916–2923.
- (19) Van Berkel, G. J.; Zhou, F. *J. Am. Soc. Mass Spectrom.*, in press.
- (20) Zhou, F.; Van Berkel, G. J. *J. Am. Chem. Soc.* 1994, 116, 5485–5488.
- (21) Zhou, F.; Van Berkel, G. J. *Anal. Chem.* 1995, 67, 3643–3649.
- (22) Xu, X.; Nolan, S. P.; Cole, R. B. *Anal. Chem.* 1994, 66, 119–125.
- (23) Dupont, A.; Gisselbrecht, J.-P.; Leize, E.; Wagner, L.; Van Dorsselaer, A. *Tetrahedron Lett.* 1994, 35, 6083–6086.
- (24) Liu, T.-Y.; Shiu, L.-L.; Luh, T.-Y.; Her, G.-R. *Rapid Commun. Mass Spectrom.* 1995, 9, 93–96.
- (25) Bord, A. M.; Colton, R.; D'Agostino, A.; Downard, A. J.; Traeger, J. C. *Anal. Chem.* 1995, 67, 1691–1695.

* Current address: Department of Chemistry, University of Wisconsin–Eau Claire, Eau Claire, WI 54702.

(1) Kebarle, P.; Tang, L. *Anal. Chem.* 1993, 65, 972A–986A.
(2) Ikononou, M. G.; Blades, A. T.; Kebarle, P. *Anal. Chem.* 1991, 63, 1989–1998.

phase by the mass spectrometer. Nevertheless, the imprecise understanding of this process has blocked its routine use for analyte ionization/detection. For example, in the previous studies,^{17,22} analytes with redox potentials less than about 0.3 V (vs SCE) were found to be almost completely oxidized by this process. However, the efficiency of electrochemical ionization dramatically decreased for analytes with redox potentials greater than 0.3 V. For analytes with redox potentials greater than about 0.6 V, gas-phase ion signals were detected only at relatively high analyte concentrations (i.e., 0.01–0.1 mM or more). If analyte redox potentials exceeded about 1.0 V, detection even at much higher analyte concentration proved difficult.

Recently, we have been able to determine from a solution-based optical study that the electrolytic nature of ES is analogous to that of a controlled-current electrolytic (CCE) flow cell.^{18,26} On the basis of that understanding, the key requirements for efficient neutral analyte oxidation/ionization in solution via this electrolytic process, including ionization of difficult to oxidize species (i.e., $E > 1.0$ V), and subsequent gas-phase detection of these electrochemically generated ions became apparent.¹⁸ In this paper, we expand on that solution-based optical study by demonstrating that ES-MS, when operated under conditions that meet these key requirements, can be used routinely for efficient ionization and detection of neutral analytes from any one of several compound classes (e.g., metallocenes, metalloporphyrins, and polycyclic aromatic hydrocarbons (PAHs)).

EXPERIMENTAL SECTION

Analyte/Electrolyte Solutions. All analytes, solvents, and the electrolytes were obtained from commercial suppliers and used without further purification. The various solvent systems and analyte solutions were prepared daily using the appropriate amounts of the respective analytes, HPLC-grade methylene chloride and acetonitrile, and lithium trifluoromethane sulfonate, i.e., lithium triflate. The conductivity of various prepared acetonitrile/methylene chloride solutions (1:1 v/v) containing known amounts of lithium triflate were measured at 25 °C using a YSI Model 35 conductivity detector (Yellow Springs, OH) with a YSI 3400 series dip cell, as previously described.¹⁸ The conductivities of these acetonitrile/methylene chloride solutions (0, 0.001, 0.01, 0.10, 1.0, and 9.0 mM lithium triflate) were measured as 1.4, 3.1, 3.7, 15, 97, and $880 \times 10^{-6} \Omega^{-1} \text{ cm}^{-1}$, respectively.

Mass Spectrometry. All ES-MS experiments were carried out using a Finnigan-MAT ion trap mass spectrometer (ITMS) adapted in-house for pneumatically assisted ES-MS.^{27–29} A syringe pump (Harvard Apparatus, Inc., Cambridge, MS) was used to deliver analyte solutions at a rate of 5–40 $\mu\text{L}/\text{min}$ through a short length of 254 μm i.d. Teflon tubing that connected to a dome-tipped 304 stainless steel capillary (6.5 cm long, 127 μm i.d., 500 μm o.d.; Scientific Instrument Services, Ringoes, NJ) or a dome-tipped platinum capillary (6.5 cm long, 210 μm i.d., 400 μm o.d.; Hamilton, Reno, NV) within a pneumatically assisted ES source.²⁹ Nitrogen gas, at a backing pressure of 30–60 psi, was used for pneumatically assisting the ES process. The ES capillary was held

at a potential of 1.0–5.0 kV and placed ~ 2.0 cm from the front aperture plate of the ITMS. The ES current was measured at the front aperture plate of the ITMS by grounding this plate through a Keithley Model 610C electrometer (Cleveland, OH).

Flow injection experiments were carried out at 20 $\mu\text{L}/\text{min}$ using the syringe pump to deliver the carrier solution through Teflon tubing, to a Rheodyne (Cotati, CA) Model 7520 injector with a 0.5 μL internal sample chamber and then through a short length (~ 15 cm) of 100 μm i.d. fused-silica capillary to which the pneumatically assisted ES source (stainless steel spray capillary, 4 kV) was connected.

RESULTS AND DISCUSSION

CCE Nature of an ES Ion Source. The electrolytic process inherent in ES, as demonstrated in our previous solution-based optical study,¹⁸ is operationally analogous to controlled-current electrolysis carried out in a CCE flow cell. (For clarity, the discussion will be limited to the positive ion mode of ES operation and the concomitant oxidation reactions that occur in the ES capillary. Similar considerations are valid for analyte reduction in the negative ion mode of operation.) In this electrolytic system, the ES current, i_{ES} , and the faradaic current resulting from the electrolysis reactions occurring at the metal/solution interface within the metal ES capillary, i_{F} , are equal in magnitude because of charge balance considerations. This relationship is expressed by Faraday's law, shown in eq 1, where

$$i_{\text{ES}} = i_{\text{F}} = \sum_j n_j A_j F v_j \quad (1)$$

n_j is the number of electrons involved in the oxidation of one molecule of species j , A_j is the concentration of species j oxidized, F is the Faraday constant (9.648×10^4 C/mol), and v_j is the solution flow rate through the ES capillary. The individual species, j , oxidized to supply i_{F} are oxidized in order of their increasing redox potentials until the required current is supplied. The actual charge balancing redox reactions that occur at the metal/solution interface in the ES capillary, and the extent to which those reactions take place, are a function of the relative concentrations and redox potentials of the various species in the solution (including the metal capillary), the availability of a species for reaction at the metal/solution interface (which is related to capillary dimensions, solution flow rate, and species concentration), and the magnitude of i_{ES} (which is related to the nature of the solvents, solution conductivity, and the electric field at the capillary tip).^{1,18}

Utilization of the CCE Process in ES for Analyte Ionization/Detection. On the basis of the operation of an ES ion source as a CCE cell, three key requirements for effective utilization of this inherent electrolytic process for neutral analyte ionization and sensitive gas-phase detection in ES-MS are evident.¹⁸ First, the magnitude of i_{ES} must be sufficient for oxidation of the molar equivalent of all species available for reaction in the ES capillary that are as easily or more easily oxidized than the targeted analyte, including all of the analyte (see eq 1, $i_{\text{ES}} = i_{\text{F}}$). Second, the analyte must be available for reaction at the metal/solution interface in the ES capillary. Third, the steps taken to ensure the first two requirements must not inhibit the formation of gas-phase ions from the ions generated electrolytically in solution.

To meet the first requirement, the magnitude of i_{ES} required for oxidization of a given amount of analyte could be reduced by

(26) Bard, A. J.; Faulkner, L. R. *Electrochemical Methods*; John Wiley & Sons, Inc.: New York, 1980.

(27) Van Berkel, G. J.; Glish, G. L.; McLuckey, S. A. *Anal Chem.* **1990**, *62*, 1284–1289.

(28) McLuckey, S. A.; Van Berkel, G. J.; Glish, G. L.; Henion, J. D.; Huang, E. C. *Anal Chem.* **1991**, *63*, 375–383.

(29) Van Berkel, G. J.; Quinones, M. A.; Quirke, J. M. E. *Energy Fuels* **1993**, *7*, 411–419.

eliminating from the solvent system all species whose redox potentials are lower than that of the analyte, which might include particular solvents, contaminants, electrolytes, other analytes, or even the ES capillary.^{2,3,18} In addition, the magnitude of i_{ES} might be increased by adjusting one or more experimental parameters that affect i_{ES} , as shown in the Hendricks equation (eq 2).¹ In

$$i_{ES} = H\nu_i^{\nu} \sigma^{\nu} E_{ES}^{\epsilon} \quad (2)$$

$$\sigma = \lambda_m^0 C_E; \quad E_{ES} = 2V_{ES}/r_{ES} \ln(4d/r_{ES})$$

this equation, the term H is a constant, the value of which depends on the dielectric constant and surface tension of the solvent, ν_i is the solution flow rate through the ES capillary, σ is the conductivity of the solution, and E_{ES} is the imposed electric field at the capillary tip. The value of σ is a function of λ_m^0 , the limiting molar conductivity of the electrolyte, and C_E , the concentration of the electrolyte in solution. The value of E_{ES} is a function of the voltage applied to the ES capillary, V_{ES} , the outer radius of the capillary, r_{ES} , and the distance of the capillary tip from the counter electrode, d . The value of the individual exponents in the equation, viz., ν , n , and ϵ , are interrelated and may vary as the individual experimental parameters are varied.¹⁸ In practice, we found that the simplest means to substantially increase i_{ES} over that current obtained under optimized ES conditions (i.e., $V_{ES} \approx 4\text{--}5$ kV with a fixed solvent system, capillary size, and ES source geometry) was to increase solution conductivity, σ , by addition of an electrolyte to the solvent system.^{18,19} The electrolytes normally employed in electrochemical experiments²⁰ are most suitable for this purpose as they are difficult to oxidize and therefore do not contribute to the faradaic current.

To ensure the second requirement, the time for transport of the analyte to the metal/solution interface (mainly via diffusion) must be short relative to the time the analyte remains within the capillary (i.e., the electrolysis time). The flow rate of the analyte through the capillary and the capillary dimensions, along with analyte concentration, will affect this availability. In general, operating at slower flow rates was found in our previous studies to enhance electrolysis efficiency, presumably through increased availability of the analyte for reaction.^{18,19} Although not investigated here, the use of narrower bore capillaries might also enhance analyte availability by shortening analyte diffusion time.

The major obstacle to meeting the third requirement is the necessary addition of an electrolyte to the analyte solution to increase the magnitude of i_{ES} for efficient analyte electrolysis, as discussed above. Tang and Kebarle^{4,8} have shown that the mass spectrometrically detected ion current for an analyte of interest, I_{A^+} , may be suppressed by the presence of other ions ("foreign electrolytes") in solution that have a greater propensity (termed k) for formation of gas-phase ions, as expressed by eq 3, where p

$$I_{A^+} = pf \frac{(k_A \cdot C_{A^+})}{(k_A \cdot C_{A^+}) + (k_E \cdot C_{E^-})} i_{ES} \quad (3)$$

is a constant expressing the efficiency of the mass spectrometer for detecting the gas-phase ions produced by the ES source, f is the fraction of droplet charge converted to gas-phase ions, C_{A^+} and C_{E^-} are the concentrations of analyte and electrolyte ions present in the electrosprayed solution, respectively, and k_{A^+} and

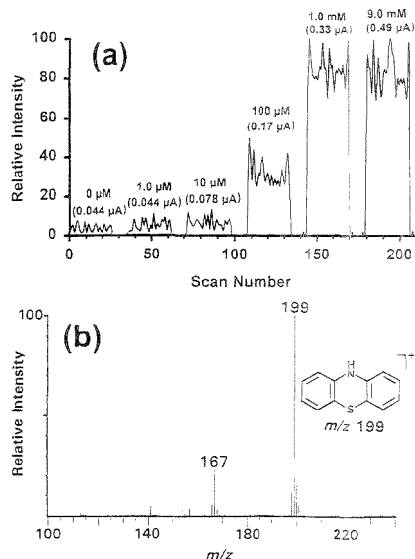


Figure 1. (a) Ion current intensities for the radical cation of phenothiazine (m/z 199, $E = 0.56$ V vs SCE²⁰) measured in six separate continuous infusion experiments in which acetonitrile/methylene chloride (1:1 v/v) solutions of phenothiazine (30 μ M) containing various amounts of lithium triflate were sprayed. The amounts of electrolyte added and the resultant magnitude of i_{ES} (in parentheses) are shown over the respective ion currents. The solution flow rate (40 μ L/min) and ES voltage (4 kV) were held constant. (b) ES mass spectrum obtained by averaging over the ion current profile in (a) that corresponds to the phenothiazine solution containing 1.0 mM lithium triflate.

k_{E^-} are the rate constants expressing the rate of transfer of the respective ions from the charged droplets to the gas phase. Therefore, to minimize problems with signal suppression, it is necessary to select an electrolyte whose propensity for gas-phase ion formation, k , is small relative to the analyte ion, and to use it at the lowest concentration possible to provide the required i_{ES} . In the present study, acetonitrile/methylene chloride (1:1 v/v) was used as the solvent system to provide experimental consistency, as it dissolved all the analytes investigated and provided sufficient polarity for electrolyte dissociation. The electrolytes used most commonly for electrochemistry in such nonaqueous solvent systems (i.e., quaternary ammonium salts) have a very large propensity for gas-phase ion formation, and concentrations even as low as ten to a few hundred micromolar were found to lead to significant analyte ion signal suppression. Fortunately, an alternative electrolyte, viz., lithium triflate, was found to have a much lower suppression effect, which enabled its use in the present work at concentrations up to the few millimolar needed for efficient analyte electrolysis.^{18,19,21} Signal suppression caused by this lithium salt is assumed to be less severe than that caused by the quaternary ammonium salts because the small, highly solvated lithium cation has a low propensity to form gas-phase ions relative to both the quaternary ammonium ions and the analyte ions under study.¹

Gas-Phase Detection of the Electrolytically Generated Analyte Ions. Figure 1a shows the ion current intensities for

the radical cation of phenothiazine (m/z 199) that were recorded in six separate continuous infusion experiments. The voltage applied to the stainless steel capillary (4 kV), the solution flow rate through the system (40 $\mu\text{L}/\text{min}$), and the concentration of the phenothiazine (30 μM) in the solutions were kept constant, but the solution conductivity was increased stepwise through the addition of increasing amounts of lithium triflate to the solution. Also shown in this figure are the respective electrolyte concentrations and measured values of i_{ES} . These data show that the abundance of the phenothiazine radical cation increases by over an order of magnitude as the electrolyte concentration (and, therefore, solution conductivity) is increased, because of the concomitant increase in the magnitude of i_{ES} (see eq 2). This outcome indicates that at least a portion of the increasing faradaic current, i_{F} (where $i_{\text{ES}} = i_{\text{F}}$), is supplied by oxidation/ionization of phenothiazine ($E = 0.56 \text{ V vs SCE}^{30}$). At 9.0 mM electrolyte added, the increase in the gas-phase ion signal for the radical cation levels off, even though i_{ES} increases. Even if one assumes that all of i_{F} is supplied by analyte oxidation, the recorded i_{ES} for 1.0 mM added electrolyte is calculated using eq 1 to be sufficient for oxidation of only about 17% of the 30 μM phenothiazine sample continuously flowing through the system. The increase in i_{ES} as the electrolyte concentration is increased to 9.0 mM might, therefore, be expected to result in oxidation of more of the phenothiazine, leading to a further increase in the radical cation signal. The signal probably levels off, however, because of the competition between increased analyte oxidation/ionization (i.e., more analyte ions in solution) and suppression of gas-phase analyte ion signal due to the higher electrolyte concentration (eq 3). An additional factor to consider is the availability of the analyte for reaction. At this relatively high flow rate, diffusion of the analyte to the metal/solution interface might be a limiting factor in allowing further analyte oxidation.

Panel b of Figure 1 is the mass spectrum obtained from the phenothiazine sample containing 1.0 mM lithium triflate, illustrating the quality of the mass spectra that can be obtained in this manner. The two major peaks observed, with an excellent signal/background ratio, correspond to the radical cation (m/z 199) and a lesser abundant fragment ion (m/z 167) produced in the atmospheric sampling interface of the ES source. Note that no ions associated with the lithium triflate are observed within this m/z window.

Similar experiments were carried out with five additional neutral analytes, including perylene ($E = 1.04 \text{ V vs SCE}^{30}$) and anthracene ($E = 1.19 \text{ V vs SCE}^{30}$), which are relatively difficult to oxidize, and one salt, viz., tetrabutylammonium tetrafluoroborate. These data are summarized by the plots in Figure 2, which show the normalized relative intensities of each molecular monocation as a function of the electrolyte concentration in the solution (Figure 2a) and as a function of the measured i_{ES} (Figure 2b). The general trends in the data are the same as those noted in Figure 1a, but several points are noteworthy. First, the gas-phase ion signal observed for the tetrabutylammonium cation (TBA^+ , m/z 242) first increases as electrolyte is added, but as electrolyte concentration increases beyond 0.1 mM, the signal is suppressed. It is well known that ES performs best with some electrolyte in solution because of more efficient electrophoretic charge separation and more efficient droplet formation.¹ Therefore, the increase

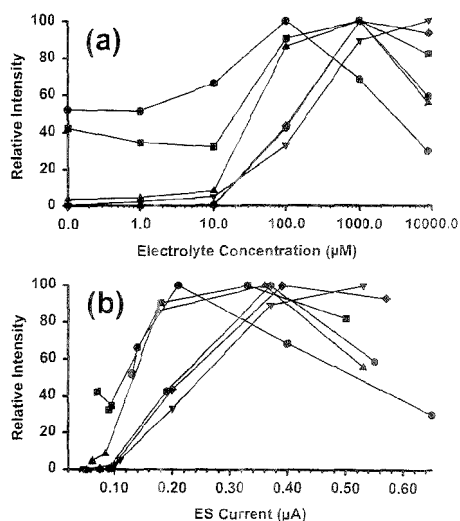


Figure 2. Normalized relative intensities recorded for the respective molecular monocations of six separate analytes as a function of (a) the concentration of electrolyte (lithium triflate) added to the solution and (b) the measured i_{ES} . The voltage applied to the stainless steel ES capillary (4 kV), the solution flow rate through the system (acetonitrile/methylene chloride (1:1 v/v), 40 $\mu\text{L}/\text{min}$), and the concentration of the respective analytes were kept constant: tetrabutylammonium tetrafluoroborate (\bullet , 15 μM , m/z 242), decamethylferrocene (\blacksquare , 25 μM , m/z 326, $E = -0.11 \text{ V vs SCE}^{31}$), ferrocene (\blacktriangle , 25 μM , m/z 186, $E = 0.31 \text{ V vs SCE}^{26}$), $\text{Ni}^{\text{II}}\text{OEP}$ (\blacktriangledown , 8.5 μM , m/z 590–593, $E = 0.73 \text{ V vs SCE}^{26}$), perylene (\blacklozenge , 22 μM , m/z 252, $E = 1.04 \text{ V vs SCE}^{30}$), and anthracene (\bullet , 34 μM , m/z 178, $E = 1.19 \text{ V vs SCE}^{30}$).

in TBA^+ signal with small amounts of electrolyte added is not surprising. Interestingly, however, the TBA^+ signal is suppressed at much lower concentrations of the electrolyte than all other analytes examined. This observation may be explained by the fact that TBA^+ is a preformed ion, while the other analytes are originally neutral in solution and are oxidized/ionized via the CCE process. As discussed above, as the electrolyte concentration increases, the extent of neutral analyte electrolysis (i.e., ionization in solution) may increase because the magnitude of i_{ES} increases. It is probable, therefore, that the positive effect that increasing electrolyte concentration has on the degree of neutral analyte oxidation outweighs the detrimental effect of signal suppression until millimolar concentrations of electrolyte are added. Thus, the suppression effect does not reduce the gas-phase ion signals for neutral analytes ionized via the electrolytic process until higher concentrations of electrolyte are present in the solution. Note also that the signals from the most easily oxidized analytes, viz., decamethylferrocene ($E = -0.11 \text{ V vs SCE}^{31}$) and ferrocene ($E = 0.31 \text{ V vs SCE}^{26}$), are the highest among all the analytes at the lower magnitudes of i_{ES} . Presumably, these neutral species are more efficiently oxidized at lower values of i_{ES} relative to the other

(30) Janz, G. J.; Tomkins, R. P. T. *Nonaqueous Electrolytes Handbook*; Academic Press: New York, 1973, Vol II.

(31) Geiger, W. E. In *Organometallic Radical Processes*; Troglor, W. C., Ed.; Journal of Organometallic Chemistry Library 22; Elsevier Science Publishing Co., Inc.: New York, 1990.

(32) Fuhrhop, J.-H.; Kadish, K. M.; Davis, D. G. *J. Am. Chem. Soc.* 1973, 95, 5140–5147.

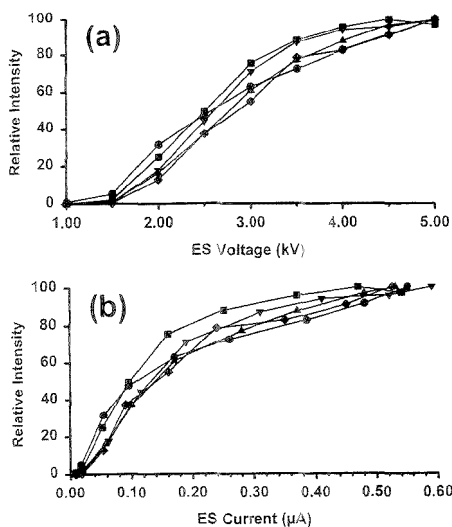


Figure 3. Normalized relative intensities recorded for the respective molecular monocations of five separate analytes as a function of (a) the voltage applied to the ES capillary and (b) the measured i_{ES} . The concentration of the electrolyte in the solutions (acetonitrile/methylene chloride (1:1 v/v), 1.0 mM lithium triflate), the solution flow rate through the system (40 $\mu\text{L}/\text{min}$), and the concentration of the respective analytes were kept constant: tetrabutylammonium tetrafluoroborate (\bullet , 15 μM , m/z 242), ferrocene (\blacksquare , 25 μM , m/z 186, $E = 0.31$ V vs SCE^{28}), $\text{Ni}^{\text{II}}\text{OEP}$ (\blacktriangle , 8.5 μM , m/z 590–593, $E = 0.73$ V vs SCE^{32}), perylene (∇ , 22 μM , m/z 252, $E = 1.04$ V vs SCE^{30}), and anthracene (\blacklozenge , 34 μM , m/z 178, $E = 1.19$ V vs SCE^{30}).

compounds tested because few other species in the system are more easily oxidized.

The data in Figure 3 show that the gas-phase ion signals for electrolytically ionized analytes also increase dramatically as the voltage applied to the ES capillary, V_{ES} , is increased. This figure shows the normalized relative intensities of the molecular monocations for most of the same analytes discussed above as a function of V_{ES} , which affects the electric field at the capillary tip, E_{ES} , and therefore also affects the magnitude of i_{ES} (see eq 2). In this case, the solution flow rate (40 $\mu\text{L}/\text{min}$) and electrolyte concentration (1.0 mM lithium triflate) were kept constant but V_{ES} was varied from 1 to 5 kV. The data show that as V_{ES} increases, the magnitude of i_{ES} increases, and the gas-phase ion signals due to the electrolysis products also increases. For each of the analytes studied, their respective gas-phase ion signals increase dramatically as V_{ES} increases from 1 to 3 kV and continue to increase more gradually from 3 to 5 kV. From our previous work,¹⁸ we know that the extent of analyte electrolysis continues to increase as i_{ES} increases, provided the analyte is available for reaction. Therefore, this leveling off of ion signal, which occurs for the tetrabutylammonium cation as well as for the neutral analytes, is probably due to aspects of the ES process involved with liberation of ions from solution or sampling of ions by the mass spectrometer. In any case, the highest gas-phase ion signal levels are recorded at the highest values of V_{ES} , providing the highest values of i_{ES} , which correlates with the conditions expected to provide maximum analyte oxidation.

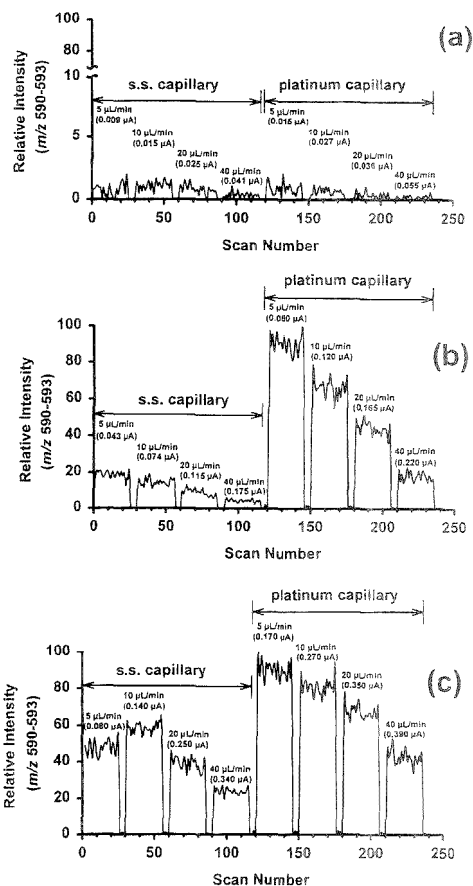


Figure 4. (a) Ion current intensities for the radical cation of $\text{Ni}^{\text{II}}\text{OEP}$ (m/z 590–593) measured in continuous infusion experiments in which acetonitrile/methylene chloride (1:1 v/v) solutions of $\text{Ni}^{\text{II}}\text{OEP}$ (10 μM , $E = 0.73$ V vs SCE^{32}) containing (e) no added electrolyte, (b) 0.1 mM lithium triflate, and (c) 1.0 mM lithium triflate were sprayed from stainless steel and platinum capillaries at flow rates of 5, 10, 20, and 40 $\mu\text{L}/\text{min}$. The respective flow rates and measured values of i_{ES} are shown in the figures. The signal levels in (a), (b), and (c) are each normalized to the maximum signal recorded in (b).

The data presented in Figure 4 illustrate how the composition of the metal ES capillary, either stainless steel or platinum, and the solution flow rate through these respective capillaries affected the observed intensity of the gas-phase ion signal for an electrolytically generated analyte ion. These data were recorded by continuously infusing a 10 μM solution of nickel(II) octaethylporphyrin ($\text{Ni}^{\text{II}}\text{OEP}$, $E = 0.73$ V vs SCE^{32}), containing either no electrolyte, 0.1 mM electrolyte, or 1.0 mM electrolyte, through the respective metal capillaries at flow rates of 5, 10, 20, and 40 $\mu\text{L}/\text{min}$. The value of i_{ES} recorded in each experiment is shown, along with the flow rate, above the respective ion current profiles in the figure. In the case where no electrolyte is added to the solution (Figure 4a), the value of i_{ES} and the gas-phase analyte ion signal for the radical cation of $\text{Ni}^{\text{II}}\text{OEP}$ are low for both

capillaries at all flow rates. On the basis of Faraday's law (eq 1), the magnitudes of i_{ES} necessary for complete oxidation of the porphyrin (10 μM) at each of the respective flow rates, assuming that no other reactions supply i_F , are 0.08 (5 $\mu\text{L}/\text{min}$), 0.16 (10 $\mu\text{L}/\text{min}$), 0.32 (20 $\mu\text{L}/\text{min}$), and 0.64 μA (40 $\mu\text{L}/\text{min}$). The currents measured at each flow rate (assuming again only oxidation of the porphyrin) are sufficient to oxidize a maximum of only 5%–20% of the total amount of porphyrin present, which explains the low gas-phase ion signals.

With 0.1 mM electrolyte added to the solution (Figure 4b), the magnitude of i_{ES} with both capillaries, at all flow rates, substantially increased. As a result, the degree of oxidation and the gas-phase ion signal levels also increased. In general, these are the results expected on the basis of the discussion and data already presented above. Of particular note in this data set, however, is the fact that the $\text{Ni}^{\text{II}}\text{OEP}$ radical cation signal observed when the platinum capillary was used is substantially greater than that observed when the stainless steel capillary was used. We attribute this to the resistance of platinum to oxidation compared to stainless steel. Evidence presented by both Kebabian and co-workers³ and our group¹⁹ has demonstrated that a substantial fraction of the total faradaic current in ES may be supplied, in the absence of more easily oxidized species, by oxidation of the iron in the stainless steel ES capillary. The occurrence of this oxidation reaction reduces the amount of i_F that might otherwise be supplied by oxidation of an analyte in solution. Using the ES capillary fabricated from platinum, which is much more difficult to oxidize than the iron in stainless steel,^{19,26} allows for a greater fraction of i_F to be supplied by the oxidization of solution species, including the analyte. As such, more $\text{Ni}^{\text{II}}\text{OEP}$ ions are created in the solution within the platinum capillary compared to within the stainless steel capillary, all other factors being equal. However, a closer examination of the data indicates that this is not the only factor at work. At each flow rate, the magnitude of i_{ES} measured is always greater in the case of the platinum capillary, which translates to a greater degree of analyte oxidation and a correlated increase in the gas-phase ion signal. The slightly different dimensions of the respective metal ES capillaries and slightly different geometries of the ES sources might explain this difference in i_{ES} . Another, more speculative, possibility might be the change in solution composition (e.g., the type and amount of ionic and neutral species present) that results from the different redox reactions that take place in the two metal capillaries. Such solution composition changes might affect the solution conductivity or degree of charge separation that can occur in the capillary and, therefore, also affect the magnitude of i_{ES} .

The data in Figure 4b (and Figure 4c) also show that, regardless of the capillary material, the gas-phase signal for the $\text{Ni}^{\text{II}}\text{OEP}$ radical cation decreases as flow rate increases. On the basis of Faraday's law (eq 1) and the measured values of i_{ES} in Figure 4b for the platinum capillary, we calculate that 100%, 75%, 52%, and 34% of the current needed for complete analyte oxidation is available at flow rates of 5, 10, 20, and 40 $\mu\text{L}/\text{min}$, respectively. The gas-phase ion signals change in these same relative proportions as flow rate is changed. Therefore, this decrease in ion signal with increasing flow rate probably results, at least in part, because of the increased rate of $\text{Ni}^{\text{II}}\text{OEP}$ transfer through the capillary without a sufficient increase in i_{ES} to enable the same degree of analyte oxidation. Another contributing factor to reduced signal levels as flow rate increases may be the diffusion-

limited availability of the analyte for reaction at the metal/solution interface in the capillary.^{18,19}

The data in Figure 4c were obtained with a $\text{Ni}^{\text{II}}\text{OEP}$ solution containing 1.0 mM electrolyte. This further increase in electrolyte concentration resulted in approximately a factor of 2 increase in the magnitude of i_{ES} measured at all flow rates, with both capillaries, when compared to the data in Figure 4b (0.1 mM electrolyte). Furthermore, the gas-phase ion signal levels recorded increased in all cases except for those measured at 5 $\mu\text{L}/\text{min}$ when the platinum capillary was used. On the basis of Faraday's law and the amount of porphyrin present, this exception might be explained by the fact that the current necessary for complete oxidation of the porphyrin was already provided with 0.1 mM electrolyte in the solution (i.e., 0.08 μA , Figure 4b). Thus, a further increase in the magnitude of i_{ES} results in no additional analyte oxidation, and the gas-phase ion signal does not increase. Nonetheless, the signal levels recorded at the higher flow rates are enhanced when more electrolyte is used, because the higher magnitudes of i_{ES} do provide, in these cases, for a greater degree of electrolysis (eq 1). The data in Figure 4c relating to the stainless steel capillary show that although the increase in i_{ES} serves to increase the gas-phase ion signals, these signal levels are still less than those recorded using the platinum capillary. As discussed above, this result is attributed to the oxidation of iron in the stainless steel capillary, which limits the proportion of i_F that can be supplied by oxidation of $\text{Ni}^{\text{II}}\text{OEP}$. Another interesting feature in these data is the slight decrease in i_{ES} and the $\text{Ni}^{\text{II}}\text{OEP}$ signal intensity at 5 $\mu\text{L}/\text{min}$. At this point, we have no solid explanation for this behavior.

Application to Low-Level Detection. As the data presented above have already demonstrated, the CCE process inherent to the operation of the ES ion source can, if used properly, efficiently oxidize/ionize neutral analytes in solution for subsequent gas-phase detection by the mass spectrometer. Furthermore, we have found that by operating under these conditions, the detection levels obtained for the ES-MS analysis of many neutral compounds, even when operating with the stainless steel capillary, are often comparable to those levels achieved for preformed ionic compounds. This is true even for species relatively difficult to oxidize (i.e., $E > 1.0$ V vs SCE), as demonstrated by the data in Figure 5. This figure shows the extracted ion current profiles for the radical cation of perylene (m/z 252, $E = 1.04$ V vs SCE²⁰) obtained from three replicate injections of a blank solution and increasing quantities of perylene into a flowing stream of acetonitrile/methylene chloride (1:1 v/v, 20 $\mu\text{L}/\text{min}$) containing either no electrolyte (Figure 5a) or 1.0 mM electrolyte (Figure 5b). The detection level for perylene when no electrolyte was added to the solvent system appears to be between 1.3 and 13 pmol. However, the detection level is reduced to between 0.13 and 0.27 pmol when the solvent system contains 1.0 mM lithium triflate. This is an enhancement of the detection levels by about an order of magnitude. These detection levels of a few hundred femtomoles are comparable to or better than those levels that we have recorded with our instrumentation for many preformed ionic compounds under similar flow rate and solution conditions (see e.g., ref 28). Shown in Figure 5c is the averaged, background-subtracted mass spectrum obtained from the first 270 fmol injection recorded in Figure 5b. The signal level for the radical cation is several times higher than that of the background noise, providing a clear identification of the compound.

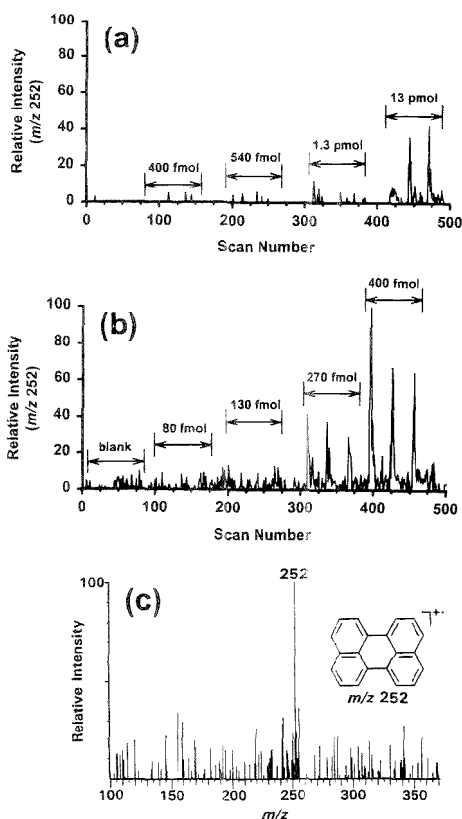


Figure 5. Extracted ion current profiles for the radical cation of perylene (m/z 252, $E = 1.04$ V vs SCE³⁰) obtained in flow injection experiments in which three replicate injections ($0.5 \mu\text{L}$) of a blank solution and analyte solutions of increasing analyte concentration (concentration shown in figure) were made into a flowing solution ($20 \mu\text{L}/\text{min}$) composed of (a) acetonitrile/methylene chloride (1:1 v/v) or (b) acetonitrile/methylene chloride (1:1 v/v) containing 1.0 mM lithium triflate. The perylene standards were prepared in a solution of the same composition as the carrier solution in the respective experiments. The blank injections are not shown in (a). Signal levels in (a) and (b) are each normalized to the maximum signal recorded in (b). (c) The averaged, background-subtracted ES mass spectrum obtained from the first 270 fmol injection of perylene as recorded in (b).

SUMMARY

Previous work has shown that the electrolytic process inherent to the operation of an ES ion source might have analytical utility

as a means to ionize and detect analytes originally neutral in solution using ES-MS. However, the incomplete understand of this electrolytic process hindered its general use in this regard. Our recent characterization of the ES ion source as a CCE cell¹⁸ provided the understanding necessary (i.e., knowledge of the proper ES operational conditions) to fully exploit the electrolytic process for neutral analyte ionization/detection in ES-MS. In this paper, we have demonstrated that an ES ion source, when operated under the appropriate conditions, can function as a very efficient CCE flow cell for oxidation/ionization of analytes originally neutral in solution with subsequent gas-phase detection of the ions. In comparison to previous work in this area,^{17,22} we demonstrated in this paper the ability to ionize/detect even relatively difficult to oxidize species ($E > 1.0$ V vs SCE) at levels comparable to those levels at which we detect preformed ionic species. Thus, using the ES source in the manner described in this work provides the means to expand further the neutral compound types amenable to sensitive analysis/detection by ES-MS as well as expanding the universality of ES as an ionization source.

From the electrochemical point of view, this operation of the ES ion source might be viewed as a means to monitor the products of controlled-current electrolysis on-line with mass spectrometry. Electrolysis carried out in this fashion certainly requires much less sample than traditional electrolytic methods and provides molecular weight and possible structural information for the ionic products of the reactions. Moreover, this electrolysis scenario is instrumentally much simpler than combining discrete electrochemical cells on-line with ES-MS for this same purpose.^{21,25}

ACKNOWLEDGMENT

This research was sponsored by the U.S. Department of Energy (USDOE), Office of Basic Energy Sciences, under contract DE-AC05-84OR21400, with Lockheed Martin Energy Systems, Inc. The authors thank Dr. Michelle V. Buchanan (ORNL) for critical review of the manuscript and for helpful comments. F.Z. acknowledges an appointment to the USDOE, Laboratory Cooperative Postgraduate Research Training Program, administered jointly by the Oak Ridge Institute for Science and Education (ORISE) and ORNL.

Received for review May 2, 1995. Accepted August 10, 1995.*

AC950426+

* Abstract published in *Advance ACS Abstracts*, September 15, 1995.

Direct Temperature Resolved HRMS of Fire-Retarded Polymers by In-Source PyMS on an External Ion Source Fourier Transform Ion Cyclotron Resonance Mass Spectrometer

Ron M. A. Heeren,* Chris G. de Koster, and Jaap J. Boon

FOM-Institute for Atomic and Molecular Physics, Kruislaan 407, 1098 SJ Amsterdam, The Netherlands

Rapid microscale analysis with high mass accuracy is demonstrated by direct temperature resolved desorption and pyrolysis from a Pt/Rh filament probe inside the external ion source of a 7-T FTICR-MS. High pressure generated during desorption and pyrolysis in the ion source does not interfere with analysis in the hydrocarbon-free UHV of the ICR cell, thus allowing short observation cycles at high resolution. The typical conditions achieved, a mass resolution $(m/\Delta m)_{50\%}$ equals 50 000 at m/z 600 with cycle times of 100 ms, were used to analyze isobaric compound mixtures generated by pyrolysis of brominated fire-retarded polymers spiked with antimony-containing synergists. Unknown fire-retarded polymer blends sampled from household appliances were found to contain brominated biphenyls, brominated diphenyl ethers, tetrabromobisphenol-A and its butylated isomers, polystyrene, and antimony oxides. High-resolution temperature-resolved analysis by "in-source" pyrolysis FTICR-MS confirms the elemental composition. The resolution is sufficient to separate the nominally isobaric ions from the antimony(III) oxide (Sb_4O_6) synergist and the *n*-butyl ether derivative of tetrabromobisphenol-A.

Identification of additives in compounded polymers is generally rather difficult because of the wide variety of available substances. Complex additive mixtures will normally be present at quite low (<1-5% w/w) concentrations compared to polymer and filler levels. Extraction of the additives from the polymer matrix is often required prior to chromatographic and spectroscopic analysis. Methods used for structural determination, separation, and quantitation of residual monomers and additives and determination of the molecular weight of polymers and additives include liquid chromatography, X-ray fluorescence, UV analysis, pyrolysis techniques, infrared and Raman spectroscopy, mass spectrometry, nuclear magnetic resonance spectroscopy, electron spin resonance spectroscopy, and thermal analysis.¹ Particularly, mass spectrometry offers a sensitive and selective method for the analysis of polymer systems and is widely applied in this field of research. Laser desorption (LD), laser-assisted pyrolysis, secondary ion mass spectrometry (SIMS), fast atom bombardment (FAB), plasma desorption (PD), and electrospray (ESI) ionization have been used to detect and to identify various nonvolatile compounds in polymers.²⁻⁷

Direct temperature resolved pyrolysis mass spectrometry (PyMS) has proven to be an analytical tool for fast analysis of unknown mixtures of polymers and for the presence of flame-retarding additives.^{8,9} Employment of a "hair-pin-type" filament pyrolysis probe in an in-source configuration provides faster heating rates and exact knowledge of the temperature of the sample on the probe during the experiment. Only minimal amounts of sample, typically 1 μ g, are necessary to obtain the total desorption/pyrolysis profiles. The high heating rate contrasts to the more conventional DPMS techniques using a small oven with a crucible inserted (or direct probe), where heating rates are much slower and sample temperature is dependent on thermal conductivity of the oven, the crucible, and both the IR absorption coefficient and the thermal conductivity of the sample, especially when a large amount of sample is used.¹⁰⁻¹⁴ In-source filament pyrolysis offers the possibility of studying the degradation characteristics of fire-retarding polymer blends as a function of temperature with a minimal sample amount and minimal sample pretreatment.^{15,16} Volatile molecules are thermally desorbed at the low-temperature end; pyrolysis of macromolecules and evaporation of metals take place at the high end of the temperature scale. Structural identification of unknown materials would be facilitated by performing accurate mass measurements of their molecular and fragment ions at high resolving power. If mass measurement accuracy of 5-10 ppm or better is obtained, elemental compositions of fragment ions can usually be deter-

* Fax: +31-20-3684106. E-mail: heeren@amolf.nl.
(1) Smith, G. S.; Smith, P. B.; Pasztor, A. J., Jr.; McKelvy, M. L.; Meunier, D. M.; Froelicher, S. W.; Ellaboudy, A. S. *Anal. Chem.* **1993**, *65*, 217R-243R.

(2) Lattimer, R. P.; Harris, R. E. *Mass Spectrom. Rev.* **1985**, *4*, 369-390.
(3) Lattimer, R. P.; Harris, R. E.; Rhee, C. K.; Schulten, H.-R. *Anal. Chem.* **1986**, *58*, 188-195.
(4) Hsu, A. T.; Marshall, A. G. *Anal. Chem.* **1988**, *60*, 932-937.
(5) Asamoto, B.; Young, J. R.; Citerin, R. J. *Anal. Chem.* **1990**, *62*, 61-70.
(6) Johlman, C. L.; Wilkins, C. L.; Hogan, J. D.; Donavan, T. L.; Laude, D. A., Jr.; Youssefi, M.-J. *Anal. Chem.* **1990**, *62*, 1167-1172.
(7) Creasy, W. R. *Polymer* **1992**, *33*, 4486-4492.
(8) Boon, J. J. *Int. J. Mass Spectrom. Ion Processes* **1992**, *118/119*, 755-787.
(9) Luijk, R.; Fureveen, J.; Comrandeur, J. M.; Boon, J. J. *Makromol. Chem. Macromol. Symp.* **1992**, *74*, 235-251.
(10) Dumler, R.; Thoma, H.; Lenoir, D.; Hutzinger, O. *Chemosphere* **1986**, *19*, 2023-2031.
(11) Dumler, R.; Lenoir, D.; Thoma, H.; Hutzinger, O. *J. Anal. Appl. Pyrolysis* **1989**, *16*, 153-158.
(12) Thoma, H.; Hauschulz, G.; Knorr, E.; Hutzinger, O. *Chemosphere* **1987**, *16*, 277-285.
(13) Hutzinger, O.; Dumler, R.; Lenoir, D.; Teuffl, C.; Thoma, H. *Chemosphere* **1989**, *18*, 1235.
(14) Dumler, R.; Lenoir, D.; Thoma, H.; Hutzinger, O. *Chemosphere* **1990**, *20*, 1867-1873.
(15) Luijk, R.; Wever, H.; Olie, K.; Govers, H. A. J.; Boon, J. J. *Chemosphere* **1991**, *22*, 1173-1183.
(16) Luijk, R.; Govers, H. A. J.; Eijkel, G. B.; Boon, J. J. *J. Anal. Appl. Pyrolysis* **1991**, *20*, 303-319.

mined, or at the very least, the number of compositions that need to be considered can be drastically reduced.

Important parameters for accurate mass measurement with a sector instrument are the scan rate and the setting of the ion optical slits. The slow scan rate, however, reduces the temperature resolution in direct temperature resolved high-resolution mass spectrometry (DT-HRMS). DT-HRMS on sector instruments also requires the continuous presence of a calibrant during the measurement to assign the mass scale and to compensate for the irreproducibility of the magnetic scans. As a result, the desorption and pyrolysis may be influenced by the presence of the calibrant. Finally, there is also a sensitivity problem as the resolution of the instrument increases. Narrowing the ion optical slits reduces the ion current and therefore reduces the signal-to-noise ratio.

The hyphenation of pyrolysis with FT ICR-MS provides a fast analytical method with a high mass resolving power. FT ICR-MS, as an established method for achieving high mass resolution and performing accurate mass measurements,¹⁷⁻²² has numerous features that make it a powerful method for the identification of polymer additives with "in-source" filament pyrolysis on an external ion source. Possible sources of error, such as magnetic field inhomogeneity²³ and magnetic drift,²⁴ are insignificant with superconducting magnets. The temporal stability of the superconducting magnetic field enables us to use FT ICR-MS to obtain highly reproducible results in mass measurement with signal averaging and without the use of internal mass reference compounds. Another important feature of FT ICR mass analysis is that sensitivity increases with mass resolution.²⁵ As a consequence of simultaneous (multichannel) ion detection, the acquisition rate exceeds the performance of quadrupole and magnetic sector mass analyzers, providing an ideal setting for temperature resolved in-source pyrolysis studies. An additional advantage of FT ICR-MS in the study of pyrolysis processes is that MSⁿ can be readily used for structural identification of desorption and pyrolysis products. In this work, the coupling of direct temperature resolved in-source pyrolysis with FT ICR-MS is, using flame-retarding additives in polymer or polymer blends as a test material, evaluated. The advantages of both methods have been combined thus drastically improving both the mass resolving power and the temporal resolution with which the desorption/pyrolysis process is studied.

EXPERIMENTAL SECTION

The direct temperature resolved pyrolysis experiments are performed on a modified Bruker APEX 7.0e FT ICR-MS equipped with a 7-T superconducting magnet. For these experiments we developed a new easy to use, hydrocarbon-free ultrahigh vacuum

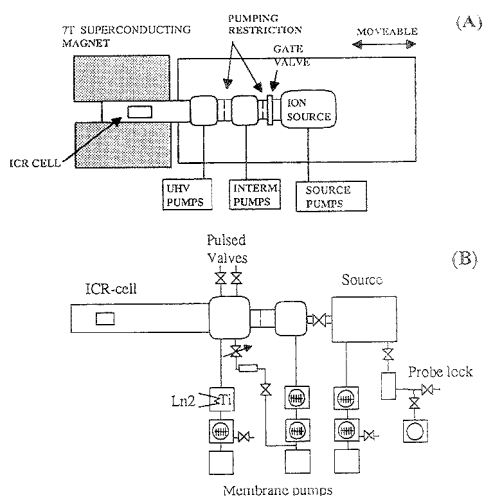


Figure 1. Experimental setup of the external ion source FT ICR-MS. Depicted are an overview of the experimental layout of the FT ICR-MS (A) and the schematical layout of the new hydrocarbon-free UHV system (B).

system as well as an in-house designed switchable EI/CI ion source. We have also equipped the instrument with a Bruker Infinity cell²⁶ for improved sensitivity. A system of electrostatic ion optical elements is used to transfer the ions produced in the external ion source to the ICR cell without radial losses. The Bruker data acquisition, control, and processing program XMASS is run on a SGI Indigo R4000 UNIX-based workstation in conjunction with an ASPECT X32/3 UNIX computer. Communication between both computers is achieved through an ethernet link.

A schematic drawing of the novel vacuum system is depicted in Figure 1. The use of a combination of turbomolecular pumps and turbodrag pumps backed by oil-free membrane pumps allows for a 4 orders of magnitude higher compression ratio for helium. The lack of oil-dependent rotary pumps leads to a vacuum system that combines the cleanliness of a cryopumped system and the ease of operation associated with a turbopumped system. This is advantageous while working with collisionally activated dissociation or during quadrupolar axialization experiments.²⁷ A differential pressure of 5 orders of magnitude between the ICR cell region and the source can be maintained without the use of cryopumps. This also eliminates disruptive vibrations originating from the rotating compressor typical for cryopumps. The base pressure in the ICR cell region amounts to 5×10^{-11} mbar during EI operation. This pressure can be achieved after a 2-day bakeout. The whole system can be heated to 175 °C while inserted in the room-temperature bore of the superconducting 7-T magnet.

In combination with the vacuum system development, a new switchable EI/CI ion source has been designed. Next to EI/CI operation and VUV ionization in combination with a direct insertion probe (DIP) or a direct inlet filament pyrolysis probe,

- (17) Marshall, A. G.; Comisarow, M. B. *J. Chem. Phys.* **1976**, *64*, 110-119.
 (18) Marshall, A. G.; Schweikhard, L. *Int. J. Mass Spectrom. Ion Processes* **1992**, *118/119*, 37-70.
 (19) Sack, R. M.; Gross, M. L. *Anal. Chem.* **1983**, *55*, 2419-2421.
 (20) Sack, R. M.; McGreery, D. A.; Gross, M. L. *Anal. Chem.* **1985**, *57*, 1290-1295.
 (21) Johlman, C. L.; Laude, D. A., Jr.; Wilkins, C. L. *Anal. Chem.* **1985**, *57*, 1040.
 (22) Johlman, C. L.; Laude, D. A., Jr.; Brown, R. S.; Wilkins, C. L. *Anal. Chem.* **1985**, *57*, 2726-2728.
 (23) Schuch, D.; Chung, K.-M.; Hartmann, H. *Int. J. Mass Spectrom. Ion Processes* **1984**, *56*, 109-121.
 (24) White, R. L.; Onyiriuka, E. C.; Wilkins, C. L. *Anal. Chem.* **1983**, *55*, 339-343.
 (25) White, R. L.; Ledford, E. B., Jr.; Ghaderi, S.; Wilkins, C. L.; Gross, M. L. *Anal. Chem.* **1980**, *52*, 1525-1527.

- (26) Caravatti, P.; Alleman, M. *Org. Mass Spectrom.* **1991**, *26*, 514-518.
 (27) Wood, T. D.; Ross, C. W., III; Marshall, A. G. *J. Am. Soc. Mass Spectrom.* **1994**, *5*, 900-907.

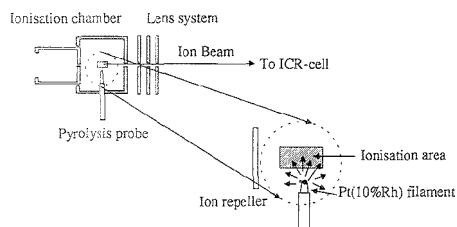


Figure 2. The in-source pyrolysis setup used for analysis of polybrominated fire retardants on the FT ICR-MS.

the same source can also be used for MALDI, SIMS, and FAB. To the knowledge of the authors, no commercially available FT ICR-MS external ion source has this high degree of flexibility. Using the SIMION²⁸ ion optics simulation program, the source has been designed to have maximum ion extraction efficiency in combination with the existing ion transfer optics. Moreover, the design makes the gas tightness of this source in CI mode 1 order of magnitude better than the conventionally used ion sources on commercial FT ICR-MS instruments.

The direct temperature resolved Py-FT ICR-MS experiments discussed in this paper have been performed using commercial mixtures of brominated fire retardants, their synergists, and polymer matrices as model compounds. In order to obtain a sufficiently large heating rate for pyrolysis to occur, we used a filament pyrolysis probe, with a 0.01-mm-diameter Pt-Rh (10%) wire. The probe is introduced into the ion source through a home-built, fully automated vacuum lock. After introduction in the source as depicted in Figure 2, the filament is on the same potential as the source housing in order not to disturb the electric field used for ion extraction. After a sample is applied to the filament, a home-built, workstation-controlled programmable power supply is activated by the acquisition software. For the experiments discussed in this paper, this power supply ramps a direct current starting at 0 A, with a slope of 1 A/min to a value of 1.1 A (unless otherwise noted). After the ramp has reached its maximum value, the 1.1 A is maintained for an additional 10 s before the power supply switches off. The filament temperature can be measured during a current ramp with an Iron Model 600C radiation thermometer as the filament can be observed through a quartz window when it is inserted into the source. The results of these measurements have been corrected for the IR transmission of the window. These temperature measurements have been used to calibrate the temperature scales throughout this paper.

During this ramp, the source pressure is monitored, which is indicative for the total amount of molecules desorbing from the probe, provided there is a sufficient amount of sample available to cause a measurable pressure rise during desorption.

The experimental sequence used for these types of experiments is depicted in Figure 3. After initialization of the current ramp through the filament, a delay is introduced, which enables us to examine a specific temperature region of the thermal desorption profile. This delay is followed by a set of m FT ICR-MS scans, each of which acquires n data points. In the present

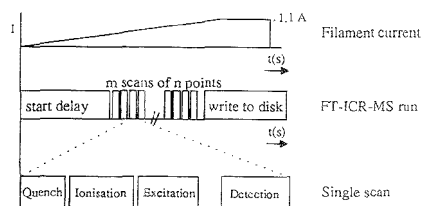


Figure 3. Experimental FT ICR-MS sequences used for high-resolution time-resolved thermal desorption experiments with a filament desorption probe.

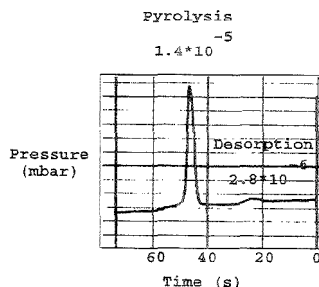


Figure 4. Source pressure measured above the source pump during a pyrolysis run of a complex polymer blend. Indicated are the maximum pressures in both the desorption and the pyrolysis regions. Baseline pressure is $\sim 1.3 \times 10^{-6}$ mbar.

experiments, we are limited to a total amount of 128K data points, which provides the upper limit for the product nm . Each FT ICR-MS scan in turn consists of a quench pulse, which removes all ions from the cell, and a postquench delay. This is followed by an ionization and ion introduction pulse and a postionization delay allowing the externally generated ions, generated with either 20- or 70-eV electron ionization, to equilibrate in the cell. The subsequent ion excitation pulse is followed by a postexcitation delay to allow the rf signal to decay. During acquisition of the time domain signal in the detection delay, the acquired data are stored into memory, and the memory address pointer is advanced after each data point taken. After one scan has been completed, the memory address pointer is not reset and this whole cycle is repeated m times until the whole 128-kB acquisition memory is filled. At that time, the data stored in memory are written to a hard disk for later processing. This processing consists of a sequence of m Fourier transformations of n points followed by a magnitude calculation for each spectrum thus obtained. No apodization or zero-filling was applied on any of the time-resolved spectra shown. The main advantage of this approach originates from the lack of "write-to-disk" events in between each mass spectrum. This results in a larger number of mass spectra acquired per unit time, and hence a higher time resolution.

For the calculation of the actual mass of an ion of a given elemental composition, we used the atomic masses tabulated in the 1983 atomic mass table composed by Wapstra et al.²⁹⁻³² The

(28) Dahl, D. A.; Dahlmann, J. E. SIMION v. 4.0, Idaho National Engineering Laboratory, Report No. EGG-CS-7233, Idaho Falls, ID, April 1988.

(29) Wapstra, A. H.; Audi, G. *Nucl. Phys. A* 1985, 432, 1-54.

(30) Wapstra, A. H.; Audi, G. *Nucl. Phys. A* 1985, 432, 55-139.

(31) Bos, K.; Audi, G.; Wapstra, A. H. *Nucl. Phys. A* 1985, 432, 140-184.

(32) Wapstra, A. H.; Audi, G.; Hoeksra, R. *Nucl. Phys. A* 1985, 432, 185-362.

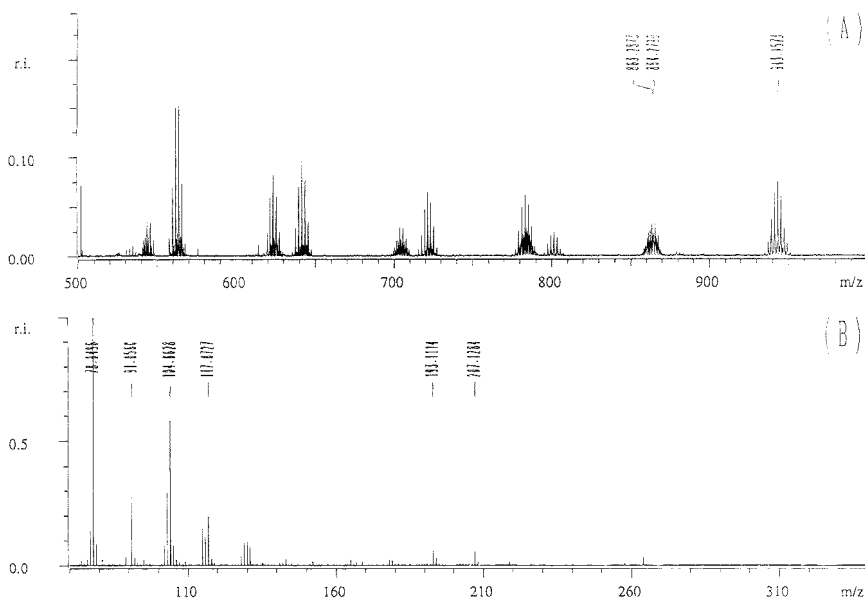


Figure 5. In-source pyrolysis FT ICR-MS of a commercially available polymer blend: (A) broad-band mass spectrum after an initial delay of 32 s; (B) mass spectrum after a delay of 36 s. Both spectra are single scans of 128K data points.

definition of mass accuracy (in ppm) in this study is

$$\text{mass accuracy} = (m_{\text{actual}} - m_{\text{measured}}) / m_{\text{averaged}} \times 10^6$$

Sample Preparation. The samples were taken from common household appliances. The polymeric materials of interest were inhomogeneous and not directly soluble in common solvents. These samples were pulverized with a SPEX 6700 freezer/mill. The mill operates at liquid nitrogen temperature ($-195.8\text{ }^{\circ}\text{C}$) and effectively pulverizes many materials that would stretch, distort, degrade, coagulate, or melt when ground at room temperature. The average polymer sample size varies from 1 to 2 g. The final size of the ground powder was approximately mesh 50–200 after three grinding periods of 2 min each with recooling of ~ 4 min between grinds. The powder (10 mg) was suspended in 2 mL of toluene (p.a). 1–2 μL aliquot of this solution was applied to the filament of the pyrolysis probe and subsequently dried in vacuo for 2 min. The filament probe was cleaned after each experiment by heating it to $\sim 1400\text{ }^{\circ}\text{C}$ in a gas flame for several seconds in air. The reference compounds were commercially available and used without further purification.

RESULTS AND DISCUSSION

I. Broad-Band Screening. Several polymer blends from household appliances like television sets, computer monitors, etc., were surveyed for the presence of flame-retarding additives with in-source pyrolysis FT ICR-MS. A few typical examples of these experiments will be discussed in this paper. The first step in the analytical protocol is a screening of the polymer sample for the presence of flame-retarding additives in broad-band mode with a wide mass range (m/z 21–5000). The delay between initialization

of the pyrolysis temperature program (current ramp through the filament) and the injection of the ions into the ICR cell is varied in order to sample desorption and pyrolysis products at different cross sections of the temperature profile. A typical pressure profile induced by thermal degradation of the sample is given in Figure 4. In this figure, two regions can be distinguished. The pressure rise at low temperatures (at ~ 25 s) is caused by evaporation of the nonbonded additives, whereas the second pressure rise is due to the pyrolysis of the polymer matrix. The correlation of the time scale mentioned in Figure 4 is obviously strongly dependent on sample size, sample composition, and filament length. The in-source pyrolysis FT ICR mass spectrum of a polymer system from a television set at 32 s after triggering of the heating program is given in Figure 5A. After a delay of 30–32 s, the temperature of the filament is sufficient to evaporate part of the additives by desorption from the polymer melt. The 32-s delay was followed by a single FT ICR-MS scan of the ions produced by electron ionization of the desorption products in broad-band mode with a bandwidth of 1.67 MHz and 128K data points. The lower mass limit was set at m/z 64.46. In this experiment the ICR cell was open to ions for 30 ms. A series of two peak clusters is observed in Figure 5A. These clusters are separated by ~ 80 Da. Both series show characteristic isotope patterns for deca-, nona-, octa-, hepta-, hexa-, and pentabromo compounds centered around m/z 943 (Br_{10}), 879 and 863 (Br_9), 801 and 783 (Br_8), 721 and 703 (Br_7), 641 and 623 (Br_6), and 561 and 543 (Br_5), respectively. Molecular ions at m/z 937 ($\text{C}_{12}^{79}\text{Br}_8^{81}\text{Br}_2$), 939 ($\text{C}_{12}^{79}\text{Br}_7^{81}\text{Br}_3$), 941 ($\text{C}_{12}^{79}\text{Br}_6^{81}\text{Br}_4$), 943 ($\text{C}_{12}^{79}\text{Br}_5^{81}\text{Br}_5$), 945 ($\text{C}_{12}^{79}\text{Br}_4^{81}\text{Br}_6$), 947 ($\text{C}_{12}^{79}\text{Br}_3^{81}\text{Br}_7$), and 949 ($\text{C}_{12}^{79}\text{Br}_2^{81}\text{Br}_8$) are indicative of the presence of decabromobiphenyl in the polymer

blend. Such brominated biphenyls are widely applied as flame retardants in polymer blends. The nominal masses of these ions are odd as a result of the almost unit mass deficiency of decabromo compounds. The $(m/\Delta m)_{50\%}$ mass resolution measured at m/z 943 is 1890. At this resolution, the $^{12}\text{C}_{11}^{13}\text{C}^{79}\text{Br}_5^{81}\text{Br}_5$ isotope peak at m/z 944 is more than unit mass resolved from the $^{12}\text{C}_{12}^{79}\text{Br}_5^{81}\text{Br}_5$ peak at m/z 943. The measured mass of the $^{12}\text{C}_{12}^{79}\text{Br}_5^{81}\text{Br}_5$ radical cation in broad-band mode is m/z 943.1574 giving a 16 ppm mass accuracy. This accuracy could only be achieved by calibrating the instrument on the molecular ions of a mixture of commercially available polybrominated diphenyl ethers. Calibration with perfluorotetrabutylamine (PFTBA), a known calibration compound, results in higher mass accuracies because there are no peaks higher than m/z 501 in the PFTBA EI/MS spectrum. The experimental bromine isotope distribution is in good agreement with the calculated one (not shown). The $^{79}\text{Br}/^{81}\text{Br}/^{12}\text{C}/^{13}\text{C}$ isotope distribution of peaks centered around m/z 863 points to the conclusion that this cluster of peaks is a mixture of nonabromobiphenyl $\text{C}_{12}\text{HBr}_9^{+}$ molecular ions and $\text{C}_{12}\text{Br}_9^+$ cations. The measured masses of the $\text{C}_{12}\text{H}^{79}\text{Br}_5^{81}\text{Br}_4^{+}$ molecular ions and $\text{C}_{12}^{79}\text{Br}_5^{81}\text{Br}_4^+$ in broad-band mode are m/z 863.2852 (-25 ppm) and 864.2790 (-35 ppm), respectively. The cluster around m/z 879 (m/z 863 + 16) is most likely the result of electron ionization (70 eV) of desorbed nonabromodiphenyl ether $\text{C}_{12}\text{HBr}_9\text{O}$ molecules. In analogy with deca- and nonabromobiphenyl and nonabromodiphenyl ether, lower homologues of brominated biphenyls and diphenyl ethers could be identified in the polymer blend.

Thermal degradation products of the polymer are observed in the 70-eV broad-band mass spectrum at 36 s (Figure 5B). The lower part of the mass spectrum (Figure 5B) contains peaks at m/z 78 C_6H_5^+ , 91 C_7H_7^+ , 104 $\text{C}_6\text{H}_5\text{CH}_2\text{CH}_3^+$, 117 C_9H_9^+ , 193 $\text{C}_{15}\text{H}_{13}^+$, and 207 $\text{C}_{16}\text{H}_{15}^+$ which are indicative of a polystyrene matrix. It is well-known that polystyrene thermally degrades mainly to styrene monomers with some 2,4-diphenyl-1-butene dimers and trimers (2,4,6-triphenyl-1-hexene) in the absence of oxygen giving molecular ions at m/z 104, 208, and 312, respectively.³³⁻³⁷ In addition to monomers, dimers, and trimers, several byproducts such as toluene, α -methylstyrene, and 1,3-diphenyl-1-propene are formed upon pyrolysis of polystyrene.³⁵ The measured mass of the styrene radical cation is m/z 104.062 81, giving a mass accuracy of -7.3 ppm. The resolution $(m/\Delta m)_{50\%}$ at m/z 104 is 12 983. The m/z 312 2,4,6-triphenyl-1-hexene molecular ion is not observed in Figure 5B. Usually, in-source pyrolysis spectra of polystyrene are recorded at 16 eV, giving radical cations that are readily correlated with the molecular weight of the pyrolysis products. Under our experimental conditions, the pyrolysis products were ionized with 70-eV electrons in order to obtain an abundant ion production. This ionization energy causes subsequent fragmentation of the molecular ions, yielding even electron fragment ions at odd m/z values. However, the mass spectrum remains characteristic for a polystyrene polymer matrix.

- (33) Sugimura, Y.; Nagaya, T.; Tsuge, S. *Macromolecules* **1980**, *14*, 520-523.
 (34) Ohtani, H.; Tsuge, S.; Matshushita, Y.; Nagasawa, M. *Polym. J.* **1982**, *14*, 495-499.
 (35) Sousa Pessoa de Amorim, M. T.; Bouster, C.; Vermande, P.; Veron, J. J. *Anal. Appl. Pyrolysis* **1981**, *3*, 19-34.
 (36) Dacust, D.; Bormann, S.; Legras, R.; Mercier, J. P. *Polym. Eng. Sci.* **1981**, *21*, 721-726.
 (37) Ohtani, H.; Yuyama, T.; Tsuge, S.; Plage, B.; Schuten, H.-R. *Eur. Polym. J.* **1990**, *26*, 883-899.

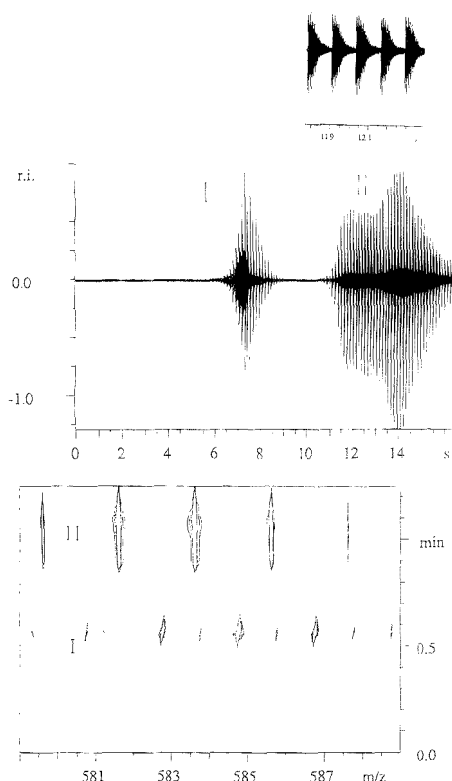


Figure 6. Temperature-resolved in-source pyrolysis FT ICR-MS of a polymer blend: (A, top) time domain data, consisting of 128 scans of 1024 data points each. In the inset, the region between 11.8 and 12.1 s has been enlarged. Note that the time on the axis is the accumulated detection time and differs from the total acquisition time of 20.5 s. The difference is explained in the text. (B, bottom) Time-resolved mass spectra after Fourier transformation of each individual scan from Figure 5A.

II. Time-Resolved Studies at High Resolution. In order to be able to examine the desorption behavior of the additives in the polymer blend, we have used the experimental sequence already described in Figure 3. The time (proportional to temperature) resolved raw in-source pyrolysis FT ICR-MS signal from a polymer sample from the housing of a TV set (different from the sample used in Figure 5) is presented in Figure 6A. This particular scan consists of 128 transients, which in turn consist of 1024 data points each. In this measurement, 30 s expired after the start of the current ramp through the desorption filament and the start of the measurement depicted in Figure 6A. Each transient is preceded by a quench pulse, an ion introduction pulse, and a shot excitation pulse, each followed by a delay. The electron energy during electron impact ionization in the ion source is 70 eV. The source and ion optics settings remain constant throughout the entire pulse sequence. The ion excitation is performed using a 70- μs shot excitation with a frequency corresponding to the cyclotron frequency of m/z 583 in a 7.02-T magnetic field. The data points for each transient are acquired in the heterodyne

mode with a sample frequency of 8000 Hz. The acquisition time for each data set is 128 ms, which combined with the preceding 32 ms for quench (1 ms), ion introduction (30 ms), ion excitation (70 μ s), and the corresponding delays (1 ms total) yields a cycle time of 160 ms. The acquired transients in Figure 6A clearly show two desorption regions. Region I starts at 37.5 s after the start of the current ramp, which corresponds to a filament temperature of ~ 700 K ($I_{fil} = 0.41$ A). Region II starts at ~ 43.1 s ($I_{fil} = 0.52$ A) after the start of the desorption ramp, corresponding to a filament temperature of ~ 1000 K. This second desorption profile shows a structure that closely resembles the characteristics of a combined first- and second-order thermal desorption process.³⁸ The envelope of the absolute signal intensity of the first point of each transient depicted in Figure 6A corresponds to the ion chromatogram for the mass range m/z 589.4–576.7. If the transients in Figure 6A are examined more closely (see inset Figure 6A), it can be seen that the acquisition stops before the coherently excited ions in the cell have fully dephased. This obviously causes the resolution of the individual mass spectra to be significantly lower than what would be possible based on the dephasing time of the ions. This is an example of a situation where mass resolution has been sacrificed in order to obtain a higher temporal and, therefore, higher thermal resolution.

After Fourier transformation of each individual data set, the resulting mass spectra have been combined in a contour plot as shown in Figure 6B. In this figure, the two desorption regions I and II are shown to originate from two different compounds. Region I originates from the thermal desorption of the *n*-butyl ether of tetrabromobisphenol-A (TBBA), with a cluster of peaks centered around the $[^{12}C_{19}H_{20}O_2^{79}Br_3^{81}Br_2 - CH_3]^+$ peak at m/z 584 displaying the $^{79}Br/^{81}Br/^{12}C/^{13}C$ isotope distribution indicative of a tetrabrominated compound given the $\sim 50\%$ natural abundance for both bromine isotopes. The polymer matrix of this particular sample was determined to be polystyrene and is not shown in Figure 6 as it falls outside of the mass range examined. Region II contains a cluster of peaks centered at m/z 583.2 ($^{122}Sb_2^{123}Sb_2O_6^+$) with an isotopic spacing typical for antimony. Sb_2O_6 is commonly used as a synergist in combination with TBBA to enhance the fire-retarding action of this compound.¹⁵ If we examine the individual peaks in both regions, a resolution $(m/\Delta m)_{50\%}$ of 10947 is found for the $^{12}C_{18}H_{17}O_2^{79}Br_2^{81}Br_2^+$ peak at scan 60 and a

(38) Woodruff, D. P.; Delchar, T. A. *Modern techniques of surface science*; Cambridge University Press: Cambridge, UK, 1988.

resolution $(m/\Delta m)_{50\%}$ of 11 646 for the $^{121}Sb_2^{123}Sb_2O_6^+$ peak in scan 110. A 4-fold increase in the number of data points taken increases the resolution by a factor of ~ 4 . The mass of the individual compounds has been determined with a 7 ppm accuracy which, in combination with the short cycle time of 160 ms, to the knowledge of the authors has not been previously shown in in-source pyrolysis MS studies on, e.g., magnetic sector mass spectrometers.¹⁶

In conclusion, we have successfully coupled direct temperature resolved in-source pyrolysis with an external ion source FT ICR-MS. The ultrahigh vacuum conditions achieved with the newly designed vacuum system resulted in a sufficiently long ion dephasing time to enable the rapid dynamic high-resolution analysis required for temperature-resolved in-source PyMS. For these experiments, the trade-off between high mass resolution and high temporal resolution has resulted in a typical scan time of 0.1 s with a mass resolution of $(m/\Delta m)_{50\%}$ equal to $\sim 50\,000$ at m/z 747 for a 4096 points data set in heterodyne mode. In our opinion, these instrumental capabilities open new pathways for a sensitive and selective mass spectrometric analysis of polymers and their additives. Moreover, the high temporal resolution of our experimental sequence also allows for fundamental studies of the kinetics involved in desorption and thermally induced dissociation processes of macromolecules.

ACKNOWLEDGMENT

The authors gratefully acknowledge A. Vijftigschild, M. de Wilde, and I. Stavenuiter for their technical assistance during the various stages of the experiment. We also acknowledge Dr. P. Caravatti for useful discussions in the design stage of the external ion source. Dr. T. Weeding is acknowledged for her careful reading of the manuscript. This work was financially supported by the IAS instrument development program for Advanced Mass Spectrometry, the Foundation for Fundamenteel Onderzoek der Materie (FOM), and the Nederlandse Organisatie voor Wetenschappelijk Onderzoek, NWO (Dutch organization for scientific research).

Received for review March 24, 1995. Accepted August 9, 1995.*

AC950294K

* Abstract published in *Advance ACS Abstracts*, September 15, 1995.

C-Terminal Ladder Sequencing via Matrix-Assisted Laser Desorption Mass Spectrometry Coupled with Carboxypeptidase Y Time-Dependent and Concentration-Dependent Digestions

Dale H. Patterson, George E. Tarr, Fred E. Regnier, and Stephen A. Martin*

PerSeptive Biosystems, 500 Old Connecticut Path, Framingham, Massachusetts 01701

The utility of matrix-assisted laser desorption/ionization time-of-flight (MALDI-TOF) mass spectrometry for the analysis of C-terminal peptide ladders from carboxypeptidase Y (CPY) digestions is discussed. MALDI analysis of aliquots of an optimized time-dependent CPY digestion of ACTH 7-38 fragment allowed for the sequence of the first 19 amino acids from the C-terminus to be determined in 25 min of digestion time. A strategy for performing parallel concentration-dependent digestions on the MALDI plate is proven to be superior to the time-dependent approach as the method development time and practical amounts of both peptide and enzyme consumed are reduced significantly. The on-plate approach offered the same sequence information from the ACTH 7-38 fragment and was used to digest 22 peptides of various amino acid composition, size, charge, and polarity. Of the 22 peptides digested on-plate, sequence information was derived from 19 of them. A statistical analysis strategy for ladder sequencing utilizing *t*-statistics is offered as a method for placing confidence intervals on residue assignments.

Protein and peptide chemists frequently desire reliable and fast determinations of amino acid sequences. This information is crucial for the identification and analysis of (1) known and novel proteins as an end in itself or as a preliminary to cloning or further analysis by other methods, (2) peptides isolated from protein digests or from the screening of combinatorial or natural libraries, and (3) synthetic products as one component of quality control. Existing methods for sequence determination include the N-terminal chemistry of the Edman degradation, N- and C-terminal enzymatic methods, C-terminal chemical methods, and MS/MS approaches, with the first and last being most widely used. Each method possesses inherent limitations that frustrate its use alone for the complete primary structure identification of all proteins and peptides. The most glaring deficiency in the current set of methods is one that offers reliable C-terminal information.

C-terminal sequencing via chemical methods has proven difficult and is marginally effective, at best, after many years of development.¹⁻³ For this reason, the C-terminus remains a region

of proteins and peptides that is often not analyzed because of lack of a dependable probe. An alternate approach to chemical sequencing is enzymatic sequencing. Serine carboxypeptidases have drawn attention over the last two decades as they offer a simple method by which amino acids can be sequentially cleaved from the C-terminus of a protein or a peptide. Carboxypeptidase Y (CPY), in particular, is an attractive enzyme as it has been reported to nonspecifically cleave all residues from the C-terminus, proline included.⁶⁻¹⁰ Sequencing of peptides by carboxypeptidase digestion has traditionally been performed by the direct analysis of the released amino acids, which is complicated by amino acid contaminants in the enzyme and protein/peptide solutions as well as enzyme autolysis. Further hindering the sequencing effort is the requirement for good kinetic information concerning the hydrolysis of each residue.

With the advancement of mass spectrometric techniques capable of high mass analysis such as field desorption,^{11,12} electrospray,^{13,14} 252-Cf plasma desorption,¹⁵⁻¹⁸ FABs,¹⁹⁻²⁴ and thermospray,²⁵⁻²⁷ it has become possible to perform direct mass

(1) Siark, G. R. *Methods Enzymol.* 1972, 25, 369-384.
(2) Tarr, G. E. In *Methods in Protein Sequence Analysis*; Wittmann-Leibold, B., Ed.; Springer-Verlag: Berlin, 1989; pp 129-136.
(3) Tsugita, A. S. *Anal. Biochem.* 1991, 195, 183-196.
(4) Tsugita, A.; Masaharu, K.; Takamoto, K.; Satake, K. *J. Protein Chem.* 1994, 13, 476-479.

(5) Bailey, J. M.; Tu, O.; Issai, G.; Ha, A.; Snively, J. E. *Anal. Biochem.* 1995, 224, 588-596.
(6) Martin, B. *Carlsberg Res. Commun.* 1977, 42, 99-102.
(7) Breddam, K.; Ottesen, M. *Carlsberg Res. Commun.* 1987, 52, 55-63.
(8) Breddam, K. *Carlsberg Res. Commun.* 1986, 51, 83-128.
(9) Hayashi, R. *Methods Enzymol.* 1977, 74, 84-94.
(10) Hayashi, R.; Moore, S.; Stein, W. H. *J. Biol. Chem.* 1973, 248, 2296-2302.
(11) Hong, Y.-M.; Takao, T.; Aimoto, S.; Shimomishi, Y. *Biomed. Mass Spectrom.* 1983, 10, 450-457.
(12) Tsugita, A.; Broek, V. D.; Przybylski, M. *FEBS Lett.* 1982, 137, 19-24.
(13) Smith, C. E.; Duffin, K. L. In *Techniques in Protein Chemistry IV*; Angeletti, R. H., Ed.; Academic Press, Inc.: San Diego, CA, 1993; pp 463-470.
(14) Rosnack, K. J.; Stroh, J. G. *Rapid Commun. Mass Spectrom.* 1992, 6, 637-640.
(15) Kiarskov, K.; Breddam, K.; Roepstorff, P. *Anal. Biochem.* 1989, 180, 28-37.
(16) Woods, A. S.; Cotter, R. J.; Yoshioka, M.; Bullesbach, F.; Schwabe, C. *Int. J. Mass Spectrom. Ion Processes* 1991, 111, 77-88.
(17) Wang, R.; Cotter, R. J.; Meschia, J. F.; Sisodia, S. S. In *Techniques in Protein Chemistry III*; Angeletti, R. H., Ed.; Academic Press, Inc.: San Diego, CA, 1992; pp 505-513.
(18) Woods, A. S.; Gibson, W.; Cotter, R. J. In *Time-of-Flight Mass Spectrometry*; Cotter, R. J., Ed.; ACS Symposium Series 549; American Chemical Society: Washington, DC, 1994; pp 194-216.
(19) Wagner, R. M.; Fraser, B. A. *Biomed. Environ. Mass Spectrom.* 1987, 14, 235-239.
(20) Caprioli, R. M.; Fan, T. *Anal. Biochem.* 1986, 154, 596-603.
(21) Self, R.; Parente, A. *Biomed. Mass Spectrom.* 1983, 10, 78-82.
(22) Bradley, C. V.; Williams, D. H.; Hanley, M. R. *Biochem. Biophys. Res. Commun.* 1982, 4, 1225-1230.
(23) Kim, J.; Kim, K.; Kim, J.; Ok, J. H.; Kim, J. *Biochem. Mol. Biol. Int.* 1994, 33, 53-64.
(24) Hirayama, K.; Ando, T.; Takahashi, R.; Murai, A. *Bull. Chem. Soc. Jpn.* 1986, 59, 1371-1378.

analysis on peptide fragments resulting from CPY digestion where the sequence order is preserved in a simple qualitative way, circumventing the need for amino acid analysis. In this "ladder" sequencing approach, a sequence can be read, in the correct order, by simply calculating the differences in mass of adjacent peptide peaks, representing the loss of amino acids. More recently, matrix-assisted laser desorption/ionization time-of-flight (MALDI-TOF) mass spectrometry has been shown as a suitable tool for ladder sequence analysis due to its high sensitivity, resolution, and mass accuracy.²⁸⁻³⁴ Chait and co-workers exploited the assets of MALDI-TOF for the ladder sequencing of N-terminal ladders formed from partial blockage at each step of an Edman degradation.^{28,29} Pappin and co-workers used MALDI-TOF to study N-terminal ladders made by adding fresh peptide at the start of each Edman cycle.³⁰ These two methods still suffer from the same limitations of traditional Edman chemistry, including the lack of C-terminal information, but demonstrate the utility of MALDI-TOF for direct sequence determination from ladders. Combining the MALDI-TOF detection scheme with carboxypeptidase digestion of peptides, direct analysis of the resulting mixture of truncated peptides can be performed, thereby offering easy-to-interpret sequence information. This has been shown to be a promising technique as eight consecutive amino acids were reported sequenced from the C-terminus of human parathyroid hormone 1-34 fragment.³¹ Recent articles from Cotter's laboratory^{32,34} have reported the transfer of classical time course digestions with carboxypeptidases and aminopeptidases to an "on-slide" format for convenient integration with MALDI-TOF analysis.

This paper demonstrates the viability of C-terminal enzymatic sequencing using a time-dependent carboxypeptidase Y digestion coupled with MALDI-TOF mass analysis of the resulting peptide ladders. An alternate and novel digestion strategy involving the use of the microliter wells machined into the Voyager MALDI plate for a concentration-dependent digestion of the peptide is presented. Sequence information analogous to the optimized time-dependent digestion is obtained in a matter of a few minutes while circumventing time-consuming method development. This method is shown to require only a few picomoles of total peptide as a combined result of the sensitivity of MALDI and no sample loss upon moving from digestion to analysis. Using this on-plate concentration-dependent digestion strategy, 22 peptides of various amino acid composition, size, charge, and polarity were digested to explore the generality of the technique. Finally, a statistical

analysis strategy is offered as a tool for applying statistical levels of confidence to amino acid assignments.

EXPERIMENTAL SECTION

Solution-Phase Digestion of ACTH 7-38 Fragment. For the time course digestion, 500 pmol of synthetic human adrenocorticotrophic hormone fragment (7-38) (FRWGKPVGKKRRPV-KVYPNGAEDESAEAFPLE) from Sigma Chemical Co. (St. Louis, MO), previously dried down in a 0.5-mL Eppendorf vial, was resuspended with 33.3 μL of HPLC grade water (J. T. Baker, Phillipsburg, NJ). In a previously dried down 0.5-mL Eppendorf tube, 3.05 units (one unit hydrolyzes 1.0 μmol of *N*-CBZ-Phe-Ala to *N*-CBZ-phenylalanine + alanine per minute at pH 6.75 and 25 °C) of carboxypeptidase Y from baker's yeast (EC 3.4.16.1), purchased from Sigma, was resuspended with 610 μL of HPLC grade water. To 20 μL of the ACTH 7-38 fragment solution was added 10 μL of the CPY solution to initiate the reaction. The final concentrations were 10 pmol/ μL ACTH and 1.67×10^{-3} units/ μL CPY, yielding an enzyme-to-substrate ratio of 1.67×10^8 units of CPY/mol of ACTH (1:37 molar ratio by assuming the CPY MW = 61 000). Aliquots of 1 μL were taken from the reaction vial at reaction times of 15 s, 60 s, 75 s, 105 s, 2 min, 135 s, 4 min, 5 min, 6 min, 7 min, 8 min, 9 min, 10 min, 15 min, and 25 min. At 25 min, 15 μL of 5×10^{-3} units/ μL CPY was added to the reaction vial. Aliquots of 2 μL were removed at total reaction times of 1 and 24 h. The reaction proceeded at room temperature until 2 min, when the temperature was elevated to 37 °C. All aliquots were added to 9 μL of the MALDI matrix, α -cyano-4-hydroxycinnamic acid (CHCA) from Sigma, at a concentration of 5 mg/mL in 1:1 acetonitrile (ACN)/0.1% trifluoroacetic acid (TFA) with the exception of the 1 and 24-h aliquots that were added to 8 μL of the matrix. The final total peptide concentrations of the ACTH digestion aliquots in the matrix solutions were 1 pmol/ μL . A pooled peptide solution was prepared by combining 2 μL of the 15-s, 105-s, 6-min, and 25-min aliquots. Into individual microliters wells on the MALDI sample plate was placed 1 μL of each aliquot solution and allowed to evaporate to dryness before insertion into the mass spectrometer.

On-Plate Digestions. All on-plate digestions were performed by pipeting 0.5 μL of the peptide at a concentration of 1 pmol/ μL into each of 10 1- μL wells across one row of the Voyager sample plate (Figure 1). All peptides given in Table 1 were purchased from Sigma and were of the highest purity offered. To initiate the reaction in the first well, 0.5 μL of 0.0122 units/ μL CPY was added. To the subsequent nine wells was added CPY at concentrations of 6.10×10^{-3} , 3.05×10^{-3} , 1.53×10^{-3} , 6.10×10^{-4} , 3.05×10^{-4} , 1.53×10^{-4} , 7.63×10^{-5} , 3.81×10^{-5} , and 0 unit/ μL , respectively. Mixing was assured in each well by pulling the 1- μL reaction back and forth through the pipet tip. The reaction was allowed to proceed at room temperature until the 1- μL total volume evaporated on the plate (~10 min). At such time, 0.5 μL of 5 mg/mL CHCA in 1:1 ACN/0.1% TFA was added to each well, with no further mixing, and allowed to evaporate for ~10 min before mass analysis.

MALDI-TOF Mass Spectrometry. MALDI-TOF mass analysis was performed using the Voyager Biospectrometry Workstation (PerSeptive Biosystems, Framingham, MA). A 28.125-kV potential gradient was applied across source containing the sample plate and an ion optic accelerator plate in order to introduce the positively charged ions to the 1.2-m linear flight tube for mass

- (25) Stachowiak, K.; Wilder, C.; Vestal, M. L.; Dyckes, D. F. *J. Am. Chem. Soc.* **1988**, *110*, 1758-1765.
- (26) Kim, H. Y.; Pilosof, D.; Dyckes, D. F.; Vestal, M. L. *J. Am. Chem. Soc.* **1984**, *106*, 7304-7309.
- (27) Pilosof, D.; Kim, H. Y.; Vestal, M. L.; Dyckes, D. F. *Biomed. Mass Spectrom.* **1984**, *11*, 403-407.
- (28) Chait, B. T.; Wang, R.; Beavis, R. C.; Kent, S. B. H. *Science* **1993**, *262*, 89-92.
- (29) Wang, R.; Chait, B. T.; Kent, S. B. H. In *Techniques in Protein Chemistry IV*; Angelelli, R. H., Ed.; Academic Press, Inc.: San Diego, CA, 1993; pp 471-478.
- (30) Bartlett-Jones, M.; Jeffery, W.; Hansen, H. F.; Pappin, D. J. C. *J. Protein Chem.* **1994**, *13*, 455-456.
- (31) Schar, M.; Bornsen, K. O.; Cassmann, E.; Widmer, H. *Chimia* **1991**, *45*, 123-126.
- (32) Aldrich, C. J.; DeCloux, A.; Woods, A. S.; Cotter, R. J.; Soloski, M. J.; Forman, J. *Cell* **1994**, *79*, 649-658.
- (33) Thiede, B.; Wittmann-Liebold, B.; Bienert, M.; Krause, E. *FEBS Lett.* **1995**, *357*, 65-69.
- (34) Woods, A. S.; Huang, A. Y. C.; Cotter, R. J.; Pasternack, G. R.; Pardoll, D. M.; Jaffe, E. M. *Anal. Biochem.* **1995**, *226*, 15-25.

Table 1. Peptides of Various Charge and Polarity Digested On-Plate by CPY and Analyzed by MADLI^a

peptide	sequence	av mass ^b	charge ^c	polarity
sleep-inducing peptide	WAGGDASGE	848.8	-2.0	polar
amino-terminal region of Hbs β chain ^d	VHLTPVEK	922.1	+0.5	mid
interleukin-1 β 163-171 fragment ^d	YQGDESNDK	1005.0	-2.0	polar
TRH precursor	KRQHPGKR	1006.2	+4.5	very
bradykinin	RPPGFSFRR	1061.2	+2.0	mid
luteinizing hormone releasing hormone ^d	pyro-EHWSYGLRPG-amide	1182.3	+1.5	mid
physalaemin	pyro-EADPNK FYGLM -amide	1265.4	0	mid
angiotensin 1	DRVYIHPFHL	1296.5	+1.0	non
renin inhibitor	PHPFHFFVYK	1318.5	+2.0	non
kassinin	DVPKSDQ FVGLM -amide	1334.5	-2.0	non
substance P	RPKPQQ FFGLM -amide	1347.6	-3.0	mid
T antigen homolog	CGYGPKKKR KVGG	1377.7	-5.0	polar
osteocalcin 7-19 fragment	GAPVYPD PLEPR	1407.6	-1.0	mid
fibrinopeptide A	ADSGEGD FLAEGGGVR	1536.6	-3.0	mid
thymopoietin II 29-41 fragment	GEQRKD VYVQLYL	1610.8	0	polar
bombesin	pyro-EQRLGN QW(AVGH)LM -amide	1619.9	+1.5	mid
ACTH 11-24 fragment	KPVGK KRRPVKVYP	1652.1	+6.0	mid
α -melanocyte stimulating hormone	acetyl-STSM EHFRWGKPV -amide	1664.9	+1.5	mid
angiotensinogen 1-14 fragment	DRVYIHP FHLLVYS	1759.0	+1.0	non
angiotensin	ENGLPV HLQSI(F)R	1781.0	-0.5	mid
glucagon	HSQGT FTSDYSKTLDSRRRAQDFVQW(LMN)T	3482.8	+1.0	polar
ACTH 7-38 fragment	FRW GK(R)RFPVKVYPNGAEDSEAEAFPLE	3659.15	+2.0	polar

^a The boldface residues indicate that a peak was observed in one or more of the mass spectra that represented the loss of that amino acid. The residues in parentheses indicate that the sequence order of the enclosed amino acids could not be determined. ^b Calculated. ^c At pH 6.5. ^d No sequence information was obtained.

analysis. For data acquisition of the ACTH 7-38 fragment and glucagon digests a low-mass gate was used to prevent the matrix ions from striking the detector plate. For the application of the low-mass gate, the guide wire was pulsed for a brief period deflecting the low-mass ions ($\sim <1000$ Da). All other spectra were recorded with the low-mass gate off. To enhance the signal-to-noise ratio, 64-128 single shots from the nitrogen laser (337 nm) were averaged for each mass spectrum. The data presented herein were smoothed using an 11-point Savitsky-Golay second-order filter. All data were calibrated using an external calibration standard mixture of bradykinin ($MH^+ = 1061.2$) and insulin B-chain, oxidized ($MH^+ = 3496.9$) (both purchased from Sigma) at concentrations of 1 pmol/ μ L in the 5 mg/mL CHCA matrix solution.

Statistical Mass Assignments. The statistical protocol presented here uses the equation for the two-tailed *t*-test:

$$t_{\text{calcd}} = \frac{|\bar{x} - \mu| \sqrt{n}}{s}$$

where \bar{x} is the average experimental mean, μ is the asserted mean, n is the number of replicates, and s is the experimental standard deviation. For the assignment of residues to experimentally derived Δ masses, a t_{calcd} for each asserted mean mass (each possible amino acid assignment) was compared to the tabulated value for a given confidence interval³⁷. A $t_{\text{calcd}} > t_{\text{table}}$ indicated that the experimental mass came from a population possessing a mean different from the asserted mass at the given confidence level.

RESULTS AND DISCUSSION

Solution-Phase Digestion. Given in Figure 2 are the MALDI spectra of the 1-, 5-, and 25-min aliquots that were removed from a solution-phase time-dependent CPY digestion of ACTH 7-38 fragment. The lack of phase control of the enzymatic digestion

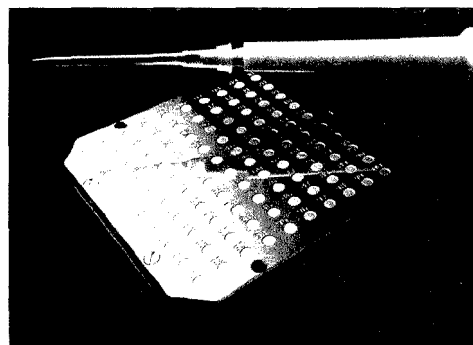


Figure 1. Voyager sample plate for MALDI analysis comprised of a 10 \times 10 matrix of 1- μ L wells etched into the stainless steel base. These wells serve as microreaction vessels in which on-plate digestions may be performed. The physical dimensions of the plate are 57 \times 57 mm and the wells are 2.54 mm in diameter.

creates the peptide ladders that are observed in this figure. After 1 min of digestion (Figure 2A), nine detectable peptide populations exist including the intact ACTH 7-38 fragment and peptides representing the loss of the first eight amino acids from the C-terminus. The 5-min aliquot (Figure 2B) shows that the peptide populations representing the loss of Ala(32) and Ser(31) have become much more predominant than the 1-min aliquot. Amino acid losses of 11 residues, Ala(32) through Val(22), are present at this digestion time. Figure 2C shows the final detected amino acids of Lys(21) and Val(20) as four major peptide populations are detected. Upon increasing the enzyme concentration 2-fold at 25 min, no further digestion was observed through 24 h (data not shown). The digestion proceeded through the Val(20) and stopped at the amino acid run of peptide-KKRRP. Although CPY may proceed rapidly through proline [e.g., Pro(24)], the basic

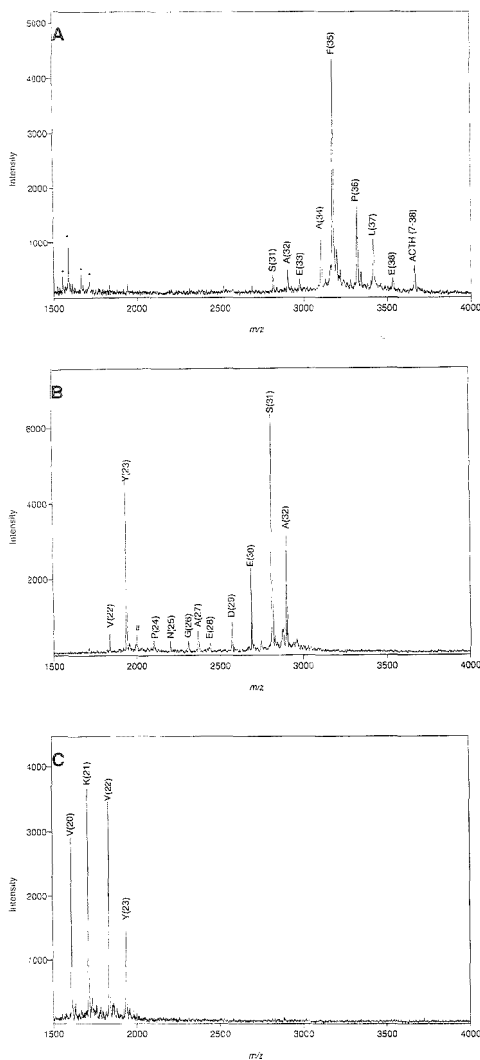


Figure 2. MALDI spectra of the 1- (A), 5- (B), and 25-min (C) aliquots from a time-dependent CPY digestion of ACTH 7-38 fragment (FRWGKPVGKRRRPVKVYPNGAEDESAEAFPLE). The nomenclature of the peak labels denotes the peptide populations resulting from the loss of the indicated amino acids. Peaks representing the loss of 19 amino acids from the C-terminus are observed. The * indicates doubly charged ions, and # indicates an unidentified peak at $m/z = 2001.0$ Da. All conditions are stated in the text.

residue, arginine, at the penultimate position in this case proved to be a combination refractory to CPY.

The lack of phase control coupled with the varied rates of hydrolysis poses problems unique to enzymatic sequencing. Varying ion intensities for the peaks in Figure 2 are due primarily to the rates of hydrolysis that vary according to the amino acids at the C-terminus and penultimate position. When a residue is hydrolyzed at a low rate compared to the neighboring residues,

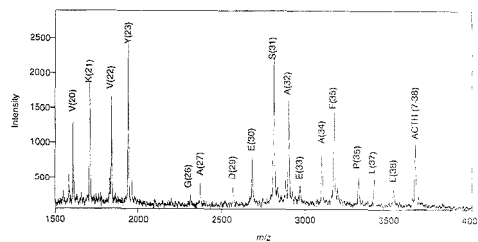


Figure 3. MALDI mass spectra resulting from the pooling of the 15-s, 105-s, 6-min, and 25-min quenched aliquots. All amino acid losses are observed except for those of Glu(28), Asn(25), and Pro(24), which were present as small peaks in the 6-min aliquot and subsequently diluted to undetectable concentrations in this pooled fraction. All conditions are stated in the text.

the concentration and, therefore, signal of the peptide population representing the loss of that residue will be small relative to that of the preceding amino acid. This is seen in the mass spectra given in Figure 2. The cleavage of Ala(34) is shown to be slow, resulting in the large signal representing the loss of Phe(35). The hydrolysis of glycine and valine are also shown to be slow as the peaks representing the loss of Ala(27) and Tyr(23) are comparatively more intense than those of Gly(26) and Val(22), respectively.

The time-dependent reaction presented here is the result of extensive method development and is optimized for obtaining the maximum sequence information in the shortest amount of time. For this optimized case, detectable amounts of all populations are observed over 25 min in the three selected time aliquots. This was not the case for numerous preliminary solution-phase digestions that were performed during the method development that led to the use of these optimized conditions. At higher concentrations of CPY, the peaks representing the loss of Glu(28) and Pro(24) were often not observed, indicating that CPY cleaves these residues very readily when alanine and tyrosine are at the penultimate positions, respectively. Lower concentrations of CPY allowed for all amino acids to be sequenced but often required long periods of time (e.g., days) for total digestion. An enzyme-to-substrate ratio of 1.67×10^8 units CPY/mol of peptide was found to offer all available sequence information in 25 min of digestion.

Upon pooling aliquots from 15 s, 105 s, 6 min, and 25 min of total reaction time, MALDI analysis shows that a peptide ladder is formed that contains peaks that represent the loss of almost all amino acids from the C-terminus (Figure 3). A sequence gap is observed here as the peptide populations representing the loss of Glu(28), Asn(25), and Pro(24), exist below a signal-to-noise ratio of 3. These populations were observed as small peaks in the 6-min aliquot mass spectrum but, upon the 4-fold dilution with the other aliquots, exist in too small a concentration to be detected. This emphasizes the necessity of recording individual mass spectra for each time aliquot. The less time-demanding procedure of recording a single spectrum representing pooled results not only creates sequence gaps but loses the time-dependent history of the digestion. Solution-phase digestions suffer from a number of disadvantages. A large amount of time, enzyme, and peptide is required for method development in order to obtain significant digestion in a short amount of time while preserving all possible sequence information. For each peptide from which sequence information is to be derived, some time-consuming method development must be performed since a set of optimum conditions

for one peptide is not likely to be useful for another peptide given the composition-dependent hydrolysis rates of CPY. An alternative strategy is to perform the digestion on the MALDI sample surface using a concentration-dependent approach.

On-Plate Concentration-Dependent Digestions. Given in Figure 1 is a picture of the MALDI sample plate that is used in the Voyager workstation. This plate is comprised of a 10×10 matrix of microliter wells etched into the stainless steel surface offering microliter reaction vessels in which digestions can be performed. Aliquots ($0.5 \mu\text{L}$) of both enzyme and substrate are placed in a well and mixed with the pipet tip. The digestion continues for ~ 10 min until solvent evaporation terminates the reaction. At this time, the digestion mixture is resuspended by placing $0.5 \mu\text{L}$ of the matrix in the well. Since the CHCA matrix is solubilized in 1:1 ACN/0.1% TFA, both hydrophilic and hydrophobic peptide populations from the digest mixture should be resuspended, with the low pH prohibiting any further CPY activity. The matrix crystal formation does not appear to be altered (as compared to the time course experiment) by performing the digestion on-plate. This on-plate strategy significantly decreases the method development time by allowing multiple concentration-dependent (time-independent) digestions to be performed in parallel. Also, sample losses upon transfer(s) from reaction vial to analysis plate are circumvented using the on-plate approach as all digested material is available for mass measurement.

MALDI analyses of the on-plate concentration-dependent digestions of the ACTH 7–38 fragment for CPY concentrations of 6.10×10^{-4} and 1.53×10^{-3} units/ μL are respectively given in panels A and B of Figure 4. The lower concentration digestion yields 12 significant peaks representing the loss of 11 amino acids from the C-terminus. The digestion from the higher concentration of CPY shows some overlap of the peptide populations present at the lower concentration as well as peptide populations representing the loss of amino acids through the Val(20). The concentration of the peptides representing the loss of the first few amino acids has decreased to undetectable levels (< 10 fmol) with the exception of the Leu(37) peak. By combining the information in both panels, the ACTH 7–38 fragment sequence can be read 19 amino acids from the C-terminus without gaps, stopping at the same amino acid run of peptide-RRKKP as the time-dependent digestion. Figure 4 represents two of the nine CPY concentrations that were performed simultaneously. The method development, in this case, is inherent in the strategy. The total time of method development (optimal digestion conditions), digestion, data collection, and data analysis is under 30 min using this on-plate approach. The consumption of both peptide and enzyme is minimal as a total of 5 pmol of total peptide is digested across the 10 well row containing 9 digestions and 1 well with peptide plus water. Also, only 1.97 pmol of CPY (assuming 100 units/mg and MW = 61 000) was required for the entire experiment.

Listed in Table 1 are the peptides that have been digested and analyzed using this novel on-plate strategy. These peptides were selected to represent peptides of varying amino acid composition, size (up to MW = 3659.15), charge, and polarity. The boldface amino acids indicate that a peak representing the loss of that residue was observed in one or more of the MALDI spectra taken across the row of digestions. In order to be able to call a residue, the peak representing the loss of that amino acid and the preceding amino acid must be present. The residues that are

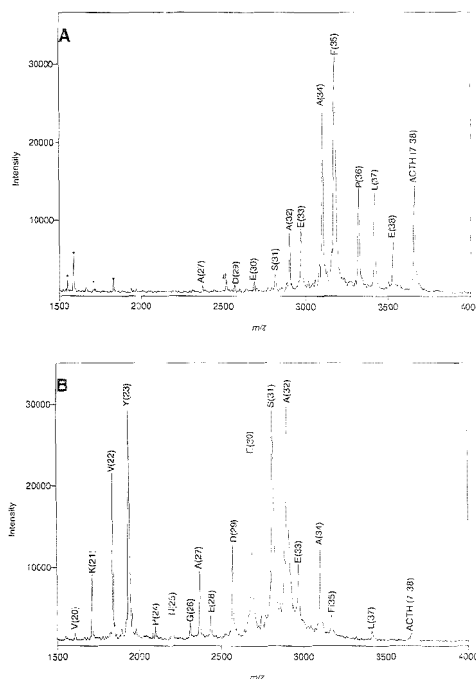


Figure 4. MALDI spectra of on-plate concentration-dependent CPY digestions of ACTH 7–38 fragment. Panels A and B show the spectra obtained from digests using CPY concentrations of 6.10×10^{-4} and 1.53×10^{-3} units/ μL , respectively. Laser powers significantly above threshold were used to improve the signal-to-noise ratio of the smaller peaks in the spectrum at the expense of peak resolution. The * indicates doubly charged ions, and # indicates an unidentified peak at $m/z = 2517.6$ Da. All other experimental conditions are stated in the text.

enclosed in parentheses are those for which the sequence order could not be deduced. Overall, CPY was able to offer some sequence information from the C-terminus for most of the peptides digested, lending no sequence information in only three of the 22 cases. In two of these three cases, the C-terminus is a lysine followed by an acidic residue at the penultimate position. CPY has been reported to possess reduced activity toward basic residues at the C-terminus,^{35,36} and the presence of the neighboring acidic residue seems to further reduce its activity. In the case of the luteinizing hormone releasing hormone (LH-RH), the C-terminal amidated glycine followed by proline at the penultimate position inhibits CPY activity, which agrees with reports of CPY slowing at both proline and glycine residues.^{35,36} CPY is known to hydrolyze amidated C-terminal residues of dipeptides³⁵ and is shown here to cleave those of physalaemin, kassinin, substance P, bombesin, and α -MSH. As can be seen from Table 1, CPY was able to derive sequence information from all of the peptides, except LH-RH, that possess blocked N-terminal residues (phys-

(35) Hayashi, R.; Bai, Y.; Tadao, H. *J. Biochem.* **1975**, *77*, 69–79.

(36) Hayashi, R. *Methods Enzymol.* **1976**, *45*, 568–587.

(37) McCormick, D.; Roach, A. In *Measurement, Statistics and Computation*; Chapman, N. B., Ed.; John Wiley and Sons: New York, 1987; p 152.

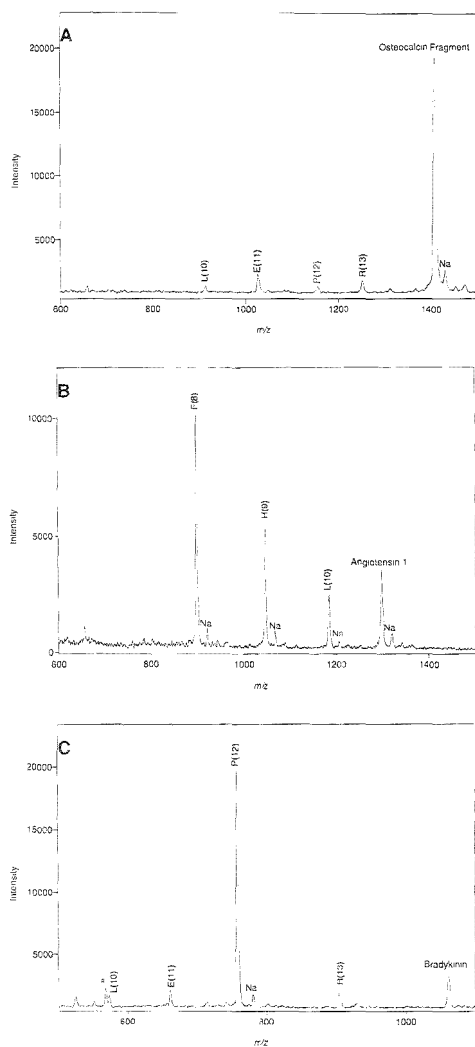


Figure 5. MALDI spectra of three selected peptides, osteocalcin 7–19 fragment (GAPVPYPDPLEPR) (A), angiotensin 1 (DRVYIHPFHL) (B), and bradykinin (RPPGFSPFR) (C) resulting from on-plate digestions using CPY concentrations of 3.05×10^{-4} , 3.05×10^{-4} , and 6.10×10^{-4} units/ μL , respectively. The symbol Na denotes a sodium adduct peak, and # denotes a matrix peak at $m/z = 568.5$ Da.

alaemin, bombesin, and α -MSH). This is significant as these peptides would lend no information to the Edman approach. A number of the peptides were sequenced until the detection of the truncated peptide peaks was impaired by the presence CHCA matrix ions (<600 Da). The sequencing of the other peptides did not go as far as a combination of residues at the C-terminus and penultimate position that inhibited CPY activity was encountered. Bombesin, angiogenin, and glucagon gave gaps in the sequence as residues that were cleaved slowly were followed by

Table 2. Comparison of the Actual Masses and Experimental Derived Masses for the Indicated Residues of ACTH 7–38 Fragment Obtained for the Time-Dependent Digestion^a

amino acid (position)	actual mass ^b	exptl mass ^{b,c}	replicates
Val (20)	99.13	98.97 \pm 0.52 (1.29)	3
Lys(21)	128.7	128.15 \pm 0.48 (0.44)	7
Val (22)	99.13	99.20 \pm 0.35 (0.27)	9
Tyr (23)	163.17	162.43 \pm 0.11 (0.99)	2
Pro (24)	97.12	97.49 \pm 0.14 (1.25)	2
Asn(25)	114.10	114.21 \pm 0.82 (0.69)	8
Gly (26)	57.05	57.22 \pm 0.88 (0.68)	9
Ala (27)	71.07	70.19 \pm 0.49 (4.40)	2
Glu (28)	129.12	130.22 \pm 0.47 (4.22)	2
Asp (29)	115.09	114.81 \pm 0.58 (0.41)	10
Glu (30)	129.12	129.27 \pm 0.61 (0.39)	12
Ser (31)	87.08	87.14 \pm 0.47 (0.30)	12
Ala (32)	71.07	70.94 \pm 0.49 (0.51)	6
Glu (33)	129.12	129.39 \pm 0.42 (0.44)	6
Ala (34)	71.07	71.09 \pm 0.30 (0.28)	7
Phe (35)	147.18	147.03 \pm 0.73 (0.77)	6
Pro (36)	97.12	96.83 \pm 0.64 (1.18)	4
Leu (37)	113.16	113.63 \pm 0.54 (1.34)	3
Glu (38)	129.12	128.40 \pm 0.52 (1.29)	3

^a The number of replicates indicate the number of spectra that possessed the detectable adjacent peaks required for the mass difference measurement of that particular residue. ^b The mass given are average masses and in units of Da. ^c The uncertainties of the experimental mass measurements are given as standard deviations (those in parentheses are 95% confidence intervals of the mean).

residues hydrolyzed more rapidly, as discussed above. The feasibility of the on-plate CPY digestion/MALDI detection strategy appears to be independent of the overall polarity and charge of the peptide.

Figure 5 shows selected on-plate digestions of osteocalcin 7–19 fragment, angiotensin 1, and bradykinin. Each spectrum represents the results of one of the nine digestions that was performed across the row of wells. Osteocalcin 7–19 fragment and angiotensin 1 were sequenced until a proline was encountered at the C-termini. Although CPY can proceed through proline,^{6–10} the presence of Asp and His at the respective penultimate positions of the two peptides prohibits further CPY activity. Bradykinin is shown to sequence until the matrix begins to interfere with peak detection. For all three of the selected peptides, the total sequence information obtained for the overall nine-well digestion is represented in the single digestion shown. For many other peptides this was not the case. The total sequence information is often derived from two or more of the wells as is the case with ACTH 7–38 fragment given in Figure 4.

Statistical Analysis of Ladder Sequencing by MALDI. To date, most reports of ladder sequencing have concentrated on demonstrations of methodology using known materials, but to be useful, these techniques must be extended to unknown sequences. The confidence with which those sequences may be called rests on instrumental mass accuracy, that is, on numerical analysis (in sharp contrast to Edman sequencing calls, which are essentially qualitative judgments). However, no individual mass measurement can lend statistical validity to a sequence call.

In order to apply the correct statistical analysis to multiple measurements, the nature of the experimental errors must first be defined. The Δ mass differences (i.e., experimental mass difference minus actual amino acid mass) for all amino acid assignments made in the 15 aliquots (one spectrum per aliquot)

Table 3. Calculated *t*-Values (Upper) for the 19 Experimental Means Given the Asserted Masses of the 20 Common Unmodified Amino Acids^a and the Subsequent Statistically Accurate Residue Assignments (Lower)

asserted amino acid	ACTH 7-38 fragment amino acid position																		
	20	21	22	23	24	25	26	27	28	29	30	31	32	33	34	35	36	37	38
	(4.30)	(2.45)	(2.31)	(12.7)	(12.7)	(2.37)	(2.31)	(12.7)	(12.7)	(2.26)	(2.20)	(2.20)	(2.57)	(2.57)	(2.45)	(2.57)	(3.18)	(4.30)	(4.30)
	Calculated <i>t</i> -Value																		
G							0.58	37.9					89.4		123				
A							47.2	2.54				118	0.65		0.18				
S					105			48.7				0.44	80.7		141		30.5		
P	6.16		17.8		3.74							73.6							0.91
V	0.53		0.60		16.6														7.19
T	7.03		16.3																
C																			
L(I)						3.62													33.6
N						0.38					3.87								1.51
D	72.0				3.04					45.5	1.53							4.68	44.3
Q	0.11									6.29	72.6								0.90
K	0.11									6.17									0.77
E	5.35									3.31	0.85			7.12					2.40
M										2.95	11.0			10.6					9.33
H									20.8										33.2
F																			0.50
R					80.4														30.7
Y					9.64														
W					305														

CI	ACTH 7-38 fragment amino acid position																		
	20	21	22	23	24	25	26	27	28	29	30	31	32	33	34	35	36	37	38
	Statistical Assignment ^{c,d}																		
CI > 99.8%		Q/K	V				G					E	S	A	E	A	F		
99% < CI < 99.8%				Y						D							P		
98% < CI < 99%						N	A												Q/K/E
95% < CI < 98%	V				P			Q/K/E/M									L(I)/N		

^a All cases where $t_{\text{calcd}} < t_{\text{table}}$ (the t_{table} values for the 95% confidence interval¹ are given in parentheses in the second row), shown in *italics*, indicate that the mean of the asserted residue is not significantly different than that of the experimental mean at 95% confidence. ^b The tabulated t -value associated with an area of 0.025 in one tail of the t -distribution corresponding to the appropriate degrees of freedom, ν , where $\nu = n - 1$. ^c The residues in boldface indicate the known residue at each position. ^d Assuming that only the 20 common unmodified amino acids are probable candidates.

removed from the time-dependent digestion of ACTH 7-38 fragment described above yielded a Gaussian distribution with a mean of 0.0089 ± 0.604 ($n = 107$). Using simple t -statistics, t_{calcd} (0.152) < t_{table} (1.99), indicating the null hypothesis of the average Δ mass difference of 0 cannot be rejected at a 95% confidence level (i.e., the error is random). This is expected as any systematic errors in the mass assignment of individual peptide peaks such as incorrect y -intercept values for two-point mass calibration should cancel out when the mass difference of adjacent peaks is calculated. One systematic component of error that would not be canceled is incorrect computation of the mass center of one of two adjacent peaks due to partial resolution of the isotopes. We minimize this problem with the use of a smoothing filter such that all peaks are detected at the actual average mass values.

Table 2 compares the actual average masses of the sequenced residues of the ACTH 7-38 fragment and the experimental mass differences with associated standard deviations and 95% confidence intervals calculated for the time-dependent digestion. Multiple measurements are clearly needed to narrow the 95% confidence interval of the mean. For all of the residues sequenced, the actual mass falls within $\pm 3\sigma$ the experimental mass distribution. Calculated t -values for each case are less than the tabulated t -value for the 95% confidence interval, signifying that the experimental mass is not significantly different from the actual known mass. But, in order to statistically assign these residues, all other possible assignments must be rejected. In other words, the actual mass of each possible amino acid must be used as an asserted mean,

μ , and each null hypothesis (i.e., $\bar{x} - \mu = 0$) assessed. The calculated t -values for the ACTH fragment are given in the top portion of Table 3. Values shown in *italics* are those which could not be rejected at the 95% confidence level. Again, the need for adequate population sampling is apparent. The two measurements for the Glu(28) gave a 95% confidence interval of 4.22 Da (Table 2), encompassing three other possible assignments (Table 3), while 12 trials for Glu(30) yielded a 95% confidence interval of 0.39 Da, statistically excluding the Gln, Lys, and Met.

Ideally, for the assignment of unknown sequences, the actual confidence interval for each residue call should be calculated and a reasonable minimum established. This is done for the ACTH fragment in the lower portion of Table 3. Unsurprisingly, residue 21 could be Gln or Lys (Δ mass = 0.04 Da). Similarly, residue 37 is ambiguous as the experimental mean (113.16 Da) bisected the asserted means of Leu(Ile) (113.16 Da) and Asn (114.10 Da). Residue 28 was assigned Gln/Lys/Glu/Met at a confidence interval greater than 95% but less than 98%, with Met (an incorrect assignment) yielding the smallest t_{table} (upper portion of Table 3). Using a confidence interval of 80%, the correct assignment of Glu is deemed statistically improbable. This example highlights the caution one must heed when using low levels of confidence (e.g., 80% confidence means a wrong call 20% of the time).

The protocol currently being implemented for statistical assignment of residues using the on-plate strategy involves multiple sampling from each well in which the digestion offers sequence information. The number of replicates that are required depends

on the amino acid(s) that is(are) being sequenced at that CPY concentration. For example, more replicates are required for mass differences around 113–115 (Ile/Leu, Asn, and Asp) and 128–129 Da (Gln/Lys/Glu) than for mass differences around 163 (Tyr) or 57 Da (Gly) in order to be able to assure that all but one assignment are statistically unlikely. The experimental errors for this method appear to be as random (multiple replicates per sample) as for the time-dependent digestion (one replicate per sample).

This general statistical approach to residue assignment can be extended to adjacent peaks that represent the loss of two or more amino acids. In this case, the asserted means of all dipeptides, tripeptides, etc., can also be used to calculate *t*-values. The information concerning the order of the residues will be lost but the composition can be deduced. Using only single amino acid and dipeptide masses as asserted means, this is done for angiogenin, which has a sequence gap of Phe-Arg (Table 1). The average experimental mass difference between the peaks representing the loss of Arg(15) and Phe(13) was 303.45 ± 0.328 ($n = 5$). For all single amino acid and dipeptide masses except Phe/Arg, the calculated *t*-values are greater than the tabulated *t*-value at a confidence interval of 99.8%. This statistical strategy can easily be incorporated into a computer algorithm that performs interactive data acquisition, analysis and interpretation of ladder sequencing/MALDI experiments.

CONCLUSIONS

The use of CPY digestion coupled with MALDI detection has been shown to be an effective method for obtaining C-terminal sequence information. The ACTH 7–38 fragment yielded sequence information 19 amino acids from the C-terminus without

gaps for a 25-min optimized time-dependent digestion. The on-plate concentration-dependent approach was demonstrated as a novel method for performing multiple digestions in parallel, which circumvents the need for time- and reagent-consuming method development. This on-plate strategy requires less physical manipulations and practically less total amounts of enzyme and peptide. Of the 22 peptides attempted using the on-plate approach, all but three were successfully digested to yield some C-terminal sequence information. CPY was also shown to cleave amidated C-terminal residues, but possessed no activity toward certain combinations of residues existing at the C-terminus and penultimate position.

A protocol for statistical analysis of the resulting peptide mass ladders was offered. Statistical levels of confidence can be placed on amino acid assignments of residues using simple *t*-statistics. This strategy affords the opportunity to derive primary amino acid composition information from experiments that produce sequence gaps. It also offers quantitative information regarding the role that reduction in the experimental error plays on the number of measurements needed for accurate amino acid assignment. This general statistical strategy can be implemented for any type of mass ladder experiment (i.e., DNA, PNA, and polysaccharide) and can be used to offer composition information in the cases where sequence gaps are present.

Received for review May 24, 1995. Accepted August 9, 1995.*

AC950501G

* Abstract published in *Advance ACS Abstracts*, September 15, 1995.

Structural Characterization of Phospholipids by Matrix-Assisted Laser Desorption/Ionization Fourier Transform Ion Cyclotron Resonance Mass Spectrometry

Jarrold A. Marto[†]

Department of Chemistry, The Ohio State University, Columbus, Ohio 43210

Forest M. White, Staci Seldomridge, and Alan G. Marshall^{†,*}

Center for Interdisciplinary Magnetic Resonance, National High Magnetic Field Laboratory, 1800 East Paul Dirac Drive, Florida State University, Tallahassee, Florida 32310

Matrix-assisted laser desorption/ionization (MALDI) Fourier transform ion cyclotron resonance mass spectrometry provides for structural analysis of the principal biological phospholipids: glycerophosphatidylcholine, -ethanolamine, -serine, and -inositol. Both positive and negative molecular or quasimolecular ions are generated in high abundance. Isolated molecular ions may be collisionally activated in the source side of a dual trap mass analyzer, yielding fragments serving to identify the polar head group (positive ion mode) and fatty acid side chains (negative ion mode). Azimuthal quadrupole excitation following collisionally activated dissociation refocuses product ions close to the solenoid axis; subsequent transfer of product ions to the analyzer ion trap allows for high-resolution mass analysis. Cyro-cooling of the sample probe with liquid nitrogen greatly reduces matrix adduction encountered in the negative ion mode.

Phospholipids are the principal components of biological cell bilayer membranes and of various subcellular organelles. The basic phospholipid structure consists of a glycerol backbone joined to an alkyl chain at *sn*-1, through either an ester or ether linkage, and a second alkyl group esterified at *sn*-2. A phosphate diester at the *sn*-3 position joins one of four typical polar head groups, which in turn define the particular phospholipid class: phosphatidylcholine (PC), -ethanolamine (PE), -serine (PS), or -inositol (PI). The alkyl chain length(s) and degree of unsaturation further specify a particular phospholipid within each class. (Other phospholipid classes, such as sphingomyelins and cardiolipins, are not considered here.) The biological role of phospholipids in fact extends beyond that of membrane building blocks. For example, glycerophosphatidylcholines (GPCs) containing arachidonic acid yield, upon hydrolysis, free arachidonic acid, which is in turn converted to oxygenated species such as prostaglandins, thromboxanes, and leukotrienes.¹⁻³ In addition, glycerophos-

phatidylethanolamine (GPE) and -inositol (GPI)⁴⁻⁶ have been identified as key elements in anchoring various proteins to cell membranes. Finally, glycerophosphatidylserine (GPS) has been shown to stimulate histamine secretion from mast cells.⁷⁻⁹

Mass spectrometric analysis of phospholipids has previously been attempted by electron ionization (EI),¹⁰⁻¹² field desorption,¹³⁻¹⁷ chemical ionization (CI),¹⁸⁻²² plasma desorption,²³ thermospray/EI,^{24,25} laser desorption,²⁶⁻²⁸ and fast atom bombardment (FAB),²⁹⁻³³ To date, FAB has been the most successful ionization method for phospholipid mass analysis; much of that work has been

- (3) Lewis, R. A.; Austen, K. F. *J. Clin. Invest.* **1984**, *73*, 889-897.
- (4) Low, M. G.; Saliel, A. R. *Science* **1988**, *239*, 268-275.
- (5) Thomsen, J. R.; Dwek, R. A.; Rademacher, T. W. *Biochemistry* **1990**, *29*, 5413-5422.
- (6) Kamitani, T.; Menon, A. K.; Hallaq, Y.; Warren, C. D.; Yeh, E. T. H. *J. Biol. Chem.* **1992**, *267*, 24611-24619.
- (7) Goth, A.; Adams, H. R.; Knoohuizen, M. *Science* **1971**, *173*, 1034-1035.
- (8) Martin, T. W.; Lagunoff, D. *Nature* **1979**, *279*, 250-252.
- (9) Martin, T. W.; Lagunoff, D. *Biochemistry* **1980**, *19*, 3106-3113.
- (10) Klein, R. A. *J. Lipid Res.* **1971**, *12*, 123-131.
- (11) Klein, R. A. *J. Lipid Res.* **1971**, *12*, 628-635.
- (12) Ohashi, M.; Iino, H.; Tsujimoto, K.; Ohashi, Y.; Shida, Y. *Org. Mass Spectrom.* **1985**, *20*, 642-643.
- (13) Wood, G. W.; Lau, P. Y. *Biomed. Mass Spectrom.* **1974**, *1*, 154-155.
- (14) Wood, G. W.; Lau, P. Y.; Rao, G. N. S. *Biomed. Mass Spectrom.* **1976**, *3*, 172-176.
- (15) Wood, G. W.; Lau, P. Y.; Morrow, G.; Rao, G. N. S.; Schmidt, D. E.; Tuebner, J. *J. Chem. Phys. Lipids* **1977**, *18*, 315-333.
- (16) Sugatani, J.; Kino, M.; Saito, K.; Matsuo, T.; Matsuda, H.; Katakuse, I. *Biomed. Mass Spectrom.* **1982**, *9*, 293-301.
- (17) Lehmann, W. D.; Kessler, M. *Chem. Phys. Lipids* **1983**, *32*, 123-135.
- (18) Foltz, R. L. *Lloydia* **1972**, *35*, 344-353.
- (19) Crawford, C. G.; Plattner, R. D. *J. Lipid Res.* **1983**, *24*, 456-460.
- (20) Bissere, P.; Nakatani, Y.; Ourisson, G.; Hueber, K.; Teller, G. *Chem. Phys. Lipids* **1983**, *33*, 333-332.
- (21) Jungalwala, F.; Evans, J. E.; McCluer, R. H. *J. Lipid Res.* **1984**, *25*, 738-749.
- (22) Ayanoglu, E.; Wegmann, A.; Piet, G.; Marbury, G. D.; Hass, J. R.; Djerassi, C. *J. Am. Chem. Soc.* **1984**, *106*, 5246-5251.
- (23) Demirev, P. A. *Biomed. Mass Spectrom.* **1987**, *14*, 241-246.
- (24) Kim, H. Y.; Salem, N. *Anal. Chem.* **1986**, *58*, 9-14.
- (25) Kim, H. Y.; Salem, N. *Anal. Chem.* **1987**, *59*, 722-726.
- (26) Cotter, R. J.; Tabet, J. C. *Int. J. Mass Spectrom. Ion Phys.* **1983**, *53*, 151-166.
- (27) Seydel, U.; Lindner, B.; Zahring, U.; Rietschel, E. T.; Kusumoto, S.; Shiba, T. *Biomed. Mass Spectrom.* **1984**, *11*, 132-141.
- (28) Wahl, M. C.; Kim, H. S.; Wood, T. D.; Guan, S.; Marshall, A. G. *Anal. Chem.* **1993**, *65*, 3669-3676.
- (29) Fenwick, G. R.; Eagles, J.; Self, R. *Biomed. Mass Spectrom.* **1983**, *10*, 382-386.

[†] Current address: National High Magnetic Field Laboratory, Florida State University.

^{*} Also a member of the Department of Chemistry, Florida State University.
(1) Samuelsson, B.; Goldyne, M.; Graustrom, E.; Hamberg, M.; Hammarstrom, S.; Malmsten, C. *Ann. Rev. Biochem.* **1978**, *47*, 997-1029.
(2) Samuelsson, B. *Science* **1983**, *220*, 568-575.

thoroughly reviewed by Murphy and Harrison.³⁴ Recently, Kim and co-workers³⁵ and Han and Gross³⁶ have applied electrospray ionization to phospholipid mass analysis.

From its introduction in 1988,^{37,38} matrix-assisted laser desorption/ionization (MALDI) has provided a versatile and sensitive means for producing singly-charged gas-phase biomolecules for mass analysis.^{39,40} In particular, the combination of MALDI and Fourier transform ion cyclotron resonance mass spectrometry (FT-ICR/MS) offers ultrahigh mass resolution, unparalleled mass accuracy, and MSⁿ capabilities. Recent advances in FT-ICR instrumentation, most notably ion axialization,⁴¹ allow for all of these advantages to be realized simultaneously. For example, Huang et al.⁴² have recently shown that simultaneous application of dipolar and azimuthal quadrupolar excitation in the source side ion trap of a dual trap mass analyzer allows for MSⁿ up to $n = 4$; at each stage, product ions formed during collisional activation may be refocused along the central axis of the electrostatic trapping potential and passed through a conductance limit to a second low-pressure analyzer ion trap for analysis at ultrahigh mass resolving power.

Here, we demonstrate the as-yet unrecognized potential of MALDI FT-ICR/MS for mass analysis of phospholipids. We find that MS/MS based on sustained off-resonance (dipolar) irradiation (SORI)⁴³ of both positive and negative molecular ions generates structurally informative fragment ions, which may be axialized by broadband azimuthal quadrupolar irradiation in the presence of argon collision gas.^{42,44} The fragment ions may then be transferred to a second low-pressure analyzer ion trap for high-resolution mass analysis. We discuss and interpret preliminary results for a variety of matrices. We also demonstrate a sample cryo-cooling technique which minimizes matrix adduct formation encountered in negative ion mode.

EXPERIMENTAL SECTION

Instrumentation. All FT-ICR mass spectra were acquired at 3 T with an Extrel FTMS-2000 FT-ICR mass spectrometer (Extrel-Waters, Madison, WI), equipped with a dual ion trap mass analyzer, an automatic insertion probe, and an Odyssey data station. A UV laser beam from either a frequency-tripled 355 nm Nd:YAG (Surelite II, Continuum, Inc., Santa Clara, CA) or a 337 nm nitrogen laser (VSL-337, Laser Science, Inc., Newton, MA)

was directed through a window in the analyzer side of the main vacuum chamber. The beam was focused by a telescope lens assembly (Nd:YAG laser) or a 1 m focal length lens (nitrogen laser) through the conductance limit separating the source and analyzer traps and onto the sample probe. The relay for switching between dipolar and quadrupolar excitation was similar to that described previously.⁴⁵ Due to the high capacitive load presented by this circuit, a low-power ($\sim 27 V_{p-p}$) Nicolet excitation amplifier was used in place of the high-power amplifier supplied with the FTMS-2000 mass spectrometer.

Sample Preparation. Appropriate aliquots of stock solutions, 1 mM phospholipid (Sigma Chemical Co., St Louis, MO) in either chloroform or 50:50 (v/v) chloroform/methanol, and 0.5–1 M matrix in methanol acidified with 0.1% (v/v) trifluoroacetic acid, were combined to make sample solutions, each containing (unless otherwise noted) matrix/analyte at 5000:1 mole ratio. Note that all phospholipids were used as received from Sigma, without further purification. Twenty microliters of sample solution, containing ~ 3.5 nmol of sample, was then applied to a stainless steel probe tip and allowed to dry completely before insertion into the mass spectrometer. Based on the relative size of the sample probe and laser spot, and assuming even sample distribution on the probe surface, we estimate that ~ 1.5 pmol of lipid is desorbed per laser shot.

FT-ICR Experimental Event Sequence. Ion trapping was facilitated by biasing the conductance limit plate to ± 9 V (positive ion/negative ion), the source trap plate to ground potential, and the sample probe to ± 2 V for 50–75 μ s during the laser fire event [laser pulse width was ~ 7 ns (Nd:YAG) or ~ 3 ns (nitrogen)]. After ionization, the source trap and conductance limit plates were set to ± 2 V, and the ions were allowed to relax to the central trap axis for 2–4 s. Note that each spectrum presented was generated from a single laser shot. For broadband excitation and detection [Figures 1 and 6 (top)], standard chirp excitation (1–500 kHz at a sweep rate of 100 Hz/ μ s at $\sim 27 V_{p-p}$ amplitude) and dipolar detection (256K time domain data acquired with a 1 MHz Nyquist bandwidth) were then carried out in the source-side ion trap. The time domain signal was Fourier transformed without zero-filling or apodization and displayed in magnitude mode.

For collisional activation [Figures 2–5 and 6 (bottom)], the molecular ion isotopic distribution of interest was first isolated by use of SWIFT radial ejection of undesired ions,^{46,47} followed by sustained off-resonance (single-frequency) irradiation ($\sim 9.5 V_{p-p}$ for 300–500 ms).⁴³ One hundred milliseconds later, a series of broadband SWIFT azimuthal quadrupolar excitation waveforms (spaced 250 ms apart) served to axialize the product ions.^{42,44} Pressure in the source-side ion trap was held constant at $\sim 1.0 \times 10^{-7}$ Torr during collisionally activated dissociation and axialization. Following transfer of ions through a conductance limit to the analyzer ion trap, dipolar frequency sweep excitation (1–500 kHz at a sweep rate of 1000 Hz/ μ s at $\sim 78 V_{p-p}$ amplitude) and detection (1 M time domain data acquired with a 1 MHz Nyquist bandwidth) were performed. The time domain signal was Fourier

- (30) Sherman, W. R.; Ackermann, K. E.; Bateman, R. F.; Green, B. N.; Lewis, I. *Biomed. Mass Spectrom.* **1985**, *12*, 409–413.
- (31) Jensen, N. J.; Tomer, K. B.; Gross, M. L. *Lipids* **1986**, *21*, 580–588.
- (32) Jensen, N. J.; Tomer, K. B.; Gross, M. L. *Lipids* **1987**, *22*, 480–489.
- (33) Cole, M. J.; Enke, C. G. *Anal. Chem.* **1991**, *63*, 1032–1038.
- (34) Murphy, R. C.; Harrison, K. A. *Mass Spectrom. Rev.* **1994**, *13*, 57–75.
- (35) Kim, H. Y.; Wang, T. C. L.; Ma, Y. C. *Anal. Chem.* **1994**, *66*, 3977–3982.
- (36) Han, X.; Gross, R. W. *Proc. Natl. Acad. Sci. U.S.A.* **1994**, *91*, 10635–10639.
- (37) Karas, M.; Hillenkamp, F. *Anal. Chem.* **1988**, *60*, 2289–2301.
- (38) Tanaka, K.; Waki, H.; Ido, Y.; Akita, S.; Yoshida, Y.; Yoshida, T. *Rapid Commun. Mass Spectrom.* **1988**, *2*, 151–153.
- (39) Hillenkamp, F.; Karas, M.; Beavis, R. C.; Chait, B. T. *Anal. Chem.* **1991**, *63*, 1193A–1203A.
- (40) Karas, M.; Bahr, U.; Giessman, U. *Mass Spectrom. Rev.* **1991**, *10*, 335–357.
- (41) Guan, S.; Kim, H. S.; Marshall, A. G.; Wahl, M. C.; Wood, T. D.; Xiang, X. *Chem. Rev.* **1994**, *94*, 2161–2182.
- (42) Huang, Y.; Paša-Tolić, L.; Guan, S.; Marshall, A. G. *Anal. Chem.* **1994**, *66*, 4385–4389.
- (43) Gauthier, J. W.; Trautman, T. R.; Jacobson, D. B. *Anal. Chim. Acta* **1991**, *246*, 211–225.
- (44) Guan, S.; Wahl, M. C.; Marshall, A. G. *J. Chem. Phys.* **1994**, *100*, 6137–6140.

- (45) Speir, J. P.; Gorman, G. S.; Pitsenberger, C. C.; Turner, C. A.; Warg, P. P.; Amster, I. J. *Anal. Chem.* **1993**, *65*, 1746–1752.
- (46) Marshall, A. G.; Wang, T.-C. L.; Ricca, T. L. *J. Am. Chem. Soc.* **1985**, *107*, 7893–7897.
- (47) Marshall, A. G.; Wang, T.-C. L.; Chen, L.; Ricca, T. L. In *Fourier Transform Mass Spectrometry: Evolution, Innovation, and Applications*; ACS Symposium Series 359; Buchanan, M. V., Ed.; American Chemical Society: Washington, DC, 1987; pp 21–33.

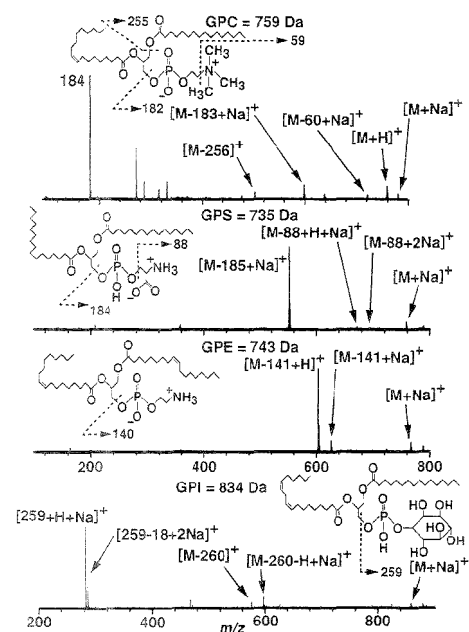


Figure 1. Positive ion FT-ICR magnitude mode mass spectra for, from top to bottom, GPC-16:0,18:1, GPS-di16:0, GPE-di18:1, and GPI-16:0,18:2. In each case, the molecular ion or its sodium adduct is observed, as well as ions indicative of the polar head group (choline, serine, ethanolamine, and inositol, respectively).

transformed without zero-filling or apodization and displayed in magnitude mode.

RESULTS AND DISCUSSION

Matrix Selection. We initially used a frequency-tripled Nd:YAG laser (355 nm) with 2,5-dihydroxybenzoic acid (DHB) as the MALDI matrix. The optimum matrix-to-analyte ratio was found to be ~5000:1 for a variety of phospholipids. Abundant positive and negative ions were observed, although matrix adduct peaks frequently appeared in the negative ion mass spectra (see below). For the same matrix-to-analyte ratio, *trans*-4-hydroxy-3-methoxycinnamic acid (TCA) gave abundant negative ions but little or no positive ion signal. Among several other matrices tested (5000:1 matrix-to-analyte ratio), including 4-hydroxy-3-methoxybenzoic acid (HMBA), 3,4-dihydroxycinnamic acid (DCA), 3-hydroxypicolinic acid (HPA), 4-nitroaniline (NA), 3,5-dimethoxy-4-hydroxycinnamic acid (DHCA), and α -cyano-4-hydroxycinnamic acid (CHCA), only DCA and NA yielded phospholipid ions, albeit at much lower abundance than for either DHB or TCA. It is possible that optimization of the matrix-to-analyte ratio could improve the ion yield for those matrices.

GPC, GPS, GPE, and GPI Positive Ion Mass Spectra.

Figure 1 shows our more recent results with a nitrogen laser; those mass spectra were obtained with a DHB matrix, in a 5000:1 molar ratio with respect to the lipid analyte. Figure 1 (top) shows a positive ion FT-ICR mass spectrum for GPC-16:0,18:1. Both protonated ($m/z = 760$) and sodiated ($m/z = 782$) molecular ions are observed, as well as sodiated fragments corresponding to loss

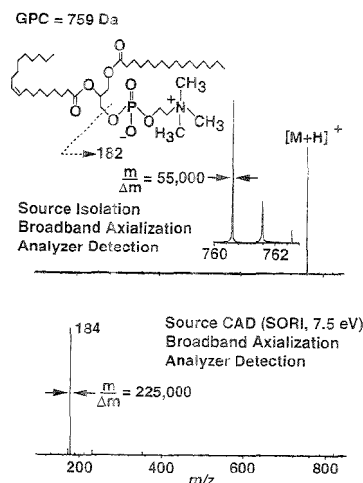


Figure 2. Collisional dissociation of GPC-16:0,18:1 positive ions. Following isolation of protonated molecular ion isotopic distribution, $m/z \approx 760$ –763 (top), collisional activation yields abundant phosphocholine ions, $m/z = 184$, which may be efficiently axialized and transferred to the analyzer ion trap for high-resolution mass analysis (bottom). Identification of the choline polar head group defines the phospholipid class (GPC).

of trimethylamine ($m/z = 722$) and loss of the polar head group ($m/z = 599$). In addition, fragments corresponding to the polar head group ($m/z = 184$) and loss of palmitic acid ($m/z = 504$) are also observed. The next spectrum in Figure 1 shows positive ions from GPS-di16:0, for which the most abundant fragment is a sodium adduct, corresponding to loss of the polar head group ($m/z = 573$). Sodiated molecular ion is also present ($m/z = 758$), as well as sodium adducts of dipalmitoylglycerophosphatic acid ($m/z = 671, 693$), formed by loss of serine.

Proceeding downward to the third spectrum in Figure 1, the most abundant positive ion observed for GPE-di18:1 is the loss of the polar head group ($m/z = 603$), along with the corresponding sodium adduct ($m/z = 625$). The sodiated molecular ion ($m/z = 766$) is also observed. Finally, the lowermost spectrum in Figure 1 is from GPI-18:2,16:0, for which the most abundant fragment is the sodiated polar head group ($m/z = 283$), along with the sodiated molecular ion ($m/z = 857$) and an ion formed by neutral loss of the polar head group ($m/z = 597$). Note that for positive ions from each phospholipid class, there is an abundant ion serving to identify the polar head group: phosphocholine ($m/z = 184$) for GPC, sodiated phosphoinositol ($m/z = 283$) for GPI, and ions corresponding to the neutral loss of the polar head group for GPS and GPE.

Collisional Activation of GPC Positive Ions. Although the ions observed in Figure 1 allow, in principle, for assignment of phospholipid class, unambiguous identification of a specific lipid present in an unknown mixture requires tandem mass spectrometric analysis. For example, Figure 2 shows MS/MS of GPC-16:0,18:1 positive ions. First, the molecular ion isotopic distribution ($m/z \approx 760$ –763) is isolated by SWIFT (dipolar) ejection of ions of other m/z values. Next, a series of azimuthal quadrupolar SWIFT (broadband) waveforms axializes the remaining ions. After transfer to the analyzer-side ion trap, standard dipolar excitation

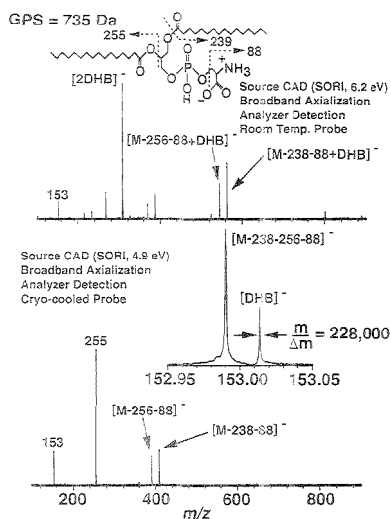


Figure 3. Collisional activation of GPS-dil6:0 negative ions desorbed/ionized from a room temperature (top) or cryo-cooled (bottom) solids probe. After isolation of the deprotonated isotopic distribution, $m/z \approx 734-737$, collisional activation yields abundant fragment ions, which are subsequently axialized and transferred to the analyzer ion trap for high-resolution mass analysis. Note that cryo-cooling the probe eliminates matrix adduct formation.

and detection yields the spectrum shown in Figure 2 (top). Clearly, isolation of protonated molecular ions, $(M + H)^+$, is quite efficient, and high mass resolving power is easily obtained after axialization and transfer to the analyzer ion trap. To collisionally activate the molecular ion, sustained off-resonance irradiation is applied between the isolation and axialization events. The average (lab frame) ion kinetic energy, calculated according to the method of Huang et al.,¹² attained during off-resonance irradiation is ~ 7.5 eV. Figure 2 (bottom) shows that CAD yields abundant ions of $m/z = 184$, corresponding to the PC head group. CAD efficiency is high, as is the collection efficiency due to axialization of product ions after dissociation.

Collisional Activation of GPS Negative Ions. Matrix Adducts. Although each phospholipid class yielded negative ions in abundance, matrix adduction proved problematic, especially for DHB matrix. For example, if a 5 s postisolation delay is inserted prior to (dipolar) excitation and detection (source-side ion trap), then equal magnitudes of deprotonated GPE molecular ion ($m/z \approx 716$) and its matrix adduct ($m/z \approx 870$) are observed (not shown). If the postisolation delay is increased to 30 s, then the matrix adduct ($m/z \approx 870$) is the only anion observed (not shown).

Matrix adduction is also problematic for collisional activation. Although off-resonance irradiation is applied promptly (i.e., within 500 ms) after isolation of the deprotonated molecular ion isotopic distribution, so that matrix adducts are not formed initially, the postdissociation product axialization process can require from 5 to 30 s to achieve efficient focusing of ions along the central z-axis of the ion trap. As a result, matrix adduction can dominate the mass spectrum. For example, Figure 3 (top) shows product ions observed after CAD of GPS-dil6:0. The experimental event sequence here consists of ionization, 4 s ion cooling period,

isolation of the molecular ion isotopic distribution ($m/z \approx 734-737$, not shown), 100 ms delay, collisional activation (SORI at average parent ion kinetic energy of ~ 6.2 eV), 100 ms delay, product ion broadband axialization, and ion transfer to the analyzer trap for standard (broadband) dipolar excitation and detection. Matrix ($m/z = 153, 307$) and matrix adduct species ($m/z = 546, 563$) clearly dominate the mass spectrum and complicate its interpretation.

Sample Cryo-cooling. The automatic insertion solids probe of the FTMS-2000 instrument is equipped with a small port, through which cryogenic gas may be fed to the probe tip for effective sample cooling under vacuum. Figure 3 (bottom) shows collisional activation of GPS-dil6:0 while the sample probe is kept cold with liquid nitrogen. Collisional activation of the molecular ion isotopic distribution (SORI at an average parent ion kinetic energy of ~ 4.9 eV), followed by broadband axialization and transfer of product ions to the analyzer trap, yields the bottom spectrum: note the absence of matrix adduct ions. We are now able to observe abundant fragment ions corresponding to palmitate anion ($m/z = 255$), neutral loss of palmitic acid and serine ($m/z = 391$), and neutral loss of the ketene analog of palmitic acid and serine ($m/z = 409$).

The inset in Figure 3 (bottom) provides a mass scale expansion of the region near $m/z = 153$. The lower-mass ion ($m/z = 152.996$), a monodehydrated glycerophosphoric acid resulting from loss of serine, palmitic acid, and the corresponding ketene of palmitic acid, differs by only 0.023 u from the matrix anion ($m/z = 153.019$); nevertheless, these species are easily resolved (mass resolving power, $m/\Delta m_{50\%} = 228\,000$ for the matrix anion, where $\Delta m_{50\%}$ is the full peak width at half-maximum peak height).

At room temperature (Figure 3, top), the matrix dimer is the most abundant species, even though initial isolation of the GPS molecular ion effectively removes matrix anions from the ion trap. Figure 3 (top) also shows no signal for either palmitate anion ($m/z = 255$) or its matrix adduct for the probe at room temperature. Since palmitate anions are clearly present in abundance from the cold probe, it appears that DHB neutrals subliming from the room temperature probe transfer a proton to palmitate anions, thus forming abundant matrix anions at the expense of the palmitate anions. We therefore conclude that cryo-cooling the probe tip greatly reduces matrix sublimation. In support of that view, note that the neutral loss species involving loss of palmitate [$m/z = 392, 409$ in Figure 3 (bottom) for the cryo-cooled sample] appear with added matrix in the room-temperature sample [$m/z 546, 563$ in Figure 3 (top)]. Finally, Nelson et al.⁴⁸ have previously obtained laser desorption/ionization time-of-flight mass spectra from frozen aqueous solutions of DNA and protein, but their experiments were performed at a laser wavelength (~ 580 nm) designed to match the *minimum* absorbance of the (water) matrix, whereas the present experiments are conducted at a laser wavelength designed to *maximize* matrix absorption.

Collisional Activation of GPC Negative Ions. Abundant negative ions were also observed with *trans*-4-hydroxy-3-methoxycinnamic acid (TCA) as the matrix. Matrix adduction was not as severe with TCA as for DHB, and cryo-cooling the sample probe was thus not necessary. Figure 4 shows collisional activation for GPC-dil6:0 formed from TCA matrix. Because of the trimethylamine moiety, deprotonated molecular ions are not observed in

(48) Nelson, R. W.; Thomas, R. M.; Williams, P. *Rapid Commun. Mass Spectrom.* **1990**, *4*, 348-351.

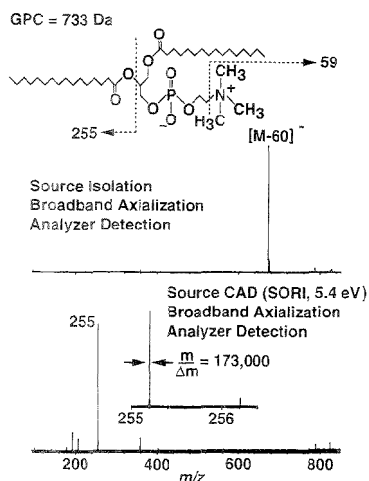


Figure 4. Collisional activation of GPC-d16:0 negative ions. Abundant quasi-molecular ions, corresponding to loss of the trimethylamine moiety ($m/z \approx 673-677$), are easily isolated in the source-side ion trap, axialized, and transferred to the analyzer trap (top). Collisional activation in the source trap yields abundant palmitate anions ($m/z = 255$), which may subsequently be axialized and transferred to the analyzer ion trap for high-resolution mass analysis (bottom).

negative ion GPC FAB mass spectra; rather, quasi-molecular species corresponding to loss of a methyl group $[M - 15]^-$, loss of quaternary amine $[M - 60]^-$, and loss of choline $[M - 86]^-$ are typically seen.³¹⁻⁴⁹ At a matrix-to-analyte ratio of 5000:1, we obtained roughly equal abundances of the $[M - 15]^-$ and $[M - 60]^-$ anions (not shown). As reported for MALDI analysis of other bio-molecules,⁵⁰ the degree of fragmentation may be adjusted by changing the matrix-to-analyte ratio. For a matrix-to-analyte ratio of 500:1, loss of trimethylamine became the most abundant species in the negative ion FT-ICR mass spectrum of GPC-d15:0. Figure 4 (top) shows the quasi-molecular anion ($m/z \approx 673-677$) isotopic distribution after isolation (source-side ion trap), axialization, and transfer to the analyzer ion trap. Upon collisional activation (SORI at average parent ion kinetic energy of ~ 5.4 eV), the quasi-molecular ion dissociates, yielding abundant palmitate anions ($m/z = 255$). The bottom spectrum in Figure 4 shows the dissociation product ions after axialization and transfer to the analyzer side of the dual ion trap. Again, both the dissociation and axialization processes are extremely efficient, yielding product ions in high abundance with high mass resolving power.

Collisional Activation of GPE Negative Ions. Deprotonation of the terminal ammonium group results in abundant $[M - H]^-$ anions for glycerophosphatidylethanolamines.^{32,51} Figure 5 shows our results from collisional activation of GPE-16:0,18:1 $[M - H]^-$ anions, with TCA matrix at a 5000:1 molar ratio relative to the analyte. The top spectrum shows GPE-deprotonated molecular anion isotopic distribution ($m/z \approx 716-720$) after isolation in the source ion trap, broadband axialization, and transfer to the

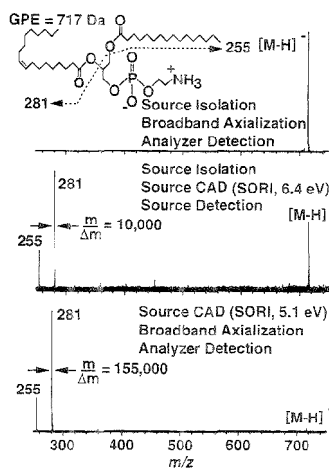


Figure 5. Collisional activation of GPE-16:0,18:1 negative ions. The top spectrum shows deprotonated molecular ions detected in the analyzer ion trap, after isolation and axialization in the source trap. Following collisional activation, product ions corresponding to the palmitic ($m/z = 255$) and oleic ($m/z = 281$) acid side chains may be detected in the source-side ion trap (middle) or axialized and transferred to the analyzer ion trap (bottom) for high-resolution mass analysis.

analyzer trap. We then performed collisional activation of the molecular ion in the source-side trap, followed by either source-side (dipolar) excitation and detection (Figure 5, middle) or broadband axialization and transfer to the analyzer trap for (dipolar) excitation and detection (Figure 5, bottom). In each case, collisional activation was achieved by off-resonance dipolar excitation at ~ 1 kHz below the reduced cyclotron frequency, ω_{-} , whereas other parameters (SORI excitation voltage amplitude and duration) were optimized for maximum product ion signal magnitude. Collisional activation results in formation of palmitate ($m/z = 255$) and oleate ($m/z = 281$) anions. Comparison of middle and bottom mass spectra in Figure 5 clearly establishes the much greater observed ion abundance and higher mass resolving power resulting from product ion axialization and ion transfer to the low-pressure analyzer trap following collisional activation. For example, the signal-to-noise ratio for the oleate anion ($m/z = 281$) increases by a factor of at least 5, whereas the mass resolving power increases 15-fold ($m/\Delta m_{50\%} \approx 10\,000$ for source trap detection vs $m/\Delta m_{50\%} \approx 155\,000$ for analyzer trap detection). Note that in the middle and bottom spectra, the acyl substituent at *sn*-2 is observed at an abundance of $\sim 3:1$ relative to the *sn*-1 substituent.

Collisional Activation of GPI Negative Ions. An obvious long-term goal of the present line of experiments will be to analyze biological mixtures of phospholipids, as from biological cell extracts. Toward that end, we begin here by analyzing a GPI mixture, consisting of phospholipids of a common class (i.e., the same inositol polar head group) but with various possible fatty acid side chains. The sample is a soybean extract (Sigma Chemical Co., 98% pure) reported to contain mainly palmitic (16:0) and linoleic (18:2) acids. We used TCA matrix at a 5000:1 molar ratio relative to GPI. Figure 6 (top) shows a standard broadband FT-ICR mass spectrum obtained in the source-side ion trap. Of

(49) Zirrelli, J. A.; Clay, K. L.; Murphy, R. C. *Lipids* 1991, 26, 1112-1116.
 (50) Sotouki, C.; Russell, D. H. *Appl. Spectrosc.* 1993, 47, 211-217.
 (51) Murphy, R. C. *Mass Spectrometry of Lipids*; Plenum Press: New York, 1993; Vol. 7, 290 pp.

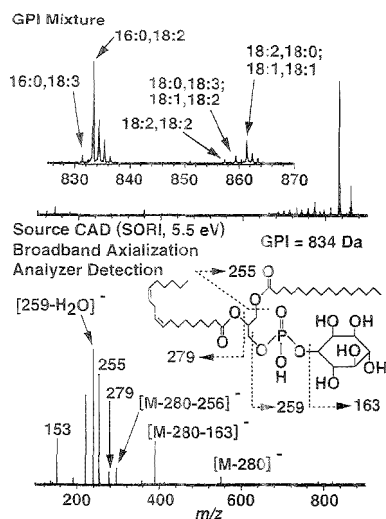


Figure 6. Identification of components of a mixture of phospholipids with the same polar head group (GPI) but different fatty acid side chains. The most abundant GPI molecular anion isotopic distribution ($m/z \approx 833\text{--}837$) in a mixture of soybean GPI (top) is isolated (not shown) and subjected to collisional activation. Product ions are then axialized and transferred to the low-pressure analyzer ion trap for high-resolution (average $m/\Delta m_{50\%} \approx 145\,000$) mass analysis (bottom).

the various observed possible GPI molecular ions, varying widely in abundance, GPI-16:0,18:2 was assigned on the basis of CAD (see below), whereas other molecular ions were assigned on the basis of prior reports.^{32,34} The inset is a mass scale expansion of the molecular ion region ($830 \leq m/z \leq 870$). The most abundant anion isotopic distribution ($m/z \approx 833\text{--}837$) was isolated in the source ion trap (not shown) and subjected to collisional activation (SORI at average parent ion kinetic energy of ~ 5.5 eV). Product ions were axialized following CAD and transferred to the analyzer ion trap, where standard (dipolar) excitation and detection yielded the spectrum shown in Figure 6 (bottom). The many structurally informative anions include palmitate ($m/z = 255$) and linoleate ($m/z = 279$) anions, loss of both acyl groups from the molecular ion ($m/z = 297$), loss of water from the polar head group ($m/z = 241, 223$), loss of both linoleic acid and inositol moieties ($m/z = 553, 391$) from the molecular ion, and monodehydrated glycerophosphoric acid ($m/z = 153$). Again, axialization of product anions after dissociation and subsequent transfer to the analyzer ion trap provide high mass resolving power (average $m/\Delta m_{50\%} \approx 145\,000$

for GPI product ions). From CAD analysis, we are able to identify the most abundant species in the GPI mixture as GPI-16:0,18:2. In this case, the relative positions (*sn*-1 or *sn*-2) for the palmitic and linoleic acyl groups cannot be determined from the present data; the structure shown in Figure 6 (bottom) is based on prior work by Myher and Kuksis.³²

CONCLUSIONS

Matrix-assisted laser desorption/ionization produces abundant molecular or quasi-molecular phospholipid ions, which are readily identified by Fourier transform ion cyclotron resonance mass spectrometry. The 2,5-dihydroxybenzoic acid (DHB) matrix yields both positive and negative ions, whereas *trans*-4-hydroxy-3-methoxycinnamic acid (TCA) provided mainly negative ions. Cryo-cooling the sample probe effectively eliminated matrix adduction for negative ions produced from a DHB matrix. For either matrix, abundant ion signal was observed for phospholipids in the low picomole range.

Collisional activation of quasi-molecular ions yielded product ions from which the polar head group and fatty acid side chains could be identified: the observed fragmentation patterns are similar to those previously reported for FAB and electrospray ionization. Azimuthal quadrupole excitation following dissociation efficiently focuses product ions close to the central axis; subsequent transfer to the low-pressure analyzer ion trap provides high-resolution ($m/\Delta m_{50\%} > 100\,000$) mass analysis. Additional CAD stages should be feasible: for example, MSⁿ could serve to identify fatty acid side chains and the location of double bond(s) (by means of charge-remote fragmentation) within each side chain.

Compared to prior FAB ionization with triple-quadrupole MS/MS, phospholipid analysis with MALDI FT-ICR MS/MS provides much higher mass resolving power, particularly in the second MS stage, thus facilitating identification of acyl groups differing by only two mass units (e.g., one double bond). Furthermore, MALDI minimizes extraneous matrix peaks, clusters, and adducts. Finally, the sensitivity of the present method compares favorably to prior ionization methods (FAB, electrospray). We are currently investigating the ultimate MALDI FT-ICR/MS detection limit for phospholipids and peptides, for ultimate applications to the analysis of complex biological mixtures.

ACKNOWLEDGMENT

We gratefully acknowledge L. Paša-Tolić, M. Senko, and T. Solouki for many helpful discussions. This work was supported by NSF (CHE-9021058 and CHE-93-22824), NIH (GM-31683), The Ohio State University, and the National High Magnetic Field Laboratory at Florida State University.

Received for review May 9, 1995. Accepted August 10, 1995.*

AC950440M

* Abstract published in *Advance ACS Abstracts*, September 15, 1995.

(52) Myher, J. J.; Kuksis, A. *Biochim. Biophys. Acta* **1984**, *795*, 85–90.

Electrospray Liquid Chromatography/Mass Spectrometry of Ginsenosides

Richard B. van Breemen,* Chao-Ran Huang, Zhi-Zhen Lu, Agnes Rimando,[†] Harry H. S. Fong, and John F. Fitzloff

Department of Medicinal Chemistry and Pharmacognosy, University of Illinois at Chicago (m/c 781), 833 South Wood Street, Chicago, Illinois 60612-7231

An electrospray liquid chromatography/mass spectrometry (LC/MS) method has been developed for the analysis of ginseng saponins (ginsenosides) contained in extracts of the root of *Panax ginseng* (Korean ginseng) and *Panax quinquefolius* (American ginseng). The LC/MS method consists of separation of ginsenosides using an (aminopropyl)silica HPLC column, followed by detection using a photodiode array UV absorbance detector and then on-line electrospray mass spectrometry. Ginsenosides eluted from the HPLC column in order of increasing molecular weight and were detected as $[M + Na]^+$ or $[M - 138]^-$ adducts. Occurrence of $[M + 138]^+$ adducts was most prominent when new HPLC columns were used, and none were observed when solutions of ginsenoside standards were infused into the mass spectrometer without use of HPLC. The cation weighing 138 was identified as (3-ammoniumpropyl)trihydroxysilane, $^+NH_4(CH_2)_3Si(OH)_3$, which was either a byproduct of stationary phase synthesis or a stationary phase degradation product. LC/MS chromatograms of extracts of Korean ginseng and American ginseng demonstrated substantial differences between the relative amounts of each ginsenoside. Based on molecular weight and coelution with standards, ginsenosides R_{g1} , R_c , R_d , R_e , R_{f2} , and R_{f1} (in order of elution from the HPLC column) were identified in both ginseng extracts. Four other ginsenosides were detected by mass spectrometry for which no standards were available, and their molecular weights were 801 (possibly corresponding to ginsenoside R_f), 817, 947, and 963 (possibly 20-gluco- R_g). The ginsenosides weighing 817 and 963 were detected only in the Korean ginseng extract.

Millions of U.S. consumers employ unconventional therapy in their health care,¹ and the use of herbal medicines constitutes a major portion of this total. In particular, ginseng products marketed as roots, capsules, tablets, and liquid extracts are widely consumed. Because of the widespread interest in ginseng products, analytical methods are needed to determine the integrity of ginseng products sold in health food stores, pharmacies, and Oriental food markets and to identify their constituent ginsenosides, which are the components that are most likely responsible for exerting the biological effects attributed to ginseng.

American or Korean ginseng each contains a series of triterpene saponins called ginsenosides in distinctive proportions or profiles. (See ginsenoside structures in Table 1.) Several analytical approaches to the identification of ginsenosides in ginseng extracts have been published, involving analysis of either hydrolyzed ginsenosides, intact, derivatized ginsenosides, or intact, native ginsenosides. Because their high hydrophilicity precludes analysis by some techniques, ginsenosides are often hydrolyzed using concentrated acid,^{2,3} alkali,^{3,4} or acid followed by alkali⁵ and then purified and analyzed as their corresponding sapogenins. For example, sapogenins from several ginsenosides were trimethylsilylated and then analyzed using gas chromatography/mass spectrometry.⁴ Problems associated with this approach include incomplete hydrolysis (i.e., yields from 27%³ to 85%⁴), formation of rearrangement products (especially during acid hydrolysis⁶), extra sample handling and time for hydrolysis and derivatization, and loss of information regarding the original composition of ginsenosides. Therefore, the analysis of intact ginsenosides would be preferred in order to overcome all of the problems associated with ginsenoside hydrolysis and derivatization.

Isolation of intact, underivatized ginsenosides has been carried out using high-performance liquid chromatography (HPLC) with stationary phases consisting of reversed phase silica⁶ or ion exchange chromatography⁷ using either UV absorbance detection or pulsed amperometric detection, respectively. Alternatively, specialized carbohydrate analysis columns have been used containing aminopropyl functional groups on the silica-based stationary phase.⁸⁻¹¹

After isolation, ginsenosides have been derivatized (i.e., peracetylated or pertrimethylsilylated) in order to increase their volatility prior to analysis using EI mass spectrometry.¹⁰ However, derivatized ginsenosides fragment extensively during EI and

(2) Brieskorn, C. H.; Mosandl, A. *Sri. Pharm.* **1978**, *46*, 106-116.

(3) Chen, Y. J.; Nose, M.; Ogihara, Y. *Chem. Pharm. Bull.* **1987**, *35*, 1653-1655.

(4) Cui, J.-F.; Garle, M.; Lund, E.; Bjorkhem, I.; Eneroth, P. *Anal. Biochem.* **1993**, *210*, 411-417.

(5) Li, Y. H.; Li, X. L.; Hong, L.; Liu, J. Y.; Zhang, M. Y. *Biomed. Chromatogr.* **1992**, *6*, 88-90.

(6) Kanazawa, H.; Nagata, Y.; Kurosaki, E.; Matsushima, Y.; Takai, N. *J. Chromatogr.* **1993**, *632*, 79-85.

(7) Parr, M. K.; Parr, J. H.; Lee, M. Y.; Kim, S. J.; Park, I. J. *J. Liquid Chromatogr.* **1994**, *17*, 1171-1182.

(8) Nagasawa, T.; Yokozawa, T.; Nishino, Y.; Oura, H. *Chem. Pharm. Bull.* **1980**, *28*, 2059-2064.

(9) Park, N. H.; Park, M. K.; Choi, K. J.; Cho, Y. H. *Arch. Pharm. Res.* **1982**, *5*, 7-12.

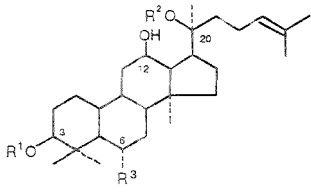
(10) Kim, B.-Y.; Lee, M. Y.; Cho, K. H.; Park, J. H.; Park, M. K. *Arch. Pharm. Res.* **1992**, *328*-332.

(11) Chang, Y. S. Chemical and Pharmacological Studies of *Panax quinquefolius* and *Panax ginseng*. Ph.D. Dissertation, University of Illinois at Chicago, Chicago, IL, 1989.

* Current address: USDA, Richard B. Russell Agriculture Research Center, Athens, GA 30605-2720.

[†] Eisenberg, D. M.; Kessler, R. C.; Foster, C.; Norlock, F. E.; Calkins, D. R.; Delbanco, T. L. *N. Engl. J. Med.* **1993**, *328*, 246-252.

Table 1. Ginsenoside Structures



compd	R ¹	R ²	R ³	formula	theor MW
R _{g1}	H	Glc-O-	Glc-	C ₄₂ H ₇₂ O ₁₁	801
R _g	H	Rha-Glc-O-	Glc-	C ₄₈ H ₈₂ O ₁₈	947
R _d	Glc-Glc-	H	Glc-	C ₄₈ H ₈₂ O ₁₈	947
20-gluco-R _f	H	Glc-Glc-O-	Glc-	C ₄₈ H ₈₂ O ₁₉	963
R _e	Glc-Glc-	H	Ara(β)-Glc-	C ₅₃ H ₉₀ O ₂₂	1079
R _{b2}	Glc-Glc-	H	Ara(α)-Glc-	C ₅₃ H ₉₀ O ₂₂	1079
R _{b1}	Glc-Glc-	H	Glc-Glc-	C ₅₄ H ₉₂ O ₂₃	1109

produce no molecular ions or molecular ions of very low abundance.¹² To determine molecular weights of underivatized ginsenosides, desorption ionization mass spectrometry has been used, including ionization methods of ²⁵²Cf-plasma desorption,¹³ field desorption,¹⁴ and liquid secondary ion mass spectrometry.¹⁵ All of these desorption ionization techniques produced abundant [M + Na]⁺ or [M + K]⁺ ions. However, no liquid chromatography/mass spectrometry (LC/MS) methods have been reported for ginsenoside analysis.

This investigation reports the first LC/MS analysis of ginsenosides and ginseng extracts. This study is also the first application of electrospray to ionize this class of compounds. In addition, unusual ginsenoside adduct ions, [M + 138]⁺, are described for the first time, and their origin as artifacts arising from the (aminopropyl)silica HPLC stationary phase is described.

EXPERIMENTAL SECTION

Roots of *Panax quinquefolius* L. (Araliaceae), commonly known as "American ginseng", were obtained from Kirkwood Associates, Chicago, IL, in 1989. Herbarium specimens of this material were deposited at the University of Illinois Pharmacognosy Field Station herbarium. Roots of *Panax ginseng* C. A. Meyer (Araliaceae), commonly known as "Korean ginseng", were kindly provided by Dr. Il-Moo Chang, Natural Products Research Institute, Seoul National University, Korea. Herbarium specimens of this material were retained at the herbarium of Seoul National University.

Ginseng (American or Korean) root powder, 5.0 g, was extracted three times with 30 mL aliquots of 80% methanol. The combined methanolic extract was evaporated to dryness under vacuum at 55 °C, and the dried residue was dissolved in 10 mL of water. The aqueous solution was applied to an Extrelut QE extraction column (EM Industries, Inc.) and then eluted with 40 mL of water-saturated butanol. The butanol eluate was evaporated to dryness under vacuum at 80 °C, and the residue, which contained the ginsenosides, was redissolved in methanol and filtered prior to LC/MS analysis.

Electrospray mass spectra were obtained using a Hewlett-Packard (Palo Alto, CA) 5989B MS engine quadrupole mass spectrometer equipped with a ChemStation data system and pneumatic nebulizer-assisted electrospray LC/MS interface. The mass spectrometer was interfaced to a Hewlett-Packard 1090 gradient HPLC system including an autoinjector and photodiode array UV/vis absorbance detector. The quadrupole analyzer was maintained at 120 °C, and unit resolution was used for all measurements. Nitrogen at a pressure of 80 psi was used for nebulization of the HPLC eluate, and nitrogen bath gas at 300 °C and a flow rate of 10 L/min was used for evaporation of solvent from the electrospray. The range *m/z* 600–1300 was scanned over ~4 s during LC/MS. During other mass spectrometric measurements, selected ion monitoring was carried out using a dwell time of 100 ms/ion.

HPLC separations were carried out using a Waters Associates (Milford, MA) carbohydrate analysis column (10 μm (aminopropyl)silica; 125 Å pore size; 3.9 × 300 mm) at a flow rate of 1.0 mL/min. Burdick and Jackson HPLC solvents were purchased from Baxter Diagnostics (McGaw Park, IL). The mobile phase consisted of isocratic water/acetonitrile (17:83 v/v) for 8 min, followed by a linear gradient from 17:83 (v/v) to 30:70 (v/v) over the next 22 min. During some analyses, a solution of water/methanol/acetic acid (50:50:1.05 v/v/v) was added postcolumn at 50 μL/min to potentially enhance the formation of protonated molecules. For negative ion electrospray, a solution of water/methanol/ammonia (concentrated aqueous) (50:50:1 v/v/v) at 50 μL/min was added postcolumn. During LC/MS, the flow was split 1:50 so that 21 μL/min entered the electrospray ionization source of the mass spectrometer.

Ginsenoside standards (~100 ng/μL in water/methanol/acetic acid, 50:50:0.05 v/v/v) were infused into the electrospray ionization source at 10 μL/min using a Harvard Apparatus (South Natick, MA) Model 22 syringe pump. Because ginsenoside standards were detected as [M + Na]⁺ ions, addition of 100 μM NaCl to the carrier solution was investigated as a means of enhancing electrospray ionization. In other experiments, 100 μM (3-aminopropyl)triethoxysilane was added to the carrier solution in order to generate (3-aminopropyl)trihydroxysilane (MW 137) and investigate the formation of ginsenoside adducts, [M + H + 137]⁺.

RESULTS AND DISCUSSION

During initial mass spectrometric experiments, ginsenoside standards were analyzed by infusing solutions directly into the electrospray ion source. Positive ion electrospray produced abundant cationized ginsenoside ions, [M + Na]⁺, but no protonated molecules. For example, the positive ion electrospray mass spectrum of ginsenoside R_e is shown in Figure 1A, and the corresponding ginsenoside structure is shown in Table 1. An abundant [M + Na]⁺ ion was detected at *m/z* 970 with no detectable fragmentation. The observation of sodium adducts of ginsenosides during electrospray mass spectrometry is similar to the observation of [M + Na]⁺ and [M + K]⁺ ions instead of protonated ginsenosides that have been reported during plasma desorption,¹³ field desorption,¹⁴ and liquid secondary ion mass spectrometry.¹⁵ Because no sodium had been added to the samples or solvents, possible sources of sodium were trace amounts from the HPLC-grade solvents, glassware, and the standards. However, addition of sodium to the mobile phase (100 μM NaCl) did not significantly enhance the abundance of [M + Na]⁺ ions.

(12) Chen, S. E.; Staba, E. J. *Lloydia* 1978, 41, 361–366.
 (13) Elkin, Y. N.; Makhankov, V. V.; Uvarova, N. L.; Bondarenko, P. V.; Zubarev, R. A.; Knysh, A. N. *Acta Pharmacol. Sin.* 1993, 14, 97–100.
 (14) Schulten, H.-R.; Soldati, F. *Chromatogr.* 1981, 212, 37–49.
 (15) Yamamoto, M.; Sugiyama, K.; Ichio, Y.; Yokota, M.; Maeda, Y.; Senda, N.; Shizukuishi, K. *Shoyabugaku Zasshi* 1992, 46, 394–396.

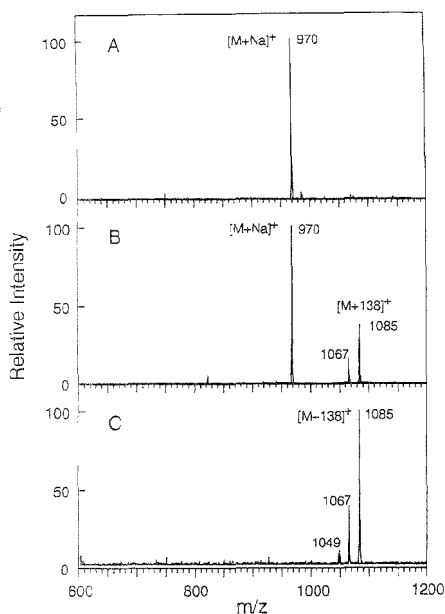


Figure 1. Positive ion electrospray mass spectra of ~100 pmol of ginsenoside R_e , obtained as follows: (A) ginsenoside standard introduced into the ion source by infusion, (B) ginsenoside standard introduced into the ion source using HPLC with an (aminopropyl)silica column, and (C) ginsenoside R_e contained in an extract of Korean ginseng introduced into the ion source using HPLC with an (aminopropyl)silica column.

Because abundant cationized ginsenoside molecules were observed during positive ion electrospray, no negative ion experiments were carried out. Acidification of the carrier solution with acetic acid was investigated as a means to enhance the formation of protonated molecules, but still no $[M + H]^+$ ions were observed. Therefore, postcolumn addition of acid was determined to be unnecessary.

Next, ginsenoside standards were injected onto an (aminopropyl)silica HPLC column and then detected upon elution using a photodiode array absorbance detector, followed on-line by positive ion electrospray mass spectrometry. The positive ion electrospray mass spectrum of ginsenoside R_e , which eluted from the HPLC column at 11.6 min, is shown in Figure 1B. In addition to the expected sodium adduct detected at m/z 970, an unexpected adduct ion, $[M + 138]^+$, was detected at m/z 1085, and an ion corresponding to loss of water from this unusual adduct was detected at m/z 1067. During LC/MS analysis of an extract of American ginseng, ginsenoside R_e was detected with a retention time of 11.6 min as the adduct, $[M + 138]^+$, m/z 1085, but no sodium adduct was observed (see mass spectrum in Figure 1C). Ions corresponding to the loss of one or two molecules of water from the ion of m/z 1085 were detected at m/z 1067 and 1049, respectively. Although sodium adducts and $[M + 138]^+$ ions were observed together in the electrospray mass spectra of all ginsenoside standards obtained during LC/MS analysis, ginsenosides contained in ginseng extracts were detected only as $[M + 138]^+$ ions.

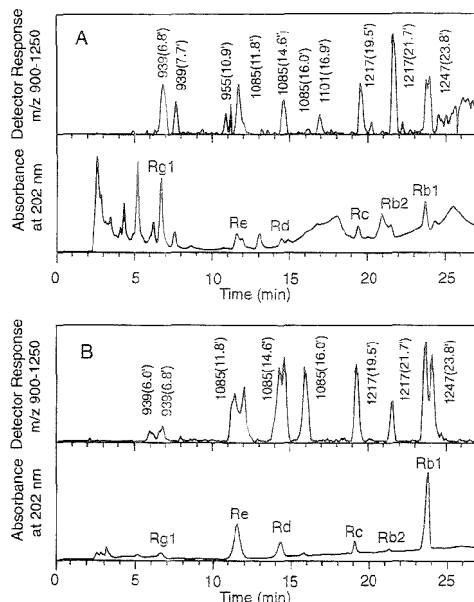


Figure 2. Positive ion electrospray LC/MS analysis with on-line UV absorbance detection of extracts of (A) Korean ginseng and (B) American ginseng. The upper chromatogram of each set shows the computer reconstructed mass chromatogram over the range m/z 900–1250. Each major peak is labeled with the most abundant m/z value (corresponding to the $[M + 138]^+$ ion), followed by the chromatographic retention time in parentheses.

Positive ion electrospray LC/MS analyses of Korean and American ginseng extracts are shown in Figure 2. Ginsenosides (R_{g1} , R_e , etc) labeled in Figure 2 were identified on the basis of comparison to standards with respect to retention times and m/z values (detected as $[M + 138]^+$ ions). In all cases, ginsenosides eluted from the (aminopropyl)silica column in order of increasing molecular weight (see Table 2). Although most ginsenosides were identified in both extracts, the relative proportions of each were different. For example, R_{g1} was the most abundant ginsenoside in the extract of Korean ginseng, whereas R_e was the predominant ginsenoside in the American ginseng extract. These variations were probably the result of genetic differences between the two strains of ginseng. However, differences in ginsenoside content of the two ginseng species might be influenced by geographical or seasonal growing conditions.

Three ginsenoside peaks were observed in the Korean ginseng LC/MS chromatogram that were not detected for the extract of American ginseng. These unique peaks were detected at retention times of 7.7, 10.9, and 16.9 min with m/z 939, 955, and 1101, respectively (Figure 2). Because these ions were detected as adducts, $[M + 138]^+$, the corresponding molecular weights were calculated to be 801, 817, and 963 (Table 2). Although no standards were available for comparison, two of these peaks were tentatively identified as R_f (MW 801) and 20-gluco- R_f (MW 963) on the basis of their molecular weights and retention times. A summary of retention times, observed adduct ions, calculated molecular weights, and corresponding ginsenoside assignments

Table 2. Summary of LC/MS Analysis of Ginsenosides and Ginseng Extracts

t_R (min) ^a	MW	ginsenoside standards ^b		Korean ginseng ^c [M + 138] ⁺	American ginseng ^c [M + 138] ⁺
		name	[M + Na] ⁺		
6.0	801				939
6.8	801	R _{d1}	824	939	939
7.7 ^d	801			939	
10.9	817			955	
11.8	947	R _e	970	1085	1085
14.6	947	R _{d1}	970	1085	1085
16.0	947			1085	1085
16.9 ^e	963			1101	
19.5	1079	R _e	1102	1217	1217
21.7	1079	R _{g2}	1102	1217	1217
23.8	1109	R _{b1}	1132	1247	1247

^a Retention time; see chromatogram in Figure 1. ^b Both [M + Na]⁺ and [M + 138]⁺ ions were detected during LC/MS of standards. ^c No sodium adducts were detected during analysis of ginseng extracts. ^d No standard available; tentatively identified as R_e. ^e No standard available; tentatively identified as 20-gluco-R_e.

for the LC/MS analyses of both ginseng extracts is shown in Table 2.

An additional unidentified peak was observed at a retention time of 16.0 min and m/z 1085 in the LC/MS chromatograms of both the Korean and American ginseng extracts. Because the abundance of the unidentified m/z 1085 ion was low in the Korean ginseng extract compared to the American ginseng sample, and because this ion was isobaric with ions corresponding to R_e and R_{d1} eluting at 11.8 and 14.6 min, the Korean ginseng extract was reanalyzed using selected ion monitoring to verify the presence of the new peak (Figure 3). The selected ion chromatogram showing the detector response at m/z 1085 and the corresponding electrospray mass spectrum for the LC/MS analysis of the Korean

ginseng extract confirmed the presence of a third ginsenoside of m/z 1085 in the Korean ginseng extract (Figure 3).

Because adducts ions, [M + 138]⁺, were only observed during LC/MS and not during infusion of standards, the origin of this unusual set of ions was determined to be the stationary phase. (3-Aminopropyl)trialkoxysilanes may be used in the synthesis of 3-aminopropyl stationary phases and for end-capping active sites in HPLC columns. Consequently, (3-aminopropyl)trihydroxysilane (MW 137) would be a hydrolysis product that might strongly adsorb to the column and bleed off over a long period of time. The column manufacturer confirms that this molecule might be present on the (aminopropyl)silica column used in this investigation. An alternative source of (3-aminopropyl)trihydroxysilane might be degradation of the (aminopropyl)silica stationary phase. Therefore, the most likely identity of the cation of MW 138 is protonated (3-aminopropyl)trihydroxysilane, ⁺NH₃(CH₂)₃Si(OH)₃.

In support of the identification of the unusual cation as protonated (3-aminopropyl)trihydroxysilane, ions were observed at m/z 138 in all the positive ion electrospray LC/MS spectra obtained using (aminopropyl)silica columns (data not shown), and [M + 138]⁺ ions were more abundant than [M + Na]⁺ adducts in LC/MS spectra of ginsenoside standards when a new (aminopropyl)silica column was used compared to a column that had been in service for an extended time period. Although too unstable to be isolated, (3-aminopropyl)trihydroxysilane could be generated at low concentrations by hydrolysis of (3-aminopropyl)triethoxysilane in aqueous solution, followed by detection as the protonated species using positive ion electrospray mass spectrometry. Because a neutral molecule of water was eliminated from protonated ginsenoside adducts, [M + 138]⁺, but not from [M + Na]⁺ ions (see Figure 1), the probable source of the eliminated water molecule was the less stable silanol moiety instead of a ginsenoside hydroxyl group.

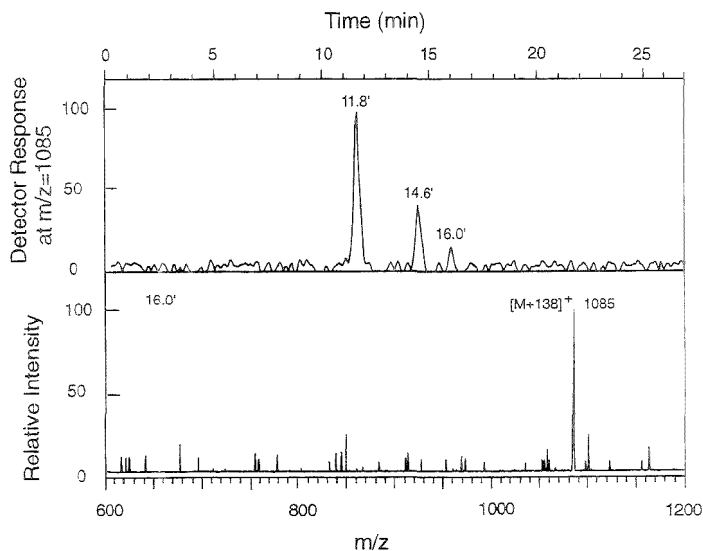


Figure 3. Positive ion electrospray LC/MS analysis using selected ion monitoring of the [M + 138]⁺ ion at m/z 1085 from the Korean ginseng extract. (Top) Three peaks are detected including R_{d1} and R_e at 11.6 and 14.4 min, respectively, and an unidentified ginsenoside at 15.9 min. (Bottom) The electrospray mass spectrum of the unidentified ginsenoside eluting at 15.9 min (recorded during the LC/MS analysis shown in Figure 2).

CONCLUSION

The first application of electrospray mass spectrometry and LC/MS to the analysis of ginsenosides is reported. Besides facilitating the identification of ginsenosides in extracts of ginseng, electrospray LC/MS also provided a ginsenoside profile that distinguished one variety of ginseng from another. Ginsenosides eluting from the (aminopropyl)silica HPLC column were detected as adducts, $[M + 138]^+$, which were the result of (3-ammoniumpropyl)trihydroxysilane (probably a manufacturing byproduct of the HPLC stationary phase) eluting from the column. Because (aminopropyl)silica HPLC columns are frequently used for a variety of carbohydrate analyses, including ginsenoside separations, and since electrospray LC/MS is rapidly becoming more widely used and available, other researchers using electrospray

LC/MS for carbohydrate research are likely to encounter $[M + 138]^+$ adducts and should be careful when determining the molecular weight of the analyte.

ACKNOWLEDGMENT

Use of the electrospray mass spectrometer was generously provided by the Hewlett-Packard Co. Support from the American Botanical Council (Austin, TX) is gratefully acknowledged.

Received for review May 2, 1995. Accepted August 23, 1995.*

AC950420K

* Abstract published in *Advance ACS Abstracts*, October 1, 1995.

Sequence-Specific Fragmentation of Matrix-Assisted Laser-Desorbed Protein/Peptide Ions

Robert S. Brown* and John J. Lennox

Department of Chemistry And Biochemistry, Utah State University, Logan, Utah 84322-0300

By utilizing delayed pulsed ion extraction of ions generated via the matrix-assisted laser desorption/ionization (MALDI) technique, fast (<320 ns) metastable ion fragmentation is observed for both peptide and protein analytes in the ion source of a linear time-of-flight mass spectrometer. Small peptides such as the oxidized B chain of bovine insulin exhibit fragmentation at the amide linking bond between peptide residues. Overlapping sequence information is provided by fragmentation from both the C- and N-terminal ends of the peptide (c_n , y_n , and z_n^+ -type fragment ions). Larger proteins can also exhibit a wealth of sequence specific fragment ions in favorable cases. One example is cytochrome c, which undergoes substantial (~80%) fast fragmentation at the amide bonds along the amino acid backbone of the protein. Only amide bond cleavages initiating from the C-terminal end (c_n fragments) are observed. The observed fragmentation pattern provides a significant amount of potential sequence information for these molecules. External mass calibration of the intact protonated molecular ions is demonstrated with mass accuracies typically around 100 ppm. Mass accuracies for the observed fragment ions ranged from ± 0.20 Da for the smaller peptides studied (i.e., oxidized B chain of bovine insulin) to ± 0.38 Da for the largest protein studied (cytochrome c), based upon the known sequences.

Matrix-assisted laser desorption/ionization (MALDI) has until recently been thought of as primarily a technique for the simple and fast determination of the molecular mass of an analyte. Numerous reports on its successful application in this area have appeared in recent years.¹⁻⁹ In this regard, MALDI is generally perceived as a "soft" ionization technique. A high degree of

metastable behavior of MALDI-generated ions is known from reflector time-of-flight (REFTOF) mass spectrometer experiments.¹⁰⁻¹² For larger proteins, this metastable decay in the field-free region prior to the ion mirror can severely limit the obtainable mass resolution with these instruments. This "postsources decay" (PSD) has been utilized¹³⁻¹⁵ in conjunction with the stepping of the REFTOF mass spectrometer's reflector voltages^{16,17} to correct for the lower kinetic energies of the PSD ions. Significant amounts of structural information can be obtained for moderate mass-to-charge (m/z) peptides via this technique. These PSD ions appear to be due at least in part to collisional activation processes during ion acceleration in the initially dense MALDI "plume" or with background gases in the field-free drift region.¹⁵ One drawback to this approach is the need to change the ion mirror voltages in discrete steps in order to produce a complete energy focused mass spectrum. These individual sections of the mass spectrum are then combined to produce a composite mass spectrum of the fragment ions. Accurate mass calibration is a much more demanding process in this experiment than with conventional time-of-flight mass spectrometers (TOF-MS). With precursor ion selection prior to the field-free region (typically via pulsed deflection methods), tandem mass spectrometry (MS/MS) can be performed.

In linear MALDI TOF-MS equipped with continuous ion acceleration, such metastable ion behavior is normally not observed. Ions which fragment during the initial acceleration period appear as incoherent background ion signals. Those ions which fragment in the field-free region (PSD ions) retain essentially the same velocity as intact ions and cannot be distinguished from stable ions. The use of delayed pulsed ion extraction combined with a linear TOF-MS and MALDI has already been discussed¹⁸ for mass resolution enhancement. This same technique can also be utilized to observe any fast (<300-4000 ns) metastable ion fragmentation which occurs during the MALDI

(1) Karas, M.; Ingendoh, A.; Bahr, U.; Hillenkamp, F. *Biomed. Environ. Mass Spectrom.* **1989**, *18*, 841-843.
(2) Karas, M.; Bahr, U.; Ingendoh, A.; Nordhoff, E.; Stahl, B.; Strupat, K.; Hillenkamp, F. *Anal. Chim. Acta* **1990**, *241*, 175-185.
(3) Beavis, R. C.; Chait, B. T. *Rapid Commun. Mass Spectrom.* **1989**, *3*, 432-435.
(4) Beavis, R. C.; Chait, B. T. *Proc. Natl. Acad. Sci. U.S.A.* **1990**, *87*, 6873-6877.
(5) Stahl, B.; Steup, M.; Karas, M.; Hillenkamp, F. *Anal. Chem.* **1991**, *63*, 1463-1466.
(6) Hill, J. A.; Annan, R. S.; Biemann, K. *Rapid Commun. Mass Spectrom.* **1991**, *5*, 395-399.
(7) Castoro, J. A.; Köster, C.; Wilkins, C. L. *Rapid Commun. Mass Spectrom.* **1992**, *6*, 239-241.
(8) Castoro, J. A.; Wilkins, C. L. *Anal. Chem.* **1993**, *65*, 2621-2627.
(9) Karas, M.; Bahr, U.; Ingendoh, A.; Hillenkamp, F. *Angew. Chem., Int. Ed. Engl.* **1989**, *28*, 760-761.

(10) Spengler, B.; Kaufmann, R. *Analysis* **1992**, *20*, 91.
(11) Karas, M.; Bahr, U.; Strupat, K.; Hillenkamp, F.; Tsarbobopoulos, A.; Pramanik, B. N. *Anal. Chem.* **1995**, *67*, 675-679.
(12) Yu, W.; Vath, J. E.; Huberty, M. C.; Martin, S. A. *Anal. Chem.* **1993**, *65*, 3015-3023.
(13) Spengler, B.; Kirsch, D.; Kaufmann, R.; Jaeger, E. *Rapid Commun. Mass Spectrom.* **1992**, *6*, 105.
(14) Spengler, B.; Kirsch, D.; Kaufmann, R. *Rapid Commun. Mass Spectrom.* **1991**, *5*, 198.
(15) Kaufmann, R.; Kirsch, D.; Spengler, B. *Int. J. Mass Spectrom. Ion Processes* **1994**, *131*, 355-385.
(16) Tang, X.; Ens, W.; Standing, K. G.; Westmore, J. B. *Anal. Chem.* **1988**, *60*, 1791.
(17) Tang, X.; Ens, W.; Mayer, F.; Standing, K. G.; Westmore, J. B. *Rapid Commun. Mass Spectrom.* **1989**, *3*, 443.
(18) Brown, R. S.; Lennox, J. J. *Anal. Chem.* **1995**, *67*, 1998-2003.

process. Unlike the PSD ions observed in MALDI with ion mirror-based TOF mass spectrometers, the metastable ions observed with delayed pulsed ion extraction are produced much earlier in the desorption process. Although not formed early enough to be observed with continuous ion extraction TOF mass spectrometers (i.e., not prompt fragmentation), they are observed as early as 300 ns after the laser desorption event and do not appear to increase in intensity at longer extraction delay times. Energetic collisions, believed to play a major role in the generation of PSD ions in MALDI, should be absent with delayed pulsed ion extraction due to the expansion of the desorbed neutral plume during the extraction delay period. Possible mechanisms for this fast metastable ion fragmentation process, the effects on the observed fragmentation of simple peptides and proteins of chemically different MALDI matrices, and the influence of the laser fluence are reported elsewhere.¹⁹

This report will demonstrate the analytical utility of these fast time frame metastable ions with several peptides and a protein of known sequence. It will be shown that delayed pulsed ion extraction TOF-MS coupled with MALDI ionization offers a simple and relatively fast method which can provide significant amounts of detailed structural information for small quantities of moderate-sized peptides. In favorable cases, small proteins have also provided significant primary structure information.

EXPERIMENTAL SECTION

The experimental arrangement for the delayed pulsed ion extraction linear TOF-MS employed in these studies is presented in detail in a separate report.¹⁸ MALDI-generated ions are produced in an initially field-free region of a standard three-grid ion source maintained at high (24 kV) voltage. The repeller grid of the source is connected to a high-voltage pulser (0–3 kV) floated at the source potential. After a variable delay period (300–4000 ns), the repeller grid is pulsed to higher voltage (positive ions), and the MALDI ions are accelerated through the second region of the ion source into the ground potential flight tube of the TOF mass spectrometer.

The samples of substance P (S 6383), melittin (M 2272), the oxidized B chain of bovine insulin (I 6383), porcine insulin (I 3505), and equine cytochrome *c* (C 7752) employed in these studies were purchased from Sigma Chemical Co. (St. Louis, MO) and used as received without additional purification. MALDI matrices were purchased from Aldrich Chemical Co. (Milwaukee, WI) and used as received. Matrix solutions were prepared as ~10 mM solutions in acetonitrile/water (30:70 v/v) to which 0.1% trifluoroacetic acid was added. Analyte solutions were prepared in distilled deionized water at the 10 μ M concentration level. Samples were deposited (1 μ L of analyte followed by 2 μ L of matrix) via a microsyringe onto a 3 mm diameter stainless steel probe tip and allowed to air-evaporate. We have found that this sample preparation procedure produces MALDI results identical to those obtained with premixing the solutions prior to depositing them on the sample target, as long as the less volatile analyte solution is applied first to the probe tip.

A pulsed nitrogen laser (337.1 nm) is focused to a spot size of ~100 μ m \times 250 μ m. The laser thus samples on any given surface a maximum of ~40 fmol of analyte (assuming equal deposition of analyte across the probe tip). Total analyte loading on the sample

probe tip (from which at least 10–20 surfaces may be sampled) is 10 pmol. These somewhat higher than normal MALDI analyte concentrations were employed to ensure good S/N for the resulting low-intensity fragment ions. As the analyte concentration is lowered, fragment ion S/N degrades until only major fragment ions are discernible. For the MALDI TOF-MS spectra presented, the ion signals from 50 laser shots were signal averaged at 5 ns/point time resolution (LeCroy 8828 transient digitizer). Ion source bias voltages of 24 kV and pulsed ion extraction delay times of 340 ns were utilized for all of the results presented.

Mass calibration of the time-of-flight spectra utilized a simple linear fit of two ions with known m/z values and their experimental flight times. This procedure is discussed in more detail in the Results and Discussion section. Because of the small abundance of the fragment ions relative to the protonated molecular ion, the limited dynamic range of the transient digitizer (200 MHz/8 bits) becomes problematic. Accurate sampling of the low-abundance fragment ions cannot be accomplished if the large intensity protonated molecular ion is kept on scale. To avoid this, the gain on the signal amplifier was initially adjusted so that the dominant protonated molecular ion signal was within the range of the transient digitizer. A signal-averaged time-of-flight spectrum for the initial 20 laser shots on a sample surface was collected, and the center of mass of the $[M + H]^+$ and the $[M + 2H]^{2+}$ ions was determined. The gain of the signal amplifier was then increased so that the analyte-protonated molecular ions were no longer on scale. A time-of-flight spectrum was then accumulated from the next 50 laser shots on the same sample surface. This approach effectively improves the dynamic range of the experiment for the much lower intensity fragment ions. The previously determined flight times can then be used in the mass calibration procedure.

RESULTS AND DISCUSSION

The extent of fast metastable ion fragmentation that is observed with delayed pulsed ion extraction in a linear TOF mass spectrometer is very matrix dependent. All of the common MALDI matrices studied to date exhibit fast metastable fragment ions. The effects on the fast metastable ion fragmentation of several common MALDI matrices are reported elsewhere.¹⁹ The most generally useful MALDI matrices found to date which provide extensive, nonspecific fragmentation include 3-methoxy-4-hydroxycinnamic acid (ferulic acid), 3,5-dimethoxy-4-hydroxycinnamic acid (sinapinic acid), and 2,5-dihydroxybenzoic acid (DHB). The two cinnamic acid derivatives tend to produce better results for larger peptides and small proteins, while the DHB matrix provides some enhancement in fragmentation with small and intermediate-sized peptides. The results presented here will be restricted to DHB and sinapinic acid matrices. Ferulic acid produces results very similar to those obtained with sinapinic acid.

The peptides and proteins chosen for study are listed in the Experimental Section, and their known sequences and average chemical molecular weights are provided in the corresponding tables of fragment ions. The analytes chosen produce fast metastable ion fragmentation results which are typical for peptides in the 1000–6000 Da mass range that have been examined in our laboratory to date by this technique. The fast metastable ion decay process appears to be complete¹⁹ within the shortest pulse delay time (340 ns) possible with current instrumentation.¹⁸ As the widest mass range of ions is optimally focused at the shortest delay time,¹⁸ all fragmentation studies reported involve a 340 ns delay period after initiation of the laser event.

(19) Brown, R. S.; Lennon, I. J. Submitted for publication in *J. Am. Soc. Mass Spectrom.*

A standard nomenclature²⁰ that is widely utilized to describe the amide bond cleavages that normally occur in the mass spectrometry of peptides is employed in these discussions. Such cleavages have primarily been observed with various collisional activation²¹ or unimolecular^{22,23} ion decay processes. Possible mechanisms for these bond cleavages in the case of fast metastable MALDI ion decay have been discussed elsewhere¹⁹ and will only be briefly summarized here. Our current model of the fast fragmentation process observed for MALDI-generated ions centers around the proton transfer event. It is believed that the exothermicity of this proton transfer reaction controls the degree of fast fragmentation that is observed. Other researchers have proposed²⁴ such a model previously to account for longer term metastable ion decay in MALDI (i.e., post-source metastable ion decay). This model can also account for the dependence on the fast fragmentation ion species observed with the MALDI matrix that is utilized.¹⁹ Differences in the exothermicity of the proton transfer reaction as a function of the chemical structure of the MALDI matrix would be expected, and this would determine the relative extent of internal activation of the analytes. This would presumably affect the favored fast metastable ion decay pathways.

Fast metastable ion decay of smaller to moderate-sized peptides is dominated by the production of y_n and c_n fragment ions. In addition, complementary N-terminal fragments are also observed with a distribution similar to the y_n series of ion fragments. These ions are observed at a somewhat unusual 15 amu below the y_n series ions (i.e., $y_n - 15$) and are believed to be due to a rearrangement around the amide bond with a loss of NH from the y_n series ions. They occur in a distribution similar to that of the y_n series of ions with approximately equal intensity. They have tentatively been designated as z^*_n ions to be most compatible with the common nomenclature²⁰ utilized to describe peptide fragmentation. For the present studies, only the c_n and y_n ion series will be discussed. The fast time frame metastable fragment ions observed with MALDI are similar to the prompt ion fragmentation observed with fast atom bombardment (FAB) ionization of peptides.²⁵

A major benefit of utilizing the fast metastable ion fragments observed with the delayed pulsed ion extraction TOF-MS technique instead of the more abundant PSD ions with a reflecting TOF mass spectrometer involves the ease of conducting the experiment. For a moderately sized protein such as cytochrome *c*, the entire analytical useful mass range (400–13 000 Da) can be examined in a single TOF mass spectrum. This can be obtained with good mass resolution ($m/\Delta m$ between 450 and 800) across the entire mass range of the spectrum. Mass calibration is accomplished in the same manner as with continuous ion extraction linear TOF-MS by employing a simple linear fit of two known masses and their associated flight times.

As the molecular mass of the analyte is increased, some tradeoff in optimal focusing conditions (i.e., the pulse voltage

employed) must be made when employing the delayed pulsed ion extraction technique. This typically involves optimizing the experimental pulsed extraction conditions to maximize the obtainable mass resolution for the largest ion of interest. Some degradation in the optimal mass resolution occurs for lower m/z ions in the spectra. In the case of the largest analyte (cytochrome *c*) which has currently produced useful fast metastable ion decay products, the mass resolution for lower m/z ions is typically no worse than what is observed in the best case with continuous ion extraction on the same instrument ($m/\Delta m \approx 500$). If improved mass resolution is required, additional fast metastable ion decay spectra can be acquired under pulsed extraction conditions optimized for lower m/z fragment ions. All of the results presented here were obtained with a single set of pulsed extraction conditions optimized for the singly protonated molecular ion.

In order to sort out the structural information contained in the fast metastable ion decay fragment spectra that are observed with MALDI, sample prepurification is required. Unlike with PSD fragmentation, there is no way to presort protonated molecular ion species from samples containing multiple analytes (i.e., no MS/MS capability). As long as any potential peptide impurities are minimized, the probability of interferences due to low-level peptide impurities fragmenting and producing spurious ions is extremely small. This is due to the small fraction (about 1% in favorable cases) of protonated molecular ions that exhibit fast metastable ion fragmentation under typical MALDI conditions. Any low-level impurity species present that generate stable ions can be distinguished by continuous ion extraction from the metastable ion species. All of the fast metastable ions reported here are not observed when the instrument is operated in continuous ion mode. In this regard, care must be taken with synthetic peptide samples not to confuse the protonated molecular ions from low levels of incomplete synthesis impurities with actual fast metastable ion decay fragmentation.

The mass calibration employed for all of the fast metastable ion fragmentation spectra presented utilized the known molecular weights of the analytes based upon their published sequences. The singly and doubly protonated molecular ion flight times were recorded as described in the Experimental Section and were utilized along with the known sequence-based molecular weights to internally calibrate each spectrum. In the case of true unknown analytes, an additional initial step would be required to accurately determine an unknown's molecular weight. This would involve utilizing other calibrant compounds of known m/z , as is typically done in MALDI TOF-MS. The mass accuracy possible using conventional internal and external calibration (average of six determinations) with delayed pulsed ion extraction for a series of common peptides is presented in Table 1. For the internal calibration results, a standard procedure typically employed with linear TOF mass spectrometers was utilized.^{25,26}

For the external calibration procedure, an alternative approach was utilized. Two samples were applied sequentially to alternate halves of the direct insertion probe's sampling area in such a manner that they did not mix during solvent evaporation. One dried sample spot contained only the analyte whose molecular mass was to be determined. The other sample spot contained the required mass calibrants. The calibrant sample was brought

(20) Johnson, R. S.; Martin, S. A.; Biemann, K. *Int. J. Mass Spectrom. Ion Processes* 1988, 86, 137–154.

(21) Bean, M. F.; Carr, S. A.; Thorne, G. C.; Reilly, M. H.; Gaskell, S. J. *Anal. Chem.* 1991, 63, 1473–1481.

(22) Kinsel, G. R.; Lindner, J.; Grote-meyer, J.; Schlag, E. W. *Proceedings of the 39th ASMS Conference on Mass Spectrometry and Allied Topics*, Nashville, TN, May 19–24, 1991; pp 350–351.

(23) Downard, K. M.; Biemann, K. *J. Am. Soc. Mass Spectrom.* 1993, 4, 874–881.

(24) Strupat, K.; Karas, M.; Hillenkamp, F.; Eckerskorn, C.; Lottspeich, F. *Anal. Chem.* 1994, 66, 464–470.

(25) Beavis, R. C.; Chait, B. T. *Anal. Chem.* 1990, 62, 1836–1840.

(26) Brown, R. S.; Gilfrich, N. L. *Anal. Chim. Acta* 1991, 248, 541–552.

Table 1. Comparison of the Mass Accuracy Obtained for Selected Peptides/Proteins by Delayed Pulsed Ion Extraction MALDI with Internal and External Calibration

analyte	known mass, Da	calcd mass, Da (internal calibrant)	error, % (ppm)	calcd mass, Da (external calibrant)	calibrants employed	error, % (ppm)
bovine insulin B chain	3495.95	3495.79 ± 0.36	0.0046 (46)	3495.52 ± 0.44	b, c	6.012 (120)
bovine insulin	5733.52	5733.66 ± 0.19	0.0028 (28)	5734.15 ± 0.62	a, d	0.011 (110)
bovine ubiquitin	8564.85	8565.21 ± 0.43	0.0042 (42)	8563.97 ± 0.88	b, e	0.010 (100)
equine cytochrome c	12360.1	12359.6 ± 0.7	0.0040 (40)	12361.3 ± 0.5	d, f	0.010 (100)

^a Bovine insulin B chain [M + H]⁺. ^b Bovine insulin [M + H]⁺. ^c Bovine insulin [M+2H]²⁺. ^d Bovine ubiquitin [M + H]⁺. ^e Equine cytochrome c [M + H]⁺. ^f Equine myoglobin [M + H]⁺.

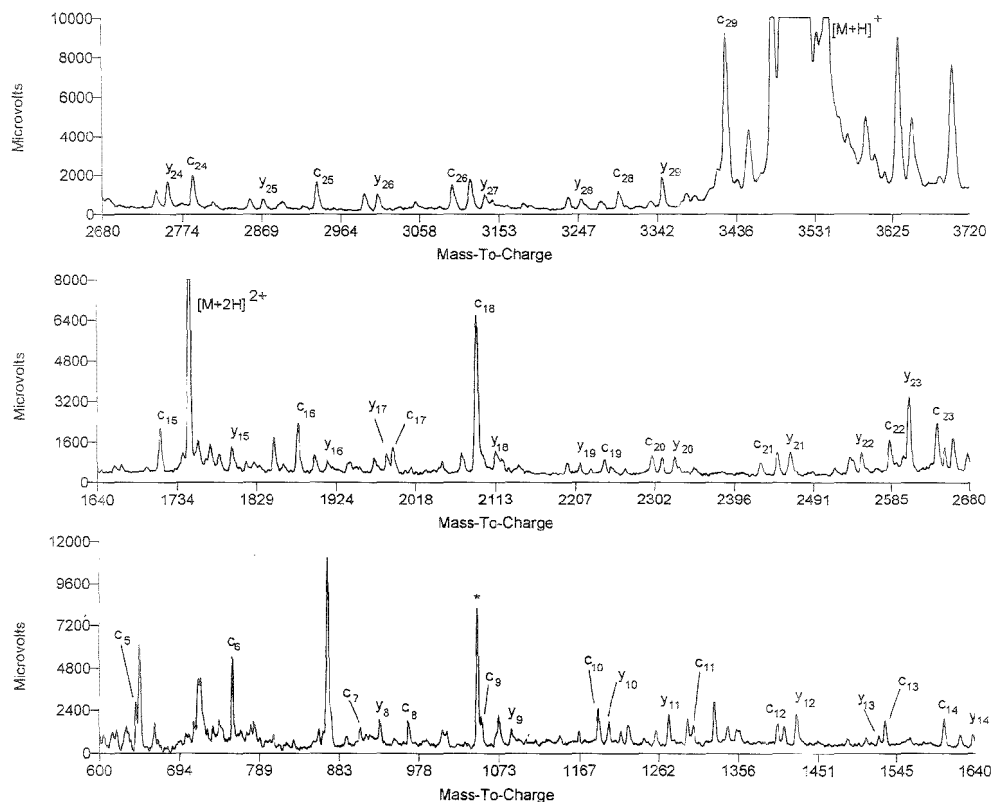


Figure 1. MALDI fast metastable ion decay spectrum of the oxidized B chain of bovine insulin obtained with delayed pulsed ion extraction. 2,5-Dihydroxybenzoic acid matrix and 1.50 kV pulsed extraction voltage. (Note: asterisk-marked peak is due to a small amount of angiotensin II impurity from an earlier analysis).

into the laser beam by rotation of the sample probe, and the flight times of the calibrant compounds were determined. The probe was then rotated so that the analyte was brought into the laser beam, and a TOF spectrum was recorded. The masses and flight times of the calibrants were then utilized to mass calibrate the analyte. The results of this approach (also the average of six determinations) are also shown for comparison in Table 1.

The internal mass calibration procedure produced average mass accuracies of 30–50 ppm, which is typical for internally mass calibrated MALDI spectra. Externally calibrated spectra on linear TOF mass spectrometers usually provide substantially poorer

results. This is normally attributed to sample surface irregularities which change the extraction fields that ions experience from surface to surface. In the case of delayed pulsed ion extraction, where the ions do not experience an extraction field until they have moved away from the sample surface, it was expected that some improvements would be possible in external mass calibration. The results in Table 1 for the external mass calibration show that mass accuracy deteriorates to about 100 ppm by this approach. The poorer results for the external mass calibration would suggest that for maximum accuracy in calibrating the fast metastable ion decay spectra of unknowns, internal mass calibra-

Table 2. MALDI Fast Metastable Decay Ions Observed for the Oxidized B Chain of Bovine Insulin (MW = 3495.95) in 2,5-Dihydroxybenzoic Acid Matrix

residue	mass, Da	N-terminal loss, Da (y_n fragments)		C-terminal loss, Da (c_n fragments)	
		calcd	exptl (error)	calcd	exptl (error)
Phe	147.18	(y_{28}) 3349.78	3349.32 (-0.46)		
Val	99.13		3250.64	165.20	
Asn	114.10		3136.55	264.34	
Gln	128.13		3008.42	378.44	
His	137.14	(y_{25}) 2871.27	2871.11 (-0.16)	596.57	
Leu	113.16		2758.11	(c_5) 643.71	643.08 (-0.63)
Cys	151.14		2606.97	756.87	756.84 (-0.03)
Gly	57.05		2549.92	908.01	908.24 (+0.23)
Scr	87.08		2462.84	965.06	964.92 (-0.14)
His	137.14	(y_{20}) 2325.70	2325.90 (+0.20)	1052.14	1051.79 (-0.35)
Leu	113.16		2212.54	(c_{10}) 1189.28	1189.13 (-0.15)
Val	99.13		2113.41	1302.44	1302.06 (-0.38)
Glu	129.12		1984.29	1401.58	1401.75 (+0.17)
Ala	71.08		1913.21	1530.69	1530.82 (+0.13)
Leu	113.16	(y_{15}) 1800.05	1799.71 (-0.34)	1601.77	1601.56 (-0.21)
Tyr	163.18		1636.87	(c_{15}) 1714.93	1714.91 (-0.02)
Leu	113.16		1523.71	1878.10	1878.50 (+0.20)
Val	99.13		1424.58	1991.26	1991.23 (-0.03)
Cys	151.14		1273.44	2090.40	2090.52 (+0.12)
Gly	57.06	(y_{10}) 1216.39	1216.43 (+0.04)	2241.54	2241.93 (+0.39)
Glu	129.12		1087.27	(c_{20}) 2298.59	2298.60 (+0.01)
Arg	156.19		931.08	2427.71	2427.66 (-0.05)
Gly	57.05		874.03	2583.89	2584.03 (+0.14)
Phe	147.18		726.86	2640.95	2641.12 (+0.17)
Phe	147.18		579.68	2788.12	2787.97 (-0.15)
Tyr	163.18		416.50	(c_{25}) 2935.30	2935.65 (+0.35)
Thr	101.11		315.40	3098.48	3098.22 (-0.26)
Pro	97.12		218.28	3199.58	
Lys	128.17		90.11	3296.70	3296.37 (-0.33)
Ala	71.08			(c_{28}) 3424.87	3425.02 (+0.15)
av error			-0.09 ± 0.22		-0.03 ± 0.25
av abs error			0.20 ± 0.12		0.20 ± 0.15

Table 3. MALDI Fast Metastable Decay Ions Observed for Substance P (MW = 1347.65) in 2,5-Dihydroxybenzoic Acid Matrix

residue	mass, Da	N-terminal loss, Da (y_n fragments)		C-terminal loss (c_n fragments)	
		calcd	exptl (error)	calcd	exptl (error)
Arg	156.19	(y_{10}) 1192.46	1192.57 (+0.11)		
Pro	97.12		1095.35	174.29	
Lys	128.17		967.18	271.40	
Pro	97.12		870.06	399.58	399.87 (+0.29)
Gln	128.13		741.93	496.69	496.77 (+0.08)
Gln	128.13	(y_5) 613.80	613.98 (+0.18)	(c_5) 624.82	624.97 (+0.15)
Phe	147.18		466.63	752.95	753.18 (+0.23)
Phe	147.18		319.45	900.07	899.89 (-0.18)
Gly	57.05		262.40	1047.25	1046.99 (-0.26)
Leu	113.16		149.24	1104.30	1104.08 (-0.22)
Met-NH ₂	131.20			(c_{10}) 1217.46	1217.51 (+0.05)
av error			+0.01 ± 0.17		+0.02 ± 0.21
av abs error			0.14 ± 0.09		0.18 ± 0.08

tion should be utilized. However, it should be remembered that mass differences (as opposed to absolute fragment ion masses) would most likely be utilized in the case of true unknowns to determine sequences. In such cases, external mass calibration with this approach might prove adequate. Additional improvements in external mass calibration may be possible utilizing a recently reported sample preparation technique²⁷ which appears to produce more uniform samples for analysis.

The analytes chosen to demonstrate the potential analytical utility of the fast metastable ion decay process in MALDI were

(27) Vorm, O.; Mann, M. *Rapid Commun. Mass Spectrom.* 1994, 5, 955-958.

selected to complement some of the analytes more widely studied by the PSD MALDI technique. Major differences observed in the two decay processes include differences in cleavage sites (a_n , $a_n - 17$, b_n versus c_n , y_n , and z^+_n ions) and substantially lower intensities of the fast metastable decay ions relative to PSD ions. The results that can be obtained for a moderate-sized peptide which is not internally cross-linked with delayed pulsed ion focusing of the fast metastable ion decay products produced in MALDI are best demonstrated for the oxidized B chain of bovine insulin (MW = 3495.95). A typical fast metastable ion decay mass spectrum which can be obtained for this analyte is shown in Figure 1 for MALDI from a DHB matrix. The spectrum is

Table 4. MALDI Fast Metastable Decay Ions Observed for Melittin (MW = 2846.49) in 2,5-Dihydroxybenzoic Acid Matrix

residue	mass, Da	N-terminal loss, Da (y_n fragments)		C-terminal loss (c_n fragments)	
		calcd	exptl (error)	calcd	exptl (error)
Gly	57.05	(y_{26}) 2790.45	2790.21 (-0.24)		
Ile	113.16		2677.29	75.07	
Gly	57.05		2620.23	188.23	
Ala	71.08		2549.16	245.29	
Val	99.13		2450.02	317.29	
Leu	113.16	(y_{26}) 2336.85	2337.40 (+0.54)	(c_2) 415.50	
Lys	128.17		2208.69	528.66	
Val	99.13		2109.55	656.83	656.95 (-0.88)
Leu	113.16		1996.40	755.97	756.08 (+0.11)
Thr	101.11		1895.29	869.13	869.46 (+0.33)
Thr	101.11	(y_{15}) 1794.19	1794.57 (+0.38)	(c_{10}) 970.23	970.34 (+0.10)
Gly	57.05		1737.13	1071.34	1071.67 (+0.33)
Leu	113.16		1623.97	1128.39	1128.50 (+0.11)
Pro	97.12		1526.86	1241.55	
Ala	71.08		1455.78	1338.66	1338.68 (+0.02)
Leu	113.16	(y_{10}) 1342.62	1228.94 (-0.52)	(c_{15}) 1409.74	1410.05 (+0.31)
Ile	113.16		1229.46	1522.90	
Ser	87.08		1142.38	1636.06	1636.01 (-0.05)
Trp	186.21		956.17	1723.14	1722.99 (-0.15)
Ile	113.16		843.01	1909.35	1909.19 (-0.16)
Lys	128.17	(y_3) 714.83	558.64	(c_{20}) 2022.51	2022.74 (+0.13)
Arg	156.19		558.64	2150.66	2151.01 (+0.32)
Lys	128.17		430.47	2306.88	2306.57 (-0.31)
Arg	156.19		274.28	2435.05	2435.37 (+0.32)
Gln	128.13		146.15	2591.24	2590.54 (-0.70)
Gln-NH ₂	128.13			(c_{25}) 2719.37	2719.31 (-0.06)
av error			0.03 ± 0.41		-0.01 ± 0.35
av abs error			0.35 ± 0.20		0.26 ± 0.23

Table 5. MALDI Fast Metastable Decay Ions Observed for Porcine Insulin (MW = 5777.58) in 3,5-Dimethoxy-4-hydroxycinnamic Acid Matrix

residue	mass, Da	calcd	exptl (error)
C-Terminal Loss (c_n Fragments)			
(c_{10}) ^B	Ala	71.08	5706.50
(c_{10}) ^B	Lys	128.17	5578.33
(c_{25}) ^B	Pro	97.12	5481.21
(c_{25}) ^B	Thr	101.11	5380.11
(c_{25}) ^B	Tyr	163.18	5216.93
(c_{15}) ^B	Phe	147.18	5069.75
(c_{25}) ^B	Phe	147.18	4922.58
(c_{25}) ^B	Gly	57.05	4865.52
(c_{25}) ^B	Arg	156.19	4709.34
(c_{25}) ^B	Glu	129.12	4580.22
(c_{15}) ^B	Gly	57.05	4523.17
(c_{15}) ^B	Cys	103.15	4420.02
av error			0.06 ± 0.28
av abs error			0.23 ± 0.14
N-Terminal Loss (y_n Fragments)			
(y_{20}) ^B	Phe	147.18	5631.41
(y_{20}) ^B	Val	99.13	5532.28
(y_{20}) ^B	Asn	114.10	5418.18
(y_{20}) ^B	Gln	128.13	5290.05
(y_{25}) ^B	His	137.14	5152.90
(y_{25}) ^B	Leu	113.16	5039.74
av error			-0.19 ± 0.21
av abs error			0.22 ± 0.17

dominated by c_n , y_n , and z_n^* (not labeled) ions. These fragments provide overlapping sequence information. Typical of the fast metastable ion decay spectra we have recorded, the last several possible fragment ions in a series are not observed. Fragmentation at a proline residue is also weak or absent in most fast metastable ion decay spectra. This is discussed in more detail below.

Matrix interferences also preclude observation of fragments below a m/z of around 400–500, depending upon the matrix utilized.

A detailed compilation of the c_n and y_n fragments observed and the absolute mass accuracy for each fragment which can be obtained with the above calibration procedure for a typical fast metastable ion decay spectrum of the oxidized B chain of bovine insulin is presented in Table 2. These data represent typical and not "best-case" results. Only the absolute mass accuracy based upon the predicted theoretical mass loss from the known sequence has been reported. Mass differences between metastable fragment ions can also be easily calculated and utilized to confirm (or establish) possible sequences. For each fragment type, overall average error and average absolute error have been calculated and tabulated. The small negative average error suggests a slight systematic bias in the calibration procedure. Overall average absolute errors are about 0.2 Da for both the c_n and y_n fragment series. This mass accuracy is sufficient to differentiate all common amino acid residues except for leucine versus isoleucine and lysine versus glutamine. Due to the similar (or identical) residue masses of these two pairs of amino acids, their identification will probably always remain problematic without additional fragmentation information to aid in their identification. Side chain cleavage fragments that can be utilized to distinguish these amino acids²⁰ do not appear to be produced in the fast metastable ion decay process.

In the case of the oxidized B chain of insulin, delayed pulsed ion extraction coupled to a linear TOF mass spectrometer does not afford sufficient mass resolution to resolve the isotopic multiplets for the majority of fragment ions. While mass resolution of about 4000 (fwhm) is not difficult to obtain under ideal MALDI conditions for smaller peptides such as melittin with our current delayed pulsed ion extraction design, the higher laser

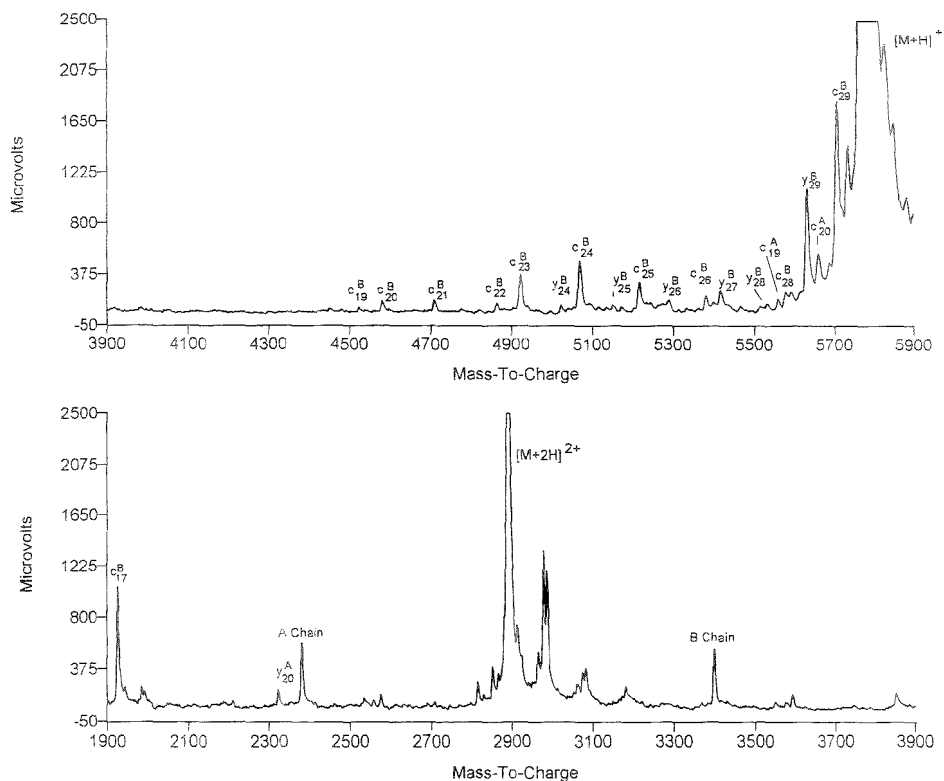


Figure 2. MALDI fast metastable ion decay spectrum of porcine insulin obtained with delayed pulsed ion extraction. Sinapinic acid matrix and 1.65 kV pulsed extraction voltage.

fluence and the mass dependence of the optimal pulsed extraction voltage typically reduce the mass resolution to between 450 and 800 when wide mass ranges are examined in a single mass spectrum. For this reason, only chemical average molecular weight data are reported for the fragment ions.

Results similar to those observed with the oxidized B chain of insulin are observed for smaller peptides. For the undecapeptide substance P, the same cleavage types (y_n , z_n^* , and c_n) that were observed for the oxidized B chain of insulin are produced with the DHB matrix. The probability for the observation of these fast metastable ion decay products increases only slightly for smaller analytes. Table 3 shows the observed y_n and c_n fragments along with the measured absolute experimental mass accuracies for each fragment ion that was observed. Average absolute mass accuracy for the fragments is statistically the same as the accuracy observed for the oxidized insulin B chain sample. As with the previous example, fragment ions are not observed for the loss of the last few residues in a particular series. Overlap of the y_n and c_n series allows confirmation of the entire peptide's sequence. Although not shown in Table 3, the z_n^* ion series is also observed, but only for a small number of possible fragmentations (z_4^* , z_7^* , and z_8^*). For comparison, PSD mass spectra for substance P are dominated by a_n , $a_n - 17$, b_n , and $b_n - 17$ fragment ion series.¹⁵

An example of the PSD technique that has been reported in the literature¹⁵ for a larger analyte is that for the 26 amino acid-

containing peptide melittin (from honey bee venom). The published PSD spectra for melittin contain several fragment ion series. The major metastable ion fragment series observed include the same a_n , b_n , and $b_n - 17$ series that were observed for substance P. In addition, y_n and b_n ion series are observed along with fragments identified as $y_n - 17$ ions. For comparison, Table 4 presents the fast metastable decay ions observed for melittin in a DHB matrix (same matrix as the published PSD results) utilizing the delayed pulsed ion extraction technique. In the case of melittin, there is some similarity in the metastable ion decay spectra in terms of the y_n fragment ion types observed with these two techniques. The z_n^* series of ions (not shown in Table 4) essentially mirror the distribution of the y_n series of ions that are observed.

The overall mass accuracy for the melittin fast metastable ion fragments is good, with an average absolute error for each series of about 0.3 Da. This is substantially better than the 1.5–3 Da absolute error reported for melittin determined by the PSD technique.¹⁵ For the fast metastable fragments, a few of the possible fragments in each series are not observed. One of the gaps in both the c_n and the y_n series (also the z_n^* series not shown) occurs at a proline residue. Both fragment ion series stop at the $n = 7$ fragment position along the backbone of the peptide. From the overlapping fragment data available, a large portion of the primary structure of melittin could be deduced.

Table 6. MALDI Fast Metastable Decay Ions Observed for Equine Cytochrome c (MW = 12 360.1)

residue	calcd	exptl error	residue	calcd	exptl error
Glu	12230.99		Asn	6130.79	6131.16 +0.37
Asn	12116.88		Ala	(c ₅₀) 6059.71	6059.67 -0.04
Thr	12015.78		Asp	5944.62	5945.02 +0.40
Ala	(c ₁₀₀) 11944.70	11944.34 -0.36	Thr	5843.51	5843.58 +0.07
Lys	11816.52	11814.43 -2.09	Tyr	5680.34	5680.20 -0.14
Lys	11688.35	11686.54 -1.81	Thr	5579.23	5578.96 -0.27
Leu	11575.19	11575.62 +0.43	Phe	(c ₁₅) 5432.06	5431.99 -0.07
Tyr	11412.01	11412.12 +0.11	Gly	5375.00	5374.74 -0.26
Ala	(c ₉₅) 11340.94	11342.68 +1.74	Pro	5277.89	
Ile	11227.78		Ala	5206.81	5207.17 +0.36
Leu	11114.62	11113.76 -0.86	Gln	5078.68	5079.05 +0.37
Asp	10999.53	10999.71 +0.18	Gly	(c ₄₀) 5021.63	5022.35 +0.72
Glu	10870.41	10871.29 +0.88	Thr	4920.52	4920.21 -0.31
Arg	(c ₉₀) 10714.22	10714.32 +0.10	Lys	4792.35	4793.13 +0.78
Glu	10585.11	10584.40 -0.61	Arg	4636.15	4636.39 +0.23
Thr	10484.00	10484.10 +0.10	Gly	4579.11	4579.14 +0.03
Lys	10355.83	10355.55 -0.33	Phe	(c ₃₅) 4431.93	4431.82 -0.11
Lys	10227.66	10227.81 +0.15	Leu	4318.77	4318.71 -0.06
Lys	(c ₈₅) 10099.48	10099.10 -0.38	Gly	4261.72	4261.80 +0.08
Ile	9986.32	9986.09 -0.23	His	4124.58	4123.42 -1.16
Gly	9929.27	9928.67 -0.60	Leu	4011.42	4011.50 +0.08
Ala	9858.19	9858.63 +0.44	Asn	(c ₃₀) 3897.31	3897.69 +0.38
Phe	9711.01	9710.28 -0.73	Pro	3800.20	
Ile	(c ₈₀) 9597.85	9598.44 +0.59	Gly	3743.14	3743.39 +0.25
Met	9466.66	9466.73 +0.07	Thr	3642.04	3642.15 +0.11
Lys	9338.48	9338.60 +0.12	Lys	3513.87	3514.03 +0.16
Thr	9237.38	9237.48 +0.10	His	(c ₂₅) 3376.72	3376.83 +0.11
Gly	9180.32	9179.73 -0.59	Lys	3248.55	3248.71 +0.16
Pro	(c ₇₅) 9083.21		Gly	3191.50	3191.46 -0.04
Ile	8970.05	8970.12 +0.07	Gly	3134.45	3134.21 -0.24
Tyr	8806.87	8806.43 -0.44	Lys	3006.27	3006.09 -0.18
Lys	8678.70	8678.81 +0.11	Glu	(c ₂₀) 2877.16	2877.27 +0.11
Lys	8550.52	8550.26 -0.26	Val	2778.02	2778.47 +0.45
Pro	(c ₇₀) 8453.41		Thr	2676.92	2677.15 +0.23
Asn	8339.30	8339.40 +0.10	His	2539.78	2539.66 -0.12
Glu	8210.19	8210.86 +0.67	Cys-heme		
Leu	8097.03	8097.10 +0.07	Gln		
Tyr	7933.85	7934.38 +0.53	Ala		
Glu	(c ₆₅) 7804.74	7804.86 +0.12	Cys-heme		
Met	7673.54	7672.99 -0.55	Lys	1389.64	
Leu	7560.38	7560.21 -0.17	Gln	1261.51	
Thr	7459.27	7458.66 -0.61	Val	1162.37	
Glu	7330.16	7330.18 +0.02	Phe	1015.20	
Glu	(c ₆₀) 7201.04	7200.53 -0.51	Ile	902.04	
Lys	7072.87	7072.41 -0.46	Lys	773.86	
Trp	6886.66	6887.04 +0.38	Lys	645.69	
Thr	6785.55	6784.97 -0.58	Gly	588.64	
Ile	6672.39	6672.69 +0.30	Lys	460.46	
Gly	(c ₅₅) 6615.34	6614.74 -0.60	Glu	331.35	
Lys	6487.17	6486.62 -0.55	Val	232.22	
Asn	6373.06	6373.55 +0.49	Asp	117.13	
Lys	6244.89	6245.38 +0.50	Gly-NH(CO)CH ₃		
			av error		-0.03 ± 0.54
			av abs error		0.38 ± 0.38

One area where both the fast metastable ion decay and PSD fragmentation process produce substantially less structural information is in the case of internally cross-linked peptides. The presence of internal disulfide bonds in the case of porcine insulin (MW = 5777.58 Da) is an excellent example. Table 5 lists the limited number of fast metastable ion decay fragments observed for porcine insulin with sinapinic acid as the MALDI matrix. Mainly c_n and some y_n fragment ions are observed, almost exclusively coming from the B chain portion of porcine insulin. This is consistent with the generally observed trend that as the mass of the peptide is increased, c_n fragments tend to be favored. Ion fragments are labeled both in Table 5 and in a representative mass spectrum (Figure 2) according to the subchain from which the fragmentation occurs. The superscript describes the chain

where fragmentation is occurring. Subscripts denote the remaining number of residues on the charge-retaining fragment in the same manner as the conventional nomenclature when only a single C and N terminus is present. Thus, a c₂₀^B fragment ion represents a c-type ion cleavage (from the C terminus) on the B chain at the residue's (phenylalanine) amide bond. This nomenclature allows fragmentation to be described for each of the four "ends" of the molecule.

All of the c_n fragments (except for proline) that would be predicted between the C-terminal end of porcine insulin and the cysteine residue where a disulfide bond links the A and B chains of porcine insulin together are observed for both chains. At this point, fragmentation is no longer observed. Additionally, equal intensity fragment ions are observed for the intact A and B chains

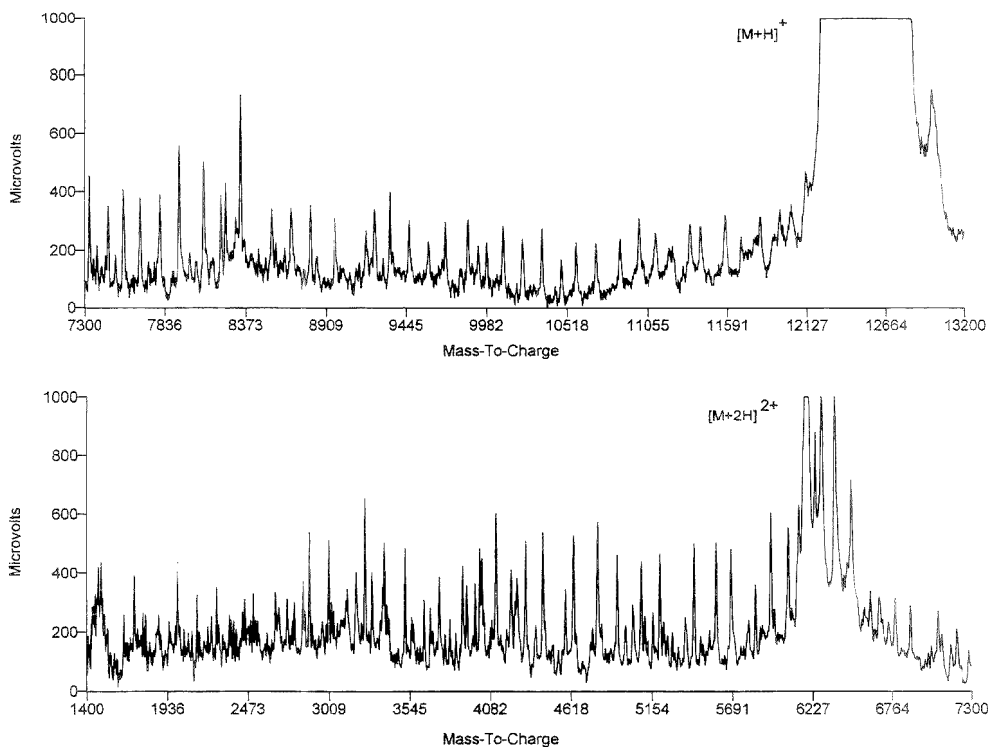


Figure 3. MALDI fast metastable ion decay spectrum of cytochrome *c* obtained with delayed pulsed ion extraction. Sinapinic acid matrix and 2.10 kV pulsed extraction voltage.

due to cleavage at both disulfide chain linkages. These are not due to a small amount of oxidation of the insulin sample prior to MALDI, as no evidence is observed for these ions with continuous ion extraction. Additionally, their m/z values indicate cleavage of the S-S bond and addition of a proton to the sulfur atom. The equal abundance of the two chain fragment ions also is consistent with a cleavage which generates equal amounts of the two chains. Additionally, ions labeled as y_2^A and c_{17}^B are observed, which are due to complete loss of an entire chain (B and A respectively), followed by additional residue loss at the indicated position. The c_{17}^B ion is positioned directly after one of the linking cysteine residues and is a particularly intense fragment ion. The mass accuracy of the limited fragment ion data that are present (B chain c_n and y_n fragments only) remains very good, with an absolute average error of around 0.2 Da.

The final example of fast metastable ion decay presented is for the protein cytochrome *c* and utilized sinapinic acid as the MALDI matrix. The fragment ions observed have been summarized in Table 6. Only c_n fragment ions are observed, continuing the trend observed with porcine insulin. Roughly 80% of the predicted c_n fragment ions are observed. Fragmentation stops at the cysteine residue closest to the C-terminal end of the protein, where the heme group of cytochrome *c* is covalently attached. There also is a very complicated series of fragment ions beginning at this point (around m/z 2500), which suggests that substantial fragmentation of the heme is also occurring.

Mass accuracy has suffered somewhat for this higher mass (and wider fragment ion mass range) analyte, with the absolute average error now about 0.4 Da for all observed c_n fragments. Despite the somewhat poorer mass accuracy, the overall quality of the fast fragmentation spectra obtained with delayed pulse ion extraction remains high, as demonstrated in Figure 3. This is particularly impressive considering it represents an estimated 40 fmol of cytochrome *c* in the laser-irradiated sample area that was collected as a single TOF spectrum in about 2 min.

The cytochrome *c* example is the only exceptional case presented for fast metastable ion decay. The extent and intensity of fast metastable ion fragmentation observed for cytochrome *c* are so far unusual for such a large protein. For example, thioredoxin (*Escherichia coli*, recombinant) is a simple linear protein that has no internal disulfide bonds and is approximately the same molecular weight (11 673.4) as cytochrome *c*. Thioredoxin (ferulic acid matrix) exhibits more limited fast metastable fragmentation with lower S/N than that observed for cytochrome *c*. As with cytochrome *c*, only c_n metastable ions are observed (~50% of the predicted thioredoxin fragments). If the factors involved in the high yield of fast metastable fragment ions for cytochrome *c* can be determined, it may be possible to substantially expand the routine usable mass range for this technique.

The only amino acid residue which consistently has been observed not to provide a usable fast fragment ion with the peptides and proteins studied to date is proline. This is best

demonstrated by the lack of a c_{27} ion for the oxidized B chain of insulin and the lack of the c_{75} , c_{70} , c_{43} , and c_{29} ions in cytochrome *c*. This is perhaps not surprising if the different bonding which occurs for proline residues is considered along with the lack of any observed tendency for multiple bond cleavages. Because of the cyclic nature of the proline residue that results in a tertiary instead of a secondary amide structure, c_n and z_n^* ions would require two bonds to be broken in order for these fragment species to be observed. The y_n fragment ion series observed for other amino acid residues can still occur, but this process must also compete with ring opening and rearrangement, which would not provide any apparent change in mass. In the case of smaller peptides, a low-intensity fragment can sometimes be seen for proline and is almost always a y_n type, as in the case of substance P (Table 3).

CONCLUSIONS

The fast metastable fragmentation data available with the delayed pulsed ion extraction technique on a linear TOF mass spectrometer have clear analytical utility in aiding in primary structure determinations of small and intermediate-sized peptides. If the unique aspects of cytochrome *c* which are responsible for the high yield of fast metastable fragment ions can be identified, the possibility exists for expanding the utility of this technique to larger peptides and proteins. While considerable work is neces-

sary before this methodology can be utilized with true unknowns, its application with small to medium-sized peptides purified from enzymatic digests of larger proteins has obvious potential. Utilization of the delayed pulsed ion extraction technique in conjunction with reflecting TOF mass spectrometers might also allow additional improvements in the obtainable mass resolution of the fast metastable ion fragmentation spectra. Such improvements in mass resolution should yield better sequence-specific information for unknowns.

ACKNOWLEDGMENT

The authors greatly acknowledge the assistance of Directed Energy, Inc., both for donation of the initial GRX 3.0K pulser and for helpful discussions with the staff concerning the pulser's use for this project. This research was supported, in part, by grants from the National Institutes of Health, Divisions of Research Resources (RR05311) and General Medical (GM47914), and with funds provided by Utah State University.

Received for review May 2, 1995. Accepted August 10, 1995.*

AC9504225

* Abstract published in *Advance ACS Abstracts*, September 15, 1995.

Effect of Hydrogen Rearrangement on the Determination of the Enrichment of [¹⁵N]Leucine by GC/MS

Annabelle Dugay, Bien Dang-Vu, Jean Christophe Moreau, and François Guyon*

Laboratoire de Chimie Analytique, Faculté de Pharmacie, Université René Descartes, 4 avenue de l'Observatoire, 75270 Paris cedex 06, France

In the determination of the enrichment of [¹⁵N]leucine by GC/MS, the measured ratio of ¹⁵/¹⁴N-labeled leucine may be affected by H rearrangement. This effect was investigated using 11 esters of ¹⁵N-labeled and nonlabeled *N*-(heptafluorobutyl)leucine. The H rearrangement is dependent on the nature of the alcohol used for the esterification. The labeling ratio increases with the length of the alkyl chain of the ester and with the number of the H atoms at the β -site and, to a lesser extent, at the γ -site on this chain. For the measurement of the enrichment of [¹⁵N]leucine, better standard curves were obtained when ion fragments not affected by H rearrangement were used.

Gas chromatography/mass spectrometry (GC/MS) is a selective and rapid method for the determination of the abundance of [¹⁵N]leucine and other amino acids in isotopic tracer experiments.¹⁻⁴ In these experiments, mixtures of ¹⁵/¹⁴N-labeled leucine are transformed into volatile esters of *N*-(heptafluorobutyl)leucine by a two-stage derivatization before GC/MS analysis.¹ Selected ions containing an atom of nitrogen are monitored and quantified. The ions from ¹⁵N-labeled leucine can be discriminated from the corresponding ones coming from nonlabeled leucine by a shift of the *m/z* values by +1 mass unit as a result of the replacement of an atom of ¹⁴N by an atom of ¹⁵N. The relative area counts of the associated ions are then used to calculate the [¹⁵N]leucine abundance. However, a shift by +1 mass unit, which is supposed to characterize [¹⁵N]leucine, may also occur when an ion containing an atom of ¹⁴N captures an atom of hydrogen by rearrangement. When the mass spectrometer has low resolution, it cannot discriminate between an ion containing an atom of ¹⁵N and an isobaric ion containing an atom of ¹⁴N and a captured H atom. This may affect the determination of the abundance of [¹⁵N]-leucine.

As H rearrangements are frequently encountered with esters of carboxylic acids⁵ and are dependent on the nature of the alcohol used for the formation of the ester, we prepared the esters of *N*-(heptafluorobutyl)leucine using 11 different alcohols and investigated their influence on the determination of the abundance of [¹⁵N]leucine in different mixtures of labeled and nonlabeled leucine.

EXPERIMENTAL SECTION

Materials and Reagents. The GC/MS system was a Fisons Instruments Model MD 800 with an 8000 series gas chromatograph. The capillary column used was a DB-5 (30 m \times 0.25 mm i.d.) J&W Scientific instrument from Interchim (Paris, France). 1-Leucine, acetyl chloride, 2-butanol, and 2-methyl-2-propanol were obtained from Labosi (Paris, France); [¹⁵N]leucine was from Sigma (St. Quentin Fallavier, France); heptafluorobutyric anhydride (HFB) was from Fluka (St. Quentin Fallavier, France); ethanol and 2-propanol were from Carlo Erba (Rueil Malmaison, France); 2,2-dimethyl-1-propanol was from Aldrich (St. Quentin Fallavier, France); 1-butanol was from Merck (Paris, France); and methanol, 1-propanol, 2-butanol, *n*-pentanol, *n*-hexanol, and ethyl acetate were from Prolabo (Paris, France).

Procedures. Leucine was derivatized according to the procedure of MacKenzie and Tenaschuk^{6,7} with minor modifications: mixtures of labeled leucine and nonlabeled leucine at different concentrations (10 μ g/mL) in aqueous solution were evaporated under a flow of dry nitrogen. To the residues was added 0.5 mL of a freshly prepared solution of alcohol-HCl (1 vol of acetyl chloride mixed with 5 vol of ice-cold alcohol at 4 $^{\circ}$ C). The sealed vials (closed with a Teflon-coated cap) were vigorously shaken and then heated to 110 $^{\circ}$ C for 30 min. When they were cooled, excess alcohol-HCl was removed under a flow of dry nitrogen. HFB (50 μ L) was added. The vials were sealed and heated anew at 60 $^{\circ}$ C for 30 min. The cooled samples were evaporated under dry nitrogen, and the ethyl acetate (500 μ L) was added. The sealed vials were vigorously shaken to ensure complete dissolution. Next, 1 μ L of the solution of derivatized leucine mixture was injected, using a CTC A200S autosampler injector. GC/MS analysis was performed under the following conditions: inlet temperature, 250 $^{\circ}$ C; detector temperature, 280 $^{\circ}$ C; oven temperature, 6 min at 130 $^{\circ}$ C, then 15 $^{\circ}$ C/min to 210 $^{\circ}$ C (run time, 12 min).

RESULTS AND DISCUSSION

Results. Under the adopted GC conditions, the retention times of all the esters were less than 10 min. The mass spectra of 1-propyl *N*-HFB and 2-propyl *N*-HFB esters of leucine are represented in Figure 1. They show the same major ion fragments at *m/z* 240, 241, 282, and 283, which appear also in the mass spectra of other amino acid derivatives. These ions contain an atom of nitrogen and may have the structures presented in Figure 2. A possible mechanism for the formation of ion fragment at

(1) Coulter, J. R.; Hann, C. S. *J. Chromatogr.* **1968**, *36*, 42-48.

(2) Adams, R. F. *J. Chromatogr.* **1974**, *95*, 189-212.

(3) Rhodes, D.; Myers, A. C.; Jamieson, G. *Plant Physiol.* **1981**, *68*, 1197-1205.

(4) Golan-Goldhirsh, A.; Hogg, A. M.; Wolfe, F. H. *J. Agric. Food Chem.* **1982**, *30*, 320-323.

(5) McLafferty, F. W. *Anal. Chem.* **1959**, *31*, 82-86.

(6) Mackenzie, S. L.; Tenaschuk, D. *J. Chromatogr.* **1974**, *87*, 19-24.

(7) Mackenzie, S. L.; Tenaschuk, D. *J. Chromatogr.* **1979**, *171*, 195-208.

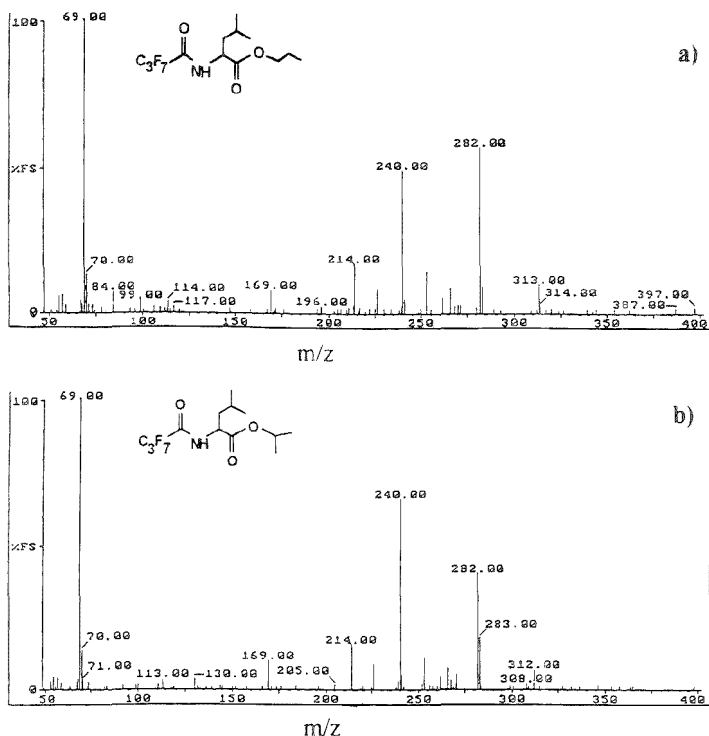


Figure 1. Mass spectra of two *N*-HFB esters of nonlabeled leucine: (a) 1-propyl [^{14}N](heptafluorobutryl)leucine and (b) 2-propyl [^{14}N](heptafluorobutryl)leucine.

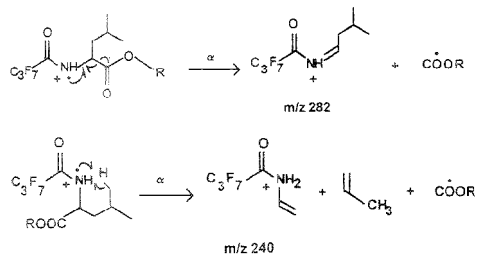


Figure 2. Possible structures of two major ion fragments of esters of *N*-(heptafluorobutryl)leucine containing an atom of nitrogen.

m/z 282 has been described previously.⁸ The formation of an ion fragment at m/z 240 may imply a McLafferty rearrangement.⁹

For the determination of ^{15}N abundance, one can use either fragment 240 or fragment 282. For [^{15}N]leucine, the masses of these fragments were shifted by 1 mass unit. The ratio of the concentration of [^{15}N]leucine to that of [^{14}N]leucine may be assumed to be proportional to the ratio of the peak area of the ion fragment at m/z 283 (or m/z 241) to that of the ion fragment at m/z 282 (or 240). Standard curves were drawn by plotting the

area % ratio (R_i) versus the molar % enrichment (E), with $i = 241$ or 283.

R_i is calculated using eq 1, where A_i is the peak area of the ion fragment at m/z 241 or 283, and A_{i-1} is the peak area of the

$$R_i = \left(\frac{A_i}{A_i + A_{i-1}} \right) \times 100 \quad (1)$$

ion fragment at m/z 240 or 282. E is known from the composition of the samples and is calculated using eq 2, where [^{15}N]Leu is the

$$E = \frac{[^{15}\text{N}]\text{Leu}}{[^{15}\text{N}]\text{Leu} + [^{14}\text{N}]\text{Leu}} \times 100 \quad (2)$$

concentration of labeled leucine and [^{14}N]Leu is the concentration of nonlabeled leucine.

Table 2 shows the intercepts, slopes, and correlation coefficients of the standard curves for esters of *N*-(heptafluorobutryl)leucine obtained using either the two ion fragments at m/z 240 and 241 or the two ion fragments at m/z 282 and 283.

According to the structures of ions at m/z 240 and 282 (Figure 2) and because of the natural abundances of ^{14}N , ^{13}C , and ^2H , ions at m/z 241 and m/z 283 will also be present in the spectra of nonlabeled leucine derivatives. For nonlabeled leucine, the relative intensities of these ions can be predicted and are expected to be independent of the nature of the alcohol used for *N*-(heptafluorobutryl)leucine.

(8) Silverstein, R. M.; Bassler, G. C.; Morrill, T. C. *Spectrometric Identification of Organic Compounds*; John Wiley & Sons, Inc.: 1991; p 38.

(9) Budzikiewicz, H.; Djerassi, C.; Williams, D. H. *Mass Spectrometry of Organic Compounds*; Holden-Day, Inc.: San Francisco, CA, 1967; p 158.

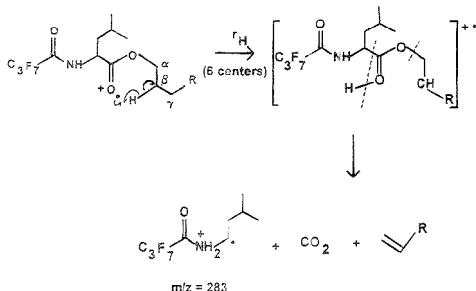


Figure 3. Suggested mechanism for the formation of the ion fragment at m/z 283 by H rearrangement.

Table 1. Influence of the Nature of the Alcohol Used for the Esterification of Nonlabeled Leucine on R_i ($i = 241$ or 283)

alcohol used for derivatization	R_{283} (%)	R_{241} (%)
1-propanol, $\text{CH}_3(\text{CH}_2)_2\text{OH}$ (predicted value) ^a	12.8 (9.33)	6.4 (6.96)
2-propanol, $(\text{CH}_3)_2\text{CHOH}$ (predicted value) ^a	26.9 (9.33)	6.4 (6.96)

^a Value calculated on the basis of the natural abundance of the higher isotopes of C, H, and N.

robutyryl)leucine esterification. We found that this is true when the two ion fragments at m/z 240 and 241 were used, but not when the two ion fragments at m/z 282 and 283 were used. Table 1 illustrates this difference. The area % ratios R_i , in the case of m/z 241, are the same regardless of whether esterification is carried out with 1-propanol or 2-propanol, whereas in the case of m/z 283, the R_i values are different (Table 1).

A similar observation may be made in the case of the standard curves. When the ions at m/z 240 and 241 are used, all the data fit the same curve: $R_{241} = 6.7 + 0.69E$. When the standard curves were drawn on the basis of the peak area of ion fragments at m/z 282 and 283, each alcohol led to a different curve: $R_{283} = 12.58 + 0.66E$ for the 1-propyl *N*-HFB ester of leucine and $R_{283} = 27.22 + 0.57E$ for the 2-propyl *N*-HFE ester of leucine. We present in Table 2 the slopes, the intercepts, and the correlation coefficients of the standard curves for the ethyl, 1-propyl, 2-propyl, 1-butyl, 2-butyl, and 2,2-dimethyl-1-propyl esters. All the standard curves obtained with the two ions at m/z 240 and 241 have high correlation coefficients ($r^2 > 0.745$) and not very different slopes (0.61–0.76) and intercepts (6.6–7.2). On the contrary, when the two ions at m/z 282 and 283 are used, the correlation coefficients are lower ($0.92 > r^2 > 0.41$). Although the slopes are not very

different from the ones observed with ions at m/z 240 and 241, each ester gave a different intercept, which may be as low as 11.2 and as high as 27.2.

Discussion. The intercept represents the peak area % ratio found with nonlabeled leucine. Theoretically, it should be independent of the nature of the alcohol used for the esterification of *N*-(heptafluorobutyl)leucine and must be close to the predicted value calculated on the basis of the natural abundances of the higher isotopes of C, H, and N. This is the case when the two ions at m/z 240 and 241 are used: the measured values of the intercept are practically the same for the two alcohols ($R_{241} = 6.7 \pm 0.3\%$) and are close to the predicted value of $R_{241} = 6.96\%$. However, when the two ions at m/z 282 and 283 are used, the intercepts (R_{283}) are very different from the predicted value ($R_{283} = 9.33\%$). They depend on the nature of the alcohol used for the derivatization of leucine. Thus, it is not possible to assume that the ion fragment at m/z 283 is exclusively an isotopic ion of ion fragment at m/z 282, generated by replacement of one atom of ^{12}C , ^1H , or ^{14}N by one atom of the corresponding higher isotope. It must also have other origins which depend on the nature of the derivatives. As the mass of an ion fragment is shifted by 1 unit when it captures a H atom by rearrangement, the dependence of R_{283} on the nature of the derivatives may be an artifact due to H rearrangement. This rearrangement is frequently encountered with esters of carboxylic acids³ and is dependent on the nature of the alcohol used for the formation of the esters. We suggest a probable mechanism for the formation of ion at m/z 283 through a two-steps H rearrangement (Figure 3).

As H rearrangement is not observed for methyl esters of carboxylic acids, we have measured the area % ratio (R_{283}) of the ion at m/z 283 and 282 using the methyl ester of nonlabeled *N*-(heptafluorobutyl)leucine. We found effectively for R_{283} the value of 9.65%, which is close to the theoretical value of 9.33%. The experimental value of R_{283} for other esters of *N*-(heptafluorobutyl)leucine are presented in Table 3, along with the number of H atoms and their location on the alkyl chain of the esters.

It can be noted from Table 3 that R_{283} increases, as expected, with the number of hydrogens in the β -site. This is very likely due to a six-center cycle McLafferty rearrangement, which is favored by an increase in the number of hydrogens at the β -site. Variation of R_{283} versus the number of hydrogens at the β -site is of second order (Figure 4). For the normal chain esters, which contain the same number of hydrogens at the β -site, R_{283} increases also as a second-order equation with the length of the chain as measured by the number of carbon atoms on the chain (Figure 5). That may be explained by an inductive effect of the alkyl chain, which may influence differently the H rearrangement. It is to be noted that in 2,2-dimethyl-1-propanol, there is no H atom at the β -site; the rearrangement must come through a seven-center cycle

Table 2. Dependence of the Intercepts, the Slopes, and the Correlation Coefficients of the Standard Curves on the Nature of the Ester of *N*-(Heptafluorobutyl)leucine and on the Choice of the Ions (at m/z 240 and 241 or at m/z 282 and 283) Used To Measure R_i

	ethanol		1-propanol		2-propanol		1-butanol		2-butanol		2,2-dimethyl-1-propanol	
	m/z 282, 283	m/z 240, 241	m/z 282, 283	m/z 240, 241	m/z 282, 283	m/z 240, 241	m/z 282, 283	m/z 240, 241	m/z 282, 283	m/z 240, 241	m/z 282, 283	m/z 240, 241
intercept	11.17	7.20	12.58	6.80	27.22	6.63	15.56	6.65	17.18	6.87	26.63	6.73
slope	0.46	0.69	0.66	0.62	0.57	0.77	0.57	0.76	0.69	0.66	0.47	0.70
corr coeff, r^2	0.41	0.78	0.82	0.75	0.45	0.90	0.79	0.92	0.72	0.86	0.74	0.87

Table 3. Variation of R_{283} (%) with the Number and the Position of Hydrogens in the Ester Chain

alcohol used for esterification	no. of hydrogens		R_{283} (%) (exptl) ^a
	β -site	γ -site	
methanol	0	0	9.65
ethanol	3	0	10.80
2-propanol	6	0	26.85
2-methyl-2-propanol	9	0	54.51
1-propanol	2	3	12.76
2-butanol	1	6	17.36
2,2-dimethyl-1-propanol	0	9	26.37

^a The value for R_{283} calculated on the basis of the natural abundance of the higher isotopes of C, H, and N is 9.33%, regardless of the nature of the alcohol used for esterification.

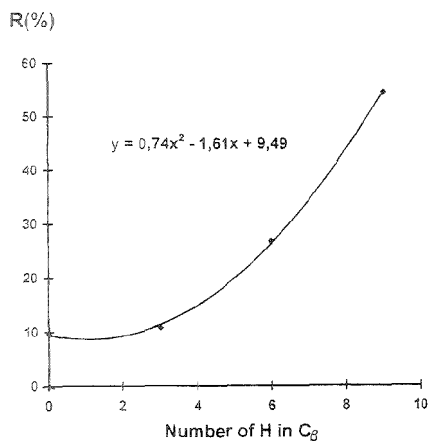


Figure 4. Variation of R_{283} with the number of β -site H of nonlabeled leucine esters.

and not through a six-center cycle. Although the number of hydrogens at the β -site decreases from ethanol to 2,2-dimethyl-1-propanol, R_{283} increases, as does the number of hydrogens at the γ -site.

When H atoms are present at both the β -site and in the γ -site, the two rearrangements contribute to the increase of R_{283} . Contribution of the H atoms in the γ -site is less important than that of H atoms in the β -site. McLafferty rearrangement through

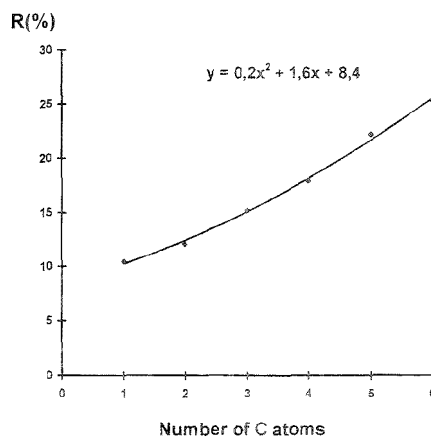


Figure 5. Variation of R_{283} with the number of carbon atoms in the normal chain of nonlabeled *N*-(heptafluorobutyryl)leucine esters.

a six-center cycle is more important than that through a seven-center cycle. The values of R_{283} for 2-methyl-2-propanol (9 H in the β -site and 0 H in the γ -site, $R_{283} = 54.51\%$) and for 2,2-dimethyl-1-propanol (0 H in the β -site and 9 H in the γ -site, $R_{283} = 26.37\%$) proved this (Table 3).

CONCLUSION

Our results show that H rearrangement may affect the determination of [¹⁵N]leucine abundance in isotopic dilution experiments. This rearrangement depends quantitatively on the nature of the alcohol used for the esterification of leucine. Better results and better standard curves were obtained when they were based on the use of the two ion fragments at m/z 240 and 241 instead of the more frequently used ion fragments at m/z 282 and 283, which may be affected by H rearrangement. Further investigations are needed to ascertain the formation of the ion fragment at m/z 283, for instance, through the use of ²H-labeled alcohol for the esterification of leucine.

Received for review May 8, 1995. Accepted July 26, 1995.*

AC950434Q

* Abstract published in *Advance ACS Abstracts*, September 1, 1995.

This Research Contribution is in Commemoration of the Life and Science of I. M. Kolthoff (1894–1993).

Measurement of Tl(III/I) Electron Self-Exchange Rates Using Enriched Stable Isotope Labels and Inductively Coupled Plasma Mass Spectrometry

Michael E. Ketterer* and Michael A. Fiorentino

Department of Chemistry, John Carroll University, University Heights, Ohio 44118

An approach is described for measuring electron self-exchange rate constants (k_{11}) in solution based upon stable isotope-labeled reactants, chemical separations, and inductively coupled plasma mass spectrometry. The technique is demonstrated for the exchange between Tl^{III} and Tl^I aquo ions in aqueous HClO₄. Tl^{III} is prepared using ²⁰³Tl-enriched Tl₂O₃ (²⁰³Tl abundance, ~36%), and Tl^I is prepared from natural abundance Tl reagents (natural ²⁰³Tl abundance, 29.52%). The exchange is monitored by mixing the labeled and unlabeled reactants and performing timewise separations through selective precipitation of Tl^I as TlBr. Isotope abundances are measured in the TlBr precipitate and Tl^{III} solution phases using ICPMS with minimal sample preparation; an NIST 981 (common lead) spike is added, and the ²⁰⁸Pb/²⁰⁶Pb is measured as an internal standard to correct for mass discrimination. The self-exchange rate constant is determined from a McKay plot obtained from the ²⁰³Tl abundances of either oxidation state. A k_{11} of $(1.0 \pm 0.1) \times 10^{-4} \text{ M}^{-1} \text{ s}^{-1}$ was obtained in 1.5 M aqueous HClO₄ at 25 °C. The obtained k_{11} compares favorably to a value of $1.1 \times 10^{-4} \text{ M}^{-1} \text{ s}^{-1}$ based upon a previously published study of this exchange reaction using radiolabeled (²⁰⁴Tl) reactants.

Research into solution-phase electron transfer reactions has been an active and productive area of study since Marcus^{1,2} first laid his theoretical framework. Marcus's theory describes single-electron transfer rate constants (k_{12}) for solution-phase reactants as follows:

$$k_{12} = (k_{11}k_{22}K_{12}f_{12})^{1/5} \quad (1)$$

$$\log f_{12} = (\log K_{12})^2 / 4 \log(k_{11}k_{22}/Z_{12}^2) \quad (2)$$

where k_{11} and k_{22} are self-exchange rate constants for the two redox couples, K_{12} is the equilibrium constant, and Z_{12} is the reactant collision frequency. For systems where both reactants are charged, additional corrective terms are used to account for the electrostatic work required to bring the reactants together

into a "precursor complex". More recently, Macartney and Sutin have also proposed extensions to these equations.³ Accurately known k_{11} values are important when comparing theoretical rate predictions for cross-reactions with experimental values, which enables inferences to be drawn about reaction mechanisms and the intrinsic properties of the reactants. Furthermore, accurately determined k_{11} values are preferred to the alternative of relying on the Marcus correlation's validity while using cross-reaction data to evaluate a given k_{11} , which has shortcomings which are mentioned elsewhere.^{4,5} Unfortunately, direct measurement of k_{11} is difficult, since no net chemical change takes place in the electron exchange (*Ox + Red = *Red + Ox). Numerous elegant procedures have been used to measure k_{11} , including loss of optical activity of chiral complexes,⁶ infrared measurements of complexes with ²H-labeled ligands,⁷ and electrochemical exchange between solution-phase and electrode-adsorbed reactants.⁸ Extensively used procedures include NMR relaxation^{4,9–15} and isotopic equilibration of radiolabeled reactants.^{16–21} The aforementioned procedures all entail certain experimental and practical difficulties, which have tended to limit the systems and conditions for which k_{11} has been directly determined.

A plausible but little-exploited approach for k_{11} measurement is to incorporate stable isotope-labeled atoms into either the Ox or the Red species, perform timewise separations of an Ox/Red

- (3) Macartney, D. A.; Sutin, N. *Inorg. Chem.* **1983**, *22*, 3530–3534.
- (4) Koval, C. A.; Margerum, D. W. *Inorg. Chem.* **1981**, *20*, 2311–2318.
- (5) Vande Linde, A. M. Q.; Juntunen, K. L.; Mols, O.; Ksebati, M. B.; Ochrymowycz, L. A.; Korabacher, D. B. *Inorg. Chem.* **1991**, *30*, 5037–5042.
- (6) Farina, R.; Wilkins, R. G. *Inorg. Chem.* **1968**, *7*, 514–518.
- (7) Meyer, T. J.; Taube, H. *Inorg. Chem.* **1968**, *7*, 2369–2379.
- (8) Lee, C. W.; Anson, F. C. *Inorg. Chem.* **1984**, *23*, 837–844.
- (9) Dietrich, M. W.; Wahl, A. C. *J. Phys. Chem.* **1963**, *38*, 1591–1596.
- (10) Chan, M. S.; Wahl, A. C. *J. Phys. Chem.* **1978**, *82*, 2542–2549.
- (11) Shpror, M.; Ron, G.; Lowenstein, A.; Navon, G. *Inorg. Chem.* **1965**, *4*, 361–365.
- (12) Yang, E. A.; Chan, M. S.; Wahl, A. C. *J. Phys. Chem.* **1980**, *84*, 3094–3099.
- (13) Macartney, D. H. *Inorg. Chem.* **1991**, *30*, 3337–3342.
- (14) Hoddenbagh, J. M. A.; Macartney, D. H. *Inorg. Chem.* **1990**, *29*, 245–251.
- (15) Takagi, H.; Swaddle, T. W. *Inorg. Chem.* **1992**, *31*, 4669–4673.
- (16) Silverman, J.; Dodson, R. W. *J. Phys. Chem.* **1952**, *56*, 846–852.
- (17) Krishnamurty, K. V.; Wahl, A. C. *J. Am. Chem. Soc.* **1953**, *80*, 5921–5924.
- (18) Bonner, N. A.; Hunt, J. P. *J. Am. Chem. Soc.* **1960**, *82*, 3826–3828.
- (19) Jolley, W. H.; Stranks, D. R.; Swaddle, T. W. *Inorg. Chem.* **1990**, *29*, 385–389.
- (20) Jolley, W. H.; Stranks, D. R.; Swaddle, T. W. *Inorg. Chem.* **1990**, *29*, 1948–1951.
- (21) Jolley, W. H.; Stranks, D. R.; Swaddle, T. W. *Inorg. Chem.* **1992**, *31*, 507–511.

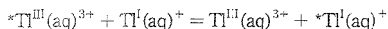
(1) Marcus, R. A. *J. Phys. Chem.* **1963**, *67*, 853–857.

(2) Marcus, R. A. *J. Chem. Phys.* **1965**, *43*, 679–701.

mixture, and monitor the change in stable isotope abundances of Ox and/or Red using mass spectrometry. Stanbury et al.²² recently used this approach for determining k_{11} for the $\text{NO}_2/\text{NO}_2^-$ couple. ^{15}N -labeled NO_2 , separations via ion chromatography, and negative ion FAB mass spectrometry were used. While this, in principle, is identical to the well-known radioisotope exchange procedure, the stable isotope approach is advantageous for two reasons. First, large advances in separation science have taken place since radioexchange studies were first performed. Newer techniques such as reverse-phase and ion-pair HPLC, ion chromatography, and continuous liquid-liquid extraction are all potentially suited to performing the requisite separations. Another relevant factor is that ICPMS enables pragmatic determinations of elemental isotope abundances to be made directly in solutions with microgram per liter levels of analyte.²³

A key limitation of both radiotracer-based and enriched stable isotope schemes for k_{11} measurements is the requirement for timewise separations of Ox and Red. Ideally, the separation process is accomplished in a time frame which is negligible compared to the time scale of the exchange. Moreover, the separation process must not cause an excessive degree of "zero-time exchange", which is the apparent degree of exchange occurring as a result of the separation process. Ultimately, separation processes and zero-time exchange, along with reactant concentrations, determine the upper rate limits of either stable or radiolabeled isotope-based measurement schemes.

The present study was undertaken to demonstrate the concept of using enriched stable isotope labels, chemical separations, and ICPMS isotope abundance measurements as a practical, versatile means of measuring k_{11} . We have chosen the well-characterized two-electron exchange of $\text{Tl}(\text{III}/\text{I})$,



as an appropriate reaction to demonstrate the concept. Using radiolabeled ^{203}Tl , Prestwood and Wahl²⁵ were able to measure k_{11} using a variety of selective precipitations. This reaction is ideal as a demonstrative example since the reactants are not air sensitive and the exchange takes place over a relatively long time scale (i.e., several hours to a few days). We have undertaken a study of k_{11} for the above reaction using ^{203}Tl -labeled Tl_2O_3 and separation by selective precipitation of Tl^{I} as TlBr , to lay the framework for a useful means of studying many additional self-exchange reactions of contemporary interest. We demonstrate herein that the time dependencies of Tl isotope abundances contain encoded kinetic information about the self-exchange process and that k_{11} may be obtained through the experiment.

EXPERIMENTAL SECTION

^{203}Tl -labeled Tl_2O_3 (97% ^{203}Tl) was obtained from Cambridge Isotope Laboratories. Based upon cost considerations, 1 part (w/w) of the labeled material was mixed with about 9 parts of the natural abundance Tl_2O_3 (Alfa Products) to produce the labeled Tl^{III} starting material for most experiments. This labeled Tl^{III}

material had a ^{203}Tl abundance of ~36–37%, which compares to the naturally occurring ^{203}Tl abundance of 29.52%. Tl^{III} solutions were prepared by microwave dissolution of labeled Tl_2O_3 in HClO_4 (70%, Baker Optima Grade) in a closed fluorinated ethylene-propylene test tube (Nalgene). **Caution:** *The microwave dissolution step is performed cautiously with 2–3 mL batches, using 5–10 s pulses of 50–100 W applied power.* Tl^{I} solutions were prepared by dissolution of natural abundance Tl_2CO_3 (Aldrich, 99.999%) in HClO_4 . Tl^{III} solutions were filtered through PTFE syringe filters to remove small amounts of undissolved Tl_2O_3 ; all solutions were diluted with deionized water to produce the desired HClO_4 and Tl concentrations. Thallium concentrations of all solutions were established by ICPMS using Pb as an internal standard.

Most kinetic experiments were conducted in 1.5 M aqueous HClO_4 at 25 ± 0.2 °C, with a $[\text{Tl}^{\text{III}} + \text{Tl}^{\text{I}}]$ of ~0.05 M, and with the Tl^{III} and Tl^{I} concentrations being approximately equal. Additional studies were conducted with unequal Tl^{III} and Tl^{I} concentrations, at a $[\text{Tl}^{\text{III}} + \text{Tl}^{\text{I}}]$ of ~0.025 M, in 3.0 M HClO_4 , and using a Tl^{III} tracer prepared from smaller relative amounts of 97% ^{203}Tl -labeled Tl_2O_3 .

Reaction mixtures were formulated by mixing equal volumes of Tl^{III} and Tl^{I} solutions in a small test tube, which was placed in a constant temperature bath. One hundred microliter aliquots were withdrawn; these were mixed with 25 μL of 2 M aqueous NaBr in the barrel of a 3 mL disposable syringe to form a TlBr precipitate; 2 mL of additional 2 M aqueous NaBr was added, and the mixture was filtered through a 0.2 μm PTFE syringe filter. The degree of zero-time exchange was somewhat sensitive to the precise steps used in forming and rinsing the precipitate; it was found to be important to perform these steps in a consistent, reproducible manner. The Tl^{III} -containing filtrate was collected and diluted to 10 mL with 5% v/v aqueous nitric acid. The TlBr precipitates were dissolved by slowly passing 2 mL of aqua regia through the syringe filter; the aqua regia solution was collected and diluted to 10 mL with deionized water. The Tl^{III} and Tl^{I} reaction mixture products were appropriately diluted with a solution of 0.6 mg/L NIST 981 Pb in 5% v/v aqueous nitric acid; the optimal Tl concentration for isotope abundance measurements was ~0.5 mg/L. The same dilution and analysis scheme (see below) was also used to measure the isotopic composition of all Tl^{III} and Tl^{I} reactant solutions.

Isotope abundance measurements were conducted using a Perkin-Elmer Sciex ELAN 500 ICPMS instrument. This instrument utilized an unpumped (free-aspirating) Meinhard TR-30-C0.5 nebulizer; the deflector and CEM detector have been replaced by an active film multiplier (Model AF561, ETP Scientific, Auburn, MA). Ion lens settings were initially adjusted to produce a $^{205}\text{Tl}/^{203}\text{Tl}$ within $\pm 4\%$ relative to the value for naturally occurring Tl . A duplicate abundance measurement was made for each sample; each measurement collected signals for a total of 30 s per m/z using peak hopping (one measurement per mass spectral peak) and a dwell time of 50 ms. Signals were collected at m/z 203, 205, 206, and 208. The NIST 981 Pb internal standard, with a certified $^{208}\text{Pb}/^{206}\text{Pb}$ value of 2.1681 ± 0.0008 , was used to correct for mass discrimination in the observed $^{205}\text{Tl}/^{203}\text{Tl}$ ratio using the raw ion intensities i_{203} – i_{208} and the equation shown below:

$$\left(\frac{^{205}\text{Tl}/^{203}\text{Tl}}{\text{corr}} \right)_{\text{corr}} = (i_{205}/i_{203})_{\text{obs}} (2.1681) / (i_{208}/i_{206})_{\text{obs}} \quad (3)$$

(22) Stanbury, D. M.; deMaine, M. M.; Goodloe, G. J. *Am. Chem. Soc.* 1989, 111, 5496–5498.

(23) Jarvis, K. E.; Gray, A. L.; Hoak, R. S. *Handbook of Inductively Coupled Plasma Mass Spectrometry*; Blackie: Glasgow, 1992.

(24) Mackay, H. A. C. *Nature* 1938, 142, 997–998.

(25) Prestwood, R. J.; Wahl, A. C. *J. Am. Chem. Soc.* 1949, 71, 3137–3145.

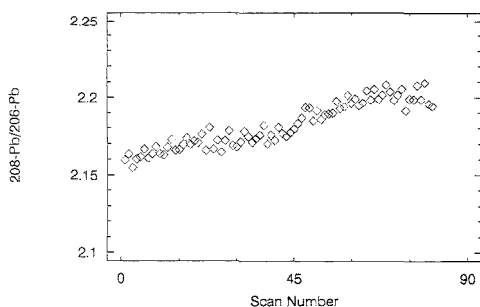


Figure 1. Drift in the degree of mass discrimination observed for the $^{208}\text{Pb}/^{206}\text{Pb}$ of the NIST 981 internal standard. The certified value for this ratio is 2.1681 ± 0.0008 . These data were collected over a single 9 h time frame and are typical of changes in mass discrimination during operation.

Reagent blank subtraction and detector dead-time corrections were found to be unnecessary. Isotope abundances were calculated from $(^{205}\text{Tl}/^{203}\text{Tl})_{\text{corr}}$.

RESULTS AND DISCUSSION

Mass Discrimination of Isotope Measurements. The problem of mass discrimination in quadrupole ICPMS is well known; furthermore, variations in the degree of mass discrimination occur during operation. Measurement of an isotope ratio for an internal standard element has been used as a basis for mass discrimination correction in quadrupole and magnetic sector ICPMS; several groups^{26–30} have used Tl as an internal standard for measurement of Pb isotope ratios, and Ga has been used as an internal standard for measurement of Zn isotope ratios.³¹ Based upon the success of this form of internal standardization, Pb has been used as an internal standard for correction of measured Tl isotope ratios. With the ELAN 500, mass discrimination correction was found to be essential to produce isotope data suitable for the intended kinetic application. Figure 1 depicts a typical example of changes in mass discrimination for the Pb internal standard observed over a 9 h time frame. Since these changes in Pb mass discrimination emulate changes in Tl mass discrimination,²⁷ Figure 1 implies that using uncorrected ^{205}Tl abundances would produce anomalous kinetic plots.

Table 1 illustrates isotope abundances measured for kinetic starting materials and completely exchanged solutions; the distributions of relative precisions (expressed as the range of two measurements) are typical of those found for all solutions investigated.

Tl^{III}–Tl^I Separation Process. The change in solution conditions required to separate the two oxidation states can itself

seriously affect the observed exchange rate; it is desirable to demonstrate agreement of the observed rates using different separation conditions. For the Tl(III/I) system, Prestwood and Wahl²⁵ found agreement between rate constants obtained using precipitation of Tl(I) using Br^- and CrO_4^{2-} as well as precipitation of Tl(III) hydroxide. To further investigate this concern, a series of kinetic runs were conducted at varying concentrations of bromide (0.5, 2.0, 4.0 M); this modification to the separation process produced rate constants which were indistinguishable.

Kinetic Data. The kinetics of a second-order self-exchange process are described by the McKay equation:²⁴

$$k_{11}[\text{Ox} + \text{Red}]t = -\ln(1 - F) \quad (4)$$

where F is the fraction exchanged. The zero-time exchange is given by the y-intercept of a plot of $\ln(1 - F)$ or $\log(1 - F)$ vs time. Prestwood and Wahl²⁵ have shown that reproducible degrees of zero-time exchange and/or incomplete separations do not impede self-exchange rate measurements, since these effects do not alter the slope of the McKay plot. k_{11} is obtainable using the McKay equation and the isotope abundances of either oxidation state:

$$(1 - F) = \frac{[(^{205}\text{Tl})_t - (^{205}\text{Tl})_{\text{infin}}]}{[(^{205}\text{Tl})_0 - (^{205}\text{Tl})_{\text{infin}}]} \quad (5)$$

In the above expression, $(^{205}\text{Tl})_t$ is the isotope abundance measured at time t expressed as a fraction of unity, $(^{205}\text{Tl})_0$ is the abundance measured at $t = 0$ (i.e., immediately upon mixing), and $(^{205}\text{Tl})_{\text{infin}}$ is the abundance found at infinite time (i.e., after driving the reaction to completion).

It was found that the self-exchange process could be readily monitored using the ^{205}Tl abundance data from either oxidation state. Figure 2 illustrates this point for three distinct self-exchange formulations. The experimental curves for ^{205}Tl abundance vs time are in accordance with the simplified second-order rate process expected by the McKay equation, and the information contained in the Tl^{III} and Tl^I curves is very similar. When the reaction is monitored to completion, the isotope abundances for the two oxidation states approach an equilibrium value which is (within the experimental uncertainty of the measurements) the concentration-weighted average of the initial values. Figure 2A depicts the results of run 2; the Tl^{III} and Tl^I concentrations are close to equal, as are the relative changes in ^{205}Tl abundance for the two oxidation states. The effect of using unequal Tl^{III} and Tl^I concentrations is evident in Figure 2C; in this case, the Tl^{III} and Tl^I concentrations were 0.0263 and 0.0159 M, respectively. As expected, a larger relative change in the isotope abundance is observed for the Tl^I fraction.

The effect of using lower relative enrichments of Tl^{III} in the starting material was examined; this produces a smaller observable change in isotope abundance over the course of the exchange. Figure 2B depicts the results of run 8, in which a Tl^{III} mixture with an initial ^{205}Tl abundance of 66.93% was used; this solution was prepared from a mixture of ~1 part 97% ^{205}Tl -enriched Tl_2O_3 and 24 parts natural abundance Tl_2O_3 . Clearly, the self-exchange is still observable; the relative changes in isotope abundance with time are, as expected, smaller, and the errors in the individual

(26) Longereich, H. P.; Fryer, B. J.; Srong, D. F. *Spectrochim. Acta* **1987**, *42*, 39–48.

(27) Ketterer, M. E.; Peters, M. J.; Tisdale, P. J. *J. Anal. At. Spectrom.* **1991**, *6*, 439–443.

(28) Ketterer, M. E. *J. Anal. At. Spectrom.* **1992**, *7*, 1125–1129.

(29) Walder, A. J.; Platzner, I.; Freedman, P. A. *J. Anal. At. Spectrom.* **1993**, *8*, 19–23.

(30) Walder, A. J.; Koller, D.; Reed, N. M.; Hutton, R. C.; Freedman, P. A. *J. Anal. At. Spectrom.* **1993**, *8*, 1037–1041.

(31) Roehl, R.; Gomez, J.; Woodhouse, L. R. *J. Anal. At. Spectrom.* **1995**, *10*, 15–23.

Table 1. Isotope Abundances (Fractional Abundances of $^{205}\text{Tl}^{\text{III}}$)^a for Starting Materials and Products and Percent Zero-Time Exchange for the $\text{Tl}^{\text{III}}-\text{Tl}^{\text{I}}$ Self-Exchange Process in Aqueous HClO_4

run	Tl^{III} abundance ₀		Tl^{III} abundance _{inf.} measd	Tl^{I} abundance ₀		Tl^{I} abundance _{inf.} measd	% ZTE	
	hypothet	measd		hypothet	measd		Tl^{III}	Tl^{I}
1	0.6420 (0.0003)	0.6507 (0.0006)	0.6760 (0.0007)	0.7048 (0.0011)	0.6988 (0.0001)	0.6768 (0.0009)	24.5	18.3
2	0.6420 (0.0003)	0.6522 (0.0008)	0.6766 (0.0010)	0.7048 (0.0011)	0.6995 (0.0012)	0.6764 (0.0005)	27.0	19.3
3	0.6500 (0.0003)	0.6638 (0.0001)	0.6803 (0.0004)	0.7054 (0.0001)	0.6993 (0.0002)	0.6808 (0.0004)	41.6	26.9
4	0.6500 (0.0003)	0.6626 (0.0010)	0.6788 (0.0004)	0.7054 (0.0001)	0.6960 (0.0010)	0.6800 (0.0015)	51.1	34.2
5	0.6448 (0.0016)	0.6540 (0.0006)	0.6750 (0.0002)	0.7048 (0.0001)	0.6980 (0.0002)	0.6765 (0.0001)	26.4	21.5
6	0.6448 (0.0016)	0.6535 (0.0006)	0.6745 (0.0002)	0.7048 (0.0001)	0.6978 (0.0003)	0.6762 (0.0004)	26.5	21.3
7	0.6693 (0.0005)	0.6758 (0.0011)	0.6877 (0.0002)	0.7048 (0.0001)	0.7022 (0.0035)	0.6897 (0.0005)	29.8	16.9
8	0.6693 (0.0005)	0.6733 (0.0022)	0.6884 (0.0002)	0.7048 (0.0001)	0.6980 (0.0009)	0.6877 (0.0011)	25.9	29.7
9	0.6380 (0.0005)	0.6436 (0.0007)	0.6609 (0.0014)	0.7058 (0.0003)	0.6318 (0.0002)	0.6616 (0.0017)	24.5	51.4
10	0.6380 (0.0005)	0.6437 (0.0002)	0.6627 (0.0004)	0.7058 (0.0003)	0.6304 (0.0001)	0.6612 (0.0003)	24.0	56.2

^a All samples analyzed in duplicate; figures in parentheses reflect the range of the two values.

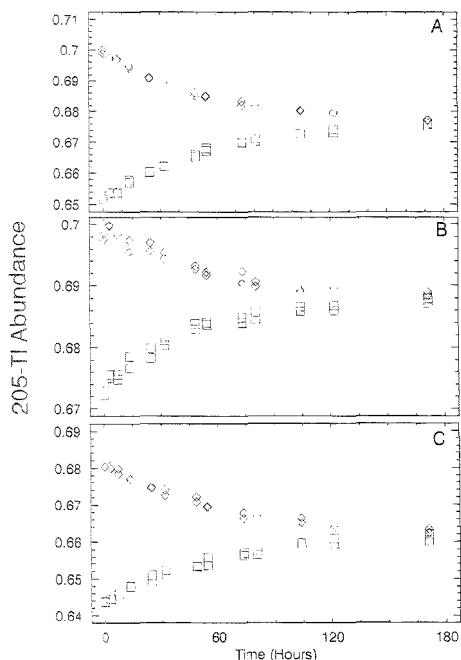


Figure 2. Temporal changes in ^{205}Tl abundance (mass discrimination-corrected) observed for Tl^{III} (\square) and Tl^{I} (\diamond) over the course of kinetic runs. Duplicate points represent isotope abundance measurement-stage replication. (A) Kinetic run 2, $[\text{Tl}^{\text{III}}]$ and $[\text{Tl}^{\text{I}}]$ approximately equal; 1.5 M HClO_4 ; 25 °C; 1:9 Tl^{III} tracer formulation; (B) kinetic run 8, $[\text{Tl}^{\text{III}}]$ and $[\text{Tl}^{\text{I}}]$ approximately equal; 1.5 M HClO_4 ; 25 °C; 1:24 Tl^{III} tracer formulation; (C) kinetic run 10, unequal $[\text{Tl}^{\text{III}}]$, $[\text{Tl}^{\text{I}}]$; 1.5 M HClO_4 ; 25 °C; 1:9 Tl^{III} tracer formulation.

abundance measurements are more pronounced. While no experiments were conducted with still lower degrees of relative Tl^{III} enrichment, it is believed that the formulation of run 8 shown in Figure 2B represents a realistic limit for quantitative determination of rate information.

Extraction of k_{11} . Rate constants were obtained from McKay plots of $\log(1 - F)$ vs time, as described by eq 4. Examples of these plots are shown in Figure 3. The McKay plots were found

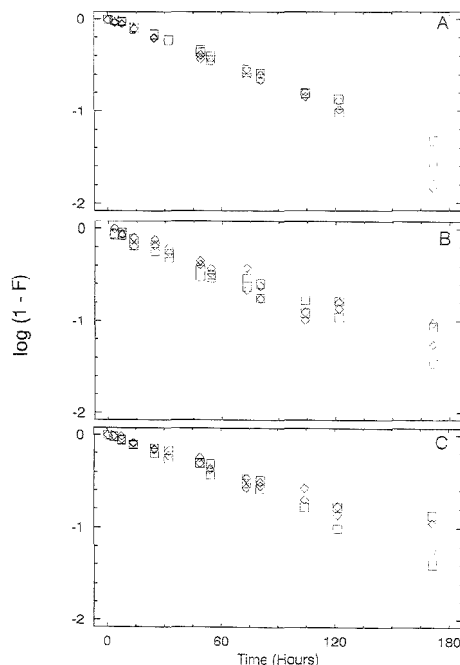


Figure 3. McKay kinetic plots of $\log(1 - F)$ vs time obtained for Tl^{III} (\square) and Tl^{I} (\diamond). Duplicate points represent isotope abundance measurement-stage replication. Plots A–C correspond to the kinetic runs depicted in Figure 2A–C.

to be linear over the course of the 2–4 half-lives which were monitored. At longer reaction times, larger relative differences in $\log(1 - F)$ for duplicate isotope ratios are observed; this is expected given eq 5. The effect of using a lower relative Tl^{III} enrichment is evident (run 8, Figure 3B).

The slopes of the McKay plots were determined using weighted least-squares regression models without an intercept term; the omission of the intercept is appropriate based upon eqs 4 and 5. In obtaining the values of $\log(1 - F)$, the value of $(^{205}\text{Tl})_0$ was taken as that observed with the first sampling of the reaction mixture, typically 1–3 min after mixing. The $(^{205}\text{Tl})_{\text{inf}}$ was obtained from the isotope abundance of a completely exchanged

Table 2. Kinetic Results Obtained for the Tl^{III}-Tl^I Self-Exchange Process in Aqueous HClO₄^a

run	[Tl ^{III}], M	[Tl ^I], M	²⁰⁵ Tl, ^b Tl ^{III}	[HClO ₄], M	<i>t</i> _{1/2}		<i>k</i> ₁₁	
					Tl ^{III}	Tl ^I	Tl ^{II}	Tl ^I
1	0.0234	0.0271	0.6420	1.50	36.3	40.0	1.06 × 10 ⁻⁴	9.61 × 10 ⁻⁵
2	0.0234	0.0271	0.6420	1.50	39.6	37.2	9.72 × 10 ⁻⁵	1.03 × 10 ⁻⁵
3	0.0117	0.0131	0.6500	1.50	78.8	76.0	9.85 × 10 ⁻⁵	1.02 × 10 ⁻⁵
4	0.0117	0.0131	0.6500	1.50	71.8	71.6	1.08 × 10 ⁻⁴	1.08 × 10 ⁻⁵
5	0.0260	0.0243	0.6448	3.00	57.4	59.6	6.71 × 10 ⁻⁵	6.47 × 10 ⁻⁵
6	0.0260	0.0243	0.6448	3.00	62.1	61.4	6.20 × 10 ⁻⁵	6.27 × 10 ⁻⁵
7	0.0251	0.0271	0.6693 ^c	1.50	39.5	34.4	9.55 × 10 ⁻⁵	1.10 × 10 ⁻⁵
8	0.0251	0.0271	0.6693 ^c	1.50	37.5	40.7	1.01 × 10 ⁻⁴	9.29 × 10 ⁻⁵
9	0.0263	0.0159	0.6380	1.50	38.4	46.0	1.19 × 10 ⁻⁴	9.92 × 10 ⁻⁵
10	0.0263	0.0159	0.6380	1.50	44.8	47.0	1.02 × 10 ⁻⁴	9.70 × 10 ⁻⁵

^a Half-lives are in hours, and self-exchange rate constants are in M⁻¹ s⁻¹. ^b Initial values of the ²⁰⁵Tl abundance (expressed as a fraction of unity) for Tl^{III} material used in the run. ^c All Tl^{III} reactants were formulated from ~1 part 97% ²⁰⁵Tl-labeled Tl₂O₃ and ~9 parts natural Tl₂O₃, except for runs 7 and 8; this reactant was prepared from ~1 part 97% ²⁰⁵Tl-labeled Tl₂O₃ and ~24 parts natural Tl₂O₃.

portion of reaction mixture, prepared as described in the Experimental Section. Weighted least-squares regression was performed using [(²⁰⁵Tl)_{*t*} - (²⁰⁵Tl)_{infin}] as weighting factors. The half-life and *k*₁₁ were obtained from the slope, *m*:

$$t_{1/2} = \log 0.5/m \quad (6)$$

$$k_{11} = \ln 2 / [Tl^{III} + Tl^I]_{t_{1/2}} \quad (7)$$

The 1σ relative uncertainties in individual *k*₁₁ measurements are expected to be ~3–5% based upon the relative uncertainties in [Tl^{III} + Tl^I] and *t*_{1/2}.

Presented in Table 2 are concentration parameters as well as *t*_{1/2} and *k*₁₁ results for 10 kinetic runs. The *k*₁₁ values derived from runs 1–4 and 7–10 provide a composite value of (1.0 ± 0.1) × 10⁻⁴ M⁻¹ s⁻¹ at 25.0 °C in 1.5 M HClO₄; this value compares very favorably to a *k*₁₁ of 1.1 × 10⁻⁴ M⁻¹ s⁻¹, which was obtained graphically from results presented by Prestwood and Wahl.²⁵ The average *k*₁₁ values obtained from Tl^{III} and Tl^I were indistinguishable at the 80% confidence level, as can be seen from Table 2. Based upon the limited data of Table 2, isotope abundance monitoring of either oxidator state would appear to suffice for determining *k*₁₁ using the technique described herein. It is certainly appropriate to investigate isotope abundance changes in both oxidation states when attempting to use this technique for new redox couples.

The effect of changing from 1.5 to 3.0 M HClO₄ is seen in the results of runs 5 and 6; a composite *k*₁₁ of (6.4 ± 0.3) × 10⁻⁵ M⁻¹ s⁻¹ is obtained at 25.0 °C in 3.0 M HClO₄. This decrease in *k*₁₁ parallels the decrease in *k*₁₁ with increasing HClO₄ concentration observed by Prestwood and Wahl.²⁵ The change in the observed *k*₁₁ may be interpreted in terms of changes in the work required to form the precursor complex and/or diminution of the importance of the hydroxide-bridged inner-sphere reaction path.

Although a rigorous test of the rate law was not conducted, the expected changes in *t*_{1/2} were produced by changes in [Tl^{III} + Tl^I], and the rate constants for runs 1–4 and 7–10 are in close agreement. It follows from the results of runs conducted at different [H⁺] and [Tl^{III} + Tl^I] that the technique is capable of producing interpretable rate constants which have chemical significance.

Zero-Time Exchange. The degree of zero-time exchange was established by using a modified form of eq 5:

$$(1 - F) = \frac{[(^{205}\text{Tl})_t - (^{205}\text{Tl})_{\text{infin}}]}{[(^{205}\text{Tl})_{\text{hyp}} - (^{205}\text{Tl})_{\text{infin}}]} \quad (8)$$

In this expression, (²⁰⁵Tl)_{hyp} refers to the hypothetical value of the isotope abundance at *t* = 0; this is simply the ²⁰⁵Tl abundance measured for the applicable reactant prior to mixing. As is seen in Table 1, the observed (²⁰⁵Tl)₀ values were systematically different from (²⁰⁵Tl)_{hyp}, which indicates that zero-time exchange exists in all cases. The effect of the zero-time exchange is to “consume” part of the observable difference between (²⁰⁵Tl)_{hyp} and (²⁰⁵Tl)_{infin}; provided the Ox/Red separation is reproducible, one can circumvent a large zero-time exchange by using a larger relative isotope enrichment in the labeled reactant.

The percent zero-time exchange (ZTE) values shown in Table 1 were determined by substituting eq 8 in eq 4; weighted linear regression parameters, including an intercept, were determined for eq 4. Weighting was again performed using [(²⁰⁵Tl)_{*t*} - (²⁰⁵Tl)_{infin}] as weighting factors; the y-intercept obtained corresponds to log(1 - F_{ZTE}). The ZTE values were fairly consistent for a given set of conditions; they are obviously influenced by the reactant concentrations. The differences in ZTE observed between run 7 and run 8 for Tl^I are most likely due to the low degree of relative Tl^{III} enrichment used.

Figure 4 illustrates the lack of any apparent relationship between *k*₁₁ and ZTE. Although similar investigations will be needed in extending our approach to additional redox couples, this finding suggests that the technique presented herein is rather tolerant of incomplete separation and/or separation-induced exchange. A plausible interpretation of the physical significance of the zero-time exchange is that it reflects a brief period of accelerated electron transfer between Tl^{III} and Tl^I. This may arise due to a bromide-bridged homogeneous inner-sphere pathway; halide ions are known to catalyze the self-exchange reaction between aquo metal ions such as Cu^{II}(aq)²¹/Cu^I(aq)^{7,32}. It is also possible that the exchange is accelerated by the presence of Tl^I-Br(s) particles, which are in contact with the exchanging solution for a few seconds until the filtration is completed.

(32) Sis'ey, M. J.; Jordan, R. B. *Inorg. Chem.* **1992**, *31*, 2880–2884.

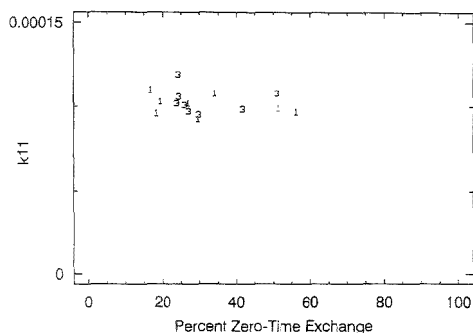


Figure 4. Plot of k_{11} vs observed percent zero-time exchange for eight kinetic runs, 25 °C, 1.5 M HClO₄. Varying [Tl^{III}] : [Tl^I] conditions influenced the % ZTE. Numerical symbols indicate the Tl oxidation state being monitored.

CONCLUSION

We have demonstrated that k_{11} can be measured using enriched stable isotope labels, chemical separations, and ICPMS. For the Tl^{III/I} reaction studied, the self-exchange rate found by this technique is in good agreement with those obtained from analogous radiotracer experiments. The stable isotope method appears to be insensitive to varying degrees of zero-time exchange and to the relative concentrations of the two redox forms; changes in isotope abundances for both redox forms are readily monitored, and it is found that the rate constants derived from either oxidation state are indistinguishable. With mass discrimination-corrected

ICPMS isotope abundance measurements of 0.1–0.5% RSD, kinetic events can be monitored with as little as a ~3% relative change in isotope abundance over the course of the reaction.

This method may potentially be extended to the study of other redox couples which can be suitably prepared in metal–ion labeled form and for which a suitable separation of the redox forms can be developed. Of obvious interest is extending the method to faster exchange reactions. Work in progress involves identifying the upper rate limits of the technique, comparing results of this technique to k_{11} values obtained by NMR line-broadening methods, and measuring k_{11} for some systems of theoretical interest where k_{11} has not been characterized to date.

Acknowledgment is made to the donors of the Petroleum Research Fund, administered by the American Chemical Society, for partial support of this research (28639-GB3). This work was also supported by the Society for Analytical Chemists of Pittsburgh (Starter Grant Award) and John Carroll University. The ICPMS instrument is a donation of VWR Corp., which the authors gratefully acknowledge. The authors also thank M. L. Waiwood for preliminary studies. J. P. Guzowski, B. Ohlson, and K. Humphries assisted with the isotope abundance measurements.

Scientific Parentage of the Author. M. E. Ketterer, Ph.D. under C. A. Koval, Ph.D. under F. C. Anson, Ph.D. under J. J. Lingane, Ph.D. under I. M. Kolthoff.

Received for review March 23, 1995. Accepted August 21, 1995.*

AC950285B

* Abstract published in *Advance ACS Abstracts*, October 1, 1995.

An Electrochemical Cell for End-Column Amperometric Detection in Capillary Electrophoresis

Mei-Cheng Chen and Hsuan-Jung Huang*

Department of Chemistry, National Sun Yat-sen University, Kaohsiung 80424, Taiwan, ROC

With end-column amperometric detection in capillary electrophoresis, precise positioning and stabilization of the working electrode are highly important. Noises from vibration and breakage of the microelectrode (e.g., carbon fiber electrode) are typical problems. To overcome these drawbacks, a new electrochemical cell assembly was designed. In this assembly, alignment of the working electrode with the capillary outlet can be achieved precisely and easily. Coupling with a disk-type Pt electrode (50 μm diameter), detection limits of 3.0 and 5.2 amol and separation efficiencies of about 70 000 and 150 000 theoretical plates for the determination of dopamine and catechol, respectively, as test compounds can be obtained. The relative standard deviations ($n = 21$) of migration time and peak current obtained are 3.5, 5.1% and 2.2, 2.7%, respectively, for these two compounds. Applicability of this assembly as an electrochemical detector for capillary electrophoresis was demonstrated by running a synthetic sample containing dopamine, serotonin, norepinephrine, epinephrine, isoproterenol, and catechol. Results obtained are comparable with those from other end-column or off-column determinations.

Capillary electrophoresis (CE) was introduced about decade ago by Mikkers et al.¹ and Jorgenson and Lukacs^{2,3} as a highly efficient method for separating ionic compounds. Since then, CE has become an important technique in the area of liquid phase separation. Typically, CE is characterized by a minimal sample volume (microliters) requirement, short analysis time, and high separation efficiency. With various separation modes, e.g., capillary zone electrophoresis, micellar electrokinetic capillary electrophoresis, and gel capillary electrophoresis, CE can be used for the separation of anions, cations, neutral molecules,⁴⁻⁷ or even

optical isomers.⁸⁻¹⁰

CE with a narrow-bore (2-10 μm i.d.) capillary offers better separation efficiency, but a very sensitive detector with minimal dead volume is needed to accommodate the extremely small sample volume (nanoliters to picoliters) injected. Although different detection schemes, such as UV absorption, laser-induced fluorescence, mass spectroscopy (MS), and electrochemical detection, have been developed for CE, not all of these detection modes are applicable to CE with a narrow-bore capillary. The UV detector commonly used^{1,4-6,8,10} is not sensitive enough because of its light-path-dependent characteristic. A laser-induced fluorescence detector^{4,8,11} provides the required sensitivity for narrow-bore CE; however, it usually requires extra procedures of pre- or postcolumn derivatization of the analytes. An MS detector¹² provides the highest sensitivity and also the structural information, but a cost problem arises as compared with other modes of detection. The electrochemical detector, which possesses high sensitivity, is inexpensive and can be coupled with the narrow-bore capillary readily. It thus becomes one of the most popular detectors used for CE with narrow-bore capillary.¹³⁻¹⁸

Two electrochemical detection modes have been developed: off-column^{7,13,14,19-25} and end-column.^{15-18,26-28} For the off-column mode, a conductive junction between the separation and detection

- (1) Mikkers, F. E. P.; Everaerts, F. M.; Verheggen, Th. P. E. M. *J. Chromatogr.* **1979**, *169*, 11.
- (2) Jorgenson, J. W.; Lukacs, K. D. *J. Chromatogr.* **1981**, *218*, 209.
- (3) Jorgenson, J. W.; Lukacs, K. D. *Anal. Chem.* **1981**, *53*, 1298.
- (4) Ludi, H.; Gassman, E.; Grossenbacher, H.; Marki, W. *Anal. Chim. Acta* **1988**, *213*, 215.
- (5) Cohen, A. S.; Terabe, S.; Smith, A.; Karger, B. L. *Anal. Chem.* **1987**, *59*, 1021.
- (6) Walbroehl, Y.; Jorgenson, J. W. *Anal. Chem.* **1986**, *58*, 479.
- (7) Wallingford, R. A.; Ewing, A. G. *J. Chromatogr.* **1988**, *441*, 299.

- (8) Gozel, P.; Gassmann, E.; Michelsen, H.; Zare, R. N. *Anal. Chem.* **1987**, *59*, 44.
- (9) Guttman, A.; Paulus, A.; Cohen, A. S.; Grinberg, N.; Karger, B. L. *J. Chromatogr.* **1988**, *448*, 41.
- (10) Honda, S.; Iwase, S.; Makino, A.; Fujiwara, S. *Anal. Biochem.* **1989**, *176*, 72.
- (11) Cheng, Y.; Dovichi, N. J. *Science* **1988**, *242*, 562.
- (12) Smith, R. D.; Wahl, J. H.; Goodlett, D. R.; Hofstadler, S. A. *Anal. Chem.* **1993**, *65*, 574A.
- (13) Wallingford, R. A.; Ewing, A. G. *Anal. Chem.* **1989**, *61*, 98.
- (14) Olefirowicz, T. M.; Ewing, A. G. *Anal. Chem.* **1990**, *62*, 1872.
- (15) Huang, X.; Zare, R. N.; Sloss, S.; Ewing, A. G. *Anal. Chem.* **1991**, *63*, 189.
- (16) Sloss, S.; Ewing, A. G. *Anal. Chem.* **1993**, *65*, 577.
- (17) Lu, W.; Cassidy, R. M.; Baianski, A. S. *J. Chromatogr.* **1993**, *640*, 433.
- (18) Lu, W.; Cassidy, R. M. *Anal. Chem.* **1993**, *65*, 2878.
- (19) Kaniansky, D.; Havasi, P.; Marak, J.; Sokolik, R. *J. Chromatogr.* **1986**, *366*, 153.
- (20) Wallingford, R. A.; Ewing, A. G. *Anal. Chem.* **1987**, *59*, 1762.
- (21) Yik, Y. F.; Lee, H. K.; Li, S. F. Y.; Khoo, S. B. *J. Chromatogr.* **1991**, *585*, 139.
- (22) O'Shea, T. J.; GreenHagen, R. D.; Lunte, S. M.; Lunte, C. E. *J. Chromatogr.* **1992**, *593*, 305.
- (23) O'Shea, T. J.; Lunte, S. M. *Anal. Chem.* **1993**, *65*, 247.
- (24) O'Shea, T. J.; Lunte, S. M. *Anal. Chem.* **1993**, *65*, 948.

capillaries is used to isolate the high voltage applied to the separation capillary from the electrochemical detection system. For the end-column detection, a microelectrode is placed directly at the end of the separation capillary without any conductive junction. Although satisfactory results can be obtained from both modes of electrochemical detection, these modes have not been applicable to routine analysis. This is primarily due to the difficulty of finding an appropriate material for making the conductive junction and the requirement of fairly elaborate work on the construction of a reliable and sophisticated electrochemical cell. For end-column detection, in order to improve the sensitivity and to eliminate the noise from mechanical vibrations, precise alignment and stabilization of the working electrode are highly demanded. Breakage of the microelectrode occurs frequently during the handling or assembling of the electrochemical cell.

In this study, a new electrochemical cell assembly similar to the off-column detector presented by Tudos et al.²⁵ was designed and used as an end-column detector. A piece of poly(tetrafluoroethylene) (PTFE) tubing enclosing a Pt electrode was employed as a guide for the alignment of the capillary and the working electrode. Precise alignment can be achieved easily with a magnifier instead of a micropositioner and a microscope. With this electrochemical cell, detection limits of 3.0 and 5.2 amol and separation efficiencies of about 70 000 and 150 000 theoretical plates are obtained for the determination of dopamine and catechol, respectively, as test compounds. The relative standard deviations (RSDs, $n = 21$) of migration time and peak current are found to be 3.5, 5.1% and 2.2, 2.7%, respectively, for these determinations in a concentration range of 5×10^{-8} – 5.0×10^{-5} M. The effects of injection time and separation potential on the separation efficiency are studied. The feasibility of this cell assembly as an electrochemical detector for CE is demonstrated by running a synthetic sample containing dopamine, serotonin, norepinephrine, epinephrine, isoproterenol, and catechol. Results obtained are comparable with those from end-column or off-column determinations.

EXPERIMENTAL SECTION

Apparatus. Fused-silica capillary of 5 μm i.d., 365 μm o.d. was obtained from Polymicro Technologies (Phoenix, AZ). A high-voltage dc powder supply (Model CZE1000 PN30R, Spellman High-Voltage Electronics Corp., Plainview, NY) was used to provide the required voltage (from 0 to $\sim +30$ kV). For the CE system, the cathodic end is maintained at ground, and pieces of Pt were used as the contacts of anode and cathode to the power supply. An acrylic box with an interlock on the access door was used to enclose the high-voltage output and to protect the operators from electric shock. The electrophoretic potential, the electrokinetic injection process, and the data acquisition were controlled by a personal computer (386DX/40 MHz) equipped with a PCL-812 high-performance data acquisition card (B&C Microsystem, Sunnyvale, CA).

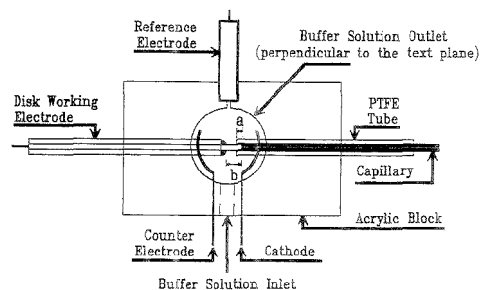


Figure 1. Top view of the electrochemical cell configuration. Components in figure are not drawn to scale. Dimensions of the acrylic block are $40 \times 25 \times 20$ cm³, and the distances a and b are about 200 μm and 3 mm, respectively. The capillary (5 μm i.d., 365 μm o.d.) is the separation capillary. The disk working electrode is formed by enclosing the Pt wire (50 μm diameter) with a piece of capillary (75 μm i.d., 365 μm o.d.). Details of the electrode configuration are given in the text.

The control program was written in Turbo C++. The post-run data processing program²⁹ was written in Quick BASIC. The data processing program displays the electropherogram on the monitor and searches the peaks of the electropherogram. The data of migration time, peak height, peak area, width at half-height, and number of theoretical plates for each detected peak can be obtained readily.

The electrochemical cell was made of an acrylic block ($40 \times 25 \times 20$ mm³). Spaces for positioning the reference electrode, the capillary tubing, and the inlet and outlet of buffer solution were tapped with a $1/4$ in. thread, while space for allocation of the working electrode was tapped with a $3/16$ in. thread. A channel with a diameter of $1/16$ in. was drilled for the connection of the working electrode and the capillary tubing. Figure 1 shows the top view of the electrochemical cell configuration. The scheme shown is not to scale, but the dimensions of several key components are labeled. A disk-type working electrode is used in this experiment. To fabricate the disk electrode, a piece of Pt wire (50 μm diameter, 5 cm length) was inserted and passed through a piece of capillary (75 μm i.d., 365 μm o.d., 1 cm length) from which the polyimide coating was removed. Epoxy glue was then applied to both ends of the capillary to secure the Pt wire. No special effort has been made to ensure that the Pt wire was secured at the center of the capillary. The capillary in which the Pt electrode was enclosed was inserted into a piece of PTFE tube (300 μm i.d., $1/16$ in. o.d., 4 cm length) from the free Pt wire end and stopped when half of the capillary (~ 5 mm) was enclosed in the PTFE tubing. Both ends of the PTFE tubing were sealed with epoxy glue. The length of capillary protruding from the cured epoxy was kept to about 3 mm. A piece of Cu wire was soldered to the free Pt wire and served as the conducting lead. The disk electrode was carefully polished before use.

To assemble the electrochemical cell, a piece of capillary (5 μm i.d., 365 μm o.d.) of appropriate length (~ 50 cm) was inserted into a short piece of PTFE tubing (same specifications as above but about 20 mm length) until the capillary was just extruded from it. Though the inside diameter of the PTFE tubing is smaller

(25) Tudos, A. J.; Van Dyck, M. M. C.; Poppe, H.; Kok, W. Th. *Chromatographia* 1993, 37, 79.

(26) Colon, L. A.; Dandoo, R.; Zare, R. N. *Anal. Chem.* 1993, 65, 476.

(27) Ye, J.; Baldwin, R. P. *Anal. Chem.* 1993, 65, 3525.

(28) Doughterty, A. M.; Woolley, C. L.; Williams, D. L.; Swaile, D. F.; Cole, R. O.; Sepaniak, M. J. *J. Liq. Chromatogr.* 1991, 14 (5), 907.

(29) Gates, S. C.; Becker, J. *Laboratory Automation Using The IBM PC*; Prentice-Hall: Englewood Cliffs, NJ, 1989; Chapter 11.

than the outside diameter of the capillary, due to the slight softness characteristic of the PTFE tubing, insertion of the capillary into the PTFE tubing can be achieved without difficulty. After the capillary was filled with buffer solution and the extruded end of the PTFE tubing submerged in the same buffer solution, the capillary was pulled gently back into the PTFE tubing until the capillary end was 150–250 μm inside the PTFE tubing. The channels of the electrochemical cell were filled with buffer solution, and the PTFE tubing in which the working electrode was enclosed was inserted into the cell along the $1/16$ in. channel and secured with a PTFE finger-tight fitting when the Pt electrode rested at the center of the channel. The PTFE tubing in which the separation capillary was enclosed was then inserted from the other end of the $1/16$ in. channel and pushed gently until the capillary outlet was in close contact with the disk electrode. The intimate contact between the disk electrode and the capillary end can be examined with a magnifier (with a magnifying factor of 20 \times). After the alignment was done, the PTFE tubing in which the separation capillary was enclosed was secured with an O-ring and a PTFE flanged fitting. As the surface of disk electrode is much larger than the dimensions of the capillary outlet, a wall-jet-type thin-layer electrochemical cell is thus formed. A home-made Ag/AgCl reference electrode surround with male screw (1/4-28 thread) was screwed into the cell. A piece of Pt wire was used as the counter electrode and was sealed into the block directly. Amperometric determination and other voltammetry experiments were done with a polarographic analyzer (Model 264A, PARC). A current preamplifier (Model PA-1, BAS) was used for the measurement of very low current. To minimize the interference of external electric noise, the electrochemical cell assembly was housed in a Faraday cage (Model C2, BAS). Current was recorded with a strip-chart recorder (Yokogawa Model 3025).

For most of the following experiments, CE was run by employing a capillary (5 μm i.d., 365 μm o.d., 50 cm length) at a separation potential of 25 or 20 kV. The buffer solution used contained of 20 mM morpholinethanesulfonic acid (MES) with pH adjusted to 6.0. Sample injection was performed by electromigration at 12 kV for 5 s. A constant electrochemical potential of 0.700 V vs Ag/AgCl was used for amperometric determination. Buffer solution in the electrochemical cell was refreshed by syringing after each electrophoretic run.

Chemicals. MES and dopamine were obtained from Tokyo Chemical Industry Co. Serotonin, norepinephrine, epinephrine, isoproterenol, and catechol were obtained from Sigma. All chemicals were used as received. The buffer solution used was 20 mM MES with pH adjusted to 6.0. Stock solutions (0.01 M) were prepared in 0.1 M perchloric acid. Sample solutions were prepared by dilution of stock solutions to the desired concentration with buffer solution.

RESULTS AND DISCUSSION

Characteristics of the Cell Assembly. Literature for CE with small capillaries indicates that the applied separation potential would drop to an insignificant magnitude at the end of the high-resistance capillaries.¹⁶ In the system currently studied, the internal resistance of the capillary (5 μm i.d., 50 cm length), R_C and the internal resistance of the PTFE tubing, R_P , can be estimated from the following equations,

$$R_C = \rho_B l_C / A_C \quad (1)$$

$$R_P = \rho_B l_P / (A_P - A_W) \quad (2)$$

where ρ_B is the resistivity of buffer solution, l_C is the length of capillary, l_P is the length of the working electrode enclosed inside the PTFE tubing ($l_P \approx 200 \mu\text{m}$), and A_C , A_P and A_W are the cross-sectional areas of capillary, PTFE tubing, and working electrode, respectively. From eqs 1 and 2, the ratio R_C/R_P is estimated to be 10^6 . As the internal resistance for the buffer-solution-filled, 5 μm i.d. capillary, R_C is approximately equal to $1 \times 10^{12} \Omega$,¹⁶ a value of $1 \times 10^6 \Omega$ is estimated for the average resistance of the buffer-solution-filled PTFE tubing. In the studied system, application of a 20 kV separation potential to the capillary should result in a 20 kV potential drop across the capillary and an ~ 10 mV potential drop across the PTFE tubing. That means the electric field across the capillary is 8 V/200 μm , and that between the capillary outlet and the end of PTFE tubing is about 10 mV/200 μm . As the surface of the disk electrode is perpendicular to the vector of applied separation potential, there should be no potential drop across the surface of the disk electrode due to the separation potential. It is feasible to carry out the amperometric detection with the designed electrochemical cell assembly. To further justify the feasibility of the conclusion made, staircase voltammetry for dopamine and isoproterenol was run in the CE system with the electrochemical cell assembly. Peak potentials found at 0.40 and 0.46 V for these two compounds, respectively, match well the half-wave potentials obtained from batch-type experiments. This implies that the voltammetric behavior of the Pt disk electrode is not affected by the possible iR drop resulting from the applied separation potential.

For end-column detection, precise alignment of the working electrode with the capillary outlet is a prerequisite and is usually achieved by careful manipulation of a micropositioner with the help of a microscope.^{16,17} Poor alignment between the electrode and the capillary outlet will result in a significant loss of sensitivity and the deterioration of the detection limit.¹⁷ For a system with a carbon fiber microelectrode, once optimized alignment is achieved, minor displacement of the electrode due to room vibrations or other unavoidable phenomena produces marked changes in the detection currents.¹⁷

In this system, the capillary and the electrode are secured within the PTFE tubing and are guided within the same channel. Additionally, the cross-sectional area of capillary outlet to the surface area of the working electrode is in a ratio of 1:100, so proper positioning and good alignment for the capillary and working electrode can be easily attained. As the working electrode and capillary are secured inside the cell assembly, the noises that arise from mechanical vibrations and air drafts are thus eliminated. This would lower the noise level and improve the sensitivity of the electrochemical detector; a similar result has been illustrated in Baldwin's work.²⁷ It takes ~ 20 min to assemble the electrochemical cell. Once assembled, it takes only about 5 min to replace either the working electrode or the capillary tubing. The reproducibility of the alignment operations is evaluated by measuring the detection current of dopamine after each operation cycle of disassembling and assembling the working electrode and separation capillary. The RSDs ($n = 8$) for the variations of migration time, peak height, and peak area obtained in alignment operations were found to be 3.0, 6.0, and 3.2%, respectively. The

RSDs obtained are better than the value of 10–15% for the wall-jet arrangement with a normal size electrode and the value of 65% for the conventional end-column scheme using a carbon fiber microelectrode.²⁷

Performance of the Cell Assembly. The characteristics of the designed cell assembly were demonstrated by running the electrophoresis with a solution containing dopamine (5.0 μM), isoproterenol (5.0 μM), and catechol (10 μM). The reproducibility of this system was tested by 21 determinations. The injected amounts were estimated to be 0.45, 0.41, and 0.54 fmol, respectively. Fairly sharp peaks were found, but peaks with minute tailing for the cationic solutes (e.g., dopamine and isoproterenol) were also found in the electropherograms. The separation efficiencies, represented by the theoretical plate number N , were estimated to be about 70 000, 82 000, and 150 000, respectively. The RSDs ($n = 21$) of migration time were 3.5, 2.5, and 2.2%, respectively. A gradual increment in the migration time for the successive determinations of the three analytes was also found. This can be attributed to the gradual decrease of the electroosmotic flow, which is caused by the adsorption of cations at the inner wall of the capillary.^{28,30} The RSDs ($n = 21$) for peak current were found to be 5.1, 6.1, and 2.7%, respectively. The slight decrement of peak current may be due to fouling of the Pt disk electrode. Due to possible fouling on the electrode surface, Pt is not the customarily chosen material for the analysis of catecholamines. In this experiment, as the concentration of catecholamines used was small, fouling of the Pt disk electrode was found to be insignificant. The performance of the Pt disk electrode should be taken as normal and is compatible with that of the conventional carbon fiber electrode.

The effect of injection time on the sensitivity of the electrochemical cell assembly was studied. It was found that the peak current increased rapidly as the injection time increased from a very short period of time but leveled off when injection time was larger than 10 s; the peak width increased linearly with the increment of injection time. The larger the amount of solute injected, the higher the sensitivity and the poorer the resolution would be. As the migration rate of analyte in the capillary was enhanced by increasing the separation potential, the wall-jet effect on amperometric detection was also enhanced,³¹ and a larger peak current thus resulted. The linear relationship found from plots of the reciprocal of migration time versus the separation potential applied for the analytes studied agrees with theory very well. Although the analysis time can be shortened by applying a larger separation potential, the larger amount of Joule heat dissipated may offset this advantage.

The response and separation efficiency are affected by the gap distance between the disk electrode and the capillary outlet in the electrochemical cell. It is difficult to control or measure the gap distance, but an effective gap distance can be obtained by pushing the PTFE tubing in which the separation capillary was enclosed gently to the working electrode until a soft contact is attained. The optimal gap distance obtained for the electrode and the capillary is evidenced by the sharp and large peak current that results. It is found that when the gap distance is larger than the optimal value, decrement of the peak current, broadening of the peak width, and thus lowering of the $SE_{i,dl}^{(1)}(t)$ efficiency will result. If the gap distance set is too small, a back pressure in the

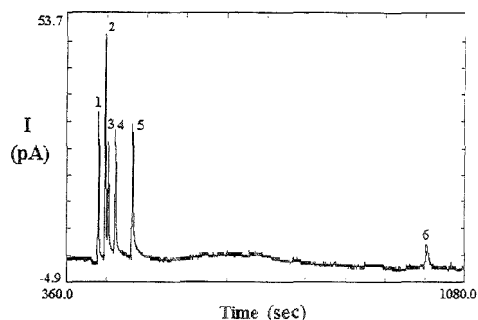


Figure 2. Electropherogram obtained for the separation of six different neurotransmitters. The concentrations used for (1) dopamine, (2) serotonin, (3) norepinephrine, and (4) epinephrine are 25 μM and for (5) isoproterenol and (6) catechol are 50 μM each. Conditions: separation capillary, 5 μm i.d., 44 cm length; separation potential, 25 kV; injection potential, 12 kV for 3 s; buffer, 30 mM MES, 20% (v/v) 2-propanol at pH 6.0.

capillary result and will subsequently induce the diminution or even the disappearance of peak current. Whenever the electrode and capillary outlet are too close, the effective gap distance can be attained by releasing the flanged fitting in a backward direction with an angle of about 5°. It is justified from the very good reproducibility obtained for alignment operation that an optimal contact between the disk electrode and the capillary outlet can be easily attained by following the assembly procedures described above.

With this electrode configuration, electrodes of smaller surface area and of different electrode material can be fabricated as long as thin wire materials are available with appropriate dimensions, i.e., instead of enclosing a piece of 50 μm diameter Pt wire with a segment of 75 μm i.d. capillary, Pt, Au wire, or carbon fiber with a diameter smaller than 25 or 10 μm can be enclosed and secured with a segment of capillary which has a specified inside diameter of 25 or 10 μm and 375 μm o.d. Although an advantage with respect to the enhancement of S/N ratio can be obtained by employing a smaller disk electrode, a problem inherent with the center alignment between the electrode surface and the capillary outlet is induced. The deterioration of electrode response due to off alignment may offset the advantage gained by using an electrode of smaller surface area. As long as the disk electrode surface is kept relatively larger than the capillary bore size, center alignment should not be a real problem. Fabrication of a smaller disk electrode may deserve further effort.

Applicability of this cell assembly is demonstrated by running a synthetic sample containing six different neurotransmitters. The neurotransmitters used in sample solution include 25 μM each of dopamine, serotonin, norepinephrine, and epinephrine and 50 μM each of isoproterenol and catechol. Figure 2 shows the electropherogram obtained by using a 5 μm i.d., 44 cm long capillary at a separation potential of 25 kV. The buffer solution used contains 30 mM MES and 20% (v/v) of 2-propanol and has its pH adjusted to 6.0. The electropherogram shown in Figure 2 is similar to that obtained by Ewing et al.¹³ Dopamine and serotonin are well resolved, but a rather small peak of catechol is also found. Tailings present in the peaks corresponding to the cationic solutes are also similar to those found when a 5 μm diameter carbon fiber microelectrode was employed.¹³ The much smaller peak of

(30) Townes, J. K.; Regnier, F. E. *Anal. Chem.* **1992**, *64*, 2473.

(31) Yamada, J.; Matsuda, H. *J. Electroanal. Chem.* **1973**, *44*, 189.

Table 1. Comparison of the Electrode Configuration and Detection Limits among Different End-Column and the Optimized End-Column Amperometric Detectors

	end-column ^a	end-column ^b	optimized end-column ^c
working electrode	Pt disk	carbon fiber	carbon fiber
electrode surface area (μm^2)	50 μm diam 2000	10 μm diam \times 200 μm 6400	11 μm diam \times 200 μm 7000
detection limit ^d for dopamine (amol)	2.0	64	18
apparent injection volume (pL)	133	>160	45
detection limit ^d for catechol (amol)	3.5	56	19
apparent injection volume (pL)	80	160	27

^a Data obtained from this work. ^b Data quoted or estimated from Ewing's results.²¹ Conditions: separation potential, 20 kV; injection, 20 kV for 5 s; electrochemical detection at 0.8 V; separation capillary, 5 μm i.d., 56.6 cm length; buffer, 20 mM MES at pH 6.0. ^c Data quoted or estimated from Ewing's results.²² Conditions: separation potential, 20 kV; injection, 10 kV for 10 s; electrochemical detection at 0.8 V; separation capillary, 2 μm i.d., 58 cm length; buffer, 25 mM MES at pH 5.65. ^d The detection limit obtained is based on S/N = 2 criterion.

catechol shown in Figure 2 is due to the effect of 2-propanol on the electroosmotic behavior of MES buffer solution. The addition of 2-propanol to the MES buffer solution results in a decrement of the electroosmotic flow in the capillary that influences favorably the separation of serotonin and dopamine in solution. The decrement of electroosmotic flow influences further the sensitivity of catechol in the studied solution. As catechol is an almost neutral molecule in the pH 6 buffer solution and the sample is injected by the electrokinetic method, the amount of catechol injected into the capillary is thus much smaller than the amount of other neurotransmitters in the sample solution. A much lower sensitivity for catechol thus results.

Standard calibration graphs based on the peak current for dopamine, isoproterenol, and catechol are plotted. With injection amounts ranging from 6.3 to 3500 amol (0.05–25 μM) for dopamine and isoproterenol and from 7.9 to 3400 amol (0.10–50 μM) for catechol, calibration graphs with linear correlation coefficients better than 0.999 are obtained. The detection limits based on the criterion of S/N = 3 are estimated to be 3.0 (23 nM), 3.6 (28 nM), and 5.2 amol (66 nM) for dopamine, isoproterenol, and catechol, respectively. Though it can be improved by proper optimization, no further effort has been made to pursue a lower detection limit. A comparison of the electrode configuration and the detection limit of the designed electrochemical cell assembly with those of carbon fiber end-column and the optimized end-column detector for the determination of the two neurotransmitters is shown in Table 1. From Table 1, the detection limit obtained from this work is about one order lower than that obtained from the optimized end-column detector and the carbon fiber end-column detector. The better performance of this work

may be attributed to the smaller electrode surface adopted in the electrochemical cell, which enhances the S/N ratio and the larger sample volume injected.

CONCLUSIONS

The primary advantage of this electrochemical cell assembly is its easier construction compared with other end-column electrochemical detectors, in which a micropositioner is needed.^{21–23} With the help of a piece of guide tubing, alignment between the capillary outlet and the working electrode can be achieved easily and reliably. The noise from mechanical vibrations and drafts is eliminated. With the proposed fabrication procedures, electrodes of various materials such as Au, Cu, Ni, or other metal wire and even carbon fiber, can be fabricated, thus extending the applicability of this cell assembly. The easy construction of this electrochemical cell assembly, the flexibility of adopting different electrode material, the high reproducibility inherent with the assembling processes, and the feasibility of reconditioning the disk electrode should make this electrochemical detector more acceptable to other CE researchers and the electrochemical detection method more useful for CE routine analysis.

ACKNOWLEDGMENT

The authors thank the National Science Council of the ROC for financial support of this work (Contract No. NSC 83-0421-M-110-025-Z).

Received for review May 2, 1995. Accepted August 18, 1995.*

AC950428U

* Abstract published in *Advance ACS Abstracts*, September 15, 1995.

Dewetting Effects on Polymer-Coated Surface Acoustic Wave Vapor Sensors

Jay W. Grate*[†]

Chemistry Division, Naval Research Laboratory, Washington, D.C. 20375-5000

R. Andrew McGill*

Geo-Centers, Inc., 10903 Indian Head Highway, Fort Washington, Maryland 20744

Thin polymer films on surface acoustic wave device surfaces sometimes dewet the surface, leading to isolated droplets of material and a degradation in sensor performance. Dewetting has been observed to lead to decreases in baseline operating frequencies and loss of oscillation in the worst cases. The influence of surface precleaning methods has been examined, and, in general, plasma cleaning was found to be the method of choice for the preparation of the device surface for polymer application. Plasma cleaning results in an increase in the surface free energy and improves polymer adhesion so that dewetting is disfavored.

For several years, we have been applying thin polymer films to surface acoustic wave (SAW) devices for use as vapor sensors.¹⁻⁷ (Reviews on SAW and other acoustic wave sensors can be found in refs 8-13.) Polymers are advantageous in this application because vapors are absorbed reversibly, chemical selectivity can be controlled by varying the polymer's chemical structure, and polymers usually form thin adherent films without difficulty. In our early empirical studies,^{1,6} some polymer-coated sensors were ill-behaved for reasons that were not obvious at the time, and such polymers were removed from consideration without further investigation. More recently, selection strategies for sorbent polymers have been developed on the basis of solubility properties.^{10,14} In some cases, however, polymers with

desirable solubility properties for vapor absorption did not yield well-behaved sensors. We have now found that well-behaved sensors can be prepared using previously troublesome polymers, provided that sufficient attention is given to factors influencing the wetting and adhesion at the interface between the polymer and sensor surface. Problems occur when the polymer films dewet the sensor surface. Dewetting leads to a number of observable effects on thin-film morphology and sensor frequency signals.

Wetting, spreading, and adhesion have been extensively studied and reviewed.¹⁵⁻²¹ Three parameters that influence spreading and adhesion are the surface free energy of the solid in contact with the vapor phase, the surface free energy of the polymer or liquid in contact with the vapor phase, and the interfacial free energy between the liquid or polymer and the solid, denoted by γ_s , γ_L , and γ_{SL} , respectively. A high solid surface energy, γ_s , is desirable since this favors both spreading and adhesion. Clean metal and metal oxide surfaces have high surface energies. A low interfacial energy, γ_{SL} , is also desirable, and this is promoted by favorable interactions between the solid and the film material (e.g., van der Waals interactions and hydrogen bonding). The liquid surface tension, γ_L , has opposing effects on spreading and adhesion. Therefore, in practice it should not be too large or too small.^{18,19}

Although wetting phenomena have been studied extensively for decades, the reverse process, "dewetting", has received little attention until recently.²²⁻²⁶ Dewetting involves changes in the shape of a thin film that reduce the area of the film/surface interface. Reiter has shown in studies of 5-60 nm thick polystyrene films at temperatures above the static glass-to-rubber transition temperature (T_g) that dewetting proceeds from the

[†] Present address: Environmental Molecular Sciences Laboratory, Pacific Northwest Laboratory, Battelle Boulevard, Richland, WA 99352.

(1) Ballantine, D. S.; Rose, S. L.; Grate, J. W.; Wohltjen, H. *Anal. Chem.* **1986**, *58*, 3058-3066.
(2) Grate, J. W.; Snow, A.; Ballantine, D. S.; Wohltjen, H.; Abraham, M. H.; McGill, R. A.; Sasson, P. *Anal. Chem.* **1988**, *60*, 869-875.
(3) Grate, J. W.; Klusty, M. *Anal. Chem.* **1991**, *63*, 1719-1727.
(4) Grate, J. W.; Klusty, M.; McGill, R. A.; Abraham, M. H.; Whiting, G.; Andonian-Haftvan, J. *Anal. Chem.* **1992**, *64*, 610-624.
(5) Grate, J. W.; Rose-Pehrsson, S. L.; Venezky, D. L.; Klusty, M.; Wohltjen, H. *Anal. Chem.* **1993**, *65*, 1868-1881.
(6) Rose-Pehrsson, S. L.; Grate, J. W.; Ballantine, D. S.; Jurs, P. C. *Anal. Chem.* **1988**, *60*, 2801-2811.
(7) Snow, A. W.; Sprague, L. G.; Soulen, R. L.; Grate, J. W.; Wohltjen, H. *J. Appl. Polym. Sci.* **1991**, *43*, 1659-1671.
(8) D'Amico, A.; Verona, E. *Sens. Actuators* **1989**, *17*, 55-66.
(9) Frye, G. C.; Martin, S. J. *Appl. Spectrosc. Rev.* **1991**, *26*, 73-149.
(10) Grate, J. W.; Abraham, M. H. *Sens. Actuators B* **1991**, *3*, 85-111.
(11) Nieuwenhuizen, M. S.; Venema, A. *Sens. Mater.* **1989**, *5*, 261-300.
(12) Grate, J. W.; Martin, S. J.; White, R. M. *Anal. Chem.* **1993**, *65*, 940A-948A.
(13) Grate, J. W.; Martin, S. J.; White, R. M. *Anal. Chem.* **1993**, *65*, 987A-996A.
(14) Grate, J. W.; McGill, R. A.; Abraham, M. H. *Proc. IEEE Ultrason. Symp.* **1992**, 275-279.

(15) Zisman, W. A. In *Contact Angle, Wettability and Adhesion*; Fowkes, R. M., Ed.; ACS Advances in Chemistry Series 43; American Chemical Society: Washington, DC, 1964; pp 1-51.
(16) Zisman, W. A. In *Adhesion and Cohesion*; Weiss, P. Ed.; Elsevier Publishing Co.: New York, 1962; pp 177-203.
(17) de Gennes, P. G. *Rev. Mod. Phys.* **1985**, *57*, 827-863.
(18) Gray, V. R. In *Aspects of Adhesion*; Alner, D. J., Ed.; University of London Press Ltd.: London, 1966; Vol. 2, pp 42-48.
(19) Gray, V. R. In *Aspects of Adhesion*; Alner, D. J., Ed.; University of London Press Ltd.: London, 1966; Vol. 3, pp 73-75.
(20) Lee, L. H. In *Adhesive Bonding*; Lee, L. H., Ed.; Plenum Press: New York, 1991; pp 1-30.
(21) Garret, H. E. In *Aspects of Adhesion*; Alner, D. J., Ed.; University of London Press Ltd.: London, 1966; Vol. 2, pp 19-41.
(22) Redon, C.; Wyart, B. C.; Rondelez, F. *Phys. Rev. Lett.* **1991**, *66*, 715-718.
(23) Reiter, G. *Langmuir* **1993**, *9*, 1344-1351.
(24) Shull, K. R.; Karis, T. F. *Langmuir* **1994**, *10*, 334-339.
(25) Wyart, F. B.; Dailiant, J. *Can. J. Phys.* **1990**, *68*, 1084-1088.
(26) Wyart, R. B.; Martin, P.; Redon, C. *Langmuir* **1993**, *9*, 3682-3690.

formation of pinhole defects in the thin film that increase in number and size with time.²³ Eventually, the polymer breaks up into isolated droplets on the surface.

We have observed that thin polymer films on sensor surfaces sometimes dewet the surface, leading to isolated droplets of material and a degradation in sensor performance. In this paper we present empirical results on polymers and sensor surfaces where dewetting has been observed and describe the effects of dewetting on sensor signals during fabrication and vapor exposures. We also describe a convenient surface cleaning method, plasma cleaning, that can alleviate these problems.

EXPERIMENTAL SECTION

Materials. A solid rubbery poly(isobutylene), a solid rubbery poly(epichlorohydrin), and poly(vinyl propionate) (as a solution in toluene) were obtained from Aldrich. A slowly pourable, viscous liquid poly(epichlorohydrin) resin was obtained from Monomer/Polymer and Dajac Laboratories, Inc. Methylphenyldiphenylsiloxane copolymer (45–55%), which we shall refer to as simply a poly[(phenylmethyl)siloxane], and poly[bis(cyanopropyl)siloxane] were obtained from Petrarch. Silar 10C, which is also a cyanopropyl-substituted polysiloxane, was obtained from Alltech. Solvents used to clean sensor devices were all HPLC grade.

SAW Devices, Electronics, and Vapor Testing. The 158 MHz SAW dual delay line devices, the individual 200 MHz SAW resonators, and the oscillators used were the same as those described in previous studies.^{2–4} The 158 MHz devices were used primarily for preliminary experiments on surface cleaning and characterization methods. Experiments on polymer coating and vapor testing were done using the 200 MHz SAW resonators unless otherwise specified, and only the polymer-coated sampling device was exposed to vapors during testing. In this paper, frequency changes during coating or vapor exposures will always be described in terms of the absolute frequency changes occurring on the individual polymer-coated sensor.

Spray-coated polymer films were applied using an airbrush supplied with compressed dry nitrogen and a dilute solution of the polymer in HPLC-grade chloroform (Aldrich), exactly as in previous studies.^{3,4,27} Spray-coated films were examined by optical microscopy with a Nikon Optiphot M microscope using reflected light Nomarski differential interference contrast. The films were examined immediately after being applied, before being exposed to vapors, and after exposure to a variety of organic vapors at ~15% of saturation at room temperature. The "standard" set of vapors included 2-propanol (17 500 mg/m³), 1-butanol (3770 mg/m³), nitromethane (16 500 mg/m³), 2-butanone (53 400 mg/m³), isooctane (45 000 mg/m³), toluene (21 200 mg/m³), dichloroethane (65 000 mg/m³), and water (3200 mg/m³). Vapor tests were conducted and data collected exactly as described in previous papers.^{3,4,27,28}

Plasma Cleaning Method. Prior to plasma cleaning, devices were rinsed with chloroform to remove gross contamination. They then were placed in a Harrick plasma cleaner. The chamber was evacuated until the pressure was low enough to sustain a plasma

(~100 mTorr), and the rf power was turned on.²⁹ The feed gas was admitted via a needle valve, and its flow was adjusted to produce the brightest plasma. We used dry nitrogen as the feed gas, but the plasma was initially an air plasma because we turned on the power as soon as the pressure was low enough to sustain a plasma, with no effort to purge the system first. Oxygen and air plasmas are more powerful cleaners than nitrogen plasmas because of their oxidizing power. Typical cleaning time was 15–20 min. It is probable that much shorter cleaning times would be sufficient, but this has not been systematically investigated.

Contact Angle Measurements. Advancing contact angles were determined using triply distilled water, with the last two distillations in an all-quartz still. A platinum wire, cleaned in a flame to produce a red tip, was used to transfer a drop of water to the test surface. Several determinations were made on each surface with a Rame-Hart contact angle goniometer, using water drops of varying sizes.

RESULTS AND DISCUSSION

Surface Cleaning and Characterization. The 158 MHz dual delay line SAW devices and the 200 MHz resonator SAW devices used in this study are fabricated with Al transducers and contact pads on ST-cut quartz substrates. The entire surface, except the contact pads, is covered with a thin layer of SiO₂.³⁰ It is this surface to which the polymer films must adhere. Typical cleaning solutions involving strong acids, bases, or oxidizers (e.g., chromic acid in H₂SO₄, mixtures of H₂SO₄ and H₂O₂, HF solution, ammonium fluoride, or alcoholic KOH)³¹ cannot be used on these devices because they consume the Al and/or SiO₂ layers. Therefore, we initially cleaned our surfaces by rinsing in organic solvents such as chloroform, acetone, and methanol.³²

Many polymers can be spray-coated onto the solvent-cleaned devices, and the resulting vapor sensors function in a normal fashion with a stable oscillation frequency. However, problems in certain cases prompted us to find a more effective cleaning method and to examine sensor surfaces more carefully. We found that nitrogen and air plasmas were quite effective for cleaning SAW sensor surfaces without damaging the devices themselves, and we first reported this approach in ref 4. We shall refer to these surfaces as plasma-cleaned to distinguish them from surfaces that are only solvent-cleaned.

Water contact angles on our 158 MHz devices were about 60° prior to cleaning and were only slightly reduced upon rinsing in chloroform. Plasma cleaning reduced water contact angles to 0–10°; in fact, these contact angles were difficult to measure because the water spread so well. After a week of storage of the devices in the laboratory, contact angles increased to ~30°, indicating that cleaned surfaces can be contaminated by adsorption of material from the air. Therefore, surfaces should preferably

(29) Our Harrick plasma cleaner was a 1974 model which we operated at power level 6. According to the manufacturer, this model corresponds to the current lower-powered model PDC-3XG (25–30 W) operated at a medium rf level setting.

(30) The SiO₂ layer is applied by a sputtering method to a thickness of ~45 nm. Horine, B., Sawtek, Orlando, FL. Personal communication.

(31) **Caution:** These aggressive cleaning solutions should be prepared and used only by knowledgeable individuals.

(32) Sonication in the organic solvent is potentially more effective, but we were discouraged from using this method because it sometimes caused the epoxy that bonds the 200 MHz devices to their headers to fail, leaving the device only loosely attached to the header by the wire bonds. Similar problems occurred with the 200 MHz devices during attempts to clean them with hot vapor and solvent in a Soxhlet extractor.

(27) Grate, J. W.; Wenzel, S. W.; White, R. M. *Anal. Chem.* **1991**, *63*, 1552–1561.

(28) Grate, J. W.; Klusty, M. Naval Research Laboratory Memorandum Report 6762; Naval Research Laboratory: Washington, DC, 1990.

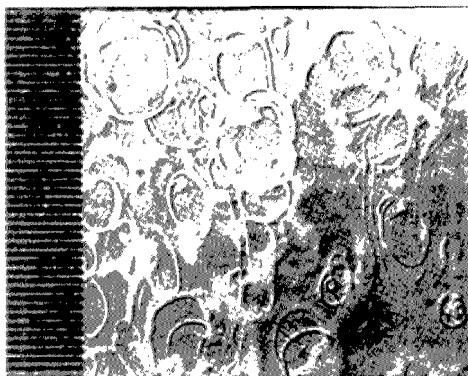


Figure 1. Image of a section of a plasma-cleaned 200 MHz SAW resonator to which poly(isobutylene) has been applied by spray coating, yielding a 267 kHz frequency shift. On the section of the sensor shown, the silica overlayer rests on top of an aluminum ground plane. The pattern of the aluminum on one edge of the image gives an indication of scale: each finger is $\sim 2 \mu\text{m}$ wide, as is the space in between fingers.

be cleaned just prior to the application of a thin film. The 200 MHz devices exhibited water contact angles of $90\text{--}95^\circ$ as received. Rinsing the as received 200 MHz devices in chloroform increased their operating frequencies by 1–2 kHz, indicating that a soluble contaminant was present. Nevertheless, solvent rinsing reduced the contact angle only slightly, to $\sim 75\text{--}85^\circ$. Plasma cleaning reduced the contact angle to $0\text{--}10^\circ$. On these narrow devices, the water spread across the entire width, and contact angles could only be estimated from the water edges that advance toward the ends. Contact angles of these plasma-cleaned surfaces were not significantly altered by rinsing with HPLC-grade organic solvents. The contact angle measurements clearly demonstrated that the plasma-cleaned surfaces differ significantly from solvent-cleaned surfaces in their wetting properties.

Dewetting Effects during Polymer Film Application. We normally select polymers whose T_g values are below the sensor operating temperature in order to obtain rapid vapor diffusion and reversible responses. Polymer materials can be applied by a variety of techniques, including spin casting, Langmuir–Blodgett (LB) film deposition (in selected cases), a spray-coating method using an airbrush. The latter method is particularly convenient because the acoustic device can be operated throughout the deposition process. The sensor's signal measures the amount of material applied, providing feedback for the control of the film thickness.

Normally, when a SAW device is spray-coated, the oscillator frequency decreases in response to the mass of material deposited on the surface. During pauses in the coating process, the frequency drifts upward slightly as solvent evaporates. The amount of frequency shift downward during spraying is proportional to the time spent spraying, and this proportionality is readily discerned. We typically apply polymer until the frequency decreases by ~ 250 kHz, for reasons discussed in previous papers.^{3,27} This corresponds to a film thickness of ~ 50 nm on a 200 MHz quartz SAW device if the material is evenly distributed.

Figures 1–3 provide examples of polymer morphologies on sensor surfaces. Figure 1 illustrates the morphology observed when poly(isobutylene) is applied to a plasma-cleaned surface by

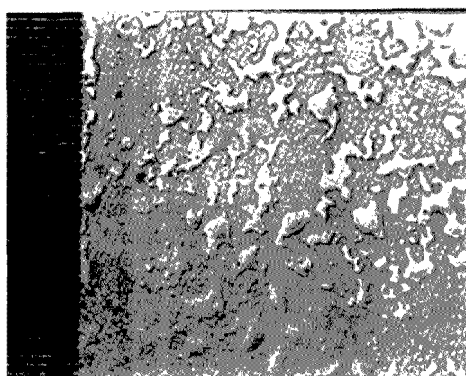


Figure 2. Image of a section of a plasma-cleaned 200 MHz SAW resonator to which Silar 10C, a poly[bis(cyanopropyl)siloxane], has been applied by spray coating, yielding a 270 kHz frequency shift.

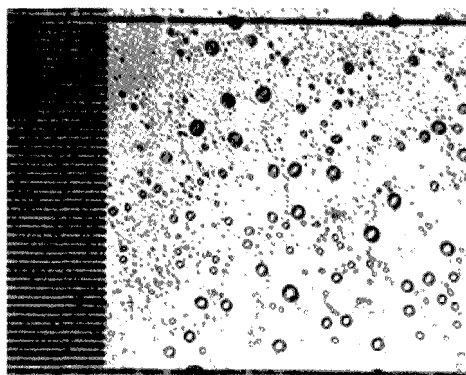


Figure 3. Image of a section of a solvent-cleaned 200 MHz SAW resonator to which Silar 10C has been applied by spray coating. This SAW resonator was placed next to the device in Figure 2 during spray coating, and therefore has a similar amount of polymer applied.

the spray-coating method. The polymer appears in small circular domains that are numerous and overlapping. This is a typical morphology for a polymer spray-coated to a thickness of ~ 250 kHz on clean surfaces. By contrast, Figure 3 illustrates a siloxane polymer that has a beaded appearance on a solvent-cleaned sensor surface. The polymer does not wet the surface. The same polymer is shown on a plasma-cleaned surface in Figure 2. In this case, the polymer is present in isolated domains but has not beaded into spheres.

When the polymer does not effectively wet the surface and beads into isolated droplets, as shown in Figure 3, two anomalous effects on sensor frequency are observed. First, the frequency drifts *downward* when spraying is interrupted, even though no more mass is being added. Normally, the frequency is shifted downward by the applied polymer and drifts slightly upward as solvent evaporates. Second, the amount of frequency shift observed for a given amount of spraying becomes less and less as the spraying process proceeds, as if the device is no longer fully sensing the material deposited. Indeed, in the worst cases, it is difficult to cause a 250 kHz decrease in frequency before the frequency becomes erratic or is quenched altogether, even though

subsequent examination under the microscope shows that a considerable amount of polymer is present.

These effects were particularly severe when poly[(phenylmethyl)- and poly[bis(cyanopropyl)siloxanes] were applied onto solvent-cleaned sensors. These polymers are viscous liquid and stiff greasy materials, respectively. On solvent-cleaned 200 MHz devices, we could not make functional vapor sensors from these polymers since oscillation became quite erratic before the device registered a 250 kHz frequency shift. Under the optical microscope, it was clear that the siloxanes had formed isolated round droplets of material on these surfaces (e.g., see Figure 3). When these two polysiloxanes were spray-coated onto plasma-cleaned devices, coating proceeded normally without the anomalous downward drift, and functional vapor sensors were obtained.

Before we investigated plasma-cleaned sensor surfaces, we made some preliminary efforts to alter the surfaces with silanizing reagents. Treatment of a solvent-cleaned device with hexamethyldisilazane vapors at room temperature overnight significantly influenced the subsequent coating process. (Hexamethyldisilazane converts surface hydroxyl groups to trimethylsiloxy groups.) Using poly[(phenylmethyl)siloxane] as the test polymer, the material could be applied in the normal fashion to the usual 250 kHz thickness. The frequency did drift downward after coating, but this phenomenon was significantly reduced relative to that observed with the solvent-cleaned devices. Another solvent-cleaned device was treated with a freshly prepared solution made by adding dichloromethylphenylsilane to methanol. In this case, coating proceeded normally (without downward drift). Although the efficiencies of the above silanization methods on the solvent-cleaned surfaces are uncertain, the results demonstrate that surface modification can influence the coating deposition process in difficult cases and that the behaviors we have described are related to the surface characteristics. Since these preliminary experiments, we have developed silanization procedures for SAW devices that block surface hydroxyls and improve polymer wetting.^{33,34}

A less severe example of dewetting behavior involved a poly-(epichlorohydrin) resin, a viscous liquid with physical characteristics similar to those of the siloxanes. It could be easily coated onto a solvent-cleaned device to a thickness of 300 kHz. Nevertheless, slight downward frequency drift observed after pauses in the coating process suggested that a dewetting problem might exist. Results consistent with this suspicion were obtained in subsequent vapor tests (see below). The application of this same resin to a plasma-cleaned device proceeded without anomalous frequency drift.

Additional evidence for improved film stability on plasma-cleaned surfaces can be seen by observing polymers on solvent- and plasma-cleaned surfaces at elevated temperatures. For example, poly(vinyl propionate) was solvent cast into continuous thin films on solvent-cleaned and plasma-cleaned 158 MHz devices. These were heated to 85 °C in a convection oven, and the film on the solvent-cleaned device broke up into isolated droplets within 15 min. However, the film on the plasma-cleaned device remained continuous, even after 24 h at the elevated temperature. Similar effects of surface cleaning have been observed on flexural plate

wave (FPW) devices.³⁵ After initial experiments where poly(vinyl propionate) dewet the FPW device surface, the device was cleaned with an H₂O₂/H₂SO₄ solution.³¹ The same polymer did not dewet this cleaned surface, even after repeated heating and cooling cycles.

Dewetting Effects during Vapor Exposures. We have observed that sensors exhibiting the anomalous effects noted above during film application sometimes cease to oscillate during exposures to organic vapors. This cannot be demonstrated in the severe cases where the sensor does not function at all, but it can be observed in "borderline" cases. For example, when a dichloromethylphenylsilane-treated sensor coated with poly[(phenylmethyl)siloxane] was exposed to vapors, it stopped oscillating. Reexposure to clean carrier gas restored oscillation, but the baseline was shifted to a lower frequency. This process was repeated many times with a variety of vapors (see Experimental Section). The shifts in baseline frequency after vapor exposures were in the same direction as the downward drift observed after the siloxanes were coated onto solvent-cleaned devices, where beading was observed. Oscillation difficulties and baseline frequency shifts were not a problem when this polymer was coated onto a plasma-cleaned sensor.

The sensor described above with poly(epichlorohydrin) resin deposited on a solvent-cleaned surface produced normal responses to most vapors at the test concentrations, but two (dichloroethane and butanone) caused it to stop oscillating. These problems did not occur when the same resin was tested on a plasma-cleaned sensor. [A solid poly(epichlorohydrin) polymer we have used in past studies coats normally and responds to vapors without loss of oscillation using either solvent- or plasma-cleaned devices.]

Discussion. To summarize, the following effects are associated with poor wetting and adhesion of the polymer: the material visibly beads into droplets (as observed under the optical microscope) after coating or after vapor exposures; the frequency drifts downward during pauses in spray coating and after stopping spray coating; spray-coated polymer may not produce consistent frequency decreases throughout the coating process, and in the worst cases, one may not be able to obtain a functional sensor because of loss of oscillation. Vapor exposures may quench the oscillation, and the baseline may be shifted after the vapor is removed. (The latter effect is observable in borderline cases.) Plasma cleaning sensor surfaces prior to film application can prevent these problems from arising; we have obtained well-behaved vapor sensors from a great variety of polymers by spray coating them onto plasma-cleaned 200 MHz SAW resonators. It is presumably the high surface energy of the plasma-cleaned device that favors wetting, although it is also likely that different polymer/surface interfacial free energies result when polymers are applied to plasma-cleaned versus solvent-cleaned surfaces.³⁶

In our experience, these effects are more likely to be observed if the polymer is a viscous liquid than if it is a solid rubber and more likely to be seen after vapor exposures than without such exposures. Presumably, lower viscosity facilitates more rapid dewetting. The physical appearance of the coated material may change with time and/or vapor exposures, depending on the viscosity and wetting properties of the polymer. Beading is observed if the polymer dewets the surface, but in other cases,

(33) McGill, R. A.; Grate, J. W.; Anderson, M. R. In *Interfacial Design and Chemical Sensing*; Mallouk, T. E.; Harrison, D. J., Eds.; ACS Symposium Series 561; American Chemical Society: Washington, DC, 1994; pp 280-294.

(34) McGill, R. A.; Grate, J. W. manuscript in preparation.

(35) Grate, J. W.; Wenzel, S. W.; White, R. M. *Anal. Chem.* 1992, 64, 413-423.

(36) One reviewer noted that plasma cleaning with Harrick plasma cleaners can change surface roughness and that this might also influence wetting properties.

sharper features of the overlapping circle morphology (Figure 1) soften, and in some cases polymer domains spread. The latter observation indicates that the surface forces favor wetting rather than dewetting, and a stable film and well-behaved sensor can be expected.

When dewetting occurs, it indicates that the coated polymer film was not in a thermodynamically stable state. Reiter²³ investigated continuous thin polymer films where dewetting was initiated by the formation of cylindrical holes whose diameters increase with time. Our sprayed-on films are not necessarily continuous and may have holes from which dewetting may proceed. Nevertheless, Reiter's studies showed that dewetting of thin films can occur regardless of whether the film has defects to begin with or not, and our own experiments with an apparently continuous thin film of poly(vinyl propionate) confirm this. Therefore, applying a polymer film by a method that gives a continuous thin film will not necessarily prevent dewetting. In this regard, the initial film morphology is probably less important than the balance of forces that determine its equilibrium morphology.

Further, we believe that it is the wetting and adhesion of the polymer on the surface, rather than simply the shape of the deposited polymer domains, that influence sensor performance. In previous studies, poly(vinyltetradecanal)-coated SAW sensors prepared with continuous thin films applied by the LB method were compared with films applied by the spray-coating method, yielding the overlapping circle morphology described above (Figure 1), and these responded similarly to organic vapors.³

The possibility of dewetting has a number of consequences for polymer-coated SAW sensor development. The SAW devices we used are purchased and used in many other laboratories, and it is common practice for polymer films to be applied and used with no microscopic observations of film morphology or behavior. The possibility that unobserved polymer dewetting processes may

influence sensor behavior could lead to irreproducible results or erroneous interpretations and conclusions. It has also been our observation that dewetting problems have become more common as our research has progressed to higher frequency SAW devices with thinner films.³ Since this is the general direction for SAW sensor development, attention to polymer film wetting and adhesion is likely to become increasingly important.

We wish to emphasize that physically adherent films with long lifetimes can be easily made provided attention is paid to the cleaning and surface preparation of the sensor prior to coating. In previous studies, we have described polymer-coated SAW vapor sensors that were repeatedly exposed to vapors over periods of months.^{2,5} In our experimental work, we routinely place a fluoropolyol-coated 158 MHz dual delay line SAW sensor in series after our test sensors whenever we test new sensors with our vapor generation system.^{3,27,28} The responses of this control sensor are used to confirm that the system is generating vapor properly. We have used the same sensor in this application for ~5 years and countless vapor exposures with consistent performance and no problems with polymer dewetting.

ACKNOWLEDGMENT

We acknowledge Mark Klusty for careful observations during several of the initial experiments that led to this study; William R. Barger and Arthur Snow for helpful discussions on wetting, adhesion, and surface characterization; and Richard Colton for suggesting the plasma-cleaning method and providing the apparatus. This work was supported by the Office of Naval Technology/Naval Surface Warfare Center, Dahlgren, VA.

Received for review March 15, 1995. Accepted August 9, 1995.*

AC950262X

* Abstract published in *Advance ACS Abstracts*, September 15, 1995.

An Improved Method for the Construction of Ultramicroelectrodes

P. Tschuncky and J. Heinze*

Institut für Physikalische Chemie, Universität Freiburg, Albertstrasse 21, 79104 Freiburg, Germany

In this paper different techniques to decrease stray capacitance effects on fast-scan cyclic voltammetry with ultramicroelectrodes are discussed. The use of new methods of connecting the electrode microwire and the development of effective shieldings for the electrode resulted in a drop of a factor of 5 in the capacitive currents obtained in a standard electrolyte solution. Furthermore, a new method for constructing ultramicroelectrodes has been developed, which is almost 100% effective in suppressing stray capacitance. Electrodes down to radii of 1 μm have been constructed. The electrodes have been used to determine the rate constant of heterogeneous electron transfer for the reduction of anthracene. The results clearly demonstrate that the proposed methods are effective for the decrease the stray capacitance and easy to perform.

Interest in ultramicroelectrodes is largely due to their unusual mass transport properties at low scan rates and the small currents measured.¹

The latter feature enabled a series of new, transient electrochemical techniques such as fast-scan voltammetry and potential step methods. The iR drop problem can be widely avoided, even at very high scan rates up to the megavolt per second range, when sufficiently small electrodes are used.²⁻¹⁴

Nevertheless, only a few groups have published papers on this special topic. The reason for this is the difficulty of constructing the potentiostat and electrode.¹⁵⁻¹⁷

Generally, all experiments performed under fast-scan conditions suffer from the problem that faradaic currents rise proportionally to $v^{1/2}$, while capacitive currents change directly proportional to the scan rate v . Unexpectedly, the capacitive current normalized for the electrode area also increases with decreasing electrode radii.

It is the so-called stray capacitance that is responsible for this effect. This capacitance is caused by the counter and reference electrodes, on the one hand, and the working electrode, on the other hand.

Normally, at very high scan rates the faradaic peak-shaped signal is predominated by a huge, mainly capacitive background signal. Under these conditions, the evaluation of cyclic voltammograms becomes difficult.

For this reason, often very high concentrations of the electroactive species are used.²

However, an increase in concentration involves disadvantages. On the one hand, the current measured at the electrode tip increases and therefore iR distortions develop. On the other hand, the reaction rates of second- and higher-order reactions increase, and thus the determination of kinetic parameters becomes more and more difficult.

In order to work with small concentrations and fast scan rates at the same time, tricks such as shielding the ultramicroelectrodes have to be used.

EXPERIMENTAL SECTION

Electrodes. Much has been written on the problem of how one connects an ultramicroelectrode, and the latest developments concern the use of shieldings¹⁸⁻²³ which enable one to decrease the stray capacitance.²⁴ But the proposed methods for the construction of shielded electrodes are often very complicated.

Usually, ultramicroelectrodes consist of a hookup wire to connect the working electrode to the potentiostat, which itself is connected to a microwire with the help of silver epoxy. The microwire is sealed into soft glass (Figure 1a).

(1) Heinze, J. *Angew. Chem., Int. Ed. Engl.* 1993, 32, 1268.
(2) Wipf, D. O.; Wightman, R. M. *Anal. Chem.* 1988, 60, 2460.
(3) Andrieux, C.; Hapiot, P.; Savéant, J. M. *J. Phys. Chem.* 1988, 92, 5987-5992.
(4) Amatore, C.; Jutand, A.; Pflüger, F. J. *Electroanal. Chem.* 1991, 305, 153-162.
(5) Larumbe, D.; Gallardo, I.; Andrieux, C. P. *J. Electroanal. Chem.* 1991, 304, 211-247.
(6) Hapiot, P.; Pinson, J.; Francesch, C.; Mhamoli, F.; Rolando, C.; Schneider, S. *J. Electroanal. Chem.* 1992, 328, 327-331.
(7) Andrieux, C. P.; Audebert, P.; Hapiot, P.; Savéant, J. M. *J. Am. Chem. Soc.* 1990, 112, 2439-2440.
(8) Anne, A.; Hapiot, P.; Moiroux, J.; Savéant, J. M. *J. Electroanal. Chem.* 1992, 331, 959-970.
(9) Yang, H.; Fletcher, D. J. *Electroanal. Chem.* 1986, 331, 913-924.
(10) Yang, H.; Bard, A. J. *J. Electroanal. Chem.* 1991, 306, 87-109.
(11) Yang, H.; Wipf, D. O.; Bard, A. J. *J. Electroanal. Chem.* 1992, 331, 913-924.
(12) Montenegro, M. I.; Fletcher, D. J. *Electroanal. Chem.* 1986, 200, 371-374.
(13) Wipf, D. O.; Michael, A. C.; Wightman, R. M. *J. Electroanal. Chem.* 1989, 269, 15-25.
(14) Amatore, C.; Lefrou, C.; Pflüger, F. J. *Electroanal. Chem.* 1989, 270, 43-59.
(15) Garreau, D.; Hapiot, P.; Savéant, J. M. *J. Electroanal. Chem.* 1989, 272, 116.

(16) Amatore, C.; Lefrou, C. J. *Electroanal. Chem.* 1989, 324, 33-58.
(17) Howell, J. O.; Kuhr, W.-G.; Ensmann, R. E.; Wightman, R. M. *Electroanal. Chem.* 1986, 209, 77-90.
(18) Bond, A. M.; Fleischmann, M.; Robinson, J. J. *Electroanal. Chem.* 1984, 168, 299-312.
(19) Besenhard, J. O.; Schulte, A.; Jannakoudakis, P. D.; Heinze, J.; Tschuncky, P. *Tagungsband DEHEMA Symp. Mikroelektrochemie*, Friedrichroda, 1992.
(20) Dayton, M. A.; Brown, J. C.; Stutts, K. J.; Wightman, R. M. *Anal. Chem.* 1980, 52, 946.
(21) Baer, C. D.; Stone, N. J.; Sweigart, D. A. *Anal. Chem.* 1988, 60, 188.
(22) Suarez Fernandez, A. L.; Garcia Calzón, J. A.; Garcia, A. C.; Blanco, P. T. *Electroanalysis* 1991, 3, 413-417.
(23) Nemura, S.; Nozaki, K.; Okazaki, S. *Anal. Chem.* 1991, 63, 2665-2668.
(24) Wightman, R. M. *J. Electroanal. Chem.* 1989, 269, 15-25.

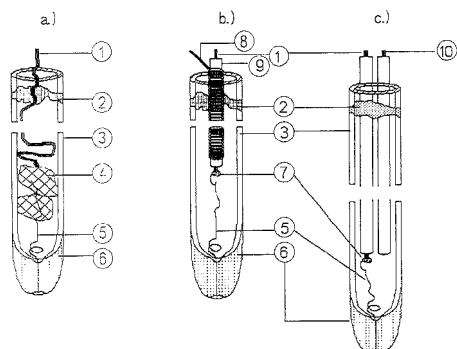


Figure 1. (a.) Conventionally constructed ultramicroelectrode; (b) improved shielded ultramicroelectrode; (c) new ultramicroelectrode for measurements in absence of stray capacitance: (1) electrical connection to working electrode, (2) adhesive, (3) soft glass tube, (4) conductive adhesive, (5) microwire, (6) fusion, (7) solder, (8) electrical connection to shielding, (9) insulation (PVC), and (10) capacity tip.

For electrodes constructed with pure metal microwires, commercially available down to radii of $2.5\ \mu\text{m}$, we suggest a facilitated method that produces an electrode as displayed in Figure 1b. The hookup wire is a coaxial cable. The shielding is connected to the virtual ground of the potentiostat. The hookup wire is connected to the microwire using a very small amount of solder instead of silver epoxy, in order to prevent the formation of big surfaces of nonshielded, conductive material inside the electrode, which is responsible for stray capacitance.

The glass tube is a soft glass (Wertheimer Geräteglas) with a transformation temperature of $650\ ^\circ\text{C}$. The tube has a diameter of $\sim 2\ \text{mm}$ at the point of sealing.

The hookup wire is passed through the glass capillary until the end stands out from the capillary. Then it is soldered to the microwire. The two wires are pulled back inside the glass tube. The hookup wire is fixed in the upper part of the glass tube using a two-component epoxy adhesive. A space of $\sim 1\ \text{cm}$ should be left between the end of the capillary (heated to $>650\ ^\circ\text{C}$) and the solder (melting point $\sim 350\ ^\circ\text{C}$).

During sealing at a temperature of $\sim 700\ ^\circ\text{C}$, no vacuum is necessary. Afterward the electrodes are carefully polished, using first emery paper, then diamond paste and, finally cerium oxide.

A completely new variant of electrode construction is outlined in Figure 1c. For this purpose, a nonshielded $5\ \mu\text{m}$ diameter gold electrode is constructed following the procedure described above. In the glass tube there is also a second wire, identical to the hookup wire, which has no microwire attached to it and hence no connection to the solution. This wire is placed parallel to the microelectrode hookup wire and will be called the capacitance tip in the further discussion. A special current follower allows one to measure and subtract the signal at the microelectrode hookup wire (1) and the response of the capacity tip (10) simultaneously. A pure capacitive signal is measured at the capacity tip (10) and displays the stray capacitance, which is a capacitance of the working electrode versus the reference and counter electrodes. The electrolyte solution, the glass capillary, and the cell environment act as a dielectric medium.

The voltammograms obtained show the faradaic signal and the difference of the capacitive currents measured at the microelec-

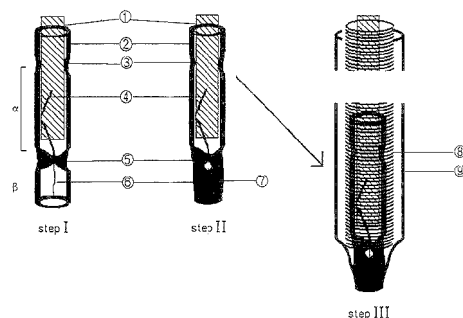


Figure 2. Construction of shielded UME obtained via Wollaston wires: (1) hookup wire, (2) inner glass tube, (3) sealing A, (4) Wollaston wire, (5) sealing B, (6) etched microwire, (7) sealing C, (8) shielding, and (9) outer glass tube.

trode hookup wire and capacity tip and, therefore, will be named subtractive scan voltammograms.

For electrodes built from Wollaston wires, we developed a new construction method following Figure 2.

In a first step I, the hookup and Wollaston wires are inserted into a soft glass tube of $\sim 3\ \text{cm}$ in length and a diameter that is slightly bigger than the whole arrangement. The two wires have a regime α where they are attached to one another without being really fixed by silver epoxy or solder. The hookup wire is fixed in this arrangement with a tight sealing (3), which can easily be done with a bunsen flame. A second sealing (5) fixes the Wollaston wire in its position.

The result is now a regime α in which the two wires are attached to each other and fixed with the help of two sealings 3 and 5, and a second regime β , in which a small piece of the Wollaston wire can be exposed to nitric acid in order to obtain the etched microwire. In step II, the etching procedure is performed with 30% HNO_3 within a few minutes. Afterward, regime β is rinsed with distilled water and then with acetone to remove impurities. At the end of step B, the microwire in regime β is sealed into the soft glass. The advantage of this method is that now a *pure metal* microwire can be sealed and no difficulties arise from movement of the *bimetallic* Wollaston wire.

A nonshielded electrode has now been constructed and is ready for measurements. However, to obtain a shielded UME, a step III is necessary. The electrode is surrounded by a shielding and sealed in a second soft glass tube.

The electrodes produced were carefully checked using scanning electron microscopy (Figure 3). The sealings of the electrodes were perfect, without any holes or air bubbles. Finally, with the help of voltammetric experiments at slow scan rates ($100\ \text{mV/s}$), the nominal diameters of the electrodes were checked. The curves obtained in these experiments are sigmoidal shaped with a limiting current proportional to the concentration of the couple and the radius of the electrode.

$$i_d = nFrcD \quad (1)$$

where n is the number of electrons transferred, F is the Faraday constant, r is the radius of the electrode, and D is the diffusion constant.

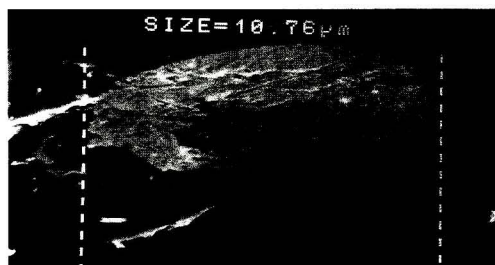


Figure 3. Electron micrograph of a 10 μm diameter Pt ultramicro-electrode.

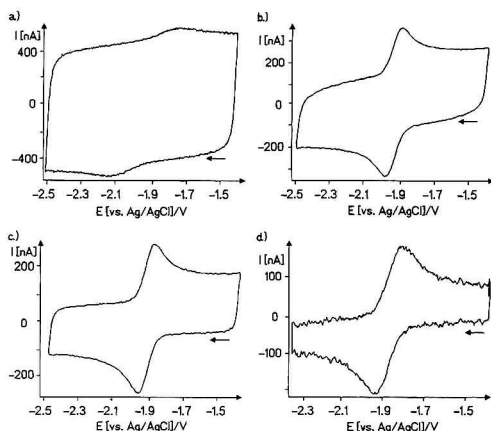


Figure 4. Cyclic voltammograms for the reduction of anthracene, $v = 20\,000\text{ V/s}$, ACN, $25\text{ }^\circ\text{C}$, 0.4 M TBAPF_6 , $c = 5 \times 10^{-3}\text{ mol/L}$, Au $r = 2.5\text{ mm}$: (a) conventionally constructed, (b) connection with solder, (c) shielded, solder connection, and (d) subtractive scan method.

Reagents and Solvents. All experiments were carried out under superdry solvent conditions. Acetonitrile (HPLC grade) was slowly passed through a column packed with basic Al_2O_3 (ICN Super D). The column was cooled to $0\text{ }^\circ\text{C}$. Afterward, the solvent was distilled from CaH_2 . All operations were performed under an Ar inert gas atmosphere.

Unless otherwise stated, all experiments were carried out at room temperature. As supporting electrolyte, 0.4 M tetrabutylammonium hexafluorophosphate [$\text{CH}_3(\text{CH}_2)_3\text{N}^+\text{PF}_6^-$] was used.

Electrochemical Cell. The electrochemical cell provided the possibility of passing the solvent/electrolyte system through thermally activated Al_2O_3 (heating for 30 min at $300\text{ }^\circ\text{C}$). As pseudoreference, a Ag wire was placed in a luggin capillary next to the working electrode. Calibration was performed via the ferrocene/ferrocenium couple. A Pt net electrode served as counter electrode.

Instrumentation. The potentiostat used was home-made, following the concept suggested by Amatore.¹⁴ The data were recorded using a 16 bit 10 MHz transient recorder (Krenz TDSO 3040). A Hewlett-Packard Model 3314a function generator was used. All measurements were carried out in a Faraday cage. The shielding of the electrodes as well as the Faraday cage was connected to the virtual ground of the potentiostat.

Table 1. Experimental Capacities

electrode diameter (μm)	C_{Exp} (pF)	C_{Norm} (F/m^2)
200 ^a	3038	0.097
25 ^a	40.98	0.083
25 ^b	38.33	0.078
10 ^a	12.23	0.157
10 ^b	7.64	0.097
5 ^a	6.25	0.32
5 ^b	4.29	0.22
5 ^c	20.0	1.0
5 ^d	2.25	0.11
2 ^e	9.2	2.93
2 ^f	0.71	0.23

^a Solder connected, shielding not connected. ^b Solder connected, shielding connected to ground (Figure 1b). ^c Conventionally constructed (Figure 1a). ^d Subtractive scan, electrode following Figure 1c. ^e Following Figure 2, shielding not connected. ^f Following Figure 2, shielding connected to ground.

RESULTS AND DISCUSSION

The success of our new construction techniques can be seen in Figure 4. The four voltammograms presented were measured under the same experimental conditions at a scan rate of $20\,000\text{ V/s}$ and with four different types of electrodes. The measurements are highly reproducible for a huge variety of electrodes.

Voltammogram a was recorded with a conventionally constructed electrode. Curve b shows the same experiment performed with an unshielded electrode, while the main hookup wire was connected to the microwire with solder. In Figure 4c, a shielded electrode was used. A further drop of the capacitive current can be achieved using our new subtractive scan method (Figure 4d). The capacitive current measured in this experiment was only 65% of what is published by other groups for the same experiment.²⁵

The capacity values determined from measurements at different electrodes are listed in Table 1 and were calculated according to

$$i_c = vC_D \quad (2)$$

where the i_c capacitive current is normalized for electrode area.

The values differ strongly, depending on the construction of the electrode used in the experiment.

The influence of stray capacitance increases with decreasing electrode radii. The shielding of the small electrodes (2 and $5\text{ }\mu\text{m}$) leads to a good value of 0.23 F/m^2 for both electrodes. This means that the effectivity of the shielding is the same in both cases.

The capacitance measured with our subtractive scan method is nearly equal to the pure double-layer capacitance, which has a value of 0.1 F/m^2 .^{26,27} Surprisingly low values are obtained for the microelectrodes with diameters of 10 and $25\text{ }\mu\text{m}$.

With this equipment, ultrafast voltammetry could also be performed. Figure 5 shows a voltammogram obtained at a scan rate of $200\,000\text{ V/s}$ for the shielded $2\text{ }\mu\text{m}$ diameter Pt electrode and a subtractive scan CV obtained at a $5\text{ }\mu\text{m}$ diameter Au electrode at a scan rate of 1 MV/s .

(25) Andrieux, C. P.; Hapiot, P.; Saveant, J.-M. *Chem. Rev.* **1990**, *90*, 723–738.

(26) Howell, J. O.; Wightman, R. M. *Anal. Chem.* **1984**, *56*, 524–529.

(27) Nicholson, R. S. *Anal. Chem.* **1965**, *37*, 1351.

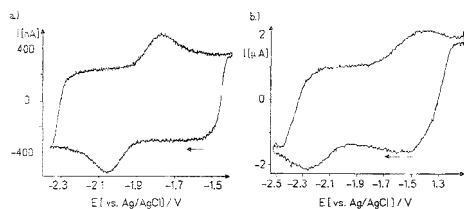


Figure 5. Cyclic voltammogram for the reduction of anthracene, ACN, 25 °C, 0.4 M TBAPF₆: (a) $v = 120\,000$ V/s, Pt $r = 1\ \mu\text{m}$, $c = 6 \times 10^{-3}$ mol/L; (b) $v = 1\,000\,000$ V/s, Au $r = 2.5\ \mu\text{m}$, $c = 5 \times 10^{-3}$ mol/L;

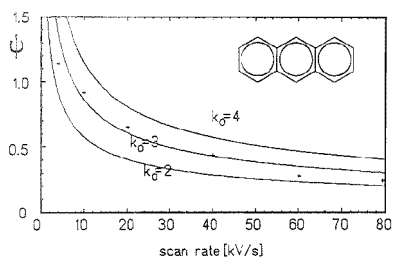


Figure 6. Plot of dimensionless kinetic parameter ψ vs scan rate v : solid lines, calculated values; crosses, experimental values.

As an example of the use of the electrodes to evaluate kinetic parameters, the rate constant of the heterogeneous electron transfer k_0 for the reduction of anthracene was determined. Although that value has already been determined by other

groups,²⁵ we decided to measure the same couple with lower concentrations, because with our new electrode the total currents measured were apparently smaller than the values in other publications, which might considerably reduce iR distortions. No positive feedback compensation, which often makes it difficult to correctly determinate the k_0 value, was necessary.

The value of k_0 was determined from the peak separation ΔE_p , using the dimensionless kinetic parameter ψ as suggested by Nicholson.²⁷

$$\psi = \frac{(D_{\text{Ox}}/D_{\text{Red}})^{a/2} k_0}{[D_{\text{Ox}} \pi v (nF/RT)]^{1/2}} \quad (3)$$

The results are summarized in Figure 6. The solid lines indicate the calculated values of ψ for $k_0 = 2, 3,$ and 4 m/s. The crosses mark the experimental values obtained with a shielded Au electrode of $5\ \mu\text{m}$ diameter. The heterogeneous rate constant was determined to be 3 m/s, which is in excellent agreement with values reported elsewhere.¹¹

ACKNOWLEDGMENT

We thank the Deutsche Forschungsgemeinschaft for financial support and Prof. C. Amatore for his advice on the construction of the potentiostat.

Received for review February 20, 1995. Accepted August 7, 1995.[®]

AC950183L

[®] Abstract published in *Advance ACS Abstracts*, September 15, 1995.

Channel Flow Cell for Attenuated Total Reflection Fourier Transform Infrared Spectroelectrochemistry

Rachael Barbour, Zhenghao Wang, In Tae Bae, Yuriy V. Tolmachev, and Daniel A. Scherson*

Department of Chemistry, Case Western Reserve University, Cleveland, Ohio 44106-7078

A channel-type spectroelectrochemical cell is described for the acquisition of potential difference (PD) attenuated total reflection Fourier transform infrared (ATR-FT-IR) spectroscopy of solution phase species generated at an electrode surface under conditions of well-defined laminar flow. The capabilities of the cell have been assessed using the reduction of bisulfite (2 M) in a weakly acidic (pH = 5.25), unbuffered, aqueous electrolyte as a model system. The PD ATR-FT-IR spectrum obtained at -0.85 V vs SCE, a potential negative enough for the reduction of HSO_3^- to proceed, compared to the spectrum recorded at a potential at which no reaction occurs (0.0 V vs SCE) as a reference, was dominated by negative- and positive-pointing contributions due to the reactant, bisulfite, and the predominant product, dithionite, respectively. Also identified in the spectrum was sulfite, which is produced by the dissociation of bisulfite induced by the increase in the pH of the medium during the reduction reaction. Theoretical aspects regarding the quantitative analysis of these data are briefly discussed.

Considerable progress has been made in this laboratory toward the development of in situ optical spectroscopic techniques in the presence of convective flow.¹⁻⁴ Attention has been centered on the coupling of UV-vis spectroscopy with rotating disk (RDE)¹⁻³ and channel-type (CE) electrodes⁴ to monitor the integrated concentration profile of solution phase species. In the first case, a beam of light is reflected off the surface of the RDE at near normal incidence, whereas for the CE, the spectrum is collected in the transmission mode through the solution past the electrode surface. More recently, UV-vis spectroscopy was employed to map the flow in a CE cell.⁵ The results of the latter investigation showed that, under steady state, diffusion-limited conditions, the absorbance measured along an axis normal to the electrode surface (y), at a fixed distance from the electrode downstream edge (x_2), denoted as $A_y(x_2)$, is invariant across the width of the electrode along the full length of the channel. In addition, it was found that $A_y(x_2)$ as a function of x_2 matches the theoretical predictions of the standard formalism,⁶ without the introduction of any adjustable parameters. Prompted by the close-to-ideal flow

pattern developed within this CE arrangement, the same cell used for the UV-vis experiments was modified to probe the solution past the electrode surface with attenuated total reflection (ATR) Fourier transform infrared (FT-IR) spectroscopy. This approach makes it, in principle, possible to take advantage of the high specificity of IR spectroscopy for the identification of solution phase products, and possibly relatively stable intermediates, formed at electrode surfaces as a function of the applied potential and other operating conditions.

This note describes the cell employed in these infrared studies and provides the first illustration of the use of ATR-FT-IR for the detection and identification of solution phase products of an electrochemical reaction under well-defined conditions of laminar flow.

EXPERIMENTAL SECTION

Spectroelectrochemical Channel Cell. The CE-type cell designed for in situ UV-vis spectroscopic measurements and described in an earlier paper⁵ (width, $a = 0.9$ cm; height, $2h = 0.11$ cm) was modified to accept a parallelepiped-type ZnSe internal reflection element (IRE, $50 \times 20 \times 3$ mm, 45° , International Crystal), placed adjacent to, and forming a common plane with, the Au working electrode (WE, length, $l = 0.5$ cm; width, $w = 0.6$ cm) cast in Kel-F (see lower section of Figure 1). As indicated in the figure, the long axis of the IRE was aligned normal to the direction of fluid flow. Contributions to the IR signal originating from sections of the channel outside the area defined by the electrode width downstream from the electrode edge (and, therefore, unaffected by the electrochemical reactions) were eliminated by sputtering a thick gold layer onto the large face of the prism (see Figure 1). The back side of the IRE was also coated with a thick layer of gold to avoid other artifactual effects. A saturated calomel electrode (SCE) and a gold piece cast in Kel-F placed downstream from the Kel-F-cast Au WE on the opposite side of the channel were used as reference and counter electrodes, respectively (see upper section of Figure 1).

Instrumentation. All FT-IR spectra were acquired in an IBM IR-98 equipped with a liquid nitrogen-cooled MCT detector at 4 cm^{-1} resolution (zero-filling factor, 2) with the cell mounted on a custom-made reflection absorption attachment. The potential of the electrode was controlled with a PAR Model 173 potentiostat and a PAR Model 175 Universal programmer. The pumping system employed in these studies was the same as that reported elsewhere.^{4,5}

(1) Zhao, M.; Scherson, D. A. *Anal. Chem.* 1992, 64, 3064.

(2) Zhao, M.; Scherson, D. A. *J. Electrochem. Soc.* 1993, 140, 1671.

(3) Zhao, M.; Scherson, D. A. *J. Electrochem. Soc.* 1993, 140, 2877.

(4) Wang, Z.; Zhao, M.; Scherson, D. A. *Anal. Chem.* 1994, 66, 4550.

(5) Wang, Z.; Scherson, D. A. *J. Electrochem. Soc.*, submitted.

(6) (a) Albery, W. J.; Coles, B. A.; Couper, A. M. *J. Electroanal. Chem.* 1975, 65, 901. (b) Coles, B. A.; Compton, R. G. *J. Electroanal. Chem.* 1983, 144, 87.

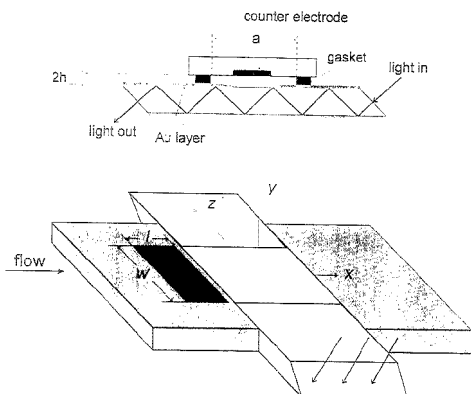


Figure 1. Schematic diagram of a channel-type spectroelectrochemical cell for ATR-FT-IR measurements of solution phase electrogenerated species under well-defined conditions of laminar flow (lower figure). For the sake of clarity, some of the cell components have been omitted. l and w are the length and width of the electrode, respectively. A partial view of the cell along the direction of fluid flow is shown in the upper figure, where $2h$ is the full height of the channel cell. The darker area in the center of the component directly above the gasket represents the counter electrode cast in Kel-F.

Electrochemical Standardization of the Spectroelectrochemical CE-Type Cell. After assembly, and prior to the spectroelectrochemical experiments, the proper operation of the CE-type cell was tested with a 10 mM $\text{Fe}(\text{NH}_4)_2\text{SO}_4$ solution in 0.1 M H_2SO_4 . A plot of the diffusion limited current vs $V^{1/2}$, where V is the flow rate (in mL/s), was linear in the range $0.07 < V < 2.0$ mL/s (slope, $S = 0.73 \pm 0.02$ mA/(mL) $^{1/2}$; intercept, 0.007; correlation, $R = 0.9993$). The magnitude of S was found to be in excellent agreement with that calculated on the basis of the dimensions of the channel and the electrode (see above) and the diffusion coefficient of the ferrous species evaluated from independent rotating disk measurements (5.3×10^{-6} cm 2 /s), i.e., $S = 0.71$ mA/(mL) $^{1/2}$.

ATR-FT-IR Spectroelectrochemical Arrangement. After thorough rinsing, the cell was mounted on the reflection absorption attachment and placed in the sample compartment (SC) of the spectrometer. Two openings on the lid of the SC were used to house the inlet and outlet solution feedthroughs to the cell. During spectral acquisition, the SC was purged with nitrogen to minimize spectral contributions due to water vapor and carbon dioxide.

In Situ ATR-FT-IR Measurements under Forced Convection. Possible spectral artifacts derived from the continuous flow of liquid through the cell were examined by ratioing two sets of 100 coadded scans obtained in sequence using a 0.22 M bisulfite solution in an aqueous phosphate buffer. The results obtained revealed no differences between ratioed spectra recorded under forced convection and stagnant conditions, indicating that the operation of the pump does not affect to any significant extent the spectral quality. Following these measurements, the solution reservoir, including the cell, was filled with a 2 M NaHSO_3 solution (Fisher, ACS analyzed) prepared with ultrapure water obtained from a modified Gilmont distillation system and adjusted to pH = 5.25 with concentrated NaOH. Spectra were recorded with the electrode polarized at a potential $E_{\text{ref}} = 0.0$ V vs SCE, at which no

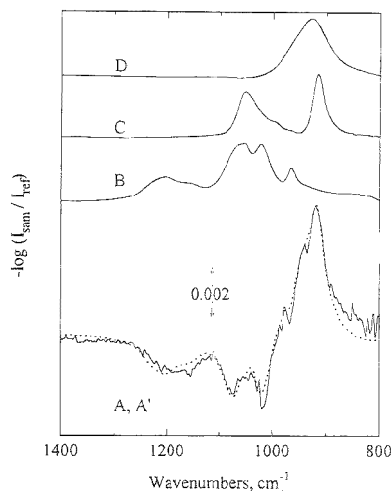


Figure 2. Curve A (solid line): Potential difference ATR-FT-IR spectrum for the reduction of bisulfite ion in an aqueous solution at pH = 5.25, obtained using the *sequential* method (see text for details) with $E_{\text{ref}} = 0.0$ V and $E_{\text{sam}} = -0.85$ V vs SCE. Flow rate, $V = 0.07$ mL/s. Curve B: Solution phase spectrum of a 2 M bisulfite ion solution ratioed against water. Curve C: Solution phase spectrum of a 0.5 M dithionite solution in 2 M bisulfite solution ratioed against a 2 M bisulfite solution. Curve D: Solution phase spectrum of a 0.5 M sulfite solution ratioed against water. Curve A' (dotted line) was obtained by a combination of spectral contributions due to bisulfite ($0.0073 \times$ curve B), dithionite ($0.011 \times$ curve C), and sulfite ($0.019 \times$ curve D) (see text for details).

reaction takes place, and at $E_{\text{sam}} = -0.85$ V vs SCE, at which the reduction of bisulfite proceeds at significant rates, for flow rates in the range 0.07 – 0.8 mL/s. The spectral collection was effected either by coadding 1000 interferometric scans *sequentially*, first at E_{sam} and then at E_{ref} , or by acquiring 10 scans alternately at E_{sam} and E_{ref} , with a 20 s time delay after each potential *switch* (by a step) to allow the concentration profile to achieve steady state. A total of 1000 scans were recorded at each potential, which were then coadded and stored in the computer for further processing. In both cases, the results are displayed in the form $-\log I_{\text{sam}}/I_{\text{ref}}$ vs wavenumber, where I_{sam} and I_{ref} represent single beam spectra obtained at the sampling E_{sam} and reference E_{ref} potentials, respectively.

ATR-FT-IR Spectra of Reference Materials. ATR-FT-IR spectra of 2 M NaHSO_3 (curve B, Figure 2) and 0.4 M Na_2SO_3 (curve C, Figure 2), ratioed against water, and 0.5 M $\text{Na}_2\text{S}_2\text{O}_4$ (sodium dithionite) in 2 M NaHSO_3 , ratioed against 2 M NaHSO_3 (curve D, Figure 2), were collected under stagnant conditions using an uncoated ZnSe crystal. These were used as references for the analysis of potential difference (PD) ATR-FT-IR spectra obtained *in situ*.

RESULTS AND DISCUSSION

Reduction of Bisulfite Ion in a Weakly Acidic, Unbuffered, Aqueous Electrolyte. A typical PD ATR-FT-IR spectrum for the reduction of a 2 M HSO_3^- , unbuffered, aqueous solution (pH = 5.25) on a gold electrode in a channel-type cell (flow rate, $V = 0.07$ mL/s), obtained using the *sequential* method ($E_{\text{ref}} = 0.0$ V

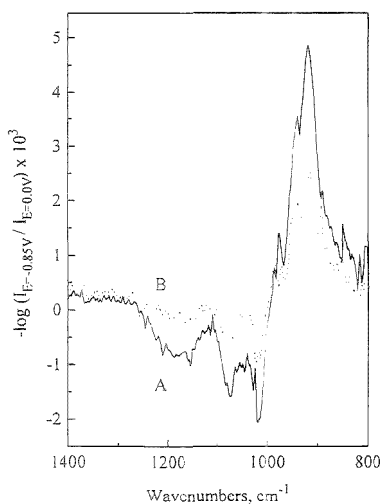


Figure 3. Comparison between PD-ATR-FT-IR spectra obtained in the *sequential* mode under the experimental conditions specified for curve A in Figure 2 for flow rates $V = 0.07$ (curve A) and 0.35 mL/s (curve B).

and $E_{\text{sam}} = -0.85$ V vs SCE), is shown in curve A (solid line) of Figure 2. As may be expected on the basis of hydrodynamic considerations, an increase in V gives rise to a decrease in the magnitude of the spectral features, as the differences in the solution composition become smaller with increased convection. This effect is illustrated in Figure 3, which compares spectra obtained for $V = 0.07$ (curve A) and 0.35 mL/s (curve B).

Only a slight improvement in signal-to-noise was observed for measurements performed using the *switching* instead of the *sequential* mode (not shown), indicating that effects due to long-term drifts are not very significant.

Spectral Assignment. The positions of the negative- and positive-pointing bands of typical PD ATR-FT-IR recorded in these experiments (see solid line, curve A, Figure 2) are in agreement with those of bisulfite and dithionite ($\text{S}_2\text{O}_4^{2-}$) shown in curves B and C in the same figure. This indicates that $\text{S}_2\text{O}_4^{2-}$ is one of the predominant products of the reduction of HSO_3^- on Au under the experimental conditions selected for these studies.

Careful inspection of these curves, however, revealed that the feature attributed to $\text{S}_2\text{O}_4^{2-}$ in the PD ATR-FT-IR spectra (918 cm^{-1}) is much broader than that of pure $\text{S}_2\text{O}_4^{2-}$ in the same medium (see curve C in this figure). The most likely explanation for this effect may be due to the presence of SO_3^{2-} , for which the spectrum shows a band centered at 927 cm^{-1} (see curve D in this figure). Sulfite can be generated via acid-base equilibrium due to an increase in pH derived from the reduction of HSO_3^- on the electrode surface in this unbuffered media. In fact, the experimental PD ATR-FT-IR spectrum (see curve A, Figure 2) could be successfully resolved in terms of the sum of negative-pointing bisulfite ($0.0073 \times$ curve B) and positive-pointing dithionite ($0.011 \times$ curve C) and sulfite ($0.019 \times$ curve D) contributions, to yield curve A' (dotted line) in this figure. Each of the numerical factors in parentheses can be multiplied by the specific concentration of the reference spectrum to obtain the *average* concentration

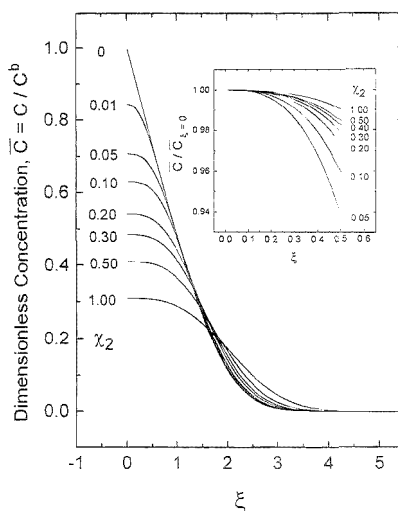


Figure 4. Plots of the dimensionless concentration of a product ($\bar{c} = c/c^b$), generated at the surface of an electrode in a channel under steady state, diffusion-limited conditions, as a function of the dimensionless distance normal to the plane of electrode ξ past the electrode surface. The values next to each of the curves represent dimensionless distances from the downstream edge of the electrode along the direction of fluid flow, χ_2 . The inset shows plots of the relative changes in the surface concentration of the product ($C/C_{\xi=0} = c/c_{\xi=0}$) as a function of the distance from the surface, over the range $0 < \xi < 0.5$, for different values of χ_2 .

of each of the species generated or consumed by the electrochemical reaction.

Theoretical Considerations. Considerable insight into a quantitative interpretation of PD ATR-FT-IR spectra of the type shown in curves A of Figures 2 and 3 can be gained on the basis of an analysis of the concentration profile past the electrode surface along x and y (see Figure 1). Figure 4 shows plots of the steady state, dimensionless concentration ($\bar{c}_0 = c/c^b$) profile of a product generated at the surface of an electrode under diffusion-limited conditions along a dimensionless axis normal to the electrode surface, $\xi = (3V/2ah^2D_0)^{1/2}y$, where c^b is the bulk concentration of the reactant, a the channel width, h the half-cell thickness (cm), and D_0 the diffusion coefficient of the product (cm^2/s). These curves were calculated by a numerical integration of the *standard* governing differential equation,⁶ for various values of the dimensionless variable $\chi_2 = x_2/l$, where x_2 is the actual distance along x measured from the downstream edge of the electrode. Except for $\chi_2 = 0$, the downstream electrode edge, the profile along ξ (or y) is characterized by a fairly flat region close to the channel surface ξ , i.e., $y = 0$, followed by a linear section, which decays exponentially into the bulk of the solution. A detailed inspection of the behavior close to the surface shows that for values of $x_2 > l/10$, the actual product concentration in the region $0 < \chi < 0.5$ differs by no more than 5% from its value on the surface (see inset in Figure 4). This observation is of much significance, as for reasonable values for the parameters involved, e.g., $h = 0.055$ cm, $a = 0.9$ cm, $D_0 = 5 \times 10^{-6} \text{ cm}^2/\text{s}$, $l = 0.5$ cm, and for flow rates in the range $V = 0.1$ – 1 mL/s, $\xi = 0.5$ corresponds to actual distances from 18 down to $8 \mu\text{m}$, and

therefore longer than the theoretical penetration depth of the IR radiation for the ZnSe/solution interface in the fingerprint region (3–5 μm). Since the concentration profile at a fixed χ_2 is invariant along the width of the electrode, the region probed by the FT-IR beam displays only χ_2 dependence.⁵ This is particularly convenient, as $c(\chi_2, \xi)$, the surface concentration of the product past the electrode surface under diffusion-limited conditions (see Figure 4 for $\xi = 0$), can be expressed in analytic form based on the integral formalism introduced originally by Lighthill.⁷

The application of chemometric techniques, such as those implemented by Bennett and co-workers⁸ for the rigorous analysis of ex situ ATR-FT-IR aqueous mixtures of sulfur–oxygen anions, may be expected to provide the necessary information to establish quantitatively reaction rates and mechanisms as a function of the applied potential for a wide variety of electrode processes. It should be pointed out that, despite the high concentration of bisulfite in the solution, the signals observed are relatively small.

(7) Lighthill, M. J. *Proc. R. Soc. London* **1950**, *A202*, 359.

(8) Helmar, D. A.; Thompson, A. W.; Bennett, D. W.; Otvos, J. D. *Anal. Chem.* **1994**, *66*, 1378.

This is due to the fact that under the conditions selected for these experiments, the current is well below its diffusion-limited value for the reduction of bisulfite, and therefore, the amount of product generated is rather small. Furthermore, the dimensions of the electrode and the cell used in these studies enable only one or two reflections at the IRE element/solution interface. Both of these factors should be carefully considered in the search of strategies for the further optimization of this type of channel cell in situ ATR-FT-IR experiments.

ACKNOWLEDGMENT

This work was supported by ARPA Grant No. N-000-14-92-J-1848. Valuable discussions with Prof. Bennett are gratefully acknowledged.

Received for review May 8, 1995. Accepted August 15, 1995.⁹

AC950436A

⁹ Abstract published in *Advance ACS Abstracts*, September 15, 1995.

Use of the Derivatizing Agent 4-Aminobenzoic Acid 2-(Diethylamino)ethyl Ester for High-Sensitivity Detection of Oligosaccharides by Electrospray Ionization Mass Spectrometry

Ken-ichi Yoshino,* Toshifumi Takao,* Hiroshi Murata, and Yasutsugu Shimonishi

Institute for Protein Research, Osaka University, Yamadaoka 3-2, Suita, Osaka 565, Japan

A method for the high-sensitivity detection of oligosaccharides by electrospray ionization mass spectrometry (ESI-MS) is reported. The method involves the chemical derivatization with 4-aminobenzoic acid 2-(diethylamino)ethyl ester (ABDEAE). This derivative, which contains a 2-(diethylamino)ethyl group, having a high proton affinity, enhances the ionization efficiency of analytes in the positive ESI mode. Experiments using maltohexaose as a model oligosaccharide revealed that derivatization with ABDEAE gave a remarkably large increase in molecular ion abundance. Using a mixture of acetonitrile, 2-methoxyethanol, 2-propanol, and water (1:1:1:1 v/v/v/v) as solvent for ESI, ABDEAE-derivatized maltohexaose could be detected at a level of 10 fmol. This represents a 5000-fold improvement in sensitivity over underivatized maltohexaose. ESI tandem mass spectrometry of the ABDEAE-derivatized maltohexaose provides structural information at the low-picomole level. In this spectrum, $1.5X'$ and $0.2A''$ series of sequence ions, arising from ring cleavage, were observed as the predominant ions.

It is widely known that the carbohydrate chains of glycoconjugates contribute significantly to the functional properties of glycoconjugates.^{1,2} As a result, one of the most challenging structural problems in cell biology and chemistry involves the structural determination of these groups. Several mass spectrometric techniques have proven to be useful analytical tools for the determination of oligosaccharide structure,^{3,4} all of which have the advantage over chemical or chromatographical methods in that they yield molecular mass information with relatively high sensitivity. Electrospray ionization mass spectrometry (ESI-MS) has been shown to be valuable in the structural characterization of carbohydrate chains of glycoconjugates.⁵⁻⁹ The poor ionization

efficiency of free carbohydrate chains in ESI, however, limits the utility of ESI-MS in structural carbohydrate studies. Attempts have been made to overcome these problems by improving the solvent system for ESI⁵ and by labeling oligosaccharides with chromophores or fluorophores, which were originally developed to improve sensitivity in high-performance liquid chromatography (HPLC).^{10,11}

In this study, we report a highly sensitive method for the detection of oligosaccharides by ESI-MS. The method involves chemical derivatization with 4-aminobenzoic acid 2-(diethylamino)ethyl ester (ABDEAE). The UV chromophore, a benzoyl group, not only permits sensitive detection by UV but also makes analytes amenable to separation on an octadecylsilica column by reversed-phase (RP)-HPLC.¹² The amino group is used for the covalent attachment of the compound to the reducing termini of oligosaccharides through reductive amination.¹³ The basic tail [a 2-(diethylamino)ethyl group] possesses a high proton affinity, which enhances the ionization efficiency of analytes in the positive ESI mode. The method has wide applicability and can be used in conjunction with any oligosaccharide which contains a reducing terminus.

EXPERIMENTAL SECTION

Chemicals. ABDEAE hydrochloride was purchased from Tokyo Chemical Industry (Tokyo, Japan). Sodium cyanoborohydride and 4-aminobenzoic acid ethyl ester (ABEE) were obtained from Sigma Chemical Co. (St. Louis, MO). A high-mannose-type N-linked oligosaccharide (Man₅GlcNAc₆), derived from ribonuclease B (RNase B), is a product of Oxford GlycoSystems (Abingdon, U.K.). Maltooligosaccharides were purchased from Nakano Vinegar (Handa, Japan). D-Glucose, maltohexaose, and other reagents of analytical grade are products of Nacalai Tesque (Kyoto, Japan).

Derivatization of Oligosaccharides. ABDEAE-derivatized oligosaccharides were prepared,¹⁴ with slight modifications, using the methodology reported for the preparation of the ABEE

Current address: Department of Infectious Diseases Research, National Children's Medical Research Center, Taishido 3-35-31, Setagaya-ku, Tokyo 154, Japan.

- (1) Radamacher, T. W.; Parekh, R. B.; Dwek, R. A. *Annu. Rev. Biochem.* **1988**, *57*, 785-838.
- (2) Cumming, D. A. *Glycobiology* **1991**, *1*, 115-130.
- (3) Dwek, R. A.; Edge, C. J.; Harvey, D. J.; Parekh, R. B. *Annu. Rev. Biochem.* **1993**, *62*, 65-100.
- (4) Burlingame, A. L.; Boyd, R. K.; Gaskell, S. J. *Anal. Chem.* **1994**, *66*, 634R-683R.
- (5) Duffin, K. L.; Welply, J. K.; Huang, E.; Henion, J. C. *Anal. Chem.* **1992**, *64*, 1440-1448.
- (6) Conboy, J. J.; Henion, J. D. *J. Am. Soc. Mass Spectrom.* **1992**, *3*, 804-814.
- (7) Huddleston, M. J.; Bean, M. F.; Carr, S. A. *Anal. Chem.* **1993**, *65*, 877-884.

- (8) Carr, S. A.; Huddleston, M. J.; Bean, M. F. *Protein Sci.* **1993**, *2*, 183-196.
- (9) Liu, J.; Volk, K. J.; Kerns, E. H.; Klotz, S. E.; Lee, M. S.; Rosenberg, I. E. *J. Chromatogr.* **1993**, *632*, 45-56.
- (10) Suzuki-Sawada, J.; Umeda, Y.; Kondo, A.; Kato, I. *Anal. Biochem.* **1992**, *207*, 203-207.
- (11) Gu, J.; Hiraga, T.; Wada, Y. *Biol. Mass Spectrom.* **1994**, *23*, 212-217.
- (12) Wang, W. T.; LeDonne, N. C., Jr.; Ackerman, B.; Sweeley, C. C. *Anal. Biochem.* **1984**, *141*, 366-381.
- (13) Hase, S.; Hara, S.; Matsushima, Y. *J. Biochem.* **1979**, *85*, 217-220.
- (14) Yoshino, K.; Takao, T.; Murata, H.; Shimonishi, Y. *Proceedings of the 42nd Annual ASMS Conference on Mass Spectrometry and Allied Topics*, Chicago, IL, May 29-June 4, 1994; p 932.

derivative.^{15,16} ABDEAE/HCl (1 μmol) dissolved in methanol (3.5 μL) was added to sodium cyanoborohydride (350 μg) in a 1.5 mL polypropylene microcentrifuge test tube (Treff AG, Degersheim, Switzerland). Glacial acetic acid (0.4 μL) was then added to the solution to form the reagent mixture. The reagent mixture (4 μL) was added to the solution of an oligosaccharide (1 nmol) in water (4 μL) in another Treff microcentrifuge test tube, and the total volume of the reaction mixture was then made up to 20 μL with methanol. The reaction tube was vortexed and heated at 80 $^{\circ}\text{C}$. After 60 min, the reaction tube was cooled, and distilled water (100 μL) was added. The resulting derivative was immediately separated from excess reagent by RP-HPLC (see below). ABEE maltohexaose was prepared according to previously described methods.^{15,16}

Purification of ABDEAE-Derivatized Oligosaccharides. ABDEAE-derivatized oligosaccharides were separated and desalted by RP-HPLC using a Waters Model 600E multisolvent delivery system (Milford, MA). The reaction mixture was applied to a column (10 mm i.d. \times 250 mm) packed with octadecylsilica having a particle diameter of 5 μm and a pore size of 12 nm (Cosmosil 5C₁₈-AR, Nacalai Tesque), which had been equilibrated with 5% acetonitrile in 0.1% trifluoroacetic acid (TFA). The reaction product was eluted using a linear gradient of acetonitrile (5–20% in 30 min) at a flow rate of 2.0 mL/min. The column effluent absorbance was monitored at 310 nm using a Waters Model 486 tunable absorbance detector. The collected ABDEAE-derivatized oligosaccharides were then lyophilized prior to examination by ESI-MS.

Electrospray Ionization Mass Spectrometry. Positive-ion ESI mass spectra were obtained in a JMS-HX/HX110A four-sector tandem mass spectrometer (JEOL, Tokyo, Japan) equipped with an ESI ion source (Analytica of Branford, Branford, CT), a collision cell, and a photodiode-based array detector. The ions accelerated at 7 kV were detected on a secondary electron multiplier operated at -1.9 kV behind the first mass spectrometer. The mass spectra were acquired with a mass resolution of 1000 in the range of m/z 300–2500 by scanning a magnetic field in 10.6 s. Mass calibration was performed using a mixture of KI and CsI (1:2 w/w) in positive-ion fast atom bombardment (FAB) mode prior to installing the ESI ion source. Solutions of the ABDEAE derivatives (10–400 fmol/ μL for MS and 1–100 pmol/ μL for MS/MS), ABEE derivative (5 pmol/ μL), and free maltohexaose (50 pmol/ μL) were infused into the ESI source with a Harvard syringe pump (Harvard Apparatus, MA) at a flow rate of 1.0 $\mu\text{L}/\text{min}$. Heated nitrogen at 120 $^{\circ}\text{C}$ was used as a drying gas and introduced into the capillary region at a flow rate of 25 L/min. All other procedures were carried out using methodology reported previously.¹⁷

Positive-ion ESI tandem mass (ESI-MS/MS) spectra were obtained from singly charged ions generated in the ESI source. The precursor ion accelerated at 7 kV was selected with a mass-resolving power by the first mass spectrometer such that only the monoisotopic ion was transmitted into the collision cell operated at 5.6 kV potential. The amount of argon collision gas introduced into the cell was adjusted to reduce the intensity of the precursor ions by half. At this point, the MS/MS product

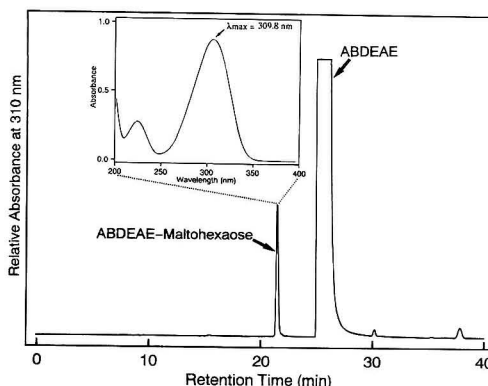


Figure 1. Separation of ABDEAE-derivatized maltohexaose by RP-HPLC. See text for chromatographic conditions. The UV absorption spectrum of the ABDEAE-derivatized maltohexaose is shown in the inset. A spectrum of the analyte solution (42.9 μM in 10% acetonitrile containing 0.1% TFA) was obtained in the range of 200–400 nm at a scan rate of 60 nm/min, using a Hitachi Model U-3400 spectrophotometer (Tokyo, Japan).

ion spectra were acquired on a photodiode-based array detector with 10% mass dispersion by stepping up the electric and magnetic fields on the second mass spectrometer, where the magnetic field was calibrated at 7 kV potential by using 20% acetonitrile solution containing LiI, NaI, KI, and CsI (1.5:4.5:0.01:1.0 mol/mol/mol/mol).

RESULTS AND DISCUSSION

Separation of ABDEAE Derivatives by RP-HPLC. ABDEAE-derivatized maltohexaose was successfully desalted and separated from the excess reagent by RP-HPLC (Figure 1). The yield of the ABDEAE maltohexaose obtained from this procedure was measured by integrating the peak observed during the RP-HPLC against an external standard and was found to be \sim 70%. Maltooligosaccharides of 2–15 degrees of polymerization (DP) were derivatized with ABDEAE using the same procedure. The retention times of ABDEAE-derivatized maltooligosaccharides in the RP-HPLC increased with a decrease in the DP value (data not shown). However, even in the case of monosaccharide, ABDEAE-derivatized glucose was eluted in \sim 1 min before elution of the excess reagent and could be purified from the reaction mixture by RP-HPLC (data not shown). The UV absorption spectrum of the ABDEAE-derivatized maltohexaose is shown in the inset of Figure 1. The derivative exhibits a characteristic absorption band (B band) with λ_{max} at 309.8 nm, which arises from the conjugation between the carbonyl group and the aromatic ring. The molar absorptivity was determined to be 20 210. These data show that monitoring at 310 nm allows the highest sensitivity for detection of ABDEAE derivatives.

Detection Limit in Positive-Ion ESI-MS. The sensitivity of the technique was tested by comparing underivatized and ABEE maltohexaose with the corresponding ABDEAE derivative (Figure 2). After various solvent systems were tested for ESI, a solvent composed of 10 mM ammonium acetate (pH 5.7) in 30% methanol^F was selected for positive-ion ESI mass measurement of underivatized oligosaccharide. Using a 50 pmol sample of underivatized maltohexaose (Figure 2a), the analyte signal at m/z 1008.4

(15) Webb, J. W.; Jiang, K.; Gillette-Castro, B. L.; Tarentino, A. L.; Plummer, T. H.; Byrd, J. C.; Fisher, S. J.; Burlingame A. L. *Anal. Biochem.* **1988**, *169*, 337–349.

(16) Poulter, L.; Karrer, R.; Burlingame, A. L. *Anal. Biochem.* **1991**, *195*, 1–13.

(17) Murata, H.; Takao, T.; Shimomishi, Y. *Rapid Commun. Mass Spectrom.* **1994**, *8*, 205–210.

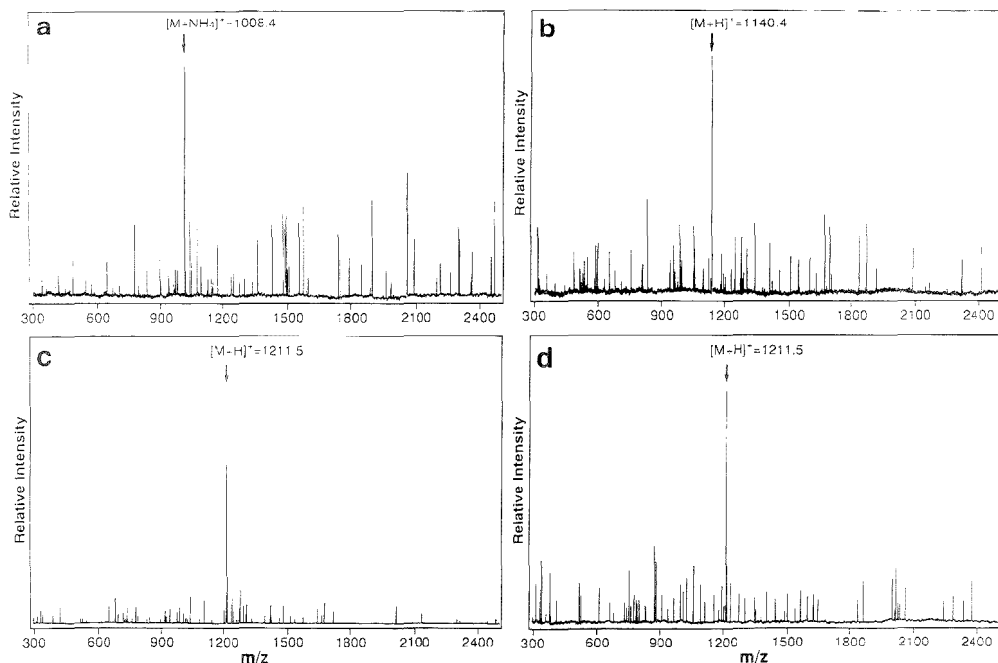


Figure 2. Positive-ion ESI mass spectra of free maltohexaose (50 pmol) (a), ABEE-derivatized maltohexaose (5 pmol) (b), ABDEAE-derivatized maltohexaose (100 fmol) (c), and ABDEAE-derivatized maltohexaose (10 fmol) (d). Each spectrum was obtained by accumulating five scans.

(corresponding to the $[M + \text{NH}_4]^+$ ion) is only slightly larger than the background. As the sample quantity was further reduced, the signal-to-background ratio decreased, and eventually the molecular ion signal became indistinguishable from the background. The ABEE derivative, which has been reported to give sensitivity in the subpicomole level on FAB ionization of oligosaccharides,¹⁶ showed a signal-to-background ratio similar to that in Figure 2a with a 5 pmol sample (Figure 2b). On the other hand, the ABDEAE derivative, which has an additional basic tail [a 2-(diethylamino)ethyl group], gave a molecular ion signal at m/z 1211.5 with a good signal-to-background ratio when a 100 fmol sample was used (Figure 2c). The solvent system, a mixture of acetonitrile, 2-methoxyethanol, 2-propanol, and water (1:1:1:1 v/v/v/v), provides the highest signal-to-background ratio and ionization efficiency in positive-ion ESI-MS of the ABDEAE derivatives compared to the other solvent systems, such as a mixture of methanol, water, and acetic acid (49:49:2) and a solvent of 10 mM ammonium acetate (pH 5.7) in 30% methanol. The signal-to-background ratio in the spectrum was clearly improved in comparison to that of the underivatized or ABEE maltohexaose, which required 500 or 50 times the amounts of sample, respectively. Decreasing the sample size to 10 fmol still allowed recognition of the protonated molecular ion (Figure 2d), in which the signal-to-background ratio is similar to those for underivatized and ABEE maltohexaose (Figure 2a,b). This represents an improvement in sensitivity of more than 5000- or 500-fold over those of underivatized and ABEE maltohexaose, respectively. As a further test of the efficiency of this derivatizing procedure for enhancing signal intensity in positive-ion ESI-MS, an N-linked

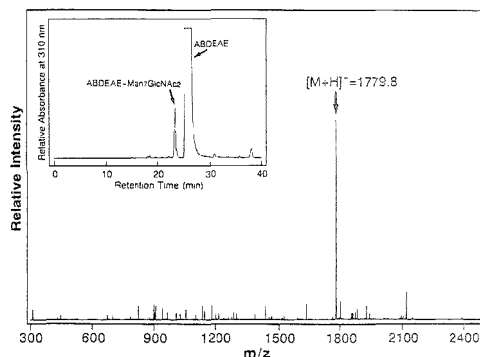


Figure 3. Positive-ion ESI mass spectrum acquired with 400 fmol of an ABDEAE-derivatized high-mannose-type oligosaccharide. The spectrum was obtained by accumulating five scans. The RP-HPLC profile during the purification is shown in the inset.

oligosaccharide (Man₇GlcNAc₂) derived from RNase B was derivatized and analyzed (Figure 3). The positive-ion ESI mass spectrum obtained using a 400 fmol sample of the ABDEAE derivative showed a major ion signal at m/z 1779.8 ($[M + H]^+$) with a signal-to-background ratio that was almost comparable to that of the spectrum obtained with 100 fmol of the maltohexaose derivative (Figure 2c).

Positive-Ion ESI-MS/MS. The left spectrum in Figure 4 shows the ESI-MS/MS spectrum of the singly charged precursor ion obtained using a 200 pmol sample of the ABDEAE-

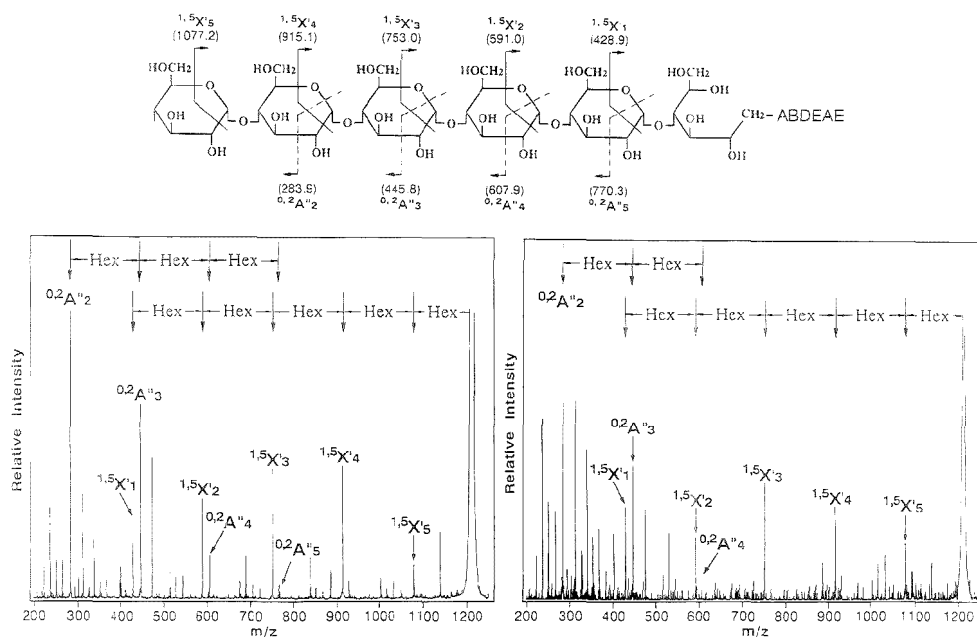


Figure 4. Positive-ion ESI-MS/MS spectra of the ABDEAE-derivatized maltohexaose (left, 100 pmol/L; right, 1 pmol/L). About 2 (left) and 4 (right) min was required to obtain whole MS/MS spectra ranging from m/z 200 to 1250, both of which are constructed with 23 segments of spectra. The nomenclature of product ions used is that of Domon and Costello.¹⁹ Hex denotes hexose.

derivatized maltohexaose. It predominantly provided $1,5X'$ and $0,2A''$ series of product ions, which correspond to the reducing and nonreducing terminal product ions that arise from ring cleavage, respectively. To further examine the detection limit of ABDEAE-derivatized oligosaccharide, the ESI-MS/MS spectrum was acquired with 4 pmol of ABDEAE-derivatized maltohexaose (Figure 4, right). The spectrum also gave both $1,5X'$ and $0,2A''$ series of product ions, which are sufficient to confirm the structure, indicating that ESI-MS/MS of ABDEAE-derivatized oligosaccharides provides structural information at the low-picomole level.

The data presented in this paper illustrate the high sensitivity of ABDEAE-derivatized oligosaccharides in ESI-MS. Recently, Gu et al.¹¹ reported the sensitivity of oligosaccharides derivatized with 2-aminopyridine in ESI-MS to be in the order of 1 pmol. The sensitivity of the ABDEAE-derivatized analyte in the order of 10 fmol could be realized with signal-to-background ratio of 3:1 (Figure 2d), which is nearly comparable to the detection limit of oligosaccharides labeled with fluorophore in HPLC analysis.¹⁸ This represents an improvement in sensitivity of at least 100-fold over the 2-aminopyridine derivative in ESI-MS. The sensitivity attained

by the ABDEAE derivatization method in the positive ESI mode can be attributed to the high proton affinity of the 2-(diethylamino)-ethyl group, based on structural comparison of ABDEAE maltohexaose to the ABEE derivative (Figure 2b,d, respectively), of which the hydrophobic characteristics are preferred for FAB ionization.¹⁶ The higher sensitivity would clearly be an advantage for structural characterization of oligosaccharides such as those derived from biologically important glycoproteins, which are often available only in limited quantities. Although HPLC of the derivative is required in order to assess its utility for carbohydrate mapping, the present method, combined with a capillary LC/ESI-MS, represents a powerful technique for sensitive and accurate analysis of carbohydrates.

ACKNOWLEDGMENT

This work was supported in part by Grants-in-Aid for Encouragement of Young Scientists [Nos. 04-2210 (K.Y.) and 05780438 (T.T.)] and for Scientific Research [No. 06680584 (T.T.)] from the Ministry of Education, Science and Culture of Japan.

Received for review March 13, 1995. Accepted August 2, 1995.*

AC950250B

* Abstract published in *Advance ACS Abstracts*, September 1, 1995.

(18) Hase, S. *Methods in Protein Sequence Analysis*; Plenum Press: New York, 1983; pp 195-198.

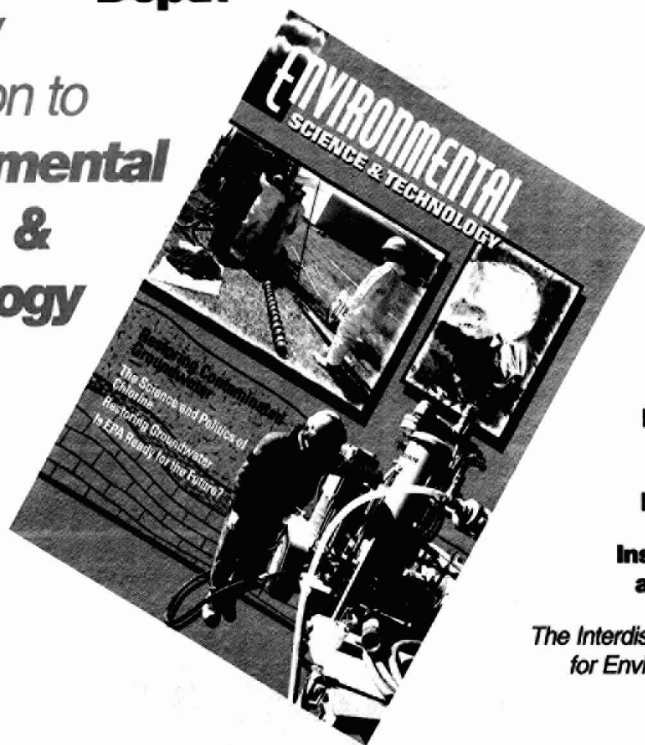
(19) Domon, B.; Costello, C. E. *Glycoconjugate J.* **1988**, *5*, 397-409.

Author Index

- Abruña, H. D., 3936
Achterberg, E. P., 3903
Annapragada, A., 3871
Armstrong, R. D., 3928
Athey, D., 3928
- Bae, I. T., 4024
Ball, M., 3928
Barbour, R., 4024
Barman, B. N., 3861
Beussman, D. J., 3925
Boon, J. J., 3965
Brown, R. S., 3990
- Carlson, R. E., 3829
Carr, P. W., 3886
Chen, M.-C., 4010
Chiu, Y.-W., 3829
Choi, M. F., 3897
- Dang-Vu, B., 4000
Dasgupta, P. K., 3853
de Koster, C. G., 3965
Dennison, M. J., 3922
Dugay, A., 4000
- Enke, C. G., 3952
- Fairbank, R. W. P., 3879
Fanali, S., 3866
Faruque, A., 3846
Fiorentino, M. A., 4004
Fitzloff, J. F., 3985
Fong, H. H. S., 3985
Fu Lu, M. Y., 3871
- Giddings, J. C., 3861
Grate, J. W., 4015
Guyon, F., 4000
- Hall, J. M., 3922
Hawkins, P., 3897
Heeren, R. M. A., 3965
- Heinze, J., 4020
Ho, W. O., 3928
Huang, C.-R., 3985
Huang, H.-J., 4010
- John, C. M., 3871
- Kar, S., 3853
Karu, A. E., 3829
Kenndler, E., 3866
Ketterer, M. E., 4004
Krause, S., 3928
Kromann, P. R., 3846
Kumke, M. U., 3945
- Lavine, B. K., 3846
Leckie, J. O., 3893
Lee, M. L., 3840
Lennon, J. J., 3990
Li, G., 3945
Linn, C. P., 3945
Liu, Z., 3840
Lorenzo, E., 3936
Lu, Z.-Z., 3985
Luque de Castro, M. D., 3916
- Marcus, K. L., 3829
Marshall, A. G., 3979
Martin, S. A., 3971
Martin, T. D., 3903
Marto, J. A., 3979
Mayfield, H., 3846
McGill, R. A., 4015
McGown, L. B., 3945
McLane, R. D., 3952
McNeff, C., 3886
McNeil, C. J., 3928
Moreau, J. C., 4000
Murata, H., 4028
- Odom, R. W., 3871
Olieman, C., 3911
Ong, C. G., 3893
- Papaefstathiou, I., 3916
Pariante, F., 3936
Patterson, D. G., Jr., 3840
Patterson, D. H., 3971
Prasad, A., 3893
- Rawson, K., 3928
Regnier, F. E., 3971
Rimando, A., 3985
Rizzi, A., 3866
- Salvati, L., 3871
Scherson, D. A., 4024
Schützner, W., 3866
Seeterlin, M. A., 3952
Seldomridge, S., 3979
Shimonishi, Y., 4028
- Takao, T., 4028
Tarr, G. E., 3971
Tobalina, F., 3936
Tolmachev, Y. V., 4024
Tschuncky, P., 4020
Turner, A. P. F., 3922
- Van Berkel, G. J., 3958
van Breemen, R. B., 3985
van den Berg, C. M. G., 3903
van Elteren, J. T., 3903
van Riel, J. A. M., 3911
Vlasak, P. R., 3952
- Walker, G. T., 3945
Wang, Z., 4024
White, F. M., 3979
Wirth, M. J., 3879
Wright, J. D., 3928
- Xiang, Y., 3879
- Yoshino, K., 4028
- Zhang, H., 3903
Zhou, F., 3958

Focus
Insight
Depth

The New
Dimension to
Environmental
Science &
Technology



New Editorial Mix
Expanded News
Research Articles

Insights into Trends
and Controversies

The Interdisciplinary Publication
for Environmental Scientists
and Professionals

Our expanded editorial coverage provides a balance of focus, insight, and depth in topics ranging from remediation and air quality to regulations and public policy. Two new departments, "Research Watch" and "EPA Watch," highlight current activities emerging at these two ends of the spectrum.

Critical analysis of policy, worldwide news, innovations in measurement, research articles by well-known authorities — all of these features offer you a broader base of knowledge than ever before. And, our new cover and interior design spotlight information so you'll know exactly where to look for new developments in areas that are beginning to affect your work.

In addition to the cutting-edge research for which this publication is highly acclaimed, the new editorial mix includes in-depth feature articles covering the areas that drive the environmental field: Science, technology, government, and society.

While many other environmental publications are devoted to one discipline or another, no other journal completely integrates all disciplines of the environmental field.

Experience the new *Environmental Science & Technology*.
Subscribe today!

To order your one-year subscription right away call toll-free, 1-800-333-9511 (U.S. only). Outside the U.S. call 614-447-3776. Fax to 614-447-3671.

Editor

William H. Glaze
University of North Carolina, Chapel Hill

Associate Editors

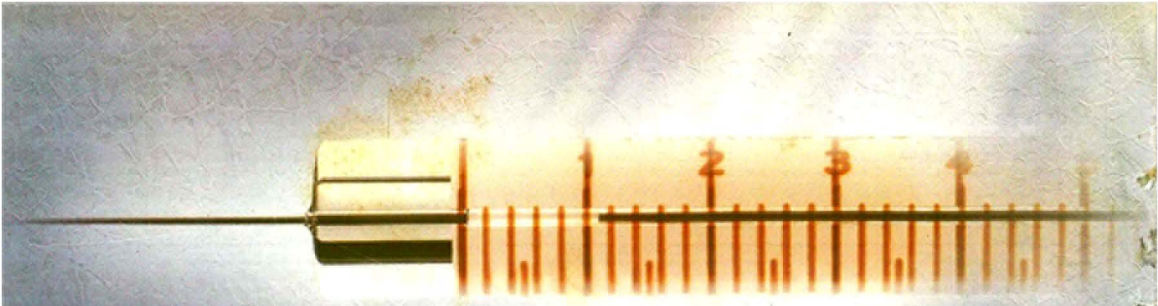
Walter Giger
EAWAG, Switzerland
Ronald A. Hites
Indiana University at Bloomington
Cass T. Miller
University of North Carolina, Chapel Hill
Jerald L. Schnoor
University of Iowa
John Seinfeld
California Institute of Technology
Joseph M. Sufita
University of Oklahoma

1995 Subscription Rates

	U.S.	Canada & Mexico	Europe*	All Other Countries*
Member	\$44	\$68	\$96	\$113
Nonmember Personal	\$90	\$114	\$142	\$159
Nonmember Institutional	\$585	\$609	\$637	\$654

*Includes air service.

ACS  PUBLICATIONS
Essential Resources for the Chemical Sciences



For Those Who Can't Always
Read Between The Lines.
We Have Your Syringe.

• Accuracy and precision,
depending on syringe series, is better
than $\pm 0.5\%$

• Plunger Drag easily adjusts
to your preference



• Large Digital Display allows
easy-to-read selection
of syringe volumes

• Digital Syringes come with their own
Certificate of Calibration based on
N.I.S.T. traceable methods

• Fine Adjustment Thumbwheel
provides ease in setting
syringe volumes

• Plunger Stop can be set for repetitive,
precise injections

The New Digital SyringeSM

HAMILTON
The Measure Of ExcellenceSM

Hamilton Company, 4970 Energy Way, Reno, Nevada 89502-4178 U.S.A.
Tel: (800) 648-5950, +1-702-858-3000 Fax: +1-702-856-7259

CIRCLE 7 ON READER SERVICE CARD

7 4 70-11 2538
D.C.M. 38